VALIDATED NUMERICAL MODELLING OF THE STRUCTURAL RESPONSE OF A SUPER-HIGH CONCRETE ARCH DAM DURING IMPOUNDMENT

R.O. CASSELLS

VALIDATED NUMERICAL MODELLING OF THE STRUCTURAL RESPONSE OF A SUPER-HIGH CONCRETE ARCH DAM DURING IMPOUNDMENT

RYAN OLIVER CASSELLS

A dissertation submitted in partial fulfilment of the requirements for the degree of

MASTER OF ENGINEERING (STRUCTURAL ENGINEERING)

in the

FACULTY OF ENGINEERING, BUILT-ENVIRONMENT AND INFORMATION TECHNOLOGY

University of Pretoria

March 2025

DISSERTATION SUMMARY

VALIDATED NUMERICAL MODELLING OF THE STRUCTURAL RESPONSE OF A SUPER-HIGH CONCRETE ARCH DAM DURING IMPOUNDMENT

R.O. CASSELLS

Supervisors: Professor S.W. Jacobsz and Professor C.P. Roth
Department: Civil Engineering
University: University of Pretoria
Degree: Master of Engineering (Structural Engineering)

Concrete arch dams are complex three-dimensional structures subject to multifaceted loading conditions. Design of concrete arch dams follow an iterative structural analysis approach; whereby advanced numerical modelling has become the current state-of-the-art tool for analysis. Advancement in the processing power of the personal computer and commercial availability of user friendly and efficient numerical modelling software packages, has enabled the development of high-resolution numerical models of arch dams with complex foundations.

The finite element method can be used to create elaborate three-dimensional models of concrete arch dams with complex foundation conditions. The models are however only as reliable as the that of the modelling assumption inputs, particularly the constitutive modelling parameters. Material testing procedures of the dam concrete and foundation conditions provide a good estimate of the modelling constitutive parameters, but the inherent variance in these test results and the difference in conditions between site and laboratory, mean these parameters may not necessarily accurately reflect those present under dam operating conditions.

As a result, it is important to validate the assumed parameters of the finite element model by calibrating its deformation response under actual loading conditions. This dissertation looks at the validation of a finite element model of the Yusufeli arch dam during reservoir impoundment, by calibrating the computed static deformation response of the model to that observed of the dam from deformation measurement instrumentation. Results from the finite element model calibration process are discussed and presented, providing insight into the sensitivity of the dam behaviour to variations in different loading and modelling parameters.

ABSTRACT

Title:	Validated Numerical Modelling of the Structural Response of a Super-High Concrete Arch Dam During impoundment
Author:	R.O. Cassells
Supervisor:	Professor S.W. Jacobsz and Professor C.P. Roth
Department:	Civil Engineering
University:	University of Pretoria
Degree:	Master of Engineering (Structural Engineering)

(may not exceed 150 words).

Concrete arch dams are complex three-dimensional structures, the design of which requires an iterative structural analysis approach to ensure the most efficient arch is adopted for site conditions. Due to a significant increase in computing capacity over the past two decades and economic viability of user-friendly numerical modelling software packages, advanced numerical modelling has become the current state-of-the-art tool for concrete arch dam design.

Structural analysis of concrete arch dams using finite element modelling, can provide valuable insight into dam function and behaviour for evaluation against design criteria and probable failure modes. Finite element analysis results, are however, only as reliable as the model input assumptions and material parameters of the dam.

Considering this, it is critical to validate assumed finite element modelling parameters, by calibrating the modelled behaviour according to the actual measured behaviour of the dam under loading. This dissertation investigates the derivation of a calibrated finite element model of a super-high concrete arch founded on complex foundations, from which various behavioural and sensitivity analyses outcomes are formulated.

DECLARATION

I, the undersigned hereby declare that:

I understand what plagiarism is and I am aware of the University's policy in this regard;

The work contained in this project report is my own original work;

I did not refer to work of current or previous students, lecture notes, handbooks or any other study material without proper referencing;

I have not allowed anyone to copy any part of my project report;

I have not previously in its entirety or in part submitted this project report at any university for a degree.

Disclaimer:

The work presented in this report is that of the student alone. Students were encouraged to take ownership of their projects and to develop and execute their experiments with limited guidance and assistance. The content of the research does not necessarily represent the views of the supervisor or any staff member of the University of Pretoria, Department of Civil Engineering. The supervisor did not read or edit the final report and is not responsible for any technical inaccuracies, statements or errors. The conclusions and recommendations given in the report are also not necessarily that of the supervisor, sponsors or companies involved in the research.

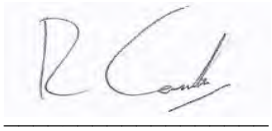

Ryan Oliver Cassells

25255216

17 March 2025

Number of words: 90 000

ACKNOWLEDGEMENT

The successful completion of this thesis would not have been possible without the support and guidance from various other persons. Appreciation is extended to the following:

a) The support and guidance given to me by my supervisors Prof Jacobsz and Prof Roth and their valuable feedback.

b) My wife Mandy Cassells for providing motivational support and for putting up with the time sacrifices this work imposed on our marriage.

c) My parents Neill and Marianne Cassells, my brother Paul Cassells, my extended family and friends for loving me and accepting me as I am.

d) My mentor Dr Quentin Shaw for the expertise, knowledge and professional guidance he has always provided in my workplace.

e) My colleague and friend Graham Roberts for always pushing me to extend my theoretical knowledge in the structural dam engineering field.

f) ARQ Dams, with special mention of Michelle Blaeser and Henry-John Wright, for sponsoring my post-graduate studies and creating a platform for me to advance my knowledge in dam engineering.

g) Mr Alan Chemaly and Mr Louis Hattingh for always being willing to impart their valuable experience and knowledge to me.

h) Dinçer Aydoğan from the DSi (Turkish State Hydraulic Works) and Fatih Çevik from Limak for granting me permission to publish literature on Yusufeli Dam.

i) Jesus Christ my Lord and Saviour for giving me insight and strength to fulfil this work and for having a calling on my life.

TABLE OF CONTENTS

LIST OF TABLES

PAGE

LIST OF FIGURES

PAGE

LIST OF SYMBOLS AND INITIALISMS

Symbol	Description	Units
FEA	Finite Element Analysis	
ICOLD	International Commission of Large Dams	
APP	Approved Professional Person	
AVM	Ambient Vibration Monitoring	
f_c	characteristic compressive strength of concrete	MPa
BC	Before Christ	
AD	Anno Domini	
USACE	United Army Corps of Engineers	
USBR	United States Bureau of Reclamation	
FERC	Federal Energy Regulatory Commission	
SANCOLD	South African National Committee of Large Dams	
ANCOLD	Australian National Committee of Large Dams	
CVC	Conventionally Vibrated Concrete	
RCC	Roller Compacted Concrete	
RMC	Roller Masonry Concrete	
CL:H	Crest Length to Height Ratio	
BW:H	Base Width to Height Ratio	
ASCE	American Society of Civil Engineers	
α	angle of incidence	°
R	resulting thrust force	MN
t/T	arch thickness	m
σ	maximum allowable stress	MPa
p/P	hydrostatic pressure	kPa
θ	arch central angle	°
B	river valley span	m
V	arch volume	m^3
A	cross section area of arch/element	m^2
H	height of dam	m
L_1	span of dam at crest	m
L_2	span of dam 0.15H above riverbed	m
T_C	arch crest width	m
T_B	arch base width	m
USP	Upstream projection	m
DSP	Downstream projection	m

Δ	extrados centre point	
O	intrados centre point	
FSL	Full Supply Level	mASL
RDF	Recommended Design Flood	mASL
PMF	Probable Maximum Flood	mASL
SEF	Safety Evaluation Flood	mASL
MOL	Minimum operating Level	mASL
NWL	Normal Water Level	mASL
TWL	Tail Water Level	mASL
T_1	concrete placement temperature	° C
T_2	maximum concrete temperature state	° C
T_3	zero-stress concrete temperature state	° C
T_4	equilibrium temperature state	° C
$T_{4minimum}$	winter equilibrium temperature state	° C
$T_{4maximum}$	summer equilibrium temperature state	° C
PGA	Peak Ground Acceleration	g
PSHA	Probabilistic Seismic Hazard Assessment	
f_{cu}	static compressive strength from cube test	MPa
f_t	allowable tensile strength of concrete	MPa
FOS	Factor of Safety	
f'_c	static compressive strength from cylinder test	MPa
f'_{cd}	dynamic compressive strength of concrete	MPa
f'_t	static tensile strength of concrete	MPa
f'_{td}	dynamic tensile strength of concrete	MPa
RMR	rock mass rating	
UCS	unconfined compressive strength	MPa
RQD	rock quality designation	
E	elastic modulus	GPa
E_c	Elastic modulus of dam	GPa
E_f	Elastic modulus of foundation	GPa
R_u	Arch radius	m
F	force	kN
K	stiffness	kN/m
U	displacement	m
[B]	strain displacement matrix	m/m
[D]	stress-strain matrix (constitutive matrix)	

[J]	Jacobian matrix
[N]	Shape function matrix
LU	lower upper factorisation
LDL^T	Lower diagonal lower-transpose
CPU	Central Processing Unit
GPU	Graphics Processing Unit

1 INTRODUCTION

This study aims to investigate how well the structural behaviour of a super-high concrete arch dam, built on a complex rock mass foundation, can be modelled using the Finite Element (FE) Method, assuming a linear elastic stress-strain relationship of the dam body and foundation material, with non-linear material behaviour at the dam-foundation interface and at the dam expansion joints, provided for through the inclusion of interface elements.

In this chapter the author briefly describes the background of the problem and defines the study objectives, scope, methodology and organisation of the study.

1.1 BACKGROUND

Concrete arch dams are complex hyperstatic civil engineering structures, for which the analysis and design require the application of complex mathematical or numerical methods, needing lengthy solver techniques. The large number of structural redundancies implicit in concrete arch dams and the different structural mechanisms that form in a loaded concrete arch dam are reason for this.

The design of an arch dam does not have a closed form solution and is an exercise that requires an iterative “trial and error” approach. There are many factors to consider when designing an arch dam, of which will be outlined later in this study. The final stages of the design comprise selection of an arch configuration and subsequent structural analysis for evaluation of deflection and stress/strain development against design criteria.

In the early days of arch dam design, the structural analysis was simplified by discretising the arch configuration into a series of arches and cantilevers. Numerous simultaneous equations were derived for these arches and cantilevers using elemental structural mechanics (elastic arch and beam theory). The large number of simultaneous equations were solved iteratively, until the superimposed deflections of the arches and cantilevers converged to a common value. This is referred to as the trial-load method (ICOLD, 1988). Before electronic computers were available, the iterative calculations of the trial-load method were done by hand. The lengthy time required to undertake these protracted computations, was later shortened through the use of the early electronic computer. Other more simplistic approaches for analysis and design of arch dams are the membrane theory method or cylinder formula method.

The advent of the personal computer and more recent exponential rise in processing power of personal computers, has resulted in the common use of computer aided numerical analysis techniques for arch dam design. Computer aided numerical analysis is not a new technology

and has been used in the academic realm and research field for many years. Numerical analysis software packages are however becoming more user friendly, powerful and accessible for the practicing civil engineer.

Despite this, numerical analysis software is merely a tool to assist the engineer in making design decisions for which experience, and a good level of judgement should come into play. Even the most advanced numerical analysis software cannot replace the problem-solving ability of experienced engineers, nor should the results they produce always be trusted blindly. The key advantage of FE analysis of dams lies in their realistic demonstration of the actual structural function of an arch dam (Shaw, 2015).

The analysis results produced by such numerical analysis software, should be tested by verification and validation against basic first principle-based calculations. This is especially relevant for the design of large concrete arch dams. The wide range of height in concrete arch dams constructed to date varies from 10 m to 300 m. This means that the typical deflection behaviour or stress that can be expected to develop in such structure, can vary by order of magnitude from one dam to the next.

Failure of any large dam is a disastrous event leading to the potential major loss of human lives, large scale economic loss, damage to valuable property and the local environment. To increase dam safety, various legislation and design guidelines stipulate the requirement for ongoing assessment of dams post-construction. According to ICOLD (2001) dams need to be continually inspected for safety. In South Africa, dam safety evaluations are to be conducted by an APP (Approved Professional Person) at regular specified time intervals, depending on dam category classification (National Water Act, 1998).

The behaviour of dams during operation, is often monitored by instrumentation installed within the dam structure and surrounding foundation. The data provided by dam instrumentation, allows for the dam to be constantly monitored for any signs of distress or unwanted behaviour, not accounted for during design. Data provided by dam instrumentation, provides invaluable information of the state of the dam for the engineer undertaking a dam safety evaluation to study. Dams are subject to changing conditions which may not have been reasonably foreseen at design stage.

Due to the nature of concrete arch dam construction, instrumentation is normally installed in the dam and foundation during construction, at various completion stages. This allows for the monitoring of the dam to commence during construction, and continue through impoundment and perpetually during operation of the dam after impoundment.

Modal analysis of concrete arch dams by way of Ambient Vibration Monitoring (AVM), may be used to obtain structural behaviour or characteristics of an existing dam, that has insufficient instrumentation data for surveillance purposes (Hattingh *et al.*, 2019). Changes in conditions or structural characteristics of concrete arch dams since initial design and construction, may be detected from the change in modal parameters and associated dam stiffness. This may indicate changes in foundation conditions or possible structural cracking/deterioration in concrete durability/strength.

Thermally induced (thermo-mechanical) loading is a critical load case for large concrete dams. Thermo-mechanical loading is caused by thermal gradients that develop within the dam body, during construction and operational phases of the dam.

During construction of the dam, the placement of massive volumes of concrete results in the generation of hydration heat energy and the containment of large temperature increases, within the core of the dam. After concrete placement, hydration heat generated in the dam quickly dissipates at the outer shell of the dam by convection into the cool atmosphere. Large thermal gradients develop in the dam body between the cool shell and the heated core. A local restraint develops between the expanding core and shrinking shell, which induces tensile stresses in the shell and may cause surface gradient cracking to occur.

After an extended period, post-construction of the dam, the heat of hydration energy fully dissipates, and the dam reaches thermal equilibrium in terms of hydration heat energy. At this point, a thermal gradient develops between the cooled core and the shell of the dam. Stresses caused by this state may cause mass gradient cracking of the dam body, as thermal shrinkage of the cooled core is restrained by the outer shell and foundation of the dam. Various instrumentation is installed in arch dams, to monitor temperatures as well as movement and stresses in the dam, during construction and operation of the dam.

After construction of the dam is complete, the most critical stage pertaining to dam behaviour monitoring is during impoundment of the water reservoir, as the new loads applied by the presence of the reservoir may induce transient stress-strain behaviour (Lombardi *et al.*, 2008).

Many engineering accidents occur during the initial impoundment period of the dam, so it is important to analyse the working behaviour of a dam during this period to ensure safe operation (Wu *et al.*, 2016). During this stage, data produced by installed instrumentation should be critically evaluated for any signs of distress or unexpected behaviour. If failure of a dam occurs, it would likely happen during impoundment.

When monitoring the behaviour of a dam during impoundment, obvious unwanted behaviour such as structural cracking, excessive displacement and major leakages may be identified by the naked eye on site. At this point the extent of the damage is assumed to be excessive, deeming the dam structure compromised. Early detection of such behaviour is an advantage and will allow for remedial work to be undertaken before major damage is experienced.

Measurement of the dam's behaviour during impoundment, using instrumentation, will provide early warning of unwanted structural action. Without a reference point indicating the expected structural action of the dam during loading, data from instrumentation provides very limited insight.

The anticipated behaviour of the dam is provided in an impoundment report or manual and is based on FE analysis results, computed at various pre-determined dam impoundment progress stages or levels. Due to possible variations in dam and foundation material parameters between design and actual values (ICOLD, 2009), it is beneficial to calibrate/validate the FE model. Calibration of a FE model against actual dam behaviour provides the ultimate confidence in the model (Moyo & Oosthuizen, 2013). This is done by comparing behaviour predicted by the analyses results, to observed dam behaviour, and then adjusting the model parameters to align the predicted behaviour with observed behaviour.

Calibration of the FE model is usually undertaken by analyses during the early stages of dam impoundment loading. If reliable instrument data is available for dam behaviour for a lengthy period prior to impoundment, a calibration analysis can be undertaken based on this early data prior to impoundment (Cassells & Shaw, 2022). This calibration work should be confirmed during impoundment, whereby the model reliability is further refined (Cassells & Shaw, 2023) and ultimately validation proves that the dam is safe and behaving as designed (Cassells *et al.*, 2024).

This dissertation specifically poses the question: "How accurately can the behaviour of a super-high concrete arch dam founded on a complex layered rock foundation, be modelled, using a three-dimensional linear elastic FE analysis, during impoundment".

The newly constructed Yusufeli Dam, in the north-east region of Turkey, was used as the prototype for undertaking this hypothesis testing study. The Yusufeli Dam comprises a 275 m high, variable thickness, double-curvature conventionally vibrated concrete arch dam. The dam was built on a complex layered rock mass foundation, and its behaviour thus far has been well monitored with instrumentation.

1.2 STUDY OBJECTIVES

The primary aim of the thesis is to develop a numerical model of the prototype dam, using the FE method, and compare the simulated structural behaviour of the model, against the actual behaviour of the prototype dam. The outcome of the comparison study will indicate how accurately the behaviour of the protype dam was predicted by the numerical model.

The secondary aim is to develop a calibrated numerical model of the prototype dam, for deriving a comprehensive understanding of the dam, by analysing the model under theoretical conditions.

The overall objective is to compare the deformation behaviour of the dam under loading to that reported by the FE analysis. The accurate numerical model of the dam can then be used to further study the dam behaviour, under an extended range of loading conditions and material parameters.

To achieve this aim various sub-objectives need to be fulfilled. The sub-objectives of this study are to:

- Find a super-high concrete arch dam, having well defined design parameters, that is thoroughly instrumented and for which meaningful output data, produced by the instrumentation, can be accessed and used,
- Obtain instrumentation output data, evaluate its reliability and post-process it into meaningful information that illustrates the behaviour modes of the dam,
- Develop a FE model that simulates the complex geometrical configuration of the 3-dimensional dam-foundation structural system, and undertake a static analysis of the dam and foundation using linear elastic material parameters,
- Compare the results of the FE analysis with the observed dam behaviour, provided by instrumentation data in terms of deformation, rotation and temperatures.

1.3 SCOPE OF STUDY

The focus of the study was to evaluate how well the behaviour of the prototype dam can be simulated, using a numerical modelling technique, assuming a linear elastic stress-strain relationship of the dam and foundation materials. Assuming a linear elastic stress-strain relationship, to model behaviour of material that is intrinsically non-linear, may seem to have inherent limitations.

Large concrete arch dams are designed according to stress criteria that specifies an allowable compressive stress, having a ratio of ¼ in relation to its actual characteristic compressive

strength (f_c). It is known that civil engineering materials, such as concrete and rock, indicate a linear stress-strain relationship at low strains. This means that properly designed concrete arch dams that experience normal design loads, will remain in a stress state below the non-linear portion of the stress-strain curve (Gunn, 2001).

The extent of the study comprises the collection of instrumentation data on a dam, for comparison with anticipated dam behaviour according to the outcome of a FE analysis. More specifically:

- The instrument data was collected during the reservoir impoundment of a concrete arch dam, to account for the response of the dam during filling of the reservoir.
- The FE analysis was undertaken to model the dam behaviour during the period for which instrumentation data was collected. The FE analysis was performed using a stage construction approach, assuming actual loading conditions as measured on site, where they differed from assumed design loads.
- The FE analysis assumed linear elastic material properties of the dam and foundation, apart from the interface between the dam and foundation and between monoliths at the expansion joint interface.
- The results of the FE analysis, were compared to the observed behaviour of the dam, as indicated by the instrumentation data.

Other assumptions that limit the scope of the study:

- Loading is limited to usual conditions which include gravity, hydrostatic and temperature loading.
- Seismic loadings were not considered.
- This abovementioned assumption will not be valid for dams overloaded to failure.

The structural numerical modelling forming part of this dissertation, were undertaken by the author according to raw digital survey files received from site.

The author formed part of a design team responsible for planning of the instrumentation, the final configuration of which was ultimately the decision of the team lead. Dam instrumentation data used for this study was captured/recorded by site personnel and sent to the author in relatively unprocessed form. The study, post-processing, interpretation and presentation of data from instruments is the work of the author.

The model calibration, sensitivity analyses and behavioural analyses of the dam as conducted in this study are the work of the author.

1.4 METHODOLOGY

The objectives of the study were achieved by following the underlying methodology:

- A literature study was undertaken, to develop a sound understanding of the various aspects and related engineering principles that collectively form part of the overall study. This will ensure that all the assumptions made, and technical theory utilised to achieve the aim of the study, are fundamentally correct. The literature review study comprised of:
    - Evaluation of dam types with specific focus on the theory of concrete arch dam analysis and design. The typical engineering properties and structural behaviour of concrete arch dams were outlined. The critical structural mechanisms of a loaded concrete arch dam were identified and the associated design assumptions and criteria, were defined.
    - A review of various dam loadings and the typical combinations considered for design, with a particular emphasis on loadings assumed for the comparison study analysis.
    - Defining arch dam foundation requirements, with emphasis on dam-foundation interaction under loading. This includes gaining an understanding of the various foundation properties to be considered and what site investigations are to be undertaken, to accurately model the foundation.
    - A review of the typical dam monitoring instrumentation, to develop an understanding of the different physical measurement data that can be reported.
    - A practical review of the theory of the FE method, its application in dams design and its limitations.

- A suite of analytical work was undertaken to test the hypothesis, by comparison of computed dam behaviour with behaviour measured on site. The analytical exercises mentioned comprised of:
    - Conducting investigations and evaluations of the dam prototype in terms of its geometrical configuration, construction, design characteristics and site-specific conditions, to obtain a basic understanding of the expected structural behaviour and the implicit mechanisms that will be instigated under loading.
    - Creating an FE model of the dam and foundation structure, for analysis, of which the results will be used for prediction of the dam behaviour, for the assumed parameters under the defined conditions. The locations of instrumentation were considered when developing the FE modelling strategy, in terms of geometrical configuration and associated mesh refinement.

  - The gathering, studying, summarising and interpreting of data received from dam monitoring instrumentation. This includes verifying the data against logical understanding of the expected behaviour of the arch dam, and elimination of flawed data from possible damaged instruments or incorrectly recorded readings.
  - A comparison study that outlines the observed behaviour of the dam, against that which was expected to occur according to the results output from the FE analysis of the dam and foundation structure. Reasons for significant differences in behaviour between the prototype dam and the predicted behaviour were proposed, and the parameters were adjusted in attempt to calibrate the model behaviour to observed/measured behaviour.
- A behavioural sensitivity analysis was undertaken of the calibrated FE model of the dam, outlining the impact of various changes in modelling assumptions and loading conditions. More specifically the investigations comprised of:
  - Evaluation of the incremental deformation and stress behaviour of the dam, under progressive reservoir loading, in terms of the typical structural behaviour modes of a concrete arch dam.
  - Evaluation of the impact of ambient temperature loading, due to changes in the seasonal temperature conditions of the dam.
  - Conducting a sensitivity analysis of the dam deformation behaviour, under a range of dam concrete elastic modulus values.
  - Conducting a sensitivity analysis of the dam deformation behaviour, under a range of foundation elastic modulus values.
  - Investigation of the sensitivity of the thermomechanical response of the dam, to a range of thermal expansion coefficients.
  - Investigation of the impact on critical stress responses of the dam, against a changing dam and foundation elastic modulus.
  - Undertaking a thorough spatial assessment of the complex time varying temperature state of the dam body.
- Formulation of a comprehensive account of the outcomes of the thesis study and ultimately providing a conclusion. This was undertaken with reference to original objectives and background of the study, putting it into perspective for the interest of academics and practising engineers.

1.5 ORGANIZATION OF REPORT

Body text.

- Chapter 1 serves as an introduction to the study
- Chapter 2 addresses all the currently known engineering theory that collectively makes up the study topic, in the form of a literature review.
- Chapter 3 presents the dam prototype, underlining specific characteristics that define the nature and constitution of the dam.
- Chapter 4 outlines the development of the FE model, including the modelling approach, parameter assumptions and defined loading conditions.
- Chapter 5 reports the FE analysis outputs along with interpretations of the results.
- Chapter 6 presents the dam instrumentation data obtained, together with meaningful observations made.
- Chapter 7 provides a direct comparison between the computed behaviour of the dam and selected instrumentation data.
- Chapter 8 discusses the results of various behavioural sensitivity analyses.
- Chapter 9 reports the overall outcome and conclusions drawn from the study, with proposed recommendations.
- Chapter 10 is the list of references pertaining to the study.
- Appendix A contains engineering drawings of the dam and excavation.
- Appendix B contains the original dam impoundment plan.
- Appendix C contains photos of dam during impoundment.
- Appendix D contains additional FE model mesh images

2 LITERATURE REVIEW

This chapter provides a comprehensive study of the recognised engineering theory and published findings, relating to the various components implicit in the study. The goal of the literature review is to highlight the key concepts that validate the analytical findings of this thesis, while providing the reader with a summary of the fundamental assumptions underlying this study.

The literature review commences with a review of dam design theory, with an emphasis on concrete arch dams looking at the typical dam design conditions and loadings. This is followed by a review of arch dam foundation requirements and typical geological investigations and testing to be done. The current dam instrumentation technology is then investigated to understand its capability and application in dam engineering. After this the FE method theory is discussed in relation to dam engineering.

2.1 DAM ENGINEERING THEORY

2.1.1 History of Dams

The first known dams were built in the regions of Egypt and Mesopotamia (Yang *et al.*, 1999). Literature is inconsistent regarding the exact dates, but evidence suggests that a rubble masonry gravity dam was built around 2950 - 2750 BC by the Egyptians using stone bricks and gravel. Around 2000 BC an earth embankment dam was constructed in Mesopotamia for flood control and to prevent erosion.

Around 100 AD the Romans were the first to use concrete and mortar for dam building. In the 17th century the Spanish were the leaders of dam building and the first book on designing dams was written in 1736 by a Spaniard. Spaniards who settled in the Americas, brought dam engineering to the continent.

The modern dam building era started in the USA in the second half of the 19th century. This was a direct result of the second industrial revolution, the growing population and the need for irrigation of large-scale farming operations.

After the end of World War 2, another population growth created further need for the construction of large dams and with it the dam engineering profession developed into an established fraternity. Technical expertise and experience on dam building became freely available through the publication of various literature, and the formation of numerous worldwide dam building committees and societies. Notable worldwide organisations formed

for the purposes of publishing dam related literature are ICOLD (International Commission on Large Dams), USACE (Unites Stated Army Corps of Engineers), USBR (United States Bureau of Reclamation), FERC (Federal Energy Regulatory Commission), SANCOLD (South African Committee on Large Dams), ANCOLD (Australian National Committee on Large Dams).

2.1.2 Dam types and selection

The evolution of dams has resulted in the design and construction of various dam types. Dams are classified according to the construction material and form (Jansen, 1988). The form of the dam is dependent on the site foundation (topography and geology) conditions and determines how the structure transfers the loading of the contained water reservoir, into the foundation. The selection of construction material is dictated by the maximum required design strength and availability of suitable raw materials in the near locality of the dam site.

The common dam forms comprise embankment dams, gravity dams, arch dams and buttress dams. The curvature and thickness of arch dams may vary according to the valley width and foundation suitability. Buttress dams may be further categorized as flat slab, multiple-arch, dome arch or massive head types.

Embankment dams and gravity dams, transfer the water reservoir loading into the underlying foundations, by way of gravity-cantilever induced shear force and moment transfer at the dam-foundation interface. It is essentially the self-weight of the mass of the structure that keeps the structure stable. Arch dams and to an extent gravity-arch dams, transfer a large portion of the water reservoir loading into the foundation by way of arch thrust action into the foundation abutments, induced by the curvature of the structure. Buttress dams behave similar to gravity dams, in that load is transferred downwards to underlying foundation by the buttresses. The buttresses provide stability to the lighter structures spanning between them. The lighter structures between the buttresses transfer load into the buttresses by arching or flexure, depending on the configuration of this lighter structure component (slab, arch, dome or massive head).

Embankment dams are constructed from earthfill or rockfill and may comprise a homogeneous or zoned material profile, having a range of permutations from clay impervious cores to concrete faces. Gravity, arch and buttress dams are normally constructed from cementitious materials such as Conventionally Vibrated Concrete (CVC), Roller Compacted Concrete (RCC), Rubble Masonry Concrete (RMC) or even Hardfill material. For the sake of brevity, dams built with cementitious materials will hereafter generally be referred to as concrete dams, unless the specific classification of concrete type is required. Embankment dams are flexible structures whilst concrete dams are relatively rigid.

Each dam site has unique local conditions, combining a specific set of properties, each having an impact on the ultimate selection of material type and form of the dam. Each of the local conditions is hereunder highlighted, with specific reference to the effect it has on the selection of the dam construction material and/or form type. The influence of a certain condition on the dam selection type, is hereunder viewed in isolation of other conditions, assuming no limitations of other conditions, to purely isolate the effect the condition addressed.

Valley Topography

The topography of a dam site normally dictates the first choice of dam form (Emiroglu, 2008), assuming the suitable material type for the form is available nearby. Low rolling planes and very flat wide valleys across a river are suitable for earth embankments dams. Wide valleys or U-shaped valleys are conducive for gravity dams built with cementitious material, whilst arch or gravity-arch dams require narrow V-shaped, wide V-shaped or narrow U-shaped river valleys. Buttress dams are suited for similar valley conditions to gravity or wide valley arch dams but are limited to small or medium size dams.

Foundation Conditions

The foundation should be able to carry the full weight of the dam as well as the water reservoir loads transferred by it. The geology and geotechnical conditions of the foundation material will indicate what dam types are suited for the foundation. The strength, bearing capacity, stiffness, homogeneity, thickness and inclination of the strata are important parameters to be considered. The physical characteristics such as permeability, fracturing, jointing and faulting of the material are also vitally important in deciding on a dam type.

Foundation conditions for a dam listed in order of competency, comprise of solid or fractured rock, gravel/coarse sand, fine sand, silt or clay. Earthfill embankment dams are suitable for all foundation types, including poor foundations with deep overburden material comprising clay, silt, fine sand or gravel. Rockfill embankment dams are not suitable for poor foundation material, with potential for differential settlement, due to large leakage potential from such settlement. Gravel or rock foundation is preferred for rockfill embankment dams.

Low height concrete gravity dams can be founded on all foundation types except for clay. Medium height concrete dams and small buttresses dams require rock or gravel material for foundation support. Medium to large concrete gravity, buttress and arch dams should only be built on rock foundations. The competency of the rock mass in terms of fracturing, faulting and permeability should be evaluated especially for the abutments of large arch dams. Highly

fractured rock mass foundation may require improvement by removal of weathered materials, consolidation grouting of deeper fractured material or geotechnical stabilisation.

Availability of Construction Material

Due to the large volumes of material required for dam construction, it is important to consider the availability of raw material in the vicinity of the dam site, when deciding on a suitable dam material type. Material hauling is a costly activity in construction and having the required raw material near to the dam site, is a great economic benefit. The availability of construction material is also linked to the local geological conditions of the valley and bedrock. If sand, gravel and stone is available, a concrete dam may be suitable. An abundant supply of well graded soil materials and impervious material may justify the construction of an earthfill dam.

Expected Flood Conditions and Dam Spillway Size,

The expected design floods from the dam catchment ultimately determine the height of the dam and the size of the spillway. For dams built on rivers with high flood potential, the spillway is often the dominant feature. Dams containing small regular floods may only need a small concrete spillway section, with earthfill sections making up the non-overflow portion of the dam. In cases where the spillway size makes up a considerable portion of the dam, combining the spillway and dam into a single dam structure type, will lead to a concrete gravity or arch dam.

Earthfill dams are more prone to failure or large-scale damage due to overtopping of the structure than concrete dams. Considering all other conditions are equal, earthfill dams are more economical to build than concrete dams.

Other conditions that may influence the dam type selection may include climate during construction and river diversion strategy, environmental impact of dam, economic conditions, availability of skilled personnel and seismicity of the region.

The ultimate selection of a suitable dam type for a given dam site, requires consideration of the various local conditions, in conjunction with the application of good engineering judgement, based on experience of dam designer.

2.2 CONCRETE ARCH DAMS

2.2.1 Arch Dam Philosophy and Design Considerations

Concrete is a composite material comprising cement, aggregate and water, that gains strength due to chemical bonds that form under hydration reactions caused by the cement. The strength properties of concrete are based on the composition of its microstructure, of which the interstitial transition zone between the aggregate and the cement paste are the weakest link. In freshly placed concrete, water films try to form around the aggregate particles due to hydrophilic behaviour. The higher water cement ratio in the interstitial transition zone of the concrete, causes the local reduction in the strength due to fewer cement particles.

The low tensile capacity of the interstitial transition zone is reason for the low tensile strength of concrete, in relation to its compressive strength (Li, 2011). A general rule of thumb states that the tensile strength of concrete is approximately 10 % of its compressive strength (Durieux & van Rensberg, 2016). This value may vary depending on the concrete mix, design strength, and method of testing (Raphael, 1984; Cement and Concrete Institute, 2009). Simply put concrete is weak and brittle in tension and strong in compression. The low strength and stiffness of the porous interstitial transition zone is also a factor that causes concrete to have nonlinear inelastic behaviour, when loaded.

These characteristics of concrete illustrate why a properly supported concrete arch loaded on the convex side, is probably the most efficient form of structural use of concrete. A loaded concrete arch restrained or supported at its ends, will transfer the loads to its supports by developing internal compression stresses or thrusts along its axis. The high compressive strength of concrete is effectively utilised if cast into an arch.

An arch dam is defined as a solid concrete structure that is curved upstream in plan (USBR, 1977), and transmits load into the upper abutments via arching action and lower foundation via cantilever action. Load transfer of an arch dam into the abutments and foundation due to resistance of movements, is illustrated in Figure 2-1 (Alfatlawi *et al.*, 2021).

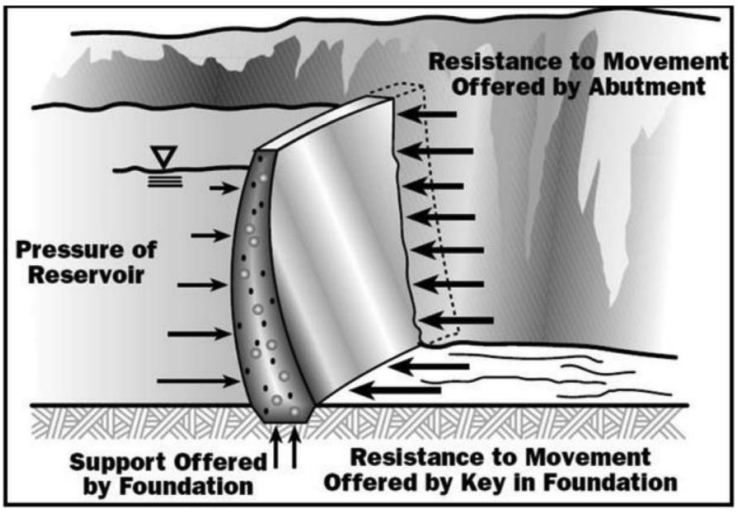

Figure 2-1: Arch dam transfer of reservoir loads into foundation (Alfatlawi *et al.*, 2021)

Arch dams are the most efficient concrete dam type (Hollingworth & Geringer, 1994) and according to Novak et al (2006), may result in an 80% concrete material saving, when compared to concrete gravity dams. Cost savings may also be experienced in the form of lesser associated foundation excavations. The complex shape and form of arch dams may cause high formwork and construction costs, which partly reduces their initial seemingly large financial advantage over concrete gravity dams.

The selection of the arch dam type is highly dictated by the local conditions of a potential dam site. Arch dams require a river site with favourable topography, comprising steep riverbank slopes and a resulting narrow valley and competent foundations.

The structural behaviour of an arch dam is commonly explained as a system of interacting cantilevers and arches, transferring loads to the foundation and abutments. The transfer of loading to the foundation and abutment, is in proportion to the relative stiffnesses of the arch and cantilever components. It is considered more efficient to transfer a greater portion of the dam load into the foundation by arching, than by cantilever action. The relative stiffness of the arch and cantilever components is dictated by the ratio of the width to height of the river valley.

Although arch dams can be constructed on wide river valleys, a narrow valley is most suitable for a very efficient arch. The typical crest length to height ratio (CL:H) of arch dams are in the range of 1 to 6. An arch dam should be given first consideration for a site with CL:H ratio of 1 to 3, whilst a ratio of 4 to 6 may also indicate an arch as the most feasible structure, assuming excessive excavation is not required (USACE, 1994). A CL:H ratio greater than 6, means that other factors and site conditions must be given careful consideration, to justify constructing an arch structure.

Arch dam sites are often classified as narrow V shaped (CL:H of 1 to 2), wide V-shaped (CL:H of 3 to 5), U-shaped or wide U-shaped (CL:H > 6). A schematic of valley profiles is shown in Figure 2-2. Generally, the limiting CL:H ratio is considered to be about 8, however exceptions exist in wide valley arch dams with CL:H > 8 (Kabell, 2014). The Gariep Dam in South Africa is a wide valley arch dam with a CL:H > 9. Numerous small wide valley arches were constructed in Zimbabwe (Wild, 1980), of which the Kariba dam cofferdam arch had a CL:H ratio of 16. Construction of an arch dam with a high CL:H ratio requires extensive analysis to ensure safety of the dam.

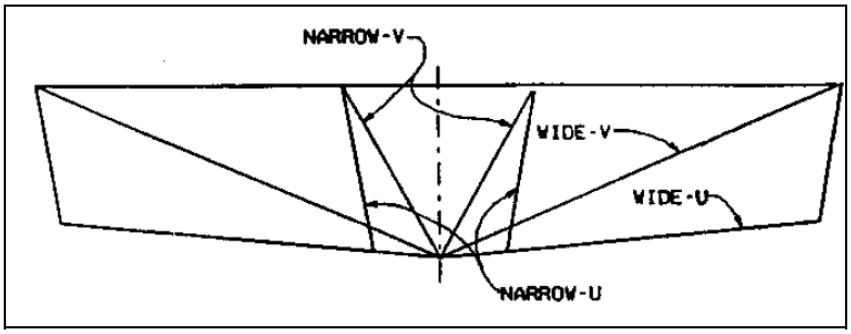

Figure 2-2: Schematic of various river valley profiles (USACE, 1994)

A narrow river valley site is suitable for construction of a thin arch; whilst wider river valleys require an arch that thickens towards the base, to ensure sufficient capacity, to resist cantilever stresses at the lower portion of the dam. Arch dam types have commonly been defined according to the dam base width over height (BW:H) ratio. Classification of arch dams according to BW:H ratio is shown in Table 2-1 (USBR, 2013).

Table 2-1: Arch dam type classification according to BW:H ratio (USBR, 2013)

Arch Dam Type	Base-width to Height Ratio
Thin arch	< 0.2
Medium-thick arch	0.2 to 0.4
Thick arch	0.4 to 0.65
Curved gravity	< 0.65

The image shown in Figure 2-3, provides a sketch of valley configurations for seven notable arch dams in Austria, and corresponding section views of the dam crown cantilever (Miranda & Farinha, 2012). The CL:H ratio of these dams ranges from the lowest of 1.5 for Dabaklamm dam, to 5.6 for Schlegeis Dam. The corresponding BW:H ratios of these dams are 0.13 and 0.26, meaning the Dabaklamm dam is classified as a thin arch structure, whilst the Schlegeis Dam is a medium-thick arch.

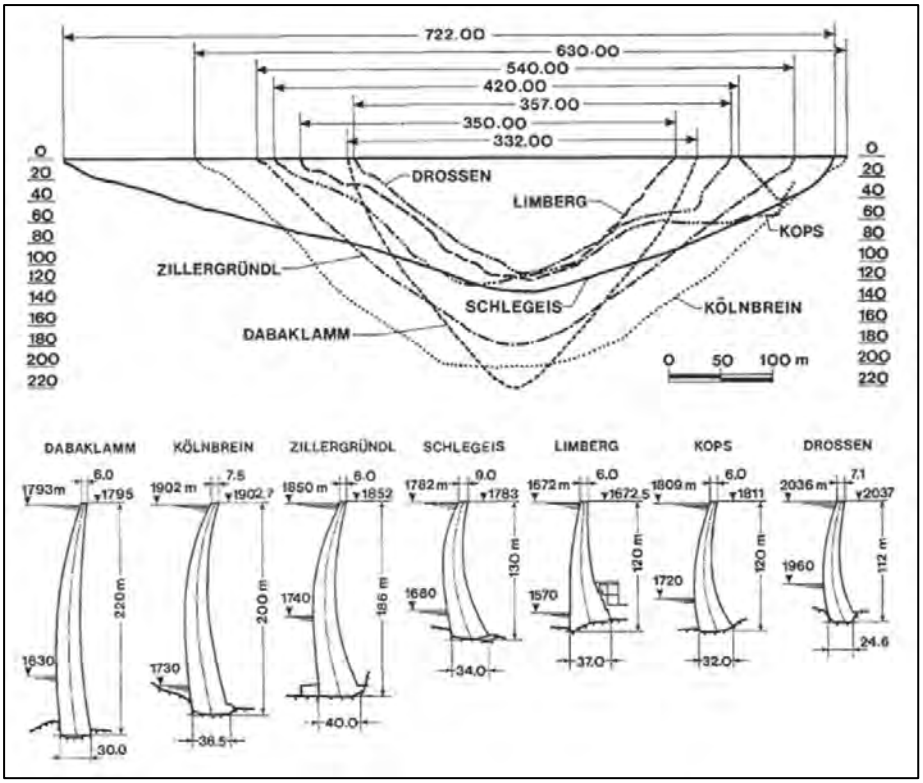

Figure 2-3: River valley configuration and dam profile for seven notable arch dams in Austria (Miranda & Farinha, 2012)

The canyon shape factor (K), which is a ratio of the total developed length of the dam foundation surface to the maximum dam height, is a more advanced site appraisal factor for suitability of an arch dam. A K value less than 5 represents conditions where an arch dam may be most feasible, assuming other conditions are also compliant (Kirn & Sarkaria, 1955).

Narrow valley arches have greater stiffness along the arch axis, causing a greater portion of the load to be transferred to the abutments via arching (Shaw, 2015). A narrow valley allows for a shorter span and higher arch curvature, resulting in greater inherent arch stiffness. Greater load transfer via arching, results in lesser load transfer by cantilever action and associated lower tensile stress development in the cantilever component. Thin arch dam structures are believed to be very efficient based on this premise.

A well-designed double-curvature thin arch dam behaves as a three-dimensional shell, that can carry a wide range of loadings through reverse membrane behaviour, developing very little bending action.

The “Thin Arch Dam Syndrome” that emerged in the 1950’s, lead European dam designers to believe that arch structures were virtually invincible to failure. The philosophy developed in this era and supported by eminent dam engineer André Coyne, was that arch dams work as self-

sealing plugs that become stronger and more taught, as thrust of forces bearing down on them increase (Coyne, 1956).

Dam designers who endorsed this philosophy, overlooked the influence that the dam foundation condition has on the structural stability of the dam (Sarkaria, 1997). It was believed that any local material failures in the dam structure, due to poor foundation conditions, would merely re-distribute and not affect the stability of the structure. While the re-distribution of tensile stresses due to cracking may occur, the stability of the dam is highly reliant on the support provided by a competent foundation.

Documented arch dam failures such as Malpasset (Duffaut, 2013), Le Gage and Tolla; comprised very thin arch structures built on poor foundations. Investigations of these dam failures have resulted in valuable lessons learnt, and highlighted that the foundation, is an integral component in the global structural integrity of an arch dam. This is especially critical for thin arch structures.

Complications that may arise from poor foundations are summarised below:

- Low or varied deformation modulus of the foundation may result in excessive or asymmetrical deformations of the dam structure. Stress distribution in an arch dam is critically influenced by excessive deformations.
- Localised zones of low deformation modulus foundation rock immediately below the dam base, may result in the formation of excessively high tensile stresses in the dam concrete. This is due to the bridging effect of the stiff concrete spanning this localised “soft” zone of foundation rock mass. The bridging over sections of foundation with low deformation modulus, may also result in elevated hydraulic gradients through poor rock materials (Shaw & Becerik, 2016).
- Localised low bearing strength regions in the rock mass near to the dam-foundation contact area, may result in local foundation material failures and unfavourable stress re-distribution in the dam and foundation.
- Low rock mass shear strength resulting in increased susceptibility to abutment failure in shear.
- Geological faults or joints in the foundations, may result in local instability due to movement or dislodging of joint-bound rock formations (Londe, 1987).
- Loose or unconsolidated foundation material at the toe of the dam, may erode during overtopping, causing the dam to lose stability due to undermining.

- Highly fractured rock is permeable and may result in excessive seepage and uplift below the dam. Inadequate drainage in the foundation and dam-foundation contact area may create stability issues (Terzaghi, 1929).

At the time of the 1990 International Arch Dam Workshop, it was stated that although arch dams have failed, as far as is known all failures were due to foundation issues (Serafim & Clough, 1990). More recent literature has stated that foundation problems are the only recorded cause of failure for arch dams (Zhang et al, 2016; ASCE Task Committee, 2018).

It has been shown from investigations of concrete dam failures, that seemingly quite minor geological, geotechnical and hydrogeological details in foundations can have major impacts on the performance and overall stability of a concrete dam (Brown, 2016). There is no other dam type for which the foundation is of such importance, than arch dams.

Considering the above, it is critical that the rock mass structure making up the foundation abutments of the arch structure, comprises competent material, with a relatively high stiffness and sufficient strength properties. Simply stated, the foundation rock mass is required to withstand the thrusts caused by the arch action of the structure under water loading, without undergoing failure or excessive deformation (Lombardi, 1989).

Rock masses are made up of material between major shears and faults. Rock mass contains joints, narrow shears, discontinuous shears and other discontinuities (USBR, 1977). Rock mass comprises a complex medium, with various formation zones moulded into place, by a combination of historical geological fault movements of existing rock and progressive formation of new rock, from molten rock extrusions/intrusions. Rock masses are rarely homogenous and normally comprise a heterogeneous material of interlocking and interwoven zones, with varying geological properties and conditions.

In light of the inherent complexities in the structural formation of rock masses, ensuring a dam site is suitable for seating of an arch dam requires the consideration of various geological and geotechnical aspects, of the local rock mass conditions. Some general factors to consider are listed below (Brown, 2016):

- Geological history of the dam site,
- In situ field stresses present in incised river valleys,
- The depth and degree of rock mass weathering,
- The locations, orientations, slopes and characteristics of faults, shear zones and other major discontinuities,
- Rock mass strength, bearing capacity and deformation moduli,

- Concrete-rock and rock-rock shear and tensile strength parameters,
- Susceptibility of rock mass to creep and relaxation,
- Permeability of rock under high pressure and in situ pressure conditions,
- Groutability of rock mass,
- Formation of high uplift within rock mass discontinuities.

Assuming compliance of the site condition criteria, there are various advantages of building an arch dam over other dam types:

- An overflow for arch dams is harmless, while an overflow for other concrete dams can be troublesome. For embankment dams it is catastrophic (Milavanovic, 1990).
- Relatively few arch dams have failed, in comparison with the more numerous failures of other types of dams (Linsley & Franzini, 1992).
- Arch dams are resistant to earthquake forces, and there are no recorded failures of arch dams from earthquakes (ASCE Task Committee, 2018).
- Although formwork for curved faces may be expensive, this is normally overcompensated by large savings in concrete material.
- Simpler river diversion opportunities due to allowance for overtopping during construction.
- Safe accommodation of outlet works and large spillway openings (ICOLD, 1988).
- Superior aesthetic properties, often exhibiting elegance and beauty through exploitation of structural intelligence of concrete material, by using organic shaping (Kreuzer, 2000).

After all the above conditions are considered, an arch dam is generally the safest and cheapest dam type to build (Goulas, 2016). It is noted that the notion whereby a potential arch dam site is dismissed in favour of a concrete gravity dam, due to possible unstable abutments should not be entertained without careful consideration. According to Dungar et al (2018), if the foundation abutments are unstable for a concrete arch dam, they are more likely to be unstable for a concrete gravity dam.

2.2.2 Arch Dam Configuration Design and Layout

The design process of an arch dam is iterative (Boggs *et al.*, 1988). An initial configuration is developed according to site topographies and a preliminary static analysis conducted. The results of the analyses comprise deflections and stresses, which are checked against design objectives, to satisfy allowable design criteria. If the results do not meet the criteria or exceed the criteria by large margins, configuration modifications are implemented. The modified

design is then analysed, the results checked, and further modifications undertaken. This process is repeated until the criteria are met with a reasonable exceedance.

The modifications undertaken may be in the form of changing the shape, curvature or thickness of the arch to achieve the most suitable form to meet the design criteria. Design criteria are most economically achieved by proper shaping of the dam, and using both horizontal and vertical curvature, as opposed to thickening the structure (Jonker & Espandar, 2014). Shape design of an arch is based highly on the experience of the designer and there are various methods that can be adopted. There are several geometrical aspects to be considered by designers.

An arch dam is designed as a solid concrete structure, shaped in plan by an extrados and intrados curve, on the upstream and downstream face. The extrados and intrados curves are defined as an arc from a circle, ellipse, parabola or log spiral. The arc and its central angle are subtended by a centre point that lies on the downstream side of the arch, and the curvature at a point is defined by the radius of the arc. A smaller radius results in an arc with greater curvature, whilst large circles have less curvature. The arch is formed to be seated in the river valley with ends abutting into the canyon, and the plan view profile transitions from crest to base to follow the contours and river valley profile.

Normally the arch thickness increases towards the base, unless the structure is specifically designed as a constant thickness arch. The decrease in required span towards the base of the arch, allows for a decrease in arc radius and consequent increase in curvature. This is ideal as the reservoir hydrostatic loading increases towards the base.

For design and analysis purposes an arch dam is dissected into an array of arch and cantilever units or elements. Arch units refer to portions bounded by horizontal planes and cantilever units are contained between two vertical radial planes. A typical arch and cantilever section are shown in Figure 2-4.

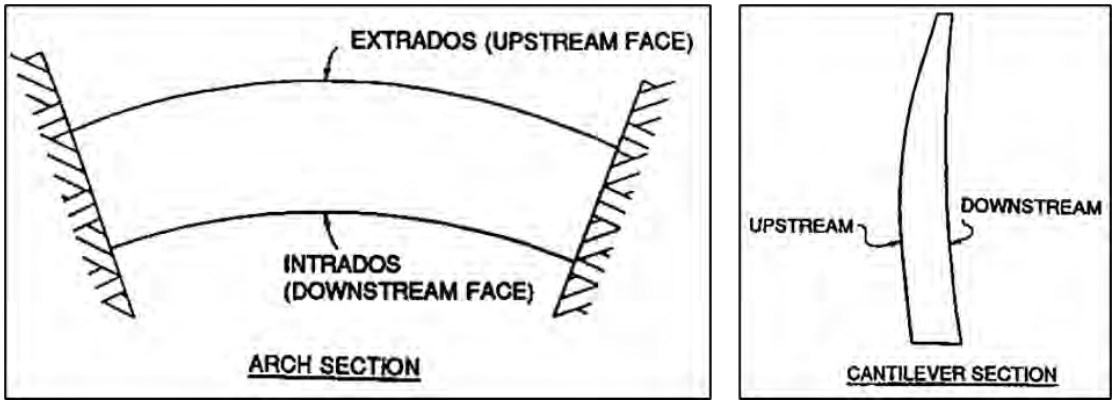

Figure 2-4: Typical arch and cantilever units of a double-curvature arch dam (USACE, 1994)

Arch dams may be designed to have curvature in the vertical radial plane, on the upstream and downstream face of the cantilever unit. This results in the design of a double-curvature arch dam. Double-curvature arch dams are shaped to have a degree of overhang and undercutting in the cantilever units, allowing for favourable utilisation of the weight of the concrete to a greater degree than the single-curvature type.

The overhang refers to the concrete on the downstream face, where the upper portion overhangs the lower portion. The undercut formation refers to the upstream face where the dam-foundation contact undercuts the dam concrete above it. The overhang and undercut of a typical cantilever unit is shown in Figure 2-5. Overhang and undercutting, negate the development of tensile stresses in the dam body at mid-height on the downstream face, and at the lower upstream portion (heel) of the dam.

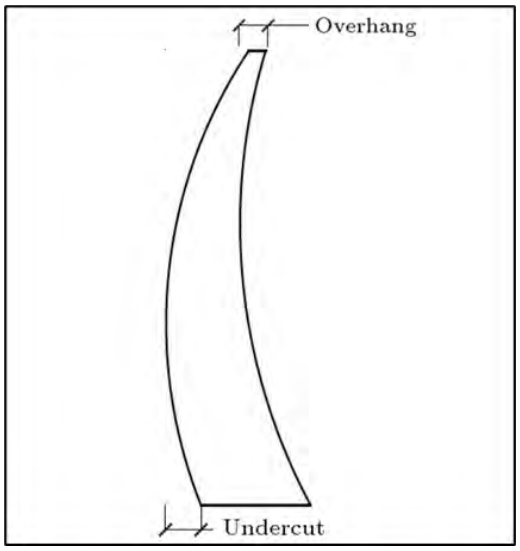

Figure 2-5: Overhang and undercut of a typical arch dam cantilever (Takalloozadeh & Ghaemian, 2014)

Classic arch shapes are normally configured around the crown cantilever, its reference plane, and the lines of centres of the arch and their corresponding radii. The crown cantilever is the

maximum height cantilever unit, normally at the lowest location in the river valley. The reference plane is a vertical radial plane, based in the streambed, that contains the crown cantilever section and the axis radius centre. The axis of the dam is a vertical reference surface, curved horizontally and defined by the upstream edge of the crest of the top of the dam. The line of centres of an arch, is a locus running through the centre points of the arcs, defining the various arch units that make up the structure from crest to base. Depending on the height of the dam, the vertical interval of the arch units may be in the order of 5 to 30 m.

Each arch unit is defined by the radius and centre point of the extrados and intrados arcs and the central (aperture) angle. Depending on the local site topography and valley width the arch dam may be designed as any of the following:

- Constant centre dam, where the arch unit centres for the extrados and intrados faces are coincident with the arch axis centre, meaning the dam has a single line of centres that plots as a vertical locus line in profile view. The various arch units are of uniform thickness from crest to base. This is also known as a constant radius dam.
- Single-centred dams have a single set of lines of centre in the reference plane. A single set refers to two lines of centres, one for the extrados and one for the intrados face of the arch units of the dam. The lines of centres are both in the reference plane. These dams can be uniform or variable thickness arches and are suitable for narrow symmetrical valleys (CL:H < 3).
- Two-centred dams have two sets of lines of centres, one for each side of the dam, being the left and right flanks. Both sets of lines of centres are coplanar with the reference plane. The extrados and intrados face of an arch element are described by the compound arc formed by the two various arcs, that intersect at the reference plane. This type of arch is suitable for narrow asymmetrical valley sites.
- Multi-centred dams have multiple sets of lines of centres. These lines of centre are not all coplanar with the reference plane. Lines of centres are spread horizontally in plan, perpendicular to the riverbed. The radii associated with the lines of centre also vary in the horizontal. This configuration produces dams with elliptically shaped or multi-centred arch elements. Shorter radius curves are usually used in the central portions of the arch and longer radius curves towards the abutments. These dams can be uniform or variable thickness dams.
- A constant-angle dam is a variable-centred dam where the central angles of the arches are approximately the same at all elevations, of the arch structure.

Sketches of preliminary designs of a single-, two- and three- centred arch dam are shown in Figure 2-6 through Figure 2-8 (USBR, 1977). A reference plane view of a single-centred arch

dam showing a single set of extrados and intrados lines of centre, is shown in Figure 2-9. Elevations and distances in these figures are shown in feet.

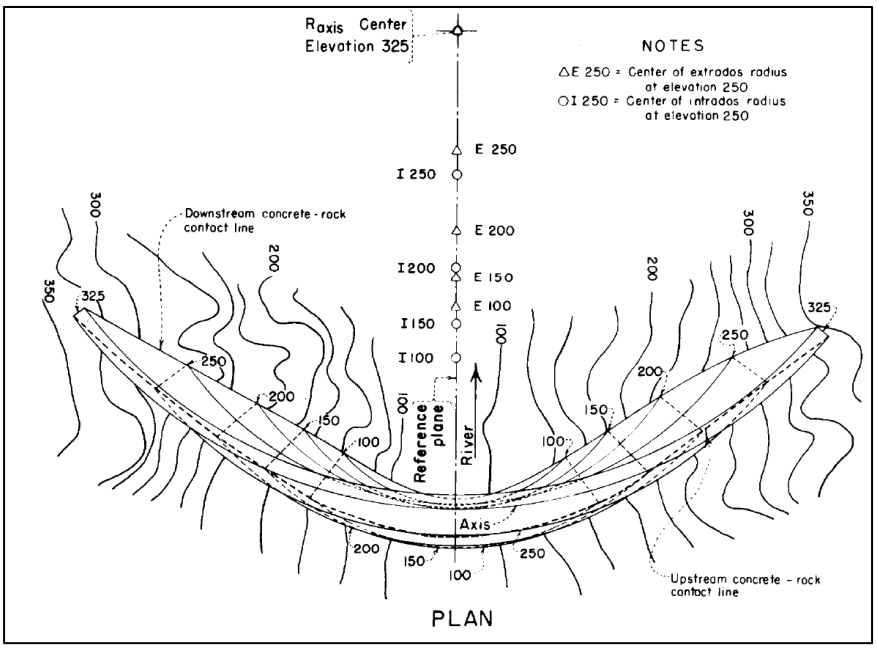

Figure 2-6: Single-centred arch in a symmetrical canyon (USACE, 1994)

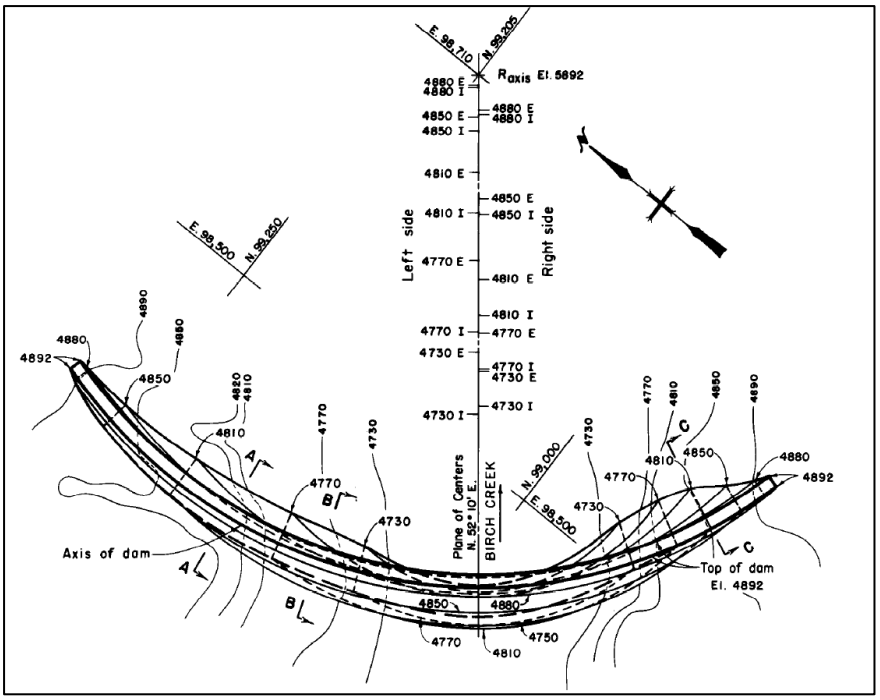

Figure 2-7: Two-centred arch dam with variable thickness arches in an asymmetrical canyon (USACE, 1994)

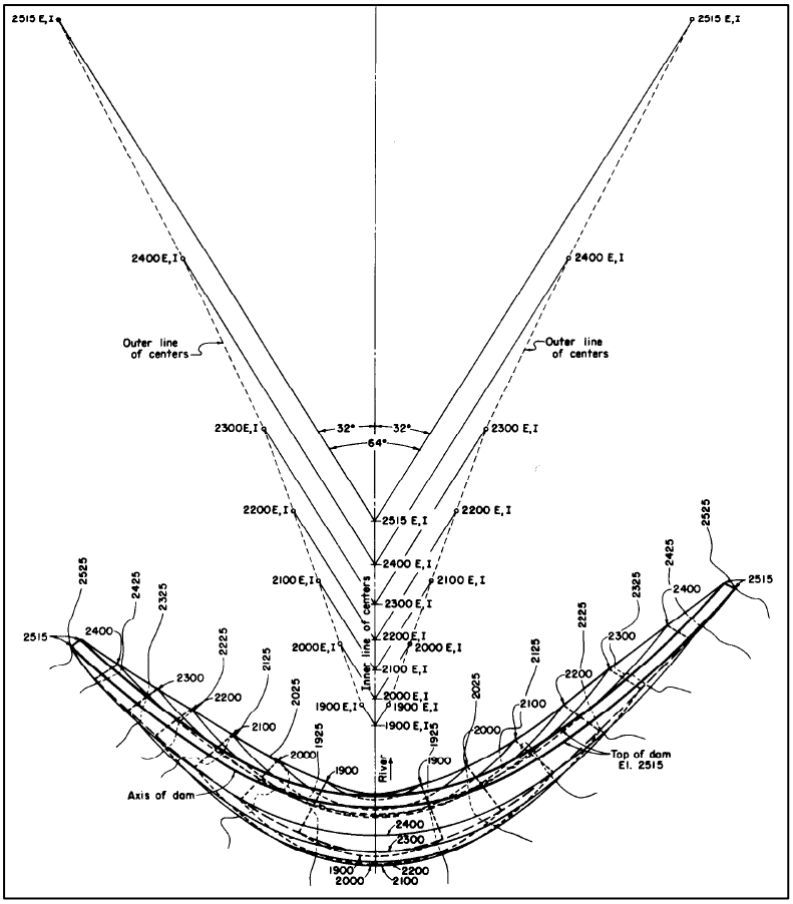

Figure 2-8: Three-centred arch dam with uniform thickness arches (USACE, 1994)

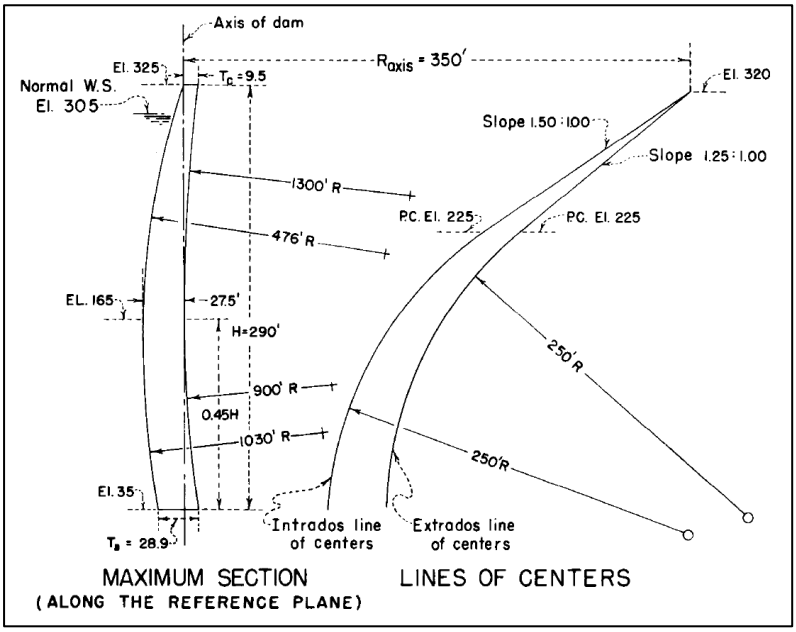

Figure 2-9: Typical reference plane view of a single-centred arch (USACE, 1994)

It is beneficial for an arch dam to be symmetrical or as close to symmetrical as possible, without the need for excessive excavations. Asymmetrical arches are likely to develop zones of stress concentrations resulting in the requirement of an uneconomical section.

The arch dam profile should be made as smooth as is possible under the given site conditions. Discontinuities or abrupt changes in the horizontal and vertical profile will create local weak zones in the arch, due to development of stress concentrations upon loading. Changes in arch thickness, curvature or abutment formation should be sculpted to occur gradually.

Local foundation irregularities under the dam footprint should be removed, and the dam footprint face of the excavation smoothly graded, to avoid concentrated stress distributions at the base and abutments of the dam.

The dam footprint excavation should be well keyed into the rock mass foundation to a level of sound rock, to provide additional sliding support. Marginal over excavation of the dam footprint is preferred to avoid local stress concentration from protruding irregularities, and to avoid shallow keys due to disintegration of material surrounding the key lip.

An arch should be orientated that the angle of incidence (α) between the arch and the rock mass abutment, is greater than 30°. The angle of incidence is taken between the tangent of the arch at the abutment, and the average rock contour lines in the region of the arch-foundation contact, as shown in Figure 2-10. An angle of incidence (β) of 40° may be adopted as a conservative approach, at the planning or appraisal stage of design. This is important to ensure that the arch can safely transfer compression forces into the abutment, without developing shear stress concentrations at the rock surface.

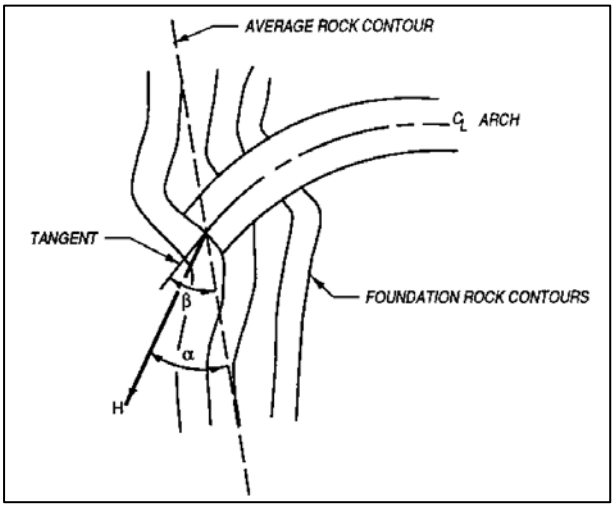

Figure 2-10: Angle of incidence between arch and rock mass abutment (USACE, 1994)

The arch abutments are to be shaped with full radial faces, meaning the face orientation is perpendicular to the dam axis. This ensures good bearing of the arch against the rock, avoiding localised high stress formations. If high volumes of excavation are required at the extrados or intrados to accommodate full-radial abutments, half-radial or greater than radial abutments may be used as shown in Figure 2-11. This alternative may only be considered if the local rock has sufficient strength, stiffness and stability and if shearing resistance is properly considered.

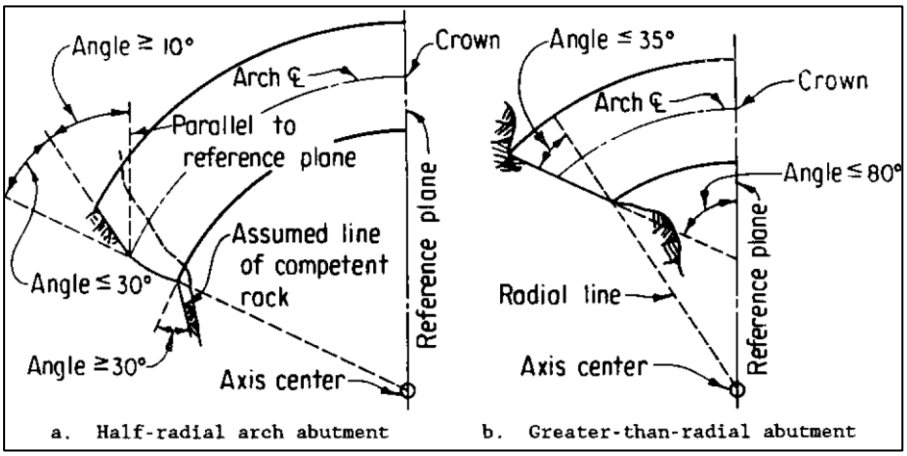

Figure 2-11: Half-radial and greater-than-radial abutment configuration alternatives (USACE, 1994)

The most efficient central angle of an arch structure for design purposes is 133.6°. The typical ratio of the arch radius to river valley span for a preliminary design cantilever arch shape, has been shown to be 0.6.

Equilibrium equations representing the forces of a free body diagram of an arch unit as shown in Figure 2-12, are derived and re-arranged to make the resulting thrust force (R) the subject of the formula. The required thickness (t) of the rib can be determined according to the maximum allowable stress (σ). These formulae are shown in Equation 2-1 through Equation 2-3.

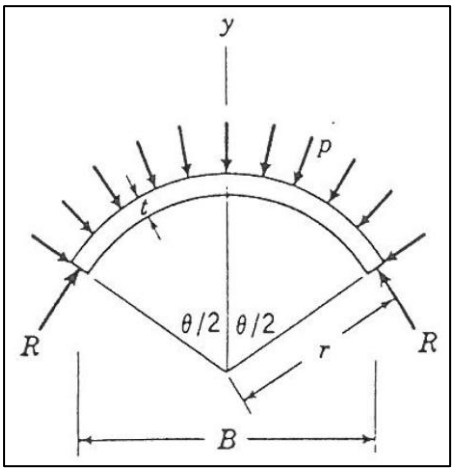

Figure 2-12: Free body diagram of an arch unit rib (Linsley & Franzini, 1992)

$$2R \sin\frac{\theta}{2} = 2pr \sin\frac{\theta}{2} \quad \textbf{2-1}$$

$$R = pr \quad \textbf{2-2}$$

$$t = \frac{pr}{\sigma} \quad \textbf{2-3}$$

Where

R = arch thrust force (kN)

p = hydrostatic pressure (kPa)

r = arch radius (m)

t = arch thickness (m)

σ = allowable compressive design stress (kPa)

θ = arch central angle (°)

B = span of river valley (m)

The volume of concrete required for a single arch unit 1 m in height is calculated by Equation 2-4.

$$V = rA\theta \quad \textbf{2-4}$$

Where

V = arch volume (m^3)

A = cross section area of arch (m^2)

Since area (A) is a function of t, which is a function of r, the volume (V) can be determined as shown in Equation 2-5.

$$V = kr^2\theta \quad \textbf{2-5}$$

Where

k is a constant

From the trigonometry of the arch diagram the radius (r) as a function of arch span (B) is shown in Equation 2-6.

$$r = \frac{B}{2 \sin\frac{\theta}{2}} \quad \textbf{2-6}$$

Ultimately the volume (V) can be calculated as shown in Equation 2-7.

$$V = k\left(\frac{B}{2\sin\frac{\theta}{2}}\right)^2\theta \qquad \textbf{2-7}$$

Differentiating Equation 2-7 with respect to arch central angle (θ), equating it to zero and solving for θ gives θ = 133.6°. It is indicated that this is the most efficient arch central angle. Data from existing arch dam sites indicates that this angle is scarcely attainable on site, and normally the largest practicable angle varies between 100 and 120°.

Assuming an arch central angle θ = 110° and solving Equation 2-7 gives a result of r = 0.61B, which indicates why the ratio of 0.6 is taken as a first estimate, to determine arch radius from river valley span distance.

A classic arch dam design procedure, published by the United States Bureau of Reclamation (USBR, 2013), is normally implemented at appraisal or planning stage of an arch dam project, to derive the arch design concept for a given site. This allows for planning of required concrete volume, minimal excavation, and associated time and costs. The design procedure followed while considering geometrical aspects mentioned above, provides a standard methodology according to which a conventional arch can be developed. A brief discussion of the procedure follows.

Dam Axis

A topographic map of the river site is required to plot and design the arch layout. The topographic contours should be based on assumed foundation rock levels. Normally only surface contours are available, and a fair amount of overburden is assumed according to which the rock level contours are predicted.

The crest elevation level of the arch dam is determined according to the design flood conditions of the river, as obtained from hydrological data studies, in conjunction with required freeboard height. The vertical distance from the crest of the dam to the elevation of the streambed at the general location of the dam, is the height of the dam (H). This is obtained from the topography map.

Knowing the location of the dam and its crest elevation, the maximum span of the dam (L_1) at crest elevation level is determined and measured as a straight line from abutment to abutment, at the dam location. The radius of the dam axis is then calculated as a function of L_1 using Equation 2-8.

$$R_{axis} = 0.6L_1 \qquad \textbf{2-8}$$

The dam axis arc with radius R_{axis} is then plotted on the topography map to span the length L_1 between abutments, at the dam crest elevation level. The straight-line distance between the abutments of the dam at elevation 0.15H, should also be measured and is defined as L_2.

Images providing typical topographical maps with plots of arch span and axis layout are shown in Figure 2-13. The largest practicable central angle below 133.6° should be used for the dam axis. The central angle is normally taken to be between 100° and 120°. This is a conservative approach as the rock topography may be incorrect, resulting in the need for deeper excavations and an extension of the arch abutments.

According to Shaw (2023) an alternative good estimation of arch dam radius can be taken as 0.5H.

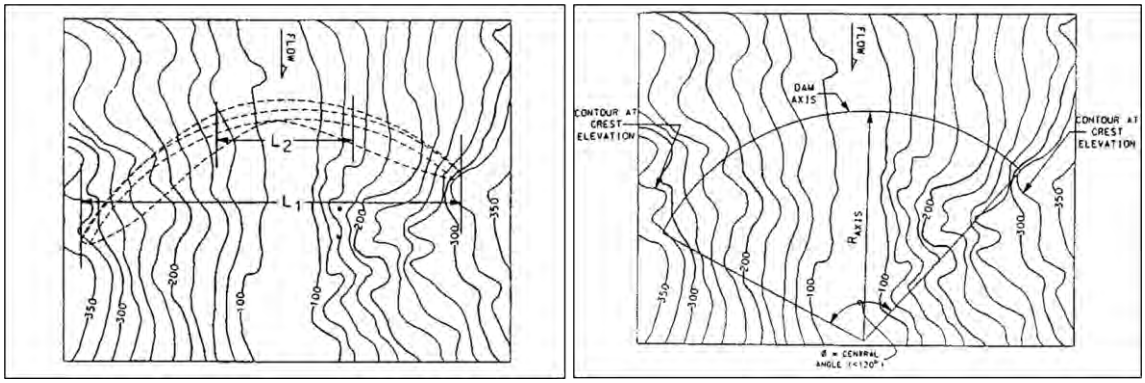

Figure 2-13: Topographical maps indicating typical layout of plotted dam axis and span (USACE, 1994)

Crown cantilever and reference plane

The crown cantilever profile is then designed according to the dam's height, axis radius and span. The crown cantilever is located at the intersection of the dam axis and the riverbed. This is the highest profile section of the dam at the lowest foundation. A vertical plane passing through the point of maximum height of the dam and the axis centre point, represents the reference plane. The crown cantilever dictates the ultimate configuration of the entire dam.

The shape of the crown cantilever is defined by the arch thickness at three elevation levels, and relating upstream and downstream projections of the extrados and intrados faces of the dam, from the dam axis. These elevation levels are at the crest, the base and at a distance 0.45H above base of the dam. The crest width (T_C), base width (T_B) and width at 0.45H ($T_{0.45}$) are calculated using the empirical equations, Equation 2-9 through Equation 2-11. A minimal crest thickness of 1 m is generally required.

$$T_C = 0.01(H + 1.2L_1) \qquad \textbf{2-9}$$

$$T_B = \sqrt[3]{0.0012HL_1L_2\left(\frac{H}{121.92}\right)^{\frac{H}{121.92}}} \quad \textbf{2-10}$$

$$T_{0.45} = 0.95T_B \quad \textbf{2-11}$$

Where

H = height of dam (m)

L_1 = span of dam at crest (m)

L_2 = span of dam at 0.15H above riverbed (m)

These equations are based on dam design data collected from a sample of existing dams by the USBR, and were derived as an aid for formulating an initial crown cantilever profile and arch dam layout.

The upstream and downstream projections of the extrados and intrados face of the dam, from the axis, are derived from the empirical Equations 2-12 through Equation 2-17. These projection distances are used to plot six points of the cantilever profile in the reference plane, as shown in Figure 2-14. The extrados and intrados curves, of the crown cantilever, are created by tracing two smooth curvilinear lines through the projection points in elevation view, one curve through the upstream points and another through the downstream points.

$$USP_{crest} = 0.0 \quad \textbf{2-12}$$

$$USP_{base} = 0.67T_B \quad \textbf{2-13}$$

$$USP_{0.45H} = 0.95T_B \quad \textbf{2-14}$$

$$DSP_{crest} = T_C \quad \textbf{2-15}$$

$$DSP_{base} = 0.33T_B \quad \textbf{2-16}$$

$$DSP_{0.45H} = 0.0 \quad \textbf{2-17}$$

Where

USP = Upstream projection (m)

DSP = Downstream projection (m)

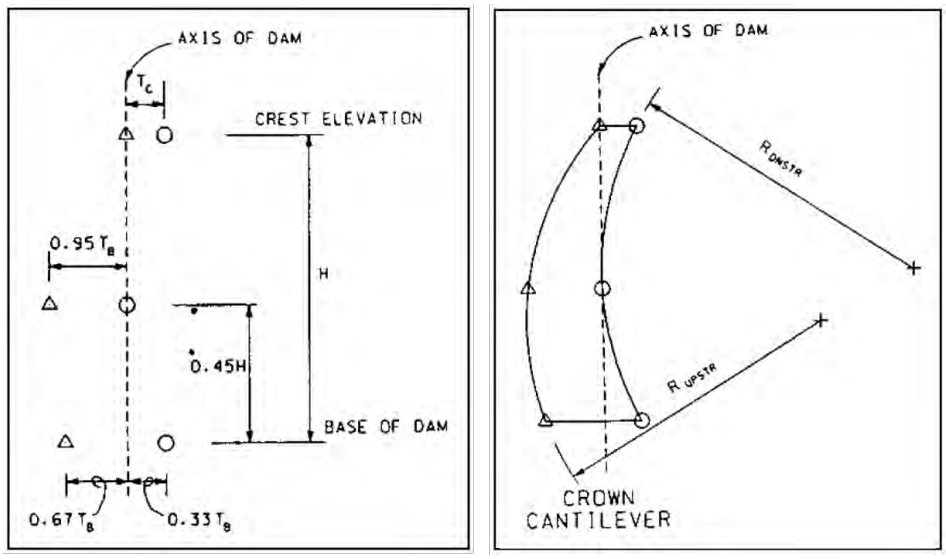

Figure 2-14: Construction of cantilever profile from projection points (USACE, 1994)

With the arch crown cantilever profile defined, upstream and downstream projections of the arch are available for the full height of the arch, according to which the layout of the arch units from crest to base will be based.

Dam footprint

With the dam axis curve representing the upstream face of the dam at crest level, the downstream face is constructed by plotting another curve with the same centre as the axis centre, having a radius equal to R_{axis} reduced by the crest thickness (T_C). The footprint of the dam is estimated by plotting a smooth curve in plan, that passes through the upstream projection point of the cantilever at the base of the dam, that meets the dam abutments on the upstream face at crest elevation level. This line is known as the contact line, and it defines the interface between the dam and foundation on the upstream face, as shown in Figure 2-15. Point C indicates the upstream projection point of the crown cantilever at the base level, with points A and B the upstream points of the dam abutments. A similar approach is followed to plot the downstream contact line.

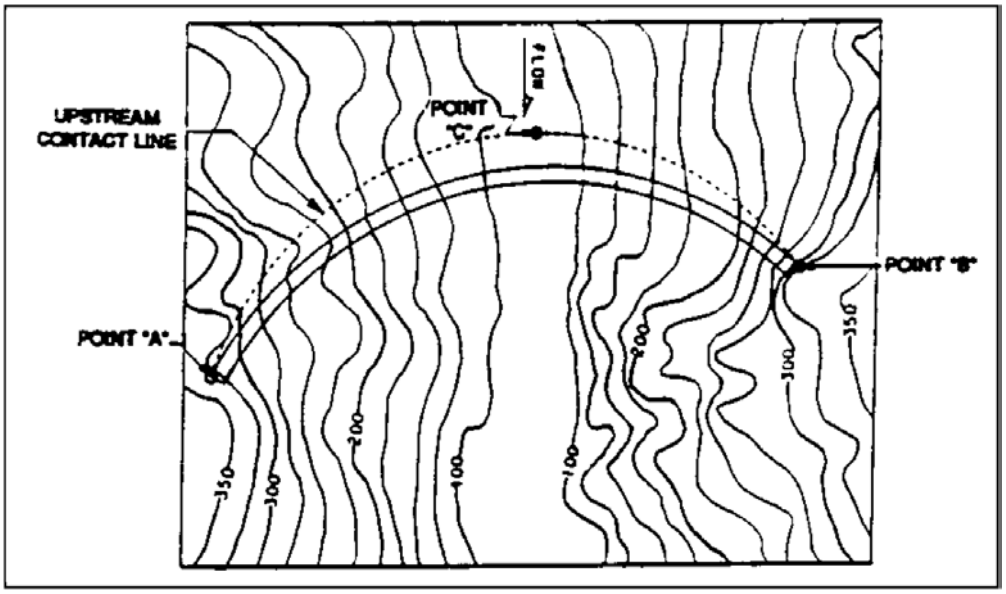

Figure 2-15: Contact line indicating dam-foundation interface on upstream side (USACE, 1994)

Layout of the Arches

To keep a smooth profile shape, the arch should be developed with between 5 and 10 arch units. Each arch unit should have a vertical height between 5m and 30 m, depending on the total height of the dam. The lowest arch unit should be placed at an elevation of 0.15H to 0.2H.

Starting from the crest of the dam, the arch unit directly below the crest is developed first. The upstream and downstream projections of the crown cantilever, at the arch unit elevation, are determined and plotted on the plan view along the reference plane line. Trial arcs are constructed to represent the upstream face of the dam, at the given elevation, and tested against criteria until one is found that complies. The following criteria need to be satisfied:

- The arc centre must lie along the reference plane.
- The arc must pass through the upstream projection of the crown cantilever, at the given elevation.
- The ends of the arc must extend to the upstream contact line at a foundation elevation, equal to, or marginally deeper than the arch elevation.

Constructing an arch which satisfies all these criteria is a trial-and-error process and may require a multi-centre arch layout. The above procedure is repeated to produce the downstream face of the arch.

Arch units are then produced for the remaining elevations by following the same process. It is important to ensure that the dam footprint is smooth and free flowing when viewed in plan, having no abrupt changes or kinks.

Final Arch Layout

The general layout of an arch dam is normally drawn from three primary viewpoints. The first drawing is a plan view showing the dam axis and various cascading arch units. The various arch unit centre points are plotted along the reference plane. Adopted standard practice indicates extrados centre points with a triangle and intrados centre points with a circle. Figure 2-16 shows a plan view of an arch dam, of which the extrados (Δ) and intrados (O) centre points for elevation 180 are plotted on the reference plane.

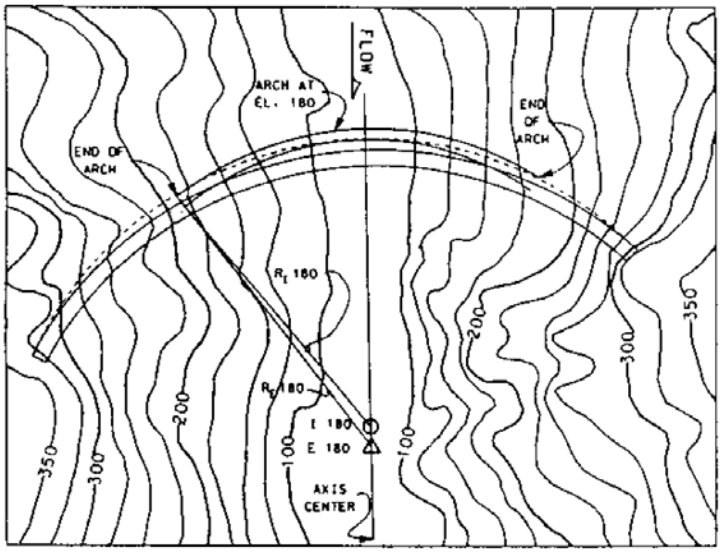

Figure 2-16: Plan view of arch dam layout (USACE, 1994)

The second drawing is an elevation section view, passing through the crown cantilever and reference plane. An example of this view is shown in Figure 2-17. The line of centres of the extrados and intrados arches are drawn in on the image. It is noted that the lines of centres are smooth lines without kinks or discrete changes in shape. The line is created by a combination of straight lines and circular arcs. The axis centre is also shown in the elevation view.

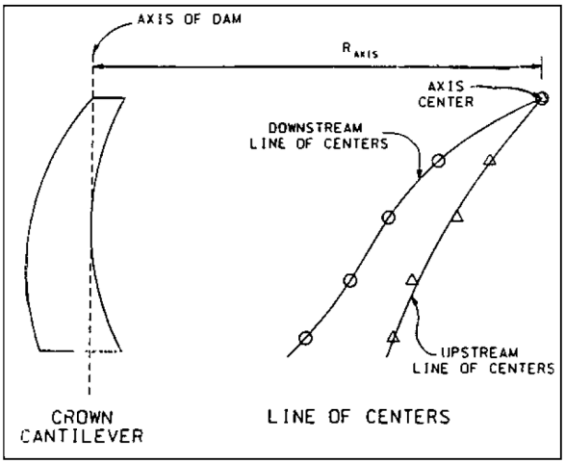

Figure 2-17: Elevation view of section passing through crown cantilever and reference plane (USACE, 1994)

The third drawing of the dam is a longitudinal profile view of the dam axis and foundation. This view constitutes a developed elevation of the dam upstream face and the foundation topography, as shown in Figure 2-18. This drawing indicates the extent of excavation required for a particular design layout. It should be ensured that the whole base of the dam fits safely below the foundation surface, whilst keeping a smooth and free-flowing form. It is undesirable to have gaps forming between dam base and foundation, as these will need special treatment.

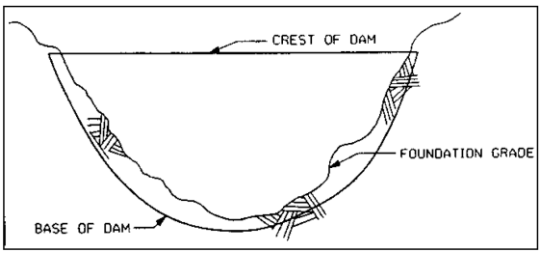

Figure 2-18: Developed longitudinal profile view of dam and foundation (USACE, 1994)

The arch dam configuration developed according to the above method, is an initial design that will require further refinement to produce the final construction design. The design refinement approach comprises an iterative sequence of structural evaluation studies of the dam, against acceptable criteria. The iterative process commences with undertaking a structural analysis of the initial dam design and revising its form according to the analysis results. The revised dam design is then analysed again, the results studied, and further revisions made. This process is repeated until a suitable arch is developed, that complies with the criteria as discussed in 2.2.4.

The structural evaluation of the dam entails ensuring the safety of the dam as per accepted design codes, publications and generally accepted guidelines established in the dam engineering fraternity. This involves ensuring the structural integrity of the dam against possible material failure or global instability. The structural integrity and safety of the dam are directly related to its response under loading and its associated capacity.

The structural response of the dam under expected loading conditions, is modelled and analysed by undertaking a stress and deflection analysis of the structure, according to the loadings. The results output by the analysis are compared to the dam design criteria. The various analysis results, should be interpreted in relation to the overall behaviour of the dam and its possible failure modes.

There are various structural analysis methods acceptable for the design of arch dams. A few of these methods are briefly discussed later.

2.2.3 Arch Dam Loadings

Arch dams may undergo a host of various loading conditions during the lifetime of the structure. The probability of the occurrence of a given loading condition, determines whether a defined load case, made up of a combination of loadings is likely or unlikely and dictates what the required design criteria will be for such load case.

Loading combinations are defined as usual (normal), unusual or extreme. Guidelines exist for typical loading combinations, but each arch dam is a unique structure and there are many factors to consider when defining loading conditions.

The typical loadings that a concrete arch dam will experience are:

- Gravity loading caused by self-weight of the dam concrete and appurtenance structures.
- Hydrostatic loading due to pressure from the contained water body.
- Uplift loading from hydrostatic pressure of water seepage under the base of the dam, or through the interface between horizontal lift joints.
- Silt loading, as a result of lateral earth pressure caused by the build-up of silt in the reservoir.
- Short-term thermal induced temperature (thermo-mechanical) loading induced by temperature gradients between core and shell of dam, arising from generation of hydration heat during concrete curing.
- Long-term thermo-mechanical loading, based on the temperature change occurring between the zero-stress temperature state (T_3) of the dam, and the minimum (winter) or maximum (summer) seasonal temperature state.
- Cyclic operational temperature loading due to changing seasonal temperature conditions.
- Seismic loading, as a result of earthquake induced ground acceleration loading of the dam and foundation system.

- Ice loads imposed on the dam body due to formation of ice layer at the surface of the dam, during winter months.
- Debris loads experienced from floating debris impounded after floods.
- Pre-stressing loads.
- Various operational loads due to aging, weathering/deterioration or chemical reaction of dam concrete such as alkali-silica reaction induced swelling, long-term creep or loss of concrete stiffness.

Different hydrostatic loadings are defined according to the various design flood water reservoir levels. Typical design flood levels may comprise full supply level (FSL), recommended design flood (RDF), probable maximum flood (PMF), safety evaluation flood (SEF) and minimum operating level (MOL). The annual exceedance probability for a selected design flood, depends on the size of the dam and its risk category in terms of consequence of failure (ICOLD, 1992).

Uplift pressure loads on the dam will differ for drained and undrained conditions. Uplift pressure is assumed to take the form of a pressure distribution at the base of the dam, the configuration of which is determined by the drain location, upstream flood level and tailwater level of the dam.

Silt loading of a concrete dam takes the form of a lateral earth pressure, caused by active wedge mobilisation of the silt material. The silt material is fully submerged by water and normally has a low internal friction angle. Typical static load diagrams of an arch dam are shown in Figure 2-19, where NWL denotes normal water level and TWL denotes tail water level.

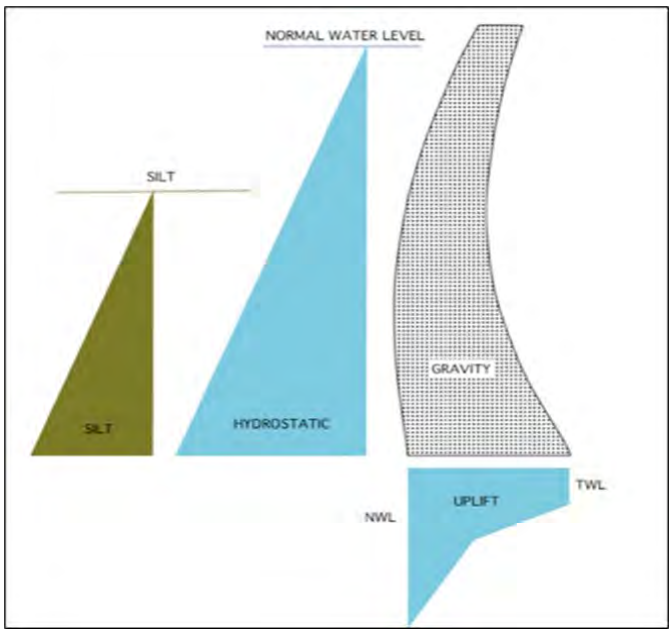

Figure 2-19: Typical static load diagrams of a concrete arch dam

Thermomechanical loading of a dam is caused by shrinkage or expansion induced movement of the dam, which is constrained by the dam foundation, and the internal structural interaction between the core and shell of the dam. Shrinkage occurs due to cooling of the concrete, and expansion arises from hydration heat generated by exothermic reaction of the concrete, during early stages of curing.

Surface gradient thermomechanical stresses develop within the shell of the dam, due to temperature differentials between the core and shell of the dam at early stages of construction. The core of the dam builds up a body of heat, while the shell (outer 2 m – 4 m) of the dam cools, due to convectional dissipation of heat into the atmosphere. Surface gradient stresses may induce tensile cracking at the surface of the dam at early stages of the dam's life, as illustrated in Figure 2-20.

Mass gradient thermomechanical stresses occur when the core of the dam cools, and the thermally stabilised shell of the dam restrains the core against shrinkage. This develops compression at the surface and tension in the core, which can result in internal cracking as illustrated in Figure 2-20.

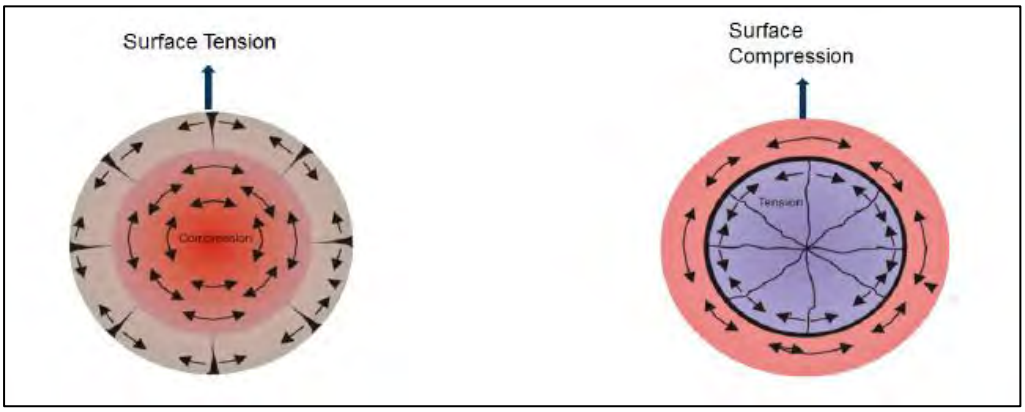

Figure 2-20: Illustration of surface gradient cracking (left) and mass gradient cracking (right) of concrete (Greyling & Zhang, 2017)

Long term thermomechanical loading occurs due to global shrinkage and expansion of the dam, caused by seasonal ambient temperature cycles of the dam. This occurs after the hydration heat of the dam has fully dissipated. The stress condition develops, due to constrained movement occurring as a result of temperature change from the zero-stress state (T_3) of the dam, to seasonal equilibrium state (T_4). Stress relaxation creep of concrete causes the zero stress state of the dam to closely coincide with the maximum temperature state (T_2), resulting in a large temperature drop occurring between zero stress state and long-term stabilised temperature state. A typical long-term temperature history plot of a concrete dam, from placement temperature (T_1) to seasonal equilibrium state (T_4) is shown in Figure 2-21.

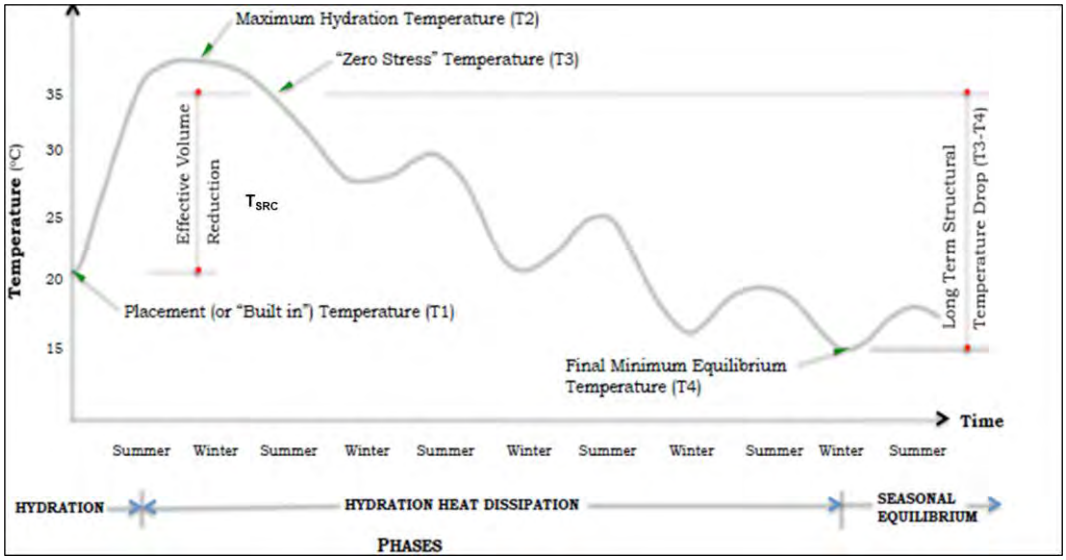

Figure 2-21: Typical long-term thermal history of a concrete dam with definition of T_1 to T_4

The long-term (operational) global temperature change of an arch dam changes the geometrical configuration of the arch structure, and effectively the associated structural load carrying capacity.

When the global temperature state of the dam decreases from the zero-stress state (T_3) to a winter temperature state (T_4), the temperature drop causes the arch to shrink, shorten its span and move forward. This forward deflection mechanism increases the radius of the arch and decreases the aperture angle, effectively reducing the load carrying capacity and efficiency of the arch. This action also causes bursting tension stresses to develop along the downstream face of the arch dam, as depicted in Figure 2-22.

A rise in temperature state of the dam arch causes an elongation of the arch, inducing an increase in the arch capacity and efficiency under static loading, due to a decrease in arch radius and increase in aperture angle. This behaviour can be seen to cause a state of pre-compression of the dam as the foundation restrains the full elongation of the arch.

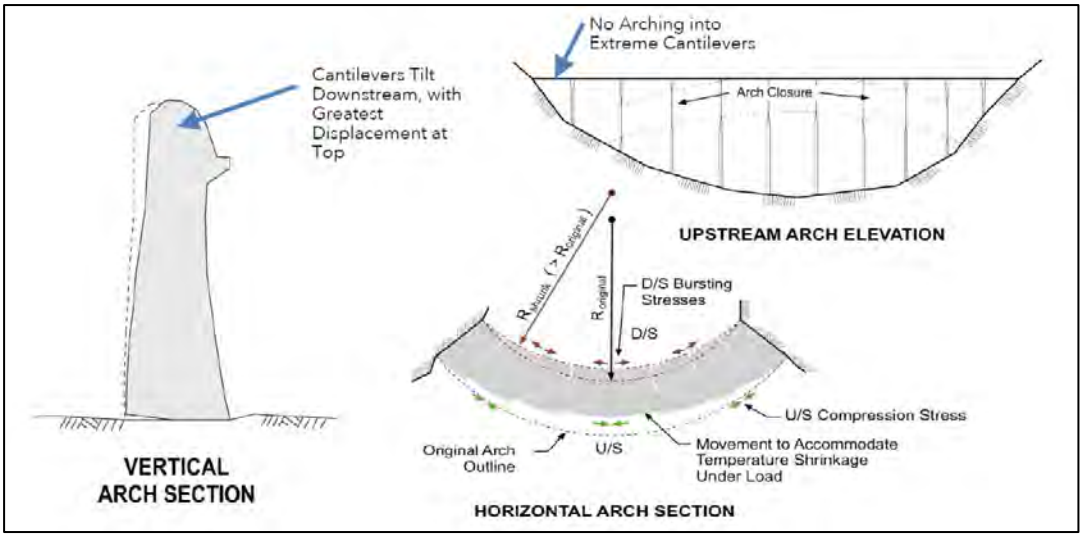

Figure 2-22: Structural behaviour of an arch dam response to a global temperature drop (Shaw, 2010)

Traditionally, arch dams have been constructed with mass conventionally vibrated concrete (CVC) placed in monolith blocks. The recent advancement in the understanding of the material behaviour of roller-compacted concrete (RCC) technology, has resulted in more arch dams being constructed with this material. Construction time of RCC dams is substantially quicker than CVC dams. The thermomechanical loading of RCC material is vastly different to that of CVC dams, and the designer should be careful not to use traditional CVC thermal design principles for RCC arch dams. The difference in thermomechanical behaviour of these materials is due to the low stress relaxation creep properties of RCC (Shaw, 2010). It has been shown that generally the low stress relaxation creep properties of RCC, increases surface gradient stresses during construction stages of the dam and decreases mass gradient stresses during operation of the dam.

The operating temperature loading of a large concrete dam is cyclic, and follows seasonally induced changes in temperature conditions imposed on the dam. The increase and decrease of the dam temperature state as the thermal conditions change between Summer and Winter, induce a conductive sinusoidal time-varying heat transfer through the dam, between the outer faces and the core. This operational heat transfer mechanism is independent of heat of hydration generated during curing of the concrete and will continue to occur after complete dissipation of hydration heat energy.

The operating temperature state of the Katse Dam body at elevation 1997.5 mASL, is shown in Figure 2-23. The suite of sinusoidal curves depicts the temperature state at various locations, along the thickness of the dam profile. The temperature state at the core of the dam is relatively stable, whilst at the upstream (US) and downstream (DS) face, temperatures approximately follow the temperature conditions of the water reservoir and atmosphere (ambient temperature).

The impact of solar radiation is noticeable, as the downstream face temperature state is marginally higher than the ambient temperature. The lag between the sinusoidal temperature curve at the core and at the faces of the concrete dam can be seen due to the thermal buffer created by the concrete material, which has a relatively low thermal diffusivity value. The low variation between the Summer and Winter temperature state of the reservoir and upstream face, is due to the relatively high specific heat capacity of water in relation to the atmosphere (air).

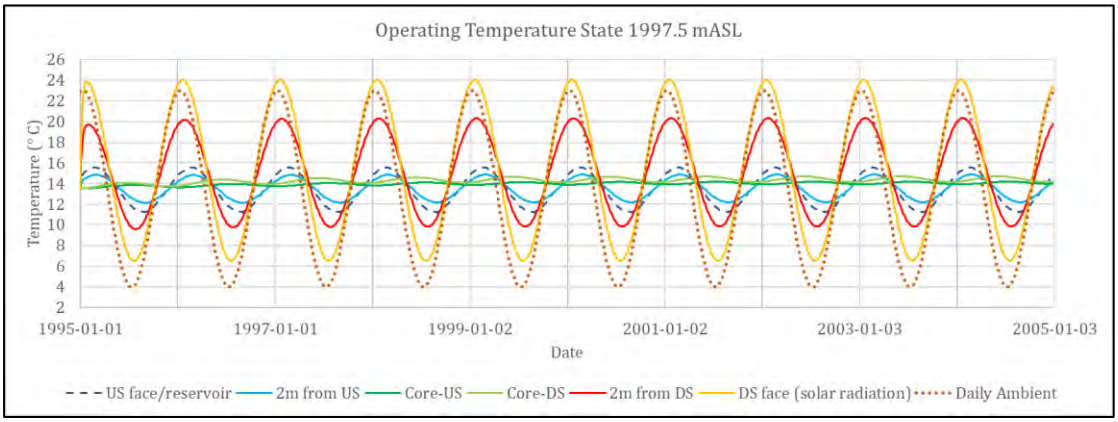

Figure 2-23: Katse Dam operating temperature state at elevation level 1997.5 mASL

Large dams are not inherently safe against earthquake hazards, and in the Southern African context, significant earthquakes that can impact the safety of dams have occurred and will continue to occur in the future (Kijko *et al.*, 2023). Large South African dams should be evaluated against seismic hazard using state-of-the-art methods that have surpassed outdated methods accepted prior to 1989 (Wieland, 2023), when ICOLD first released guidelines on seismic hazard analysis of dams (ICOLD, 1989).

Seismic loading of dams is induced by ground accelerations from earthquake events that may occur in the near vicinity of the dam. Seismic loading of a dam is often a critical loading condition, especially when the dam site is in an active seismic zone or near active geological faults. The magnitude of seismic loading of a dam is indicated by the site-specific PGA (peak ground acceleration), expected to occur for different earthquake event return periods.

The PGA of a dam site is obtained from seismic survey maps or from the results of a site-specific PSHA (probabilistic seismic hazard assessment). A PSHA considers the regional historical earthquake events and tectonic behaviour or fault conditions of the site, and implements statistical models to determine the expected PGA, and an associated site-specific design response spectrum, for a range of interested earthquake event return periods. PGA values and response spectra curves are of significance in dam design for the OBE (operating basis earthquake) and SEE (safety evaluation earthquake) events (ICOLD, 2010).

Earthquake induced seismic acceleration signals trigger a complex dynamic response of the dam, according to its dynamic (mass, stiffness and damping) characteristics. The dynamic response of the dam is directly related the mass and stiffness of the dam-foundation-reservoir structural system, and results in a complex time-based application of inertia and hydrodynamic forces.

A rise in temperature state of the dam, during a low reservoir level condition is not favourable under earthquake loading. The seismic induced ground acceleration forces acting in the upstream direction, will load the arch from the unfavourable side inducing tension along the axis and cause possible opening of dam monolith joints. Opening of joints under seismic loading may cause the dam arch to lose its monolithic behaviour, which will allow each monolith to behave as an independent cantilever structure, compromising the arch action of the dam.

A list of typical dam loading combinations is shown in Table 2-2. This list is not exhaustive, and unique circumstances may arise for a dam requiring additional load cases to be formulated to account for these. The temperature load cases indicated in the table refer to long-term temperature drop from zero stress state (T_3) to the winter (T_{4min}) and summer (T_{4max}) temperature state, after full dissipation of concrete hydration heat.

Table 2-2: Typical arch dam loading combinations

Load Condition	Gravity	Hydrostatic	Uplift	Silt	Thermal	Seismic	Ice
Usual	Yes	FSL	Drained	Yes	No	No	No
Usual	Yes	FSL	Drained	Yes	$T4_{min}$ - T3	No	No
Usual	Yes	FSL	Drained	Yes	$T4_{max}$ - T3	No	No
Unusual	Yes	Empty	N/A	Yes	No	No	No
Unusual	Yes	FSL	Undrained	Yes	No	No	No
Unusual	Yes	Empty	N/A	No	$T4_{min}$ - T3	No	No
Unusual	Yes	RDF	Drained	Yes	No	No	No
Unusual	Yes	FSL	Drained	Yes	No	OBE	No
Extreme	Yes	PMF	Drained	Yes	No	No	No
Extreme	Yes	FSL	Drained	Yes	No	MCE	No

*FSL – Full Supply Level

**RDF – Regional Design Flood

***PMF – Probable Maximum Flood

A comprehensive discussion of the modelling of loadings in the analysis of dams using the FE method is given in Section 4.

2.2.4 Dam Design Criteria

Design criteria of arch dams ensure that there is a sufficient factor of safety in the design of the concrete structure. The design criteria specify the stress allowed to develop in the dam according to the various loading conditions, and the associated risk or probability of occurrence. The design stress criteria are based on the compressive strength (f_c) of the concrete, adjusted by the relevant factor of safety for the loading condition.

There is no generally accepted South African arch dam design code and the engineering manuals or design guidelines published by ICOLD, USACE, USBR, and FERC have been adopted as suitable for developing a design philosophy. ICOLD Bulletin 61 (1988), states that due to existence of various evolving criteria developed by technical institutions throughout the world, there can be no definitive criteria to be followed rigidly by dam designers. Concepts and philosophies published in the guidelines should be considered by dam designers in light of the specific conditions of the dam, and not simply applied without discrimination. The dam designer will define criteria according to experience of similar dam design problems.

Typically design criteria of a concrete arch dam comprise allowable compressive strength (f_c), allowable tensile strength (f_t) and a minimum required limit equilibrium sliding FOS (factor of safety). Various design guidelines may use different symbols to present these criteria.

The required compressive strength of the concrete is determined from the structural analyses of the dam. A mix design should be selected so that the characteristic strength exceeds the required strength. Arch dams are designed to not utilise steel reinforcing for strength enhancement, and therefore the concrete may be seen as mass concrete. Arch dams however rely predominantly on the strength of the concrete and only a lesser extent its mass, for load bearing capacity.

The design criteria guidelines proposed by the USACE are shown in Table 2-3. The static compressive strength (f'_c) refers to the results from a static concrete cylinder test. The compressive strength of normal strength concrete, based on a cylinder test, is normally 80 % of that taken from a cube test of the same concrete (Neville, 2011).

The dynamic compressive strength (f'_{cd}) of concrete is strain rate sensitive and is thus higher than the static compressive strength (f'_c), under high strain rate loading conditions, as experienced under earthquake induced seismic loading, of concrete dams. The dynamic compressive strength (f'_{cd}) of concrete, should be derived from laboratory tests done assuming strain rates similar to expected seismic loading. Typically, the dynamic compressive strength of concrete is 30 % higher than the static value (ACI 207.1R-96, 1996).

The static tensile strength (f'_t) may be obtained from a direct tension test, splitting tension test or a modulus of rupture test. The direct tension test gives the most accurate uniaxial tensile strength but is prone to challenges in execution. The splitting tension test is the easiest test to perform and gives consistent results. The modulus of rupture test calculates the tensile strength, assuming linear elastic theory of the tested beam specimen. It is proposed that the modulus of rupture test is best suited, as it is consistent with the linear elastic material behaviour assumed in analysis of arch dams.

The tensile strength of concrete is also strain rate dependant, and thus the dynamic tensile strength (f'_{td}) is assumed to be 50 % higher than the static tensile strength (f'_t) (Raphael, 1984).

The limiting factor in the design of concrete arch dams is normally the tensile strength, and tensile stresses are largely avoided by shaping and designing the dam for a smooth load transfer. The development of local zones of tension in an arch dam, especially at the heel of the dam, may not be problematic as tensile cracking and associated forming of local hinges, causes the load to re-distribute and be taken up by the compression in the arch (Cassells & Wright, 2023).

If extensive tensile cracking occurs in the dam, excessive plastic deformation of the cantilevers may result in overloading of the arches, and subsequent failure in compression from crushing of the concrete arches. Assuming a competent foundation, compression failure is the primary mode of failure of an arch dam, and it is for this reason that a material factor of safety of four is considered to establish the allowable compressive strength (f'_c). The allowable design strengths for concrete arch dams as shown in Table 2-3, are therefore derived on the basis of the primary failure mode of an arch dam.

Table 2-3: Arch dam design criteria (USACE, 1994)

Load Condition	Allowable Compressive Stress (f_c)	Allowable Tensile Stress (f_t)	Minimum Required Sliding Factor of Safety
Static Usual	$f'_c/4.0$	f'_t	2.0
Static Unusual	$f'_c/2.5$	f'_t	1.3
Static Extreme	$f'_c/1.5$	f'_t	1.1
Dynamic Unsual	$f'_{cd}/2.5$	f'_{td}	1.3
Dynamic Extreme	$f'_{cd}/1.5$	f'_{td}	1.1

The design criteria of concrete arch dams proposed by the USBR are shown in Table 2-4. The USBR design factors of safety are more conservative than those of USACE, when considering sliding stability, but more liberal in terms of the allowable material strengths. The USBR design

manual requires a post-earthquake cracked section analysis to be undertaken, to evaluate the stress state of the cracked section against criteria.

Table 2-4: Arch dam design criteria (USBR, 1977)

Load Condition	Allowable Compressive Stress (f_c)	Allowable Tensile Stress (f_t)	Minimum Required Sliding Factor of Safety
Static Usual	$f'_c/3$	f'_t	3.0
Static Unusual	$f'_c/2$	f'_t	2.0
Static Extreme	$f'_c/1$	f'_t	1.0
Dynamic Unsual	$f'_{cd}/2$	f'_{td}	1.0
Dynamic Extreme	$f'_{cd}/1$	f'_{td}	1.0

FERC proposes that the design of new dams follow the guidance and criteria published by USACE and USBR. FERC however proposes less conservative factors of safety for deriving allowable stress and stability criteria, of existing dams as shown in Table 2-5. This is testament to the wide spectrum of design criteria published for arch dams and how important it is that a dam designer consider the unique conditions of the dam, and lessons learnt from past experience, when selecting dam design criteria.

Table 2-5: Arch dam design factors of safety for existing dams (Federal Energy Regulatory Commission, 1999)

Load Condition	Compressive Strength	Tensile Strength	Internal Shear Strength	Sliding Stability
Usual	2.0	1.0	2.0	1.5
Unusual	1.5	1.0	1.5	1.5
Extreme (seismic)	1.1	1.0	1.1	1.1

2.2.5 Foundation Design Criteria

While a basic concept of each dam type requiring certain minimum foundation properties certainly holds true, each foundation should be measured on its own merits (Davis, 2010). There is no universally defined founding criterion applicable to all situations.

Generally concrete dams, especially concrete arch dams require rock foundations. Two primary criteria to be considered for concrete arch dams, are the strength and deformability of the foundation rock mass. The rock mass is required to have sufficient compressive and shear strength to resist failure by rupture, and sufficient deformation modulus to prevent excessive deformations (Bieniawski & Orr, 1976).

The existence of faults and highly fractured/clay lineations within a rock mass foundation, may collectively result in the formation of joint-bound rock wedges within it. Unfavourable orientation of the dip angle and azimuth, of these low strength interfaces, may potentially cause the formation of kinematically free rock wedges. The stability of these rock wedges should be evaluated under dam loading and stabilisation measures considered if necessary (Cassells & Roberts, 2017).

Allowable foundation design strength and stability safety factors according to USACE and USBR guidelines are shown in Table 2-6. According to the USBR, higher safety factors are normally assumed for foundation material as there is a greater amount of uncertainty involved in assessing the load-resisting capacity, when compared to that of concrete material. The USACE guidelines, do not specifically define FOSs for foundation design strength criteria, but simply propose that the compressive strength of rock should be tested, and be sufficient to resist thrusting of the dam into the abutment.

Table 2-6: Arch dam foundation design criteria (USACE & USBR)

Load Condition	Required Design Strength FOS		Required Sliding Stability FOS	
	USACE	USBR	USACE	USBR
Static Usual	N/D	4.0	2.0	3.0
Static Unusual	N/D	2.7	1.3	2.0
Static Extreme	N/D	1.3	1.1	1.0
Dynamic Unusual	N/D	2.7	1.3	2.0
Dynamic Extreme	N/A	1.3	1.1	1.0

According to the USACE design guidelines, if the elastic moduli of arch dam foundations are less than 3.5 GPa, consolidation grouting should be considered for improvement of foundation deformability, and extensive testing done to evaluate impact of improvement.

According to Romana (2003), the minimal sure elastic modulus value required for the foundations of an arch dam is 5 GPa. This is not without problems, as there are reported cases of arch dams founded on rock masses with elastic modulus greater than 5 GPa, of which some of these problems include cracking of the dam.

Chinese dam designers are using consolidation grouting, together with the optimisation of structural interaction at the dam-foundation interface, to achieve harmonisation of the arch dam and foundation. By following these design methods, the Chinese engineers are building dams on rock mass foundations with very low deformation moduli. The Ertan dam is a 240 m high

concrete arch dam successfully built on rock mass foundations with an elastic modulus ranging from 1 GPa to 3 GPa (Qixiang *et al.*, 2015).

To South African dam designers these values may seem quite low, but due to the frequent incidence of favourable geotechnical conditions, South African dams have been built in accordance with quite conservative foundation design conditions (Shaw, 2017). According to Van den Berg and Parrock (2009), large concrete dams with a height above 60 m need to meet the minimum criteria as shown in Table 2-7.

Table 2-7: Foundation design criteria for large concrete dams with height above 60 m (Van den Berg & Parrock, 2009)

E Mod (GPa)	RMR	RMR Components				
		Weathering Grade	UCS (MPa)	RQD (%)	Joint Spacing (mm)	Joint Condition
> 4.5	> 40	Moderate to slightly	20 – 40	> 30	300	Rough, hard

The RMR (Rock Mass Rating) system has gained widest acceptance amongst dam engineers and is generally adopted. The extent of deformability problems experienced by concrete arch dams, in relation to the foundation RMR and height, are shown in Table 2-8 and range from normal to very serious problems.

The RMR value is based on six rock mass parameters readily determined in the field being UCS (unconfined compressive strength) of intact rock, RQD (rock quality designation), spacing of discontinuities, condition of discontinuities, ground water conditions and orientation of discontinuities (USACE, 1994).

Table 2-8: Extent of deformability problems in concrete dams according to RMR value (Romana, 2003)

Dam Height (m)	RMR Value		
	Normal	Problems	Serious Problems
< 100	>45	35 – 45	<35
100 – 150	<60	45 – 60	<45
150 - 200	<70	55 - 70	<55

Various published recognised methods are available for determining the elastic modulus of rock mass, in terms of the derived RMR value. The mathematical correlation proposed to determine the elastic modulus from the RMR value is shown in Equation 2-18 (Serafim & Pereira, 1983).

$$E = 10^{\frac{(RMR-10)}{40}} \qquad \textbf{2-18}$$

Where

E = elastic modulus (GPa)

RMR = Rock mass rating

As a design criterion, the deformability of the rock mass foundation should not be evaluated in isolation. A varying deformation modulus of rock mass along the axis of the dam base, may present design problems. A stiff loaded concrete arch dam, founded on a rock mass with a varying deformation modulus, may result in the development of high tensile stresses at the base of the dam. This is caused by bridging of the flow of minor principal stresses over low deformation modulus rock mass zones, as shown in Figure 2-24. These issues can be overcome by excavation of local "soft" regions of the foundation and replacement with dental (foundation replacement) mass concrete, foundation improvement by consolidation grouting or designing for local zones of high strength fibre reinforced concrete, with high tensile strain capacity.

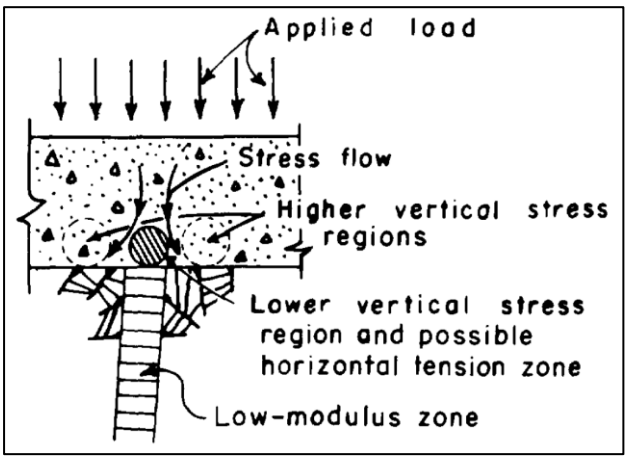

Figure 2-24: Bridging mechanism causing minor principal stress flow over low deformation modulus zone (USBR, 1977)

The deformability of the foundation rock mass should be considered in relation to the elastic modulus of the dam concrete. A classic reference for concrete dam designers when considering foundation suitability for arch dams, is to derive a ratio of the dam elastic modulus (E_c) over the foundation elastic modulus (E_f). The influence of the foundation on dam behaviour and the extent of anticipated problems in accordance with this ratio, is shown in Table 2-9 (Rocha, 1965). It can be seen from the E_c/E_f values in the table, that arch dams with a low E_c/E_f value are not as highly influenced by the deformability of the foundation, as may initially be assumed.

Table 2-9: Effect of E_c/E_f on arch dam behaviour (Rocha, 1965)

E_c/E_f	Influence on Dam	Deformability Problems
< 1	Negligible	None
1 – 4	Low importance	None
4 – 8	Moderate importance	Minor
8 – 16	High importance	Serious
> 16	Special measures	Very dangerous

The influence of the deformability of the foundation on the state of stress of an arch dam, is only significant for E_c/E_f ratios of 4 and greater. Assuming early tests of rock mass foundations indicate an elastic modulus well above 10 GPa, and based on an assumption that the elastic modulus of concrete will not realistically be more than 40 GPa, further high cost, large scale in situ tests of the foundations, should not be necessary as a more accurate E_f will not influence the design of the arch dam (Oliveira, 1990).

Although ideal founding conditions for arch dams comprise a narrow river valley with stiff rock mass formations, several arch dams have been successfully built in wide valleys and on rock foundations with a relatively deformable nature (Swaminathan, 1965).

2.2.6 Structural Analysis

Design of an arch dam is not a closed form solution and therefore analysis is an integral part of the design procedure. Mathematical analyses are used to determine stresses/strains and deflections in the structure due to loads. The design is accomplished by following an iterative process of alternatively modifying the structure geometrically and checking the results, until the design objective is satisfied within the design criteria (Jansen, 1988).

The technology of arch dam analysis has progressed much since the birth of analysis of arch dams in the early 1900's in the USA (ICOLD, 1988). Before the birth of analysis of arch dams, designers were aware of the advantages provided by an arch shape structure loaded into compression but were not able to calculate stresses in arch dams. Very early arch dams were designed as gravity structures with the curve adopted purely to enhance the safety of the dam, from a non-measurable qualitative perspective.

Since the 1900's various structural analysis methods have been used to design arch dams. The progressive advancement in application of scientific and mathematical technology, has caused the sophistication and accuracy of these methods to increase, allowing for the design of larger and more efficient arch dams, previous thought to be impossible.

Essentially analysis undertakes to model the dam according to the geometrical configuration of the structure and support, its material stiffnesses, suitable boundary conditions and anticipated loadings. This is normally achieved by deriving simultaneous equations, based on first principles and fundamental concepts, being equilibrium of forces and compatibility of displacements. The complexity and accuracy of the modelling technique is based on its ability to accurately simulate the mechanisms of the constrained, loaded, non-rigid (flexible) dam.

In the early days of arch dam design, very basic and conservative design methods were adopted for arch dam design. The arch dam was simply analysed assuming thin cylinder (ring) theory, as derived by French mathematician Louis Navier in 1826 and commonly referred by dam engineers as Cain's arch formula. The free body diagram of a loaded thin cylinder is shown in Figure 2-25. The required thickness of the arch is calculated from Equation 2-19.

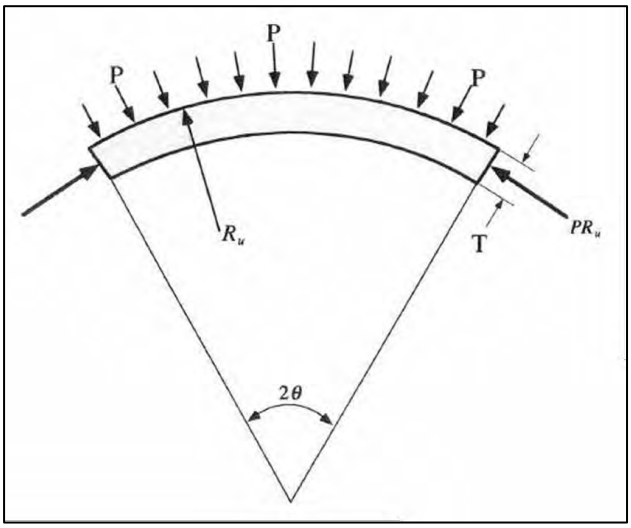

Figure 2-25: Free body diagram of Louis Navier's thin cylinder structural theory

$$T = \frac{PR_u}{f_c} \qquad \textbf{2-19}$$

Where

T = arch thickness (m)

P = water pressure (Pa)

R_u = arch radius (m)

f_c = allowable compressive strength

This approach assumes the loaded arch to be supported at the abutment ends by pin supports, developing pure uniform compressive stress along a unit height section of the arch, at a given elevation level. The arch structure is designed as a vertical array of independent cascading thin

cylinder structures, not interacting with each other, and each transferring compressions to the abutment supports. The compressive stress at a point in the arch is related to the hydrostatic water pressure load at that level, which is a linear function of depth below water surface. This method does not consider bending moments along the horizontal arches nor cantilever action across the arches.

This conservative approach was deemed acceptable as designers were wary of the fact that many unknowns existed, due to the complex nature of a loaded arch. The calculated compressive stress of the loaded dam was evaluated against a given concrete/masonry characteristic strength, reduced by an acceptable factor of safety. This method is sometimes still deemed suitable for initial studies of simple single-curvature, constant radius arch dams of modest height.

Other design methods used in the early days of arch dam design, comprised analysing models according to thin membrane theory, or building physical scaled models, for testing and analysis in a hydraulic laboratory. Thin membrane theory assumed that a catenary chord suspended from two supports, will hang and form a curved profile to allow the entire chord to be in tension. Similarly, a planar sheet or rubber membrane hung from a series of supports will also find its most efficient form.

According to Allen et al (2016), a structure with funicular form can take a form that follows the flow of tension forces. A three-dimensional shell can carry a wide range of forces through membrane behaviour without bending. If the funicular shaped membrane structure is turned upside down and all the tension forces reversed, equilibrium is preserved and the tensile stresses become compression stresses (Da Silva & Julio, 1995). Assuming an inverted funicular structure has an zero bending stiffness, this condition would be true, and the arch will only develop compressions within it. Due to flexural stiffness some bending will be induced under load, especially at the supports.

The membrane method entails deriving the most efficient arch shape by hanging a rubber membrane to span across a 90°-rotated model of the dam river valley, with the streambed direction aligned to the vertical, and loading it with a linear increasing load distribution to simulate hydrostatic water loading.

A unique South African approach to the membrane method of analysis, not to be confused with the FE method is the mesh model method (Myburgh, 1960). This method involves creating a mesh of perpendicular wires, stretched, and hung across a model of the foundation valley, applying simulated hydrostatic and gravity loads at the nodes of the mesh. The shape taken up

by the mesh, is measured and considered to embody the optimum condition of compressive equilibrium.

The current main existing analysis methods for the arch dam are the trial-load and FE method (Ren *et al.*, 2009). The complete trial-load method developed in the 1920's, is based on the concept that an arch dam is composed of a system of horizontal arches and vertical cantilevers (ICOLD, 1988) as shown in Figure 2-26.

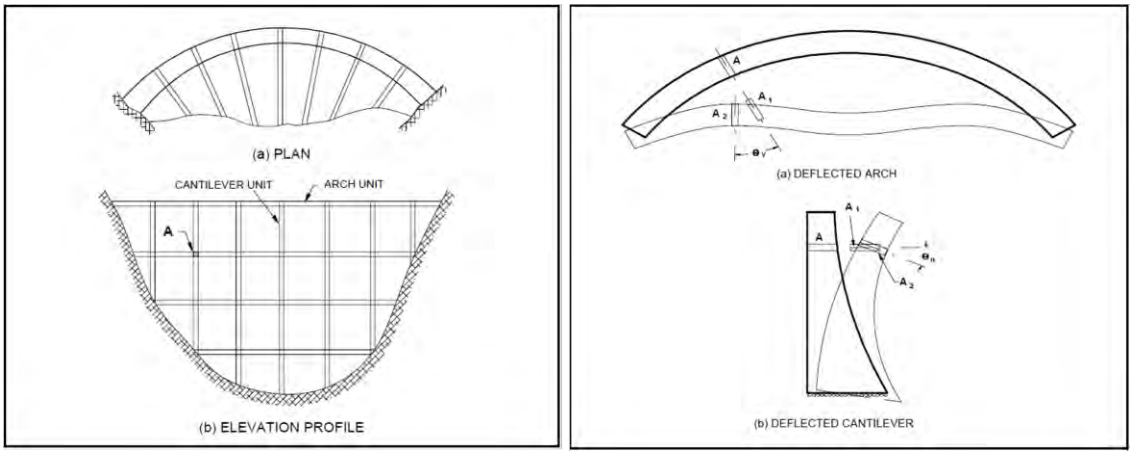

Figure 2-26: Arch and cantilever units (left) and their deformations (right) as derived from trial load method

The stresses and deflections of the individual elements are calculated by means of the usual elastic arch and beam formulae (Karnovsky, 2012). It is assumed that the water load is divided between the arch and cantilever systems, and that each carries a proportion of the load and the deflections of the two systems due to radial, tangential and twist loadings are equal. The distribution of the load is such to cause equal arch and cantilever deflections in the tangential, rotational and radial directions.

The solution to the overall arch structure problem can be inferred from Kirchoff's uniqueness theorem which states the following (Love, 1906):

- The elastic properties of the body must be expressible in terms of elastic modulus and Poisson's ratio;
- If a volume of body is divided into small elements by passing through a series of intersecting planes or surfaces, each formed element will be in equilibrium under forces and stresses acting on it;
- Each element that undergoes deformation due to internal stress development from loading, will continue to be compatible with its neighbours on all sides;
- Stresses or displacements at boundaries of the body must conform to the stresses or displacements imposed on it.

Earlier more simplistic methods loosely referred to the trial-load method, are the crown cantilever analysis method and the radial deflection analysis method. Shortcomings of these methods are that they do not consider the effects of tangential shear and twist, on deformation of the dam. The difference between these two methods being that the crown-cantilever method aligns the radial deflections of arches and cantilevers only at the crown cantilever, whilst the radial deflection method considers compatibility of radial deflection at arch quarter points.

The FE method is the most comprehensive and technologically advanced analysis method for arch dam design. It is the current state-of-the-art for advanced analysis of concrete arch dams, and it is often considered the real breakthrough for arch dams (Shaw, 2015). Whilst this method was developed in the 1960's, the application of the FE method continues to develop today in terms of commercial availability of FE analysis software, advances in PC processing power for large models, efficient modelling tools and techniques, accessible graphic user interfaces and powerful post-processing and reporting of analysis outcomes.

The FE method is a numerical modelling approach, whereby a complex structural body is divided into an equivalent system of smaller bodies or units (finite elements), interconnected at points (nodes) common to two or more elements and/or boundary lines or surfaces (Logan, 2019).

In terms of arch dam analysis, the dam and foundation geometry structure are modelled into a system of interconnected elements, as shown in Figure 2-27, which illustrates one half of an FE model developed during the early stages of the FEA technology. The elements are connected by nodal points and related to each other in terms of the fundamental compatibility and force equilibrium equations, applied in terms of the nodal continuity. Loadings of the dam are applied as nodal forces and boundary conditions as nodal constraints. The behaviour within each element, is modelled according to displacement shape (interpolation) functions that incorporate the constitutive behaviour and geometric shape of the element.

Other numerical modelling techniques available for analysis of arch dams are the finite differences method and variational method. The discussion of these is beyond the scope of this study. A comprehensive account of the FE method is provided in Section 2.5 of this dissertation.

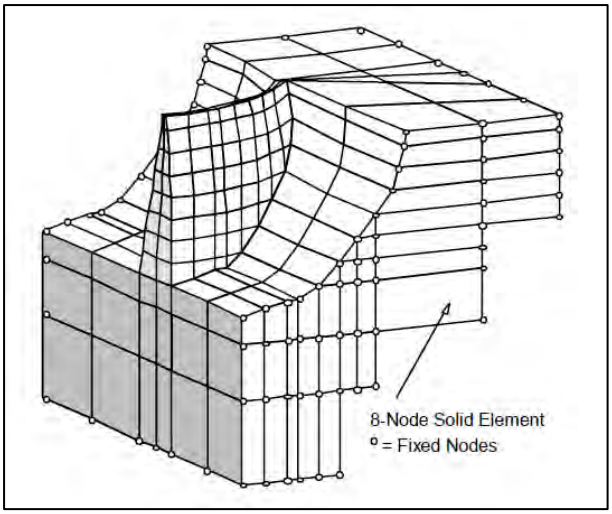

Figure 2-27: Perspective view of a dam-foundation FE model developed using early technology (Federal Energy Regulatory Commission, 1999)

2.2.7 Structural Behaviour of Arch Dams

Traditionally, loaded arch dam structures have been described to behave as a an interlinked and interacting system of elementary beam and arch units. Although this approach is currently seen as outdated, the analogy is useful in distinguishing the extent to which a dam relies on horizontal load transfer, to ensure its structural integrity.

More specifically, the beam elements behave as vertical cantilevers partly fixed at the base of the dam, supported/propped by a series of elastic springs on the downstream side, and loaded on the upstream side by a linear hydrostatic pressure. Effectively the elastic springs that prop the cantilevers model the non-rigid support provided by the stiffness of the crossing arches.

The vertically cascading series of arch elements span horizontally, are supported at the foundation abutments, orientated with the convex side on the upstream face, and loaded by hydrostatic pressure which is uniform along a given arch span. The arch units near the base of the dam behave as short arches with high bending stiffness and partly fixed at the supports. The arches near the crest of the dam behave as longer spanning arches with less bending stiffness, and pinned at the abutment supports. Arches with less bending stiffness and more curvature, are more inclined to transfer load as compressive thrusts along the axis, rather than bending moments.

The structural behaviour of any loaded arch dam is assumed to entail a combination of cantilever and arch action, to transfer loads to the foundation as shown in Figure 2-28. The geometrical configuration and stiffness of the dam and foundation, will dictate how the internal forces that develop in the loaded dam, pass into the foundation. Strict cantilever action results in vertical load paths and strict arch action in horizontal load paths. Effectively most internal

force transfer occurs as a hybrid across both cantilever and arches, and the arch dam structural mechanism is seen to be more representative of a loaded shell.

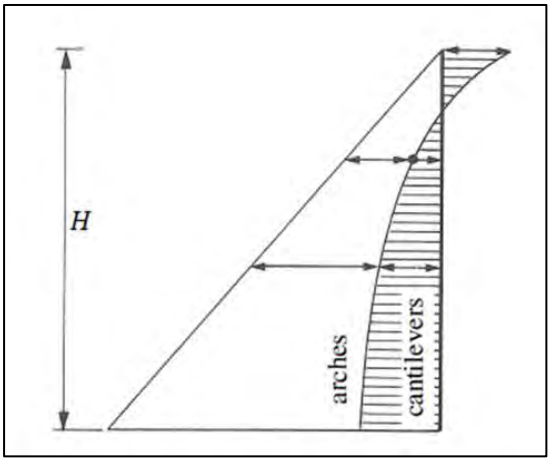

Figure 2-28: Hydrostatic load distribution between cantilever and arch action (Schleiss & Pougatsch, 2022)

The typical structural function of a hydrostatically loaded arch dam is shown in Figure 2-29. The principal compression stress vectors indicate the primary thrust or load transfer of the dam structure. The internal principal compressive stress state of an arch dam varies according to the shape of the foundation valley and the associated design formation.

Essentially an arch dam exuding greater arch curvature and more flexible cantilevers will transfer a greater portion of stress horizontally. Alternatively, an arch dam formed with stiff cantilevers and arches with less curvature, will transfer a greater portion of stress vertically into the foundation.

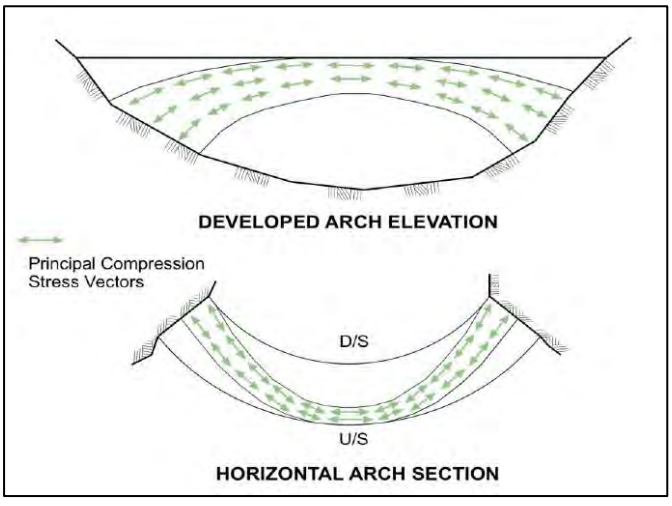

Figure 2-29: Primary load transfer mechanism depicted by principal compressive stress vectors (Shaw, 2015)

In arch dam design the fundamental means by which the structural performance of a concrete arch is evaluated is according to the pattern of biaxial, principal stresses under hydrostatic

loading (ICOLD, 2024). The principal stress pattern describes definitively how the structure transfers load from the impounded water into its foundation, while the magnitude of these stresses are used to determine the required concrete strength. The efficiency of the structural function can be evaluated, by plotting the biaxial principal stress vectors on the upstream and downstream faces, and along horizontal sections as shown in Figure 2-30.

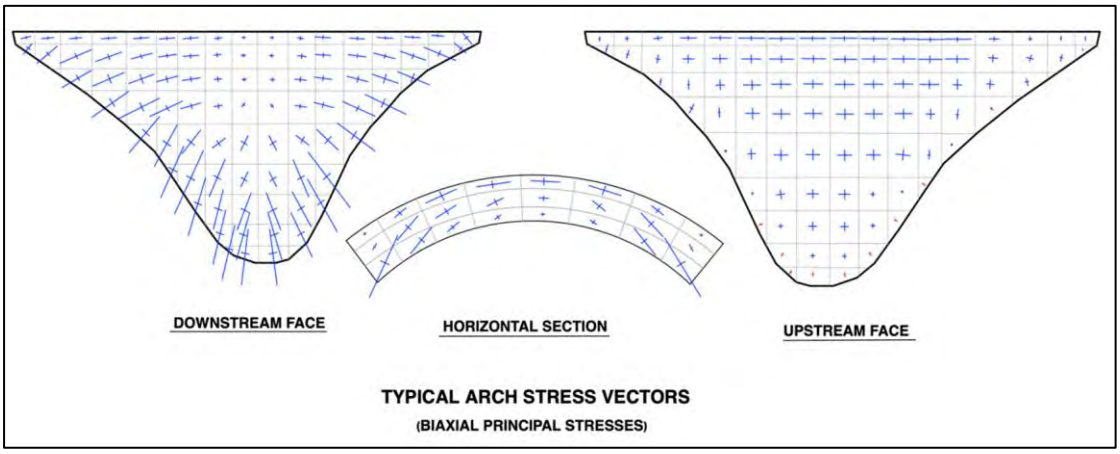

Figure 2-30: Biaxial principal stress vectors in an arch dam under normal loading conditions (ICOLD, 2024)

Minor principal stress vector results from FE analyses undertaken on 8 varying arch/gravity dams of different heights, spans, curvature, thickness and foundation conditions are presented, indicating the variance in stress transfer of these structures according to the different forms. The FE analysis results are taken from existing dams for which the author was involved in the analysis and design.

The minor principal stress directions of a variable thickness arch (dam 1) constructed in a narrow V-shaped valley with a CL:H value of 1.8, are shown in Figure 2-31. The stress vector plot on the downstream face of the dam, at the centre of the arch, show that the top 2/3 of the dam height transfers load horizontally by arching, into the abutments. The lower 1/3 of the dam, near to the base is shown to transfer load by vertical stresses. It can be seen from the minor principal stress vectors on the upstream face, that horizontal arch action is evident over virtually the full height of the dam.

The thrust drop from central arching to abutments, depicts a uniformly perpendicular angle of incidence between the minor principal stress vector and the abutment face. This shows that the arch form is efficient, and that it maintains an effective distribution of balanced stresses along the dam abutment.

Although the variable arch dam thickens towards the base making the cantilevers inherently stiffer at the base, the dam is a variable radius, multiple-centred arch meaning that the lower

arches have more curvature inducing considerable horizontal stress transfer in the lower portion of the dam.

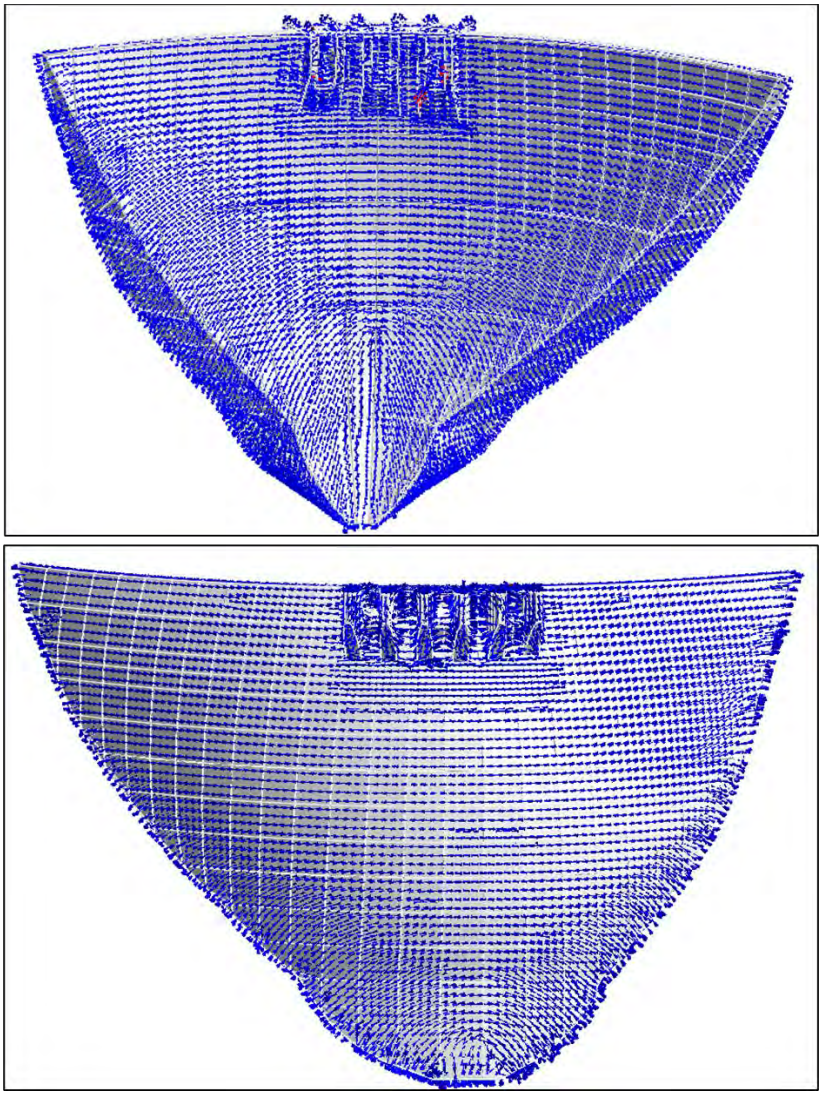

Figure 2-31: Dam 1 minor principal stress distribution on downstream (top) and upstream (bottom) face of arch dam with narrow V-shaped valley foundations

The minor principal stress direction vectors of a thin arch (dam 2) constructed in a wide V-shaped valley with a CL:H value of 4.3, are shown in Figure 2-32. The stress distribution on the downstream face, at the centre of the arch, show that the top 60 % of the dam height transfers load horizontally by arching, while the lower 40% of the dam transfers load by vertical stresses. It can be seen from the minor principal stress compressions on the upstream face, that horizontal arch action is evident over virtually the full height of the dam.

Whilst the CL:H ratio of dam 2 is substantially higher than that of dam 1, dam 2 is a thin arch with flexible cantilevers resulting in a low vertical stiffness at the base and subsequent transfer of loads horizontally. This is a very efficient structure with high dependence on foundation competency.

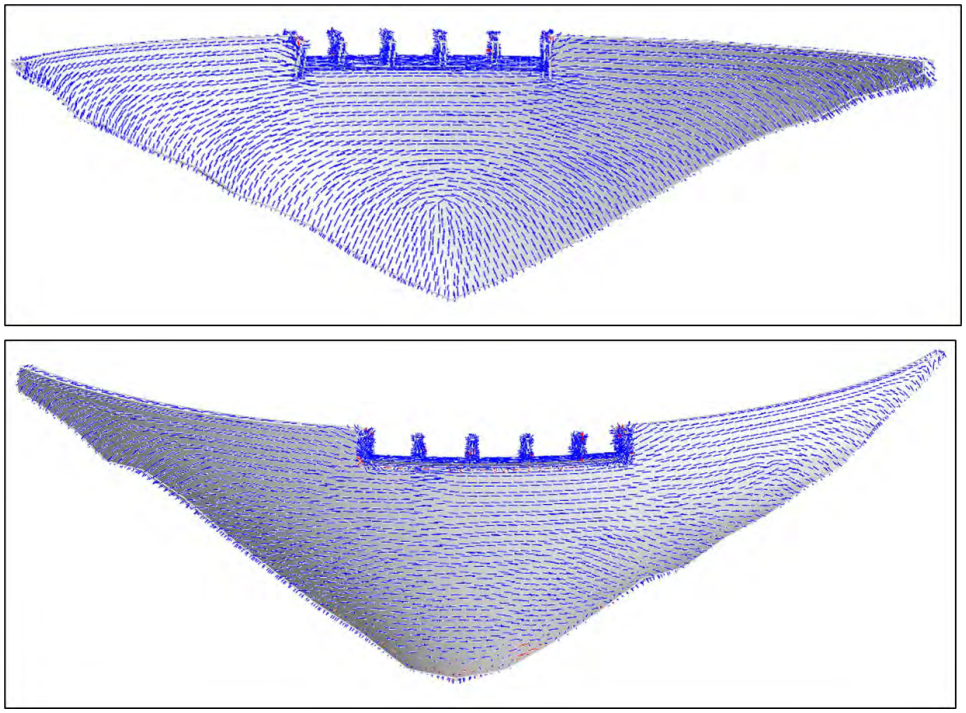

Figure 2-32: Dam 2 minor principal stress distribution on downstream (top) and upstream (bottom) face of arch dam with wide V-shaped valley foundations

The minor principal stress vectors of two single-curvature arches (dam 3 and dam 4), constructed in a narrow U-shaped valley with a CL:H value of 3.8 and 4.2, are shown in Figure 2-33 and Figure 2-34. The stress distribution on the downstream face, at the centre of the arch, show that the top 50 - 55 % of the dam height transfers load horizontally by arching, while the lower 50 - 45% of the dam transfers load by vertical stresses. It can be seen from the minor principal stress compressions on the upstream face, that horizontal arch action is evident over the top 80 – 90 % of the dam height.

Granting that the CL:H ratio of dams 3 and 4 are similar to dam 2, the valley is wide at the base of the dam, requiring a thicker base resulting in stiffer cantilevers and substantially more transfer of loads to the foundation through vertical stresses. Although, as arch structures, these dams are not as efficient in transferring load horizontally as dam 1 and 2, the dam profile configuration in terms of thickness and downstream slope are substantially leaner and more efficient than a gravity dam. A gravity dam designed in the same location will rely virtually only on vertical stress transfer for stability, requiring a thick section and relatively flat downstream slope.

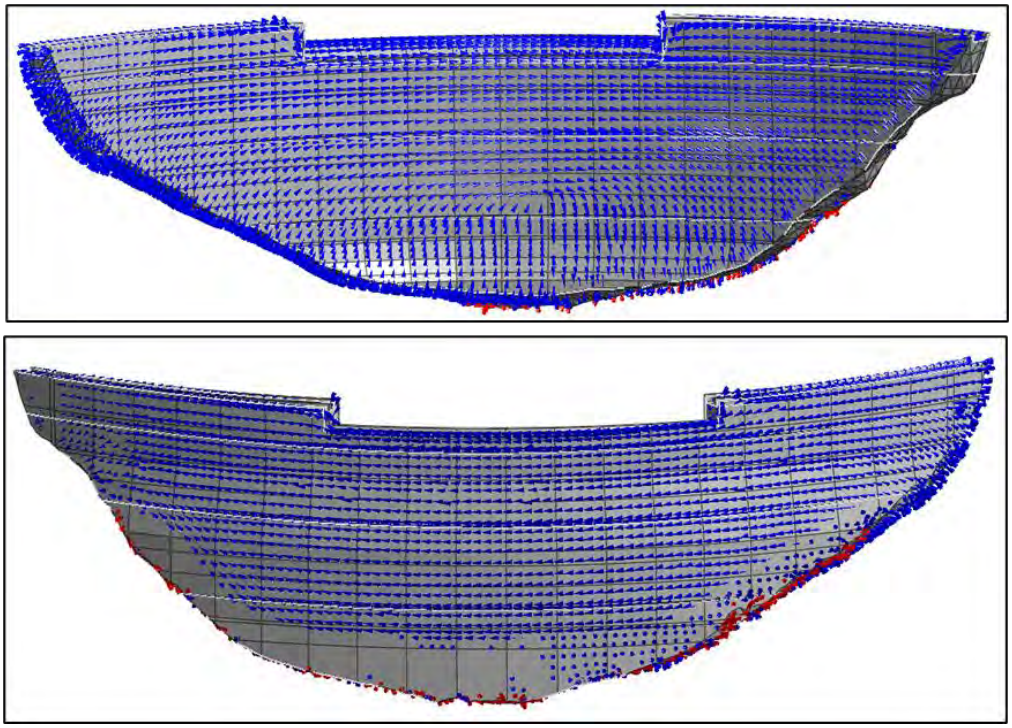

Figure 2-33: Dam 3 minor principal stress distribution on downstream (top) and upstream (bottom) face of arch dam with narrow U-shaped valley foundations

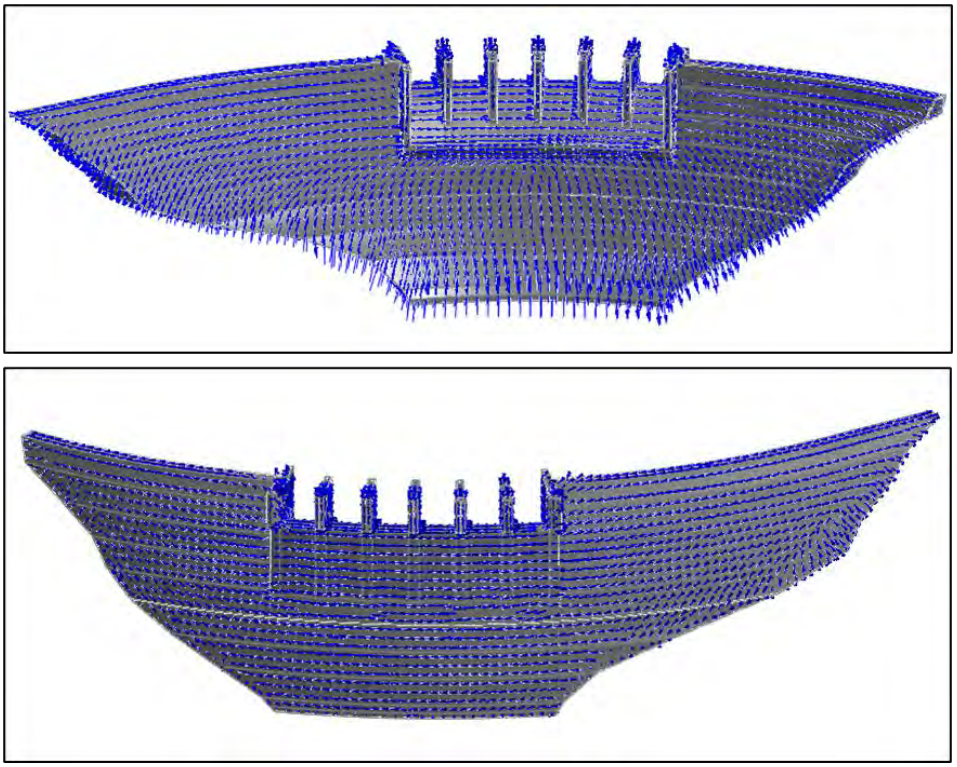

Figure 2-34: Dam 4 minor principal stress distribution on downstream (top) and upstream (bottom) face of arch dam with narrow U-shaped valley foundations

The minor principal stress vectors of the double-curvature arch (dam 5) constructed in a wide U-shaped valley with a CL:H value of 5.1, is shown in Figure 2-35. The stress distribution on the downstream face, show that the top 60 % of the dam height transfers load horizontally by arching, while the lower 40% of the dam transfers load by vertical stresses. It can be seen from the minor principal stress compressions on the upstream face, that horizontal arch action is evident over the top 80 % of the dam height.

Dam 5 has a CL:H value greater than dams 3 and 4. Despite the wide U-valley, the dam stress pattern shows that the dominant load transfer mechanism is through horizontal stress transfer. The double-curvature of the structure and the varying radius with height allow for higher curvature towards the base and horizontal stress transfer.

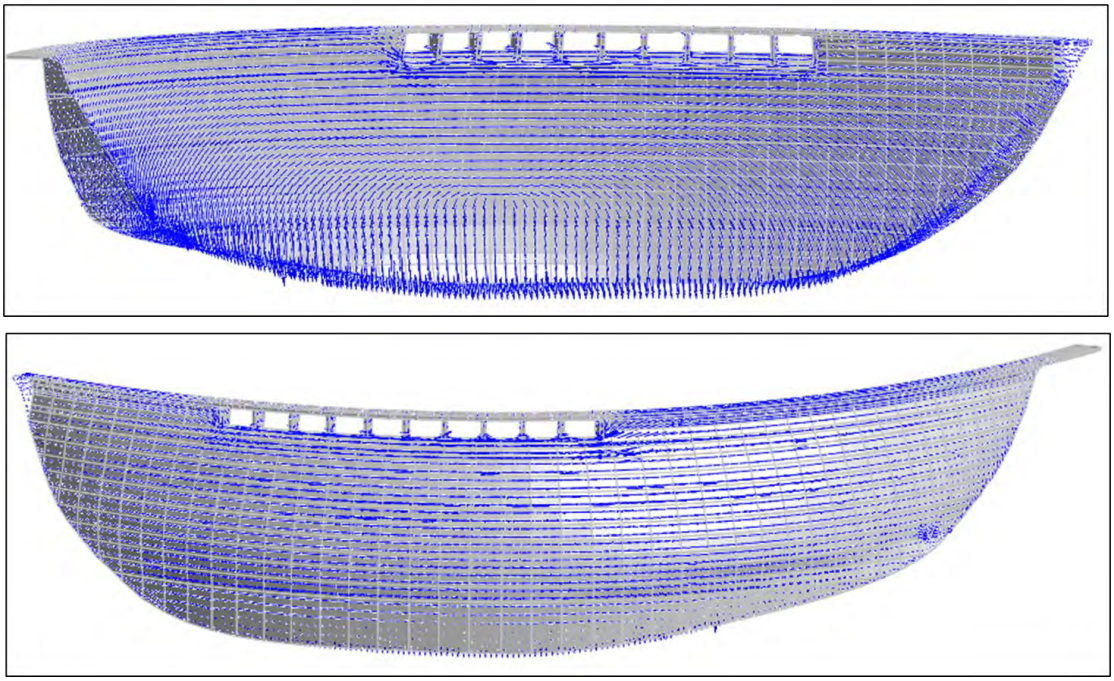

Figure 2-35: Dam 5 minor principal stress distribution on downstream (top) and upstream (bottom) face of arch dam with wide U-shaped valley foundations

Dam 6 is an arch-gravity dam constructed in a wide U-valley with a CL:H value of 4.0. The minor principal stress vector plot of the dam is shown in Figure 2-36. The stress vectors on the downstream face shows that the top 50 % of the dam height transfers load horizontally by arching, while the lower 50% of the dam transfers load by vertical stresses. It can be seen from the minor principal stress compressions on the upstream face that horizontal arch action is evident over the top 90 % of the dam height.

The CL:H value of dam 6 is similar to that of dam 2, 3 and 4, yet a substantially lower portion of the load is transferred via horizontal stresses, than is the case for the aforementioned dams. Dam 6 is an arch gravity structure having a thick section profile and flat downstream slope. The

thick base and associated stiff cantilever response of the dam on the downstream lower half, is reason for large transfer of vertical stresses into the foundation.

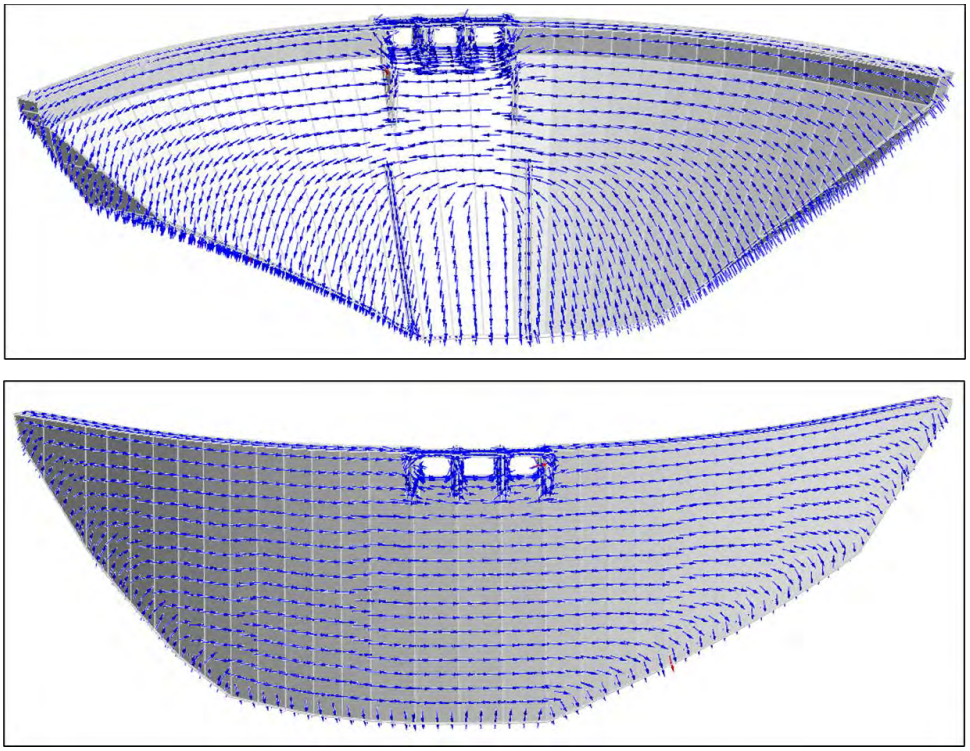

Figure 2-36: Dam 6 minor principal stress distribution on downstream (top) and upstream (bottom) face of arch-gravity dam with wide U-shaped valley foundations

Dam 7 is a thick gravity-arch dam constructed in a wide valley with a CL:H value of 5.8. The minor principal stress vector plot as shown in Figure 2-37, indicate that on the downstream face the top 40 % of the dam height transfers load horizontally by arching, while the lower 60% of the dam transfers load by vertical stresses. It can be seen from the minor principal stress compressions on the upstream faces that horizontal arch action is evident over the top 75 % of the dam height.

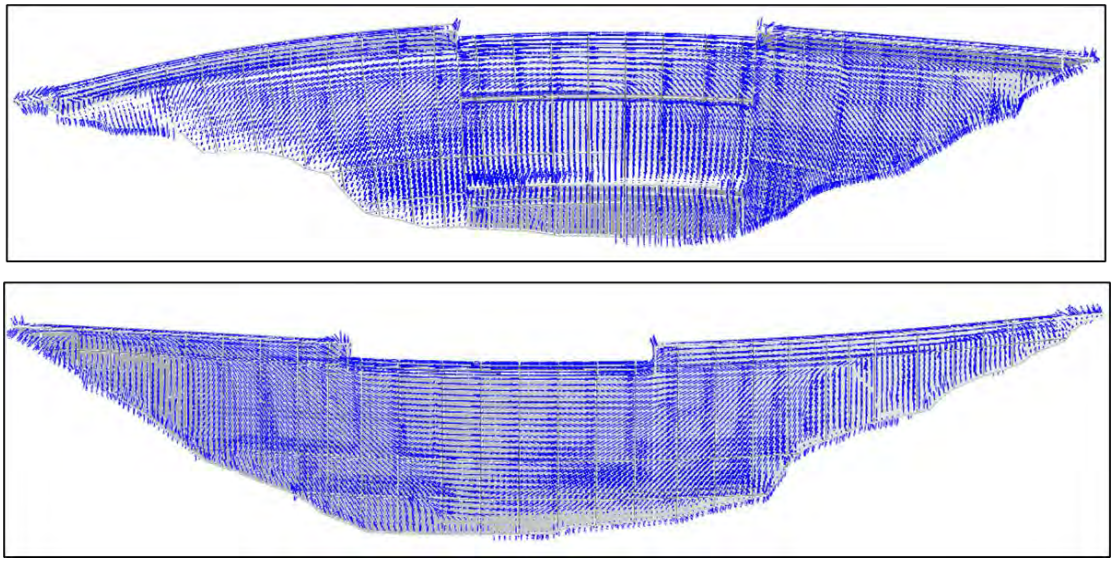

Figure 2-37: Dam 7 minor principal stress distribution on downstream (top) and upstream (bottom) face of gravity-arch dam with wide valley foundations

Dam 8 is a gravity dam constructed in a wide valley with a CL:H value of 4.5. The minor principal stress vectors as shown in Figure 2-38, indicate that on the downstream face there is virtually no horizontal load transfer, while on the upstream face there is some horizontal arch action evident over the top 60 % of the dam height.

Dam 8 is strictly speaking a gravity dam, the axis of which has a kink on the left flank giving the structure discrete upstream convexity inducing marginal horizontal compressive stress transfer, on the upstream face in response to loading.

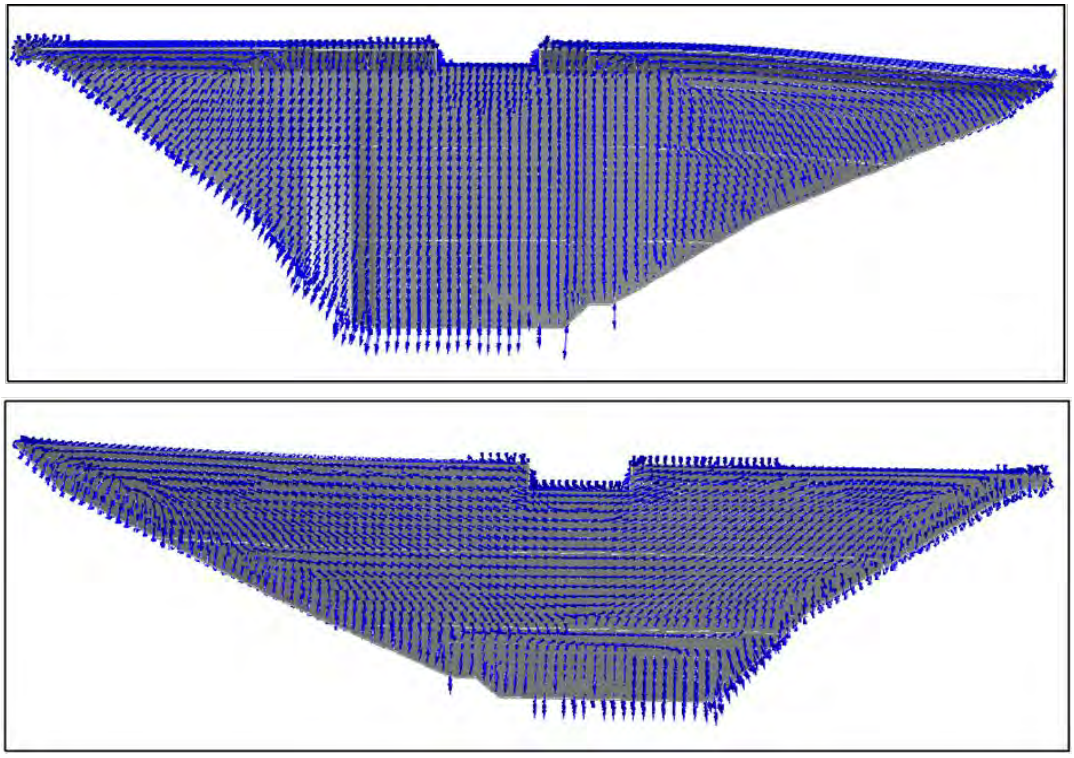

Figure 2-38: Dam 8 minor principal stress distribution on downstream (top) and upstream (bottom) face of gravity dam with wide valley foundations

The principal stress patterns of the 8 dams presented depict how all the arches demonstrate a different stress behaviour pattern on the upstream face, compared to the downstream face. This is evidence of the truly 3-dimensional function of an arch dam.

There is a clear relationship between the dam arch form, the CL:H ratio and the stress transfer mechanisms. These should be taken into consideration when postulating possible failure modes of an arch dam. A summary of the geometrical configuration and characteristics of the 8 dams as well as the E_c to E_f ratios are shown in Table 2-10.

Table 2-10: Summary of dam configuration data

Dam Name	Height (m)	Crest Length (m)	E-dam (GPa)	E-foundation (GPa)	CL:H	Ec/Ef
Dam 1	275	490	24	4	1.8	6.0
Dam 2	66	285	25	50	4.3	0.5
Dam 3	42	159	12	30	3.8	0.4
Dam 4	83	350	15	5	4.2	3.0
Dam 5	89	451	20	19	5.1	1.1
Dam 6	93.5	372	10	20	4.0	0.5
Dam 7	101.6	590	18	6.5	5.8	2.8
Dam 8	95	424	16	1.5	4.5	10.7

2.2.8 Failure Modes of Arch Dams

An arch is a stable structural form and assuming the integrity of the supporting abutments is assured, failure can only occur due to material overstress (Novak *et al.*, 2006). Arch dam design is centred mostly on stress analysis of the structure and the exercise of attaining a form with minimal local tensile stress concentrations, whilst avoiding excessive compressive stress.

If an arch is stressed to failure, tensions will typically develop at the upstream heel of the dam and approximately mid-height of the downstream face.

The failure of an arch dam is normally of a progressive nature and ultimately is caused by a hybrid of actions, occurring progressively over a time period. Arch dam failures are viewed to be brittle or sudden in nature, but the observed catastrophic failure is normally the ultimate culmination of a series of gradually occurring interlinked problems, not easily detected at the outset.

As with most structural failures, the event may be initiated by a local material failure that progresses to a point where the global structure develops various internal hinges, for which its external support can no longer maintain overall stability. In other words, global failure is a physical instability that starts from local material damage (Ren *et al.*, 2011).

For purposes of devising an understanding of arch dam failure modes, the arch dam system is divided into 3 components which may fail in isolation causing the other components to fail by default as the system ultimately fails. Each of these components can be seen as a link in the common analogy that “a chain is only as strong as its weakest link”.

The three isolated components comprise:

1. The arch structure;
2. The interface between the dam and foundation; and
3. The foundation structure.

Failure modes for each of the three structural components will be addressed assuming that if two of the components in the system are inherently stable or structurally sound, a failure would have to be caused by structural inadequacy of the third component.

Arch structure failure

Failure of a concrete arch may occur due to a material strength exceedance or local instability as a result of buckling of the arch. The latter failure mode is only considered for thin arch dams of a relatively long span, and is checked by simply evaluating the dam arch against Euler

buckling along its crest (Federal Energy Regulatory Commission, 1999). The configuration at the crest usually comprises the thinnest section width and the longest span (buckling length).

A material failure requires more careful consideration when designing an arch dam. It may be of a compressive (crushing), shear (slippage) or tensile (cracking) nature, although failure in tension or shear are exponentially more likely than compression, as the compressive capacity of concrete is generally ten times that of its tensile and shear capacities.

In theory the inherent nature of a perfectly formed, perfectly supported, elastic cylindrical thin arch should result only in the development of compressive stresses when loaded, even to failure. The limitations posed by uncontrollable site conditions, constructability, and the deformability of the foundation mean that some tensions will develop in an arch dam, especially if loaded to failure.

Various cracking types experienced in arch dam are shown in Figure 2-39. Although the development of tensile stresses in arch dams is regarded as undesirable, they should not necessarily be regarded as problematic, unless viewed against the structural mechanism of the dam. Development of tensile stresses and the initiation of local cracking in a hyperstatic arch structure may simply result in a redistribution of loading as the local stress concentration transfers away from the cracked area.

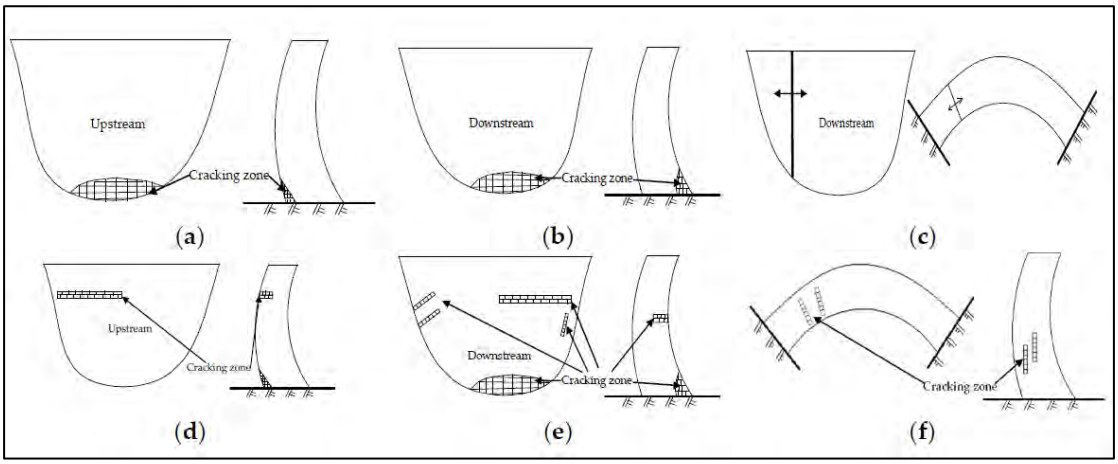

Figure 2-39: Various cracking types of arch dams (Peng *et al.*, 2018)

Under hydrostatic loading conditions tensions normally develop vertically at the heel of the dam (type a) and in both horizontal and vertical directions on the downstream face at a height approximately 40 – 60 % above the base (type e).

Minor tensile stresses have been shown to occur at the heel of the dam under design loads. The tensions normally initiate at the interface between the dam and foundation and progress

marginally into the dam heel. These tensions are inevitable due to vertical stress transfer at the dam base and cause minor localised tensile cracking to occur.

The reduced stiffness of the locally cracked heel of the dam causes a self-induced plastic hinge to form, allowing the load concentration in the region to redistribute into the arches as the dam leans progressively and marginally forward. The dam has effectively become more efficient, transferring a portion of the vertical stress into horizontal stress via the higher capacity load mechanism. The tensile crack progresses to a point where the local stress equalises to the actual tensile strength in the region, as the excess moves to regions with higher stiffness and capacity.

The design criteria assumptions of arch dams normally result in substantial additional capacity of the dam to carry compressive loads, before exceeding compressive strength criteria, meaning that a redistribution of load into the arches will not pose a problem. It has been found that certain wide valley arch dams have been allowed to undergo tensile cracking at the base over an extent of 2/3 of its thickness (Shaw, 2015). This extent of cracking would be considered highly unacceptable for a concrete gravity dam that relies on vertical load transfer for stability, and the dam would be deemed unsafe.

Notable French arch dam pioneers such as Andre Coyne have been known to design dams with a preformed horizontal joint at the heel of the dam, to “unstiffen” the cantilevers of the arch, so that arch action could be enhanced. The Katse Dam of Lesotho was constructed with a pre-formed joint (Tardieu & Carrere, 1994).

The development of tensile stresses on the downstream face of the dam, are more unforgiving than those at the heel, and are commonly referred to as bursting stresses. A loaded arch has minimal capacity for redistribution of bursting tensile stresses and these should be avoided in the design approach. Tensile cracking on the downstream face of an arch dam will cause the arch to lose stiffness, deflect excessively and open up towards the downstream face, ultimately lengthening the arch radius and reducing curvature and arch effectiveness. This behaviour may develop quickly and induce a sudden failure as the arch strength reduces whilst the stress concentrations increase.

Response of an arch dam under seismic earthquake loading may cause the monolith construction joints to open (type c) and effectively negate stabilising horizontal load transfer of the arch, particularly at the crest where the dam is more flexible and under a lower hydrostatic load, making it conducive to this dynamic response.

Ground acceleration caused by an earthquake induces vibrations on the dam, resulting in upstream-downstream shaking along the riverbed axis. The dam oscillates back and forth at a

high frequency and when it extends backwards (towards the reservoir), the arch elongates momentarily along its axis and the tensile strain results in opening of the dam joints, as their tensile capacity is exceeded.

The dam construction joints have practically zero tensile capacity and rely on the compression of the loaded arch, during normal hydrostatic loading to remain closed, whilst shear keys provide shear stability from sliding between monolith blocks only when contact is maintained. When this dynamic response occurs, the dam is highly susceptible to failure caused by vertical cantilever tensile stresses at the base or along possible horizontal planes of weakness, at construction joints between placed lifts of concrete (type a, b and e). The mobilisation of partially-free concrete blocks is shown in Figure 2-40.

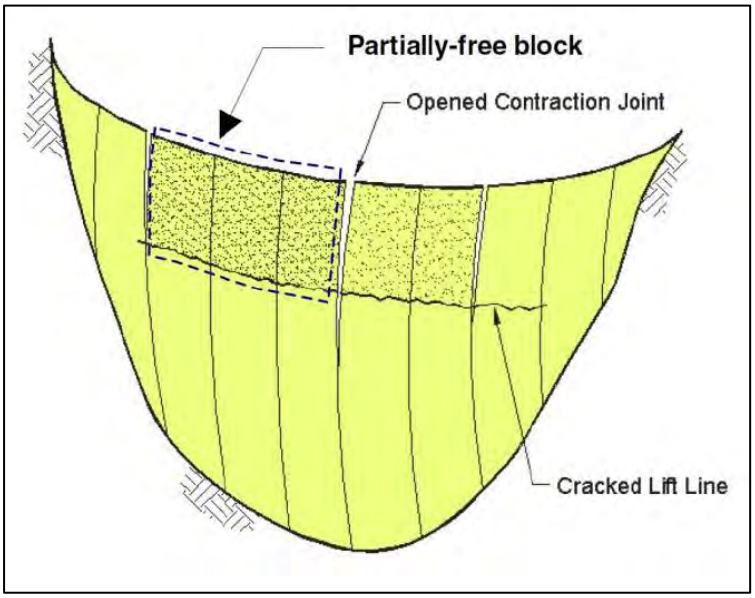

Figure 2-40: Mobilisation of partially free concrete block during dam earthquake response (Ghanaat, 2004).

Thermo-mechanical loading of an arch dam may induce cracking. Shrinkage and expansion of the body due to temperature changes, will induce stresses in the dam body due to the constraint against movement imposed by the foundation, or between the core and shell of the dam.

Shrinkage generally induces tensions (type f) at the core of the dam under mass gradient thermomechanical loading, or at the surface (type d) under surface gradient thermomechanical loading, see Figure 2-20. Temperature induced expansion of an arch dam with a low level or empty reservoir, may cause it to lean upstream inducing tensile stresses at the toe (type b). Expansion due to Alkali Aggregate Reaction may also instigate type b stresses.

A tensile concrete failure initiates when the structure load approaches capacity, with the formation of micro-cracking. Further loading causes the micro-cracks to progress and become stable macro cracks that effect the structural stiffness and the stress-strain load curve becomes

non-linear as the material yields. When the concrete is stressed beyond its capacity the cracks become unstable, fracture occurs and ultimately a material failure occurs (Gillian *et al.*, 2011).

Dam-foundation interface failure

The interface between an arch dam and the rock mass foundation, is a physical joint that forms a plane of weakness between the bodies in contact, having shear strength parameters generally less than the concrete and rock materials flanking it.

Although a predominant portion of the hydrostatic load is transferred into the foundation abutments via compressive thrusts, the forces are seen to act at an angle of incidence to the face of the abutments. This means that there is inherently a component of shear force transfer at the dam-foundation interface, and the possibility of a sliding mechanism developing if the friction (shear) resistance between concrete and rock is inferior to the driving force.

The shear forces transfer of load from the dam into the lower central foundation from cantilever action, is similarly capable of inducing a local sliding mechanism, that may progress causing a substantial portion of the dam to become unstable and slide along its foundation.

This failure mode is generally not critical and is only a concern for very large thin arches with a high slenderness ratio. According to Lombardi and Fanelli (1992) the shear resistance of an arch dam is related to its slenderness ratio.

Hydrostatic uplift pressures between the dam and foundation, reduce the effective stress between dam and foundation and lower the shear strength of the joint, as mobilised by the favourable compressive stress normal to the dam-foundation interface.

Stability against sliding is normally enhanced by incorporating a drainage system under the base of the dam, excavating a sunken key for the dam to sit in, ensuring a favourable angle of incidence and ensuring a good bond interlock between concrete and foundation during construction.

Foundation failure

History has shown that foundation instability is the most common cause for arch dam failures. Foundation failure may be in the form of local material failure or instability of the rock mass.

A material failure initiates as a local rock mass rupture under the base of the dam or excessive deformation of a localised zone of soft rock mass, under the dam base. Both these actions may cause bridging of stress transfer over the failed foundation zone, resulting in possible high tensile concentrations forming over this zone. If the tensile stresses are higher than the tensile

capacity of the arch concrete, a local fracture/rupture of the concrete will develop and if extensive enough may progress to a larger area and cause instability of the dam.

A rock mass instability failure will occur if the dam load transferred into the foundation causes a portion of the supporting rock mass to become unstable, move and/or dislodge from the main body of rock mass. This is commonly called a rock wedge failure.

The rock mass foundation of an arch is sure to have various faults, joints, bedding planes or other local planes of weakness within it and traversing under the dam footprint. The orientation and location of these planes of weakness may cause joint-bound rock wedges to form that could potentially be pushed to slide out of position, from arch dam loads.

This failure requires such rock wedge to be kinematically free, meaning that joint planes should day-light or exit the foundation at an open face. The wedge joint planes should dip out of the canyon faces and have an azimuth directing the wedge in an unfavourable direction, in relation to dam arch thrusts. The potential instability of rock wedges is exacerbated by permeation of water into the sliding planes, resulting in uplift pressures developing at these joints.

Foundation instability may occur at the lower central region of the foundation or on the upper banks. Such failure will occur if the thrust load of the dam onto a formed wedge is transferred from wedge into the parent rock mass, along potential sliding planes, and exceeds the shear strength (friction resistance) at these sliding planes. The shear strength is mobilised by forces normal to the sliding plane, caused by the weight of the wedge. An example of a rock wedge instability failure in the upper abutment and lower central foundation is shown in Figure 2-41. Failure of a substantial rock wedge size will undermine the arch dam resulting in a stability failure.

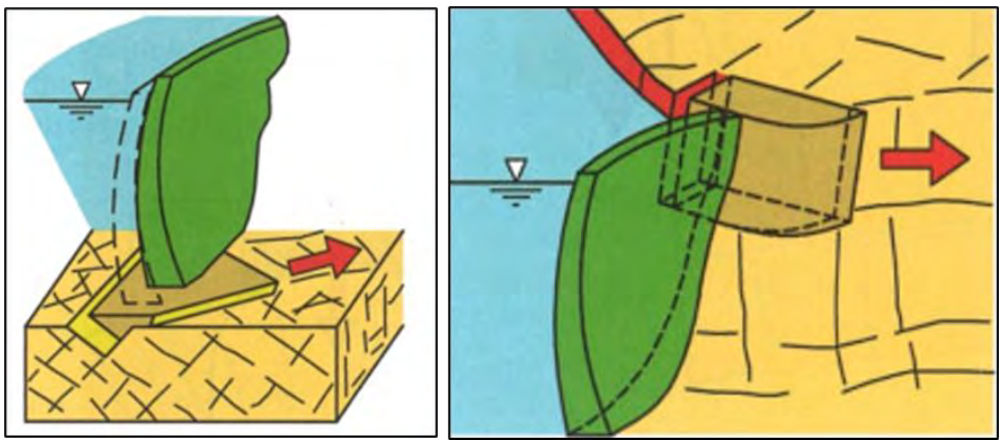

Figure 2-41: Arch dam rock wedge instability in lower central foundation (left) and upper abutments (right) (Brown, 2016)

Problematic conditions

Typical potentially problematic conditions or issues that may lead to the ultimate formation of a dam failure mechanism, are shown in Figure 2-42 and listed below:

1. Overtopping of dam and associated foundation erosion
2. Excessive uplift due to blocked drains
3. Erosion or failure of the grout/drainage curtain
4. Tension and shear cracking of dam concrete overload
5. Foundation failure
6. Scouring of downstream foundations
7. Excessive reservoir level due to unforeseen flooding
8. Earthquake induced acceleration
9. Alkali aggregate reaction induced swelling of concrete
10. Excessive pre-strain conditions from phased construction
11. Thermal cracking
12. Concrete or foundation creep
13. Abutment movement
14. Sliding or shear at dam-foundation interface

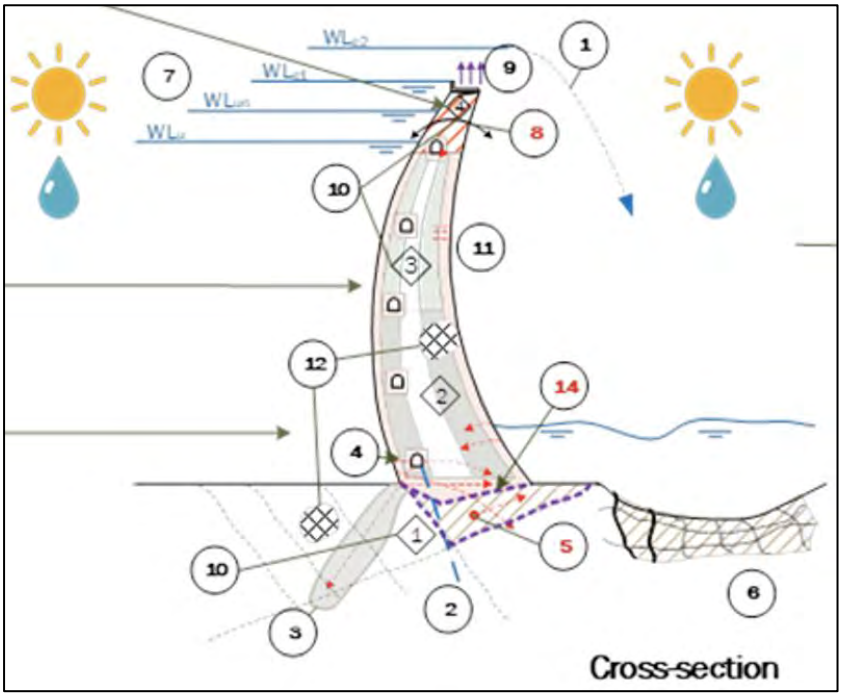

Figure 2-42: Potential issues that may lead to development of an arch dam failure (ICOLD, 2024)

2.2.9 Evaluation of Analysis Results

Various analysis methods were presented in section 2.2.6, for the structural evaluation and design of arch dams. The results these methods compute for analysis of a loaded arch, are the modelled displacements, stresses and strains to be considered for design.

Analysis results should be studied holistically in light of the overall structural behaviour of the dam and possible failure modes. The different analysis techniques each have their own shortcomings and challenges, according to the numerical and physical modelling assumptions upon which they are based, and this should be kept in mind when evaluating the outputs.

This study adopts the FE method for analysis purposes and the evaluation of results are addressed in terms of those obtained using this method.

When evaluating the FE analysis results of an arch dam, it is the nodal displacement results that are first studied. The nodal displacements are the unknowns solved in the simultaneous equations, derived using the commonly adopted stiffness (displacement) method.

Modern FE analysis software provides graphical representations of nodal displacement results in the form of contour plots. The displacement contour plots simulate the deformation response of the arch dam, under loading, and provide useful insight of the structural mechanism that develops within the loaded structure and effectively illustrates the expected physical behaviour of the dam.

The displacement results of a FE analysis show the degree of symmetry of the dam and the location of maximum displacement of the dam, which normally occurs at the most flexible portion, being the crest of the crown cantilever. The maximum displacement is importantly observed against possible serviceability constraints and provides a quantity to be considered as a sanity check, for reliability of FE computations. The smoothness of the displacement contours provides an indication of a well-developed FE model, in terms of mesh quality and compatibility. Normally radial and tangential displacements with orientation shown in Figure 2-43 are evaluated for deformation response of the dam.

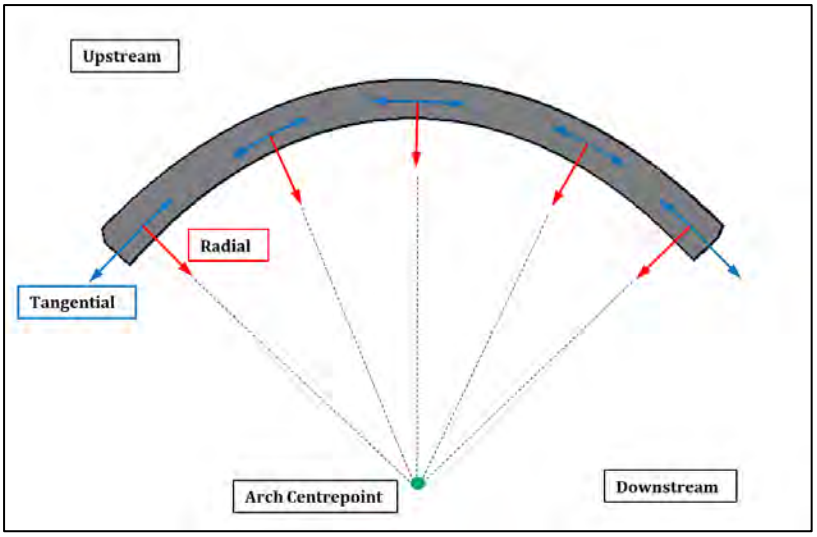

Figure 2-43: Description of radial and tangential displacement vectors

An example of typical radial and tangential displacement plots output by an FE analysis of a dam under full supply level, are shown in Figure 2-44. The results show a symmetrical displacement about the crown of the arch and smooth contour bands. The maximum in stream crest displacement of the arch dam is 96 mm towards the downstream.

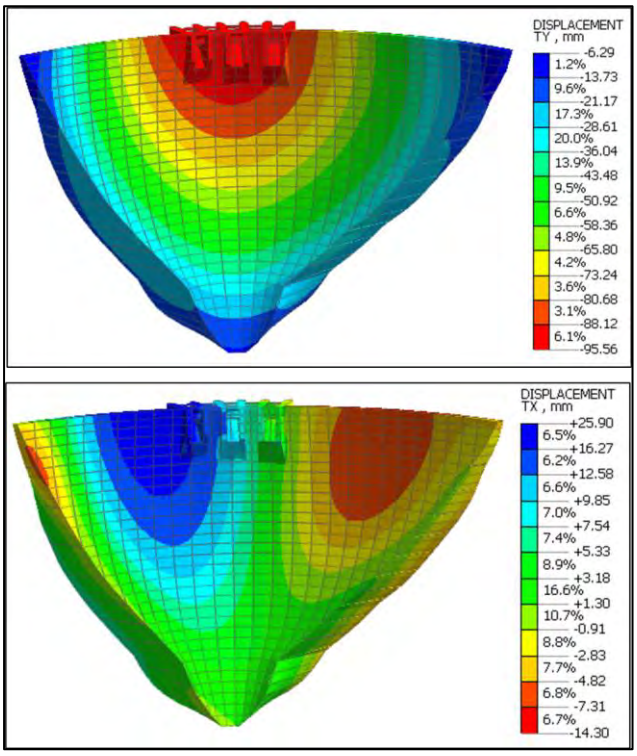

Figure 2-44: FE analysis result plots showing radial (top) and tangential (bottom) deformation of Yusufeli Dam

Vertical stress results of an FE analysis show the extent and configuration of cantilever action of the dam. A well-designed arch dam will typically show negligible tensile vertical stresses

under normal hydrostatic loading, on the upstream and downstream faces. A small zone of concentrated local tensions is however likely to be computed at the heel of the dam, even under usual loading. Although marginal tensions may be expected to truly occur at the heel of an arch dam, the tensile stress values reported by FE analysis outputs are usually an exaggeration of the true magnitude.

There are various reasons for computation of such local exaggerations of stresses when using the FE method. Due to the non-linear behaviour of concrete and rock, high-end stresses computed by the FE method assuming linear elastic material parameters, are inherently higher than true stresses expected to develop.

In addition, fictitious stress concentrations are known to be computed in the region of pronounced geometric discontinuities, especially re-entrant corners, as occurs at the interface of the dam and foundation in the 3D FE model of a dam (Durieux & van Rensberg, 2016). The elemental stresses are computed by interpolation of values derived from derivatives of element shape functions, at Gaussian integration points. These elemental stresses are exagerrated by the almost infinite nodal stresses caused by the singularity of the re-entrant corner, between the dam and foundation.

This is further exacerbated by the abrupt changed in stiffness at the interface between the dam and foundation, as well as an unrealistically high normal and shear stiffness occuring at the interface of these. The actual stiffness of the plane of weakness at the joint will be lower than both the foundation and dam. Such mechanisms can be modelled using non-linear material parameters.

According to St Venants principle a singularity stress/strain concentration is local and will subside towards a realistic nominal value, within a short distance from the affected finite element. It is assumed that the stresses computed by elements neighbouring the effected element, provide a better representation of actual stresses. In accordance with the above, the actual tensile stresses reported at discontinuities are probably double the actual nominal value (Cassells & Wright, 2023).

According to Ghanaat (1993), computation of tensile stresses at the contact between the dam and foundation, from structural analysis results of concrete arch dams assuming linear elastic material parameters, can be interpreted as a local opening of the dam-foundation interface joint or joints within the rock mass directly below.

Typical vertical stress result contours of an arch dam under full supply level hydrostatic loading are illustrated in Figure 2-45. The results show negligible tensions on the downstream (front)

and upstream (back) of the dam. Since maximum stresses in an arch dam usually occur at the faces of the structure, the relevant stress results are evaluated on the upstream and downstream faces of the arch (Ghanaat, 1993).

Local vertical tensile stress concentrations with a value close to 1 MPa are evident at the heel of the dam and can be considered exaggerations for purposes of evaluating the safety of the dam. The maximum vertical compressive stresses of the dam are of a magnitude of 4.7 MPa, and form on the lower upstream face of the dam. These compressive stresses are attributed to the undercut of the arch curvature, occuring in the radial reference plane of the dam.

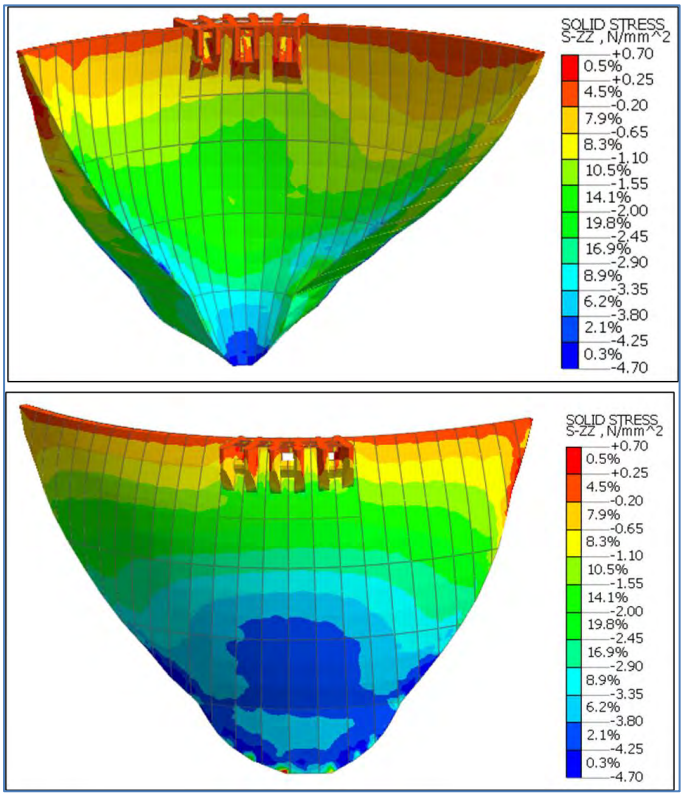

Figure 2-45: FE analysis results plot showing vertical stress contours of the front (top) and back (bottom) face of the dam

The horizontal (hoop/axial) stress results of an arch dam, indicate the magnitude and extent of the primary load thrusts of the dam. These are in the form of horizontal arch stresses developed longitudinally along the axis of the arch structure. These results typically display the most efficient load transfer mechanism of the arch, and effectiveness of the arch in transferring large compressive stresses smoothly from the mid-height and mid-span upstream face of the dam, to the abutments and predominantly the toe of the dam, along the abutments.

FE analysis horizontal stress results of an arch dam are shown in Figure 2-46. The maximum axial compressive stresses calculated by the FE analysis have a magnitude value of 7.3 MPa, (negative indicates compression) which is computed to develop mid-span and mid-height on

the upstream face, and towards the toe of the arches along the abutments. The tendency of the dam to develop horizontal tensile bursting stresses in the lower portion of the dam, on the downstream face, is also indicated. Generally this zone of tensile bursting stresses will progress to cover a larger area on the downstream face to nearly mid-height of the crown cantilever if the following unfavourable conditions are imposed on the dam:

- The dam is overstressed to failure;
- The dam lower central foundation rock mass deformation modulus is low with the dam E_c/E_f ratio exceeding 8;
- The arch is designed n a wide U-valley with a high CL:H value.

The dam for which stress results are provided in Figure 2-46, is in a favourable state in terms of the abovementioned conditions, indicating an efficient arch form with no sign of developing significant horizontal tensile bursting stresses.

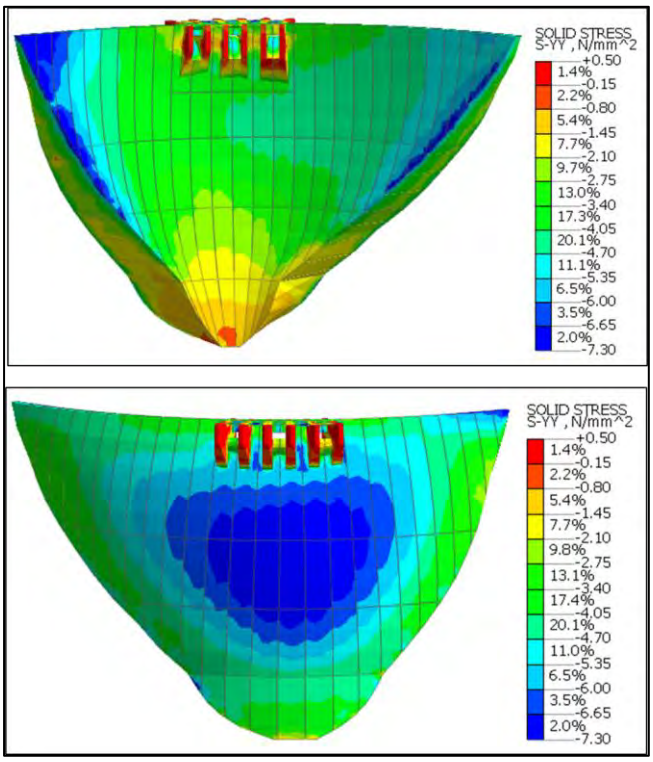

Figure 2-46: FE analysis results plot showing horizontal stress contours of the downstream (top) and upstream (bottom) face of the dam

The minor principal stress results extracted from an arch dam FE analysis show the magnitude of the expected compressive load thrusts, in the direction of the resultant load path, for load transfer between loaded dam and foundation. These values are indicative of the maximum compressive stress expected to occur in the arch dam body, and the direction is generally a

resultant of the horizontal and vertical stress transfer paths, which runs along and across the arch-cantilever elements of the dam.

The P3 minor principal stress results should be investigated in terms of the stress magnitude and stress direction vector. These results should be evaluated against the allowable compressive strength criteria of the arch dam concrete material. The minor principal stress contours and vectors of an arch dam are shown in Figure 2-47. The stress contours show the maximum compressive stress value computed to develop in the dam is of a magnitude of 7.8 MPa. The directions of the minor principal stress vectors show how the arch dam behaves akin to a loaded shell, and that the compressive arch stresses transfer into the abutments, at angles relatively normal to the face of the abutments. This is indicative of a well-formed concrete arch.

The minor principal stress vectors provide insight into the load transfer mechanism of the dam. The vector directions and orientations allow the compressive stresses to be evaluated in terms of possible problematic structural aspects of the dam, such as planes of weakness orientated unfavourably in terms of the compression thrust.

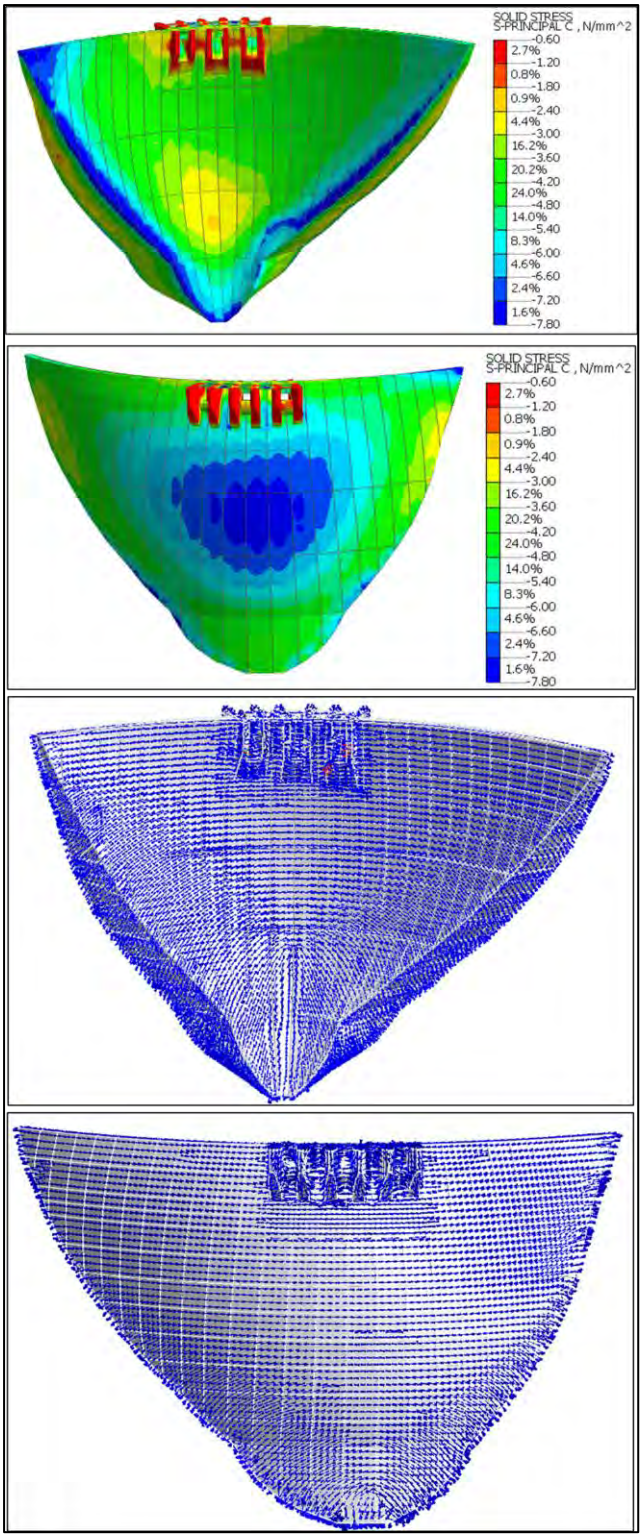

Figure 2-47: FE analysis results plot showing minor principal stress contours and vectors of the front (top) and back (bottom) face of the dam

The major principal stress results extracted from an arch dam FE analysis show the magnitude of the tensions expected to develop, acting perpendicular to the direction of the compressive thrusts. These values are indicative of the maximum uniaxial tensile stress expected to occur in

the arch dam body and should be evaluated against the allowable uniaxial tensile strength criteria, of the arch dam concrete material.

The major principal stress contours of an arch dam are shown in Figure 2-48. The stress contours show that the maximum tensile stresses simulated to develop in the dam, is negligible, apart from stress exaggerations indicated at pronounced geometric discontinuities of the FE model, at the re-entrant corner between the dam and foundation. The major principal stress results show no signs of excessive tensile bridging stresses developing at the base of the dam.

Generally, analysis results under large temperature drop loads and seismic acceleration loads will indicate tensile stress outputs that will be readily observed in P1 major principal stress plots. These loads tend to cause the dam to shrink (temperature drop) along its axis; or accelerate in the downstream direction overstressing the dam, or towards the upstream stressing the dam in its unfavourable direction, putting the arch in tension. The various FE analysis results should be checked for all defined load cases.

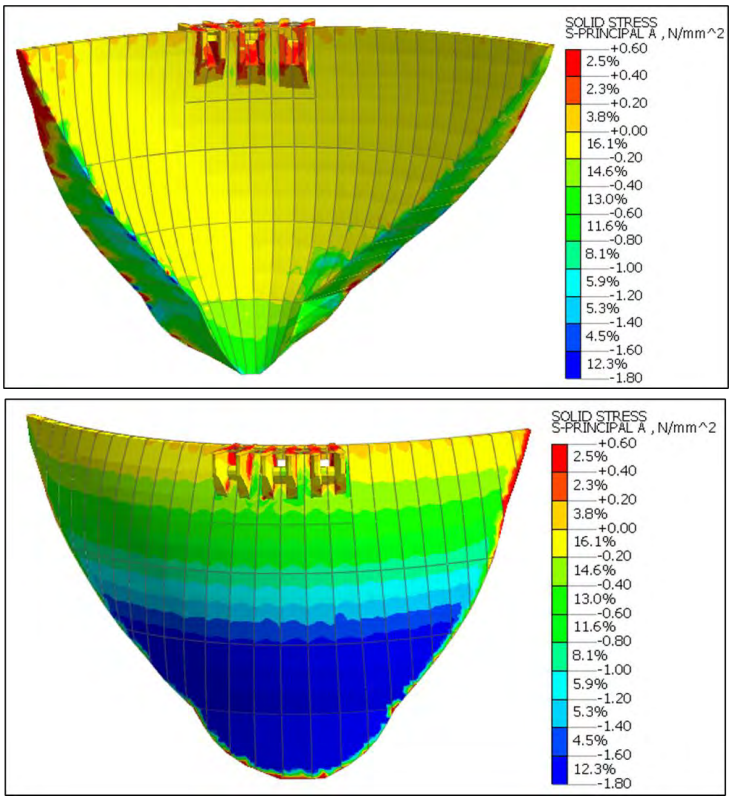

Figure 2-48: FE analysis results plot showing major principal stress contours of the front (top) and back (bottom) face of the dam

2.2.10 Dam Safety

Dam safety is defined as a dam's adequacy against an uncontrolled release of reservoir water (Federal Energy Regulatory Commission, 1999). Dams are designed to be safe under the

assumed conditions at design stage. The high construction costs of dams mean they are built to have a long lifespan typically of 50 to 100 years or more. Aging of the materials and possible changes in conditions over the lengthy lifespan of a dam, may effectively influence the safety of the dam. Many dams built in the early 1900s are still in operation, and de-commissioning of dams is not always an easy option, as communities become reliant on their supply.

A dam failure is a catastrophe often causing considerable loss of life and/or property. Past failures, have caused dam owners and engineers to give a great deal of care and attention to dam safety and ensure safety is a priority. Several dam failures have occurred, as a result of poor maintenance or operation of the dam by the owner. Typical causes of operational failures and the resulting fault that may ultimately lead to failure of the dam are shown in Table 2-11.

Table 2-11: Causes of operational failures and their associated fault (Prins, 2017).

Operational Fault and Cause		Mode of Dam Failure
Human Error	Negligence in terms of outflow release and water level control within dam	Over-topping and/or excessive outflow
Lack of Maintenance	Lack of lubrication of moving mechanical parts, fatigue fracture and loose bolts in gates	Faulty operation of gates and outlet works causing overtopping
Mechanical Malfunction	Gates fail to open, outlet works fail to operate.	Over-topping and/or excessive outflow
Technological Malfunction	Communication breakdown	No warning received of large flood inflow from upstream and no warning issued downstream in case of large outflow
Reduced Storage Capacity	Siltation	Over-topping and/or excessive outflow
Reduced Release Capacity	Debris blockages of spillway, ice attacks of outlet works, loss of access to operational controls	Over-topping and/or excessive outflow
Power Failure	Loss of operational control of gates, valves, communication and monitoring instruments	Over-topping and/or excessive outflow

In 1982 the ICOLD Committee on Dam Safety was formed in response to three noticeable developments in dam engineering that needed to be addressed:

- The occurrence of several dam incidents with severe consequences.
- The increase in size of new dams and the aging of existing dams, to a point of material deterioration.

- The increasing number of dams being built in developing countries, with little or no experience in dam engineering.

The mandate of the committee was to formulate dam safety guidelines that would serve as a formal safety approach, to be adopted in the dam engineering field. The formalisation of safety considerations, and issuance of summarised safety requirements would also be part of necessary transfer of technical know-how to countries with little dam engineering experience and exposure (ICOLD, 1987).

Dam safety international standards are largely influenced by ICOLD standards, although certain individual countries have their own legislation on dam safety, in accordance with their unique circumstances. Normally the dam safety legislation of a country will require dams above a certain size to comply with the dam safety standards prescribed by such legislation requirements. A summary of a few countries and the dam size criteria for enforcement of dam safety legislation is shown in Table 2-12.

Table 2-12: Minimum height and volume of dams that imply safety measures (Durieux, 2008)

Country/Source	Height of Wall (m)	Volume in Dam Basin (m^3)
Austria	15	500 000
ICOLD	15	1 000 000
Portugal	-	100 000
Switzerland	10	50 000
Zimbabwe	8	-
USA	7.6	62 000
Canada	7.6	62 000
South Africa	5	50 000
Sweden	5	50 000
Norway	4	500 000
Finland	3	-
United Kingdom	-	25 000

A good understanding of dam engineering was only really developed in the 19th century, when the industrial era began in Western civilisation. Dam engineering in South Arica followed trends of standards and methodologies developed in the United States of America and Western European countries.

Many South African dams were built in the 1960s and 1970s, with the first four South African dams known to be built in the 1900s. By 1992, the ICOLD world register of dams provided a record of 458 dams in South Africa.

In 1956 the Water Act of South Africa was promulgated which was the first official dam safety legislation in South Africa. The act required that a permit was needed to construct dams with a storage capacity over 250 000 m^3.

In 1965 SANCOLD was founded to represent South Africa as a National Committee member at ICOLD. Due to growing focus on dam safety worldwide, SANCOLD made proposals for legislation to control the safety of dams in South Africa. Based on this, the Department of Water Affairs drafted the necessary legislation, which was then included in the Water Amendment Act of 1984, and subsequent regulations of 1985 and 1986.

The South African National Water Act 36 of 1998 was later promulgated in parliament, containing updated dam safety legislation superseding that of 1986. As indicated in Table 2-12, a dam with a safety risk is defined in the Act as having a storage volume capacity in excess of 50 000 m^3 and a vertical height exceeding five metres.

According to Regulations of the Act, every dam with a safety risk must be classified by the Director-General of Water Affairs as a Category I, II or III dam based on its size and hazard potential rating. This is found in regulation 2.4 of the Act.

The size classification of a dam with a safety risk shall be based on the maximum wall height, in accordance with details shown in Table 2-13.

Table 2-13: Dam classification according to size

Size Class	Maximum wall height in metres
Small	More than 5 m but less than 12 m
Medium	Equal to or more than 12 m but less than 30 m
Large	Equal to or more than 30 m

The hazard potential rating of a dam with a safety risk in accordance with potential loss of life, potential economic loss and potential adverse impact on resource quality, is shown in Table 2-14.

Table 2-14: Hazard potential rating of dam

Hazard potential rating	Potential loss of life	Potential economic loss	Potential adverse impact on resource quality
Low	None	Minimal	Low
Significant	Not more than 10	Significant	Significant
High	More than 10	Great	Severe

The category classification of a dam with a safety risk is based on a combination of its size classification and hazard potential rating, as indicated in Table 2-15. Conditions and requirements to be complied with for a Category III dam, are stricter and more comprehensive than a Category II or Category I dam.

The Regulations specify requirements to be complied with in terms of the operation and maintenance of a dam. This is the responsibility of the owner or appointed person in control. A compulsory dam safety inspection must be held at least once every five years, for every dam with a safety risk. Inspections of Category I dams do not need the involvement of an approved professional engineer, whilst for Category II and III dams, a comprehensive dam safety inspection must be undertaken by an approved professional engineer.

A dam safety inspection must include a site visit to the dam from which various aspects of the dam should be evaluated, such as adequacy of the spillway capacity, dam stability, consequences of overtopping of non-overflow crest and the estimated economic loss and loss of life, as a result of a potential failure of the dam.

The APP should identify any actual and potential shortcomings in the condition of the dam and its foundation, under the current conditions. The operation methods of the dam, maintenance procedures and monitoring of the dam behaviour should also be evaluated, to ensure these are done properly and with the right adequacy to ensure the dam safety.

Table 2-15: Dam category classification

Size Class	Hazard Potential Rating		
	Low	**Significant**	**High**
Small	Category I	Category II	Category II
Medium	Category II	Category II	Category III
Large	Category III	Category III	Category III

It is the responsibility of the approved professional engineer to ensure that all the relevant design aspects of the dam are thoroughly reviewed, especially in light of any deteriorated material properties or changes in conditions to which the dam is exposed.

The APP is responsible for defining suitable standards for a dam for safety evaluations. The Regulations do not explicitly provide standards or criteria for compliance in terms of the design, construction, operation and maintenance of the dam. The standards applied by the engineer should be documented, and it is left to the dam authority (Dam Safety Office) to decide if the standards are acceptable.

2.3 GEOLOGICAL TESTING AND INVESTIGATIONS OF ARCH DAM FOUNDATIONS

Global stability of an arch dam cannot be achieved without a competent foundation rock mass, upon which it can be seated. To determine the suitability of a dam site for the safe design of an arch dam, requires extensive geotechnical investigations of the rock mass, to determine the geological and structural compositions, strength, deformability and permeability of the material.

The collection, study and evaluation of foundation data is a continuing program that progresses in detail and extent, through the various dam design stages, from appraisal/feasibility design to final design and completion of construction.

Early site investigations for design appraisal may comprise basic evaluations of geological and topographic maps, photos of site, investigations of natural outcrops, road cuttings and surface conditions. During early-stage investigations of complex foundations for large dams, a limited number of bore holes may be drilled to obtain subsurface data. Investigations required for appraisal should be sufficient to define the geologic conditions, with emphasis on those which will affect design and decision of site location. A typical geological map and profile is shown in Figure 2-49.

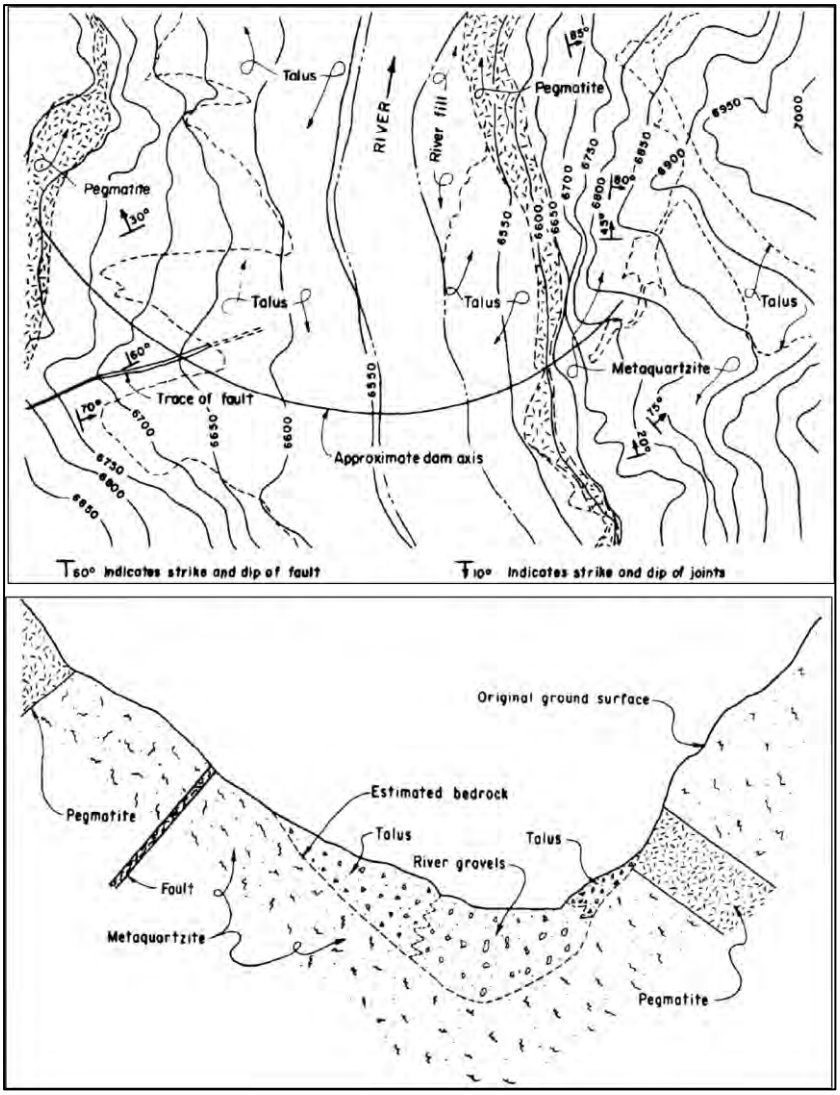

Figure 2-49: Typical geologic map (top) and profile (bottom) of an arch dam site (USBR, 1977)

More advanced and refined geotechnical investigations required for detailed design may comprise extensive borehole drilling, as well as testing of specimens, to comprehensively define the rock mass characteristic and properties in each abutment and the valley bottom. Typically, the following items need to be accurately defined (USBR, 1977):

1. Strike, dip, thickness, continuity, and composition of faults and shears in the foundation.
2. Depth of overburden.
3. Depth of weathering throughout the foundation.
4. Joint orientation and continuity.
5. Lithologic variability.
6. Physical properties of the foundation rock, including material in the faults and shears.

Test excavations are elementary and valuable aids in dam site investigation, and can provide the geologist or engineer with strategically located exposures of bedrock. Ideally, exposure of bedrock along road cuttings up and down the dam abutments, will greatly improve geological interpretation of foundation conditions.

Core borings obtained from borehole drilling provide useful hard data on the foundation conditions and stratigraphic layering of the foundation rock mass. Core loggings should include descriptions of rock type, rock quality including degree of weathering, fractures, shears, faults, rock quality designation (RQD).

A typical arch dam foundation bore layout map and profile view is shown in Figure 2-50 and Figure 2-51. The images show the judicious spacing of the borehole locations in the region of the dam footprint, to ensure sufficient coverage within the foundation, and avoid the possibility of significant adverse foundation features being undetected. Vertical and inclined orientations are utilised to maximise coverage.

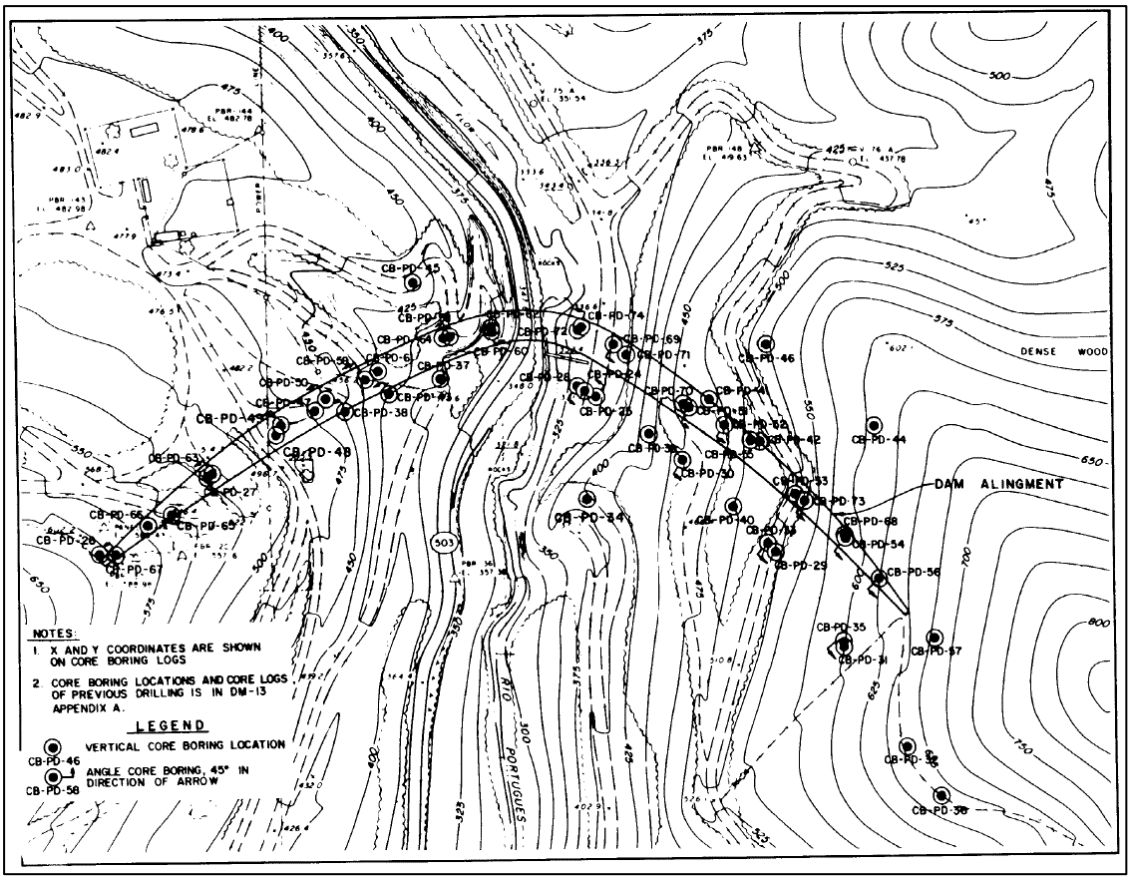

Figure 2-50: Typical arch dam boring layout plan (USACE, 1994)

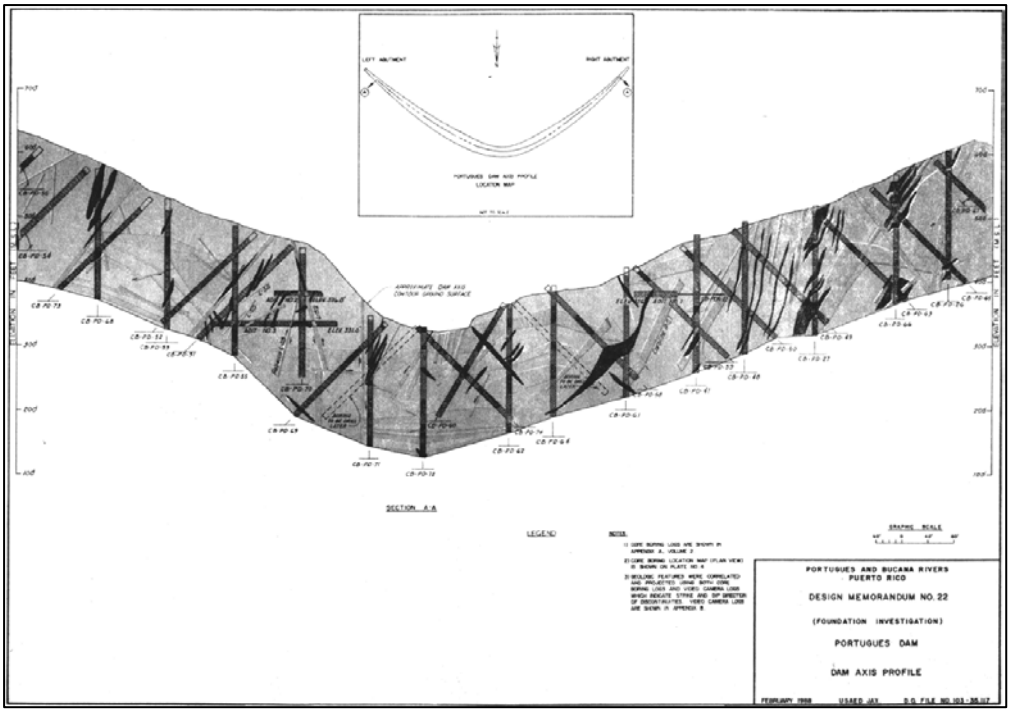

Figure 2-51: Typical arch dam boring profile schematic (USACE, 1994)

Foundation abutment adits are often excavated to provide access for in-situ observations, obtaining of samples, mapping of foundation conditions and large-scale rock mass testing. Foundation information obtained from investigation adits greatly improve the confidence that all significant foundation defects have been detected, and improve the reliability in the statistical evaluation of the rock mass fracture system. A typical isometric view of adit periphery mapping of two interconnected adits is shown in Figure 2-52.

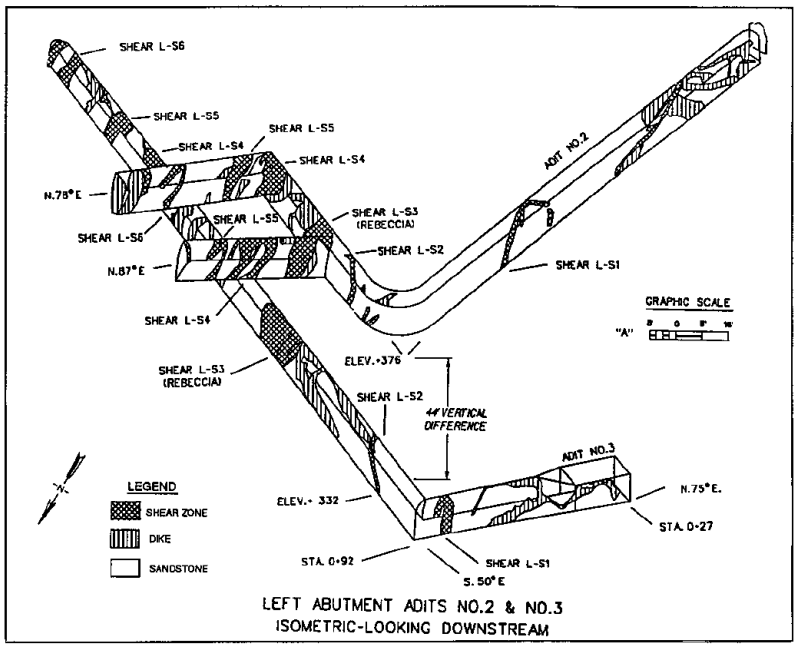

Figure 2-52: Typical isometric view of adit periphery mapping (USACE, 1994)

Insitu foundation testing is imperative for deriving undisturbed material properties of the site. Typical tests undertaken on site may include:

- Geophysical seismic refraction testing, which may be used to survey subsurface foundation conditions such as deformation properties and indicate occurrence of large faults or shear zones. This may include various forms of geophysical testing such as continuous surface wave testing, down-hole seismic testing, cross-hole seismic testing, seismic profiling and sonic borehole logging.
- Dilatometer tests to measure the deformation properties of rock mass.
- Plate load tests/uniaxial jacking tests to predict deformation modulus of material.
- Foundation Lugeon tests to determine the permeability of the rock mass.
- Groutability testing of foundation.
- Groundwater investigations of foundations.
- Large-scale shear tests of foundation rock mass.

Various laboratory testing procedures may also be performed on samples taken from site. These are normally standard material properties tests that provide data on the physical characteristics of the materials including:

- Unconfined compressive strength,
- Tensile strength (direct or split cylinder test),
- Elastic Modulus,
- Poisson's ratio,
- Specific gravity and unit weight,
- Porosity and permeability,
- Moisture content,
- Absorption.

Direct shear and triaxial shear tests are also normally undertaken to evaluate the shear strength of the rock mass on intact samples, sawed surfaces and natural fracture surfaces. This will provide a range of shear strength parameters for providing sliding resistance at various possible failure interfaces. Physical surveys of the joint roughness of sheared joints are usually undertaken for deriving the joint roughness coefficient (JRC), to be incorporated in determining the friction angle of the sheared joint.

The various forms of foundation site data obtained and the associated inferences are corroborated against each other, where coverage overlaps to increase reliability of the geotechnical investigation outcomes. A comprehensive foundation model is normally created

providing a detailed account of the various characteristics and defining aspects of the dam rock mass foundation, for design of the arch dam.

2.4 DAM INSTRUMENTATION AND BEHAVIOUR MONITORING

Concrete arch dams are complex three-dimensional solid structures that develop intricate load transfer paths, and associated deformation mechanisms when loaded. Instrumentation of an arch dam allows for monitoring of its behaviour in response to various loading conditions.

The response of the dam is normally measured in terms of components such as deformations, strains, stresses, temperatures, tilting, relative movements, joint openings, hydrostatic pressures, piezometric levels and seepage/drainage flows.

The primary purpose of these measurements is immediate safety of the dam (ICOLD, 1988). Implicitly all dam design work or surveillance is for the purpose of constructing a safe dam. More explicit reasons or objectives for instrumentation monitoring of concrete arch dams are mentioned below:

- Measurement of dam behaviour during construction and impoundment of reservoir, to identify and evaluate the severity of early signs of variations from expected design behaviour.
- Measurement of dam behaviour during operations to provide early warning signs of possible imminent failures, or the development of unfavourable scenarios or severe distress.
- Verification of design assumptions and parameters by observing measured behaviour against expected behaviour of dam. This provides the engineer with confidence in the design suitability.
- Prediction of future behaviour of the dam, according to trends derived from statistical analysis of historical cyclic behaviour.
- Provide necessary structural behaviour information for undertaking an adequate dam safety inspection or surveillance exercise.
- Progression in the technical knowledge and understanding of the complex behaviour of concrete arch dams, allowing for the transfer of expertise to the designer and dam engineering fraternity, to be used in future designs. This serves as research into the complex nature of the multitude of forces, acting in an unusually interdependent manner, on an arch dam.

In establishing a dam instrumentation strategy, the objective of the instrumentation should firstly be considered. When the objective of instrumenting a particular dam with its own unique challenges and conditions is understood, then the type of measurements required and associated instrumentation set up can be formulated by the design engineer. There is no standard minimum requirement for instrumentation of arch dams and implementation is normally based on sound judgement of the experienced dam designer. An approximate rule of thumb is that instrumentation for a concrete dam will normally make up 1 – 3 % of the dam construction cost.

Because of the monolithic behaviour of concrete arch dams, displacement is the most meaningful parameter that can be readily measured (USBR, 1987). Displacements in the horizontal plane are the most significant. All concrete arch dams should have provisions for measuring these displacements as a bare minimum. This may include relative movements between points within the dam body, and movement of the dam against a remote fixed point.

Other parameters that should be considered for concrete arch dam monitoring include foundation movements, and relative foundation movements at any major joint in the dam. It is also necessary to monitor seepage flows through formed and foundation drains.

Measurements of strains, stresses, temperatures, tilting and hydrostatic pressures may also provide valuable insight into the behaviour and state of conditions of the concrete arch dam.

Traditionally dam instrumentation has been placed in categories according to the physical measurement taken. These instrumentation categories are listed below and discussed in detail later:

- Internal movement measuring devices.
- Surface movement measuring devices.
- Stress measuring devices.
- Hydrostatic pressure measuring devices.
- Seepage measurement devices.
- Vibration measuring devices.

The various instrumentation and measuring devices that may be used for monitoring of arch dam behaviour, are presented below in terms of the various forms of dam behaviour measurements obtained.

1. Monitoring of Movement

A concrete arch dam on a rock mass foundation, may undergo several types of deformation movements within the dam body and in the local surrounding foundation. The movements that may occur and for which it is desirable to measure, or monitor may be vertical, horizontal (translational) or rotational.

Vertical movements of arch dams are normally the result of a combination of deformation and consolidation of rock mass foundation, caused by the weight of the dam and water reservoir. Resultant horizontal movements of an arch dam may be derived into components acting perpendicular and tangential to the dam axis. Such movements manifest mostly as radial translation of the dam in a downstream direction, due to a combination of large hydrostatic forces and temperature fluctuations, and tangential translation due to lateral deformation spreading of the foundation abutments. Rotational movements of the dam occur due to low shear strength of the foundation rock, causing the lower central portion of the dam to move outwards.

a. Geodetic Surveys

A geodetic survey comprises measuring deformation movement of a dam using land surveying equipment. A survey instrument is set up at a location point a sufficient distance away from the dam to not be locally influenced by the dam movement. The survey instrument is used to sight a set of target points or survey beacons on the dam body, in relation to a predetermined known benchmark point, also away from the dam body. The locations of the survey beacons are compared to the location of the benchmark point in relation to a predetermined plane common to both points, and a 3-dimensional coordinate of the survey beacon point is defined.

Geodetic surveys are done at regular time intervals and the changes in survey beacon position over the time intervals, provide data for calculating the movement of the marker point in 3-dimensional space. Mathematical theory and equations of geometry and/or trigonometry are used to transform linear and angular measurements, into deflections of alignment points.

Various measurement systems that may be used for conducting these surveys comprise collimation (tangent-line measurements), trilateration, triangulation and surveying angle-distance closure systems. An example of a triangulation system survey set-up for the Katse Dam in Lesotho is shown in Figure 2-53, indicating that five monitoring points (triangles), were set up around the dam for sighting ten survey points (black dots) in reference to one bench-mark point (P11).

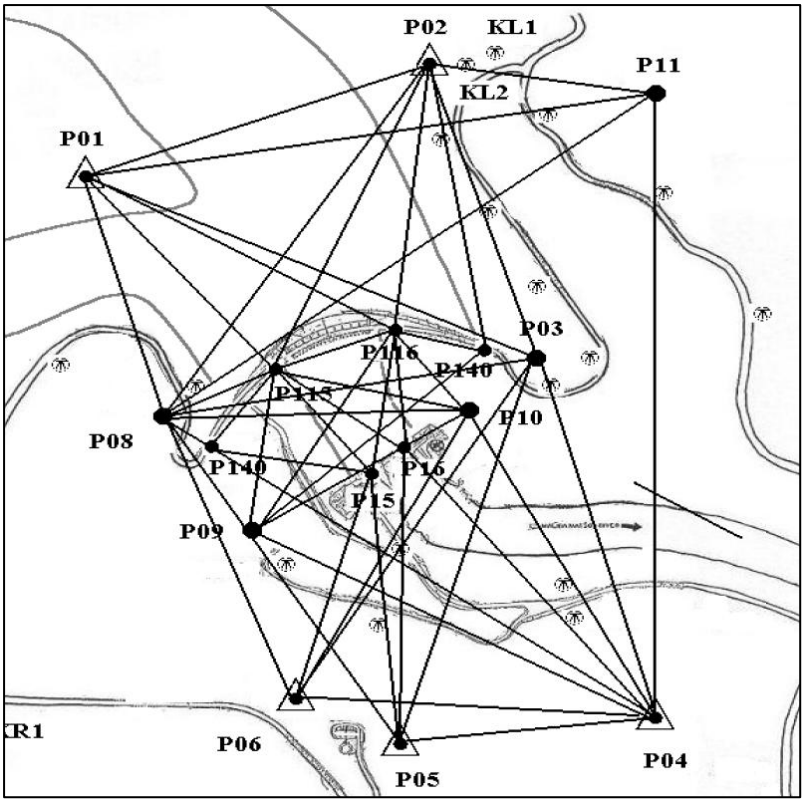

Figure 2-53: Triangulation survey network for Katse Dam (Pretorius *et al.*, 2001)

The deformation movements of an arch dam are normally plotted as 2-dimensional or 3-dimensional vectors relative to the axis of the dam configuration, as shown in Figure 2-54, for the Zervreila Dam in Switzerland. Geodetic surveys taken at regular intervals provide reliable deformation movements of the dam over time-history periods.

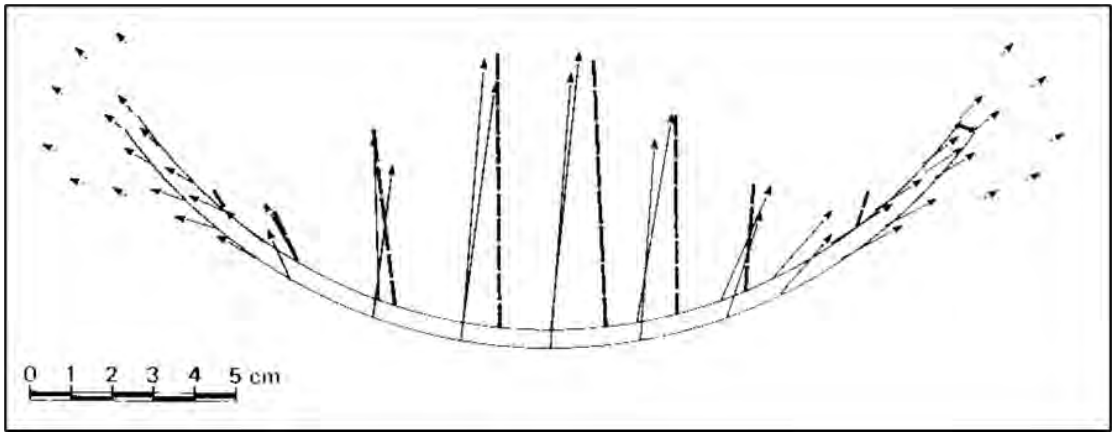

Figure 2-54: 2-dimensional displacement vectors at crest of Zervreila Dam from geodetic survey results (Dungar, 1985)

Equipment used to conduct such surveys include theodolites, auto-levellers, total stations, EDM (electronic distance measurement) instruments and conventional tape measuring tools. An example of a total station set up for dam monitoring is shown in Figure 2-55. Modern geodetic

survey instruments can measure deformation movements to an accuracy of 2 mm (Pretorius *et al.*, 2001).

Figure 2-55: Total station with EDM capability set up for measuring dam movements (USACE, 2018)

b. Pendulums

Pendulums also known as plumblines are powerful instruments that can measure the bending, tilting and deflections of concrete dams. The pendulum device is made up of a plumb bob, suspended from a steel wire in a vertically formed well within the dam body, that extends from top of dam to near the foundation level. The pendulum wire is attached at the top to a suspension device and hangs within a vertical shaft, with a dashpot vessel near the bottom to damp out local vibrations. A sketch illustrating the main components (A-E) of the pendulum is shown in Figure 2-56. Pendulum reading stations are normally located at elevations along the vertical height of the pendulum wire, where galleries intersect the vertical well, and measurement observations are made.

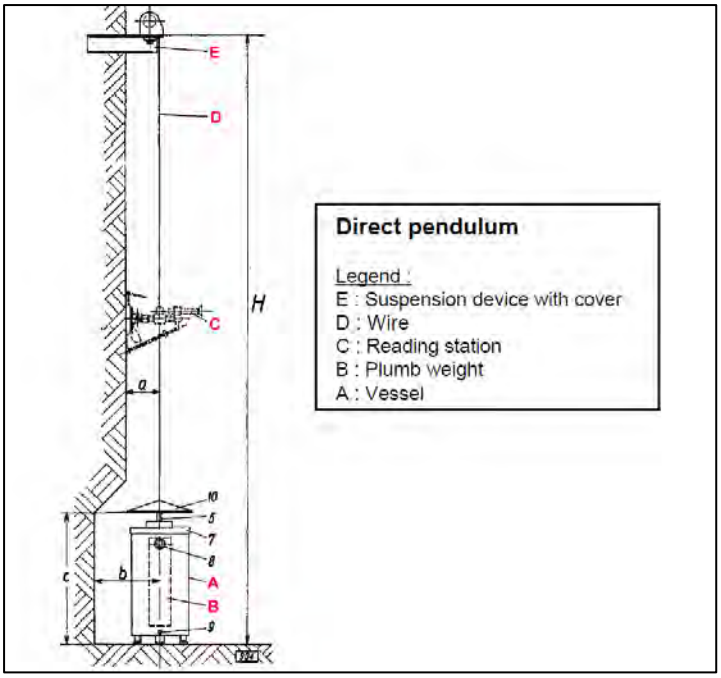

Figure 2-56: Sketch of direct hanging pendulum (ASCE Task Committee, 2018)

Conventional direct plumblines are suspended from the top of the dam, meaning that they can only be installed near to completion of construction. Inverted pendulums can be installed during construction and are configured with a float assembly at the lowest point of the instrument, serving as the fixed point of the instrument. Inverted pendulums also allow for measurements below dam base into the foundation.

A pendulum measures movement of the dam at reading points relative to the fixed point being the point of suspension. It is considered a minimum requirement to install at least three pendulums on a concrete arch dam, one at the crown cantilever (highest section) and one at each midpoint along the abutments as shown in Figure 2-57 (USACE, 1994). If pendulums are properly operated, they can be very accurate instruments for measuring dam movement, and when observed over several years will furnish valuable information regarding the elastic behaviour of the dam-foundation structure. Due to the sensitivity of these instruments, it is important to practice good quality control of the measurements and to practice good maintenance and cleaning of these instruments, to ensure the readings obtained are reliable. Poor quality control can result in inconsistent measurements. According to Dunicliff (1988) pendulums can be read to an accuracy of 0.5 mm.

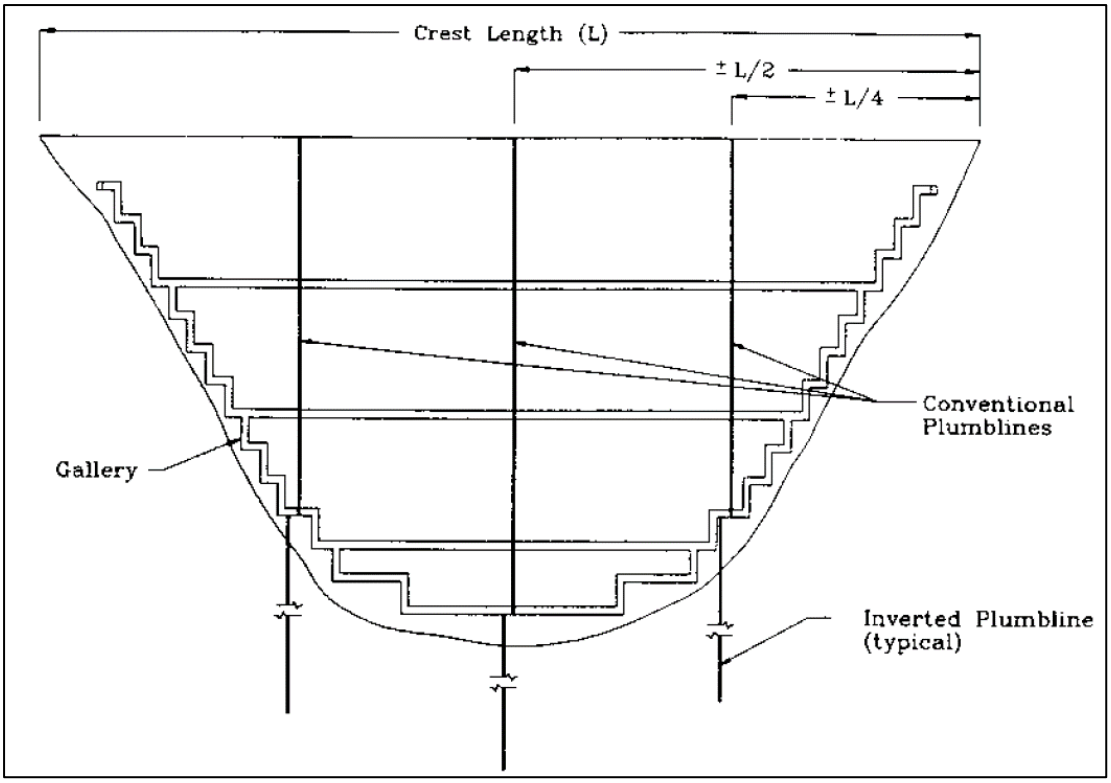

Figure 2-57: Typical layout of plumblines in an arch dam (USACE, 1995).

c. Extensometers

Extensometers measure movement of one point in the dam or foundation structure, relative to another point in the dam or foundation. The instrument is designed to measure axial displacements of one or more fixed points along its axis, in relation to a reference measuring point. The groutable fixed points are called anchor points and are configured at the end of each of a series of parallel rods or tension wires, with staggered lengths along the axis of the instrument. A rod-type extensometer with six groutable anchors is shown in Figure 2-58.

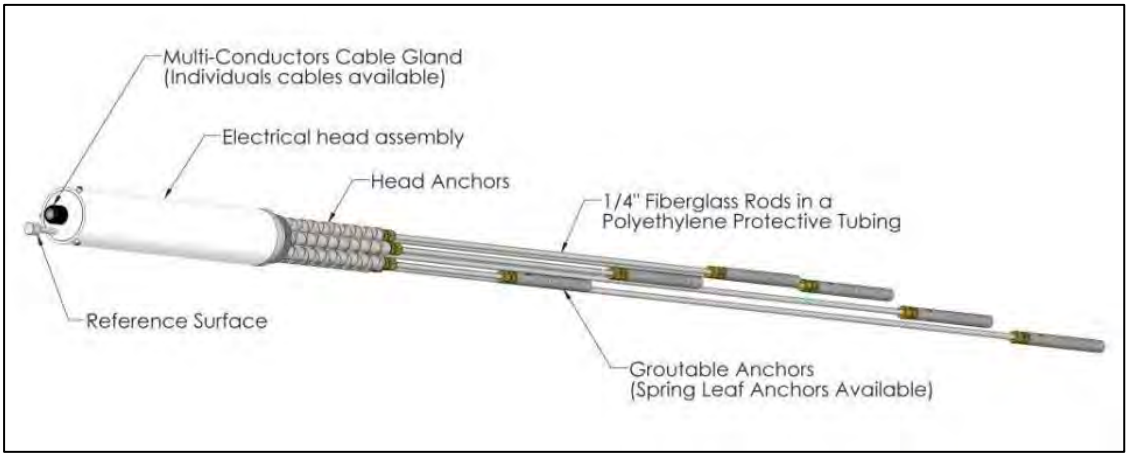

Figure 2-58: Rod-type extensometer with six groutable anchors

The extensometer is installed by drilling a borehole into the foundation/dam material, to the required depth, and fixing the anchor points into their positions along the uncased borehole from bottom up. Each anchor point is grouted into position using a thin sand-cement grout and the measuring head installed at the top. An extensometer may comprise multiple anchor points along its configuration. A typical horizontal extensometer installation sketch is shown in Figure 2-59.

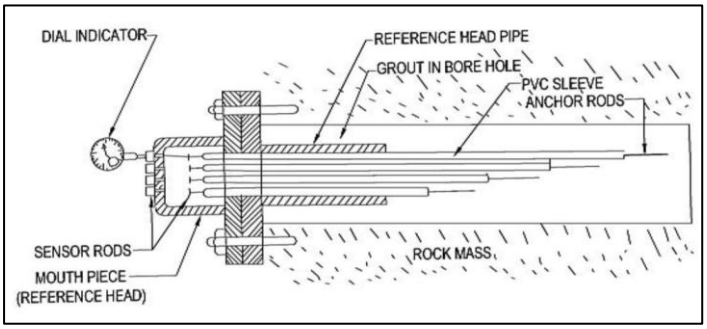

Figure 2-59: Horizontal installation of rod-type extensometer with four anchors (Dam Safety Rehabilitation Directorate, 2018)

Extensometers measure small axial deflections of 50 – 100 mm and should typically be installed to a depth 25 % - 50 % of the dam height. Extensometers are normally placed in the foundation at the base of the dam and orientated in the direction of the expected primary mode of dam-foundation deformation movement. A simple arch dam instrument configuration showing three extensometers is shown in Figure 2-60.

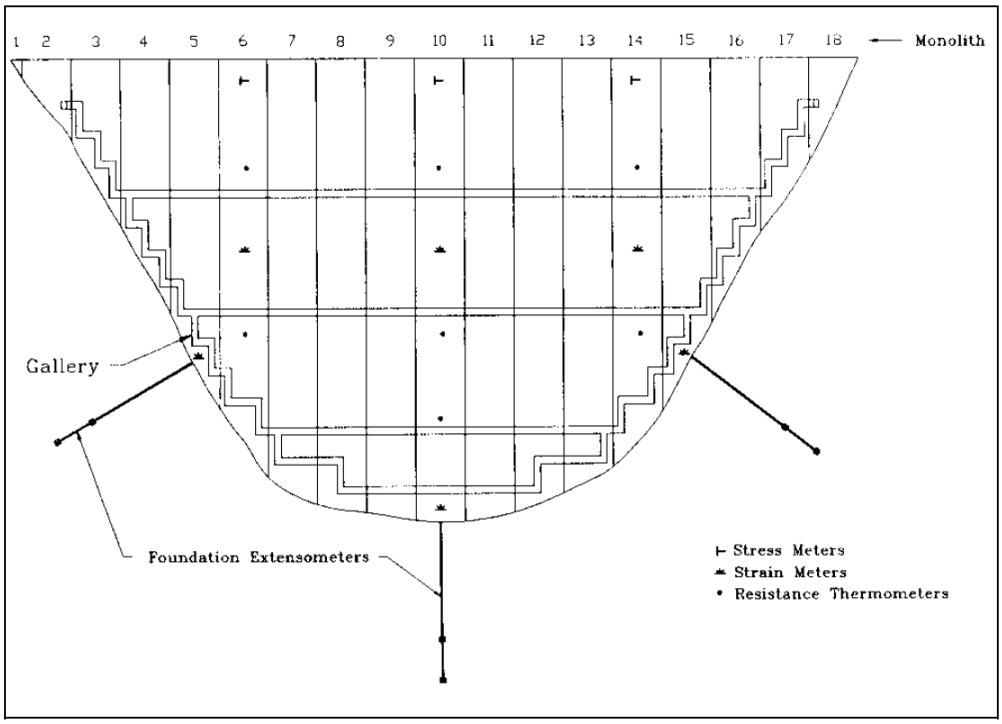

Figure 2-60: Extensometer configuration in relation to arch dam (USACE, 1994)

Extensometers should be placed to bridge between different zones of foundation rock material and across rock lineations, faults or other potential sliding planes. Extensometers should be installed in the dam foundation before commencement of concrete placement, allowing for the dam-foundation movement to be monitored during construction and provide insight to possible unforeseen foundation issues, or permanent deformation during the construction phase of the dam. A certain amount of redundancy is required in instrumentation placement for dams, and it is beneficial that the location of extensometers correspond to dam elevations for other instruments. Cross-referencing of instrument readings provides additional confidence in the measurements obtained.

d. Inclinometers

Inclinometers are used to monitor the lateral movements in the abutments and foundations of concrete arch dams. Inclinometers can be installed in the dam concrete or foundation material. Inclinometers extended into the foundation can provide information on a potential rock mass sliding plane that needs investigation.

Inclinometers are made up of a specially shaped metal or plastic casing embedded into the concrete, a probe and a readout unit. The casing is grouted into a vertically drilled hole in the dam or foundations. The probe inside the casing, has two accelerometers that detect the inclination angle of gravitational acceleration at the relative plane of their axis, by measuring the tilt of the probe in two mutually perpendicular directions. The probe measures inclination of the casing to the vertical at regular intervals, and lateral movement with respect to the bottom of the casing, is calculated by summation of the incremental measurements taken at various intervals. A cross-section of the casing (a), side view of the inclinometer (b) and an image with summation of displacements (c) is shown in Figure 2-61.

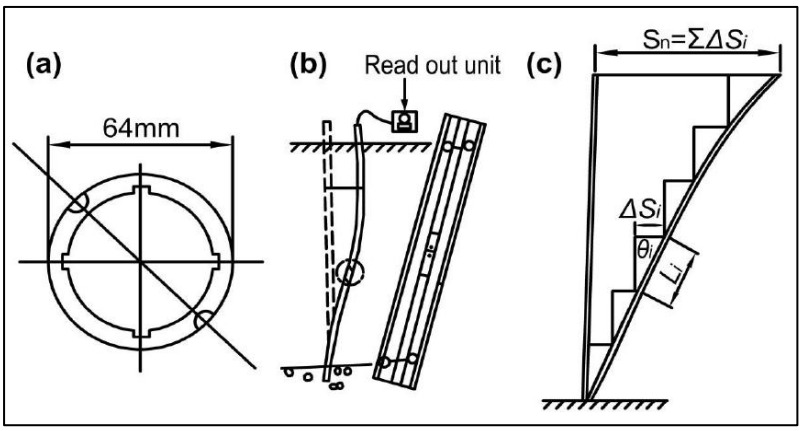

Figure 2-61: a) Cross-section of casing, b) Side view of inclinometer and c) Summation of displacements (Dam Safety Rehabilitation Directorate, 2018)

The installation of inclinometers by core holes is a useful attribute as it allows for installation post construction of existing dams.

e. **Strain meters**

Strain meters measure strain and temperature in dam concrete material by using a variety of electrical or mechanical strain gauges. Vibrating wire strain gauges are commonly used for internal measurements in the dam concrete. These operate on the principle that a tensioned wire inside the gauge, vibrates at a certain frequency that is proportional to the strain in the wire. The gauge is assembled so that a tensioned wire is held between two end flanges. When the strain meter extends the tension in the wire increases along with its vibrating frequency, and when the meter contracts the tension in the wire reduces lowering its natural frequency.

Strain gauges are installed in cluster formations known as rosettes, to evaluate a three-dimensional stress state in the concrete and calculate principal strain using Mohr's circle formulae. Formation A and B shown in Figure 2-62 are simple formations where the principal stress directions are vertical and horizontal. Rosettes C and D allow for a full triaxial strain state to be measured, whilst E and F do the same but have additional redundancies in case of malfunction of one of the strain gauges.

To convert measured strains into stresses the material parameters such as elastic modulus, thermal expansion coefficient, creep and shrinkage need to be known which can be obtained from laboratory testing of the concrete. The installation of strain gauges in a concrete arch dam requires careful consideration of the complex three-dimensional strain state, ensuring the gauges align with the directions of meaningful strain modes of the dam. These normally comprise axial, vertical and radial strains.

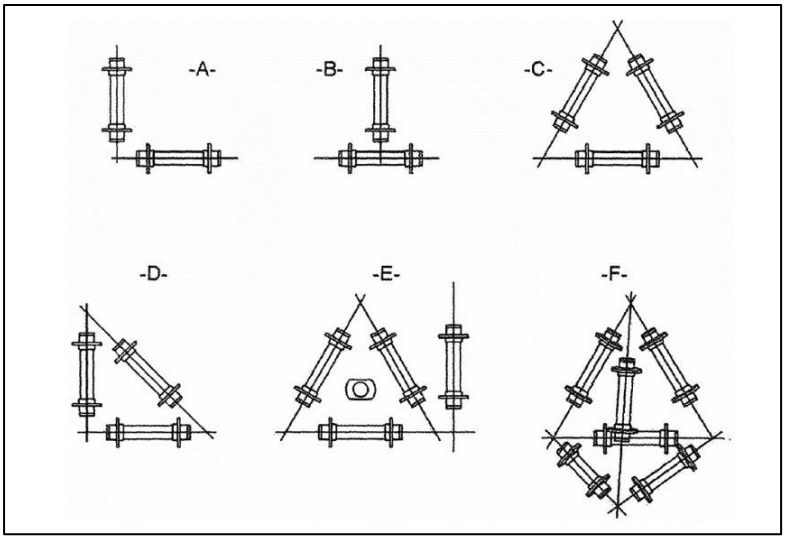

Figure 2-62: Various Rosette strain gauge formations (Dam Safety Rehabilitation Directorate, 2018)

f. Joint meters

Joint meters are used to measure the relative movements across a formed joint. The most common use is to measure the opening of contraction joints between concrete dam monoliths. Joint meters function in a manner similar to strain meters and resemble them very closely apart from their installation.

The installation configuration of a joint meter is shown in Figure 2-63. A threaded socket with anchor is cast into the leader monolith approximately 150 – 250 mm from the top of lift, with the socket open end plugged closed and attached to vertical face form work (step 1). A timber recess box is formed below the socket to house a wrapped cable which has one end fixed in the concrete and the other loose for connection to the instrument. After stripping the form and recess box, the monolith joint is prepared for casting of follower block (step 2). The follower block is then cast filling the recess void and encasing the instrument which is screwed into the socket just before placing the final 300 mm of lift (step 3). If possible, this procedure can be simplified by omitting the recess box and casting the cable lead in the follower monolith.

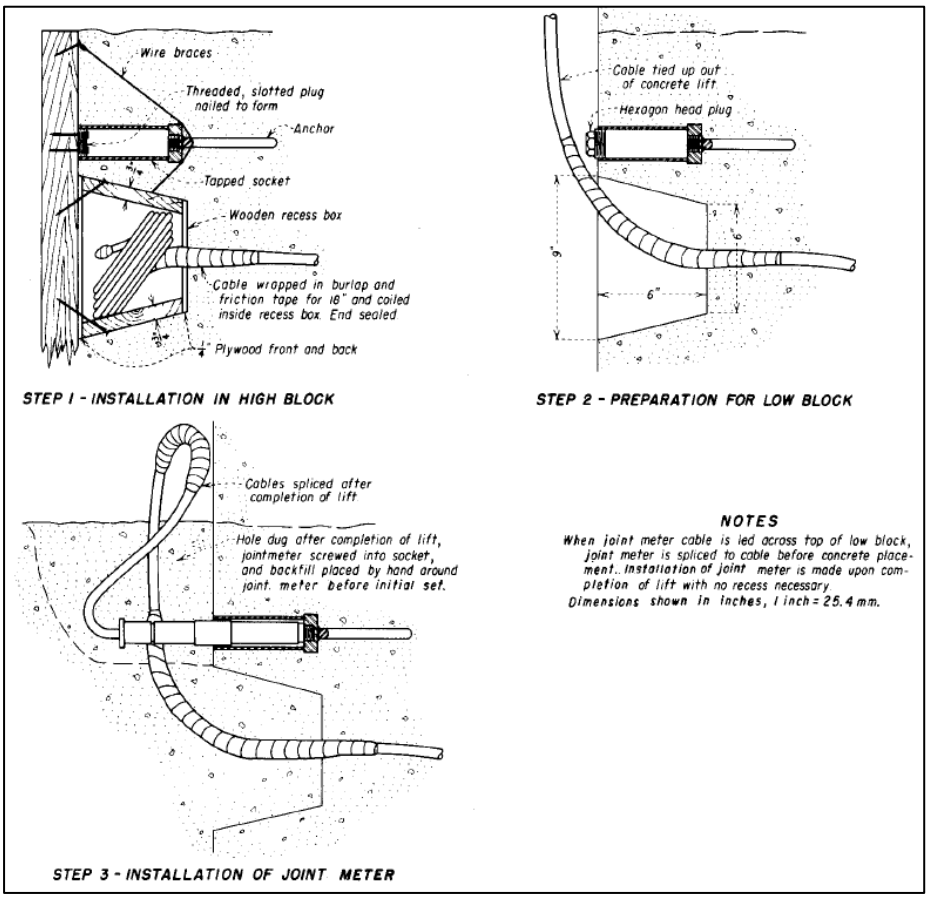

Figure 2-63: Installation set up of a joint meter across dam monolith joint (USBR, 1987).

The maximum relative movement that can be measured by strain meter is approximately 5 - 10 mm, and if larger movements are anticipated these instruments should not be used. Joint meters provide information about when the joints begin to open and if there is adequate opening for grouting. They also provide an indication of how effective the grouting is and whether further movement occurs in the joint during and after grouting.

According to USACE's Arch Dam Design Manual, joint meters are required in every other dam monolith contraction joint, at the mid height elevation, of alternative grouting lifts as is shown in Figure 2-64. Joints can be monitored with double or single joint meter configurations as per detail A and detail B in the figure. Dam joint meters provide information on the dam thermal state by measuring operational long-term temperature change induced expansion and contraction of the dam along its axis.

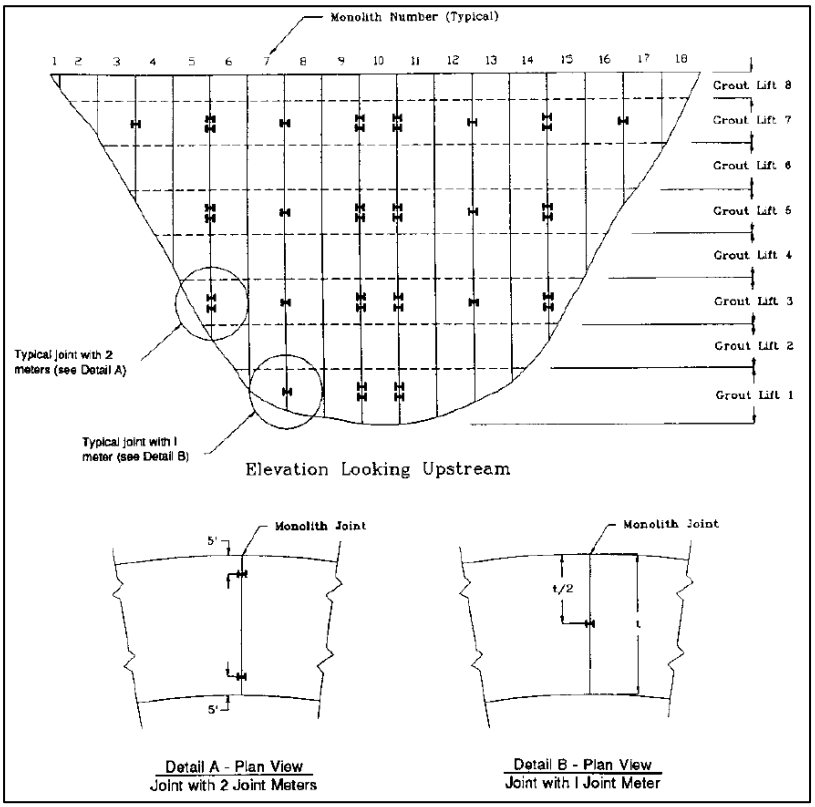

Figure 2-64: Minimum requirement arch dam joint meter layout (USACE, 1994)

Keeping a historical account of deformation movements of a dam over an extended period after filling, allows for cyclic behaviour of the dam in relation to seasonal loading conditions to be captured. The evaluation of any trends or repeated behaviour of the dam in parallel to repeated seasonal loadings, gives a good indication of what portion of the deformation movement is permanent (unrecoverable) and which portion is elastic (recoverable). Seasonal deformation of a dam that cycles back and forth between winter and summer or rainy and dry seasons, returning to the same value is considered to be elastic, whilst anything outside of this may be permanent.

2. Monitoring of Stress and Pressures

It was shown in Section 2.2.7, that an arch dam behaves like a loaded shell developing internal stress distributions that are of a three-dimensional nature and not purely vertical and horizontal. To monitor the triaxial internal stress mode of an arch dam, requires careful consideration of the principal stress paths that develop in the dam body. As a minimum requirement, the compressive axial (hoop) stress and vertical cantilever stress should be measured within the dam.

Other stresses that need to be measured are bearing stress at the base of the dam, as well as hydrostatic pore pressures acting at the dam base or within the rock foundation. The bearing stresses furnish information on the stability of the dam foundation joint in terms of sliding and indicate the development of excessive tension cracking at the heel, or development of unwanted bridging stresses, due to localised foundation rupture.

a. Stress Meters

Stress meters measure compressive stresses independently of shrinkage, expansion, creep or changes in elastic modulus. Stress meters are used for measuring vertical stresses at the base of a section, or for measuring horizontal thrust stresses along the dam axis in the upper portion of the arches. Like strain meters, stress meters can be set up to measure a triaxial stress state in the three-dimensional space. A comprehensive installation of three-dimensional stress meters, covering the body of an arch dam, may provide sufficient stress data to map the principal stress state of the loaded dam.

Various types of stress meters are available that use different methods to measure stress. The most used device is the Carlson-type cell shown in Figure 2-65. The device comprises a mercury filled diaphragm exposed to the exterior on one side, with a transducer/wire strain meter housed in a chamber within the device casing on the inside of the diaphragm. The monitored stress of the dam concrete is imposed on the diaphragm and causes a deflection, which is measured by a transducer or elastic strain meter wire and converted into a stress.

Stress meters are often used in conjunction with strain meters, for comparisons and checks of measurements deduced from strain meters.

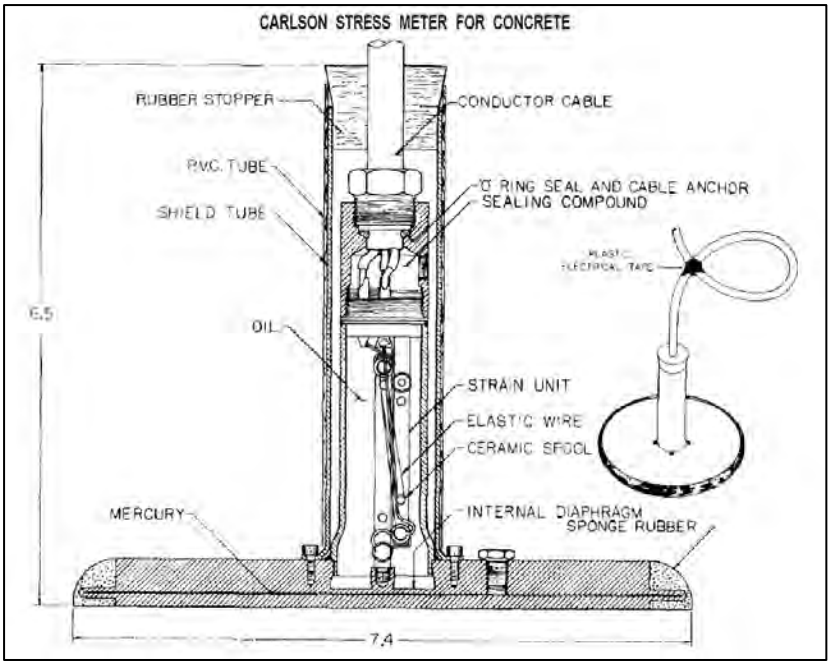

Figure 2-65: Carlson-type stress meter for concrete (USACE, 1987)

b. Piezometers

Piezometers are used to measure water pressures within the dam and foundation material. Closed piezometers can measure the uplift pressure distribution along the base length of a dam section, or within the foundation rock mass along the seepage path of the grouted drainage curtain. Piezometers are installed at desired locations by inserting into holes drilled to the desired elevation level of monitoring.

Closed piezometers typically comprise of electric resistance or vibrating wire devices. The details of a vibrating wire piezometer assembly are shown in Figure 2-66. The piezometer tip contains a porous disk that allows water to enter and press against a diaphragm. A high-strength steel wire is fixed to the centre of the diaphragm at one end and to a block at the other end. The wire is set to a predetermined tension during manufacture. Pore pressure applied to the diaphragm causes it to deflect, thereby changing the wire tension and resonant frequency of the wire. Measured vibration frequencies are converted to pressures using an equation or conversion chart.

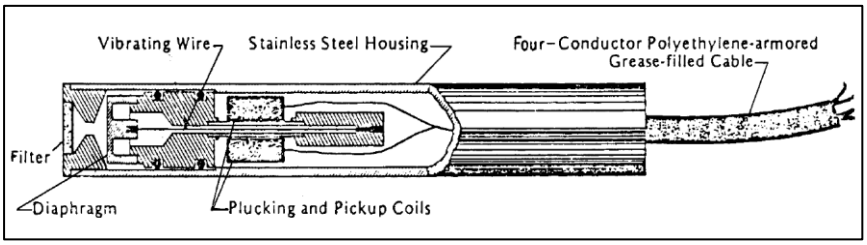

Figure 2-66: Vibrating-wire piezometer tip assembly (USBR, 1987)

Open piezometers or standpipes fitted with a pressure measuring device, also provide means to measure the hydrostatic head at a particular location along the base of the dam or the seepage path of the grout curtain.

Standpipes for measuring uplift pressure along the dam base, are installed by casting in a system of pipes at several locations along the dam axis in the first lift of the dam body, directly above the contact between the foundation and base of the dam. The top of the standpipes are fitted with Bourbon-type pressure gauges to measure the pressure in the pipe.

Drainpipes for measuring pressure along the grout curtain seepage path, are installed in drillholes that extend from lower galleries of the dam, to below the dam in directions both upstream and downstream of the grout curtain. These drainpipes are also fitted with a Bourbon-type pressure gauge. The variation in the pressure measured upstream and downstream of the grout curtain or drain location, can be used to derive a pressure head diagram by plotting the values along the seepage path or base of the dam, as shown in Figure 2-67.

The measurement of hydrostatic uplift pressure along the dam-foundation interface, is critical for establishing the effective operation of drainage systems designed to alleviate uplift pressures. Measurement of hydrostatic pressure along seepage paths around the grout curtain, indicates the effectiveness of the foundation grouting in reducing large hydraulic gradients within the fractured rock mass.

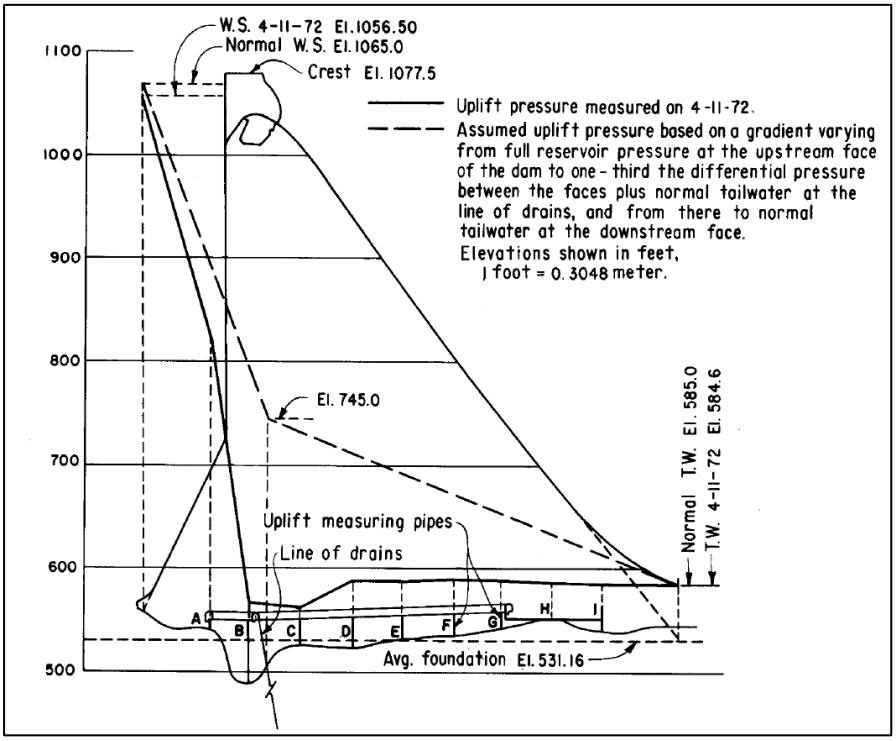

Figure 2-67: Comparison of measures dam uplift pressure with assumed design value (Casagrande, 1961)

3. Temperature

The temperature state of a concrete arch dam has a significant influence on the deformation and stress behaviour of the dam. Temperature induced loading of a dam commences from placement of concrete, when heat of hydration generated in the concrete during curing is retained at the core and dissipated at the shell. This leads to the development of stress inducing surface temperature gradients between the core and shell, as the surface shrinks whilst the core expands.

Later on, as the core temperature dissipates and the dam body temperature stabilises, the mass/core of the dam shrinks. This mass temperature gradient causes development of internal stresses as the shrinkage is restrained by the outer shell and dam foundation.

a. Resistance thermometers

Resistance thermometers are suitable for long-term temperature measurement in dams and are installed in a grid-type pattern, to measure the temperature state of a dam at various time step intervals of the dam's life. At a given section and elevation of the dam, thermocouples should be installed having one device 2 – 3 m below the upstream face, one device approximately at the core and another device 2 – 3 m below the downstream face.

Installation of thermometers is relatively simple and comprises placing the device in a shallow hole in the concrete, 150 – 200 mm deep, and covering it with fresh concrete that is lightly vibrated.

The resistance thermometer is a Carlson type instrument and consists of a wound coil copper wire, enclosed in a casing. The change in resistance of the copper wire as temperature changes, is measured by a Wheatstone bridge-type readout unit and converted into a temperature change. Details of a resistance thermometer are shown in Figure 2-68.

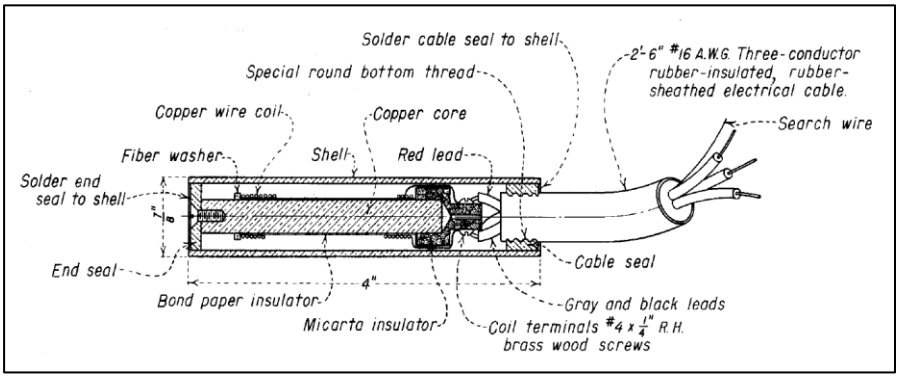

Figure 2-68: Embedded type resistance thermometer (USBR, 1987)

Thermometers are important for measuring thermal gradients in the dam during and post construction, for monitoring the concrete cooling process, determining typical heat of hydration values and to determine seasonal long term operational temperature cycles of the dam body.

b. **Thermocouples**

Thermocouples are suitable for measuring temperatures in massive concrete structures over a short period, such as the first few days after concrete placement in a dam. These devices can provide detailed temperature histories over short periods of time. The rapid response to temperature variations is due to the small sensing element and its low thermal capacity.

Thermocouples are relatively inexpensive, simple to construct and rugged, however the indicating readout instruments are comparatively elaborate and prone to precision errors and highly sensitive to extraneous influences. Generally, resistance thermometers are preferred over thermocouples in concrete installations as they are more dependable, longer lasting, show greater precision and are less complicated to operate.

Thermocouples function according to the principle that when two dissimilar metal wires are joined together, a change in temperature produces a change in voltage at the junction. The magnitude of the voltage depends on the metals used and is proportional to the temperature at the junction. The voltage change is measured by a potentiometer and used as input to calculate the temperature.

2.5 FINITE ELEMENT METHOD

2.5.1 Introduction

In general, the FE method is a numerical analysis procedure in which a structure is analysed in terms of a given field quantity, within a defined domain of interest. The approximated distribution of a field quantity is hereby obtained, where a solution is difficult when using simplified analytical approaches (Liu & Quek, 2003).

The internal response of the structure domain is evaluated as a result of external conditions imposed on it. The internal response is evaluated in terms of the field quantity distribution, being the output or results of the numerical analysis, to be evaluated against the required design criteria or serviceability constraints of the structure.

The field quantity of interest of the analysis problem may be any physical engineering phenomenon, that can be expressed by governing mathematical equations and boundary conditions. The physical phenomena may typically comprise structural behaviour, fluid behaviour, thermal heat transfer, wave propagation, and electrostatics. The analysis results of greatest interest are normally the peak value of the field quantity or its gradients.

A common use of the finite element method is for modelling (simulation) of the physical behaviour of loaded structures, in accordance with the displacement or stress that develops in the structure, as it responds to a loading condition. Normally the FE method is adopted for analysis where either the structure comprises a complex geometrical configuration, or the loading condition is of an intricate or multi-faceted composition.

In basic terms, the FE method involves dividing a structure up into several smaller regularly shaped interconnected pieces and describing the behaviour of each of these pieces in a simple way, in terms of a simultaneous equation. This process is referred to as discretisation of the structure into elements and these elements are connected to each other by common nodes, that effectively represent locations where neighbouring elements are “glued” or fixed to one another, as shown in Figure 2-69. A set of simultaneous algebraic equations, or governing equations, can be used to represent the inter-related mechanical behaviour of the system of interconnected elements.

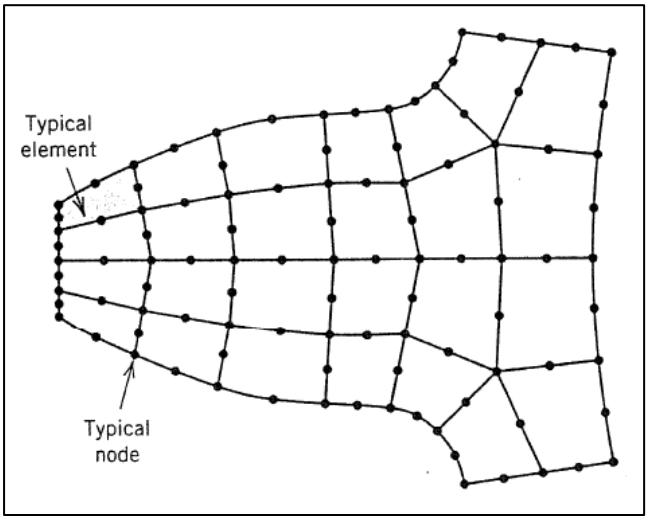

Figure 2-69: A two-dimensional FE model of a gear tooth (Cook, 1995)

Due to the fixed connection between neighbouring elements, the simultaneous equations that describe the displacement of each element, need to be compatible in terms of a common displacement at nodal points of the element. The structural nature of this interlinked matrix also means that for a static loaded structure, force equilibrium will remain across nodal points.

The loading and support conditions of the structure modelled using the FE method, are applied to the nodal points in the vicinity of the loading or support of the structure. A complex load spanning a few nodes or elements, is discretised into an equivalent system of point loads acting at the node points, whilst supports are modelled as physical nodal boundary constraints preventing local movement (translation or rotation), in terms of the degrees of freedom of the structure.

A sophisticated description of the FE method may regard it as a piecewise polynomial interpolation over the elements in the structure, from nodal values of the displacement (field quantity). As a result of the connection between elements, the displacement becomes interpolated over the entire structure in piecewise fashion, by as many polynomial expressions as there are elements (Cook, 1995).

2.5.2 The Finite Element Procedure

The finite element method is a powerful tool for undertaking a structural analysis, where a detailed analysis is required as part of the design approach, for deriving a solution to a complex engineering problem.

The finite element problem is derived by formulating algebraic equations that represent the behaviour of each element of the discretised mesh structure, according to the governing equations and boundary conditions of the physical structural mechanics phenomena.

There are three primary methods that can be used to derive finite element equations of a physical system (Logan, 2019). These are the:

- Direct method or direct equilibrium method,
- Variational methods consisting of among the subsets energy methods and the principle of virtual work,
- Weighted residual methods.

A direct method, known as the displacement or stiffness method, is one of the most common formulation approaches for deriving algebraic equations used in FE modelling for structural analysis problems. Most FE programs have adopted this approach due to its simplicity, generality and good numerical properties (Ghanaat, 1993). The displacement method is adopted in this dissertation.

According to the displacement (stiffness) method, the algebraic functions are derived in terms of known behaviour defining local constitutive stiffness parameters, defined nodal loadings

(forces) and unknown nodal displacements, with reference to a local coordinate system. These equations are normally presented in matrix form as a local stiffness matrix.

The local stiffness matrices representing the numerous elements making up the modelled structure, are then combined into a global stiffness matrix according to a global coordinate system. The stiffness approach is then used to derive a matrix algebra equation, equating the product of the global stiffness matrix and displacement vector (unknown), to the global force vector, which represents the external force loads of the system.

In terms of matrix algebra the global solution of the FE system is presented in Equation 2-20, in which the unknown displacement variable {U} is solved in terms of the known global stiffness matrix [K], and the force vector {F} which is derived from the discretised load functions.

$$\{F\} = [K]\{U\} \qquad \textbf{2-20}$$

Where

{F} = Force vector

[K] = Global stiffness matrix

{U} = Displacement vector

The solved displacement vector provides nodal displacements of the entire model, from which elemental strains can be derived by differentiating displacements across elements, and deriving strain gradient interpolating functions.

Stresses are simply computed by relating them to element strains in accordance with the constitutive material parameters.

2.5.3 Finite Element Formulation

The term finite element was first introduced by Clough in 1960, when plane stress triangular and rectangular elements were used to model two-dimensional structures such as thin plates.

The FE method can be used to solve problems of a one-, two- and three-dimensional nature. In many cases, truly three-dimensional structures are analysed according to simplified principles of one- or two-dimensional models.

The geometrical configuration and the expected response to loading of a structure, analysed using the FE method, will dictate the level of complexity required when modelling. This will

also dictate how many dimensions (degrees of freedom) of movement should be considered in the model, to accurately represent the structure behaviour.

The type of elements used to create the FE model, are based on the degrees of freedom required to accurately model the structural behaviour, according to translation and rotation of the structure. Some common element types used are shown in Figure 2-70

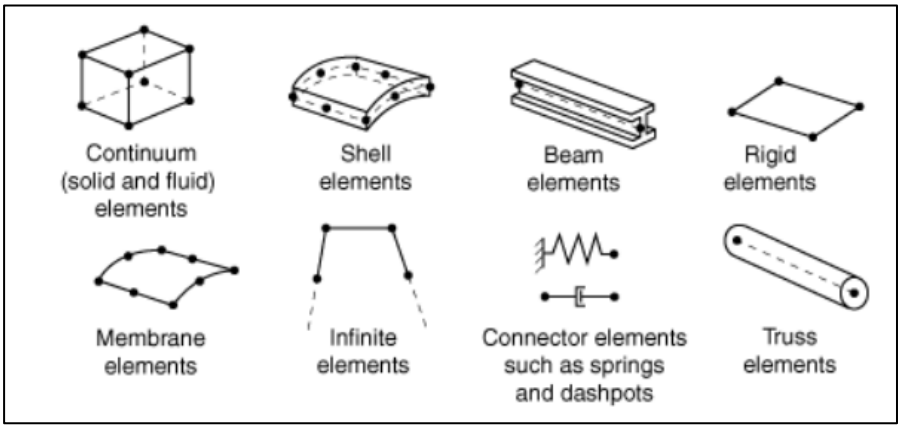

Figure 2-70: Common element types used in FE modelling (Andersson & Seppälä, 2015)

The basic element shapes commonly used to discretise structures in one-, two- and three-dimensional space, are shown in Figure 2-71. Linear type elements are shown in the top row of the figure and quadratic type elements with mid-side nodes in the bottom row.

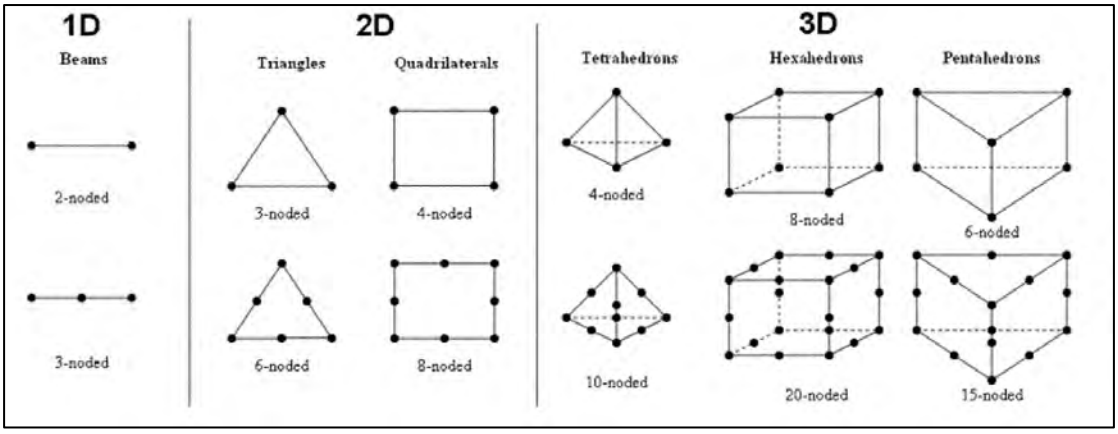

Figure 2-71: Various element shapes for discretisation of structures (Logan, 2019)

Each of the various element types require the derivation of different interpolation or shape functions, to describe the displacement of the various nodes in relation to each other. Linear element types may result in constant strain gradients across elements, due to the differentiation of linear shape functions when deriving the strain gradient interpolation functions. Quadratic elements overcome this, as the differentiation of quadratic functions result in linear strain gradients across elements.

The formulation of FE equilibrium equations is different for various element types, as a result of the different degrees of freedom modelled by each type. The general principle is however similar.

According to Rockey et al. (1975), the basis of the FE method is derived from the formulation of a simple linear spring following Hooke's law:

Force (F) = spring stiffness (K) x displacement (U)

The global stiffness matrix of the FE method as introduced earlier and shown in Equation 2-21, is an expansion of this simple principal into a system of interconnected springs (elements) connected at nodes.

$$\{F\} = [K]\{U\} \qquad \textbf{2-21}$$

The spring element according to which this analogy is made is shown in Figure 2-72. The axial force and displacement action at nodal points 1 and 2 are denoted by F_1, u_1, F_2 and u_2. The spring stiffness for a linear elastic spring element is a constant, k. Formulation of the FE method according to these principles, is known as the displacement or direct stiffness approach.

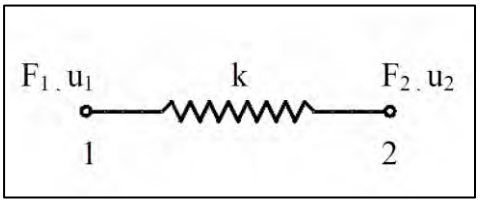

Figure 2-72: Simple one-dimensional spring element with stiffness = k (Logan, 2019)

In terms of formulation of a FE method system of equations, the force and displacement vector for the spring are represented as $\begin{Bmatrix} F_1 \\ F_2 \end{Bmatrix}$ and $\begin{Bmatrix} U_1 \\ U_2 \end{Bmatrix}$. The stiffness matrix for the spring is derived as shown in Equation 2-22.

$$\begin{Bmatrix} F_1 \\ F_2 \end{Bmatrix} = \begin{bmatrix} k_{11} & k_{12} \\ k_{21} & k_{22} \end{bmatrix} \begin{Bmatrix} U_1 \\ U_2 \end{Bmatrix} \qquad \textbf{2-22}$$

The terms in the stiffness matrix are undetermined, and are solved by allowing the spring element to adopt various independent modes of deformation, caused by the nodal forces. The three possible modes of deformation are shown in Figure 2-73. The sign convention is taken as positive to the right.

The first deflection mode of the spring (case 1) assumes node 1 moves axially and node 2 is fixed. For case 2 node 1 is fixed and node 2 is free to move axially. Case 3 allows both node 1 and 2 to deflect and can be represented by superposition of case 1 and 2.

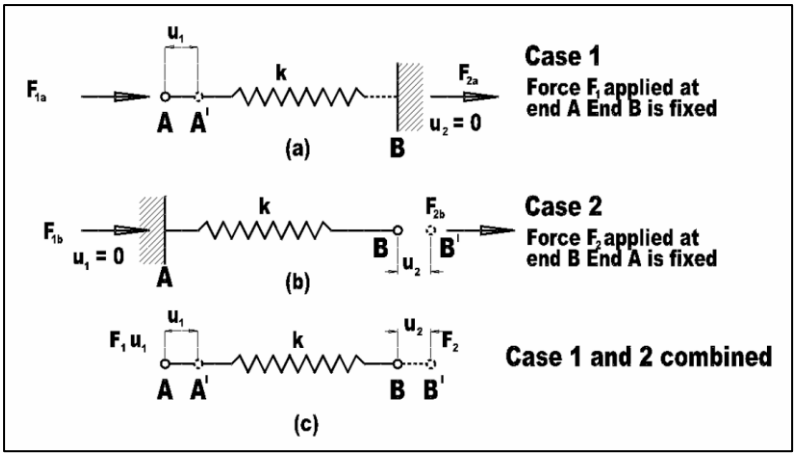

Figure 2-73: Possible deflection modes of an axially loaded spring (Logan, 2019)

According to equilibrium of forces in the springs it is required that:

$$F_{1a} + F_{2a} = 0 \quad \textbf{2-23}$$

$$F_{1b} + F_{2b} = 0 \quad \textbf{2-24}$$

And by Hooke's law

$$-F_{1a} = F_{2a} = -ku_1 \quad \textbf{2-25}$$

$$-F_{1b} = F_{2b} = ku_2 \quad \textbf{2-26}$$

To obtain the relationship for forces F_1 and F_2 of case 3 the forces from case 1 and 2 are superimposed such that for case 3 the forces acting at node 1 and node 2 are solved as follows:

$$F_1 = F_{1a} + F_{1b} \quad \textbf{2-27}$$

$$F_2 = F_{2a} + F_{2b} \quad \textbf{2-28}$$

or

$$F_1 = ku_1 - ku_2 \quad \textbf{2-29}$$

$$F_2 = -ku_1 + ku_2 \quad \textbf{2-30}$$

And presented in matrix form as shown in Equation 2-31.

$$\begin{Bmatrix} F_1 \\ F_2 \end{Bmatrix} = \begin{bmatrix} k & -k \\ -k & k \end{bmatrix} \begin{Bmatrix} U_1 \\ U_2 \end{Bmatrix} \quad \textbf{2-31}$$

The stiffness matrix for a spring element is given by Equation 2-32, where the superscript e indicates that the matrix is for a single element.

$$[K^e] = \begin{bmatrix} k & -k \\ -k & k \end{bmatrix} \quad \textbf{2-32}$$

Large or complex structures comprise an assemblage of basic structural components, connected together to form the overall global structure. To analyse the global structure the total structure stiffness matrix for the interconnected system of elements is derived. To obtain the global stiffness matrix for the two-element spring assemblage as shown in Figure 2-74, matrix equations for element 1 and 2 are formulated and then combined by using force/displacement relationships, for the spring elements together with the fundamental concepts of nodal equilibirum and compatibility (continuity).

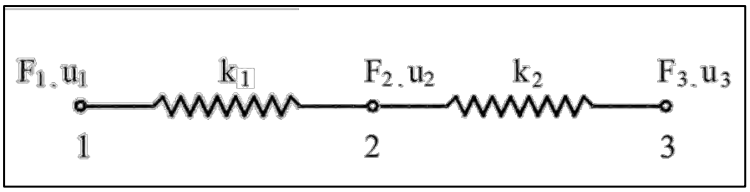

Figure 2-74: Two-element spring assemblage with 3 node points (Logan, 2019)

The matrix force/displacement equations for elements 1 and 2 of the spring assemblage are shown in Equation 2-33 and Equation 2-34.

$$\begin{Bmatrix} F_1 \\ F_2 \end{Bmatrix} = \begin{bmatrix} k_1 & -k_1 \\ -k_1 & k_1 \end{bmatrix} \begin{Bmatrix} U_1 \\ U_2 \end{Bmatrix} \quad \textbf{2-33}$$

$$\begin{Bmatrix} F_2 \\ F_3 \end{Bmatrix} = \begin{bmatrix} k_2 & -k_2 \\ -k_2 & k_2 \end{bmatrix} \begin{Bmatrix} U_2 \\ U_3 \end{Bmatrix} \quad \textbf{2-34}$$

The matrix equations representing the global FE system for the spring assemblage, as formulated by combining the individual element matrix equations, is shown in Equation 2-35. The global stiffness matrix for the sprig assemblage FE method problem is shown in Equation 2-36.

$$\begin{Bmatrix} F_1 \\ F_2 \\ F_3 \end{Bmatrix} = \begin{bmatrix} k_1 & -k_1 & 0 \\ -k_1 & k_1 + k_2 & -k_2 \\ 0 & -k_2 & k_2 \end{bmatrix} \begin{Bmatrix} U_1 \\ U_2 \\ U_3 \end{Bmatrix} \quad \textbf{2-35}$$

$$[K] = \begin{bmatrix} k_1 & -k_1 & 0 \\ -k_1 & k_1 + k_2 & -k_2 \\ 0 & -k_2 & k_2 \end{bmatrix} \quad \textbf{2-36}$$

Similarly, the stiffness matrix for a bar element loaded in tension (Figure 2-75) with a known cross-sectional area (A), elastic modulus (E) and length (L) is given by Equation 2-37.

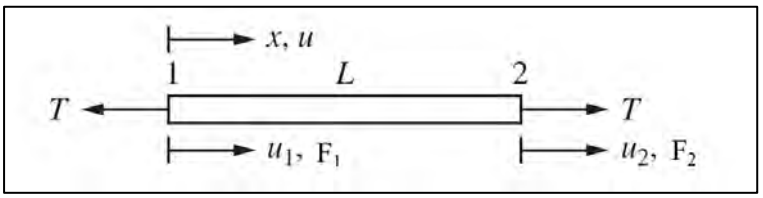

Figure 2-75: Simple bar element of length L axially loaded in tension

$$[K^e] = \frac{AE}{L}\begin{bmatrix} 1 & -1 \\ -1 & 1 \end{bmatrix} \quad \textbf{2-37}$$

A universal approach to formulating the stiffness matrix for any type of element commonly used in FE analysis, is referred to as the isoparametric method. This method adopts a local natural element coordinate system, according to which polynomial shape functions or interpolation functions are derived. These shape functions define the deflection at any location along an element, in terms of its position in relation to the nodes of the element. Essentially a mathematical function is chosen in advance to represent the deformed shape of the element under loading (Logan, 2019).

The adoption of a natural coordinate system for a simple bar element is shown in Figure 2-76. The conventional global coordinate system is depicted as (a) on the left and a natural coordinate system with the origin located at the centre, is indicated as (b) on the right.

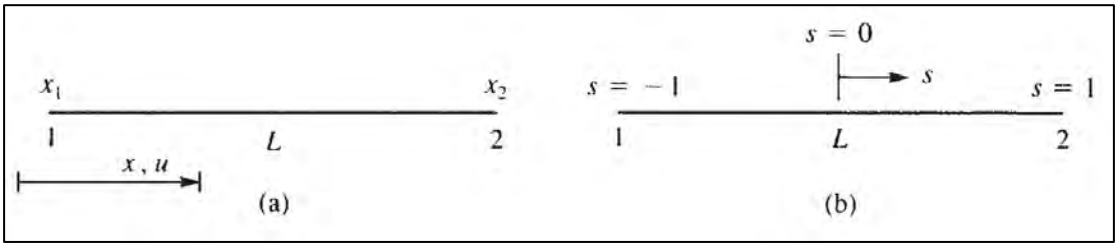

Figure 2-76: Linear bar element mapped according to global (a) and natural (b) coordinate system

The bar is considered to have two degrees of freedom, being axial displacements u_1 and u_2 at nodes 1 and 2 associated with the global x axis. The relationship between the s and x coordinates of the two differently mapped bar elements can be represented as in Equation 2-38, where x_c is the global coordinate at the centroid of the element. Assuming x_c is calculated as shown in Equation 2-39, then s can be defined as shown in Equation 2-40.

$$x = x_c + \frac{L}{2}s \quad \textbf{2-38}$$

$$x_c = \frac{(x_1 + x_2)}{2} \quad \textbf{2-39}$$

$$s = \left[x - \frac{x_1 + x_2}{2}\right]\left[\frac{2}{x_2 - x_1}\right] \quad \textbf{2-40}$$

The natural coordinate is then related to the global coordinate, by deriving a polynomial equation with coefficients a_1 and a_2 as shown in Equation 2-41. Knowing that $-1 \leq s \leq 1$, the coefficients a_1 and a_2 are defined in terms of x_1 and x_2 resulting in the displacement function given in Equation 2-42.

$$x = a_1 + a_2 s \quad \textbf{2-41}$$

$$x = \frac{1}{2}[(1-s)x_1 + (1+s)x_2] \quad \textbf{2-42}$$

These equations presented in matrix form are as shown in Equation 2-43, where the shape functions for N_1 and N_2 are provided in Equation 2-44 and Equation 2-45.

$$\{x\} = [N_1 \quad N_2]\begin{Bmatrix} x_1 \\ x_2 \end{Bmatrix} \quad \textbf{2-43}$$

$$N_1 = \frac{1-s}{2} \quad \textbf{2-44}$$

$$N_2 = \frac{1+s}{2} \quad \textbf{2-45}$$

It is important that shape functions always be continuous throughout the element domain and have finite first derivatives within the element.

The displacement function within the bar element, is based on the shape function and shown in Equation 2-46. According to this function, the displacement at any arbitrary point within the bar, is calculated in terms of its spatial location between the element nodes and in terms of their respective displacements.

$$\{u\} = [N_1 \quad N_2]\begin{Bmatrix} u_1 \\ u_2 \end{Bmatrix} \quad \textbf{2-46}$$

A graphic illustration of the shape function curves (N_1) and (N_2), plotted on the natural coordinate system of a bar element are shown in (a) and (b) of Figure 2-77. Application of the displacement function for deriving the linear displacement field of a bar element is shown in (c) of Figure 2-77. Since u and x are defined by the same shape functions at the same nodes, the element is called isoparametric.

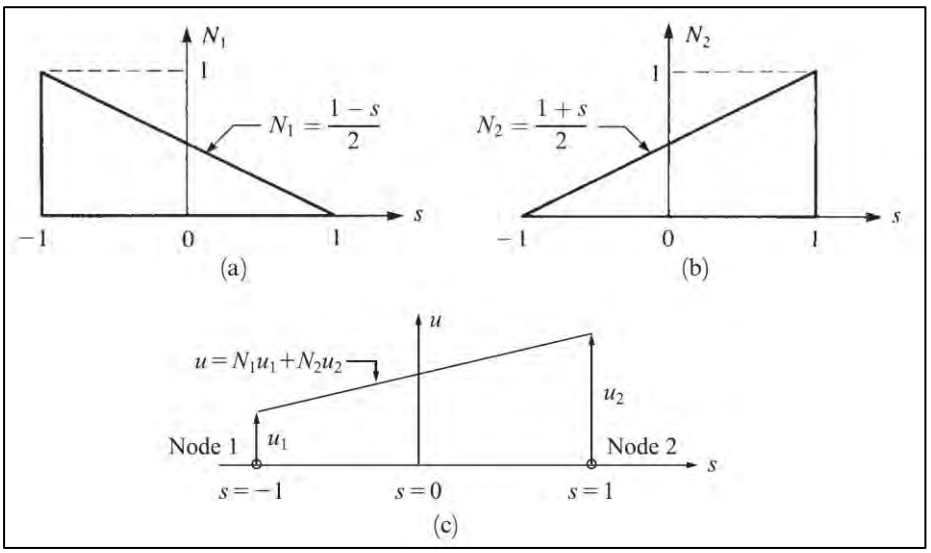

Figure 2-77: Application of element shape functions in the natural coordinate space (a and b) and resulting linear displacement field of bar (c) (Logan, 2019)

To construct the element stiffness matrix the strain-displacement and stress-strain relationships are defined. The strain of the element is defined as a derivative of the displacement with respect to x. The displacement u is however a function of s, and by applying the chain rule of differentiation to the function for u, Equation 2-47 is derived for differentiating u with respect to s.

$$\frac{du}{ds} = \frac{du}{dx}\frac{dx}{ds} \qquad \textbf{2-47}$$

Equation 2-47 is solved in terms of du/dx, giving Equation 2-48.

$$\frac{du}{dx} = \frac{du}{ds}\frac{ds}{dx} \qquad \textbf{2-48}$$

Knowing that du/dx = ε_x, du/ds and dx/ds are evaluated by differentiating Equation 2-46 and Equation 2-43 giving Equation 2-49 and Equation 2-50, because $x_2 - x_1 = L$.

$$\frac{du}{ds} = \frac{u_2 - u_1}{2} \qquad \textbf{2-49}$$

$$\frac{dx}{ds} = \frac{x_2 - x_1}{2} = \frac{L}{2} \qquad \textbf{2-50}$$

According to the strain-displacement relationship, axial strain along the bar element is written in matrix form as given in equation 2-51, which is commonly presented as shown in Equation 2-52, with [B] being defined as the strain displacement matrix as shown in Equation 2-53.

$$\{\varepsilon_x\} = \begin{bmatrix} -\frac{1}{L} & \frac{1}{L} \end{bmatrix} \begin{Bmatrix} u_1 \\ u_2 \end{Bmatrix} \qquad \textbf{2-51}$$

$$\{\varepsilon_x\} = [B]\{U\} \qquad \textbf{2-52}$$

$$[B] = \begin{bmatrix} -\frac{1}{L} & \frac{1}{L} \end{bmatrix} \qquad \textbf{2-53}$$

The axial stress-strain relationship in matrix form as per Hooke's law is given in Equation 2-54, where [D] = [E] and substituting Equation 2-52 into Equation 2-54 gives Equation 2-55.

$$\{\sigma_x\} = [D]\{\varepsilon_x\} \qquad \textbf{2-54}$$

$$\{\sigma_x\} = [D][B]\{U\} \qquad \textbf{2-55}$$

The principle of minimum potential energy, assumes that the finite element process, seeks a minimum in the potential energy within the constraint of an assumed displacement pattern, within each element, as allowed by the derived displacement functions.

The greater the number of degrees of freedom associated with an element, the more closely will the solution approximate the true solution and ensure complete equilibrium. An approximate FE solution found by using the stiffness method, always provides a value of potential energy

greater than or equal to the correct one. The stiffness method also results in a structure behaviour, that is predicted to be physically stiffer than, or at best to have the same stiffness as the actual solution. This is explained by the fact that the structure model, is only allowed to displace into shapes defined by terms of the assumed displacement field, within each element of the structure.

The element stiffness matrix derived assuming minimum potential energy is given in Equation 2-56.

$$[K^e] = \int_0^L [B]^T [D][B][A]dx \qquad \textbf{2-56}$$

The element stiffness matrix Equation 2-56 is then transformed from the x coordinate system to the s coordinate system by applying dx/ds = L/2, to formulate Equation 2-57.

$$[K^e] = \frac{L}{2}\int_{-1}^{1} [B]^T [D][B][A]ds \qquad \textbf{2-57}$$

For the case of a one-dimensional bar element the modulus of elasticity E = [D], and further simplification by substituting Equation 2-53 into Equation 2-57 and performing simple integration, the bar element stiffness is given in Equation 2-58, which is identical to the matrix Equation 2-37 derived earlier.

$$[K^e] = \frac{AE}{L}\begin{bmatrix} 1 & -1 \\ -1 & 1 \end{bmatrix} \qquad \textbf{2-58}$$

This dissertation focuses on a practical application of the FE method, and a comprehensive formulation of the element stiffness matrix, for the various types of elements is beyond its scope. The concrete arch dam FE analysis studies undertaken in this dissertation adopt the use of a hybrid of three-dimensional hexahedral, tetrahedral and pyramid linear elements for modelling of the dam structure.

A basic description of stress-strain relationships for a three-dimensional solid element, and the formulation of isoparametric shape functions for deriving the element stiffness matrix, are provided.

A three-dimensional infinitesimal solid element in Cartesian coordinates with dimensions dx, dy and dz subject to normal and shear stresses on all faces is shown in Figure 2-78. The normal stresses are perpendicular to the faces of the element and are represented by σ_x, σ_y and σ_z. Shear stresses act in the plane of the faces of the element and are represented by τ_{xy}, τ_{yz} and τ_{zx}. From moment equilibrium it can be shown that $\tau_{xy} = \tau_{yx}$, $\tau_{yz} = \tau_{zy}$ and $\tau_{zx} = \tau_{xz}$. As a result, the three-dimensional stress space has only three independent shear stresses and three normal stresses.

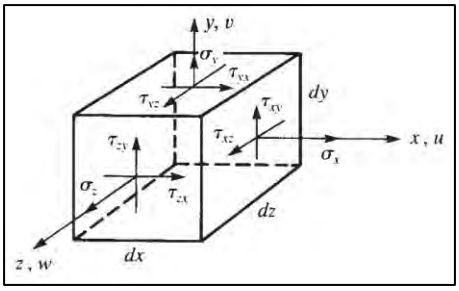

Figure 2-78: Three-dimensional stresses on a solid hexahedral element (Logan, 2019)

The element strain-displacement relationships for axial strain are given in Equation 2-59 through Equation 2-61, where u, v and w are the displacements associated with the x, y and z directions of the element.

$$\varepsilon_x = \frac{du}{dx} \quad \textbf{2-59}$$

$$\varepsilon_y = \frac{dv}{dy} \quad \textbf{2-60}$$

$$\varepsilon_z = \frac{dw}{dz} \quad \textbf{2-61}$$

Strain-displacement relationships for shear strain are provided in Equation 2-62 through Equation 2-64.

$$\gamma_{xy} = \frac{\partial u}{\partial y} + \frac{\partial v}{\partial x} = \gamma_{yx} \quad \textbf{2-62}$$

$$\gamma_{yz} = \frac{\partial v}{\partial z} + \frac{\partial w}{\partial y} = \gamma_{zy} \quad \textbf{2-63}$$

$$\gamma_{zx} = \frac{\partial w}{\partial x} + \frac{\partial u}{\partial z} = \gamma_{xz} \quad \textbf{2-64}$$

The element stresses and strains are represented in column matrix form, as given in Equation 2-65 and Equation 2-66.

$$\{\sigma\} = \begin{Bmatrix} \sigma_x \\ \sigma_y \\ \sigma_z \\ \tau_{xy} \\ \tau_{yz} \\ \tau_{zx} \end{Bmatrix} \quad \textbf{2-65}$$

$$\{\varepsilon\} = \begin{Bmatrix} \varepsilon_x \\ \varepsilon_y \\ \varepsilon_z \\ \gamma_{xy} \\ \gamma_{yz} \\ \gamma_{zx} \end{Bmatrix} \quad \textbf{2-66}$$

The stress-strain relationships for an isotropic material are given in Equation 2-67.

$$\{\sigma\} = [D]\{\varepsilon\} \quad \textbf{2-67}$$

The terms in Equation 2-67 are defined by Equations 2-65 and Equation 2-66, whilst the constitutive matrix [D] for a three-dimensional element of isotropic material, is provided in Equation 2-68.

$$[D] = \frac{E}{(1+\nu)(1-2\nu)} \begin{bmatrix} 1-\nu & \nu & \nu & 0 & 0 & 0 \\ \nu & 1-\nu & \nu & 0 & 0 & 0 \\ \nu & \nu & 1-\nu & 0 & 0 & 0 \\ 0 & 0 & 0 & \frac{1-2\nu}{2} & 0 & 0 \\ 0 & 0 & 0 & 0 & \frac{1-2\nu}{2} & 0 \\ 0 & 0 & 0 & 0 & 0 & \frac{1-2\nu}{2} \end{bmatrix} \quad \textbf{2-68}$$

The isoparametric transformation of an 8-noded solid linear hexahedral (brick) element, from a global coordinate system into a two-unit sided cube with natural coordinates, is shown in Figure 2-79, where the x, y and z coordinates are transformed into s, t and z' coordinates, with the origin at the centroid of the cube.

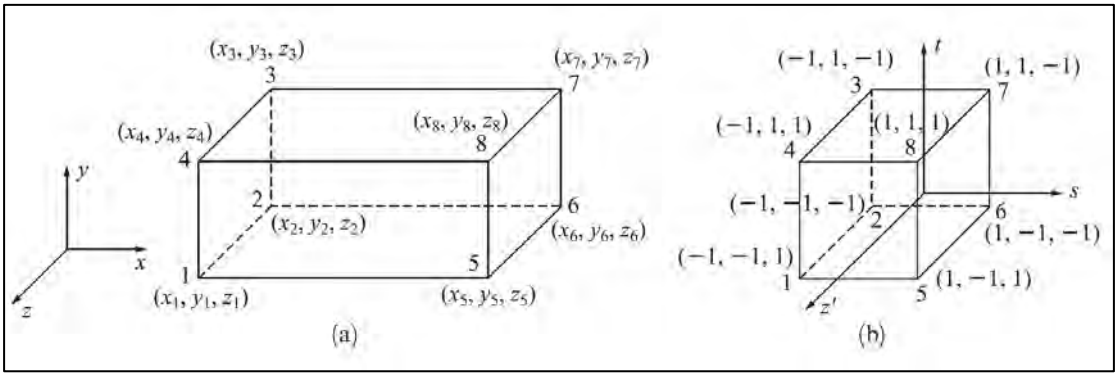

Figure 2-79: Linear hexahedral element in a global coordinate system (a) and mapped with a natural coordinate system (b) (Logan, 2019)

The functions used to describe the element geometry (shape) for x, y and z in terms of the generalised degrees of freedom a_is is given in Equation 2-69 through Equation 2-71.

$$x = a_1 + a_2 s + a_3 t + a_4 z' + a_5 st + a_6 tz' + a_7 z's + a_8 stz' \quad \textbf{2-69}$$

$$y = a_9 + a_{10} s + a_{11} t + a_{12} z' + a_{13} st + a_{14} tz' + a_{15} z's + a_{16} stz' \quad \textbf{2-70}$$

$$z = a_{17} + a_{18} s + a_{19} t + a_{20} z' + a_{21} st + a_{22} tz' + a_{23} z's + a_{24} stz' \quad \textbf{2-71}$$

The various coefficients of the above equations are then defined in terms of x, y, z, t, s, z' and shape functions defining a location within the element in relation to the eight nodes, in terms

of the natural coordinate system, are formulated. The general shape function form is given in Equation 2-72 with s_i, t_i, $z'_i = \pm 1$ and i = 1, 2, …, 8.

$$N_i = \frac{(1 + ss_i)(1 + tt_i)(1 + z'z'_i)}{8} \quad \textbf{2-72}$$

Similarly, the displacement functions for u, v and w are obtained in terms of generalised degrees of freedom, as shown in Equation 2-73 through Equation 2-75, for setting up the element stiffness matrix $[K^e]$, of a three-dimensional solid brick element with 24 degrees of freedom.

$$u = a_1 + a_2 s + a_3 t + a_4 z' + a_5 st + a_6 tz' + a_7 z's + a_8 stz' \quad \textbf{2-73}$$

$$v = a_9 + a_{10} s + a_{11} t + a_{12} z' + a_{13} st + a_{14} tz' + a_{15} z's + a_{16} stz' \quad \textbf{2-74}$$

$$w = a_{17} + a_{18} s + a_{19} t + a_{20} z' + a_{21} st + a_{22} tz' + a_{23} z's + a_{24} stz' \quad \textbf{2-75}$$

By applying the principle of minimum potential energy, the 24 x 24 stiffness matrix for a linear three-dimensional hexahedral element is given in Equation 2-76. This equation is a definite integral that can be solved by numerical integration. [J] is the Jacobian matrix as given in Equation 2-77 which transforms the global coordinate system of the element to the natural coordinate system as shown in Equation 2-78.

$$[K^e] = \int_{-1}^{1}\int\int [B]^T [D][B][J]\, ds\, dt\, dz' \quad \textbf{2-76}$$

$$[J] = \begin{bmatrix} \frac{\partial x}{\partial s} & \frac{\partial y}{\partial s} & \frac{\partial z}{\partial s} \\ \frac{\partial x}{\partial t} & \frac{\partial y}{\partial t} & \frac{\partial z}{\partial t} \\ \frac{\partial x}{\partial z'} & \frac{\partial y}{\partial z'} & \frac{\partial z}{\partial z'} \end{bmatrix} \quad \textbf{2-77}$$

$$\int_0^L f(x,y,z)dx\, dy\, dz = \int_{-1}^{1} f(s,t,z')[J]ds\, dt\, dz' \quad \textbf{2-78}$$

2.5.4 Loading and Boundary Conditions

As shown earlier, the global solution of the FE system is presented in Equation 2-79, for which the nodal displacement vector is to be solved in terms of the known global stiffness matrix [K] and global force vector {F}. To solve the FE problem, there needs to be at least one boundary condition upon at least one node and at least one nodal load on another node.

$$\{F\} = [K]\{U\} \quad \textbf{2-79}$$

The global force vector {F} is made up of various superimposed nodal forces derived from body, surface (traction) and point loads formulated as externally applied discrete forces acting at nodes only.

Body forces normally represent gravity loads (self-weight), or other acceleration loads that act through the centroid of the structure. Such gravity forces are assumed to act through the centroid of each element in the FE model. These forces are accordingly apportioned to the various nodes making up such element, in terms of the spatial location of the node, in relation to the element centroid. Apportionment of a body force acting through an element to its nodes, is done by application of the element shape functions, as derived for the formulation of the element stiffness matrix $[K^e]$.

Surface or traction forces represent distributed loads or pressure loads acting along the surface of a structure. These traction forces are discretised to nodal points according to the tributary area of the node, at the surface of the structure model. Such discretisation is undertaken according to the surface shape functions of the element geometry.

Nodal point loads represent concentrated loads occurring at the exact location of a node within the FE model assemblage.

The general forces acting on a one-dimensional bar element of length L with nodes 1 and 2 and a local vertical x-coordinate, are shown in Figure 2-80. X_b denotes the gravitational force acting through the centroid of the bar due to its self-weight, which is modelled as a body force to be apportioned to node 1 and 2 in accordance with the shape functions [N].

T_x denotes a shear stress acting along the face of the bar, which is modelled as a surface traction force apportioned to node 1 and 2, in relation to shape functions defining the surface geometry of the bar, in relation to the node positions.

F_1 and F_2 indicate concentrated point loads acting at the ends of the bar modelled directly as concentrated nodal forces, acting on the node points 1 and 2.

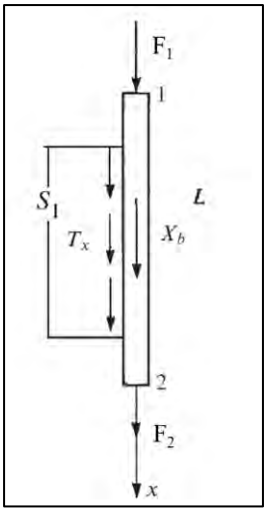

Figure 2-80: General forces acting on a one-dimensional bar (Logan, 2019)

The elemental matrix equations for modelling concentrated nodal loads {f}, surface traction forces $\{f_s\}$ and body forces $\{f_b\}$ acting on a one-dimensional bar element, are given in Equation 2-80 through Equation 2-82.

$$\{f\} = \begin{bmatrix} F_1 \\ F_2 \end{bmatrix} \quad \textbf{2-80}$$

$$\{f_s\} = \iint_{S_1} [N_s]^T \{T_x\} dS \quad \textbf{2-81}$$

$$\{f_b\} = \iiint_{V} [N]^T \{X_b\} dV \quad \textbf{2-82}$$

The global force vector is formulated by summing the general force vectors for each element as shown in Equation 2-83, and expanding the various element force vectors into a global vector representing the whole assemblage.

$$[F] = \{f\} + \{f_s\} + \{f_b\} \quad \textbf{2-83}$$

Application of boundary conditions to a FE model, essentially entails constraining certain regions in the model from translation or rotational movement, in given directions along the global coordinate system axes. This is normally implemented by fixing applicable nodal displacement or rotational degrees of freedom to zero. Note only beam and shell elements can have rotational degrees of freedom.

The zero-displacement boundary condition is defined directly in the displacement vector {U}, by equating nodal displacements of fixed nodes to zero. An axially loaded one-dimensional bar element with a fixed support at node 1 and a free end at node 2, is shown in Figure 2-81. The

nodal displacement vector {U} for the FE problem of the bar is given in Equation 2-84 and substituted into the FE solution for the bar element, as given in Equation 2-85.

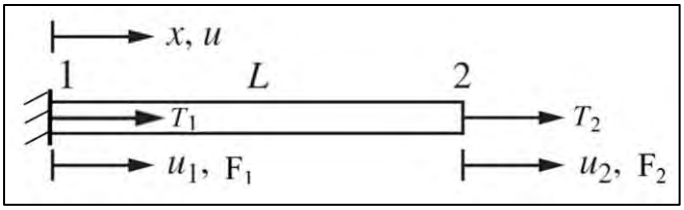

Figure 2-81: One dimensional axially loaded bar element with fixed support (Logan, 2019)

$$\{U\} = \begin{bmatrix} 0 \\ u_2 \end{bmatrix} \quad \textbf{2-84}$$

$$\begin{Bmatrix} T_1 \\ T_2 \end{Bmatrix} = \frac{AE}{L} \begin{bmatrix} 1 & -1 \\ -1 & 1 \end{bmatrix} \begin{Bmatrix} 0 \\ u_2 \end{Bmatrix} \quad \textbf{2-85}$$

2.5.5 Thermal Heat Transfer Formulation

For simplicity, the numerical modelling theory for a heat transfer analysis is addressed for one-dimensional heat flow, in a solid continuum with convection boundaries.

The laws of thermodynamics state that the rate of heat transfer through a solid continuum, is governed by the thermal conductance of the material (λ), whilst the rate of heat transfer between a solid and fluid medium is governed by the convection coefficient, for the solid-fluid interface. To correlate heat energy to temperature, the specific heat capacity (c) is a material constant defining how much heat energy is required to raise a unit volume of material, by one-degree centigrade.

The fundamental thermodynamics heat transfer equation, known as Fourier's law of heat conduction, describes the one-dimensional rate of heat transfer through a solid material by conduction. Equation 2-86 describes the heat flow in the x-direction through a unit volume solid element as indicated in Figure 2-82.

$$q_x = \lambda_{xx} \mathrm{A} \left(\frac{dT}{dx} \right) \quad \textbf{2-86}$$

Where

q_x = rate of heat transfer/conductance in x-direction (kJ/(hr))

λ_{xx} = thermal conductivity in x direction (kJ/(m.hr.˚C))

A = cross sectional area (m^2)

dT/dx = temperature gradient (˚C/m)

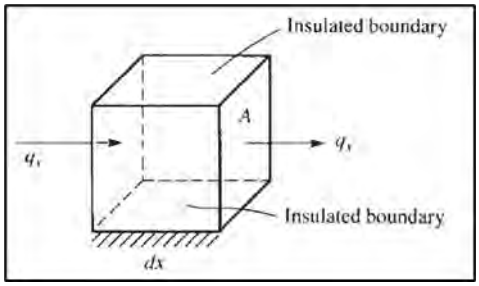

Figure 2-82: Heat conductance through a unit volume solid material (Logan, 2019)

According to Newton's law of cooling, the one-dimensional heat transfer from a solid medium to a fluid medium by way of convection is shown in Equation 2-87.

$$q_h = h(T_s - T_f) \quad \textbf{2-87}$$

Where

q_h = rate of heat transfer/convection (kJ/(hr))

h = heat transfer convection coefficient (kJ/(m^2.hr.˚C))

T_s = temperature of solid surface at solid/fluid interface (˚C)

T_f = temperature of fluid at solid/fluid interface (˚C)

The change in stored energy in a unit volume solid medium, expressed as a change in temperature of the unit volume solid body, is shown in Equation 2-88.

$$\Delta U = c(\rho A dx)dT \quad \textbf{2-88}$$

Where

ΔU = change in heat energy stored (kJ)

c = specific heat capacity (kJ/(kg.˚C))

ρ = density of solid material (kg/m^3)

A = cross sectional area (m^2)

dx = infinitesimal distance in x (m)

dT = change in temperature (˚C)

Combining Equations 2-86 through Equation 2-88 and dividing by A.dx.dt, and simplifying further, the differential equation for one-dimensional heat conduction with convection is shown in Equation 2-89.

$$\frac{\partial}{\partial x}\left(\lambda_{xx}\frac{\partial T}{\partial x}\right)+Q=\rho c\frac{\partial T}{\partial t}+\frac{hP}{A}\left(T_s-T_f\right) \quad \textbf{2-89}$$

Where

P = convection perimeter around constant cross-sectional area A (m)

Q = heat generated from an internal source (kJ/(hr.m^3))

Using similar principles followed in Section 2.5.3, and in accordance with derivation of shape functions for heat transfer in three-dimensional space considering conductance and convection, the element stiffness matrix for heat transfer due to conduction and convection for a one-dimensional bar element, is shown in Equation 2-90 and Equation 2-91. The stiffness matrix for heat transfer due to conductance and convection is shown in Equation 2-92.

$$[k_c]=\frac{A\lambda_{xx}}{\mathrm{L}}\begin{bmatrix}1 & -1\\ -1 & 1\end{bmatrix} \quad \textbf{2-90}$$

$$[k_h]=\frac{hPL}{6}\begin{bmatrix}2 & 1\\ 1 & 2\end{bmatrix} \quad \textbf{2-91}$$

$$[K^e]=\iiint_V [B]^T[D][B]dV+\iint_S h[N]^T[N]dS \quad \textbf{2-92}$$

Where

V = volume of solid material (m^3)

S = surface area of convection boundary (m^2)

2.5.6 Material Models

Material models are mathematical representations of the physical properties of materials, indicating how they behave in terms of stress, strain and displacement under loading.

Formulation of the global stiffness matrix [K] for implementation in deriving and solving a FE system, is reliant on the stress-strain behaviour of the material model assumed for the structure being analysed. The stress-strain behaviour, which models the physical response of a material, may exhibit linear or non-linear behaviour, whilst the strain deformation experienced under loading may be purely elastic, plastic or a combination of both (elastoplastic).

Purely elastic materials do not undergo permanent deformation under loading, and when unloaded, the unloading stress-strain path follows the initial loading path. The loading is fully reversible and if a loaded specimen is unloaded, the stress-strain state will return to the initial point before loading, if not loaded to failure. When elastic materials are loaded, the stress-strain

response causes the material to transfer kinetic energy into elastic strain energy, with the potential to kinematically reverse the material strain to its original state, upon removal of loading.

Elastic materials may exhibit linear or non-linear load paths. Linear elastic materials follow Hooke's law meaning the deformation is proportional to the applied stress load. This is modelled by the elastic modulus (E) of the material, which is a constant and is essentially the slope of the linear stress-strain curve. The mathematic definition of elastic modulus in terms of the stress over strain relationship, is given in Equation 2-93. Non-linear elastic materials do not exhibit a constant elastic modulus and the slope of the stress-strain load path changes, as loading progresses.

$$E = \frac{\sigma}{\varepsilon} \qquad \textbf{2-93}$$

Where

E = elastic modulus (GPa)

σ = stress (MPa)

ε = strain (m/m)

Plastic materials may experience permanent deformation under loading, and when unloaded, the stress-strain path does not trace back along the initial loading path and a certain amount of permanent strain remains, if fully unloaded. The material therefore undergoes a permanent change in shape or size. When plastic materials are loaded, a portion of the kinetic energy is transferred into elastic strain energy, which will be released when load is removed, while the remainder is absorbed by the material as it undergoes permanent deformation.

The plastic deformation normally occurs at the higher end of a loading curve, and the region of plastic deformation is characterised by the yield strength value of the material. The plastic deformation occurs when the material is loaded beyond its yield point and may experience strain hardening, strain softening or perfectly plastic behaviour.

Most materials exhibit non-linear elastoplastic properties and undergo some form of nonlinear plastic behaviour, when loaded to a stress state equivalent to the material yield strength. Simplified stress-strain curves for a uniaxial material test comparing a linear elastic material to elastoplastic materials, are shown in Figure 2-83. The material model represented by the stress-strain curve on the left is linear elastic, and the remaining three material models shown are elastoplastic indicating perfectly plastic, strain hardening and strain softening behaviour post yielding.

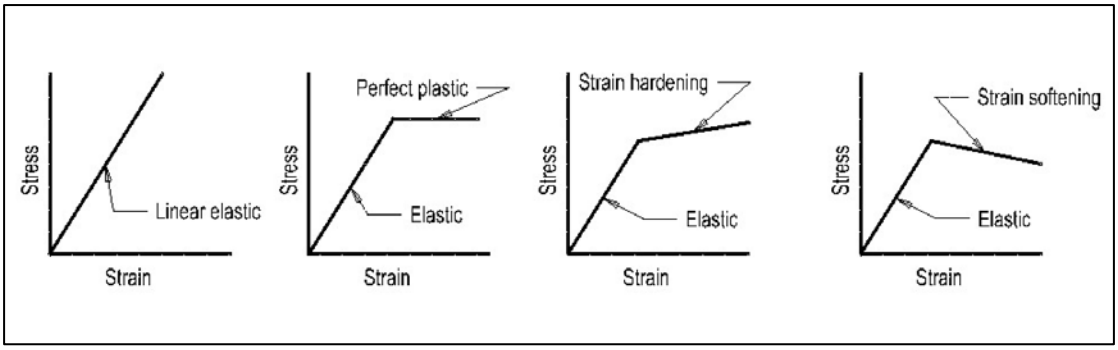

Figure 2-83: Simplified linear elastic vs elastoplastic stress-strain curves for non-linear material models (Durieux, 2008)

The FE analysis of concrete dams assuming non-linear material models, is a useful design tool if the dam response under critical loading shows, or is expected to show, stress results that marginally exceed the material yield strength of the dam (Cassells & Wright, 2023). Such an analysis, allows the designer to investigate whether localised yielding of the loaded dam will result in the formation of plastic hinges, with associated stress redistribution to regions of the dam having sufficient strength capacity for additional stress load, meaning the dam will not fail. Alternatively, the localised yielding may progress indefinitely having a cascading effect and result in global instability of the dam, in terms of a possible failure mode.

The FE analysis studies undertaken in this dissertation purposefully assume linear elastic material parameters, to investigate the hypothesis statement. A comprehensive account of the various non-linear material models commonly adopted in FE procedures is therefore not addressed.

Civil engineering materials such as geotechnical earth/rock, concrete and steel are truly non-linear but exhibit linear elastic stress-strain behaviour under small strain loading. In some instances, these materials exhibit linear elastic stress-strain behaviour to a point relatively close to the yield strength of the material, after which nonlinear plastic deformation commences. The FE analysis of a concrete arch dam founded on rock mass foundations, incorporates material models for mass concrete and rock mass.

Figure 2-84 shows a stress-strain curve of a concrete test specimen loaded to failure in tension, by the modulus of rupture test. The non-linear stress-strain curve of the loading test, showing plastic deformation is plotted as a solid line. Alongside the non-linear curve, a linear elastic stress-strain curve is plotted as a dashed line in the form of an initial tangent to the non-linear curve. A comparison between the actual non-linear curve and the estimated linear curve, reveals that the linear curve very accurately models the stress-strain behaviour of the concrete specimen to a stress value of 90 % of its tensile yield strength. Any practical differentiation between these curves only occurs past $0.9f'_t$, where f'_t is the modulus of rupture tensile strength of concrete.

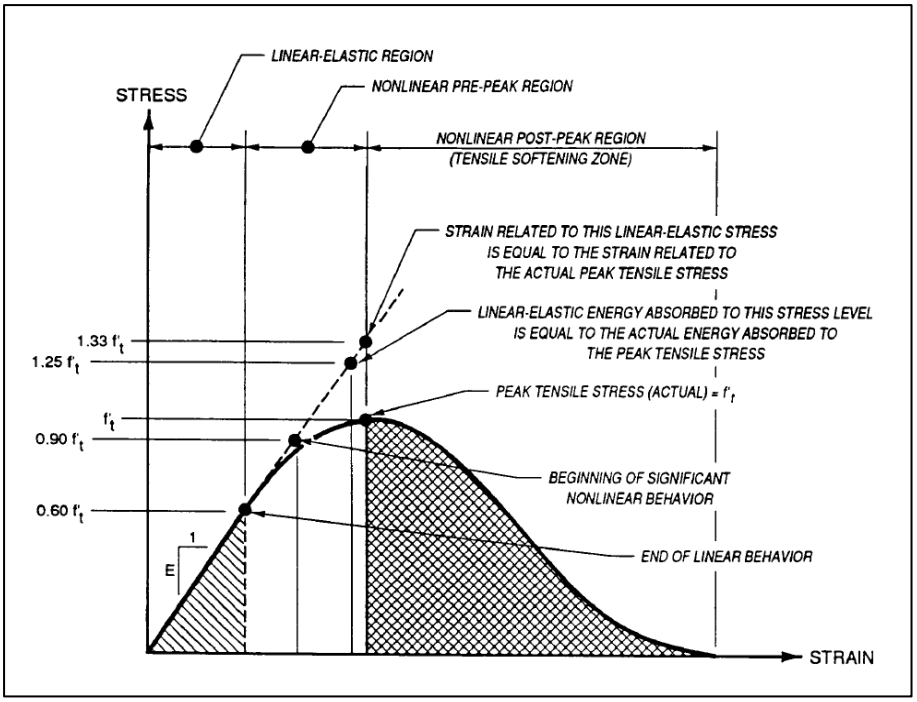

Figure 2-84: Stress-strain curve of concrete loaded in tension to failure with superimposed linear elastic curve (USACE, 1995)

According to Raphael (1984), the results of material testing studies undertaken on tensile strength of concrete as shown in Figure 2-85, indicate that the non-linear behaviour of concrete only becomes significant when it is loaded close to yield point. The stress-strain curves of the testing results show this behaviour is consistent for a set of tests, evaluating nine different concrete strength classes.

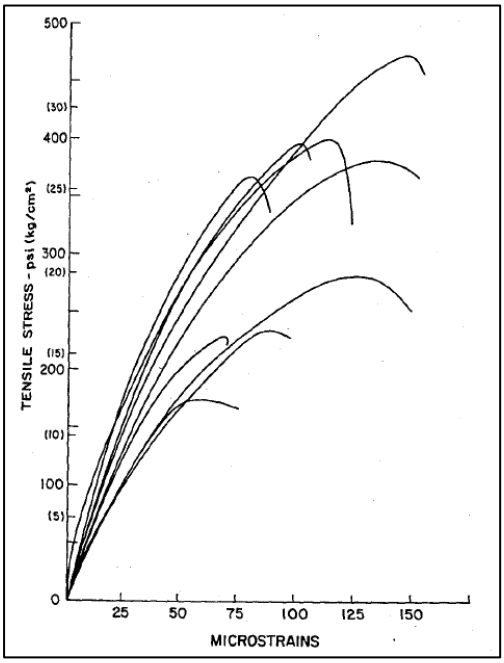

Figure 2-85: Stress-strain curves for the tensile strength test results of nine concrete strength classes (Raphael, 1984)

Similarly, it has been shown in rock mechanics, that for practical purposes, when undertaking numerical analysis on rock mass structures, the deformation properties of rock masses may be assumed to exhibit a linear elastic stress-strain relationship, until the point of yielding (Hoek, 1993). The typical configuration of stress-strain loading curves for rock mass of good, average and poor quality is shown in Figure 2-86.

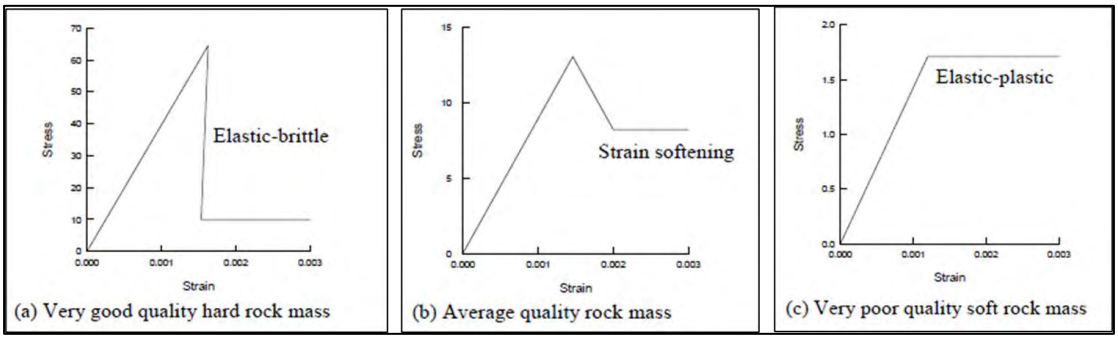

Figure 2-86: Stress-strain curves indicating the typical qualitative deformation behaviour of rock mass (Hoek, 1993).

Material models can be further categorised into isotropic, anisotropic, and orthotropic models depending on the symmetry and particle orientation making up the material continuum. Isotropic models assume that material properties are the same in all directions, while anisotropic models allow for variations in material properties in different directions. Orthotropic models are used for materials that exude different properties in three mutually perpendicular directions.

For practicality in implementing FE analysis procedures, concrete can be assumed to be isotropic if sound quality control is exercised during casting, avoiding the development of cracks, cold joints, honeycombing and segregation of materials due to poor workmanship.

Rock masses may comprise complex, interwoven, fault-bound formations of rocks with differing parameters having various intersecting joints, lineations, flow contacts and planes of weakness traversing through the continuum. Depending on the complexity of the rock mass conditions as indicated by geological site investigations results, the material model adopted for FE analysis of rock mass structures may be isotropic, anisotropic or orthotropic.

2.5.7 Solving the FE Model Problem

Solving the modern FE model problem is conveniently done on personal computers, using commercially available FE modelling software packages. The software packages utilise computer program coding to formulate the FE model, in terms of mathematical simultaneous equations in matrix form. The software employs a user-friendly graphical user interface, that allows for a visual interaction with the model via a rendered CAD view of the FE model

components including geometry, mesh bodies, loadings, boundary conditions and analysis results.

The software package ultimately creates the FE problem using matrix algebra as shown in equation 2-94, which represents a large set of simultaneous equilibrium equations to be solved in terms of the displacement vector {U}, using a solver tool.

$$\{F\} = [K]\{U\} \qquad \textbf{2-94}$$

Various software packages exist that use different solver methods. The most common direct methods for solving linear elastic static FE problems, comprise decomposition of the global stiffness matrix (coefficient matrix), followed by forward-backward substitution to solve the various unknown nodal displacement values in the problem. Common matrix decomposition methods include Gaussian elimination, LU (lower-upper) factorisation, LDL^T (lower diagonal lower-transpose) factorisation, Cholesky factorisation and many others. The solver tool is executed by running algorithm codes that follow a logical process, to decompose and solve the matrix algebra problem.

Direct methods operate on fully assembled system equations and therefore demand larger storage space, and processing power. Extensive FE problems constituting a high number of nodes and associated degrees of freedom, may require the use of indirect (iterative) solver methods, to conserve or limit the use of available processing power of the computer CPU.

Iterative solver methods include the Gauss–Jacobi method, the Gauss–Deidel method, the successive over-relaxation method, generalized conjugate residual methods or the line relaxation method.

Iterative methods may be coded in such a way as to avoid full assembly of the system matrices, to save on storage capacity and processing power. Matrices with many zeros placed away from the diagonal are considered as low-bandwidth matrices, and are especially suitable for solving using iterative methods. A typical low bandwidth coefficient matrix [K] is shown in Equation 2-95, where upper and lower triangular bandwidth = 2.

$$[K] = \begin{bmatrix} k_{11} & k_{12} & k_{13} & 0 & 0 & 0 & 0 & 0 \\ k_{21} & k_{22} & k_{23} & k_{24} & 0 & 0 & 0 & 0 \\ k_{31} & k_{32} & k_{33} & k_{34} & k_{35} & 0 & 0 & 0 \\ 0 & k_{42} & k_{43} & k_{44} & k_{45} & k_{46} & 0 & 0 \\ 0 & 0 & k_{53} & k_{54} & k_{55} & k_{56} & k_{57} & 0 \\ 0 & 0 & 0 & k_{64} & k_{65} & k_{66} & k_{67} & k_{68} \\ 0 & 0 & 0 & 0 & k_{75} & k_{76} & k_{77} & k_{78} \\ 0 & 0 & 0 & 0 & 0 & k_{86} & k_{87} & k_{88} \end{bmatrix} \qquad \textbf{2-95}$$

Modern FE modelling software packages may also utilise the GPU of powerful graphics cards, to decrease the solver time for large FE problems.

Computer resources are a decisive factor on how complex a FE model can be. It is generally a rule that the CPU time required to solve the global stiffness matrix for a static analysis, is directly proportional to the global degrees of freedom of the model, raised to a power of between two and three as given in equation 2-96 (Liu & Quek, 2003). The increase in solver time with an increase in model size is therefore exponential.

$$t_{CPU} \propto n_{DOF}^{(2\ to\ 3)} \qquad \textbf{2-96}$$

FE problems derived for large concrete arch dams founded on complex rock mass conditions, using solid 8-noded linear hexahedral (brick) elements each with 24 degrees of freedom, normally results in the solving of a matrix algebra equation, with a very large coefficient (global stiffness) matrix. This warrants the use of different solver techniques to optimise the solution process and minimise usage of valuable CPU processing power.

For solutions to dynamic FE problems, time-dependant partial differential equations may be solved using either an explicit or implicit solving technique.

An explicit solver calculates the solution at each time step using only the information from the previous time step, without involving algebraic equations. The solution in each time step is therefore calculated in a straight-forward manner without requiring much computational effort. Explicit solvers require small time steps to ensure numerical stability which may slow down the convergence process.

An implicit solver involves solving a system of algebraic equations at each time step, which involves information from both the current and previous time steps. Implicit solvers are more computationally expensive compared to explicit solvers, but they offer better numerical stability and can use larger time step sizes.

2.5.8 Post-processing of FE Solution

After the FE problem is solved, the raw unprocessed output results comprise a large matrix of nodal displacements for the global assemblage of elements making up the model. FE modelling software packages, produce graphical output plots showing the displacement of the model as banded contours, over the FE structure model. The displacements across elements are derived by substituting the nodal displacements back into the various element displacement functions, which requires numerical integration for three-dimensional 8-noded hexahedral elements. The representation of smooth banded displacement plots across graphical images of modelled FE

assemblages, is achieved by using nodal averages or interpolation functions to report element values.

The strain output results are similarly obtained by using the strain-displacement matrices, to determine the nodal strains for the various elements in the model. Element strains are commonly derived using Gaussian quadrature for integration of definite integrals, to obtain integration point values. These Gaussian integration point values are used for interpolation of strain results within an element, between the various nodal values making up the element.

Element stresses are then computed from element strains by applying the stress-strain relationship of equation 2-67 presented in section 2.5.3.

2.5.9 Practical Considerations in FE Modelling

The FE modelling of large structures with complex geometrical configurations requires some practical considerations to be considered, to ensure the analysis problem is solved efficiently and that the results produced are reliable and meaningful, in terms of the design of the structure.

The most important aspect to consider is the discretisation of the structure geometry, into an assemblage of interrelated finite elements connected at common nodes, known as a mesh.

A suitable discretisation strategy is required, to ensure that a good quality mesh is created that complies with sound meshing practices. The elements making up the mesh should always be of a regular shape and form, and not contain warped or stretched edges or faces as shown by the selection of poorly modelled two-dimensional plane elements in Figure 2-87 (Cook, 1995).

Warpage of elements will result in distorted output results, due to the transformation from the element's locally mapped isoparametric coordinate system, to the global coordinate system. Excessive warpage of an element is normally indicated by a low determinant value of the Jacobian matrix. Poor meshing may also result in the computation of local stress/strain concentrations, resulting from element singularities or other numerical instabilities.

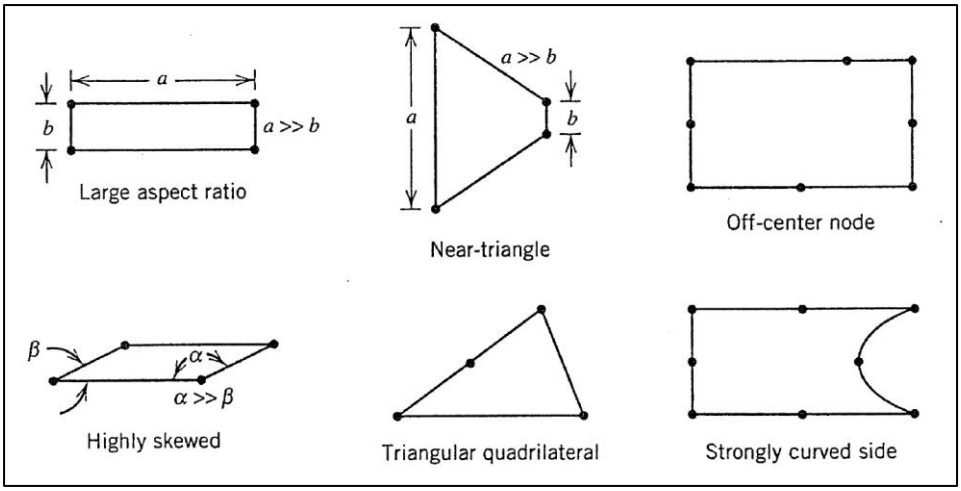

Figure 2-87: Two-dimensional plane elements with shape distortions that reduce the quality of FEA results (Cook, 1995)

To achieve a regular and uniform mesh pattern, in regions of the modelled structure having abrupt geometry changes or edges/faces with curvature, a fine mesh is normally required, to ensure these features are smoothly captured by the discretisation. In some instances where discrete geometry changes such as notched re-entrant corners or other sharp edges are encountered, adopting a fine regular mesh to capture these features, may still result in localised numerical instabilities.

The existence of sharp points or discrete edges caused by re-entrant corners or other concave structural features, may result in the development of local singularities when solving the FE problem. This is caused by nodal in-balances in equilibrium equations or compatibility conditions. Local inequalities may develop at nodal points due to evolution of physical contradictions, arising when honouring the local boundary or loading conditions, where two perpendicular edges meet at a vertex. The application of a nodal force, at a location where the local geometrical stiffness prevents or greatly restricts nodal displacement from occurring, will result in the computation of very high local stress/strain results.

A typical stress/strain concentration caused by the singularity of a re-entrant corner, which is formed at the heel of a two-dimensional plane strain model of a gravity dam, is shown in Figure 2-88. The singularity problem may be overcome by smoothing the notch at the vertex of the corner, into a filleted or chamfered corner, or using quadratic elements with mid-side nodes for modelling. Where notched re-entrant corners are unavoidable, a meshing convergence or refinement process should be undertaken, to optimise the element size in the affected zone of the FE mesh. Alternatively, a material model considering yielding or plastic deformation behaviour should be adopted.

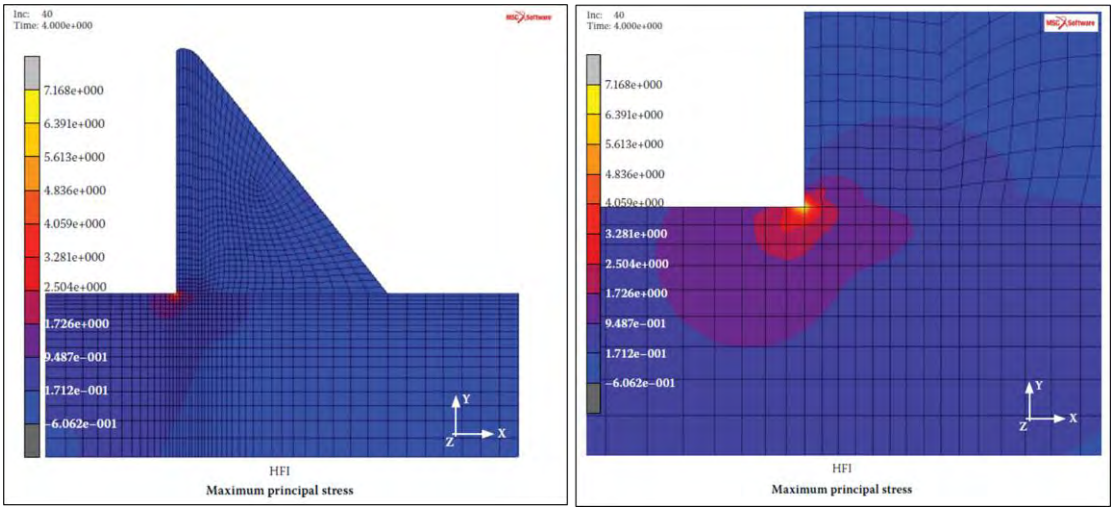

Figure 2-88: FE analysis maximum principal stress results showing a local concentration caused by re-entrant corner at the heel of dam (Durieux & van Rensberg, 2016)

Stress/strain concentrations may also be computed at the interfaces between materials having a large difference in elastic modulus, due to the abrupt change in stiffness across the interface.

According to St Venants principle, a singularity stress/strain concentration is local and will subside towards a realistic nominal value, within a short distance from the effected finite element. It can be assumed that the stress/strain computed by elements neighbouring the effected element, provide a better representation of actual stresses. In accordance with the above, the actual stress/strain reported at discontinuities/singularities may be two or even three times larger than the actual nominal value (Cassells & Wright, 2023).

When meshing geometry components of a structure, it is required to adopt a fine mesh with good quality elements in the region of interest of the structure and regions expected to develop high strain gradients under the analysed loads, to ensure a smooth representation in the stress/strain transfer results is computed. An overly fine mesh may increase the local stress/strain concentrations at notched corners and should be avoided.

The adoption of a very fine mesh will also exponentially increase the computational demand and time required to solve the FE problem. A fine balance needs to be implemented to ensure a good quality mesh is created, without the use of too many nodes and associated degrees of freedom. CPU processing time is a scarce and expensive resource to be used sparingly.

A good meshing strategy ensures that fine high-resolution elements are modelled near the structure's region of interest, where large strain gradients are expected to develop, whilst allowing for a coarse element distribution in the region of the model expected to have small strain gradients. The transition from fine to coarse mesh should be smooth and regular showing a gradual change in element size.

The process of creating a balanced FE mesh is an iterative procedure. It begins with creating a basic mesh using the fewest reasonable number of elements. The model is analysed and the quality of output results are evaluated to determine a mesh refinement process. This first mesh is a starting point, from which multiple revised meshes may follow, until the analysis results of a given mesh indicate convergence of such. This means that the analysis results of a particular mesh revision, are almost identical or very similar to results from the prior revision.

For simple structures it is possible to compare the analysis results to the exact solution derived using classical methods. For complex structures a classic solution may not be available and therefore refinement is necessary.

Large distortions in elements make them implicitly stiffer, and susceptible to producing poor output results. The amount of degradation caused by a given distortion varies with element type, mesh arrangement and the field value computed. Element distortion usually degrades stresses more than displacements and temperature fields, due to the impact of the distortion on the interpolation functions. Poor elements can still display states of constant strain, but their ability to represent stress/strain gradients across the element declines. Distortion of elements is normally most detrimental to the output results in areas of high strain gradients.

To ensure the FE model has a good quality mesh, certain geometrical limits should be imposed on the element features, to ensure they are compact and regular in shape. Guidelines for these limits have been developed by FE analysts working in the field and are provided below.

The aspect ratio of an element should be less than 3 for a stress/strain analysis, and less than 10 for a displacement analysis. An example of a two-dimensional element with a high aspect ratio is shown in Figure 2-89, where the ratio is taken as the longer dimension (b) divided by the shorter dimension (a).

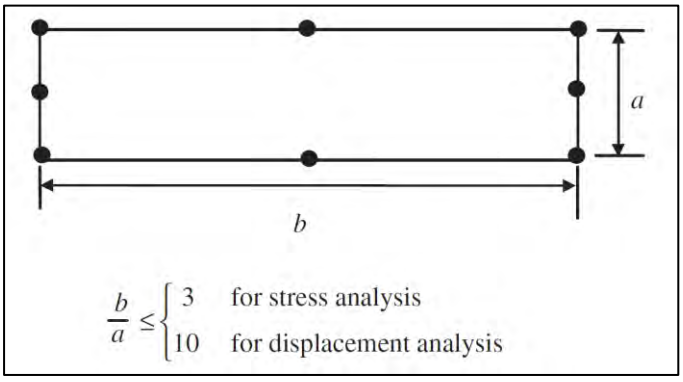

Figure 2-89: Distorted element with high aspect ratio (Liu & Quek, 2003)

The internal angles of an element should not be less than 60° and not more than 120°. An example of a two-dimensional element with angular distortion (skewness) is shown in Figure 2-90, where adjacent included angles are both out of the required range.

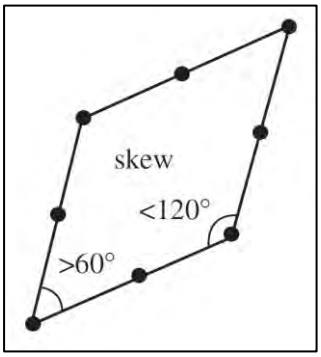

Figure 2-90: Distorted element with skewed angles (Liu & Quek, 2003)

The ratio of the dimensions of the opposite edges or faces of an element should not have a value higher than 5, as to avoid a large taper between these edges as shown in Figure 2-91.

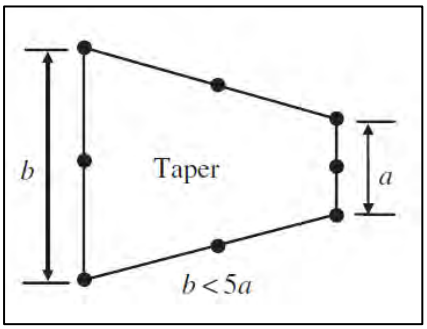

Figure 2-91: Distorted element with large taper of opposite edges (Liu & Quek, 2003)

Curvature distortion occurs when the straight edges of an element are distorted into curves, when matching the nodes to the geometric points of the structure geometry. An example of an 8-noded quadrilateral square element with a curved edge is shown in Figure 2-92.

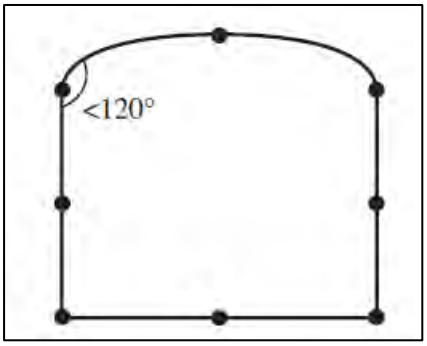

Figure 2-92: Element with curvature distortion (Liu & Quek, 2003)

Overall, poorly derived elements with high warpage or distortion can be evaluated according to the Jacobian value. This commonly refers to the determinant value of the Jacobian matrix. The Jacobian value for convex elements may range between zero and one, where one represents a perfectly shaped element and low values approaching zero indicate poor elements. Elements that have high concavity will have a negative Jacobian value and can lead to numerical instabilities when solving the FE problem. An example of an element with concave edges and the result of transformation into a mapped coordinate system is shown in Figure 2-93.

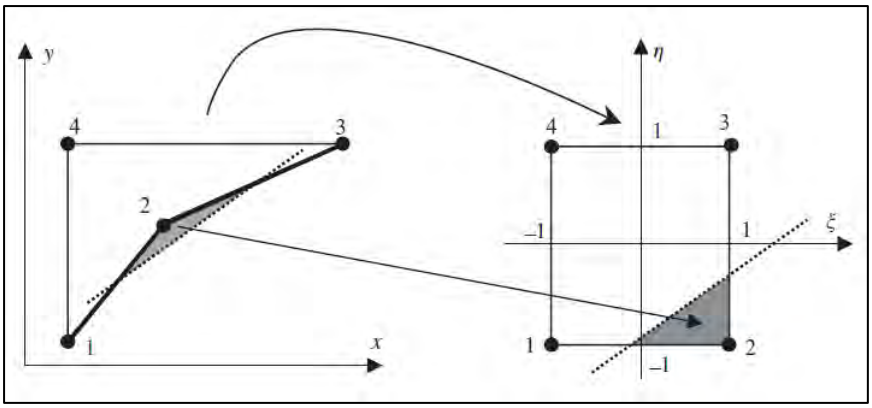

Figure 2-93: Negative area effect of a concave element transformed into a locally mapped isoparametric coordinate system (Liu & Quek, 2003)

A common benchmark geotechnical FE analysis problem, comprising the analysis of a foundation strip footing on a soil mass, is produced to indicate the difference between good and poor quality meshes.

The analysis objectives are to evaluate the deformation and stresses in the soil, due to the load from the foundation footing. Such an analysis is relatively simple and can be undertaken using two-dimensional plane strain elements, assuming the strip footing and underlying soil are infinitely long, and undergo no strain in a direction normal to the plane.

The FE model is further simplified by adopting symmetry and only modelling half the problem, to reduce model size and solving time. This is a good practice to be exercised where possible, taking special care to correctly model the loading and boundary conditions along the axis of symmetry. The plane strain model is assumed to have a one metre width normal to the plane and the strip footing load is implemented as a uniformly distributed load.

An example of three different FE models, created using Civil FEM software, and the stress plots of the resulting vertical stresses computed in each case, for the problem mentioned, is shown in Figure 2-94. The models presented were created from a combination of two-dimensional quadratic (mid-side node) triangle and quadrilateral elements.

The top FE model in Figure 2-94 presents a poorly formulated mesh with irregular elements and no application of mesh refinement in the area of interest, where large strain gradients are expected, and where the load is applied. The distributed load is coarsely discretised to a single element edge with three nodal loads. Effectively the stress results show poor stress contours having coarse/abrupt gradients and discontinuities between element stresses. The model is made up of 28 elements and 103 degrees of freedom.

The second model in Figure 2-94 shows a very fine and regular mesh, however the model is computationally expensive having many nodes and associated degrees of freedom. This model is made up of 800 elements and 2521 degrees of freedom. The quality and reliability of the output stress results show a marked improvement from the first model, but this was achieved without any optimisation and at the expense of valuable processing time. Similar or even better results could have been attained with fewer degrees of freedom and an associated shorter solving time.

The bottom model in Figure 2-94 indicates a balanced mesh with regular shaped, convex elements that transition smoothly from a high-resolution distribution near the analysis area of interest, to a sparse element distribution at the outer extents away from the loading. The final model is smaller than the second model having 733 elements and 2304 degrees of freedom. The distributed load is well captured by the smaller elements and resulting smooth distribution of nodal loads. The computed stress results are shown to be marginally better than those from the second model in terms of stress continuity across elements, and smoothness in contour bands.

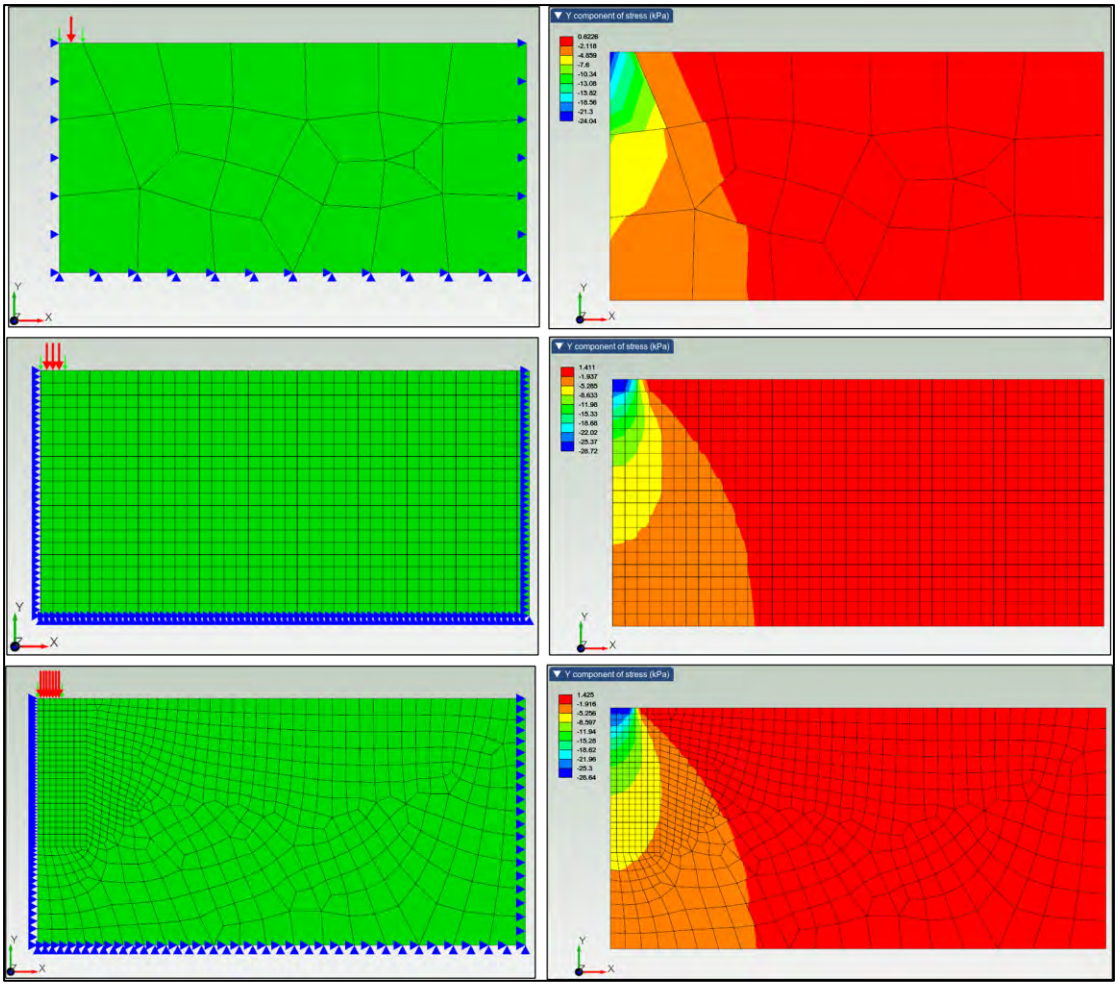

Figure 2-94: FEA modelling and vertical stress results of a strip footing problem, assuming different mesh strategies

The three FE models for which mesh quality and results were compared, are the outcome of a mesh refinement exercise for a geotechnical problem, for which the actual exact solution for the maximum vertical stress can be calculated by other tested classical methods. In such instances, where a comparison can be made to the exact solution from a classic analytical method, a patch test can be performed. This test ensures that the interpolation functions of the elements can accommodate rigid-body motion and a constant state of strain, as both these cases are physically possible in a structure.

Convergence results for a typical patch test are shown in Figure 2-95. The curve indicates that the calculated displacement of a structure obtained using the FE method, gradually approaches the exact solution as more elements are used. This relationship progresses to a point after which further mesh refinement will not bring this computed value any closer to the exact solution.

The anticipated displacement of an engineering structure computed using the FE model, assuming linear elastic material properties, will always be marginally less than the exact solution (Logan, 2019). FE models are implicitly stiffer than the actual structure modelled as

they are only allowed to displace into shapes defined by the terms of the assumed displacement field, within the FE structure, as dictated by the interpolation functions of each element. Similarly, the stress results computed assuming linear elastic material properties, will inherently, as a minimum, always be marginally higher than the true value, even if a flawless mesh is created, avoiding localised stress concentration effects of element singularities and poor elements.

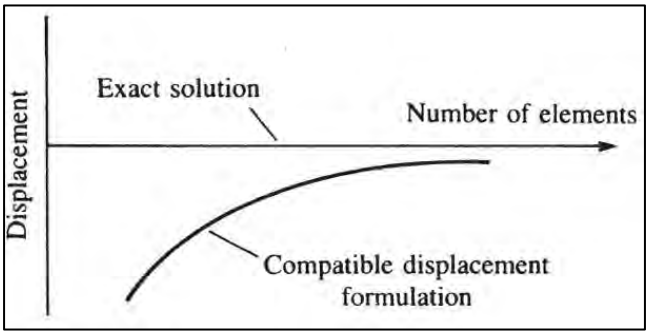

Figure 2-95: Convergence of computed displacement values from a mesh refinement exercise (Logan, 2019)

2.5.10 FE Modelling of Dams

The use of numerical modelling tools such as the finite element method, boundary element and finite difference methods, has become standard practice in dam engineering. The significant advances in software and hardware technology allow dam engineers to perform a variety of quick and efficient numerical analyses, for unusual or very complex problems in dam design, construction and operation (ICOLD, 2013).

Numerical simulation models of the dam-foundation-reservoir system, such as the FE method, have been used in dam engineering for several purposes such as:

- Evaluation of the structural stability of different dam types, and simulation of the possible failure mechanisms under the full spectrum of loading conditions (construction, normal operation, flood, thermal and earthquake).
- Design of dams and optimisation of new dams at different stages of the project.
- Interpretation of dam behaviour under operation by comparison of results of dam instrumentation measurements and monitoring system, with theoretical computed values, and subsequent assessment of dam safety.
- Design and optimization of remedial works, corrective measures, and most efficient rehabilitation methods of existing dams.
- Learning from real cases and back analysis of different problems.

It is not necessary to utilize the FE method for analysis of all dam type problems. In certain instances, traditional design methods are sufficient to evaluate a dam, negating the need for more detailed analyses using advanced numerical modelling methods. An example of such a case is the stability analysis of a concrete gravity dam, not subject to large seismic loads or other complex loading conditions, founded in a relatively flat valley. The stability of a concrete gravity dam under normal loading, can be properly undertaken by the classical method, which assumes rigid body motion of the dam and elastic stress transfer according to Bernoulli's elastic shallow beam theory.

The classic method has been in use for over 100 years (Watermeyer, 2006), and most concrete gravity dams around the world still standing today, were designed according to this approach. This approach is accepted as being conservative in most instances, (Durieux & van Rensberg, 2016) unless the dam is expected to undergo large seismic loading (PGA > 0.2), in which case numerical modelling is required to accurately model and evaluate the dynamic response of the dam (Roberts, 2017; Fell *et al.*, 2015; Chopra, 2020; Wieland, 2018).

As shown by Fu & Haflioason (2015), numerical analyses of concrete gravity dams under static loading, give nearly identical results to those of the classical method in terms of stability evaluation factors of safety. If it is deemed that numerical analyses of a dam would not result in any additional information of importance, then the classic method should be used (Malm, 2016).

Design problems where the FE method is a valuable analysis tool, comprises various dam types that experience complex loading conditions, have a complex geometric configuration or both.

Typical design problems for which numerical modelling is a valuable tool are provided below:

- Slope stability of earthen embankment dams using the strength reduction method or limit equilibrium method,
- Displacement analysis of earthen embankment dams,
- Steady state, or transient (rapid draw down) seepage analysis of earthen embankment dams,
- Liquefaction assessment of tailings dams using advanced critical state soil mechanics material models, suitable for modelling contractive soil behaviour of loose soils (O'Brien *et al.*, 2022; O'Brien *et al.*, 2021),
- Seismic analysis of earth embankment dams using the time-history method,
- Hydrostatic analysis of concrete gravity and arch dams,

- Thermal and thermomechanical analysis of concrete gravity and arch dams, making provision for low stress relaxation creep behaviour of high cementitious content paste RCC dams (Shaw & Cassells, 2023; Shaw *et al.*, 2020),
- Seismic analysis of concrete gravity and arch dams using the time-history or response spectrum approach, adopting state-of-the-art methods for modelling the complex dam-foundation-reservoir interaction during earthquake acceleration loading (ICOLD, 2022),
- Impoundment analysis of concrete gravity and arch dams, for use as a reference point of expected dam behaviour during impoundment of reservoir (Cassells & Shaw, 2022),
- Non-linear analyses of concrete gravity and arch dams assuming a suitable non-linear elastoplastic material model, to predict dam response under critical loading conditions when stress re-distribution occurs, due to the development of plastic zones in the vicinity of localised high stress zones in the dam (Cassells & Wright, 2023; United States Department of the Interior Bureau of Reclamation, 2006),
- Stability analysis of concrete gravity using fracture mechanics (Chemaly, 1995),
- Stability analysis of rock mass foundation abutments of concrete arch dams (Cassells & Roberts, 2017),
- Structural analysis of the swelling effects of alkali-silica reaction of concrete arch dams (Pourbehi, 2018),
- Risk analysis assessment of dam safety in terms of reliability-based design methods (Kreuzer & Leger, 2013),
- Dam overload analysis to determine overload capacity of concrete dam (Wang, 2016).

Every two years, ICOLD Technical Committee A (Computational Aspects of Dam Analysis and Design) hosts technical benchmarking workshops on numerical analysis of dams. Typical dam FE analysis problems, based on existing dam structures, are proposed for participants to undertake and report on findings in terms of a common set of predefined outputs and criteria.

An image taken from the publication of the 14th International ICOLD Benchmark Workshop of 2018, held in Stockholm is shown in Figure 2-96. It shows images from the four dam engineering analysis problems addressed at the 2018 workshop in accordance with the themes listed below:

- Theme A: Cracking of a concrete arch dam due to seasonal temperature variations,
- Theme B: Static and seismic analysis of an arch-gravity dam,
- Theme C: Embankment dam behaviour,
- Theme D: Risk analysis-assessment of reliability for concrete dams.

The purpose of the benchmark workshop is to share knowledge and experience regarding numerical modelling within the fields of dam safety, planning, design, construction as well as operation and maintenance of dams (ICOLD, 2018).

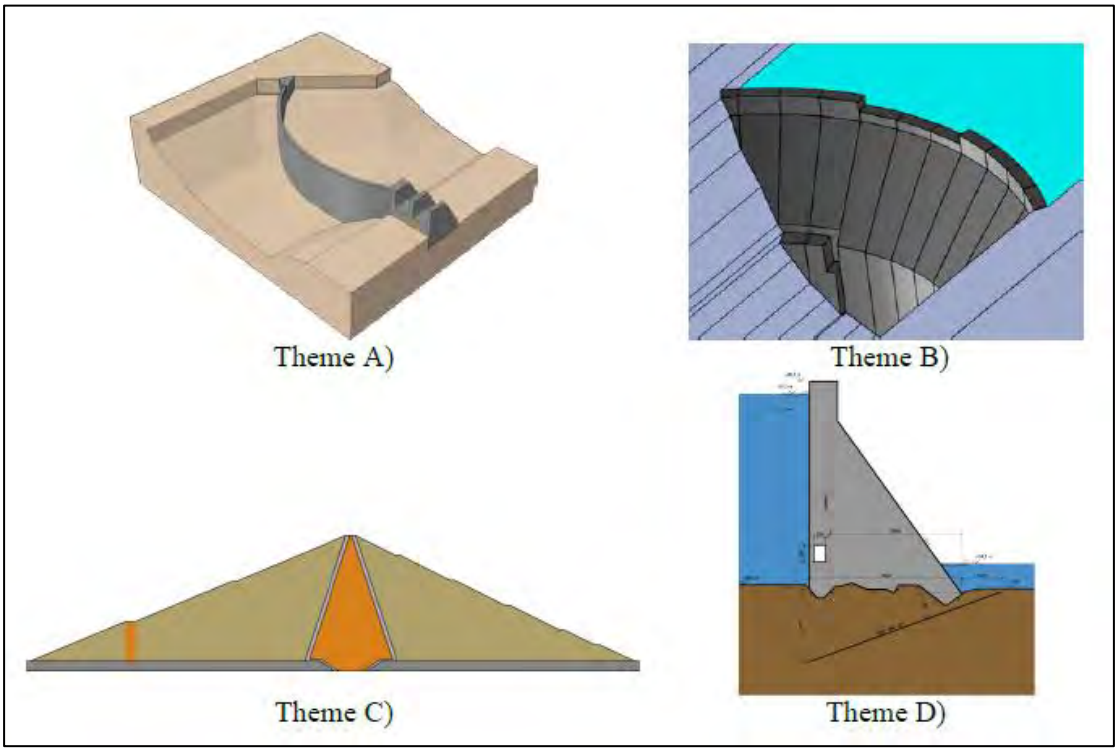

Figure 2-96: Images of four modelled dam geometries for numerical analyses studies undertaken at ICOLD benchmark workshop of 2018, in Sweden (ICOLD, 2018)

Most analysis problems are strictly speaking partial mathematical models, in that they describe or simulate some particular (partial) response of the dam, to the variations of some external agents (ICOLD, 2001). When appropriate, analyses regarding only individual mathematical models, are adopted for modelling a specific physical dam phenomenon, in isolation from the influence of other phenomena. This is to investigate the behaviour of a given dam in relation to that specific phenomenon. Alternatively, coupled analyses can be undertaken that consider multiple mathematical models in an inclusive analysis, which simulates the effects of interaction of these different physical phenomena, in relation to each other.

2.6 SUMMARY

A comprehensive literature review was undertaken investigating the current knowledge base in the dam engineering industry, that relates directly to the topic of this dissertation. The literature study has focused particularly on the important design considerations of concrete arch dams, with an emphasis on the FE method as an analysis tool for the design of large concrete arch dams.

The fundamental theoretical principles of the dissertation topic have been outlined, ensuring the assumptions adopted in the study follow sound engineering principles. The following chapter describes the prototype dam upon which the study is conducted.

3 DAM PROTOTYPE INFORMATION

3.1 GENERAL DESCRIPTION

Yusufeli Dam is a 275 m high double-curvature concrete arch dam, on the Coruh River in the Artvin Province of the Black Sea region of Turkey. The dam has a developed crest length of 540 m, and a section thickness of 8 m at the crest and 90 m at the base on the crown cantilever. The dam was constructed with conventionally vibrated mass concrete and the structure contains 4 million cubic meters of concrete, impounding 2.1 billion cubic meters of water at full supply level. Yusufeli Dam is the highest dam in Turkey, the fourth highest double curvature arch dam in the world and ninth highest dam in the world. A photograph of the completed dam structure during reservoir impoundment is shown in Figure 3-1.

Figure 3-1: Yusufeli Dam reservoir flow release through outlet during impoundment

The DSi (Turkish State Hydraulic Works) is the owner of the project, which was constructed by Limak Construction S.A. For the detailed and construction design, Limak appointed IC Consulenten of Austria for all geotechnical investigations and design, and a team comprising ARQ of South Africa and Su Yapi of Turkey for the dam design. Su Yapi was also contracted for the power station design. The ARQ-Su Yapi team for the dam design was led by Dr Quentin Shaw of ARQ. ARQ was responsible for all dam design, which included numerous complex and detailed studies to model all conditions and modes that could be experienced during

construction and operation. The dam design project won the award for best international project at the CESA engineering excellence awards in 2023 (IMIESA, 2023).

With very little geotechnical investigations for the dam site before the start of construction, as a result of difficult access due to the steep and rugged topography, the dam design process was essentially re-started at the outset of construction. Consequently, ARQ's involvement spanned from geotechnical investigations until final filling of the impoundment.

The tender design assumed a substantially simpler geotechnical situation than finally proved to be the case, and the dam structure was substantially redesigned to accommodate the actual geotechnical complexity of the site.

The dam is the largest in the Coruh River hydropower development plan commissioned by the DSi (Turkish State Hydraulic Works). The hydropower development scheme intends to build 13 large new dams to generate hydropower to meet the rapidly growing electricity demand of Turkey. The Coruh River hydropower scheme is in the Artvin Province of Turkey, and the geographical location of its dams are shown in Figure 3-2. The nearest town is the Yusufeli town which lies along the Coruh River banks about 10 km upstream of the dam.

Figure 3-2: Coruh River development scheme geographical location

Other notable large concrete dams forming part of the scheme are Artvin Dam and Deriner Dam. These dams lie downstream of Yusufeli Dam and are already in operation. Artvin Dam is a 180 m high concrete gravity-arch dam and Deriner Dam is a 249 m high double-curvature concrete arch dam. The Deriner Dam is shown in Figure 3-3.

Figure 3-3: General photograph of the downstream face of Deriner Arch Dam

3.2 DAM DESIGN CONSIDERATIONS

The Yusufeli Dam site is located in a remote mountainous area, with relatively extreme weather conditions and challenging site access. The local topography comprises a river with steeply incised canyon-like valley slopes of complex rock mass formations showing signs of surface relaxation. The steep riverbank slopes create a topography suitable for an arch dam, while the igneous rock mass forming the V-shape valley demonstrated some challenges that required particular management.

The site bedrock comprises variably fractured and sheared granites and diabase dykes, covered by Quatenary sediments of notable thickness along the river basin in the lower valley. The bedrock is intersected by six main discontinuity sets and numerous faults, that reflect the regional tectonic setting (IC Consulenten, 2018).

From a design perspective, the dam foundation conditions were the most challenging aspect of ensuring a safe dam structure that complies with all design criteria, which were established in accordance with various guidelines published by ICOLD, USACE and USBR.

The final design, as presented for tender, anticipated a simple and uniform rock mass, intercepted by a single fault of limited width, and relatively shallow excavations. Applying a single and relatively high elastic modulus for the foundation, no particular abutment stability issues were anticipated.

On the basis of the construction design investigations, a substantially more variable and complex picture was developed. The deformation modulus turned out to be generally lower and also rather variable, with zones also impacted by relaxation. Additionally, investigations revealed the requirement for deeper excavations generally, and particularly on the left flank.

All geotechnical testing and geological investigations were conducted by IC Consulenten of Austria. A comprehensive three-dimensional solid geological model was subsequently compiled by IC Consulenten using the Leapfrog software, whereby the various rock mass layers and their tested material properties were provided.

The geotechnical investigation comprised a thorough set of tests including geological surface mapping, borehole logging, standard laboratory tests (triaxial, unconfined compressive strength and shear box tests), dilatometer tests, Lugeon tests, various surface and sub-surface seismic refraction tests, plate load jacking and groutability tests.

The rock mass foundation of Yusufeli Dam comprises complex layers of rock exhibiting vertical and horizontal extrusions of material, with differing deformation moduli and strength properties. These rock formations contain various faults and discontinuities, creating local planes of weakness. Highly fractured foundation rock zones exhibit low deformation moduli. The Elastic modulus of the rock mass layers range from 2 GPa to 13 GPa. Assuming a sustained Elastic modulus of approximately 20 GPa for the dam structure, the dam-foundation stiffness ratio approaches 10 at worst case scenario.

Most of the lower riverbed foundation contains competent rock. The upper abutment materials are of a lower stiffness due to a certain degree of loss of confinement or relaxation. The rock properties of the left and right banks vary from each other, thereby creating an asymmetrical configuration for arch thrust support.

As a result of the above, a complete redesign of the arch dam and its foundation was found to be necessary.

A lower rock mass deformation modulus will not only result in higher overall structural displacements and an increased development of tensions at the heel of the cantilever, but it also causes tensile stress to develop in the concrete at the contact with the rock, in a radial direction. This last effect can be understood as similar to the system developed with a rigid beam on a flexible foundation as seen in Figure 3-4.

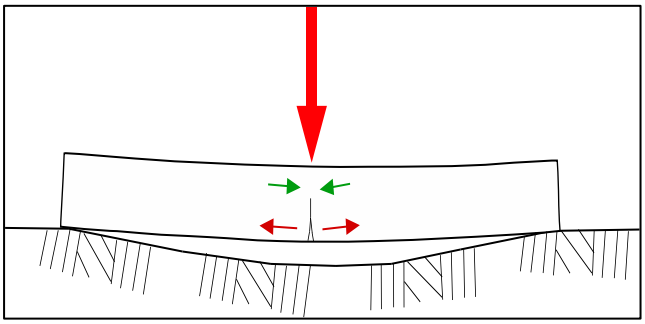

Figure 3-4: Illustration of tensions developed in a beam founded on flexible material

To mitigate the above effect, "cushion concrete" was used as a transition between the stiff dam concrete and the more flexible foundation. Where critical tensions were observed, the ductility, or concrete tensile strain capacity, of the contact zone was locally enhanced with polymer fibre reinforcement. Several options were tested to identify a means to assure a lower elastic modulus for the "cushion concrete", whilst retaining other mechanical properties, and the application of a high air content (11%) was found to be the most efficient. The cushion concrete was designed for an elastic modulus under sustained load of approximately 12.5 GPa.

The design of a concrete cushion as a low deformation modulus foundation replacement concrete, to allow smooth stress transfer between the dam and foundation with varying deformation modulus, has been adopted by designers of other super-high concrete arch dams recently completed in China (Song *et al.*, 2013).

The final revision for three-dimensional model of the rock mass foundation including dam excavation is shown in Figure 3-5. The top left image is a perspective view of the Leapfrog model showing various rock mass types in different colours, as well as joint sets represented as coloured lines. The top right image shows an aerial view of the layered rock mass and excavation footprint, whilst the bottom view shows a developed section taken along the dam axis. The model was progressively developed as excavation proceeded downwards from the upper abutments to the lower river basin.

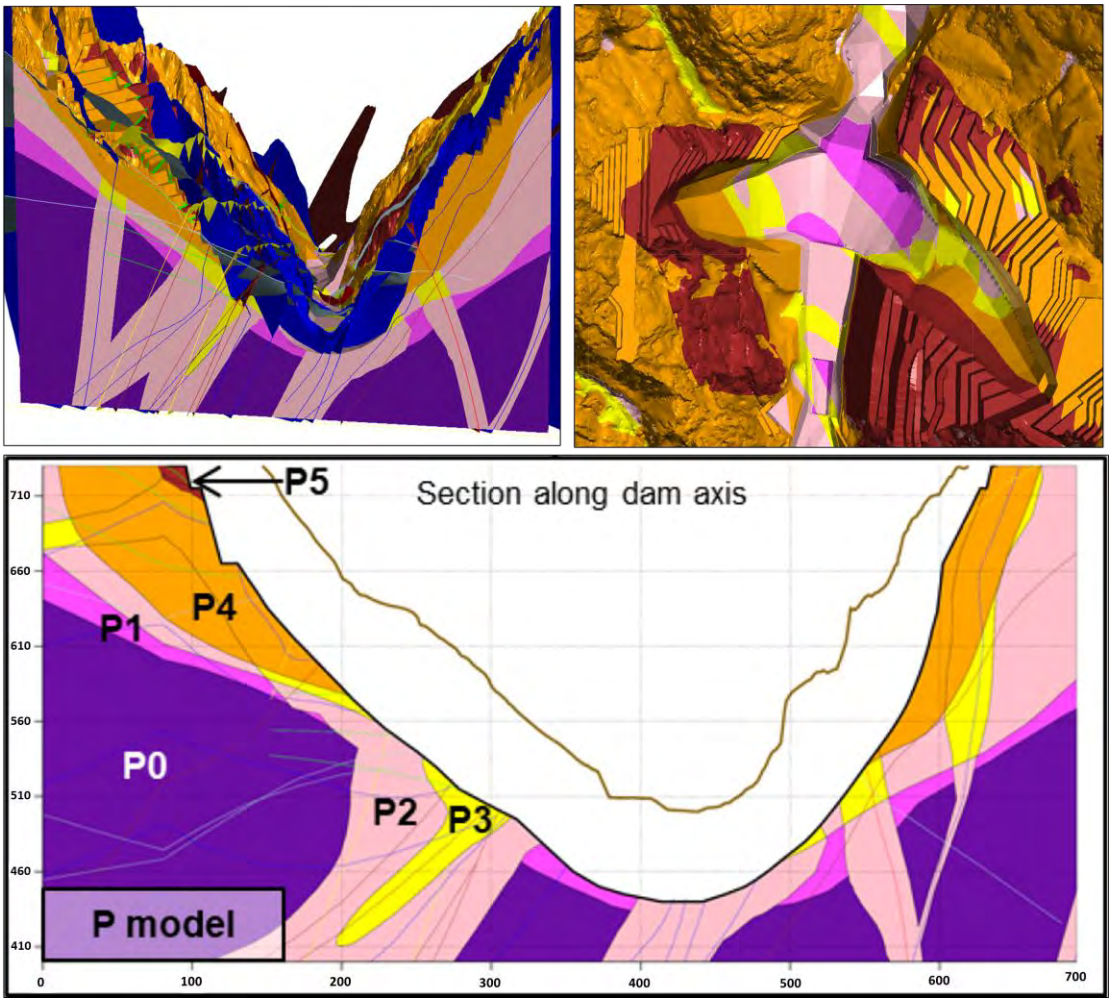

Figure 3-5: Three-dimensional model of foundation rock mass viewed in Leapfrog software

The material design parameters for the various zones of foundation rock mass prior to foundation improvement are shown in Table 3-1. Extensive consolidation grouting works were undertaken to improve the elastic stiffness of the foundation and reduce the variability in elastic modulus between foundation layers, and the cushion concrete. As a result of the grouting, a fair amount of foundation improvement was achieved and the elastic modulus of material sets P5, P4 and P3 were each improved by one level to match properties of P4, P3 and P2 respectively.

Table 3-1: Geotechnical material parameters of dam foundation rock mass (IC Consulenten, 2018)

Material Set	Density γ (kN/m^3)	Cohesion c (MPa)	Friction Angle ϕ (°)	UCS (MPa)	Elastic Modulus (GPa)	Poisson ratio ν
P5	25	1.2	32	4.3	2.0	0.45
P4	25	2.0	32	7.2	3.5	0.43
P3	26	3.0	35	11.5	6.0	0.35
P2	27	4.0	37	16.0	8.5	0.30
P1	27	6.0	40	25.7	11.0	0.29
P0	27	7.0	42	31.4	13.0	0.27

The deep zone of poor P4 rock mass material on the upper left abutment of the foundation, required a substantially deeper excavation than the right bank. The additional excavation was kept to a minimum by designing a concrete abutment, which was cast before commencement of main concrete works of the dam body. The objective of the abutment was to maintain a degree of symmetry in the arch and retain the steep valley slope at the excavation rock face.

Other foundation improvement works comprised stabilisation of the canyon cut slopes with grout-injected post-tension pre-stress rock anchors and rock bolts, that were installed as the excavation progressed down the valley slopes.

The Yusufeli Dam structure indicates a crest length to height (CL:H) ratio of 1.78. The geometric features of the dam are comparable with other notable super-high and local arch dams as shown in Table 3-2.

Table 3-2: Geometric properties of selected large arch dams

Dam Name	Height (m)	Crest Length (m)	CL/H	Year of Completion
Yusufeli Dam	275	540	1.96	2022
Jingping 1	305	568	1.86	2015
Xiaowan	292	902	3.09	2010
Xiluodo	285.5	700	2.44	2013
Inguri	271.5	680	2.51	1984
Katse	186	710	3.82	1994
Pongolapoort	89	451	5.07	1973

A crest-length/height ratio of less than 2 signifies a narrow valley arch. Narrow valley arch structures are efficient and have a high arch stiffness to cantilever stiffness ratio when compared to wide valley arch structures, such as Katse Dam, or Pongolapoort Dam. Such an arch dam configuration transfers the majority of the hydrostatic load into its foundation by arch, rather than cantilever action and the greatest efficiency in terms of least concrete volume can be achieved with such structures.

The dam comprises approximately 4 million m^3 of concrete; of which 2,5 million m^3 of concrete was placed in the arch itself, 700 000 m^3 of concrete was placed to form the foundation cushions on either flank and 450 000 m^3 concrete was placed to form a concrete abutment on the left flank. The concrete arch was zoned on the basis of maximum stresses under dynamic loading, with approximately 5% comprising 30 MPa concrete, 15% comprising 25 MPa concrete and 80% comprising 20 MPa concrete. A perspective view of a three-dimensional CAD model of the dam, indicating the various structural features is shown in Figure 3-6.

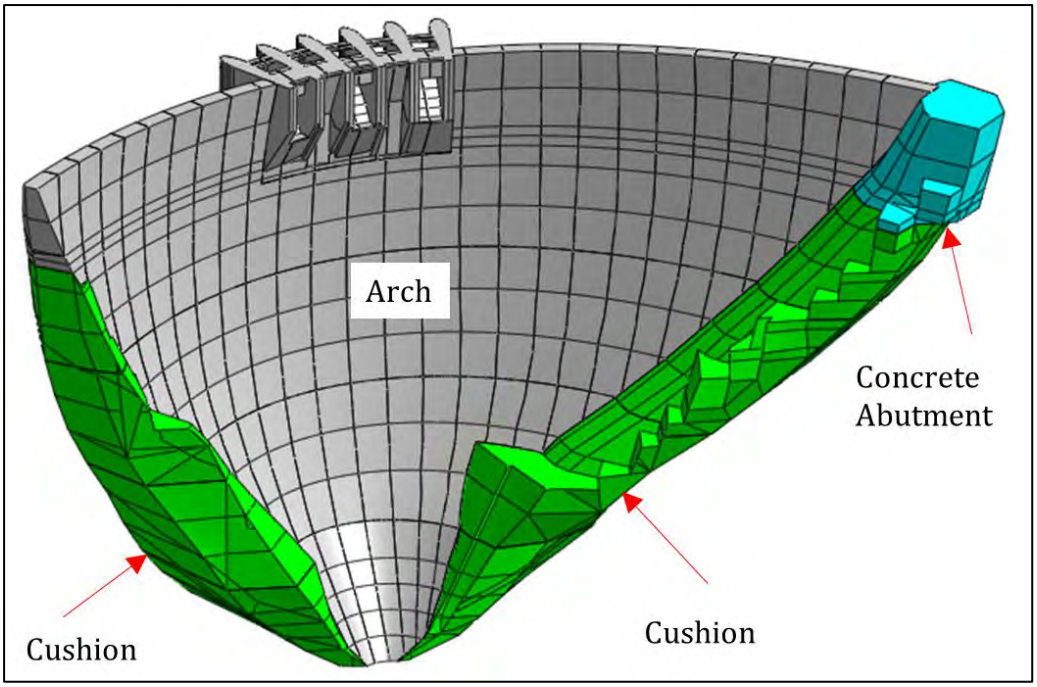

Figure 3-6: Three-dimensional CAD model of Yusufeli Dam

The cushion illustrated in Figure 3-7 is effectively foundation replacement concrete and where this lies below the rock surface, it was constructed with "cushion concrete", as described above, that ensures a smooth structural transition between the stiff mass concrete arch and the lower deformation modulus of the rock mass foundation (Shaw & Becerik, 2016).

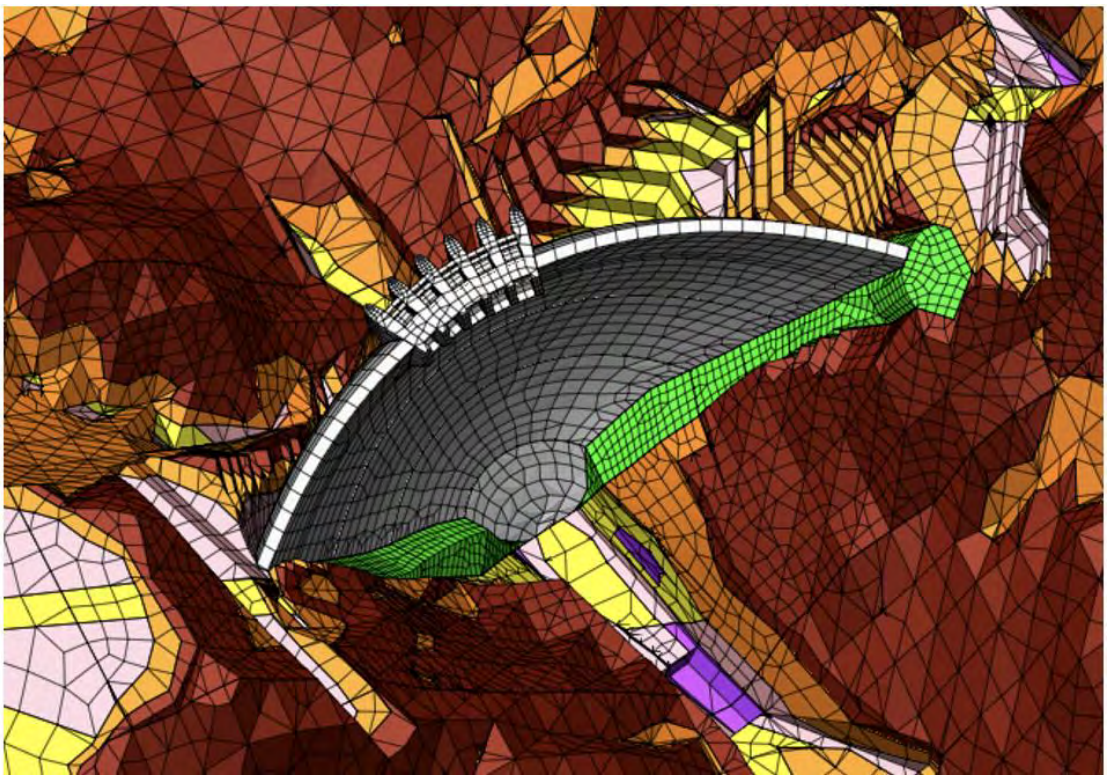

Figure 3-7: Illustration of cushion within valley rock mass

The form and extent of the cushion was designed iteratively based on the evolving foundation rock mass model, and the criteria of limiting tensile stress in the contact concrete, to within the tensile stress capacity in all cases.

The dam is 275 m high at the crown cantilever, in the deepest location of the river bed, with a foundation level of 440 mASL and a crest level of 715 mASL. The dam is a single-centre arch, formed with a combination of circular arcs at the centre and ellipsoidal arcs towards the flanks, having a variable thickness profile. A reference plane view of the crown cantilever geometric configuration in relation to the dam elevation levels is shown in Figure 3-8. The graphic indicates the dam side profile with arch axis line, the arch defining intrados (upstream) and extrados (downstream) lines of centres and the variable arch thickness of the arch.

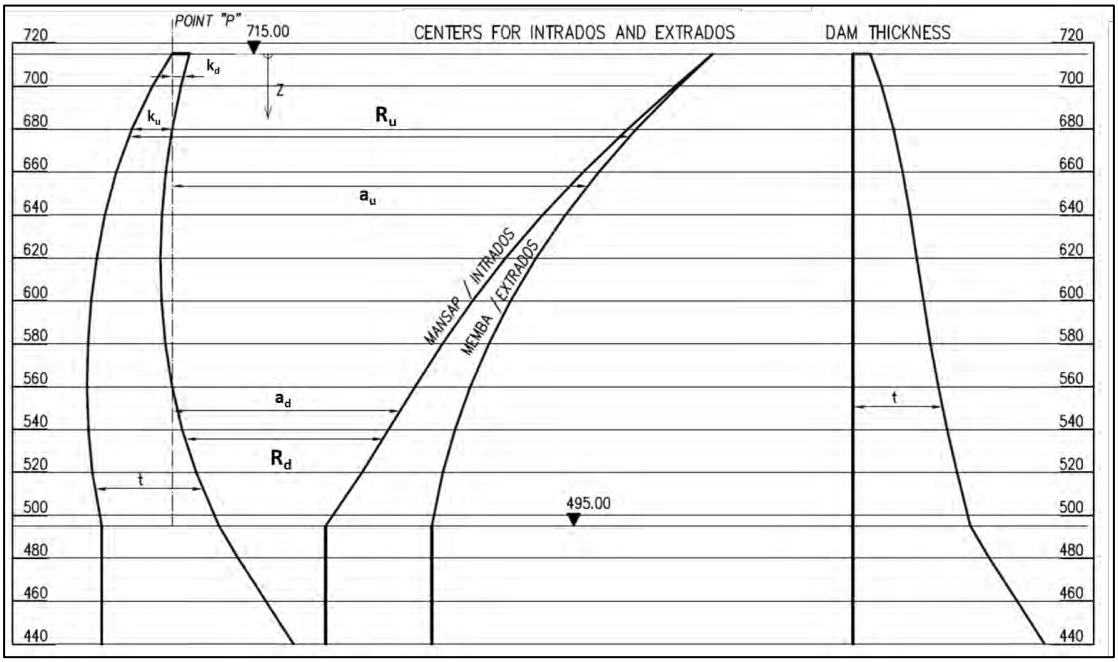

Figure 3-8: Reference plane view of the crown cantilever geometric configuration for Yusufeli Dam

The configuration of the crown cantilever is defined according to seven variables, of which three correspond to the extrados face of the dam profile and three to the intrados face of the dam profile. Each of these variables is a function of the dam height (elevation) and comprise the distance between dam axis and line of centers (a), the radius length from the line of centres to arc (R), and the projection distance of the arc from the dam axis (k).

The variables are all defined by polynomial functions in terms of the dam elevation as shown in Equation 3-1 through Equation 3-8.

$$k_d = 8.09E\text{-}9z^4 - 1.70E\text{-}6z^3 + 1.55E\text{-}3z^2 - 2.81E\text{-}1z + 8.00 \quad \textbf{3-1}$$

$$t = -2.25E\text{-}8z^4 + 1.47E\text{-}5z^3 - 3.00E\text{-}3z^2 + 4.02E\text{-}1z + 8.00 \quad \textbf{3-2}$$

$$k_u = k_d - t \quad \textbf{3-3}$$

$$R_u = -2.79E\text{-}8z^4 + 1.33E\text{-}5z^3 - 1.61E\text{-}3z^2 + 4.45E\text{-}1z + 254.00 \quad \textbf{3-4}$$

$$R_d = -4.93E\text{-}8z^4 + 1.41E\text{-}5z^3 - 6.47E\text{-}3z^2 - 9.07E\text{-}1z + 246.00 \quad \textbf{3-5}$$

$$a_u = R_u + k_u \quad \textbf{3-6}$$

$$a_d = R_d + k_d \quad \textbf{3-7}$$

$$Z = 715 - El \quad \textbf{3-8}$$

Where

El = elevation (m)

k_d = arch offset distance downstream (m)

t = arch thickness (m)

k_u = arch offset distance upstream (m)

R_u = arch radius upstream (m)

R_d = arch radius downstream (m)

a_u = arch axis to centre point upstream (m)

a_d = arch axis to centre point downstream (m)

The crown cantilever profile of the dam was designed by passing a smooth curve through discrete defining points on the extrados and intrados faces of the profile, according to the application of equations presented at predetermined elevation height intervals. These elevation intervals vary from 10 m to 25 m in height depending on extent of curvature of the profile.

The array of profile defining geometrical distances calculated for the crown cantilever extrados and intrados faces, using the mathematical equations at predetermined dam elevation levels from elevation 715 mASL at the crest to 440 mASL at the base are shown in Table 3-3. The crown cantilever was used as a reference for defining the various arch elements making up the whole arch dam. These arch elements are defined in terms of the dam axis, reference plane and lines of centres.

Table 3-3: Arch defining dimensions for extrados and intrados faces of dam crown cantilever

El (m)	Z (m)	k_d (m)	t (m)	k_u (m)	R_u (m)	R_d (m)	a_u (m)	a_d (m)
715	0	8.0	8.0	0.0	254.0	246.0	254.0	254.0
700	15	4.1	13.4	-9.3	247.0	232.3	237.7	236.4
680	35	0.0	19.0	-19.0	236.5	214.1	217.5	214.1
660	55	-3.0	23.3	-26.3	224.7	196.5	198.4	193.5
640	75	-4.8	26.8	-31.6	211.3	180.3	179.7	175.5
620	95	-5.5	29.9	-35.4	196.1	166.1	160.7	160.6
600	115	-5.0	33.0	-38.0	178.7	154.6	140.8	149.6
580	135	-3.2	36.3	-39.5	158.7	146.5	119.2	143.3
560	155	0.0	40.0	-40.0	135.3	142.4	95.3	142.4
540	175	4.7	44.1	-39.4	107.9	143.1	68.5	147.8
520	195	11.2	48.8	-37.6	75.7	149.2	38.1	160.4
495	220	22.0	55.0	-33.0	27.2	165.4	-5.8	187.4
490	225	24.6	56.3	-31.7	16.2	169.9	-15.5	194.5
480	235	30.1	58.9	-28.7	-7.1	180.3	-35.8	210.4
470	245	36.3	61.4	-25.1	-32.4	192.5	-57.5	228.7
460	255	43.1	63.9	-20.8	-59.8	206.6	-80.6	249.7
450	265	50.6	66.3	-15.7	-89.5	222.8	-105.2	273.4
440	275	58.8	68.5	-9.8	-121.7	241.1	-131.4	299.9

Due to the asymmetrical configuration of the river valley site, the centre point location of the ellipsoidal arcs defining the arch, were translated and rotated for each arch element according to its corresponding elevation level, in relation to the crown cantilever. The mathematical formulation of an arch element for the dam is shown in Figure 3-9. The arch element is configured around the crown cantilever profile, its axis and centre point (O).

The Yusufeli Dam is a double-curvature arch dam as it exhibits curvature in the horizontal and vertical planes of the dam. Construction drawings of the dam and foundation are provided in Appendix A.

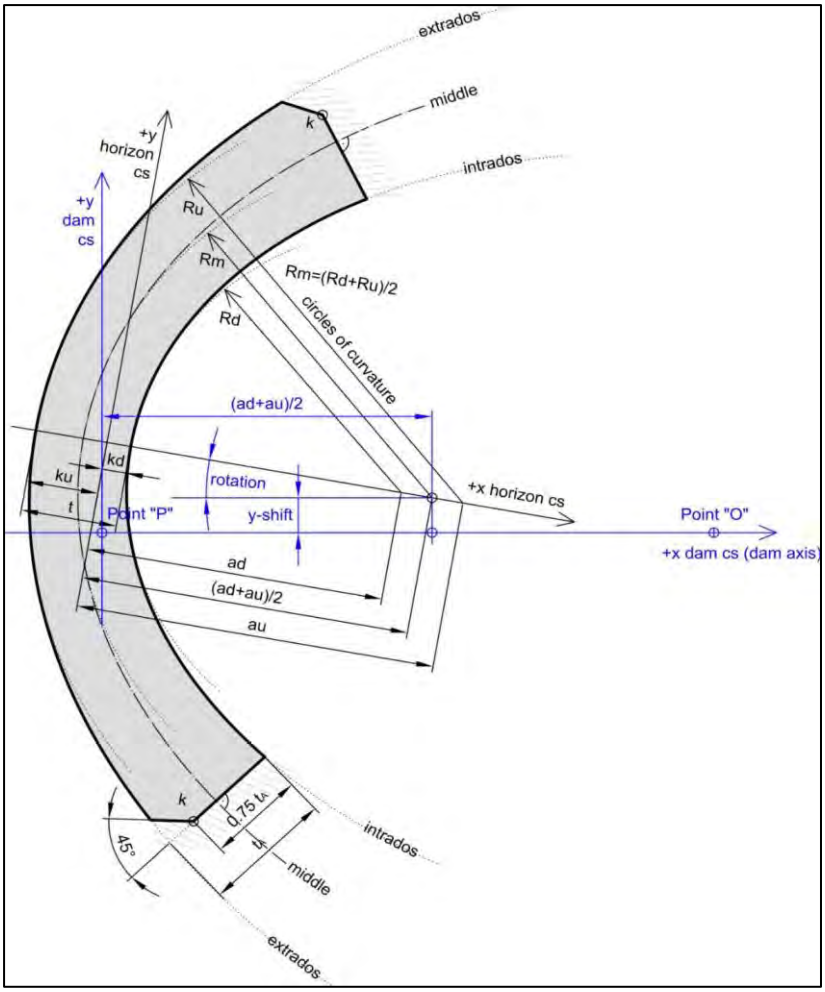

Figure 3-9: Mathematical formulation of dam arch elements and rotation angle against crown cantilever

The historical evolution of the arch dam structure indicates that the most effective arch structure comprises a double curved structure, with a variable section thickness. Assuming the arch structure is founded on competent foundation, this configuration is most effective in that it develops low internal tensile stresses when loaded by the water reservoir (Djoudi & Sabir, 1995).

Various concrete types were used for casting the dam, cushion and related structures. Structural mass concrete was designed for the arch and low elastic modulus concrete for the cushion structure. The structural mass concrete of the dam body comprised three different class types, having different characteristic strengths, for zoning of the dam body. The three concrete designations are shown in Table 3-4 where the aggregate size and minimum cement content are shown, as well as that for the cushion concrete. The characteristic strength of the dam concrete is defined as the compressive cylinder strength at 90 days.

Table 3-4: Yusufeli Dam characteristic concrete strengths and composition

Concrete Application	Concrete Class	90-day Cylinder Strength (MPa)	Max Aggregate Size (mm)	Minimum Cement Content (kg/m^3)
Structural mass concrete	C200/60	20	60	275
Structural mass concrete	C250/60	25	60	300
Structural mass concrete	C300/60	32	60	325
Cushion mass Concrete	C150/120	15	120	200

The dam allowable stress design criteria for five load conditions are shown in Table 3-5. The criteria are in accordance with the USACE's material design and stability factors of safety for concrete arch dams as presented in section 2.2.4. The assumed direct tensile strength of concrete was adopted as per ACI 207.1R-96 where $f_t = 0.32(f'_c)^{2/3}$.

Table 3-5: Arch dam design criteria (USACE, 1994)

Load Condition	Allowable Compressive Strength ($f_{c'}$)	Allowable Tensile Strength (f_t)	Minimum Required Sliding Factor of Safety
Static Usual	$f'_c/4.0$	$f'_t/1$	2.0
Static Unusual	$f'_c/2.5$	$f'_t/1$	1.3
Static Extreme	$f'_c/1.5$	$f'_t/1$	1.1
Dynamic Unusual	$f'_{cd}/2.5$	$f'_{td}/1$	1.3
Dynamic Extreme	$f'_{cd}/1.5$	$f'_{td}/1$	1.1

Ultimately the final revision of the dam-cushion configuration was comprehensively analysed and designed to withstand a full set of normal, unusual and extreme loading cases, as deemed appropriate for the design of large concrete dams. These loading cases cover a full spectrum of the loadings shown below applied as combinations expected to occur simultaneously. These comprise:

- Dam self-weight from gravity,
- Hydrostatic loading,
- Drained and undrained uplift,
- Silt loading,
- Thermally induced loading due to short-term heat of hydration during construction,

- Thermally induced loading due to long-term operational seasonal temperature variations,
- OBE and MCE seismic induced acceleration loading of dam-foundation-reservoir system,
- Staged impoundment loading.

Other structural/geotechnical components of the dam also analysed or designed by ARQ are listed below:

- Rock wedge stability analyses and stabilisation techniques,
- Auxillary spillway support platform,
- Approach for pipe cooling of concrete,
- Plunge pool lining reinforced concrete design and doweling,
- Shear keys and post-tensioned anchors for stability of various concrete dental infill structures,
- Stability of individual dam monoliths,
- Drainage path crack lengths for uplift derivations.

3.3 DAM CONSTRUCTION

Early access to the dam site for purposes of construction was obtained in 2013. Access to the upper flanks of the site for commencement of excavation, was obtained by drill and blast construction of spiral tunnels within the abutment rock mass. Excavation commenced on the upper banks in 2014 and progressed downwards towards the river course.

Excavation of the rock material was achieved by a combination of controlled blasting and mechanical excavation. As the excavation progressed downwards, the canyon cut slopes were stabilised with 250 tonne, 80 m long, grout-injected post-tension pre-stress rock anchors. These were required in the greatest measure on the upper left abutment as shown in Figure 3-10, where excavations undercut major joint planes.

Figure 3-10: Advanced stage of excavation on the left abutment

The cleaned and prepared surface of the excavated foundation rockface was protected with shotcrete on completion of excavation, as shown in Figure 3-11. The shotcrete was removed immediately before placing cushion concrete against the foundation, as the dam construction progressed upwards.

Figure 3-11: Steep excavation surface on right abutment, protected with shotcrete

A tunnel river diversion was constructed through the lower left abutment and the river was diverted using embankment coffer dams, both upstream and downstream, on top of slurry cut-off walls that were constructed through ± 50 m gravel alluvium beneath the riverbed using Hydro-mills.

The dam foundation excavation was completed in 2018, with a total of 3.9 million m^3 of rock being removed. The final stages of excavation at the deepest point are shown in Figure 3-12 and Figure 3-13.

Figure 3-12: Final stages of excavation at the deepest foundation point in the river basin

Figure 3-13: Wide angle view of the final stages of excavation at the deepest foundation point in the river basin

During excavation for the dam foundation, a cable crane and multiple batch plants were erected in preparation for casting of the concrete arch structure. The 3-line cable crane was suspended from concrete platforms on the upper banks of the excavation and each crane had a 28-tonne capacity. The primary concrete batch plant that fed the cable cranes was located on the upper left abutment and this was supported with one supplementary plant located on the downstream coffer dam and another located upstream of the dam, both feeding the placement by conveyor. The cable crane and batch plant are shown in Figure 3-14 and Figure 3-15.

Figure 3-14: View of foundation excavation looking in the direction of stream flow

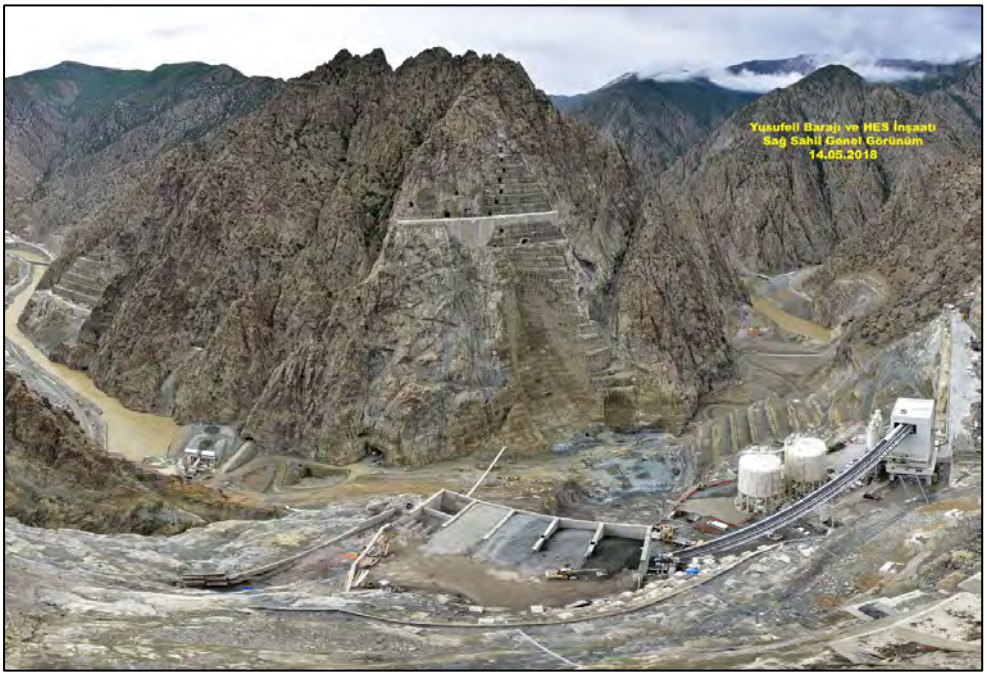

Figure 3-15: Wide angle view of dam excavation looking onto the right abutment of the dam site

The batch plants collectively had a concrete production capacity of 740 m^3/hour and were operated 24 hours a day, to meet the ambitious project production requirements. The majority of the aggregate materials were sourced from site excavations, although it was necessary to open a supplementary quarry to complete the works. The aggregate crusher was located downstream of the dam site and indicated a capacity of 2000 tonne/hour. Crushed aggregates were transported almost 2 km by conveyor, with a capacity of 200 m^3/hour, to the batching plant at the dam site. A photo of the main concrete batch plant on the upper left abutment is shown in Figure 3-16.

Concrete mix designs were optimised giving special attention to the thermal/thermomechanical properties, the design tensile strength, the durability and workability of the concrete. A concrete testing laboratory was set up on site for the primary test and this was supported by the regional DSi laboratory in Artvin, as well as the central laboratory in Ankara.

Figure 3-16: Concrete batch plant and cooling plant on upper left abutment

The placing of concrete in the dam body commenced in late 2018 and continued without interruption for 30 months until mid 2021, during which time 4 million m^3 of concrete were cast. Concrete was placed into forms by a combination of a 9 m^3 bucket suspended from the cable crane (Figure 3-17), and temporary conveyor belts leading directly to the forms. Concrete was spread in the box by rubber-tracked bulldozer, and compacted using gang-mounted immersion vibrators attached to an excavator with low-pressure tracks as shown in Figure 3-18.

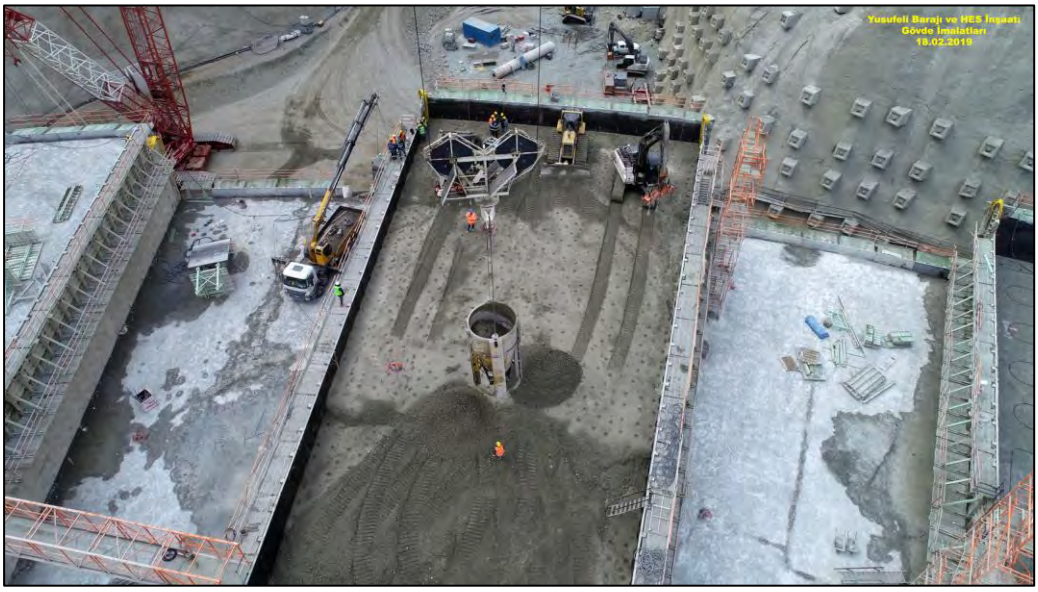

Figure 3-17: Placement of concrete with 9 m^3 bucket suspended from cable crane

Figure 3-18: Spreading and vibration of freshly placed dam concrete

The dam body comprises 28 vertical monolith blocks separated by groutable joints. The dam was cast in 3m lift heights, with a total of 1910 lifts. Placement of concrete using two conveyor belts and a bucket is shown in Figure 3-19 and an early stage of concrete construction is shown in Figure 3-20.

Figure 3-19: Delivery of concrete with conveyor belts from upstream & downstream and bucket

Figure 3-20: Early stages of concrete placement in dam body

Extensive temperature control measures were implemented at Yusufeli Dam, both in terms of pre-cooling and post-cooling of the mass concrete. Pre-cooling was implemented using a cooling plant to chill the mixing water and more importantly the coarse aggregates prior to batching, in order to meet the maximum allowable placement temperature specification of 18 °C.

Once cast, the most significant challenge was found in the need to cool the maturing concrete to approximately 11 ˚C sufficiently quickly to allow grouting of the joints between the monoliths, in sufficient time so as not to slow concrete placement. Post-cooling was achieved by circulating chilled water through 32 mm cooling pipe loops (2.5 m c/c) installed in the bottom of each lift cast as shown in Figure 3-21. The key challenge in this regard relates to ensuring that the tensile stresses due to cooling and thermal gradients are never allowed to exceed the tensile strength of the concrete, which obviously increases with time. Typically, generic rules in terms of time and temperature differentials are applied. However, with a concrete of lower stress-relaxation creep, due to the nature of the mix, and the use of fly ash in the mix, a different approach was considered appropriate. Furthermore, applying the generic rules, it would simply not have been possible to achieve the target rates of concrete placement.

Consequently, and on the basis of stress-relaxation creep measurements on the starter block cast at the top of the left abutment, a thermal-grouting model was developed, which allowed a prediction of the necessary cooling rates and compared these with the associated development of tensile stresses, compared to tensile strength. When tensile stress did not exceed strength, the required rate of cooling was confirmed. The model was both predictive and reactive, not only establishing the maximum possible cooling rates, but also identifying a situation when actual cooling rates were exceeding the allowable rate, in which case an adjustment would be made to the rate and consequently the required lift placement dates and joint grouting dates.

Figure 3-21: Pipes placed in coil formation on top of old lift for post cooling of concrete in subsequent lift

As the concrete construction progressed towards the dam crest, the thickness decreased and the crest length increased, resulting in more monoliths being cast concurrently. As is conventional practice for the construction of a conventionally vibrated concrete dam, a leader-follower block approach was applied, whereby the monolith casting heights are staggered between neighbouring monoliths. This can be seen in the photos of Figure 3-22 and Figure 3-23.

Figure 3-22: Casting of concrete monoliths using leader-follower block approach

Figure 3-23: Advanced stage of construction showing upstream face of dam

The final stages of concrete placement occurred in May and June of 2021, when the spillway piers and bridges were formed and cast as shown in Figure 3-24 and Figure 3-25. These components of the dam comprise reinforced concrete to account for concentrated loading of the structural steel spillway gates to be installed.

Figure 3-24: Final stages of concrete construction of Yusufeli Dam

Figure 3-25: Construction of the final concrete lifts of the dam spillway

Concrete construction works for the dam were completed by July 2021 at the height of summer, after which post-cooling continued until the end of August 2021, when most of the hydration heat generated had been dissipated by the pipe cooling. A view of the downstream (front) face

of the completed arch dam is shown in Figure 3-26, and an aerial view over the dam orientated with the river stream direction from left to right is shown in Figure 3-27.

Figure 3-26: Front face view of the completed Yusufeli Dam

Figure 3-27: Aerial view of the completed Yusufeli Dam orientated with upstream on the left

The Yusufeli Dam was constructed with a network of galleries and adits running along the dam axis and into the foundation. The galleries provide for drainage of internal water build up from the pressure relief drains at the base of the dam and in the foundation, as well as providing

access for monitoring of dam instrumentation and the related service lines for possible maintenance requirements. An extensive set of instruments were installed in the dam during construction for monitoring dam movement, joint opening, stress development, cracking, leaks, frainage and seepage paths through the drainage curtain. A comprehensive description of the dam instruments is shown in Section 5 of this report.

3.4 IMPOUNDMENT OF DAM RESERVOIR

Impoundment of the 2.1 million m^3 dam reservoir commenced on 21 November 2022 and is currently still progressing as of January 2024. The rate of water reservoir rise during impoundment is controlled by release from the Yusufeli Dam outlet works as well as the release from upstream dams in the Coruh River Development Scheme. The reservoir impoundment speed has been limited to a daily rate of rise not exceeding 1.5 meters per day, pending the availability of sufficient river flow volume and behaviour of the dam. Substantial volumes of river flow were anticipated as a result of run-off from snow melt in the early summer months.

A reservoir impoundment programme was drawn up making provision for impoundment stoppages at predetermined reservoir elevation heights, to allow for observing of the dam behaviour against expected design behaviour, and to detect any early signs of structural distress or permanent deformation of the dam. Early detection of distress during impoundment greatly reduces the risks of accidents or incidents occurring (Leitao *et al.*, 2023).

The original dam impoundment programme for Yusufeli Dam is shown in Appendix A. The programme was devised based on conservative assumptions, meaning if flow conditions permitted and if dam behaviour during impoundment was favourable, the actual impoundment of the dam would be expedited.

Observed dam behaviour during impoundment indicated that the dam was behaving well within design expectations showing the design to be marginally conservative. All observed displacements and stresses were below the criteria requirements, there were no signs of plastic deformation, negligible leaking of expansion joints was observed, uplift seepage conditions were favourable and virtually no concrete cracking was seen to occur. To capitalise on the substantial river flow volumes in early summer from snow melt, the dam impoundment process was accelerated. The achieved stages of impoundment are shown in Table 3-6. Impoundment of the water reservoir was temporarily halted at each of these stages to allow for evaluation of the dam behaviour, in the form of a dam impoundment study, after which impoundment recommenced.

Table 3-6: Yusufeli Dam impoundment stages

Impoundment Stage	Water Elevation Level (mASL)		Date Level Reached
	Upstream	Downstream	
0	503.5	440	2022-11-21
1	580	500.5	2023-02-13
2	610	500.5	2023-04-08
3	630	500.5	2023-04-29
4	670	500.5	2023-06-10
5	696	500.5	2023-08-18

The dam impoundment study comprised of monitoring dam behaviour against the anticipated behaviour of the dam according to predictions reported by the FE model. The FE model was calibrated according to dam behaviour during early impoundment stages and the analysis output results were further used as a reference point, for expected dam behaviour. The analysis validation work undertaken for the dam impoundment study ultimately form the backbone of the experimental data used to investigate the hypothesis of this dissertation.

At the current stage of impoundment (January 2024), the reservoir elevation level has reached a height of 256 m above lowest foundation level, requiring a further 14 m of raising until the full supply (spillway crest) reservoir level of the dam is reached. The latest dam impoundment photos as of May and June 2023 are shown in Figure 3-28 through Figure 3-32. Additional impoundment photos are shown in Appendix C.

Figure 3-28: Yusufeli Dam reservoir impoundment level 630 mASL (190 m above foundation)

Figure 3-29: Yusufeli Dam reservoir impoundment level 670 mASL (230 m above foundation)

Figure 3-30: Yusufeli Dam reservoir impoundment level 696 mASL (256 m above foundation)

Figure 3-31: Aerial view of Yusufeli Dam reservoir impoundment to level 200 m above foundation

Figure 3-32: Downstream view of Yusufeli Dam reservoir impoundment to level 230 m above foundation

3.5 ENVIRONMENTAL AND SOCIAL IMPACTS OF DAM

The project had significant environmental, ecological, archaeological and social impacts on the surrounding area of dam. Responsible decisions were made to alleviate any unfavourable impact of the dam on the surroundings. Endemic and endangered plant species and archaeological sites needed to be investigated and relocated where necessary.

The most significant feature was the relocation of the entire Yusufeli town located upstream of the dam along the banks of the river. The existing town will be fully inundated by the water reservoir of the dam when impoundment is completed. The new town was constructed above the dam having all the necessary infrastructure such as roads, schools, hospitals etc. The inundation of the town at the current stage of impoundment is shown in Figure 3-33.

Figure 3-33: Inundation of Yusufeli town upstream of dam on the banks of the Coruh River

It is noted that the dam will provide valuable infrastructure facilities to the local community and the greater Turkey in terms of the 558 MW of sustainable electricity supply, water resources for farming of the arid area as well as job creation and an economy stimulus of 1.65 billion Turkish Lira (US$ 65 million at 2023-07-31) per annum.

Hydropower is an inherently sustainable and clean form of power generation and consequently, the project implementation offers significant sustainability benefits in reducing overall CO_2 emission. Furthermore, the use of the maximum possible level of fly ash to replace cement in the dam concrete created a reduction in the carbon footprint associated with the construction, while rapid implementation further reduced total emissions.

3.6 SUMMARY

The Yusufeli Dam in Turkey was constructed from 2014 to 2021 with impoundment of the reservoir expected to reach completion in 2024. The 275 m high double-curvature concrete arch dam was used as the prototype dam for undertaking the studies presented in this dissertation. The studies specifically comprised a comparison of the observed instrumented dam behaviour during reservoir impoundment against that modelled using the FE analysis method, assuming linear elastic constitutive material parameters for the dam and rock mass foundation.

A summarised presentation of the design and construction of the dam was given in this chapter to provide background information on the dam features and its conditions. Features of the dam including the geometrical arch formulation, the design criteria, foundation properties and other unique challenges relating to the dam design were outlined herein.

The following chapter addresses compilation of the FE model of the dam.

4 FINITE ELEMENT MODEL AND ASSUMPTIONS

This chapter aims to present the numerical model of the Yusufeli Dam created for purposes of the dissertation study. A comprehensive description is provided of the FE model of the dam and foundation in terms of the modelling approach and methodology, geometrical modelling assumptions, discretization strategy, material model assumptions, loadings, boundary conditions and other unique modelling features.

The FE model of the dam was created and analysed using the Midas FEA NX software package. Midas FEA NX is a simulation program developed for the simulation of advanced linear and nonlinear analysis for civil and structural engineering applications, based on the finite element method. The program supports advanced geometric modelling functions, powerful mesh generation algorithms and various analysis conditions to simulate real phenomena. Field value conditions can be simulated using non-linear analysis methods such as linear/non-linear static analysis and linear/non-linear dynamic, linear buckling and heat transfer analysis (Midas, 2024).

4.1 FINITE ELEMENT ANALYSIS APPROACH AND METHODOLOGY

The FE modelling approach was considered in relation to the objective of the FE analysis problem in the overall context of this dissertation. The purpose of the FE model is to simulate the structural response of the Yusufeli Dam during first filling of the dam reservoir, and evaluate the actual observed and instrumented dam behaviour during impoundment, against that anticipated by the FE model. The evaluation of the structural response of a dam during first filling forms an essential part of dam safety surveillance (Perner & Obernhuber, 2010).

From a dam design perspective, the behaviour of the dam FE model provides insight into the ideal behaviour expected of the dam during impoundment, in terms of its assumed design parameters. The simulated behaviour of the dam serves as a reference point against which the observed impoundment behaviour may be compared. Any significant deviations in observed dam behaviour from those expected, may potentially indicate early signs of distress in the dam-foundation structure, and need further investigations.

The FE model is based on many assumptions which may vary from actual conditions, meaning it is unlikely that the extent of movement and stress/strain development predicted by the model, will exactly match that observed quantitatively. The model will however provide a reasonable indication of the behaviour mode of the dam as well as an acceptable envelope within which the observed dam behaviour should remain.

For purposes of this dissertation, the FE model was formulated to model the staged structural response of the dam at various reservoir impoundment levels, in accordance with the stages of the dam impoundment plan. The anticipated behaviour at each impoundment stage was then compared to that observed on site, and if necessary the model was calibrated according to observed behaviour.

The model was devised to incorporate staged hydrostatic and temperature loadings of the dam, at various time intervals during the period of impoundment. These time intervals correspond to the planned stages of temporary impoundment stoppage and behaviour monitoring. The loadings assumed for the analysis were derived according to actual loading conditions rather than design loading conditions.

The model was created with a relatively fine mesh, especially in the vicinity of installed dam instrumentation, to ensure modelled dam behaviour can be extracted at nodal or elemental locations coincident with the instrument location and to capture localised large strain gradients.

The ultimate objective in terms of the FE analysis, was to create a FE model of the dam and foundation assuming linear elastic material parameters for continuum mesh bodies, to predict its behaviour during reservoir impoundment and compare this to the dam behaviour measured on site. The predicted and observed behaviour of the dam were compared, and suitable conclusions were made according to the findings.

4.2 FINITE ELEMENT ANALYSIS METHODOLOGY

A geometrical model of the dam and foundation was created in AutoCAD. The geometry was then imported into Midas FEA NX and discretised to form a FE mesh structure suitable for analysis. Applicable linear elastic material models were defined and assigned to the relevant mesh bodies of the FE model.

Load functions were derived for the actual and observed loadings and applied to the FE mesh structure. The mesh structure was then constrained accordingly against translation at the outer boundaries of the foundation. A construction stage analysis case was set up according to the various reservoir impoundment stages, and the analysis solver tool was run.

Various verification and validation checks were carried out on preliminary analysis runs as a troubleshooting exercise to ensure that the analysis inputs were correctly applied, and that the outputs were reliable and meaningful in terms of the assumptions made.

4.3 GEOMETRICAL MODELLING OF DAM AND FOUNDATION

The Yusufeli dam and foundation were modelled as three-dimensional solid bodies using AutoCAD 3D, for subsequent discretization into three-dimensional solid elements, to create the FE model structure. The three-dimensional geometry of the dam arch structure was modelled according to the mathematical formulation of the various arch elements, and the associated arc defining conic functions.

Conic functions are particularly suitable for modelling the curvature of arch dams that have complex shapes, to avoid creating sharp geometrical points of discontinuity, which can lead to the computation of fictitious stress/strain concentrations in the FE analysis output. The conic lines pass through control points of the arch definition and their defining functions have continuous first and second order derivatives, ensuring abrupt changes in curvature or form are avoided. An example of an arch structure solid modelled in CAD, depicting the various curvature defining elliptical arches and cantilever sections is shown in Figure 4-1.

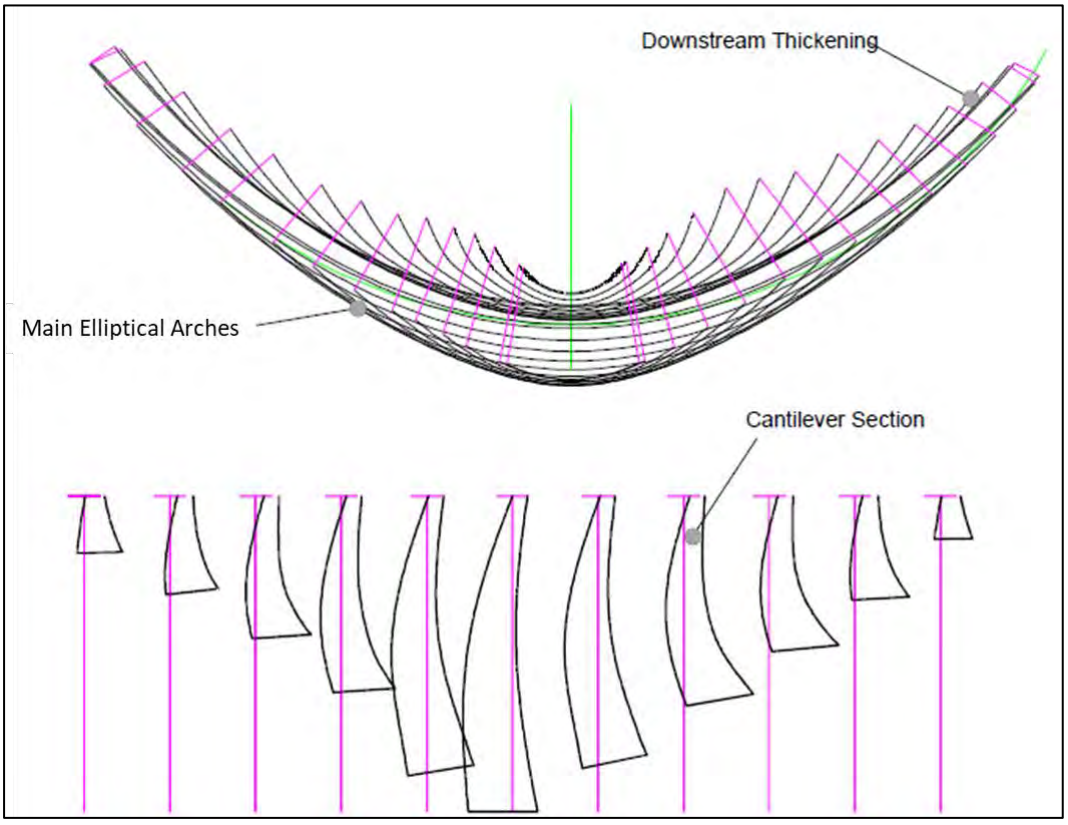

Figure 4-1: Three-dimensional CAD modelling of an arch dam solid according to the interaction between curvature arcs and profile defining points

An AutoCAD view of the various arch defining conic section arcs (ellipses, parabolas and circles) used to define the dam arch body configuration is shown in Figure 4-2. It can be seen that the radius of the arcs decrease with drop in elevation level moving from crest to base, providing for higher arch curvature towards the lower dam portions.

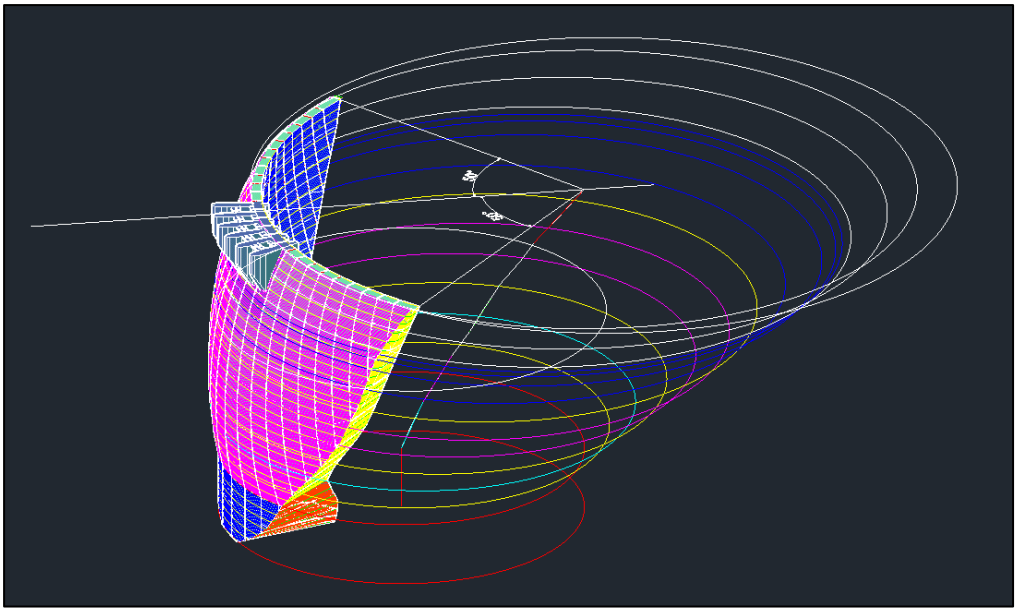

Figure 4-2: Yusufeli dam body showing the arch defining conic section arcs

The Yusufeli dam model was further refined by dividing the arch solid up into the various monoliths and concrete lift heights, in accordance with the arch design and construction strategy. The dam body has 29 monoliths with an approximate contraction joint spacing of 20 m along the dam axis at crest level.

Arch dams are large structures for which concrete casting is done by placement of individual blocks, creating contraction joints between the block. The joints are necessary for ease of construction and provide some flexibility in the structure. The joints relieve stress that may develop in the dam due to various loading responses, particularly thermally induced movements and autogenous concrete shrinkage. Contraction joints are normally grouted closed after cooling of the dam, when it is at the coldest global temperature state, to ensure a monolithic behaviour between monoliths. Figure 4-3 shows the development of an arch solid body from geometry defining arcs and polylines.

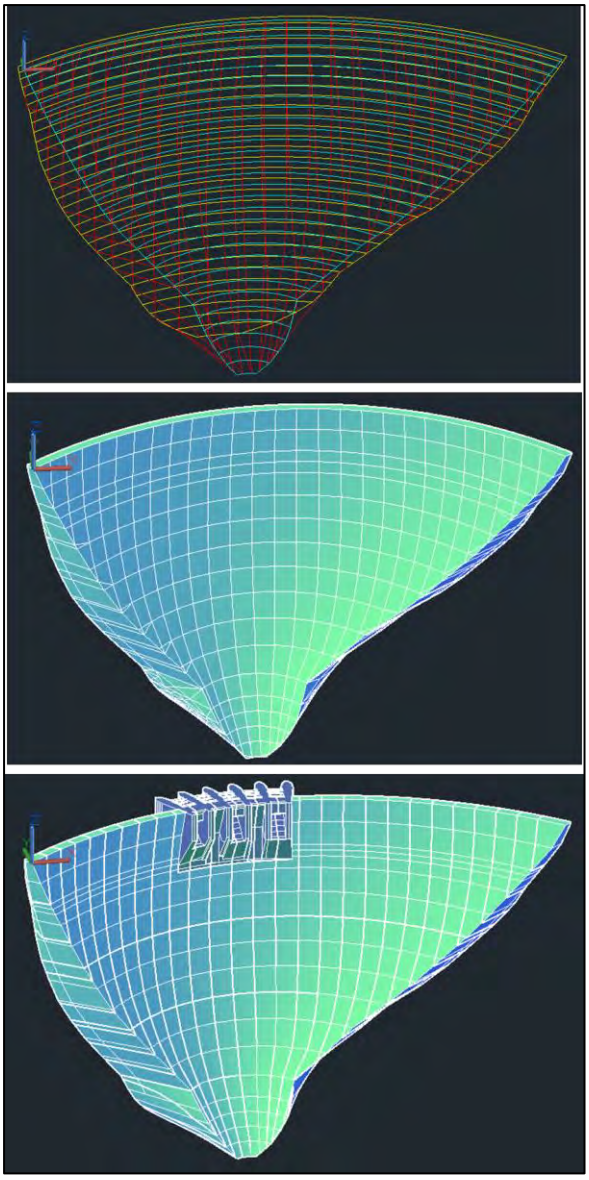

Figure 4-3: AutoCAD solid body model of Yusufeli Dam showing various arch elements and monolith joints

The dam foundation model was also created in AutoCAD as a solid body. The geotechnical model of the foundation rock mass, as derived from extensive geological/geotechnical investigations on site, was used to create the foundation solid with varying interacting rock mass formations. The foundation model rock formation zones were created by slicing up a block according to interface defining horizontal and vertical surfaces. The final geometry model of the dam and foundation is shown in Figure 4-4.

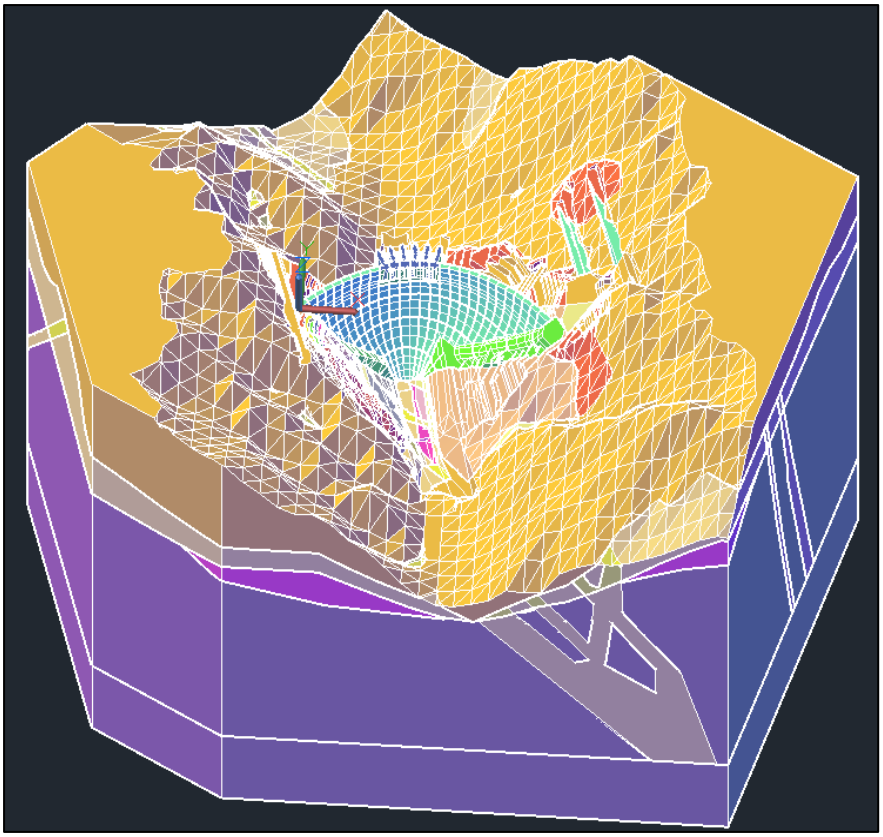

Figure 4-4: AutoCAD perspective view of Yusufeli dam and foundation solid geometry

4.4 DISCRETISATION OF DAM MODEL

The FE model of the dam was created using the Midas FEA NX software. The dam and foundation were modelled as a continuum mesh body discretised with a hybrid of hexahedral, tetrahedral, pyramid and wedge 3D solid elements. The model is hexahedral dominant with other elements only used in the vicinity of sharp edges and faces. The dam and foundation FE model are shown in Figure 4-5 and comprises 330 000 nodes and 786 000 elements.

The very complex FE model shows implementation of a sound meshing strategy with high resolution of elements within the dam body and the grouted foundation zone in close proximity of dam body and low-resolution elements on the outer extents of the foundation. This ensures the model will provide good quality analysis results whilst also being computationally efficient in terms of analysis time.

There is a smooth transition in mesh size from the dam to the outer foundation model extents. The elements within the dam body and grouted foundation zones have regular element sizes with good aspect ratios. This is the zone where large strain gradients were expected to develop. Large element sizes, with less emphasis on good aspect ratio were used to model the outer extents of the foundation model, where small strain gradients were expected.

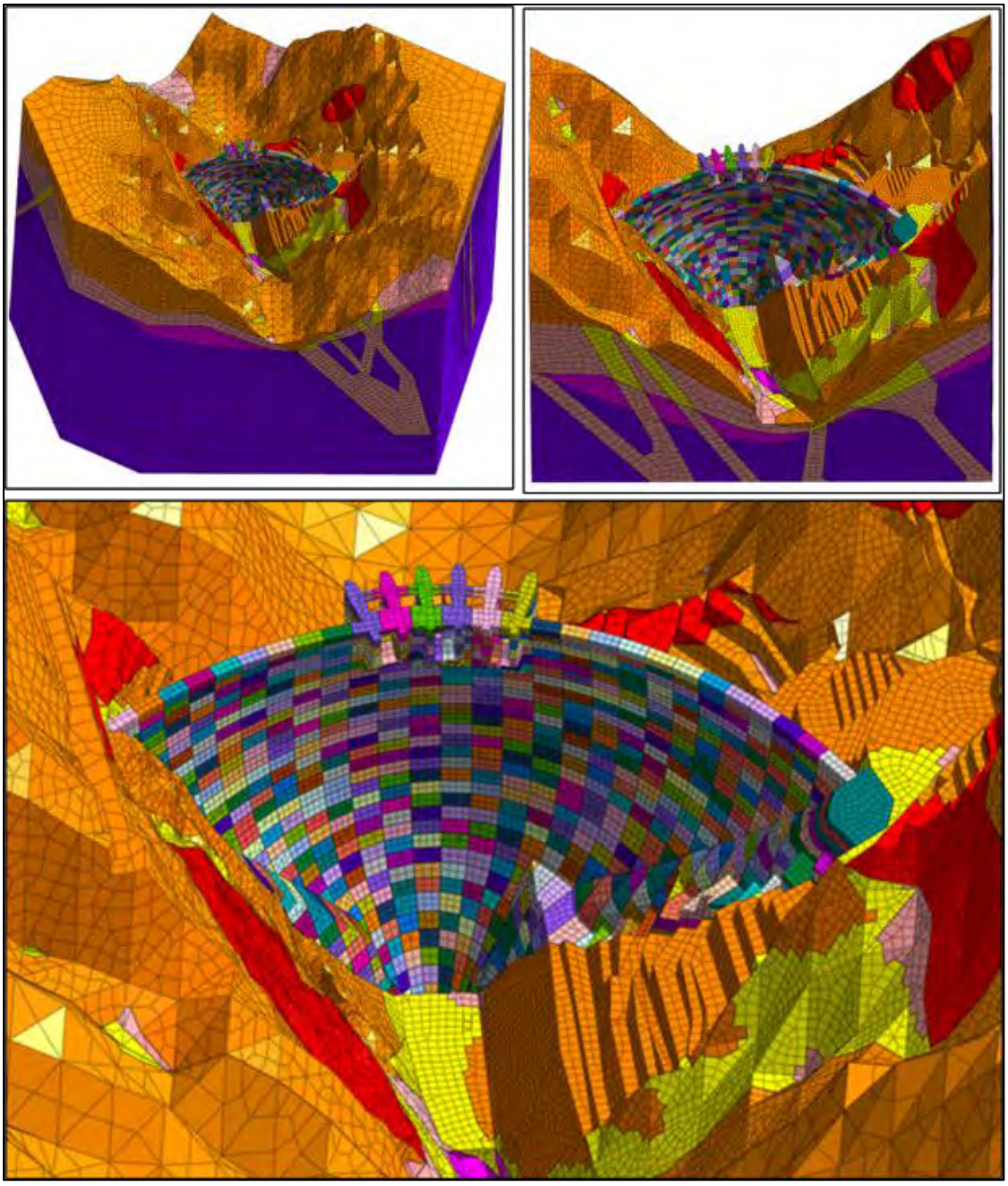

Figure 4-5: Yusufeli dam and foundation FE model as developed in midas FEA NX

A high-resolution mesh density allowed for modelling of the various construction lifts and monoliths of the dam as separate mesh bodies. This enabled a replication of the progressive construction stage activation of the dam model lifts in the analysis, according to the time-based construction sequence that was undertaken.

This high-resolution mesh was necessary to accurately model the incremental movement of the dam body under stepwise hydrostatic and temperature loadings experienced during impoundment of the reservoir.

The lower limit of the foundation continuum model extends to a depth twice the dam height below the lowest dam foundation. The horizontal outer limits of the foundation model extend to 1.5 times the dam height from the upper left abutment, upper right abutments and the most upstream face of the centre arch (Federal Energy Regulatory Commission, 1999).

Additional perspective views of the dam and foundation mesh for the FE model are shown in Appendix D.

4.5 BOUNDARY CONDITIONS

A local rectangular coordinate system was assigned to the dam FE model in which the x-axis was aligned to the cross-stream direction sense, the y-axis to the in-stream direction, and the z-axis aligned to the vertical direction (positive upwards).

The outer extents of the foundation model were constrained against translation accordingly, with the bottom face constrained against translation in all three directions of the cartesian plane, X, Y and Z. The side faces of the foundation mesh were constrained against horizontal translation. A local coordinate system was assigned to the dam in which the x-axis was aligned in the cross-stream direction sense, the y-axis to the instream direction and the z-axis aligned to the vertical direction (positive upwards).

A radial coordinate system was also assigned with the x-axis being aligned to radius of the arch, the y-axis being tangent to the arch and the z-axis aligned to the vertical.

4.6 MATERIAL MODEL ASSUMPTIONS

The dam concrete and foundation rock mass material were modelled assuming linear elastic constitutive material parameters. As indicated in the literature study of Chapter 2, an assumed linear elastic stress-strain response of concrete and foundation material is suitable when the loaded material develops a stress-strain state adequately below the yield point. This is assumed to be the case for a concrete arch dam progressively loaded during impoundment to the full supply level conditions, which is a normal loading condition.

The assumed material parameters of the dam concrete were obtained from laboratory testing of specimens cast and cured in the on-site laboratory under similar conditions to the dam. The structural analysis parameters of the dam concrete are shown in Table 4-1, and are based on the sustained static elastic modulus value of concrete to account for creep action under loading (ACI 207.1R-96, 1996).

Table 4-1: Constitutive material properties of dam concrete applied for analysis

Concrete Type	Unit weight γ (kN/m^3)	Elastic Modulus (GPa)	Poisson ratio ν
Dam Concrete	24.5	21	0.2
Cushion Concrete	23.0	14	0.2

The assumed parameters for the various zones of rock mass material making up the foundation are shown in Table 4-2. These material properties were derived from the results of the geotechnical investigations of the foundation. The rock mass material sets are colour coded to correspond with the mesh colour of the FE model shown in Figure 4-5. The unit weight for the foundation was taken as zero assuming that the foundation has fully settled under its own weight, and any displacement of the dam under gravity is only due to the weight of the dam.

Table 4-2: Constitutive material properties of dam foundation applied for analysis

Material Set	Density γ (kN/m^3)	E Modulus (GPa)	Poisson ratio ν
P5	0	2.0	0.45
P4	0	3.5	0.43
P3	0	6.0	0.35
P2	0	8.5	0.30
P1	0	11.0	0.29
P0	0	13.0	0.27

The assumed thermal and thermo-mechanical parameters of the dam and foundation materials dictate the response of the dam to thermal loading. For purposes of this analysis thermal loading refers to the change in temperature state of the dam body due to cyclic seasonal variations in ambient temperature, to which the dam is exposed, via convection boundaries at the surface of the material. The thermal loading takes the form of heat transfer through a solid medium by conductance and between the solid and the fluid environment (atmosphere and water reservoir) through convection.

The thermomechanical response of the dam refers to the displacement of the dam and development of internal stress/strains of the material, when the temperature state of the dam changes as a result of transfer of heat within the dam body and between it and the ambient surroundings.

The thermal and thermomechanical properties of the dam and foundation were assumed to be very similar, as the concrete aggregate was sourced from the local rock material. In the absence

of tested values, the thermal properties assumed for the dam and foundation were estimated as average values for similar granitic materials as taken from the publication "Thermal Stresses and Temperature Control of Mass Concrete" by Zhu Bofang (Bofang, 2014). The thermal and thermomechanical properties assumed for the analysis are shown in Table 4-3.

Table 4-3: Assumed thermal properties of dam concrete and foundation rock mass

Parameter	Dam and Cushion Concrete	Foundation Rock Mass
Specific Heat Capacity c (kJ/(kg.˚C))	0.97	0.93
Thermal Conductivity λ (kJ/(m.hr.˚C))	9.4	9.4
Density ρ (kg/m^3)	2400	2500
Convection Coefficient air β_a (kJ/(m^2.hr.˚C))	56	56
Convection Coefficient water β_w (kJ/(m^2.hr.˚C))	92	92
Coefficient of thermal expansion α (1/ ˚C)	10. 10^{-6}	10. 10^{-6}

Specific heat capacity is defined as the amount of heat required to raise the temperature of a unit mass of material by 1°C with SI units J/kg.°C. Specific heat is highly influenced by the water content in the concrete as it has a relatively high specific heat value. Specific heat generally also varies with temperature, but a constant value is deemed acceptable, for the range of temperatures applicable within mass concrete structures such as dams (USACE, 1997).

Thermal conductivity is a measure of the ability of a material to conduct heat and indicates the heat flow through the material under a given temperature gradient. Thermal conductivity can be calculated directly from the product of thermal diffusivity (the rate at which temperature change can occur), specific heat capacity (c) and density (ρ). The thermal conductivity of concrete is governed by the aggregate type, moisture content and porosity of the concrete.

For conducting solids in contact with a fluid, there will be a heat transfer taking place between the solid surface and fluid when a temperature difference occurs, which is influenced by the movement of the fluid and the conditions at the interface. The convection coefficient (heat transfer coefficient) indicates the rate at which heat energy passes (convects) from a solid medium to a fluid. In the case of a concrete dam, this occurs at the surface of the concrete where the air or water reservoir is in contact with it.

The convection coefficient (surface conductance) of the dry surfaces of the dam, is influenced by the roughness of the surface (condition) and the wind speed over it (fluid flow). The average wind speed at Yusufeli Dam is 2.5 m/s. A convection coefficient of 56 kJ/(m^2.hr.˚C) is based on the assumption of a mid-range surface roughness neither smooth nor rough (Bofang, 2014).

The convection coefficient at the concrete water interface was taken as 92 kJ/(m^2.hr.˚C) (Williams, 1963).

The thermal expansion coefficient quantifies the change in a material's dimension in response to a change in temperature of that material. The value describes the linear change in dimension per unit change in temperature. The thermal expansion coefficient induces the displacement response of the dam and associated stress-strain response, as a result of internal and external restraint against the movement.

4.7 ANALYSIS LOADING ASSUMPTIONS

With an analysis attempting to predict the actual structural response of the dam, it is particularly important to apply loadings as close as possible to those to be experienced in reality, and to model both the dam concrete and foundation rock mass as accurately as possible. While silt and seismic loadings were consequently not considered in the analyses undertaken, hydrostatic, earth back fill and uplift loads were applied in parallel with a prediction of the thermal condition of the structure, at the particular date at which each measurement impoundment level will be reached. The predicted thermal state of the structure being the results of a thermal heat transfer analysis, largely influenced by the seasonal temperature change experienced by the dam.

4.7.1 Static Structural Loading

The structural static loading of an arch dam is caused by the impounded water reservoir and the self-weight of the structure. More specifically the static loadings of the Yusufeli Dam defined for structural analysis purposes include the following:

- Gravity
- Upstream hydrostatic
- Downstream hydrostatic
- Uplift
- Upstream backfill lateral earth pressure

The action of these loads in relation to a section of the dam body is shown in Figure 4-6. The hydrostatic and uplift loading correspond to the various reservoir levels attained at the progressive stages of reservoir filling, during impoundment of the dam. The progressive stages and associated applicable loadings are discussed in Section 4.9.

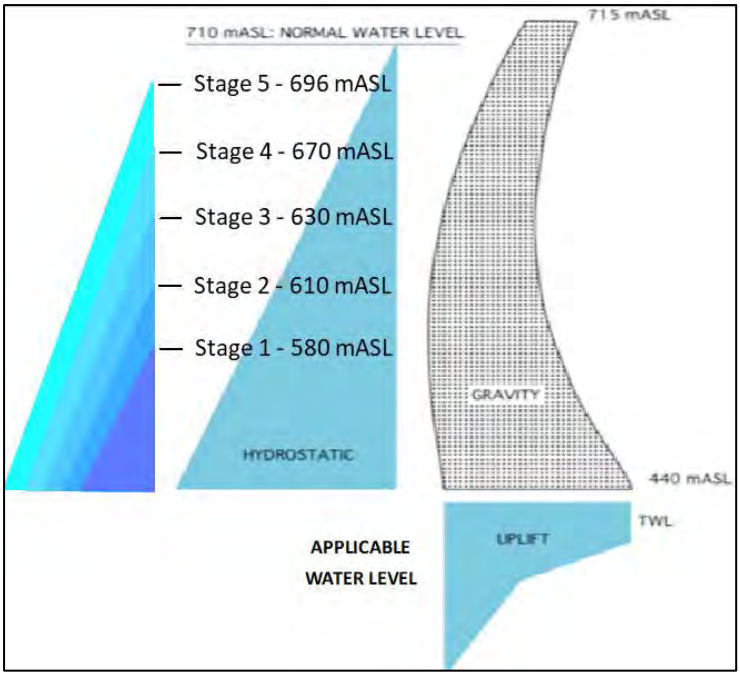

Figure 4-6: Hydrostatic loading of dam according to applicable water level

Gravity loading was modelled as a self-weight of the dam induced by vertical gravitational acceleration of 9.81 m/s^2 applied downwards, in the Z-direction of the model space. The self-weight of the dam was applied to the FE model as a body force acting through the centroid of the structure. This is applied to the FE mesh by apportioning the total free body force to the various nodes, in relation to the centroid and volume of the associated elements.

The upstream and downstream hydrostatic loading were defined as simple hydrostatic pressure loads, applied as a linear function of depth below water surface level as shown in Equation 4-1, according to the applicable reservoir impoundment water level. The pressure loads were applied to the FE mesh as discretised nodal forces imposed at nodal points, in relation to the tributary area of the nodes at the surface of the mesh.

$$p = \gamma_w g h \qquad \textbf{4-1}$$

Where

p = hydrostatic pressure (kPa)

γ_w = density of water (kg/m^3)

g = gravitational acceleration (m/s^3)

h = depth below water level (m)

The design uplift loading normally adopted for a concrete dam according to USACE is shown in Figure 4-7. It is customary to assume a drain efficiency (e) of 0.67, which makes provision for partial blockages or other malfunctioning of the drains. The uplift pressure distribution takes the form of a multi-linear pressure diagram as shown in the figure. The uplift pressure at the heel corresponds to the upstream reservoir level (H_1) and at the toe to the tailwater level (H_2).

Assuming a 67 % drain efficiency, the uplift pressure at the drain is calculated by adding one third of the difference between upstream (U_1) and downstream (U_2) pressure, to the greater of the downstream pressure (U_2) or the hydrostatic pressure of the gallery level (γH_3).

As mentioned, for purposes of this study it is necessary to model loadings as close as possible to the actual loads experienced during impoundment, rather than assuming design loads. It has been shown by Casagrande (1961) that uplift proposed by design literature is conservative, and assuming the drains are well maintained, the actual uplift is lower than design uplift as shown in Figure 4-8. For purposes of this dissertation actual uplift pressures measured by instrumentation on site as presented in Section 5, were adopted for loading of the FE model.

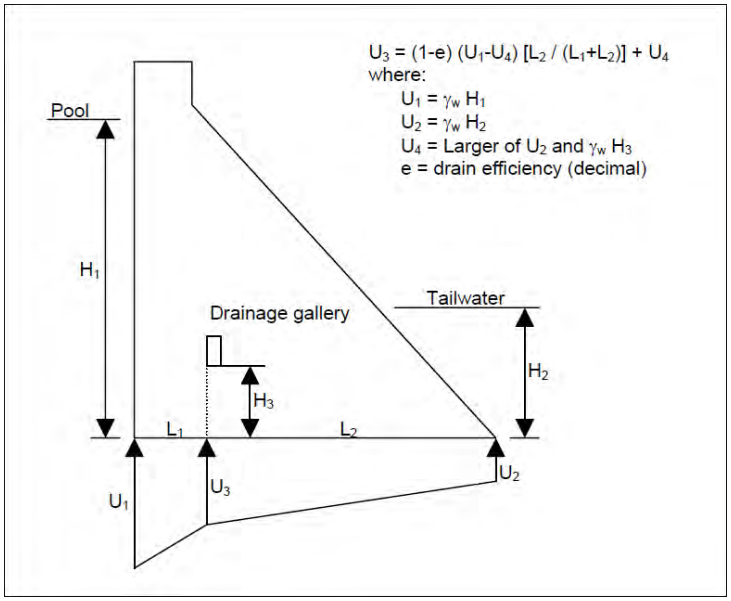

Figure 4-7: Design hydrostatic uplift pressure distribution of a concrete dam (USACE, 2005)

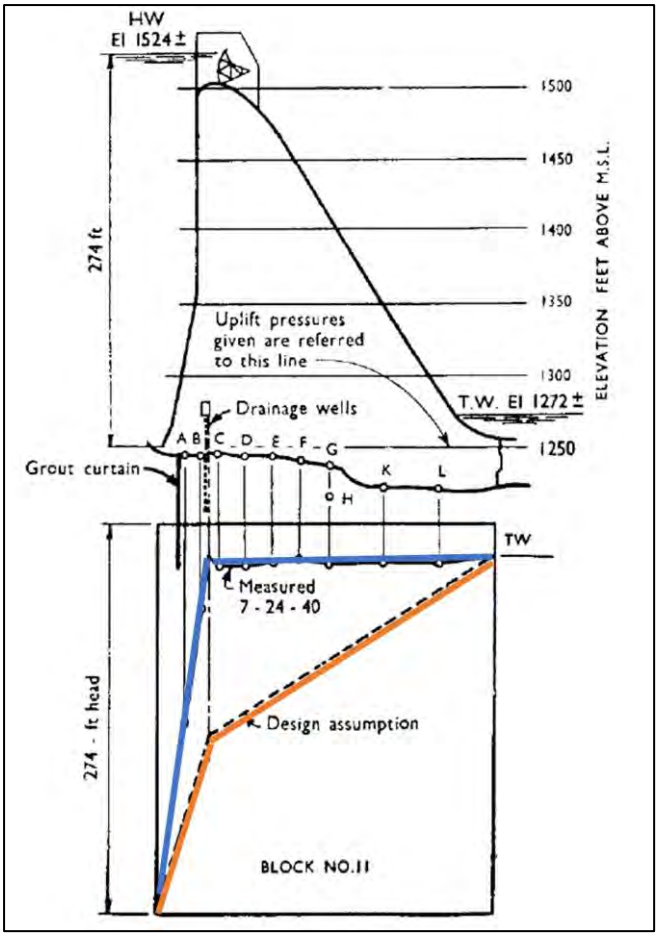

Figure 4-8: Assumed design uplift pressure distribution vs measured uplift (Casagrande, 1961)

Before impoundment, a local back fill material was placed against the lower upstream face of the dam to elevation level 531 mASL. Backfill loading of the dam was modelled as a submerged lateral earth pressure, assuming active earth conditions and adopting a lateral earth coefficient value K_A as per Equation 4-2.

$$K_A = \frac{1 - \sin\varphi}{1 + \sin\varphi} \qquad \textbf{4-2}$$

Where

φ = internal friction angle (°)

The saturated unit weight of the material was taken as 20 kN/m^3 and the effective internal friction angle (φ') as 30 °. This resulted in an active lateral earth pressure coefficient K_A of 0.33.

4.7.2 Thermal Loading

Arch dams are highly affected by temperature loadings in comparison to other dams (Daoudu *et al.*, 1997), with downstream crest displacements under maximum temperature drop loads being of the same order as displacements under maximum hydrostatic loads. The thermal loadings experienced by arch dams are complex and are caused by a variety of time-based heat contact conditions, heat transfer mechanisms and hydration heat generation all imposed on the dam simultaneously.

As a result of comprehensive post-cooling of the dam prior to reservoir filling, concrete hydration heat generated during curing of the concrete is assumed to have fully dissipated at the time of impoundment. This was confirmed by the flattening out of temperature measurement curves obtained from thermistors installed in the dam during casting of concrete. The analysis does therefore not consider heat of hydration as a generated heat source and only considers the operational thermal loading of the dam, driven by the seasonal ambient temperature change conditions experienced on site, during impoundment of the reservoir.

For FE modelling purposes the dam heat transfer problem was approached as a boundary value problem. An initial temperature state of the dam was defined, and seasonal time-varying heat conditions applied to the dam as thermal contact boundary constraints at the outer faces of the dam and foundation. The heat flow problem was then solved using the FE model according to thermodynamic laws, as governed by the various material thermal parameters and boundary constraints.

The dominant cause of operational thermal loading of a dam is the seasonal change in ambient temperature, which transfers into the dam body by various heat transfer mechanisms and changes the internal temperature state of the dam with time. The operational thermal loading conditions and associated heat flow mechanisms experienced by the Yusufeli Dam during impoundment, are shown in Figure 4-9. The changes in internal temperature state of the dam are caused by a combination of the following conditions (Andersson & Seppälä, 2015):

- Convection of heat between the dry faces of the dam and the atmosphere air,
- Convection of heat between the submerged faces of the dam and the water reservoir body,
- Conductance of heat through the dam body solid,
- Conductance of heat between the dam body and foundation,
- Absorption of heat energy at the dam surfaces exposed to solar radiation from the sun,
- Initial temperature state of dam and foundation just prior to impoundment.

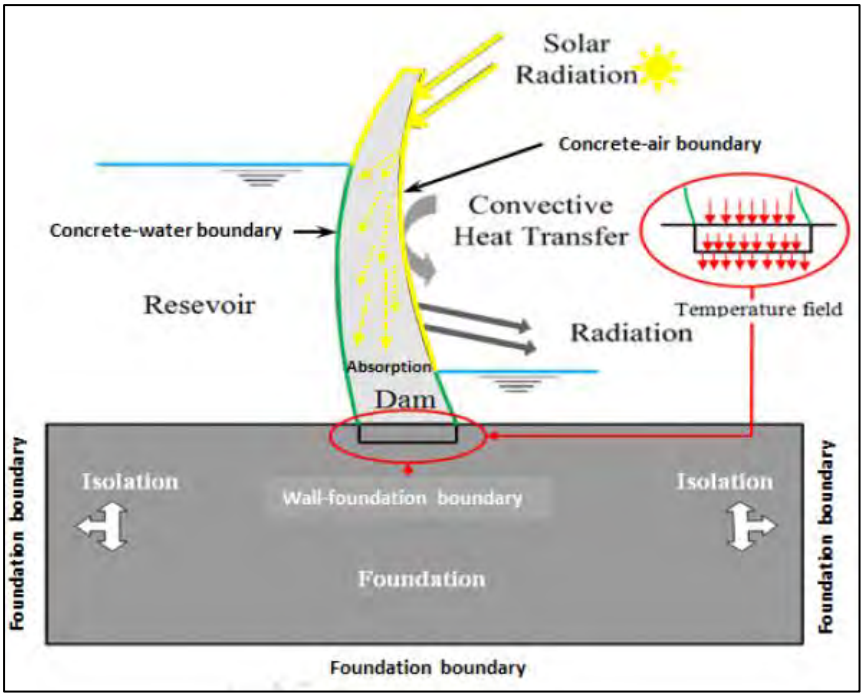

Figure 4-9: Heat transfer loading temperature contact boundary conditions (Nzuza, 2013)

Convective heat transfer between the dam and the surrounding air is a function of the dam temperature state, the ambient air temperature and the convection coefficient (β_a) value as shown in Table 4-3, at the dam-air interface. The convective heat transfer mechanism was incorporated in the dam thermal FE modelling as a time-varying seasonal temperature cycle, applied at the concrete-air boundary faces of the dam in terms of the convection coefficient. The thermodynamic heat transfer FE model simulates the time-based convective heat transfer process at the dam-air interface, in terms of the thermal gradient and convection coefficient at the interface.

For the Yusufeli Dam, the measured ambient temperature on site was used as the temperature variation data for temperature loading. Two thermometer stations were installed on the dam site, of which one is located on the south facing riverbank and the other on the north facing bank. The ambient temperature cycle measured on the north facing slope was measured by device T02 and is shown in Figure 4-10, and that of the south facing slope was measured by device T06 as shown in Figure 4-11. The time-history seasonal temperature variations follow a sinusoidal cycle typical of seasonal temperature data. The dam is exposed to extreme seasonal temperature conditions with a summer maximum of approximately 35° C and a winter minimum of -3° C. The annual mean ambient temperature is shown to be 16 ° C.

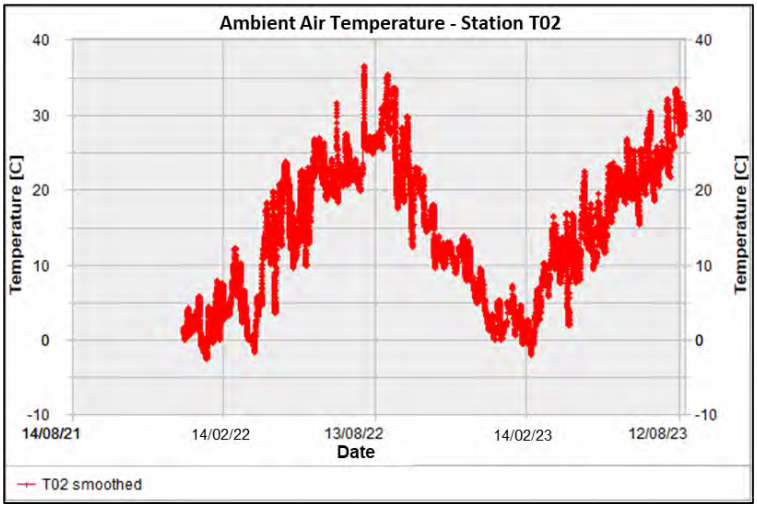

Figure 4-10: Ambient temperature cycle of Yusufeli Dam site measured on north facing river slope by T02

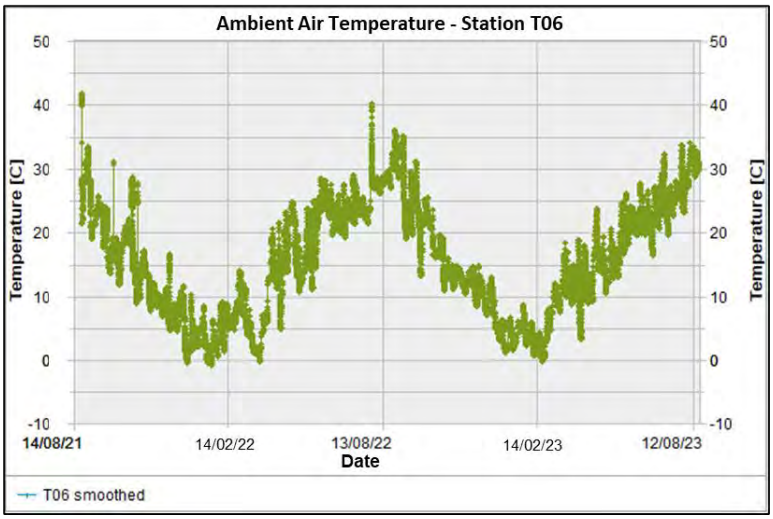

Figure 4-11: Ambient temperature cycle of Yusufeli Dam site measured on south facing river slope by T06

The impact of solar radiation on the temperatures measured by the north and south facing thermometers is evident when comparing the two temperature readings. The daily average temperatures measured on the south facing slope (T06), are 3° C warmer than the north facing slope (T02) in Summer and 1° C warmer in Winter.

The dam is located in the northern hemisphere with GPS coordinates of 40°49'0" N and 41°38'45" E. The dam is orientated with its x-axis (cross-stream direction) aligned at approximately 29° from the northing line (red line) towards the west (anti-clockwise) as shown in Figure 4-12. The orientation of the dam relative to the sun means that the left flank is exposed to solar radiation, whilst the right flank is mostly in the shade as can be seen in the Google Earth image of the dam shown in Figure 4-12.

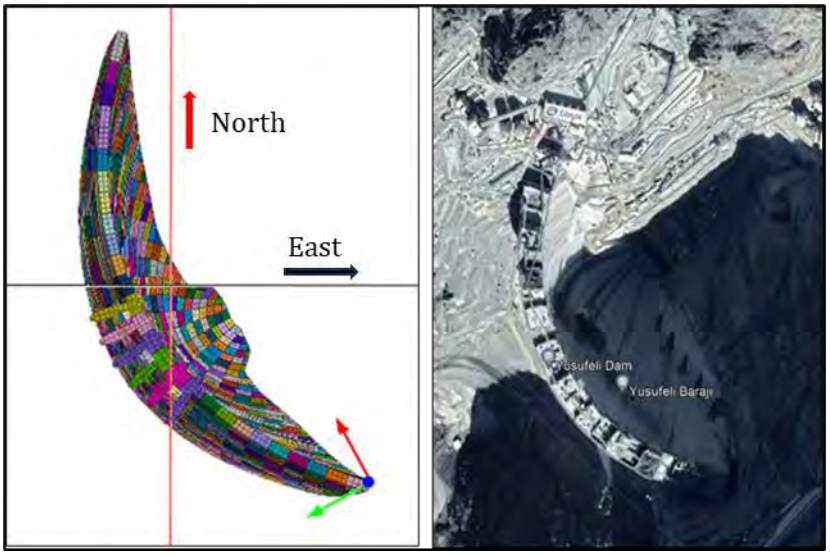

Figure 4-12: Orientation of dam relative to northing line (left) and relative to sunlight (right)

The incorporation of heat absorption from solar radiation, in the thermal analysis of concrete arch dams, is a complex process requiring thermal input assumptions for which actual values are not easily attainable.

The solar radiation has an impact on the ambient air temperature and on the surface temperature of the dam exposed to sunlight (Daoudu *et al.*, 1997). For Yusufeli Dam, the impact of solar radiation on temperature was implicitly accounted for in the temperature readings taken at the foundation surface in both the sun and shade.

In cases where measured ambient temperature data as influenced by solar radiation is not available, the increase in the surface temperature of a concrete dam due to solar radiation energy can be derived from Equation 4-3 (Bofang, 2014). The solar radiation experienced on a concrete surface is influenced by the latitude of the site in relation to the earth equator, the time of the year and the angle of the normal to the dam surface, in relation to the direction towards the sun and to the vertical. For locations in the northern hemisphere the sun direction is always taken as towards the South and vice versa for locations in the southern hemisphere.

$$\Delta T_s = \frac{\alpha_s S}{\beta_a} \qquad \textbf{4-3}$$

Where

α_s = coefficient of absorption of concrete = 0.65

S = annual mean solar radiation (kJ/(m^2.hr))

β_a = coefficient of convection at air-concrete interface (kJ/(m^2.hr.˚C))

In the absence of actual solar radiation measurements on site, the increase in temperature of the dam surface due to solar radiation, is estimated using empirical graphs derived by the United States Bureau of Reclamation. These graphs were formulated based on observations of various concrete dams in the USA. An example of such a graph as re-reproduced by Bofang (2014) for dams located within a latitude range of 40 – 45° is shown in Figure 4-13.

The orientation of the Yusufeli Dam body, in relation to the direction of the sun, is such that an angular rotation of approximately 80° exists between the northing and a normal to the dam surface midspan along the left flank, as shown on the left image in Figure 4-14. The slope of the upstream and downstream face of the dam, is such that the average angle formed between a line tangent to the upstream and downstream face of the dam, and the vertical is approximately 5° as can be seen on the right image of Figure 4-14.

Application of the dam body alignment angles as φ and ψ for the empirical derivation of the solar radiation temperature increase, is indicated in Figure 4-13 at the intersection of the horizontal and vertical red lines. The derived annual temperature rise is shown to be 3° C, which is very close to the average temperature difference of 2° C between readings measured on site by thermometers T02 placed in the shade and T06 in the sun.

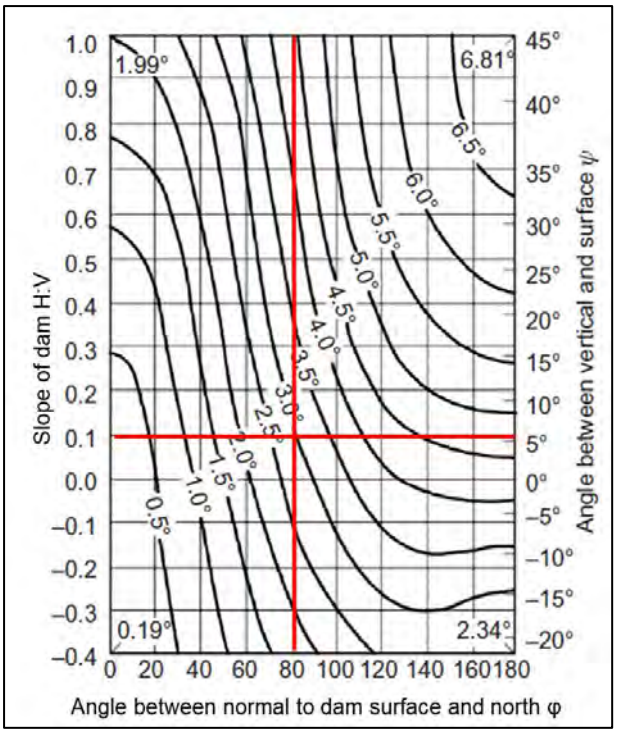

Figure 4-13: Increase in annual temperature due to solar radiation from sunshine

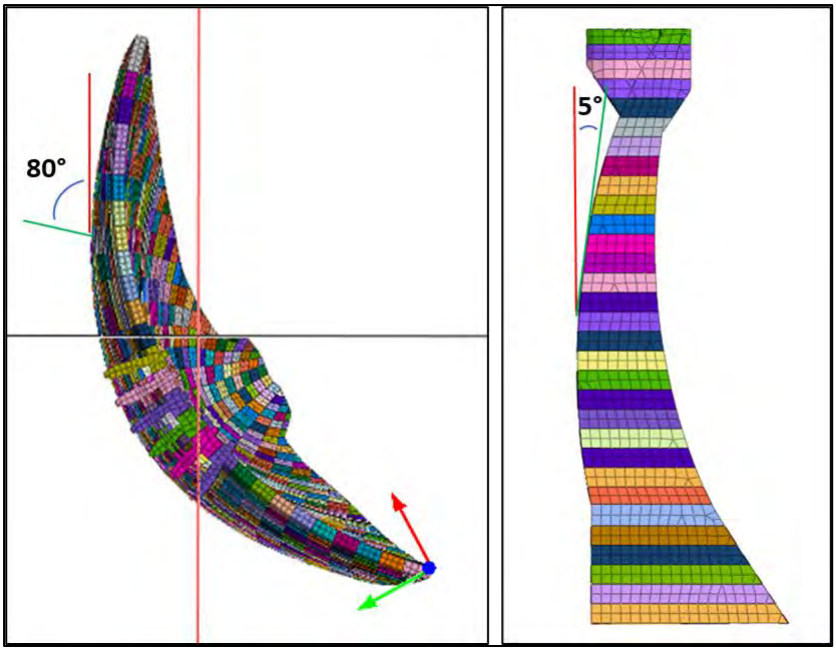

Figure 4-14: Angle between normal to left flank dam surface and northing line (left) and between dam surface and vertical (right)

The wind speed in the Yusufeli region was referenced from "world weather online" website (www.worldweatheronline.com/yusufeli-weather-averages/artvin/tr.aspx), and the typical seasonal distributions are illustrated in Figure 4-15. An average wind speed of 2.5 m/s was considered when establishing the surface convection coefficient (β_a) for the dam structure and the foundation (Bofang, 2014). The green line in Figure 4-15 confirms that the average wind speed is relatively constant year-round, and that a constant value of 2.5 m/s is a reasonable approximation.

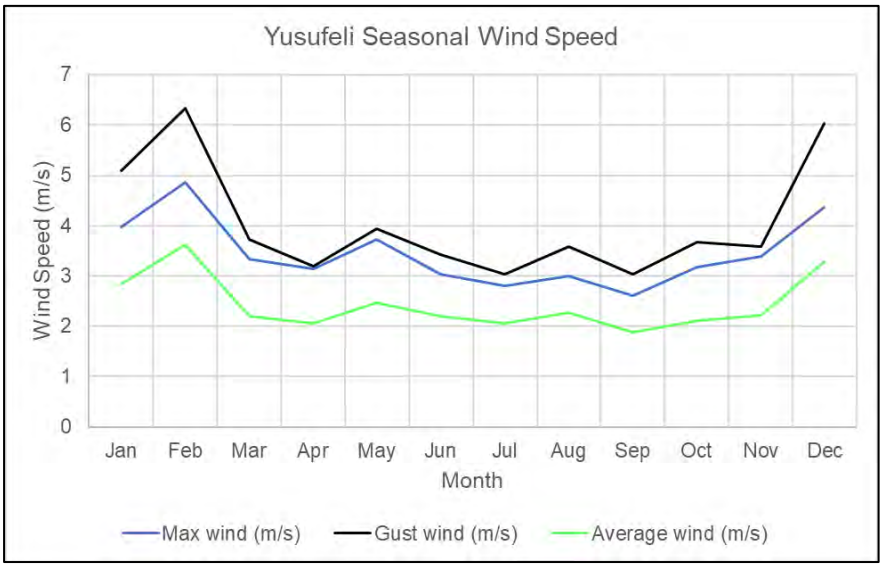

Figure 4-15: Seasonal wind speed in the Yusufeli region

The convective heat transfer mechanism between the submerged dam surface and the water reservoir was modelled as a convective boundary condition in the FE model. The convective heat transfer at the dam-reservoir interface is a function of the reservoir temperature, the dam body temperature, and the convection coefficient (β_w) at the concrete-reservoir interface.

Water has a relatively high specific heat capacity of 4.2 kJ/(kg.˚C). As a result, the temperature state of a large water body contained by a dam, takes longer to respond to seasonal temperature variations when compared to the almost instantaneous response of the ambient air temperature.

The time-based seasonal temperature variation curve of water lags the temperature curve of the ambient air temperature, meaning that the maximum and minimum temperature peaks of the sinusoidal curve for water occur later than peaks observed in ambient temperature. The extent of the lag of the water temperature variation increases with depth below the water surface, whilst the amplitude of the sinusoidal temperature cycle decreases. The lag is defined as the angular phase difference of the sinusoidal temperature variation curves.

Effectively the temperature state of the dam reservoir near the surface is more sensitive to the seasonal ambient temperature change, than the water near the bottom, which is insensitive to seasonal temperature changes and maintains a relatively constant temperature. The amplitude of the sinusoidal temperature variation curve of water near the bottom of the reservoir is very low compared to that at the surface.

The temperature state of the water reservoir is a function of time and depth below the water surface, and if measured reservoir temperature data for the dam does not exist, it can be modelled using Equation 4-4. The empirical equation was derived from observations of water reservoir temperature conditions at various concrete dams in China and the USA (Bofang, 1997).

$$T(y,\tau) = T_m(y) + A(y)\cos\omega(\tau - \tau_0 - \varepsilon) \qquad \textbf{4-4}$$

Where

y = depth below water surface (m)

τ = time (months)

τ_0 = time of peak maximum air temperature = 6.5 months

T(y, τ) = water temperature at depth y and time τ (˚C)

T_m(y) = yearly mean temperature at depth y (˚C)

A(y) = amplitude of annual variation of water temperature at depth y (˚C)

ε = phase difference of annual variation of water temperature and air temperature (months)

ω = circular frequency of temperature variation = 2π/P

P = period of temperature variation = 12 months

For northern hemisphere locations the peak summer month is taken as 6.5 and for southern hemisphere it is assumed as 0.5. All the variables for the water temperature modelling equation can be derived from a single annual air temperature variation cycle of the dam site. $T_m(y)$ is calculated from Equation 4-5 through Equation 4-7, where variables T_s and T_b can be obtained from Equation 4-8 and Equation 4-9. A(y) and ε can be calculated from Equation 4-10 through Equation 4-12.

$$T_m(y) = c + (T_s - c)e^{-0.04H_r} \quad \textbf{4-5}$$

$$c = \frac{(T_b - gT_s)}{(1-g)} \quad \textbf{4-6}$$

$$g = e^{-0.04H_r} \quad \textbf{4-7}$$

Where

T_s = yearly mean water temperature at the surface of reservoir (˚C)

T_b = yearly mean water temperature at the bottom of reservoir (˚C)

H_r = total depth of reservoir (m)

$$T_s = T_a + \Delta b \quad \textbf{4-8}$$

$$T_b = \frac{(T_1 + T_2 + T_{12})}{3} \quad \textbf{4-9}$$

Where

T_a = yearly mean air temperature (˚C)

Δb = temperature increment due to solar radiation = 2 to 4˚ C

T_1, T_2, T_{12} = monthly mean temperature in January, February and December (˚C)

$$A(y) = A_0 e^{-0.018y} \quad \textbf{4-10}$$

$$A_0 = \frac{(T_7 - T_1)}{2} \quad \textbf{4-11}$$

$$\varepsilon = 2.15 - 1.30e^{-0.085y} \quad \textbf{4-12}$$

Where

A_0 = amplitude of annual variation of water temperature at water surface (˚C)

y = depth below water surface (m)

T_7 = maximum monthly mean temperature in July for northern hemisphere (˚C)

T_1 = minimum monthly mean temperature in January for northern hemisphere (˚C)

ε = phase difference of annual variation of water temperature with surface temperature (months)

Sufficient actual time-based temperature measurement data of the water reservoir, with change in depth below water surface, was not available for Yusufeli Dam. The time-based temperature state of the dam water reservoir, at various depths below reservoir surface, was modelled using the abovementioned empirical equations and is shown in Figure 4-16. The various sinusoidal curves of the graph depict the seasonal temperature variation cycles at different reservoir depths. The time-based temperature depth profile was incorporated in the dam FE model as a convective boundary for heat transfer between the dam and reservoir bodies.

The plotted curves show that according to the modelled reservoir temperature profile, the water at the surface is expected to reach a maximum of 30 ˚C in August and a minimum of 2 ˚C in February. The temperature of the water at the bottom 100 m of reservoir depth will not vary much with time and stay relatively constant at approximately 7 ˚C, meaning that during Winter the bottom half of the reservoir has a higher temperature than the top half of the reservoir and the air above it. The average temperature variation of the reservoir is indicated by the black curve in Figure 4-16. The profile of modelled water reservoir temperature vs depth for Yusufeli Dam, is indicated for each month of the year as a separate curve in Figure 4-17. The graph depicts how the seasonal temperature variation is large near the surface of the dam reservoir, and reduces to almost zero towards the bottom of the reservoir.

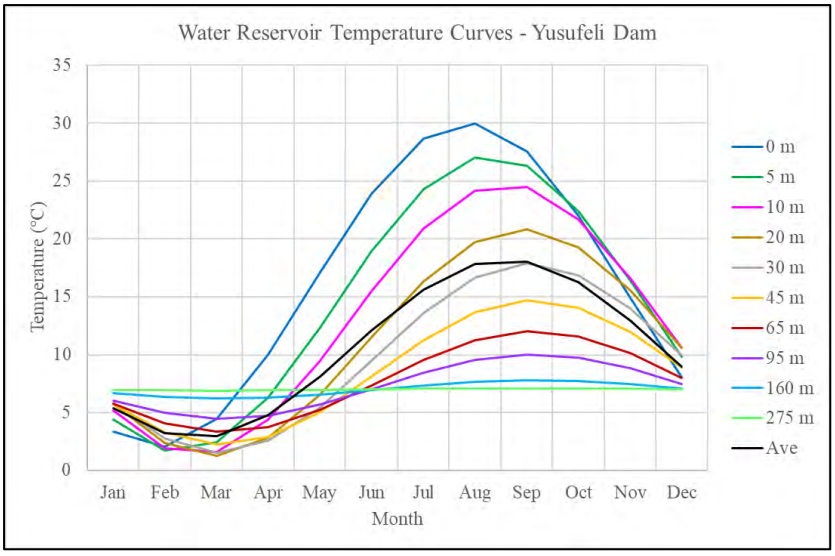

Figure 4-16: Yusufeli Dam water reservoir temperature curves

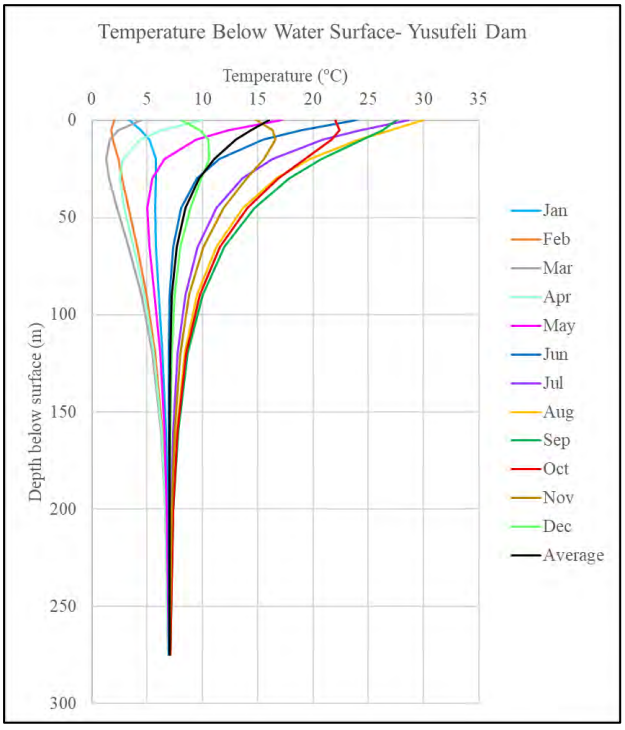

Figure 4-17: Yusufelli Dam monthly reservoir temperature depth profiles

The convective boundary loading conditions for the dam foundation were implemented in the FE model similarly to the method they were adopted for the dam body.

The initial temperature state of the dam, for purposes of the FE modelling of the operational temperature state of the dam during impoundment, was obtained from the actual temperature state of the dam as measured on site. Comprehensive temperature measurements were taken of the dam body, by thermistors installed at every 3 m concrete lift to monitor the effect of post-

cooling of the concrete during construction. The temperatures were taken at the core of the dam where the heat of hydration would be greatest.

Construction of the dam was completed on 7 July 2021, after which pipe cooling continued until 21 August 2021, when thermistor readings indicated that the generated heat of hydration of the concrete had fully dissipated. At this stage the comprehensive temperature measurement of the dam was discontinued, and only selective temperature measurements were taken post-construction cooling from thermocouples installed in the dam.

The initial temperature state of the dam at commencement of impoundment, on 22 November 2022, was modelled by running a thermal heat transfer analysis from 21 August 2021 to 22 November 2022, from which the output temperature state of the dam was used as the input of initial temperature state at commencement of impoundment on 22 November 2022.

For analysis purposes, the measured temperature state of the dam on 21 August 2021 was applied to the FE model as an initial nodal temperature state. This was achieved by application of VBA code run in Excel, to assign a temperature value to each node of the dam body FE mesh, in accordance to its spatial location in relation to the thermistor device reporting the temperature reading. The nodal temperature result of the pre-impoundment thermal analysis was extracted as a nodal temperature state for input into the impoundment thermal analysis.

The temperature state of the dam on 22 November 2022 at commencement of reservoir impoundment is shown in Figure 4-18 and is defined as T_0 for analysis purposes. This initial temperature state was taken as the starting nodal temperature of the dam for the various thermal analyses undertaken to derive the temperature state of the dam for each stage of reservoir impoundment considered in the dissertation study.

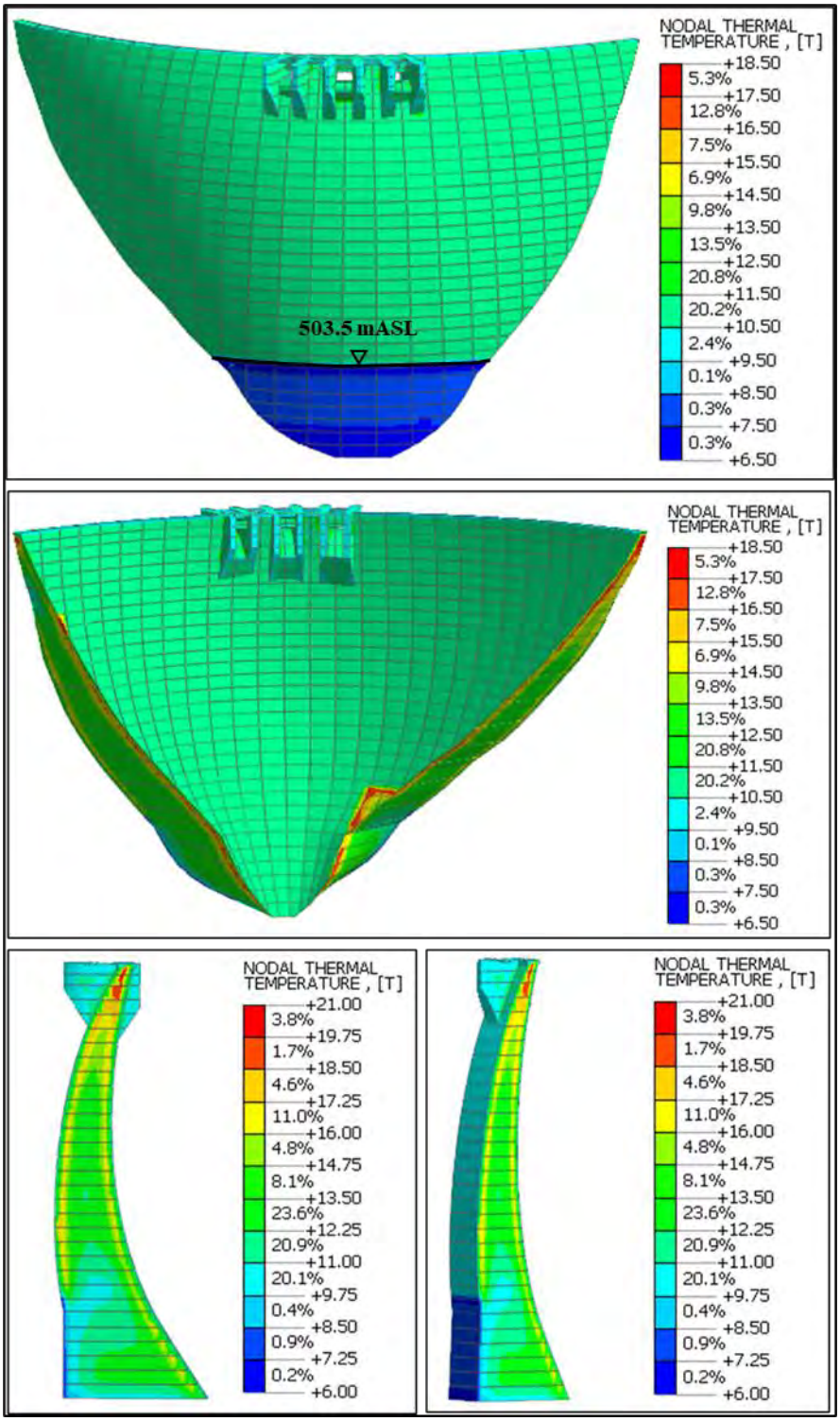

Figure 4-18: Temperature state of dam on 22 November 2022 (T_0), at reservoir level 503.5 mASL (average temperature state = 13.3 °C)

4.8 THERMOMECHANICAL LOADING

Thermomechanical loading refers to the structural loading of the dam in response to changes in the thermal state of the dam. The thermomechanical loading of Yusufeli Dam is a direct result of the change in the temperature state of the dam, from commencement of impoundment to each applicable stage of dam behaviour evaluation during impoundment. During the impoundment of the dam, the temperature state of the dam will drop in winter and rise in summer. The temperature drop of the dam will cause it to lean forward as the arch span shortens whilst the temperature rise will cause it to lean back.

The thermomechanical loading of the dam in the FE model was applied as a nodal temperature change of the dam, reflecting the change in temperature from the date of impoundment commencement (22 November 2022) to the relative date of impoundment evaluation.

4.9 STAGED CONSTRUCTION ANALYSIS

A comprehensive evaluation of the dam behaviour was undertaken at each stage of the dam reservoir impoundment, for which reservoir filling was temporary stopped and then re-started if the dam behaviour was deemed to be safe.

The analysis case of the dam-foundation FE model was set up adopting a staged construction approach, whereby each stage of the dam impoundment study was modelled according to the applicable loading conditions experienced at such stage. The assumed loading conditions for each stage of the analysis are shown in Table 4-4 where the relevant upstream (US) and downstream (DS) reservoir level, backfill loading, uplift loading and temperature change for each stage is provided. It is noted that gravity loading was applied only to analysis stage 0. Stage 0 is effectively the reference stage of the analysis for comparison of succeeding stages.

Table 4-4: Analysis construction stages adopted in FE model

Analysis Stage	Date	Gravity	US level (mASL)	DS level (mASL)	Backfill (mASL)	Uplift	Temp Change
0	2022-11-22	Yes	503.5	440	531	Measured	N/A
1	2023-02-13	N/A	580	500.5	531	Measured	$T_{580} - T_0$
2	2023-04-08	N/A	610	500.5	531	Measured	$T_{610} - T_0$
3	2023-04-29	N/A	630	500.5	531	Measured	$T_{630} - T_0$
4	2023-06-10	N/A	670	500.5	531	Measured	$T_{670} - T_0$
5	2023-08-18	N/A	696	500.5	531	Measured	$T_{690} - T_0$

4.10 SPECIAL MODEL FEATURES

The FE analysis studies of the Yusufeli Dam, under staged dam impoundment loading was done assuming linear elastic material parameters of the dam and foundation. According to this assumption the three-dimensional FE continuum solid structure was assigned isotropic linear elastic material properties.

As indicated in the literature study, this assumption has been shown to be true for the stress-strain response of the dam and foundation solid under normal static loading conditions, except for non-linear behaviour occurring at the interface between the dam and foundation. At this interface there is a definite plane of weakness that exists due to the physical joint between dam concrete and foundation rock. As a result of the low tensile strength of the dam-foundation joint, the tensile stress that develops at the heel of the dam, under normal static loading, may progress beyond the linear elastic portion of the tensile stress-strain response of the joint. Similarly tensile yielding may occur at the low tensile capacity joints between dam monoliths.

As a result, the low tensile capacity of joints at the dam-foundation contact and between dam monoliths, were modelled in Midas FEA NX using interface elements with a bi-linear penalty stiffness material model.

The interface elements allow for redistribution of computed tensile stresses if the tensile yield strength of the dam-foundation interface is surpassed, effectively allowing an elastic, perfectly plastic hinge to form.

The normal stiffness response of the interface elements modelled at the dam-foundation interface is shown in Figure 4-19. The normal stiffness of the interface elements essentially represent the relationship between the tensile stress normal to the interface and the relating displacement occurring at the interface. The normal stiffness of the interface element can be likened to the axial stiffness of a spring, except that it acts across the infinitesimal joint interface over a unit of area. It can be seen from the plot that the normal stiffness across the joint effectively reduces to zero after the tensile capacity is reached.

The assumed tensile strength ($f_{t,j}$) of the dam-foundation interface joint was taken as 600 kPa. According to Wieland (2005), the uniaxial tensile strength of mass concrete at joint interfaces of dams is less than 5 % of the uniaxial compressive strength (cube strength, f_c). As a result, the tensile strength at the dam-foundation interface was calculated using Equation 4-13 where the concrete cylinder strength of the dam cushion material is shown in Table 3-4. The value of 0.67 was assumed to substantially reduce the 5 % value. The assumed tensile strength of the dam construction joints was taken as 0 to allow for opening of the joints when tensions developed along the arch axis.

$$f_{t.j} = 0.67 * 0.05 f_c \quad \textbf{4-13}$$

Where

f_c = concrete cube strength = 1.2 x f_c' (concrete cylinder strength) (MPa)

An isometric view of the dam model showing the application of the interface elements at the base is shown in Figure 4-20.

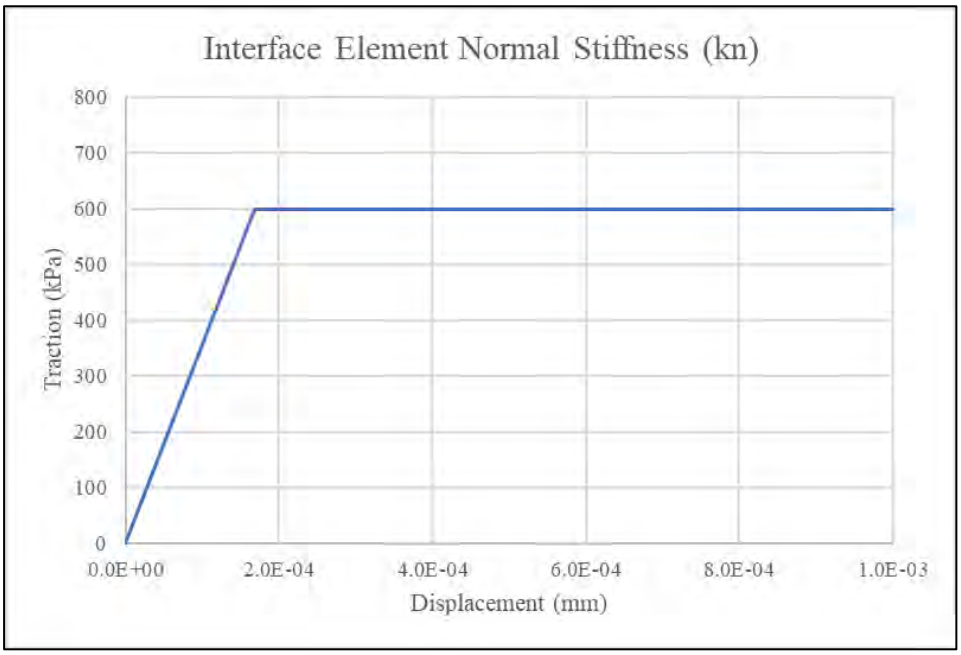

Figure 4-19: Bi-linear normal tensile stiffness of interface elements at dam-foundation joint for ft = 600 kPa

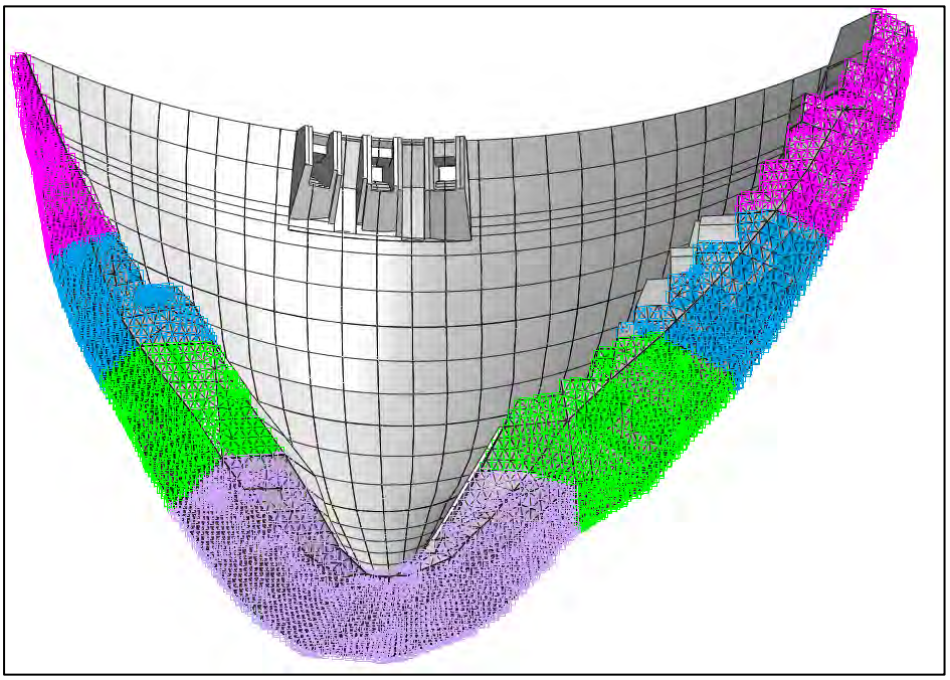

Figure 4-20: Interface elements at dam-foundation interface contact zone

4.11 SUMMARY

This chapter provides a discussion of the assumptions made and the methodology followed to create the three-dimensional FE element model of the dam-foundation structural system, for conducting the dam impoundment analysis

The various FE model components such as geometry configuration, FE mesh, boundary conditions, material models and loading conditions were presented and explained in the context of the dissertation study.

The following chapter will address the dam instrumentation data against which the outputs of the impoundment study FE analysis will be evaluated and compared.

5 INSTRUMENTATION DATA

This chapter provides a discussion on the instrumentation data of the Yusufeli Dam. A detailed account is given of the various instruments installed on the dam and the measurements obtained from these instruments during impoundment of the dam. An interpretation of the instrument readings and evaluation of the dam behaviour, in response to the reservoir impoundment is presented.

The monitoring of the dam behaviour during impoundment allows for the detection of possible early signs of distress as the progressively loaded dam displaces, transfers load into the foundation and gets seated into its rock mass foundation. Signs of distress may present in the form of the following behaviour:

- Excessive movements in a local portion of the dam or foundation, inconsistent with the overall structural mode of the dam indicating possible local material yielding and loss of stiffness,
- Permanent or plastic deformation of the structure, due to movements within the foundation caused by unknown subsurface foundation features,
- Substantial tilting or relative movement of foundation across a bedding plane or joint set, because of slippage along a plane,
- Development of large pore pressure or seepage flow rates within foundation rock mass jointing behind the dam drainage grout curtain or at the dam-foundation interface.

Ultimately, the dam behaviour under impoundment loading should not exceed the expected design behaviour, and the ideal scenario entails a dam movement and associated development of stresses/strains, marginally below the anticipated design value. This indicates a conservative design of the dam. The anticipated design behaviour of the dam is that reported by the outputs of the impoundment study FE analysis, which is seen as the reference point for evaluation of the dam behaviour during impoundment.

The dam impoundment study was undertaken by considering the cumulative dam behaviour at each of the various reservoir impoundment evaluation stages, in comparison to that observed at the impoundment commencement date. The reservoir impoundment was temporarily halted for each stage pending the favourable outcome of the dam behaviour evaluation at that stage, after which impoundment was continued. For purposes of the impoundment study the displaced state of the dam at commencement of impoundment was taken as the zero-displacement stage.

For purposes of conducting the dam impoundment evaluation study, the cumulative instrument readings observed at each stage of impoundment were summarised in table form, for ease of comparison with anticipated behaviour reported by the FE analysis outputs.

5.1 DAM INSTRUMENTATION TYPES

The Yusufeli Dam has a comprehensive set of instrumentation installed within the dam body and surrounding rock mass foundation. Various devices were placed in strategic locations of the dam and its foundation to obtain a complete range of dam behaviour measurements, for observing all the relevant forms of behaviour that occur in a loaded concrete arch dam. The primary forms of behaviour of interest comprise internal and surface movement of the dam, internal structural stress of the dam, internal and external hydrostatic pressures within the dam and foundation, temperature state of the dam and seepage flow rates within the dam and foundation.

The instrumentation system installed at Yusufeli Dam comprise the following components:

- Geodetic survey system with external beacons on the dam and surrounding foundation surface, for measuring movement of the external surfaces of the dam.
- Hanging and inverted pendulums for measuring relative movement of the dam and foundation.
- Joint meters installed across contraction joints between the dam monolith blocks, to measure the opening and closing of these joints under loading.
- Strain gauges cast within the dam concrete to measure strain development in the dam body.
- Stress meters to measure the internal axial and radial compressive stress development in the dam body.
- Thermocouples to measure temperature state within the dam body.
- Uplift stations to measure pore pressures along the seepage path at the dam-foundation interface.
- Piezometers to measure the pore pressure of the water within the dam foundation rock mass along the grout curtain seepage path.

The following section provides a discussion of each of the instruments installed on Yusufeli Dam and a presentation of the measurements obtained from them. A time-based representation of the progressive reservoir elevation levels attained during impoundment is depicted by the curve shown in Figure 5-1. It can be seen that impoundment initiated on 21 November 2022 and reached elevation level 696 mASL on 18 August 2023.

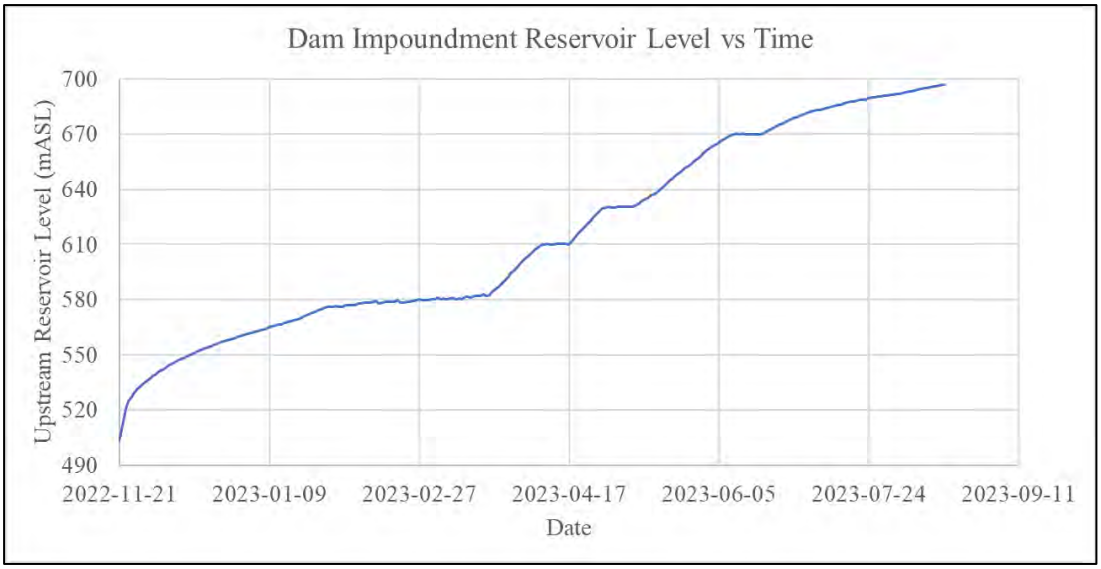

Figure 5-1: Time-based representation of the progressive dam impoundment elevation levels attained

5.2 GEODETIC SURVEY SYSTEM

The geodetic survey system of Yusufeli Dam comprises 12 survey beacons fixed on the downstream face of the dam, which are surveyed from two setting out points downstream of the dam, one on the left and one on the right bank of the river canyon. The locations of the survey beacons in relation to the dam body are shown in Figure 5-2.

The survey beacons were placed at three elevation levels, covering the top half of the dam where most of the dam displacement will take place. Survey beacons B1 and B2 were placed at elevation level 590 mASL which is approximately mid-height of the dam, beacons B3 to B6 were placed at 662 mASL near the top quarter line of the dam height and beacons B7 to B12 were placed at crest level, which is at elevation level 715 mASL. At the various elevation levels the beacons were spaced out at relatively even distances along the arch axis, to capture a good representation of the change in the displacement of the dam along its span.

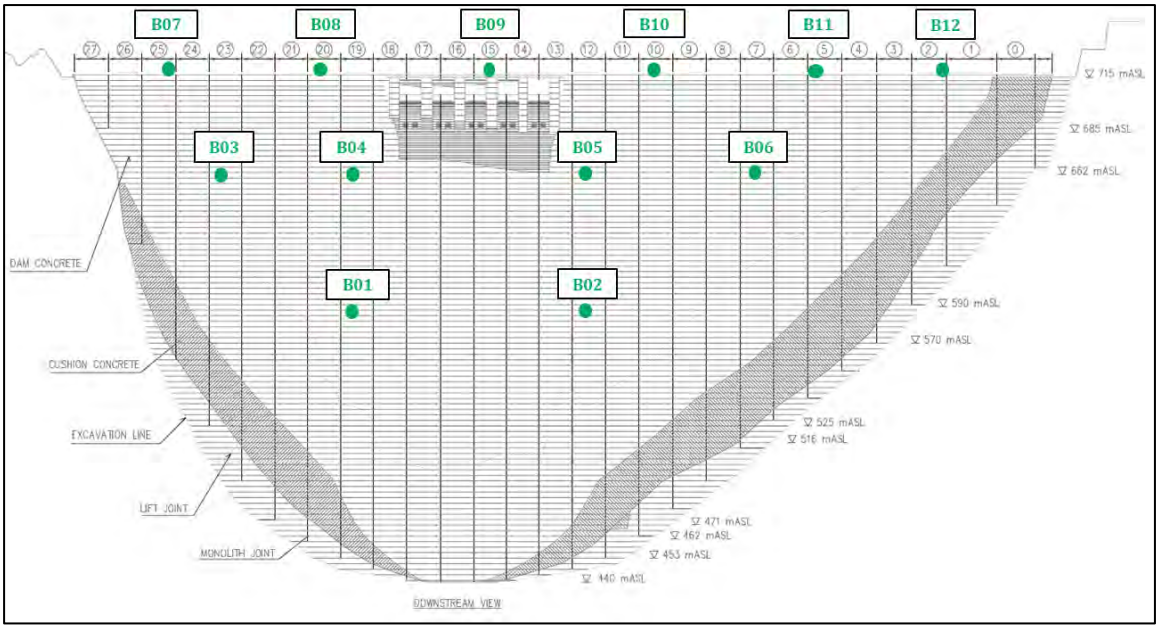

Figure 5-2: Location of survey beacons in relation to Yusufeli Dam body

The survey work was done by an independent survey contractor, GeoMosNow and displacements of the various survey beacons were taken hourly and provided in the form of time-based displacement graphs on a server website accessible via the internet. The measured horizontal displacements of the survey beacons were provided in the form of movements along the northing line and easting line, and as resultant two-dimensional vector displacements.

The dam body is orientated such that a straight line drawn from upper right flank to upper left flank of the dam body, and defined as the x-axis, lies at an angle of 29 ° to the northing line. This is indicated in Figure 5-3 where the x-axis is shown as the red local axis of the dam and the northing line as the vertical red line crossing the black easting line.

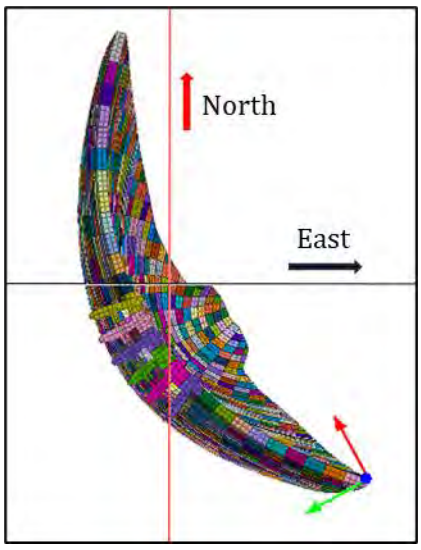

Figure 5-3: Orientation of Yusufeli Dam body axis in relation to Northing and Easting lines

The surveyed resultant horizontal displacement of the various dam beacons as a function of time, are shown in Figure 5-4. The twelve curves depict smoothed daily-average cumulative horizontal movements of the survey beacons from commencement of dam impoundment on 2022-11-21 to 2023-08-18, from which point forward impoundment is being halted at reservoir elevation 696 mASL for hydropower turbine testing. Similarly, the horizontal displacements of beacons B01 to B12 plotted as a curve function of the reservoir elevation level are shown in Figure 5-5.

The positive horizontal displacements of the beacons are all in the downstream direction. It can be seen from the graph curves that the impoundment progress was halted at reservoir elevation level 580 mASL on 2023-02-13, at 610 mASL on 2023-04-08, at 630 mASL on 2023-04-29, at 670 mASL on 2023-06-10 and at 696 mASL on 2023-08-18.

The commencement of impoundment occurred during late Autumn, at which stage the dam temperature was seen to be dropping, whilst the reservoir level was rising and associated hydrostatic load increasing. The displacement behaviour of the arch during various stages of impoundment at the different beacon locations, is a complex configuration mode that is influenced by a combination of the structural stiffness of the arch dam, the location of the survey beacon, and the loading condition of the dam at that point.

During early stages of impoundment, the lower row of survey beacons, B1 and B2 are closest to the reservoir water load and these beacons undergo significant downstream displacement. Survey beacons B4 and B5 experience a similar displacement to B1 and B2 for early to mid-stages of the impoundment even though they are higher up on the dam than B1 and B2.

Beacon B4 and B5 are higher up on the dam elevation and further from the water load, yet the dam thickness decreases significantly towards the crest meaning the dam structure is more flexible higher up, and more susceptible to deflection under load. The upper part of the dam is also more sensitive to ambient temperature drops, as the profile is thinner meaning a larger ratio of the profile thickness experiences a temperature drop than for lower thick portions.

Survey beacons B3 and B6 are at the same elevation of B4 and B5 but are closer to the dam abutments than B4 and B5 where the dam is stiffer than at the crown, resulting in these beacons experiencing smaller displacements than B4 and B5.

Survey beacons B8, B9 and B10 located mid-span of the dam at the crest level, are seen to have the largest displacements during early impoundment until approximately April 2023. A this point, the reservoir elevation reached 630 mASL and induced a substantial increase in the downstream displacements of beacons B1, B2, B4, B5 in comparison to B8, B9 and B10. This

is evident as the displacement curves of the lower mid-span beacons cross the curves of the beacons at the crest. The increase in temperature can be seen to reduce downstream displacement at the crest as it warms, expands and begins to experience relative upstream movement.

The displacement graphs show that the maximum horizontal displacement of the dam, at impoundment elevation stage 696 mASL, occurs mid-span of the arch, between mid-height and three-quarters elevation point from the bottom. The maximum horizontal displacement observed here on 2023-08-18 when the reservoir elevation has reached 696 mASL is approximately 58 mm.

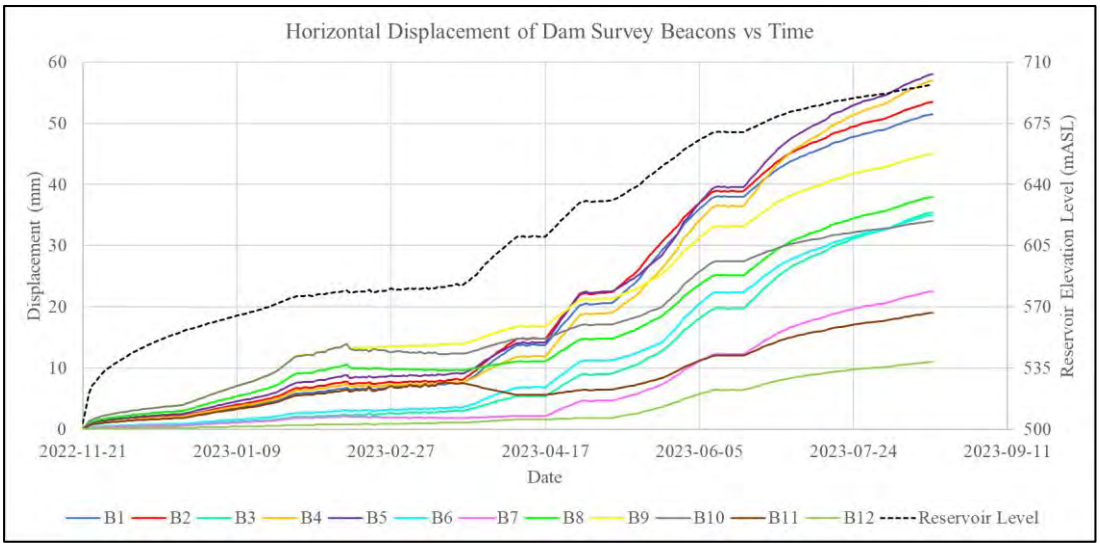

Figure 5-4: Resultant horizontal displacement of dam survey beacons vs time

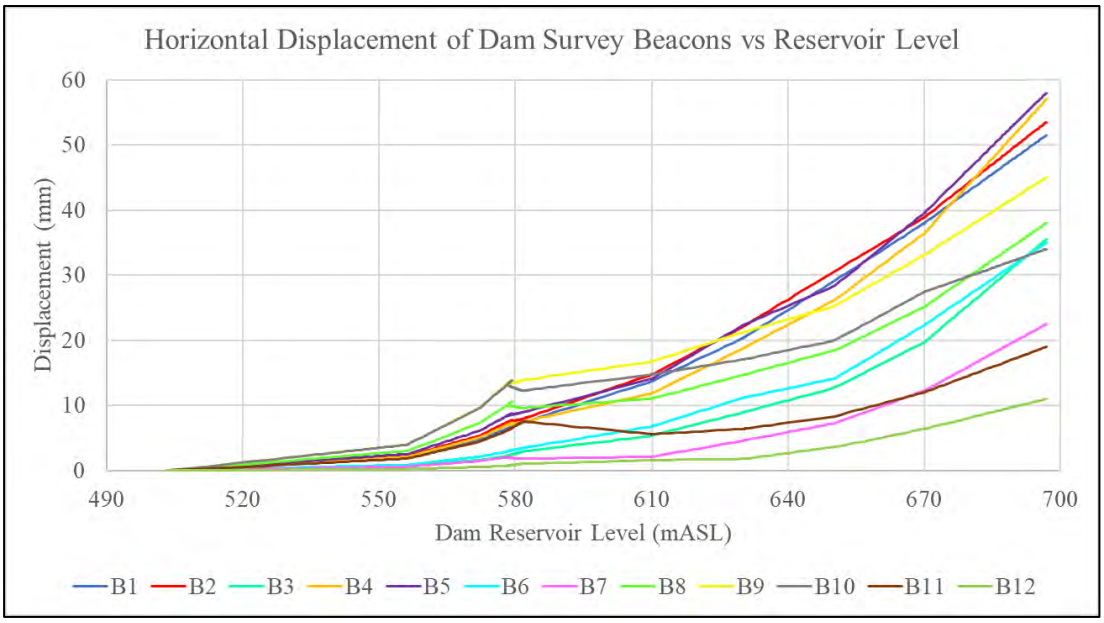

Figure 5-5: Resultant horizontal displacement of dam survey beacons vs reservoir elevation level

A summary of the observed horizontal displacements of the survey beacons at the various progressive reservoir impoundment stages is shown in Table 5-1.

Table 5-1: Summary of surveyed horizontal displacement of dam beacons at impoundment stages

Survey Beacon	Resultant Horizontal Displacement (mm)				
	580 mASL (2023-02-13)	610 mASL (2023-04-08)	630 mASL (2023-04-29)	670 mASL (2023-06-10)	696 mASL (2023-08-18)
B1	6.8	13.7	20.4	38.4	51.5
B2	7.4	15.2	22.1	39.4	53.5
B3	3.4	5.4	8.9	19.7	35.5
B4	7.2	11.9	18.4	36.1	57.0
B5	9.1	13.4	20.4	39.1	58.0
B6	3.5	6.3	9.4	22.4	35.0
B7	2.0	2.1	4.1	12.3	22.5
B8	9.9	10.6	14.2	25.1	38.0
B9	13.4	16.8	19.9	33.1	45.0
B10	12.3	14.0	16.1	27.5	34.0
B11	5.6	5.4	5.7	12.0	19.0
B12	0.8	1.5	1.6	6.4	11.0

*positive displacement denotes movement towards downstream

5.3 PENDULUMS

The Yusufeli dam has six pendulum devices installed in the central portion of dam body axis, of which three are hanging pendulums and three are inverted pendulums. One of each hanging and inverted pendulums were placed in dam monolith 13, 16 and 19. The pendulum device name assigned for the three hanging pendulums are P-13-H-525.5, P-16-H-525.5 and P-19-H-525.5, whilst for the inverted pendulums they are P-13-I-525.5, P-16-I-525.5 and P-19-I-525.5. The configuration of the pendulum set up in relation to the dam FE mesh bodies for monoliths 13, 16 and 19 is shown in Figure 5-6, where monolith 16 is the crown cantilever of the dam. A cantilever side view showing the typical pendulum configuration for monolith 19 is also provided in Figure 5-6 and a detailed drawing of the dam pendulum locations is provided in Figure 10-5 of Appendix A.

The suspension points of the hanging pendulums were positioned in the dam gallery 30.5 m below the crest of the dam at elevation 684.5 mASL. The anchor points for the inverted pendulums of monoliths 13, 16 and 19 were fixed in the foundation rock mass below the dam base at elevation levels 378 mASL, 366 mASL and 358 mASL, whilst the deepest foundation

level of the dam is at 440 mASL. The reading points of both the hanging and inverted pendulums are located in the gallery at dam elevation 525.5 mASL.

The hanging pendulums measure the radial and tangential displacement of the top of the dam, in relation to the lower portion of the dam, and the inverted pendulums measure the relative movement of the lower portion of the dam, with reference to the foundation below.

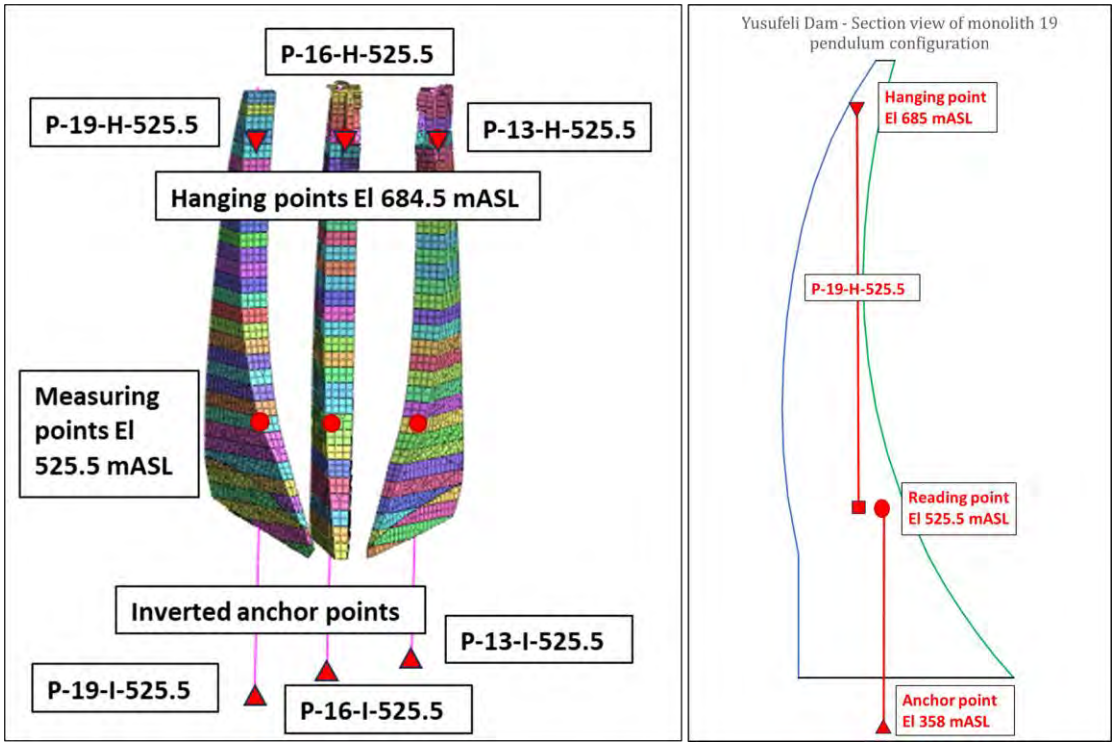

Figure 5-6: Three-dimensional view of pendulum configuration (left) and section view of monolith 19 pendulum set-up (right) for Yusufeli Dam

Pendulums are sensitive instruments as they measure relative movements between two points, over a significant vertical distance. A small angular rotation of the dam can manifest in the form of a significant relative displacement between the anchor and measuring point.

The hanging and inverted pendulum readings taken for the dam from the period of 2022-12-04 to current date of 2023-08-18 are shown by the curves of Figure 5-7 and Figure 5-8. It is noted that pendulum measurements were started two weeks after commencement of the reservoir impoundment, at which stage the dam reservoir had already reached an elevation of 545 mASL.

The hanging pendulums of monolith 13 (P-13-H-525.5) and 16 (P-16-H-525.5) show similar downstream radial displacement readings of the top of the dam in relation to the lower portion of the dam, with a maximum value of 19 mm at monolith 13 recorded at impoundment level 696 mASL. This is consistent with the surveyed downstream horizontal displacements of the dam body.

The readings taken for the hanging pendulum in dam monolith 19 (P-19-H-525.5) show some inconsistencies in behaviour which compromises the reliability of this instrument. The displacement curve for the hanging pendulum of monolith 19 shows a similar behaviour to that of monolith 13 and 16 until end of March 2023, where a vertical spike of 4 mm in the upstream direction is indicated. After the spike the downstream displacement readings are seen to progress slowly again until 2023-05-23 where another vertical spike of upstream displacement in the order of 3 mm can be seen.

It is evident that the vertical spikes in displacement towards the upstream direction, of the hanging pendulum in dam monolith 19, are inconsistent with the overall displacement mode of the dam. These spikes are assumed to be anomalies, probably caused by a source external to the dam behaviour. The instrument may have been bumped by personnel operating the dam or reading the instruments. The final readings taken from July to August also look suspicious due to the smoothness in the curve and large vertical spike at the end. If the vertical spikes in upstream and downstream displacements are eliminated from the curve for pendulum P-19-H-525.5, the final downstream displacement measured at reservoir elevation level 696 mASL would be approximately 15 - 17 mm which is relatively close to the measurements taken by pendulums P-13-H-525.5 and P-16-H-525.5.

The tangential displacement of the hanging pendulums indicate that there is lateral twisting of the dam near the mid-section. At approximately mid-height of the central portion of the arch axis, the upstream face of the dam is squeezed inwards towards the crown of the arch under hydrostatic pressure, whilst the top and bottom of the dam move outwards towards the abutments. The tangential displacement curves for hanging pendulum P-13-H-525.5, left of the crown cantilever, show movement towards the left abutment of the dam at the crest with a cumulative magnitude of nearly 3 mm at impoundment elevation level 696 mASL. The tangential displacement readings for pendulums P-16-H-525.5 and P-19-H-525.5, indicate cumulative displacements of 4 mm and 9 mm at the top of the dam, towards the right abutment at impoundment stage 696 mASL.

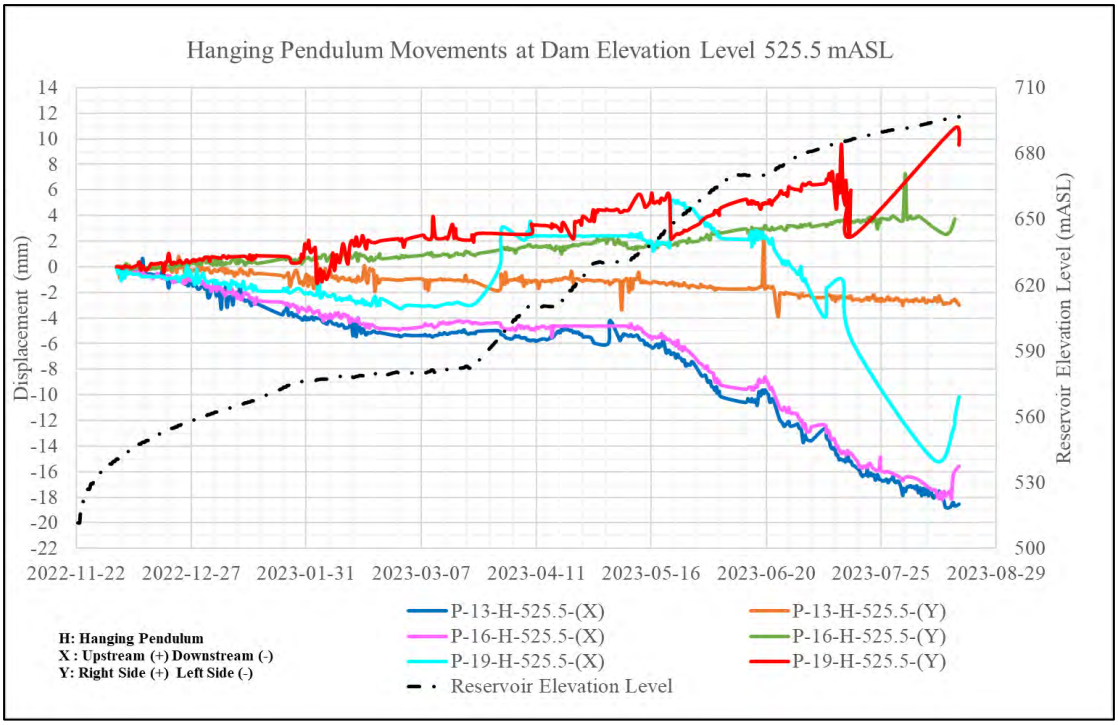

Figure 5-7: Hanging pendulum readings of dam monolith 13, 16 and 19 at reading point elevation 525.5 mASL

The inverted pendulum measurements taken for dam monoliths 13 (P-13-I-525.5), 16 (P-16-I-525.5) and 19 (P-16-I-525.5) all show a similar progressive positive radial displacement. This indicates that the mid-span portion of the dam at elevation level 525.5 mASL has moved downstream relative to the foundation. This is consistent with the movements observed in the dam survey beacons. The cumulative downstream displacement of the inverted pendulums at reservoir impoundment level 696 mASL range between 22 mm and 29 mm.

The measured tangential displacements of the inverted pendulums for monoliths 13, 16 and 19 again show the twisting deformation of the mid-heght portion of the dam upstream face, near the crown cantilever. The inverted pendulum P-13-I-525.5 just left of the crown cantilever is seen to have moved tangentially 7.3 mm to the right abutment during impoundment to reservoir elevation level 696 mASL. Inverted pendulums to the right of the crown cantilever, P-16-I-525.5 and P-19-I-525.5 move 6.5 mm and 15 mm to the left during the period of impoundment to reservoir level 696 mASL.

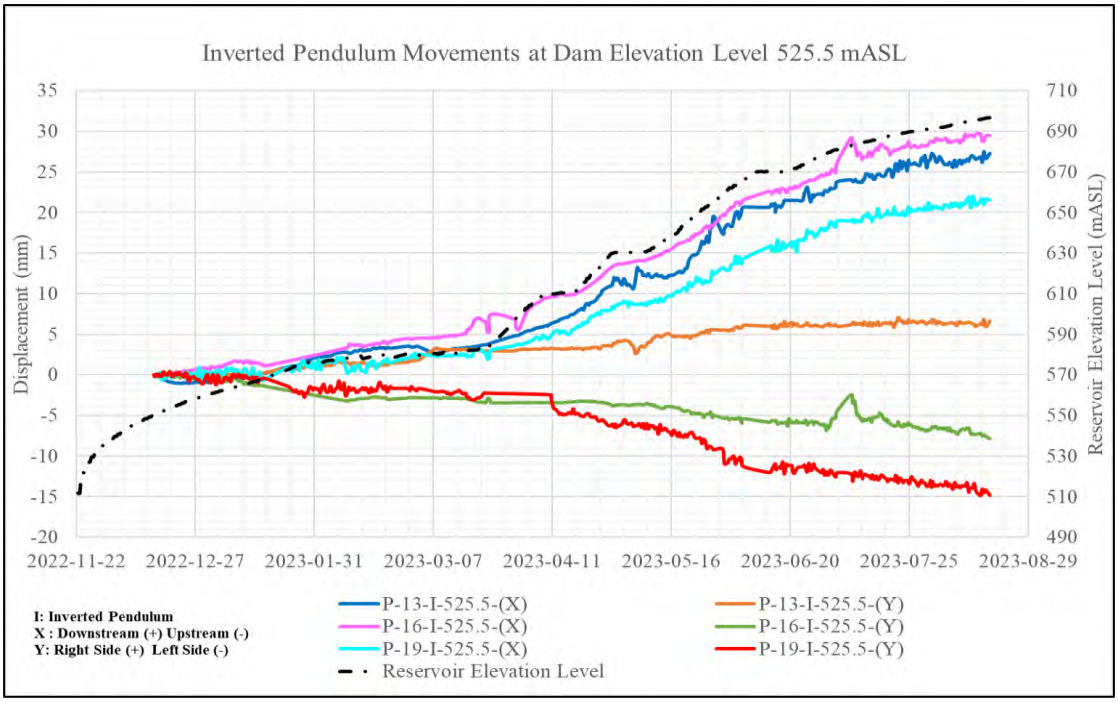

Figure 5-8: Inverted pendulum readings of dam monolith 13, 16 and 19 at reading point elevation 525.5 mASL

A summary of the pendulum radial and tangential displacement readings taken at the various dam reservoir impoundment level stages, for hanging and inverted pendulums, are shown in Table 5-2 and Table 5-3. The assumed corrected measurements for P-19-H-525.5 are shown in the summary, with the actual observed measurements given in brackets.

Table 5-2: Summary of radial relative pendulum displacements at various impoundment stages

Pendulum	Radial Relative Displacement (mm)				
	580 mASL (2023-02-13)	610 mASL (2023-04-08)	630 mASL (2023-04-29)	670 mASL (2023-06-10)	696 mASL (2023-08-18)
P-13-H-525.5	-5	-5.5	-6	-10	-19
P-16-H-525.5	-4.5	-5	-5.5	-9	-18
P-19-H-525.5	-3	-3.5 (2)	-4 (2.5)	-8 (2)	-16
P-13-I-525.5	3	6	12	21	27.5
P-16-I-525.5	4	9	14	23	29
P-19-I-525.5	1.5	5	9	16	22

*positive displacement indicates upstream movement for hanging pendulums and downstream for inverted pendulums

Table 5-3: Summary of tangential relative pendulum displacements at various impoundment stages

Pendulum	Tangential Relative Displacement (mm)				
	580 mASL (2023-02-13)	610 mASL (2023-04-08)	630 mASL (2023-04-29)	670 mASL (2023-06-10)	696 mASL (2023-08-18)
P-13-H-525.5	-0.8	-1	-1.2	-2	-2.8
P-16-H-525.5	1	1.5	2	3	4
P-19-H-525.5	2	3	4	5.5	9
P-13-I-525.5	1	3	4	6	7.3
P-16-I-525.5	-3	-3.5	-4	-5	-6.5
P-19-I-525.5	-2	-3	-6	-11	-15

*positive displacement indicates movement to the right bank for hanging and inverted pendulums

5.4 JOINT METERS

Opening of contraction joints between dam monoliths are indicative of contraction and associated formation of tensile stresses along the arch axis. This unwanted behaviour may cause the dam arch to lose monolithic behaviour. The opening of contraction joints between dam monoliths were measured with joint meters installed across the joint interfaces of the dam at various elevation levels.

Data readings for the joint meters were studied for the period from 2022-11-21 to 2023-06-10 to evaluate the extent and pattern of joint opening. The readings indicated that most of the joints either closed or remained closed for the period of impoundment and were not considered for this study. Towards the crest of the structure, however, some opening of the joints was apparent, as would be expected for a double-curvature arch dam with a low reservoir level at a time of year with low temperatures.

A developed upstream view of the dam showing the locations of joint meters considered for this study are shown in Figure 5-9. Time-history displacement plots of joint meter readings taken at elevation 715 mASL, for the impoundment period, are illustrated in Figure 5-10. During early impoundment stages in Winter, the joint meters at the crest indicated an opening of between 0.5 mm and 2 mm, with the higher value occurring at the crown of the arch and the lower values closer to the abutments. During Spring, the joints at the crest started closing due to a combination of dam expansion from temperature rise and loading of higher portions of the dam monoliths. By the time that impoundment had reached elevation level 600 mASL, all the joints had closed, showing a negative change in displacement relative to reference point measurement on 2022-11-21.

The numbering convention adopted for the joint meter naming is explained for the instrument 715/92/8-9/JM-9 where 715 represents the elevation number, 92 the lift number, 8-9 the monolith interface and JM-9 indicates the joint number.

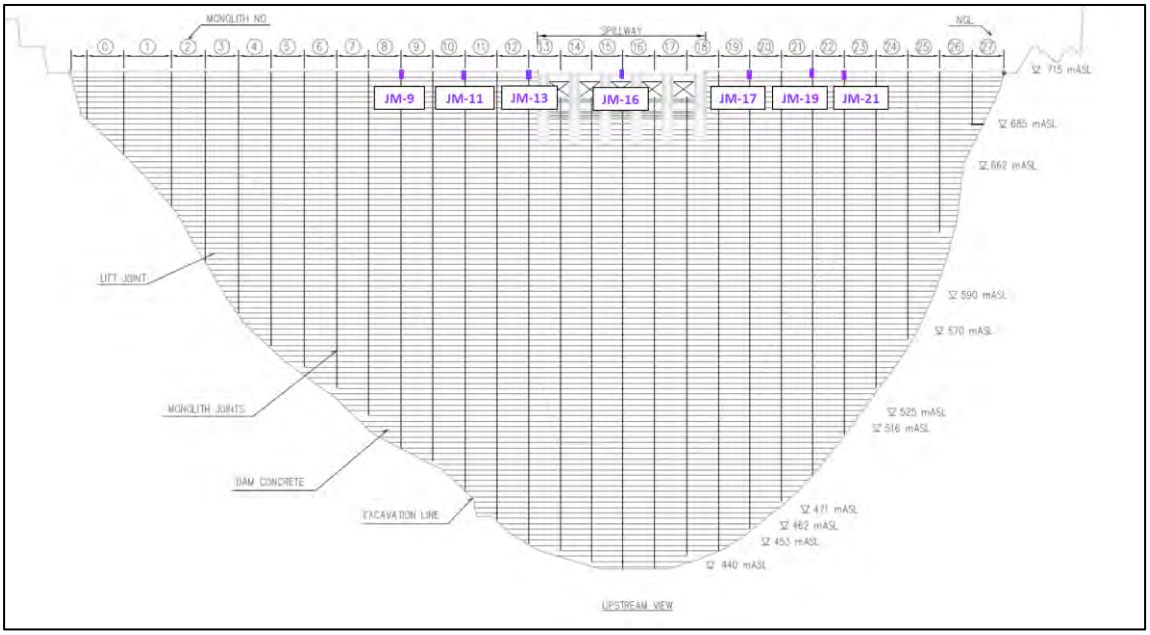

Figure 5-9: Location of joint meters at crest level of dam

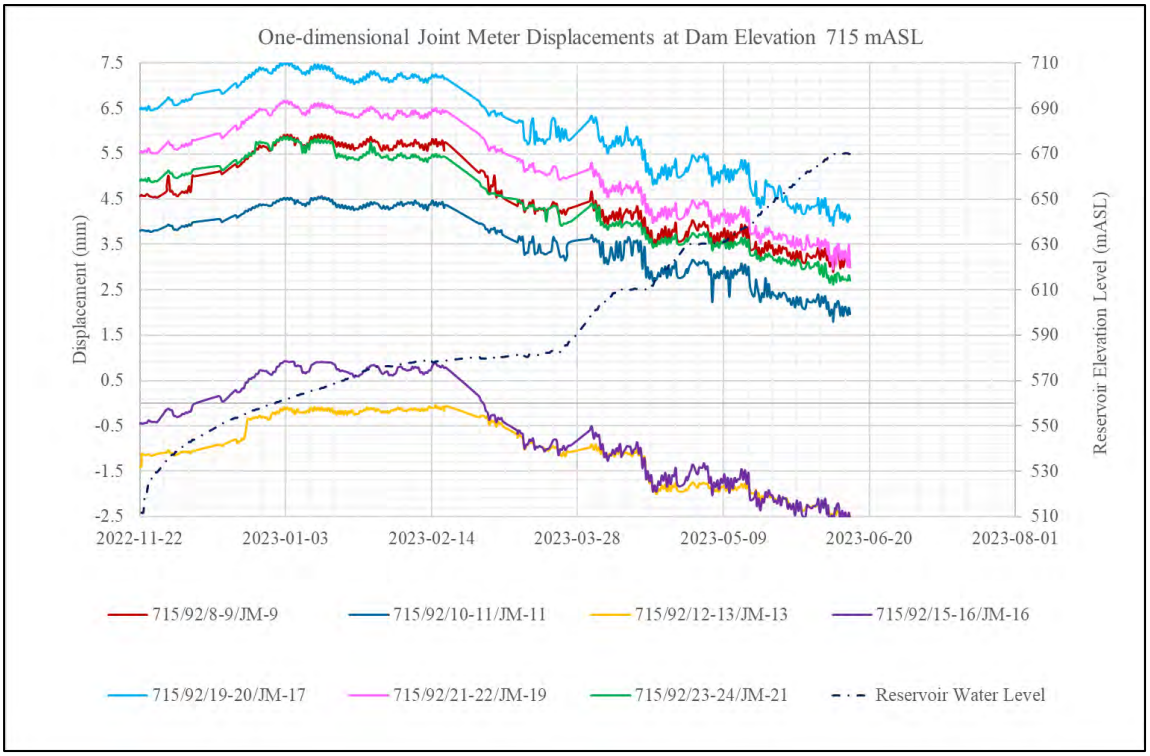

Figure 5-10: One-dimensional joint meter displacement readings at elevation level 715 mASL

A summary of the joint meter readings taken at the various stages of impoundment are shown in Table 5-4. After impoundment stage 610 mASL was reached all the joints had closed and remained closed during subsequent impoundment stages.

Table 5-4: Summary of joint meter measurements of dam at various impoundment stages

Joint meter	Elevation (mASL)	Relative Displacement Across Joint (mm)				
		580 mASL (2023-02-13)	610 mASL (2023-04-08)	630 mASL (2023-04-29)	670 mASL (2023-06-10)	696 mASL (2023-08-18)
JM-9	715	0.9	0	0	0	0
JM-11	715	0.8	0	0	0	0
JM-13	715	1.3	0	0	0	0
JM-16	715	1.3	0	0	0	0
JM-17	715	0.8	0	0	0	0
JM-19	715	0.9	0	0	0	0
JM-21	715	0.6	0	0	0	0

*positive value indicates joint opening

5.5 STRAIN GAUGES

Strain measurements in the dam were taken using strain gauges cast into the dam body concrete at pre-determined locations. The strain measurements observed in the dam were very small, particularly in the upper portions of the dam. Only measurements obtained in the lower portion of the dam body were deemed reliable enough to evaluate. The strain measurements from six strain gauges were considered for the dam impoundment study. Of the six strain gauges considered, four were located at elevation level 453.5 mASL and two at elevation 471.5 mASL. The elevation levels at which the strain gauges were installed in relation to the dam body are shown in Figure 5-11.

The instrument numbering convention for strain gauge 453.5/SR/1/17/1 refers to the strain gauge at elevation 453.5 mASL, installed in dam lift number 1 of monolith no 17, with the number 1 representing the upstream side (2 representing downstream side instrument).

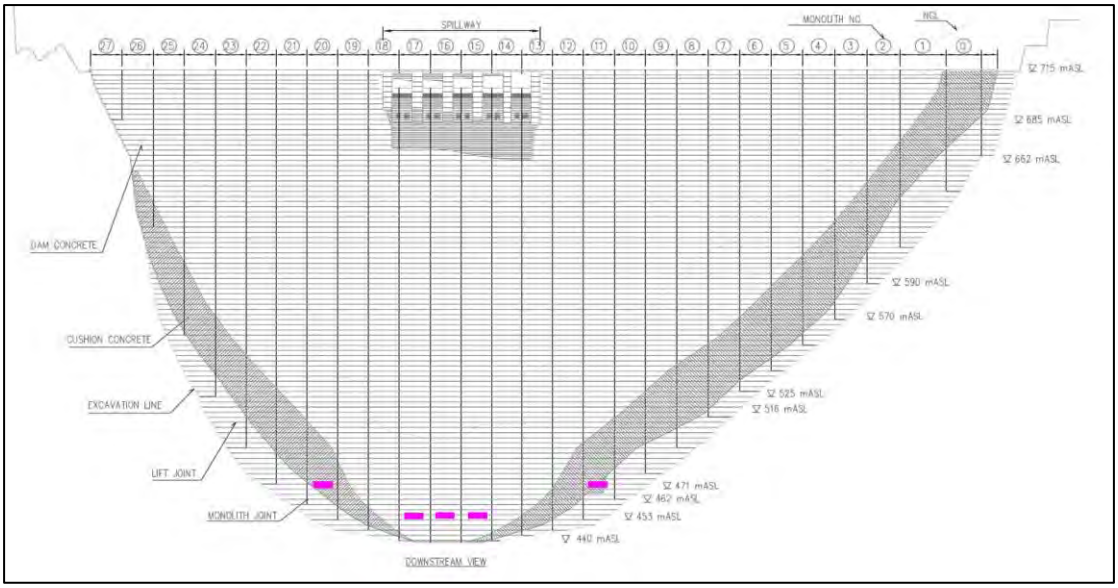

Figure 5-11: Instream view of dam showing elevation levels of strain gauges installed in dam

The location of the four strain gauges cast into the dam at elevation level 453.5 mASL, are indicated in the horizontal section of the dam shown in Figure 5-12. These strain gauges were orientated to measure tangential strain of the dam, being the direction parallel to the dam axis. Strain gauges 453.5/SR/1/17/1, 453/SR/0/16/1 and 453/SR/1/15/1 measure the tangential strain near the upstream face of the lower dam body and device 453.5/SR/1/17/2 near the downstream face.

The location of the two strain gauges installed in the dam body at elevation 471.5 mASL is depicted in the horizontal section of the dam as shown in Figure 5-13. Strain gauges at elevation 471.5 mASL were orientated to measure the radial strain development along the axis of the dam. Instrument 471.5/SR/10/11/1 and 471.5/SR/10/20/1 are located in the zone of the dam towards the downstream side, where arch thrusts into the abutments are expected to develop under full supply level loading conditions.

Strain development of the dam measured by strain gauges installed were plotted as time-history curves showing the change in strain as a function of time, alongside a curve indicating the rise in reservoir elevation level during impoundment. The change in strain values are very small and therefore not necessarily very reliable.

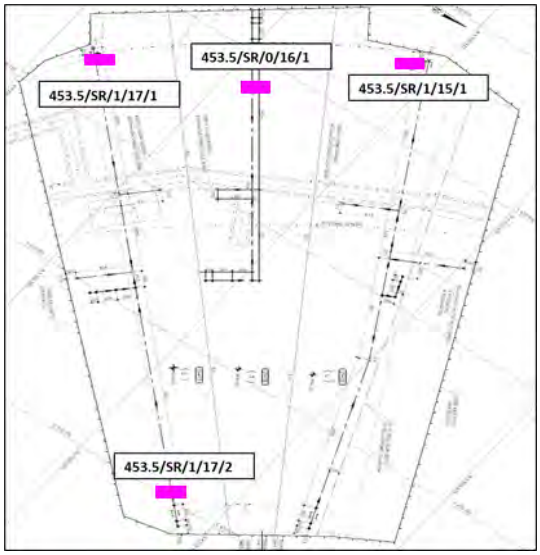

Figure 5-12: Location of strain gauges in Yusufeli Dam at elevation level 453.5 mASL

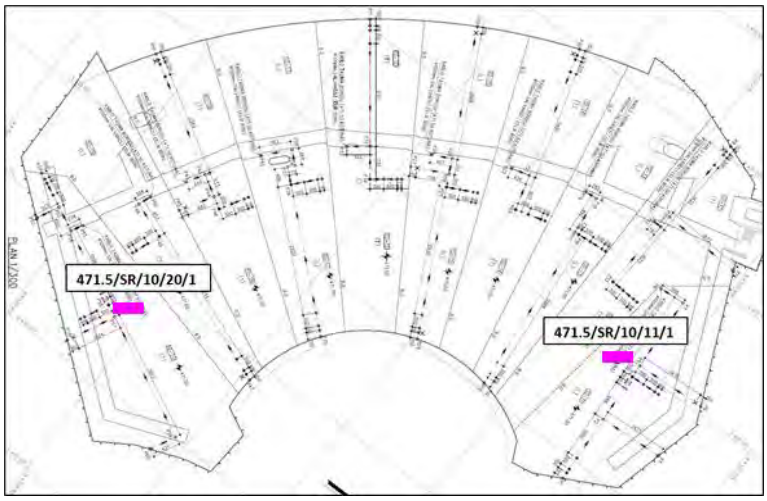

Figure 5-13: Location of strain gauges in Yusufeli Dam at elevation level 471.5 mASL

The strain gauge readings taken of the dam at elevation level 453.5 mASL from the period of 2022-11-21 to current date of 2023-18-18 are shown by the curves of Figure 5-14 and Figure 5-15. Strain gauge 453.5/SR/1/15/1 and 453.5/SR/1/17/1 both report a decrease in positive (expansive) strain which indicates the development of contractive tangential (compressive) strain at the heel of the lower dam of 18 $.10^{-6}$ m/m and 7 $.10^{-6}$ m/m. Similarly strain gauge 453.5/SR/1/17/2 measures a contractive tangential strain of 6 $.10^{-6}$ m/m. Readings from strain gauge 453.5/SR/1/16/1 show a positive (expansive) strain measurement of 18 $.10^{-6}$ m/m. The measurements are consistent with cantilever action at base of the dam.

The radial (axial) strain development measured in the dam body at elevation level 471.5 mASL for device 471.5/SR/10/11/1 is a contractive value of 5 $.10^{-6}$ m/m and that for instrument 471.5/SR/10/11/1 is an expansive value of 2 $.10^{-6}$ m/m. Both these values are very close to zero showing the development of negligible horizontal arch thrust action at the base of the dam.

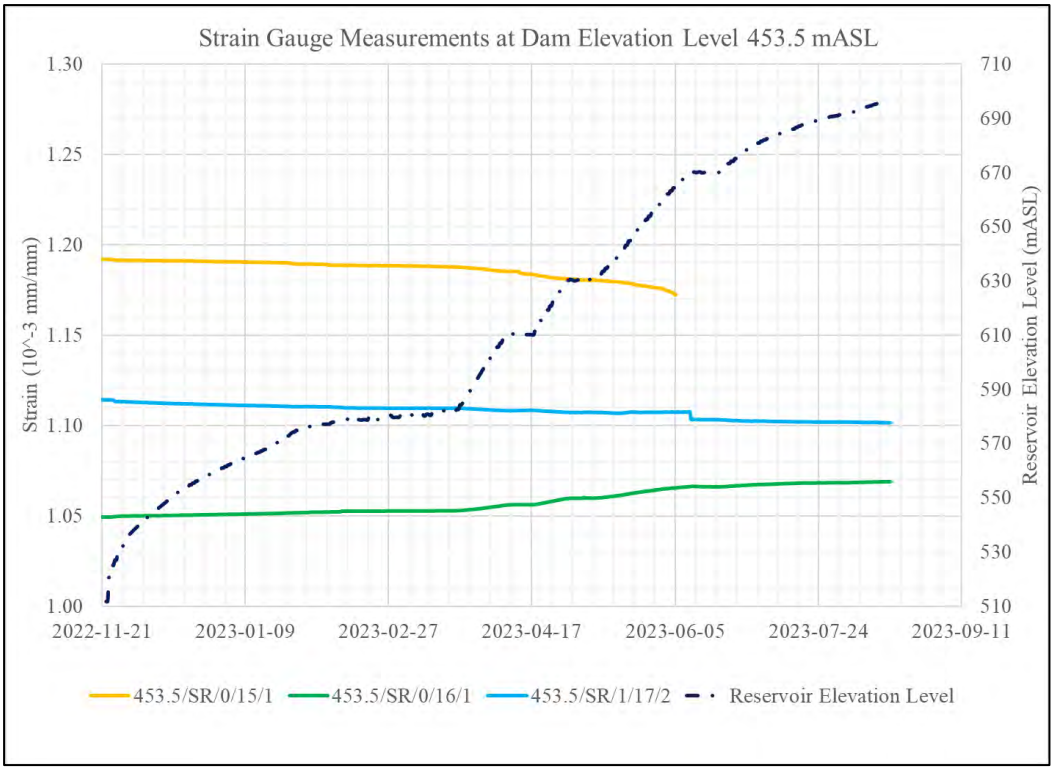

Figure 5-14: Tangential strain measured in dam body at elevation level 453.5 mASL

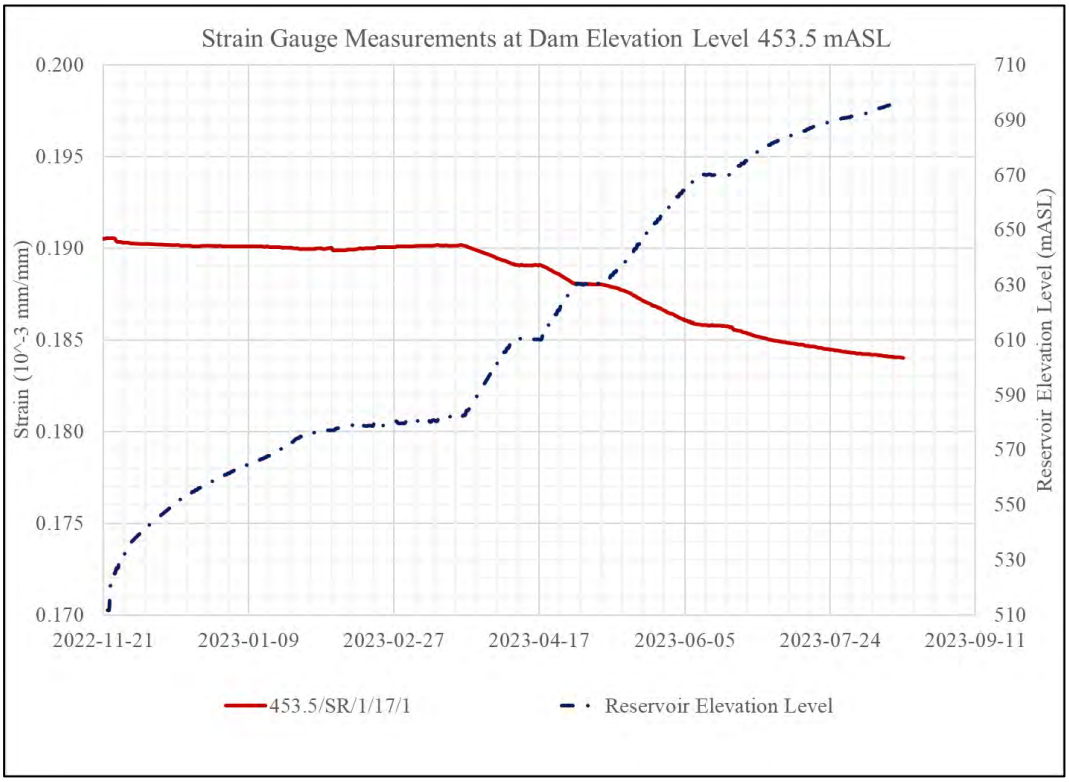

Figure 5-15: Tangential strain measured in dam body at elevation level 453.5 mASL

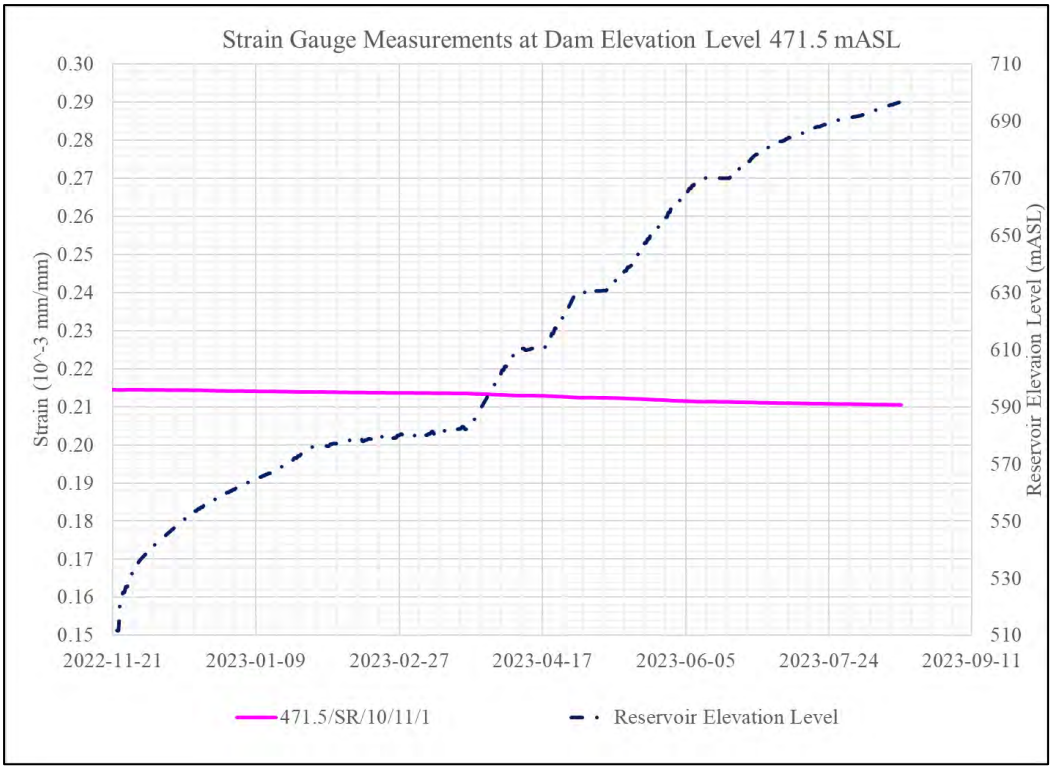

Figure 5-16: Radial strain measured in dam body at elevation level 471.5 mASL

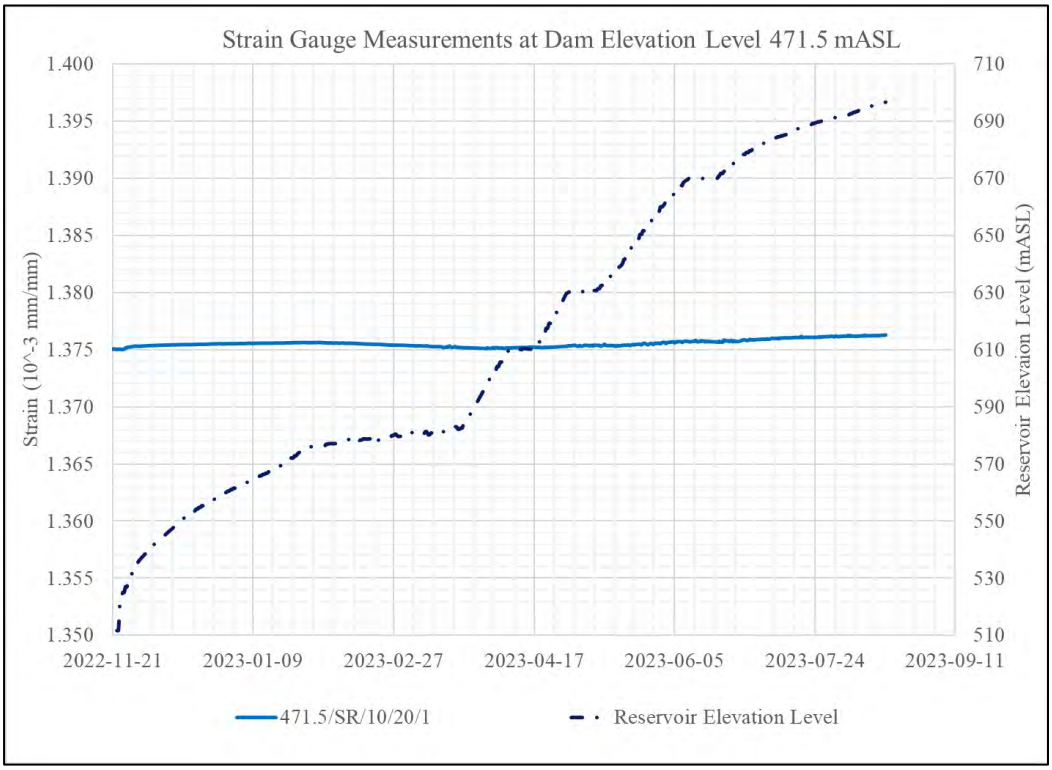

Figure 5-17: Radial strain measured in dam body at elevation level 471.5 mASL

A summary of the change in strain development of the dam structure under progressive loading during the period of impoundment is show in Table 5-5. Due to the very small strain development values observed during impoundment, only the final change in strain is evaluated.

Table 5-5: Summary of change in measured strain development during period of dam impoundment

Strain gauge No	Measured Change in Strain 10^{-6} (m/m)
453.5/SR/1/15/1	-18
453.5/SR/1/16/1	18
453.5/SR/1/17/1	-7
453.5/SR/1/17/2	-6
471.5/SR/10/11/1	-5
471.5/SR/10/20/1	2

*positive values denote expansive strain

5.6 STRESS METERS

Compressive hoop (thrust) stresses that develop in the direction of the dam axis, at the location where the dam contacts the foundation, were measured using stress meters placed at the contact between the dam and foundation. These instruments measure the normal stress between the dam concrete and foundation as a result of the dam thrusting into the foundation. Stress meters were installed at dam elevation 471.5 mASL and 525.5 mASL which is indicated in relation to the FE mesh of the dam body in Figure 5-18.

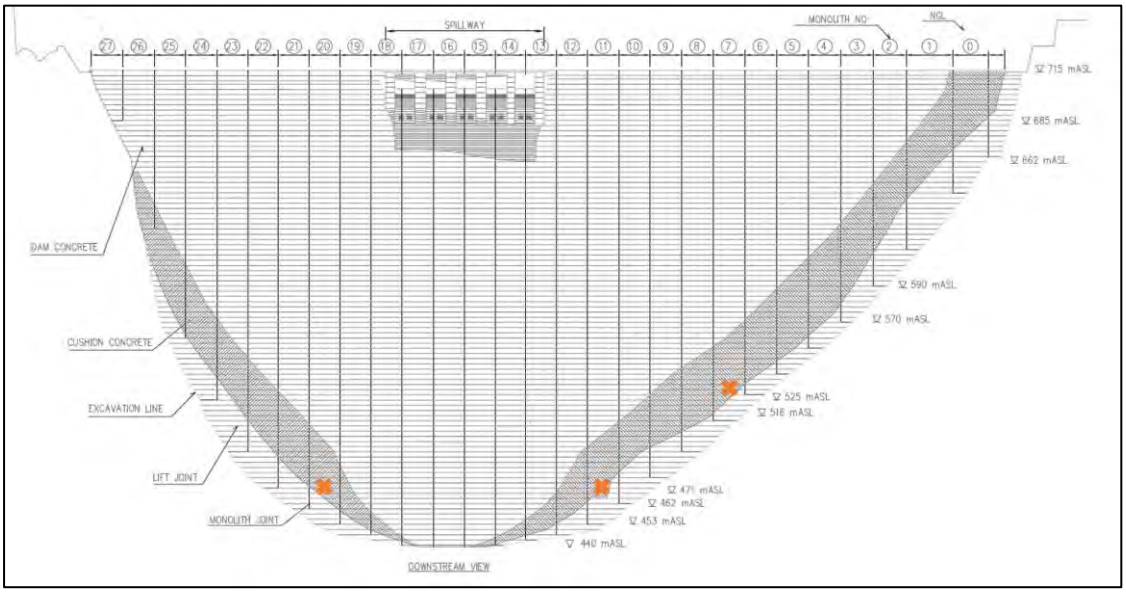

Figure 5-18: Instream view of dam showing elevation levels of stress meters installed in dam

The locations where stress meters were installed in the dam at elevation level 471.5 mASL and 525.5 mASL are shown in Figure 5-19 and Figure 5-20. The instrument numbering convention for stress meter 471.5/ST/10/20/1 refers to the instrument at elevation 471.5 mASL, installed in dam concrete lift number 10 of monolith no 20, with the number 1 representing the upstream side (2 represents the downstream side – See Figure 5-19).

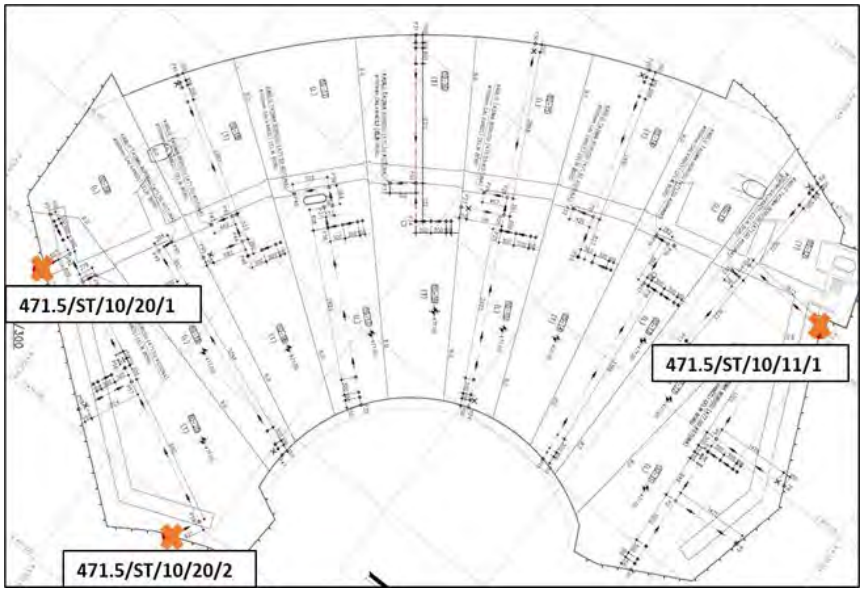

Figure 5-19: Location of stress meters installed in the dam at elevation 471.5 mASL

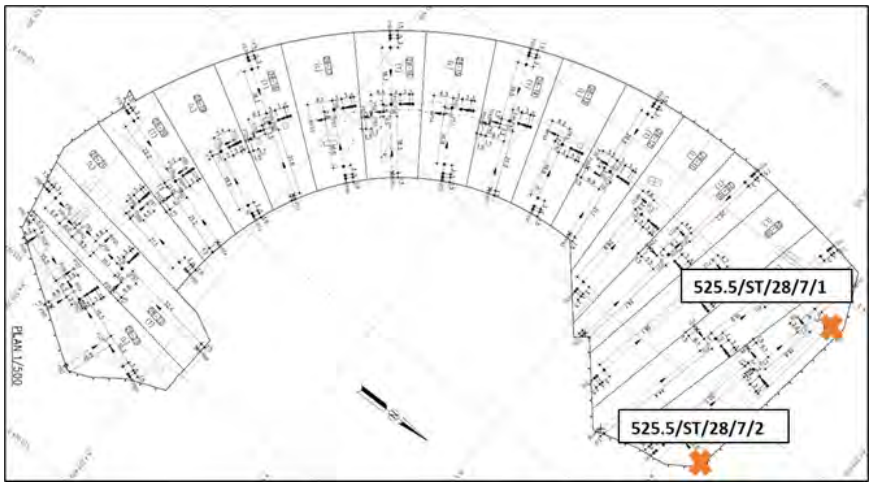

Figure 5-20: Location of stress meters installed in the dam at elevation 525.5 mASL

Axial stress developments in the dam measured at elevation 471.5 mASL and 525.5 mASL, were plotted as time-history curves showing the change in pressure as a function of time, alongside a curve indicating the rise in reservoir elevation level as shown in Figure 5-21 and Figure 5-22. Considering that positive pressure equates to compression measured on the stress

meter, it can be seen that for all instruments the dam develops an axial pressure pushing it into the foundation. All the readings indicate pressure values within a similar range of magnitude.

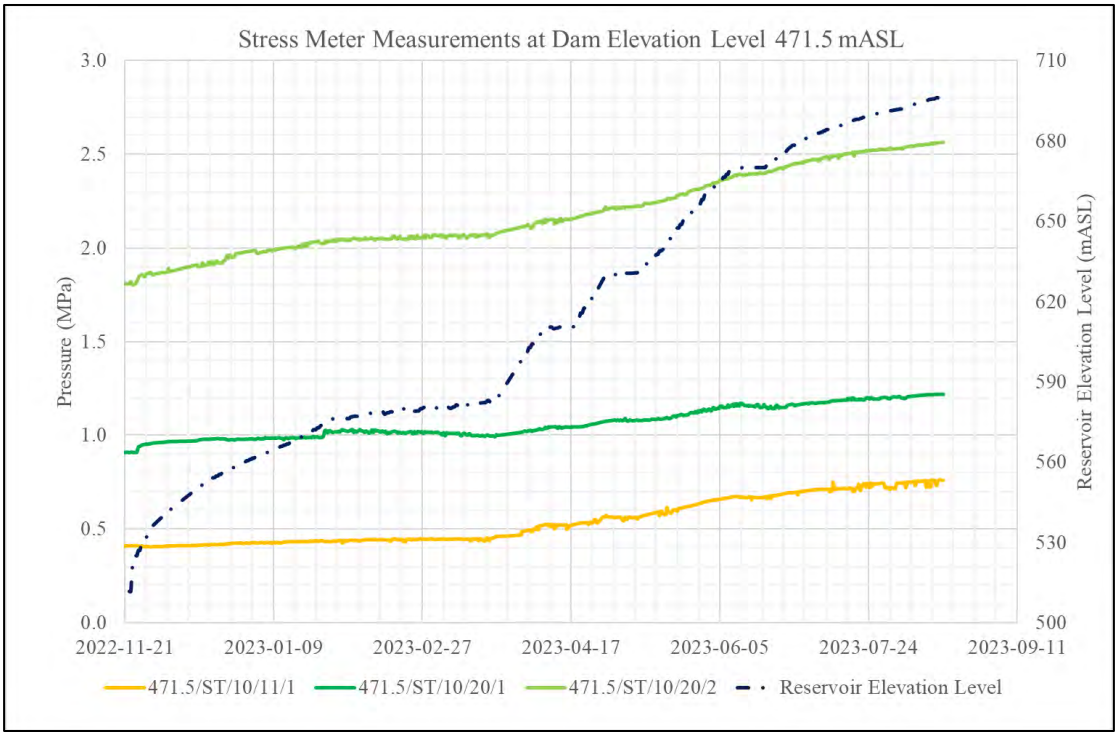

Figure 5-21: Axial stress measured in dam at elevation 471.5 mASL

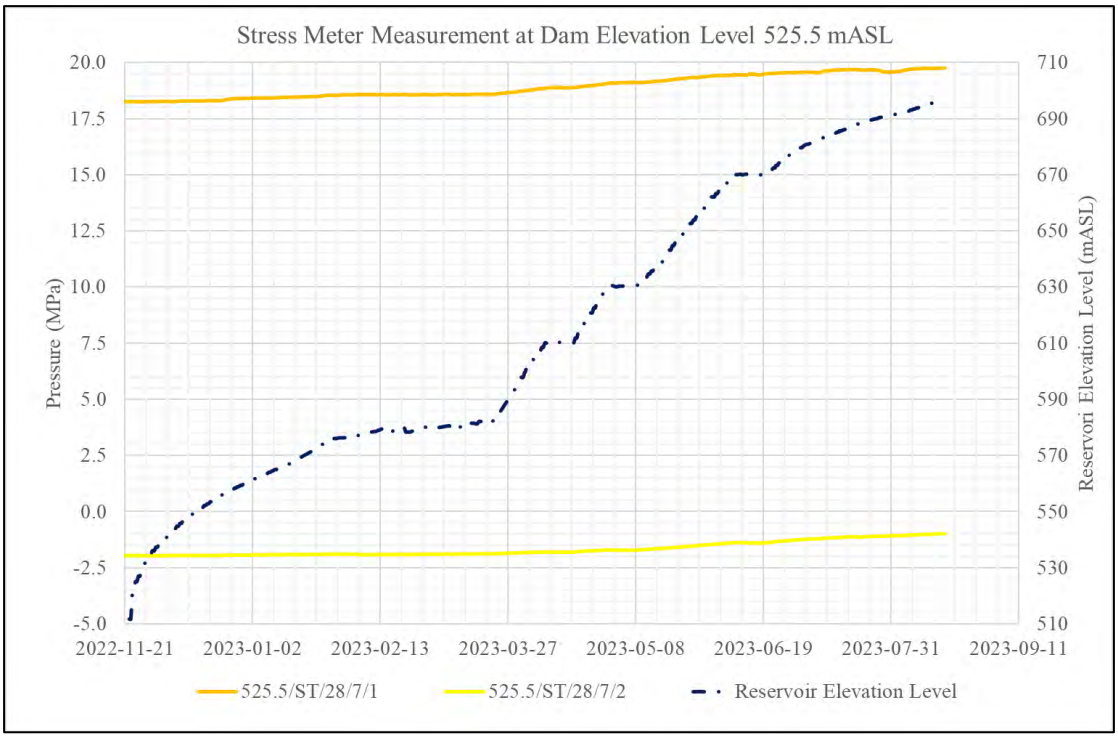

Figure 5-22: Axial stress measured in dam at elevation 525.5 mASL

A summary of the change in stress development of the dam structure under progressive loading during the period of impoundment is shown in Table 5-6. The summary shows that the stress measured at the abutments of the dam are low, due to predominantly cantilever action occurring within the lower portion of the dam, and little axial load development.

Table 5-6: Summary of change in measured stress development during period of dam impoundment

Stress meter No	Measured Change in Stress (MPa)
471.5/ST/10/11/1	-0.30
471.5/ST/10/20/1	-0.35
471.5/ST/10/20/2	-0.70
525.5/ST/28/7/1	-1.5
525.5/ST/28/7/2	-1

*negative values denote compressive stress

5.7 THERMOCOUPLES

Temperature measurements of the dam body during impoundment were taken by thermocuples cast into the dam. Thermocouples were arranged in a typical dam thermal configuration with devices placed 2 – 3 m below the surfaces of the upstream and downstream face of the dam, and at the core of the dam. The elevation levels at which thermocouples installed were considered is shown in Figure 5-23, and their locations relative to horizontal sections at the elevations indicated are shown in Figure 5-25 through Figure 5-27.

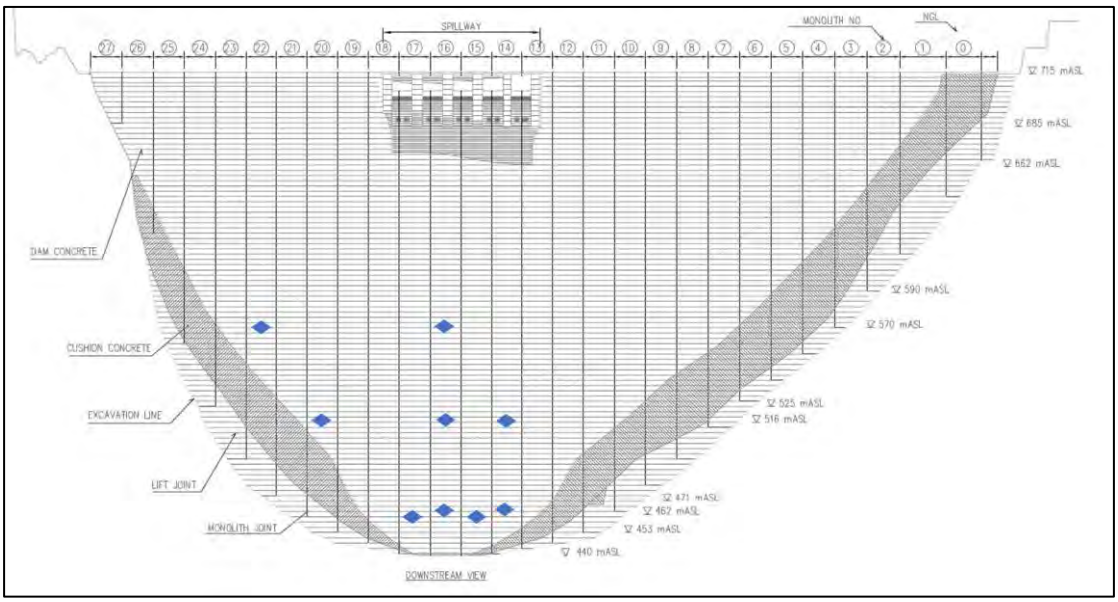

Figure 5-23: Instream view of dam showing elevation levels of thermocouples installed in dam

The instrument numbering convention for thermocouple 471.5/TK/7/17/1 refers to the instrument at elevation 471.5 mASL, installed in dam lift number 7 of monolith no 17, with the number 1 representing the upstream side (2 representing the instrument on the downstream side).

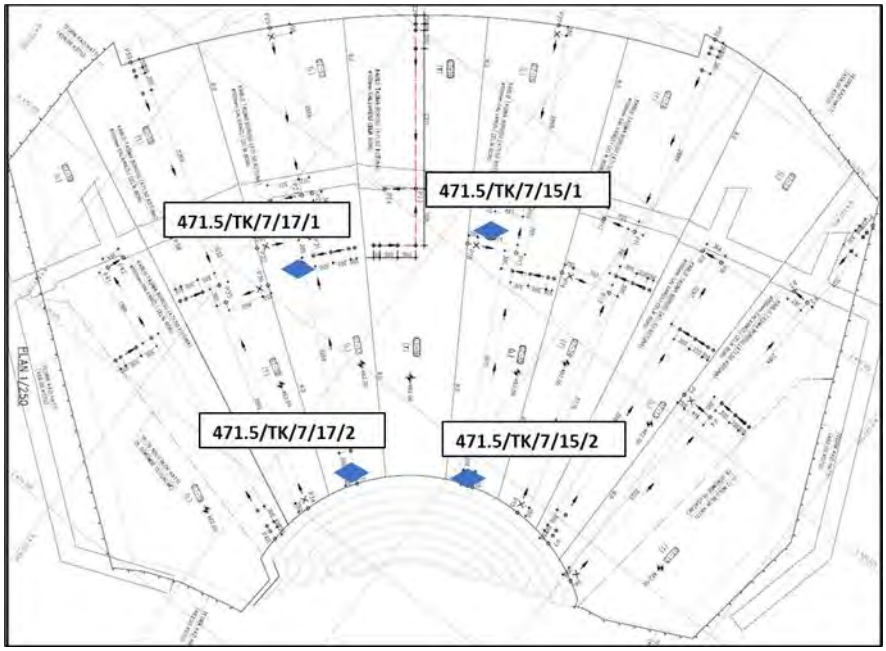

Figure 5-24: Location of thermocouples installed in the dam at elevation 462.5 mASL

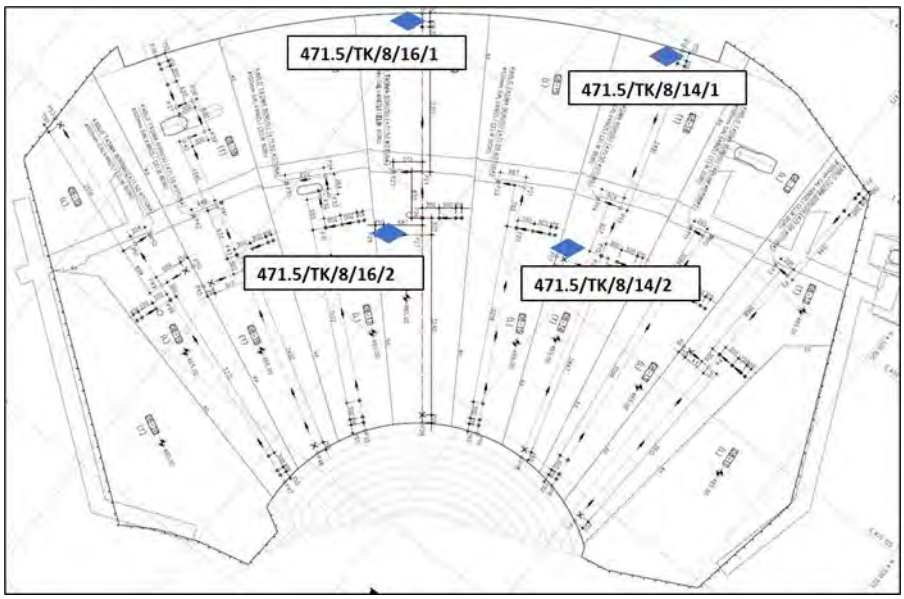

Figure 5-25: Location of thermocouples installed in the dam at elevation 465.5 mASL

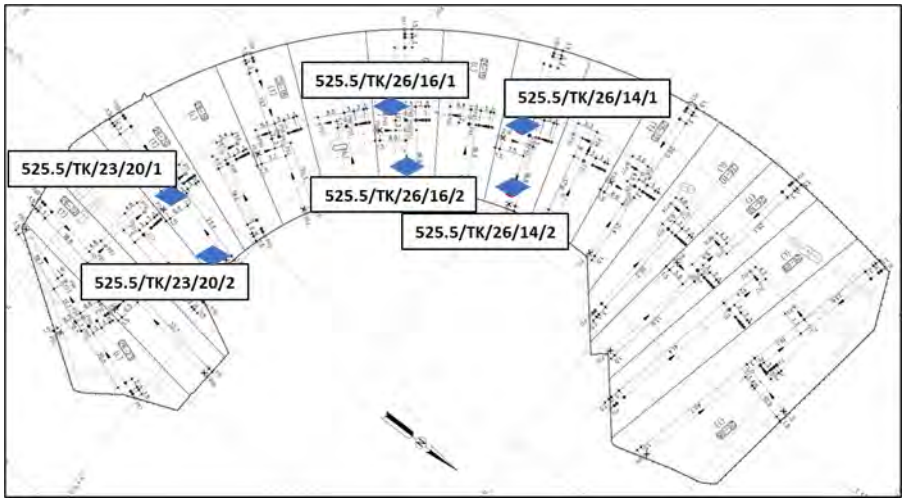

Figure 5-26: Location of thermocouples installed in the dam at elevation 516 mASL

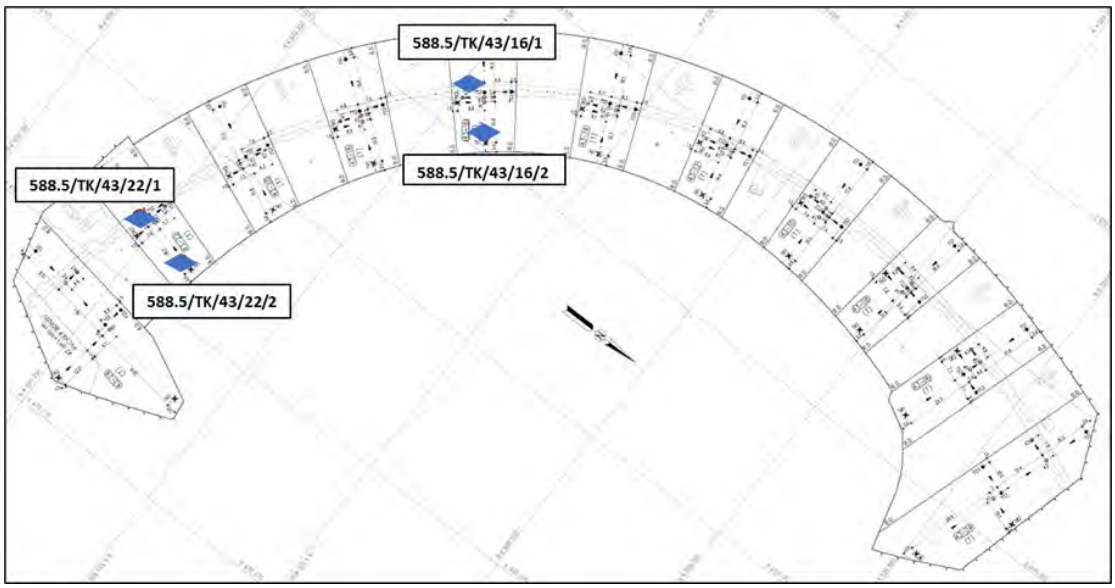

Figure 5-27: Location of thermocouples installed in the dam at elevation 570 mASL

The time-based temperature readings taken by the thermocouples installed in the dam at elevation level 462.5 mASL are shown in Figure 5-28. The curves of the time-history plot indicate that since commencement of impoundment the dam temperature has dropped. This has occurred with varying degrees depending on the location of the thermocouple device in terms of depth below the face of the dam, and proximity of the instrument relative to the impoundment water level on both upstream and downstream sides of the dam.

At elevation 462.5 mASL the dam temperature dropped due to the decrease in ambient seasonal temperatures and the cooling effect of the rising water level against the face of the dam. The temperature measurements taken at the core of the dam by instrument 471.5/TK/7/15/1 and 471.5/TK/7/17/1, show a gradual decrease in the core temperature of the dam of approximately 2.5° C from commencement of impoundment until the impoundment stage of reservoir level

696 mASL. The gradual decrease continued even during summer months of June and July 2023, and this indicates that the cooling effect of the rising water reservoir was greater than the impact of ambient temperature increases of summer, and also that there is a lag between the temperature response of the dam and ambient conditions of the air and water. This is expected due to thermal inertia of the large and thick dam (Sheibany & Ghaemian, 2006).

When the upstream water reservoir level reached the lower inlet works at elevation level 560 mASL, flow was released through the outlet works and into the tailwater pond, building up a downstream water elevation level of 500.5 mASL. As a result of this the dam was cooled from both upstream and downstream face from the exposure to the water reservoir body. As discussed in section 4.7.2, it is the upper portions of a deep reservoir pool of a dam that experiences any significant warming during summer.

The temperature state on the downstream face of the dam as measured by thermocouples 471.5/TK/7/15/2 and 471.5/TK/7/17/2, show a marked decrease in the gradient of temperature drop from January 2023 when the upstream reservoir level reached 560 mASL, and flow was released through the dam lower outlet works. The close proximity of the thermocouples to the downstream face indicates the sensitivity of the dam outer shell to temperature change at the face of the dam. In this region the dam temperature dropped by approximately 3° C from commencement of impoundment until impoundment stage at reservoir level 696 mASL. A drop of 5° C was experienced during the peak of Winter.

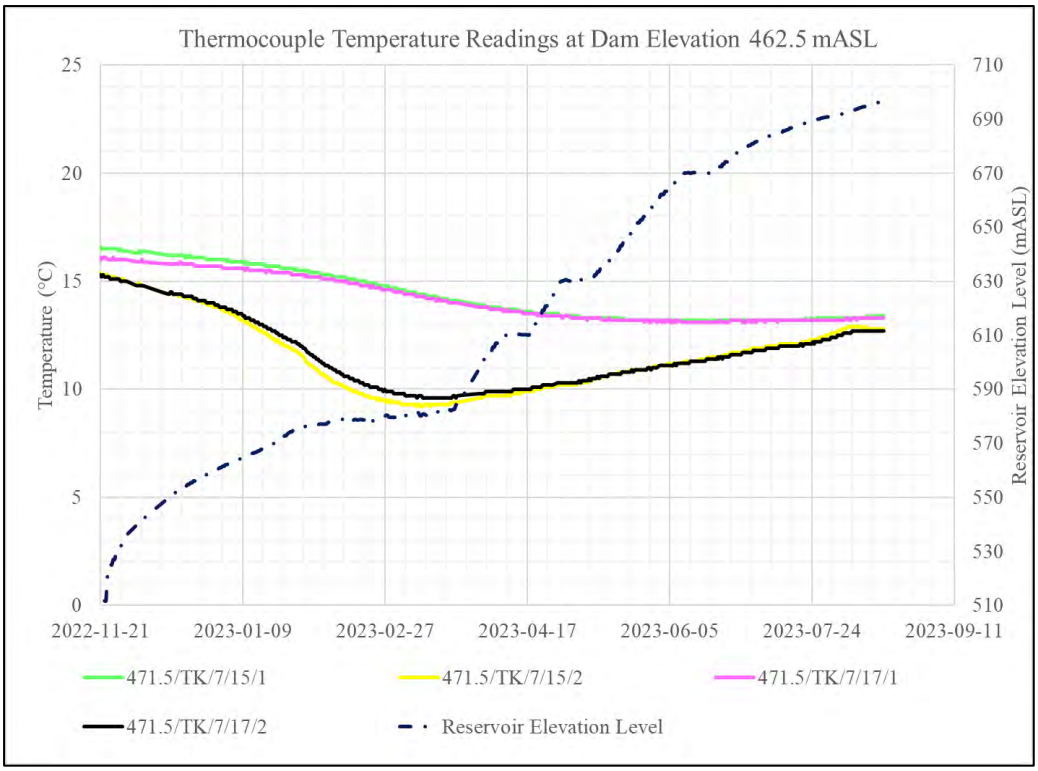

Figure 5-28: Temperature time history readings produced by thermocouples installed at 462.5 mASL

The time-based temperature readings taken by the thermocouples installed in the dam at elevation level 465.5 mASL are shown in Figure 5-29. At elevation 465.5 mASL the dam temperature dropped due to the decrease in ambient seasonal temperatures, and the cooling effect of the rising water level against the face of the dam.

The temperature measurements taken at the core of the dam by instrument 471.5/TK/8/14/2 and 471.5/TK/8/16/2, show a gradual decrease in the core temperature of the dam of approximately 1° C from commencement of impoundment until the impoundment stage of reservoir level 696 mASL. The gradual decrease continued even during summer months of June and July 2023, and this indicates that the cooling effect of the rising water reservoir was greater than the impact of ambient temperature increases of summer, and that there is a lag between temperature response of dam and ambient conditions of the air and water.

The temperature state on the upstream face of the dam at 465.5 mASL, as measured by thermocouples 471.5/TK/8/14/1 and 471.5/TK/8/16/1, indicate a temperature decrease of approximately 2.5° C, caused by the rising reservoir level on the upstream side of the dam, during impoundment.

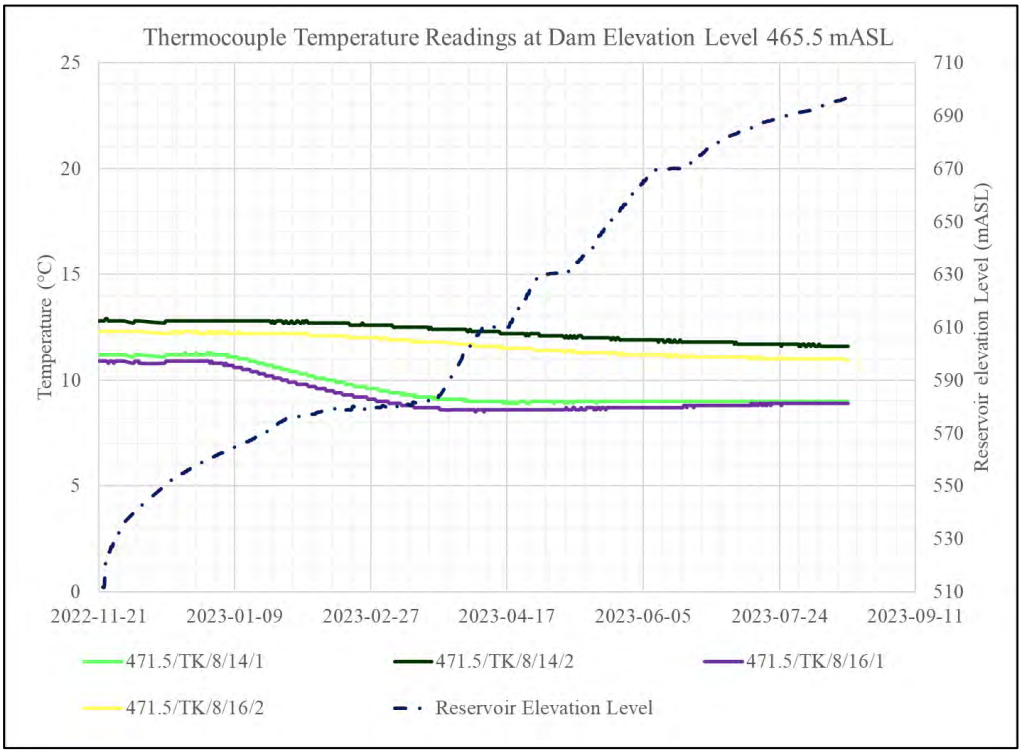

Figure 5-29: Temperature time history readings produced by thermocouples installed at 465.5 mASL

The time-based temperature measurement plots of the dam at elevation level 516 mASL are shown in Figure 5-30. The plotted curves show an overall decrease in the temperature state of the dam body, at this elevation, during impoundment of the dam reservoir. The cooling of the

dam was again caused by a combination of the initial drop in ambient temperature and later the cooling effect of the rising water reservoir on the dam body.

At elevation 516 mASL, the temperature measurements taken at the core of the dam by instrument 525.5/TK/26/14/1, 525.5/TK/26/16/1 and 525.5/TK/26/20/1, show a gradual decrease in the core temperature of the dam of approximately 2 - 3° C, from commencement of impoundment, until the impoundment stage of reservoir level 696 mASL. The gradual decrease continued even during summer months of June and July 2023, and this indicates that the cooling effect of the rising water reservoir was greater than the impact of ambient temperature increases of summer.

The temperature state on the downstream face of the dam as measured by thermocouples 525.5/TK/26/14/2 and 525.5/TK/26/16/2, show an initial average decrease in temperature of approximately 3 ° C until the peak of Winter, followed by a subsequent average increase of 2.5 ° C as the season returns to Summer. Device 525.5/TK/26/20/2 shows a constant temperature reading and is assumed to be malfunctioning as its readings are not consistent with other instruments. Device 525.5/TK/26/20/2 measurements were deemed unreliable for purpose of this calibration.

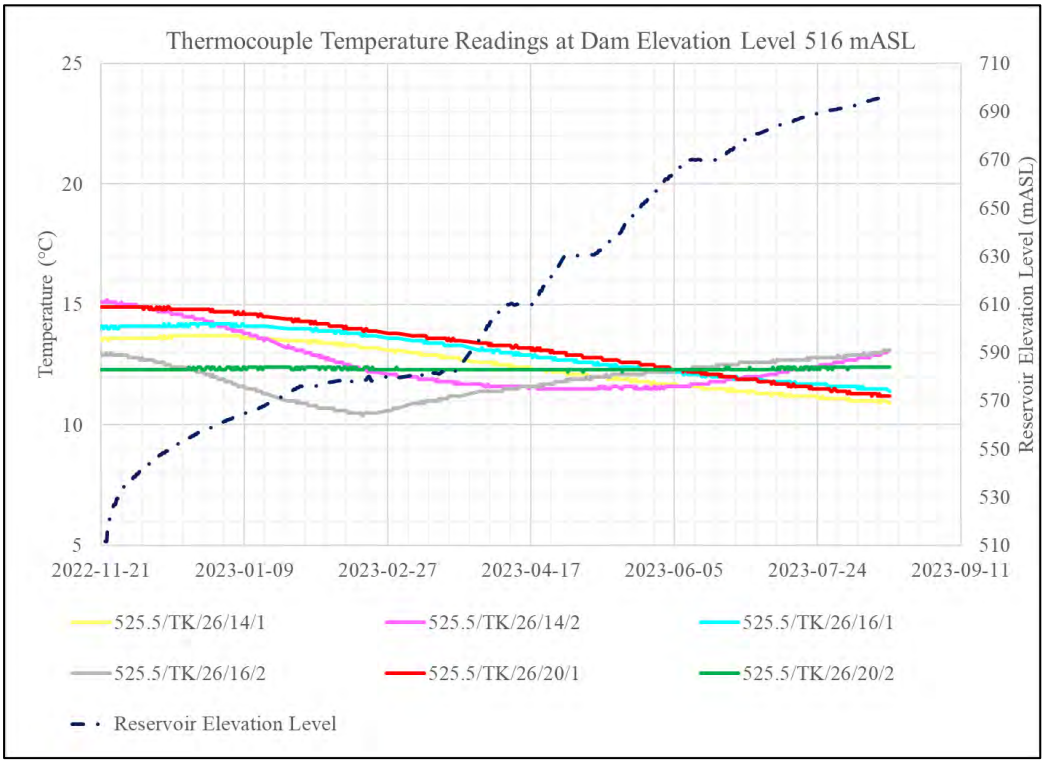

Figure 5-30: Temperature time history readings produced by thermocouples installed at 516 mASL

The time-based temperature measurement plots of the dam at elevation level 570 mASL are shown in Figure 5-31. The plotted curves show an overall decrease in the temperature state of the dam body, at this elevation, during impoundment of the dam reservoir.

At elevation 570 mASL, the temperature measurements taken at the core of the dam by instrument 588.5/TK/43/16/1 and 588.5/TK/43/22/1, show a gradual decrease in the core temperature of the dam of approximately 1 ° C from commencement of impoundment until the impoundment stage of reservoir level 610 mASL in April 2023. Subsequently the temperature increased again by 0.5 ° C until the reservoir level reaches 696 mASL in August 2023.

The temperature state on the downstream face of the dam as measured by thermocouples 588.5/TK/43/16/2 and 525.5/TK/43/22/2, show an initial average decrease in temperature of approximately 5 ° C until the peak of Winter, followed by a subsequent average increase of 4.5 ° C as the season returns to Summer.

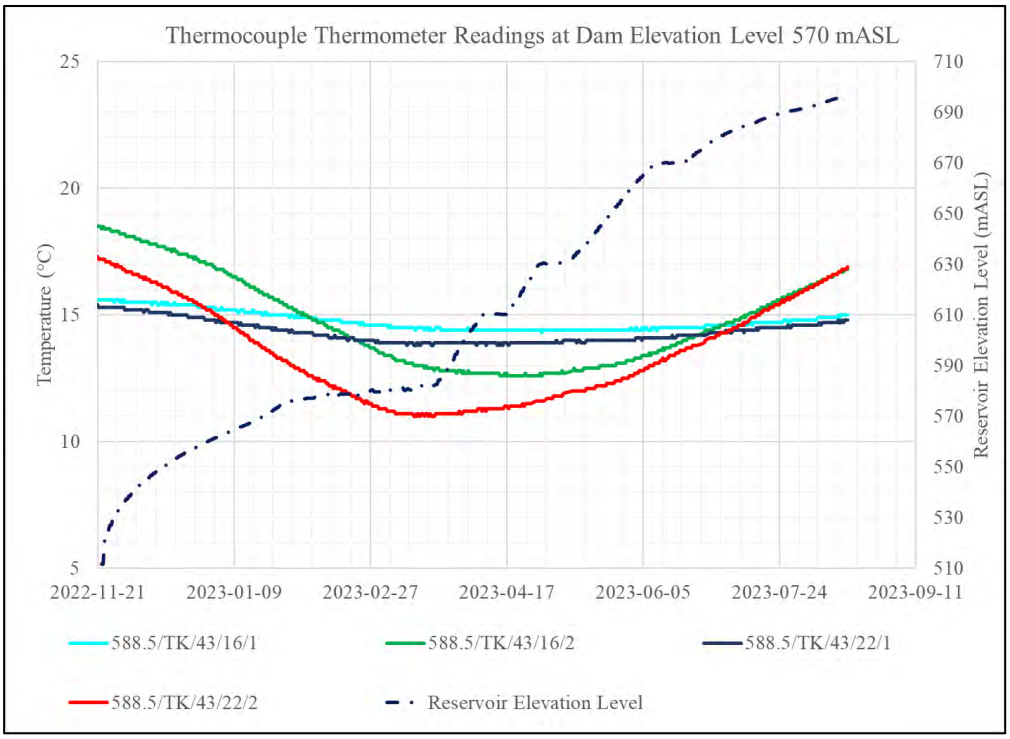

Figure 5-31: Temperature time history readings produced by thermocouples installed at 570 mASL

A summary of the temperature measurements taken of the dam structure at impoundment elevation level 696 mASL is shown in Table 5-7.

Table 5-7: Summary of thermocouple measurement values at impoundment elevation level 696 mASL

Thermocouple No	Elevation Level (mASL)	Measured Temperature (°C)
471.5/TK/7/15/1	462.5	12.7
471.5/TK/7/15/2	462.5	13.3
471.5/TK/7/17/1	462.5	12.7
471.5/TK/7/17/2	462.5	13.3
471.5/TK/8/14/1	465.5	11.6
471.5/TK/8/14/2	465.5	8.9
471.5/TK/8/16/1	465.5	10.9
471.5/TK/8/16/2	465.5	8.9
525.5/TK/26/14/1	516	11
525.5/TK/26/14/2	516	13.1
525.5/TK/26/16/1	516	11.5
525.5/TK/26/16/2	516	13.1
525.5/TK/26/20/1	516	11
525.5/TK/26/20/2	516	12.4
588.5/TK/43/16/1	570	14.8
588.5/TK/43/16/2	570	16.8
588.5/TK/43/22/1	570	14.8
588.5/TK/43/22/2	570	17.0

5.8 UPLIFT STATIONS

Uplift does not represent a particularly significant load on an arch dam, unlike the situation for a gravity dam which normally has a wide base. The standard USACE/USBR/FERC design assumption of a 66% drain efficiency is generally conservative unless drains are blocked or unfavourable foundation jointing exists, causing uncontrolled flow paths to develop around the drains.

Hydrostatic uplift pressures beneath the base of the dam were measured at several dam monoliths, using uplift stations installed at the lowest gallery in these monoliths. The uplift stations are configured with four manometer tubes installed in boreholes along an angular sweep from the upstream to the downstream side of the gallery, as illustrated in Figure 5-32. The open end of the tube is located at the interface between the dam and foundation and the closed end on a manometer pressure gauge. The uplift pressures distributions measured at the

base of the dam were evaluated and compared to the assumed design uplift distribution, and where they differed from design assumptions, the measured values were considered for uplift loading of the dam FE model as dicussed in Section 4.7.1.

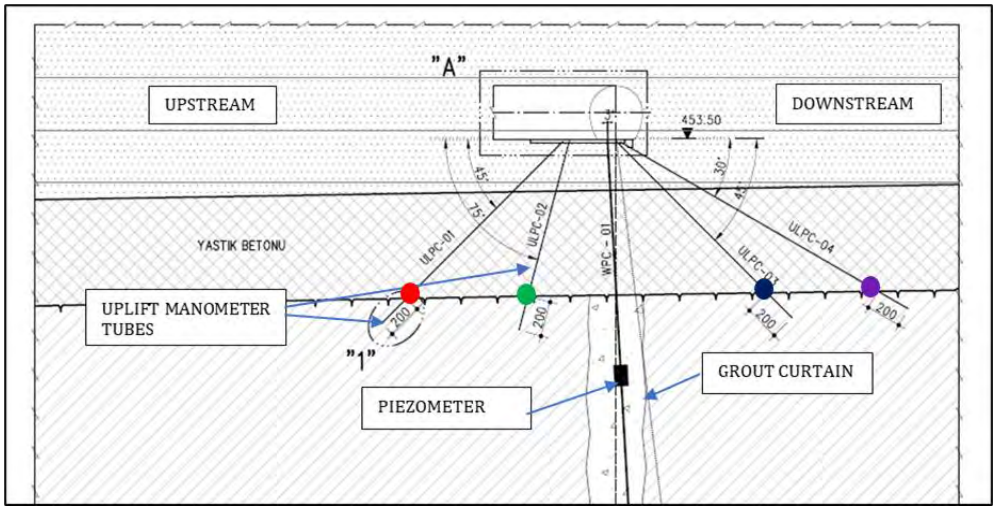

Figure 5-32: Uplift station configuration indicating sweep configuration of four manometer pipes

A view of the dam cushion base FE model showing the monoliths at which uplift stations were installed and the locations where the manometer pipes intersect with the dam-foundation interface are shown in Figure 5-33. The offset distance of each manometer tube from the heel of the dam, the offset of the drain location and the seepage path length are shown in Table 5-8. The table also indicates the gallery elevation level for each of the uplift stations. The pink line indicates the alignment of the drainage curtain at the interface between the dam and foundation.

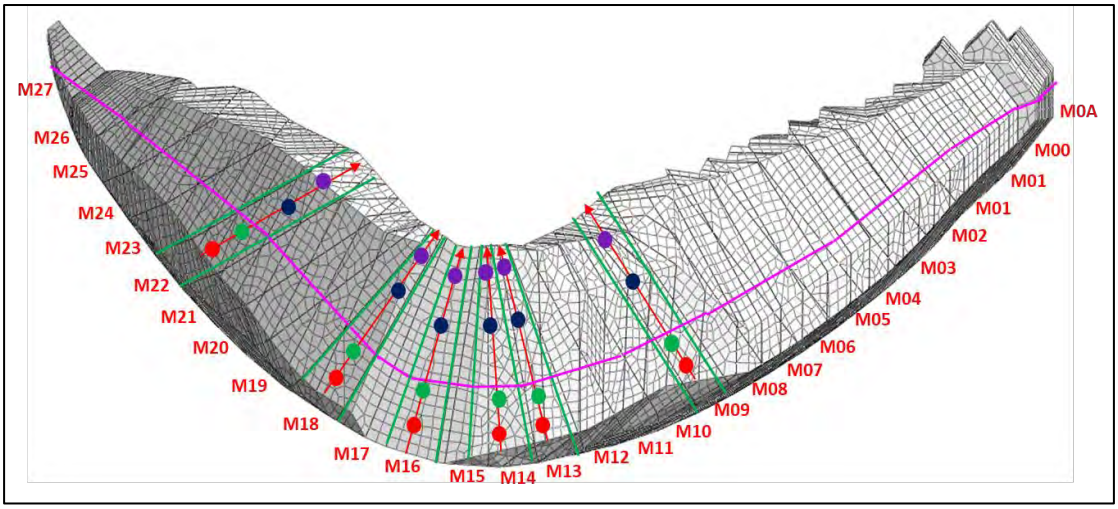

Figure 5-33: Location of uplift manometer tubes in relation to seepage path at base of dam

Table 5-8: Location of manometer tubes along seepage path of dam-foundation interface from heel

Uplift Station Monolith No (Elevation in mASL)	Offset Distance from Heel of Dam (m)					
	Tube 1	Tube 2	Tube 3	Tube 4	Drain location	Seepage Path Length along Dam Footprint
M09 (507.5)	12.9	15.7	25.6	29.1	17.0	84.0
M13 (453.5)	15.5	18.6	28.3	31.2	20.0	84.0
M14 (453.5)	12.6	20.1	36.5	43.0	23.0	87.0
M16 (453.5)	11.2	21.9	44.3	54.3	26.0	90.0
M18 (453.5)	16.3	20.3	31.4	35.1	22.0	84.0
M22 (507.5)	5.8	15.2	28.0	30.7	18.0	78.0

The uplift pore pressure measurements taken, during the impoundment period, at each of the four manometer tubes along the dam-foundation interface, for monoliths 9, 13, 14, 16, 18 and 22 are shown in Figure 5-34 through Figure 5-39. The unit of Bar is used to indicate pressure, with 1 Bar = 100 kPa.

A trend is common between the uplift pressure readings observed along the seepage paths of the various monoliths. In all instances the general pressure build up is directly proportional to the rising water level of the upstream reservoir during impoundment. With the exception of the pressure measurements taken at the base of dam monolith 9, during the very early stages of impoundment, the uplift station pressure measurements all show the highest readings taken at tube 1, and the lowest at tube 4. The effectiveness of the dam-foundation drainage system in reducing the uplift pressure is evident from the significant drop in pore pressure measured between manometer tube 1 and 2.

Instrument labelling refers to elevation/monolith/gauge type - number/installation depth and consequently, instrument 453.5/13/UPLC-01/6.35m is uplift manometer No 1, installed at a depth of 6.35 m in monolith No. 13 in gallery elevation 453.5 mASL. Indicated pressure is the water head measured at the gauge and consequently, a maximum reading of 24.3 Bar on instrument 453.5/16/UPLC-01/20.87m is equivalent to a water pressure head of 675.63 mASL (453.5-20.87+24.3 x 10) and a maximum reading of 15.4 Bar on instrument 507.5/09/UPLC-01/5.78m is equivalent to a water pressure head of 655.72 mASL (507.5-5.78 + 15.4 x 10). See Figure 5-37 and Figure 5-35.

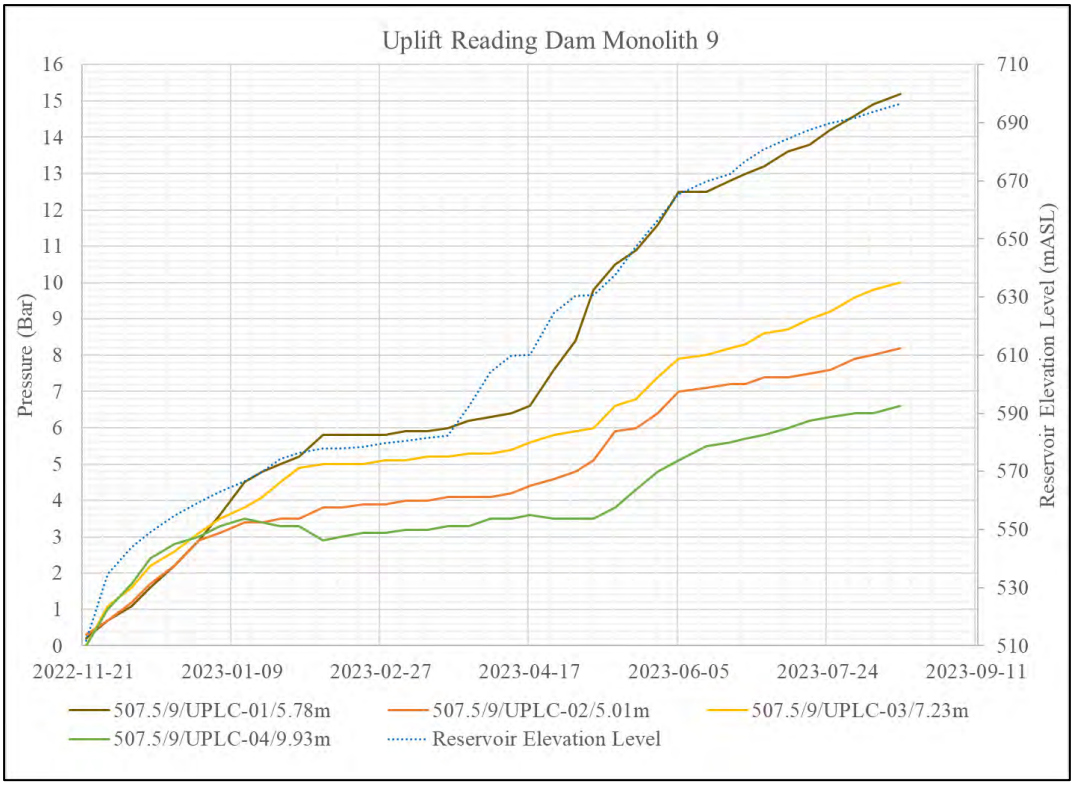

Figure 5-34: Uplift pressure measured along seepage path at dam-foundation interface for monolith 9

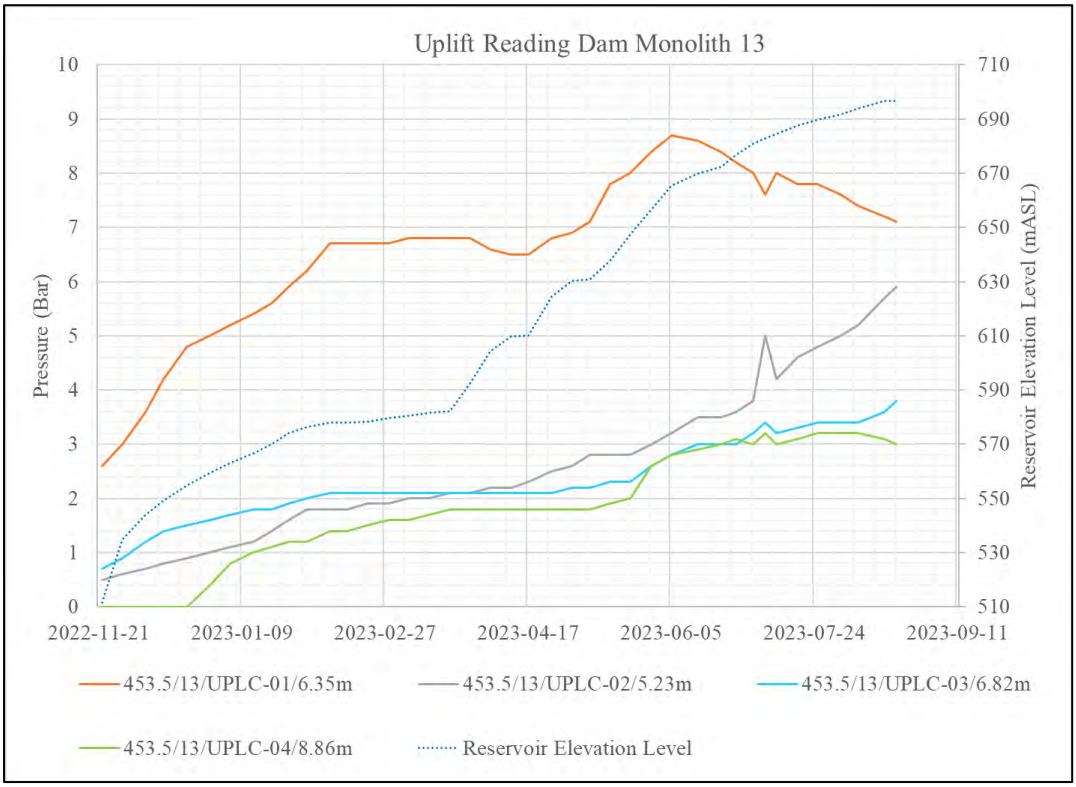

Figure 5-35: Uplift pressure measured along seepage path at dam-foundation interface for monolith 13

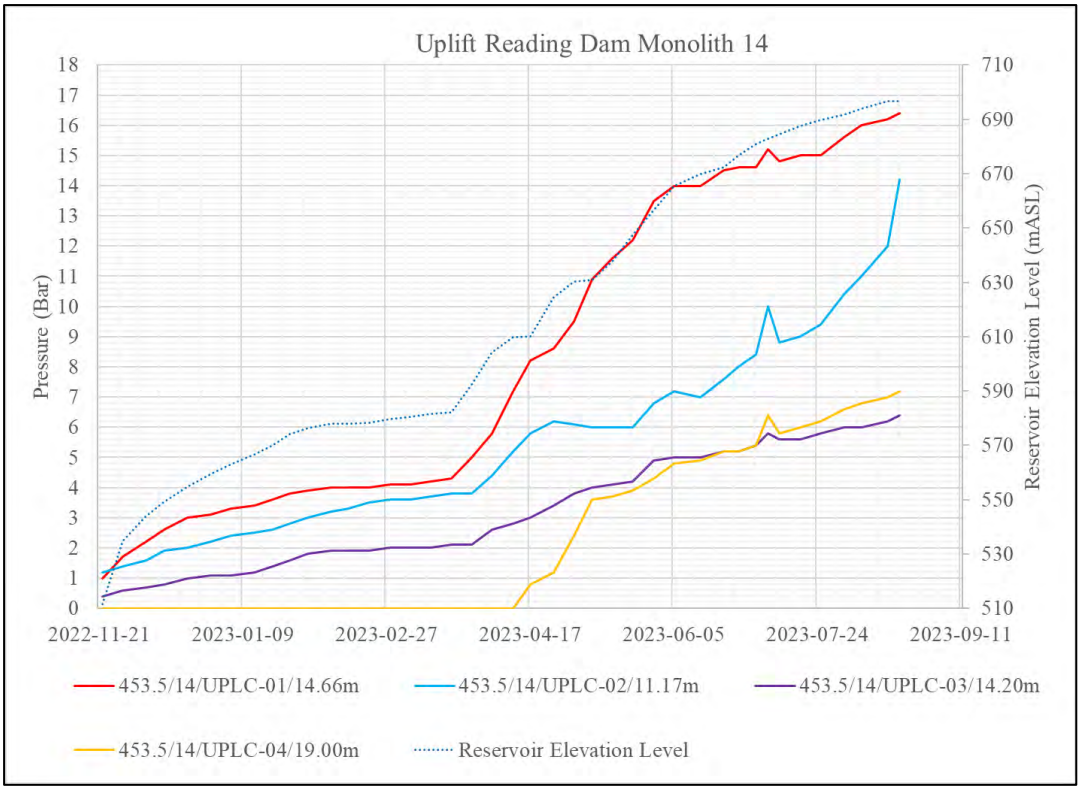

Figure 5-36: Uplift pressure measured along seepage path at dam-foundation interface for monolith 14

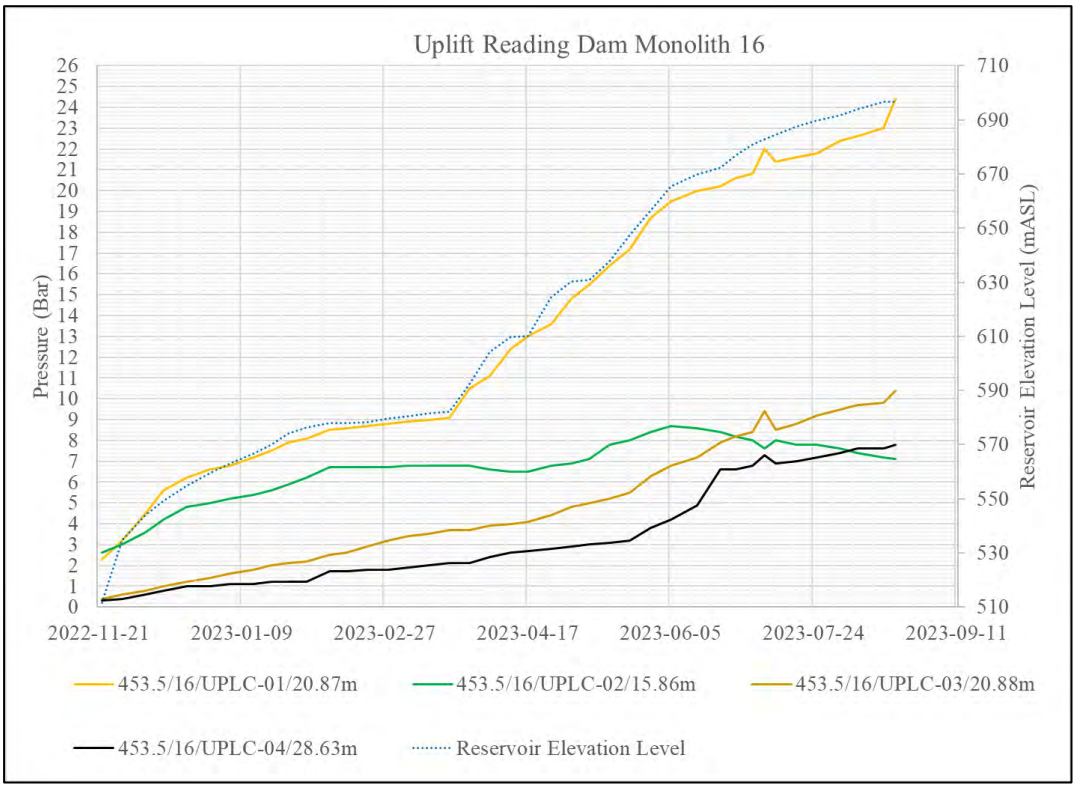

Figure 5-37: Uplift pressure measured along seepage path at dam-foundation interface for monolith 16

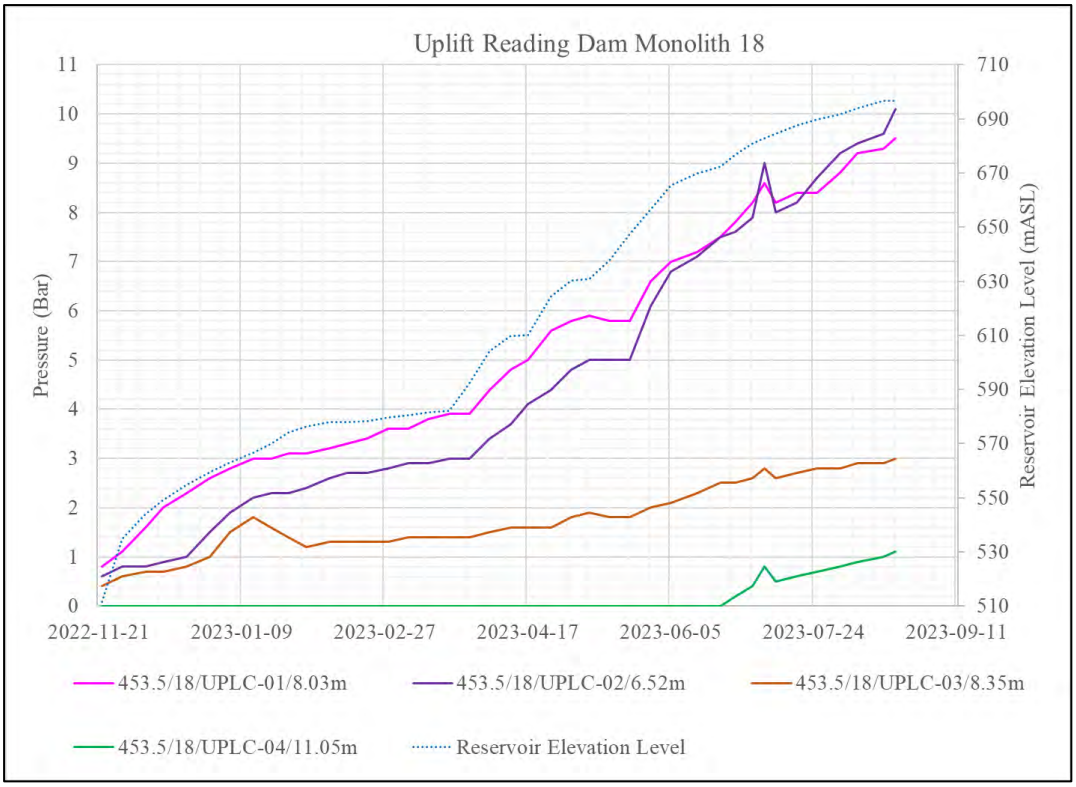

Figure 5-38: Uplift pressure measured along seepage path at dam-foundation interface for monolith 18

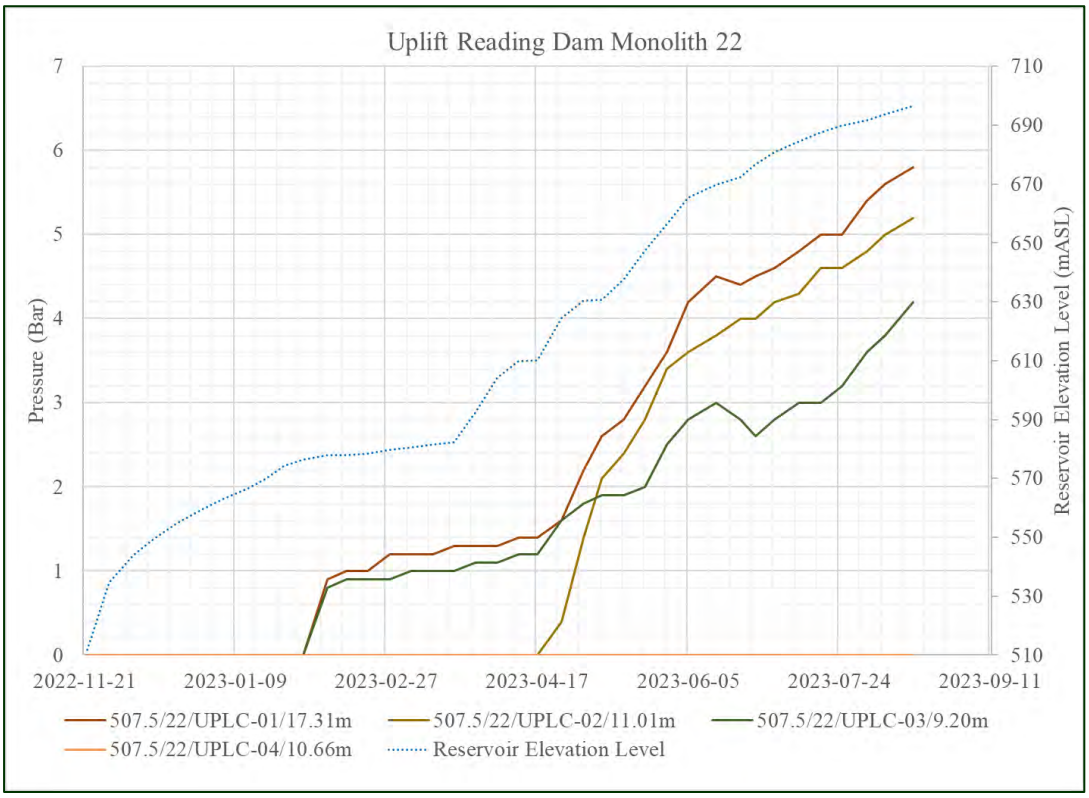

Figure 5-39: Uplift pressure measured along seepage path at dam-foundation interface for monolith 22

The four pressure readings along the uplift seepage path at the dam-foundation interface were plotted to create an uplift pressure diagram alongside plots of the design uplift pressure,

assuming 67% drain efficiency. A comparison of the design uplift and measured uplift pressure for monoliths 9, 13, 14, 16, 18 and 22 at reservoir impoundment stage 696 mASL are shown in Figure 5-40 through Figure 5-45.

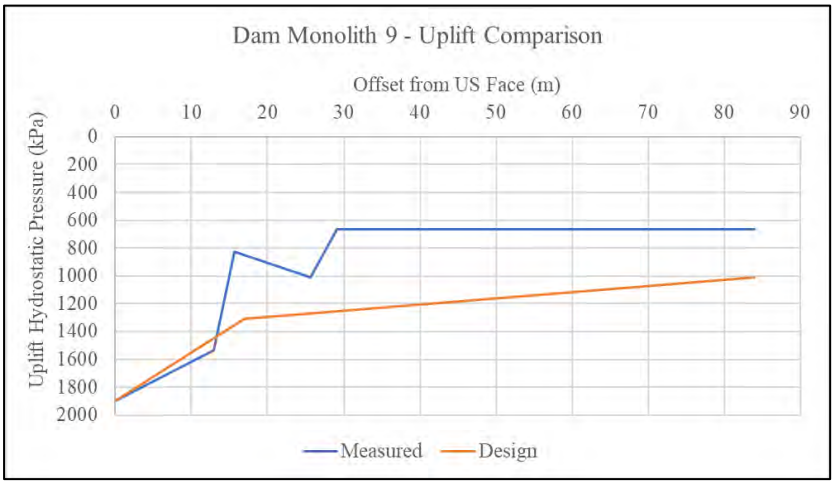

Figure 5-40: Comparison of design uplift against measured uplift pressure for monolith 9 at reservoir elevation level 696 mASL

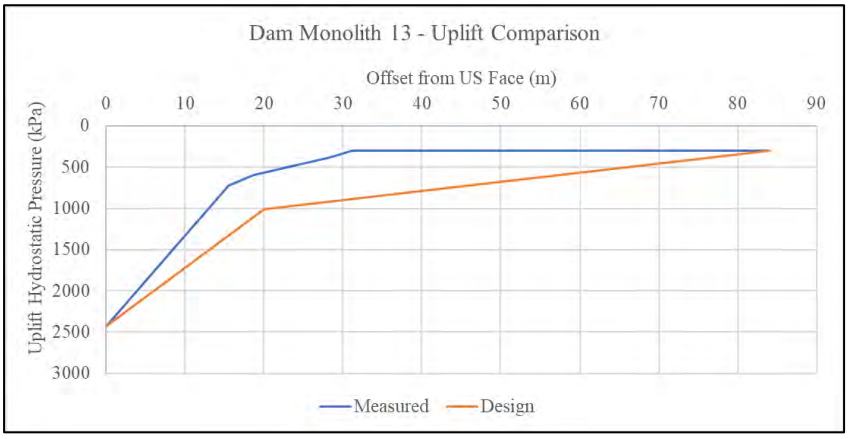

Figure 5-41: Comparison of design uplift against measured uplift pressure for monolith 13 at reservoir elevation level 696 mASL

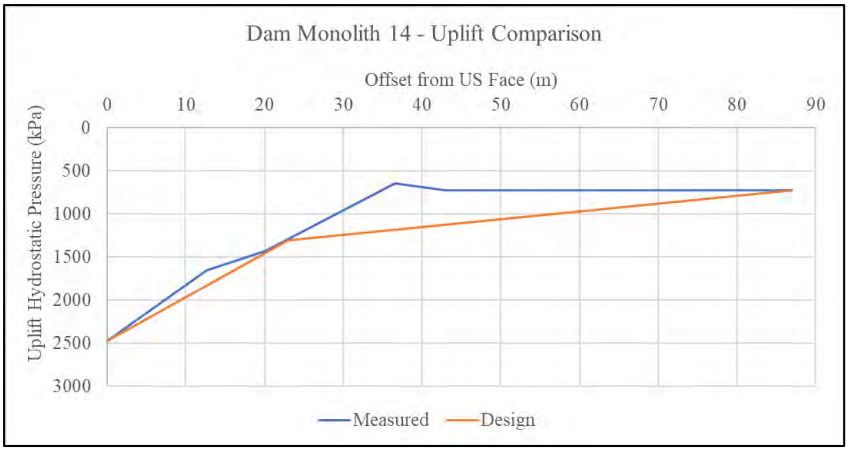

Figure 5-42: Comparison of design uplift against measured uplift pressure for monolith 14 at reservoir elevation level 696 mASL

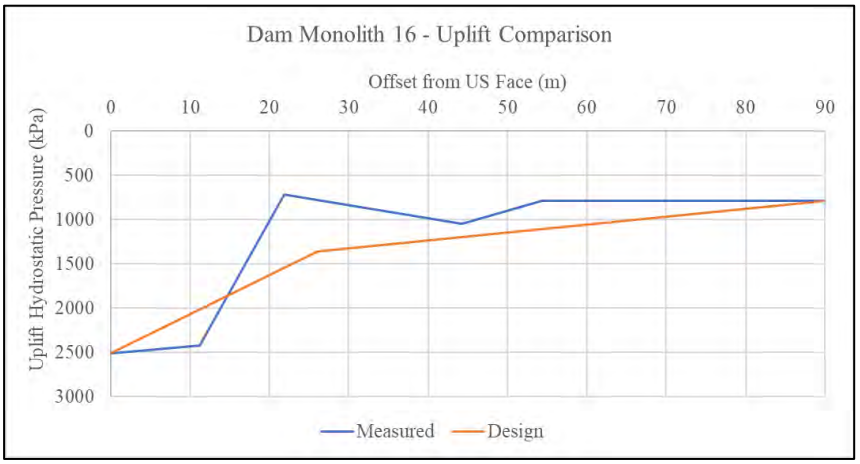

Figure 5-43: Comparison of design uplift against measured uplift pressure for monolith 16 at reservoir elevation level 696 mASL

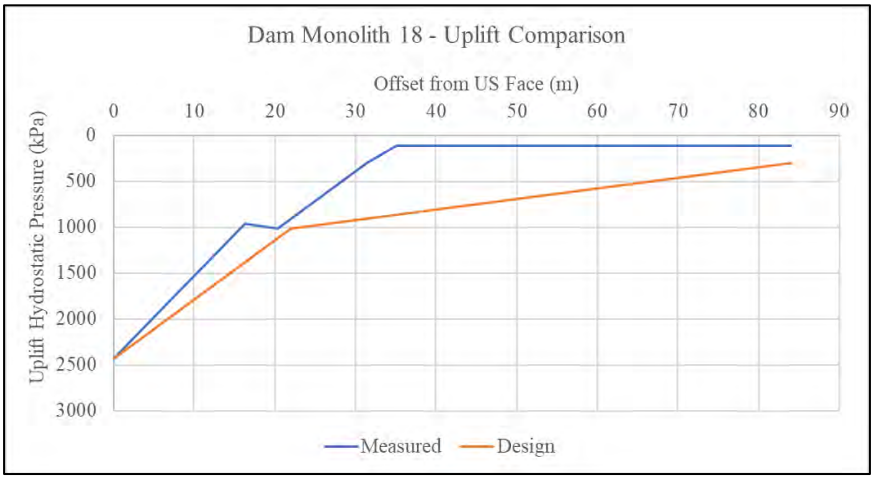

Figure 5-44: Comparison of design uplift against measured uplift pressure for monolith 18 at reservoir elevation level 696 mASL

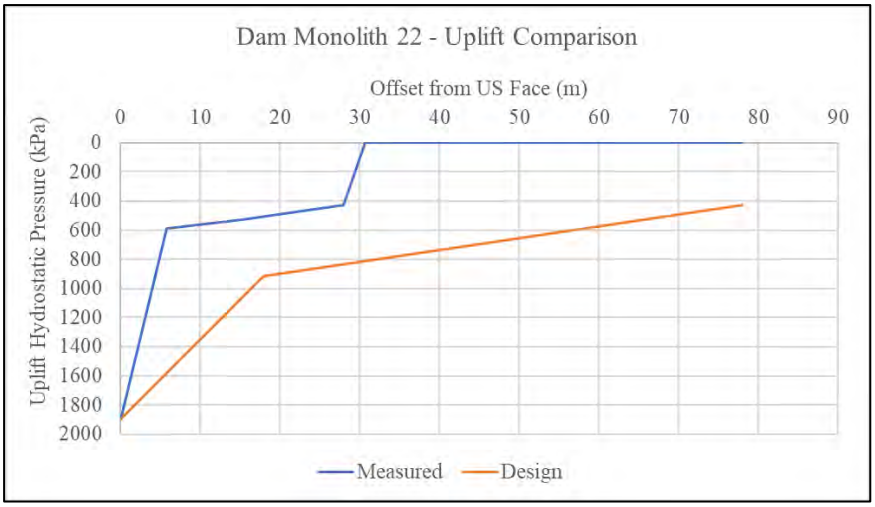

Figure 5-45: Comparison of design uplift against measured uplift pressure for monolith 22 at reservoir elevation level 696 mASL

Comparisons of the design uplift pressure distribution with actual measured uplift distribution indicate that the design assumption is conservative. This has been shown to be the case by investigations done on large American dams for which a direct comparison is illustrated in Figure 5-46 (Casagrande, 1961).

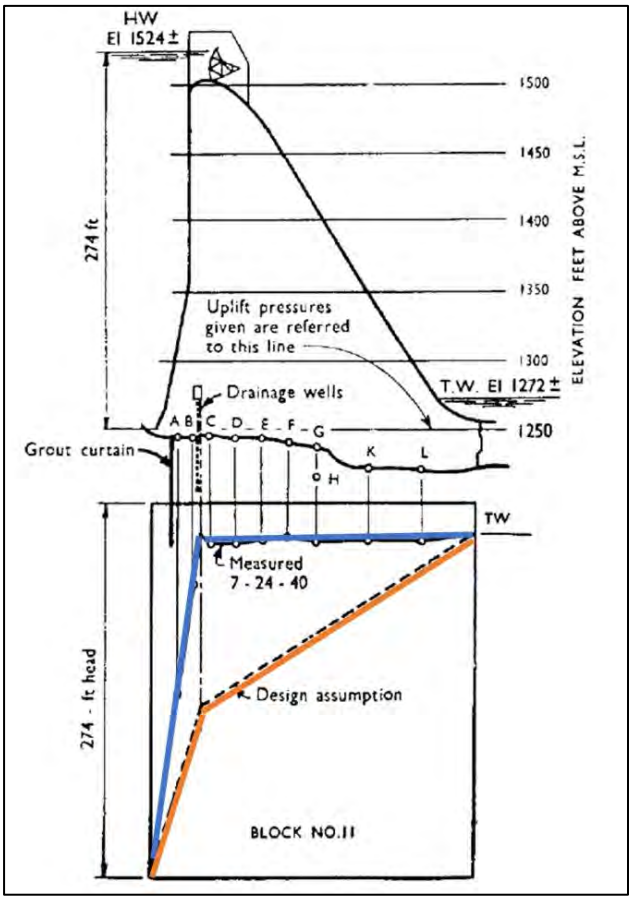

Figure 5-46: Assumed design uplift pressure distribution vs measured uplift (Casagrande, 1961)

5.9 PIEZOMETERS

Transducer piezometers were installed in the rock mass foundation below the dam galleries at elevations 453.5 mASL, 507.5 mASL, 564.5 mASL, 612.5 mASL and 660 mASL. The configuration of the piezometers in relation to the dam, drainage grout curtain and gallery are shown in Figure 5-47. The piezometers were installed below the gallery in a collinear formation of four instruments traversing a sub-vertical line on the downstream side of the drainage grout curtain, to measure the pore pressures along the seepage path around the grout curtain. The four piezometers are shown as the red, green navy blue and purple blocks in the image, with the red indicating the deepest device.

The piezometers were installed to a depth of approximately 65 m below founding level of the dam, except for the piezometer installed below dam monolith four which has a maximum depth of 58 m, due to its location high up on the abutment of the dam and associated low height of the dam at this location.

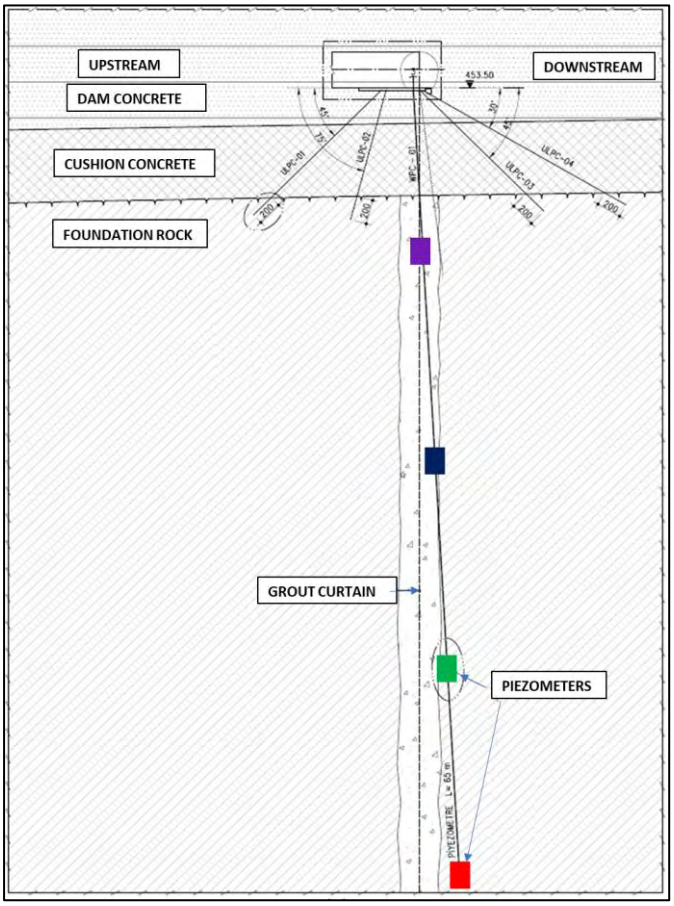

Figure 5-47: Configuration of piezometers in dam foundation

Time-based plots of the total pressure head in metres as measured by the piezometers at the various depth intervals are shown in Figure 5-48 through Figure 5-55. Gauge labelling refers to elevation level/instrument type/lift No./monolith No./installation depth (e.g. 564.5/TP/42/4/58m).

The measurement considers the elevation of the instrument and then adds the measured pore pressure in terms of metres of head. It can be seen that the sets of piezometers installed below starting impoundment reservoir level commence with the same reading, whilst those installed above impoundment starting reservoir level do not, as the water level reaches them at different stages.

A distinct reaction to the impounded water is evident in the measured pressure change of all the plots, except for the measurements taken below monolith block 18. The pore pressures measured under block 18 as shown in Figure 5-52 show an almost insignificant response to the rising water impoundment level. Assuming the instruments are not malfunctioning, this may indicate a local zone of rock mass with low permeability allowing negligible seepage to pass around the drainage curtain. The discrete change in pressure measured at all depths on 2022-12-27 may however indicate a malfunctioning of the piezometers.

The pressures measured at the various piezometers, are all substantially lower than the pressures associated with the design uplift loading, and corroborate well with the pressures measure by the uplift stations along the dam-foundation seepage path. The measurements show that the drainage system comprising of internal drains in the dam and a grout curtain, are working effectively to reduce pore pressure build up in the foundation below the dam.

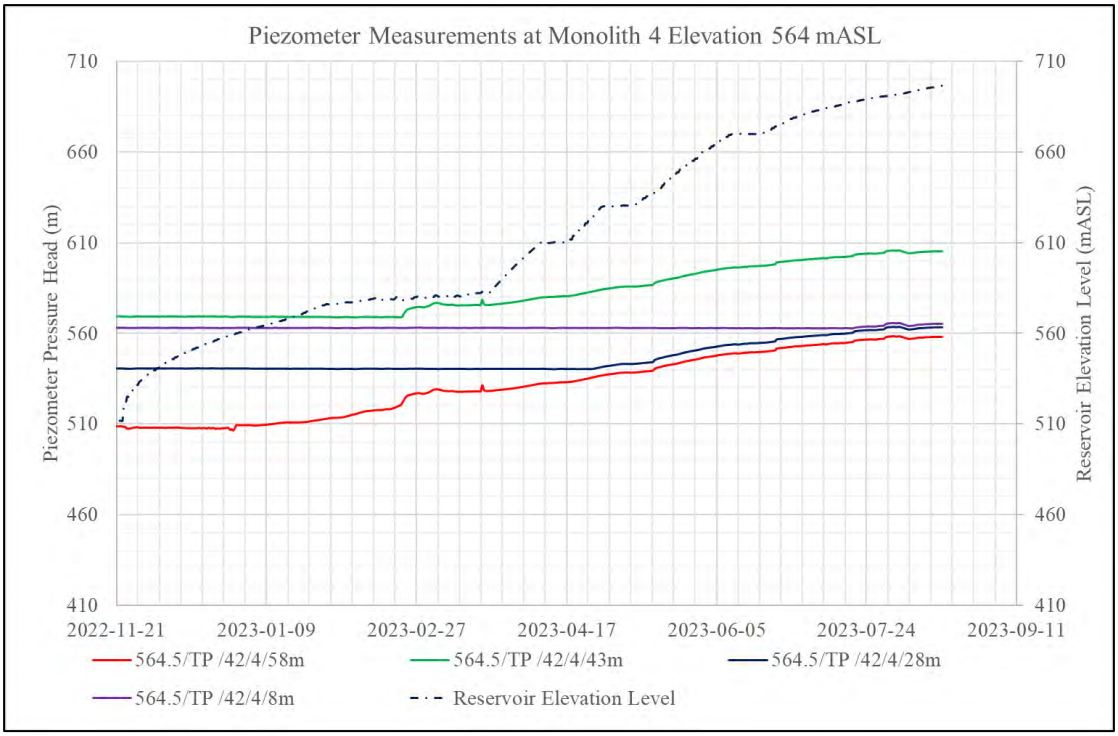

Figure 5-48: Piezometer Response at Elevation 564.5 mASL Monolith Block 4

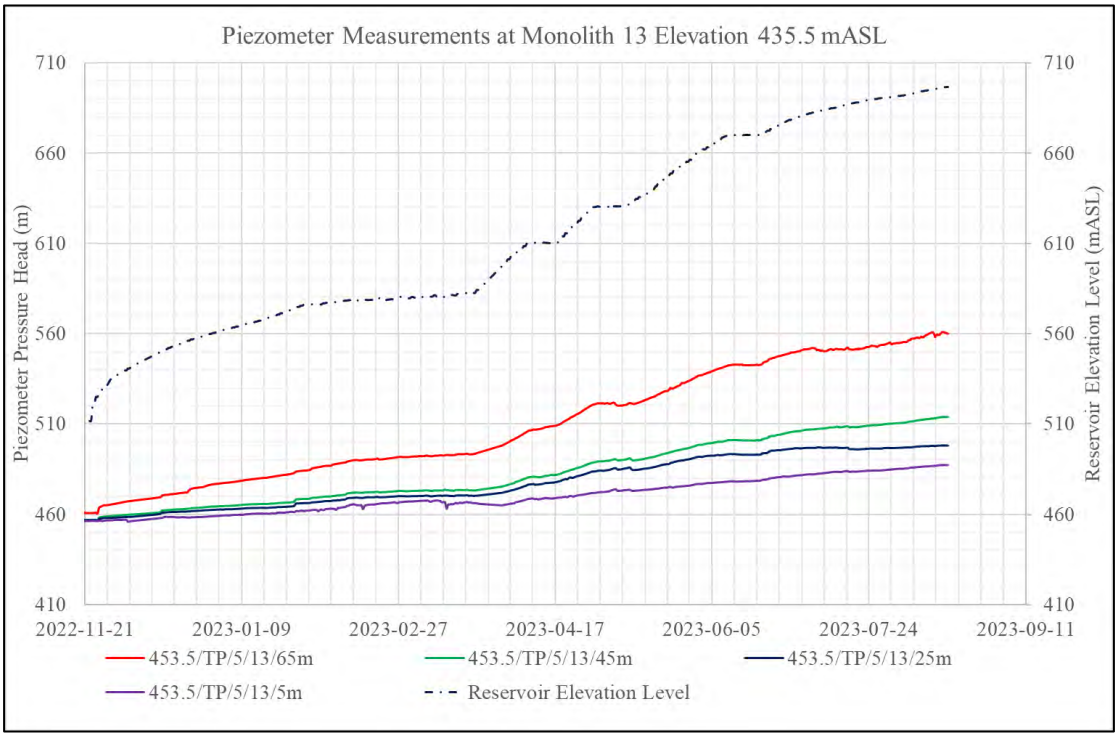

Figure 5-49: Piezometer Response at Elevation 453.5 mASL Monolith Block 13

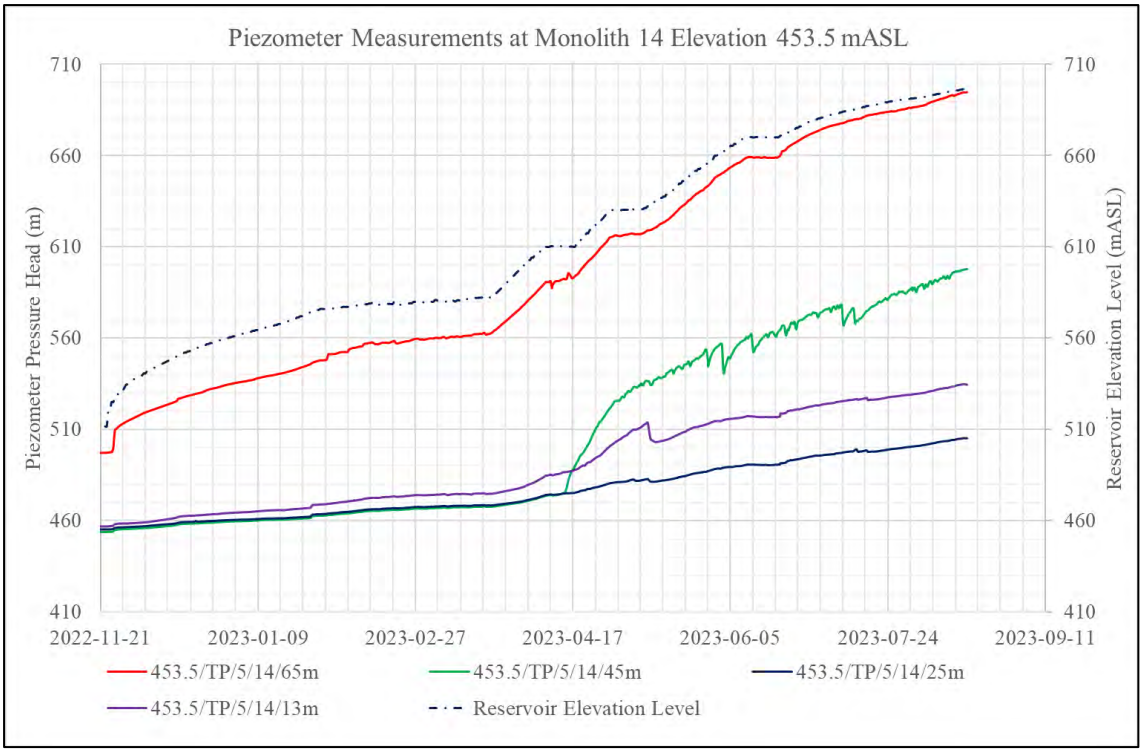

Figure 5-50: Piezometer Response at Elevation 453.5 mASL Monolith Block 14

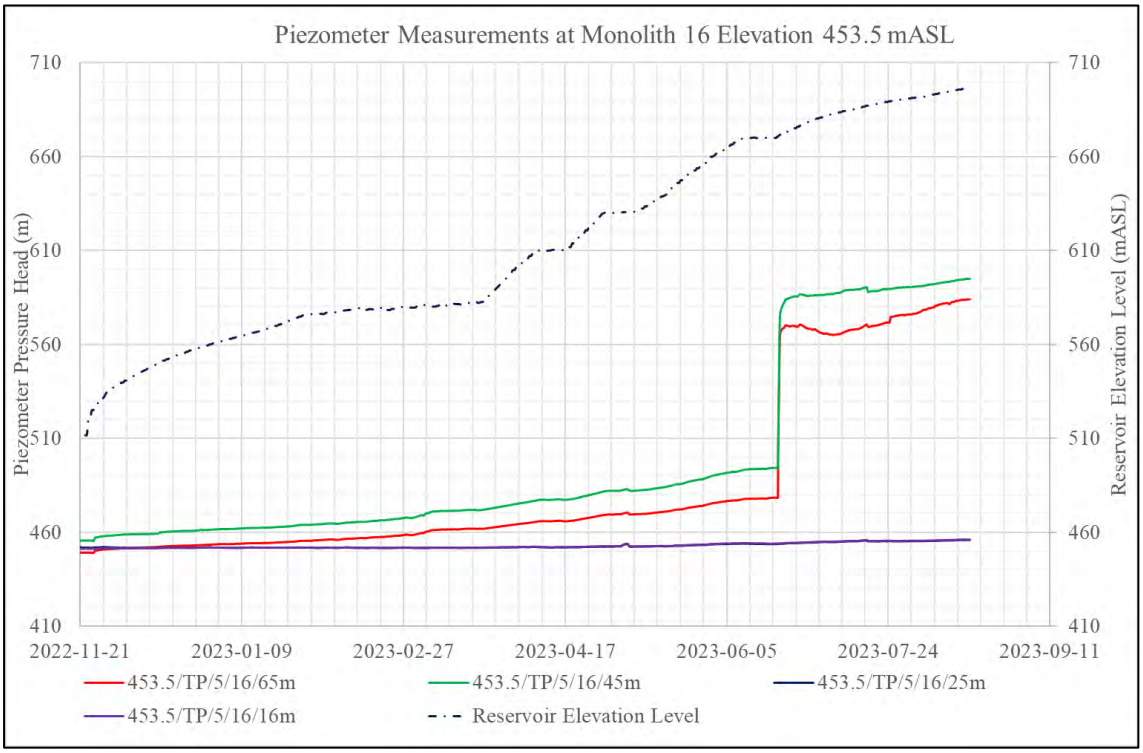

Figure 5-51: Yusufeli Dam Piezometer Readings – El 453.5 Monolith Block No. 16

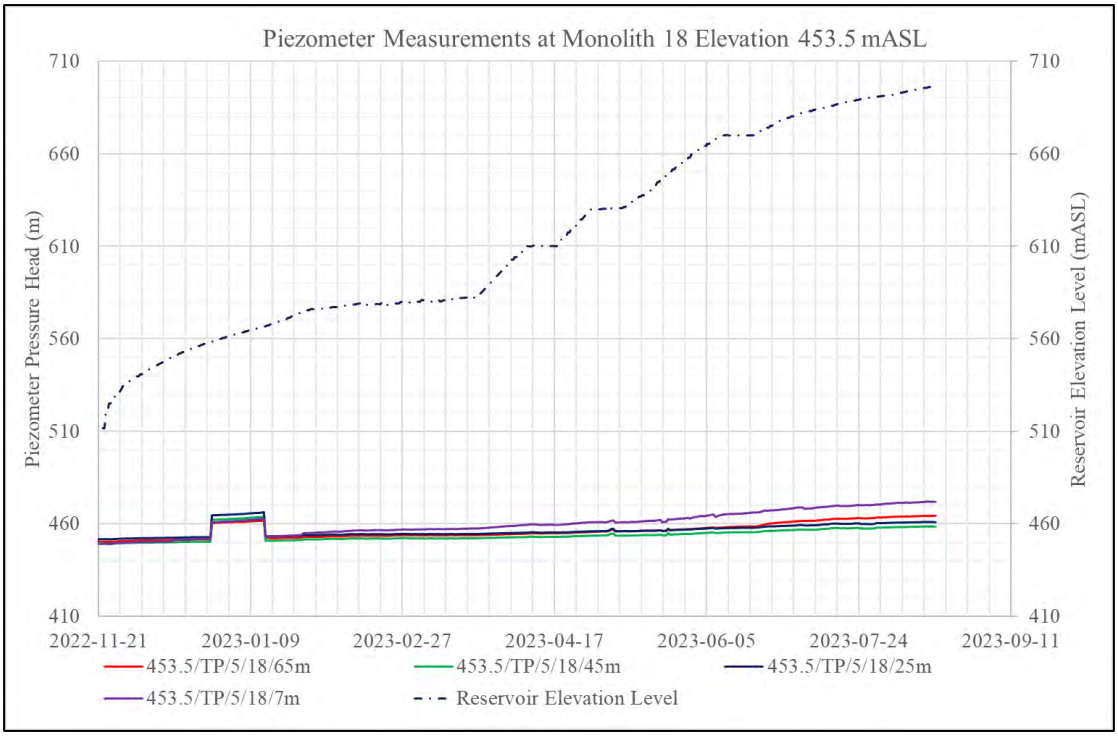

Figure 5-52: Yusufeli Dam Piezometer Readings – El 453.5 Monolith Block No. 18

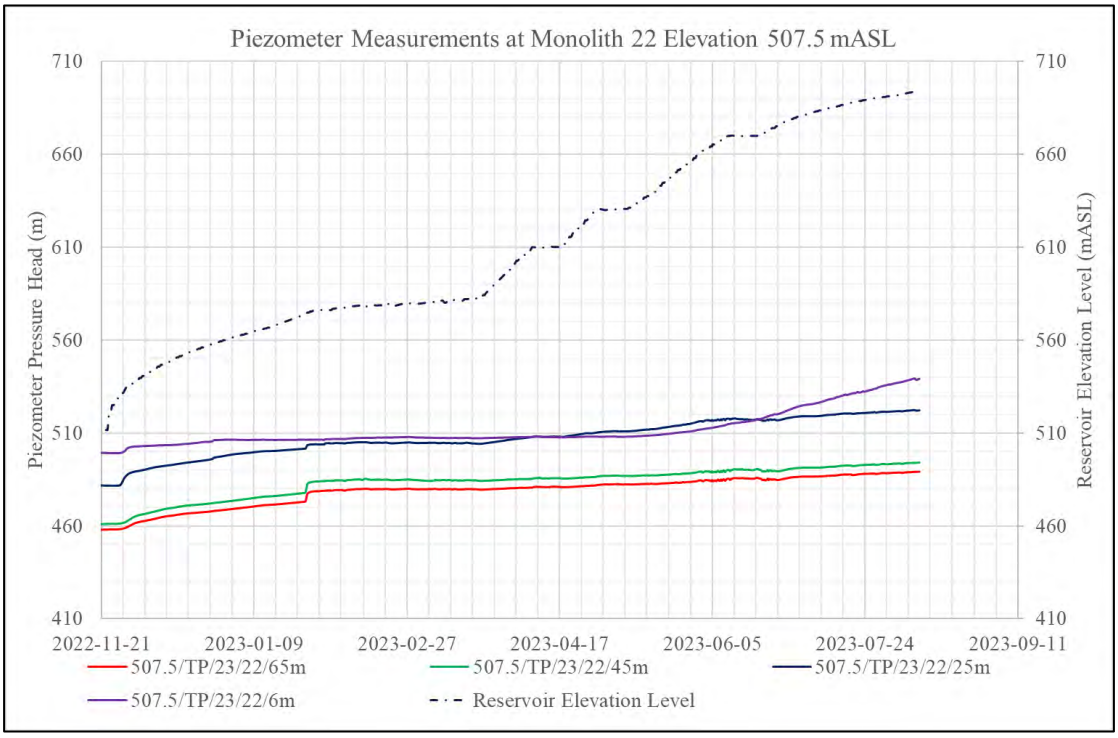

Figure 5-53: Yusufeli Dam Piezometer Readings – El 507.5 Monolith Block No. 22

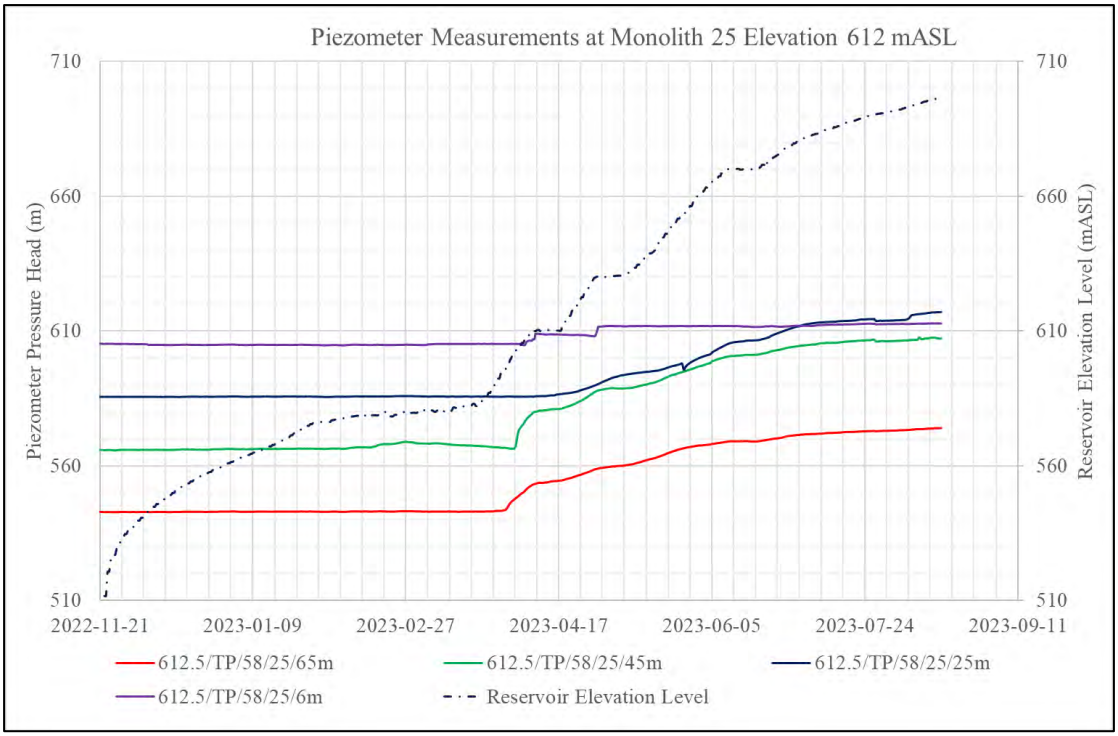

Figure 5-54: Piezometer Response at Elevation 612.5 mASL Monolith Block 25

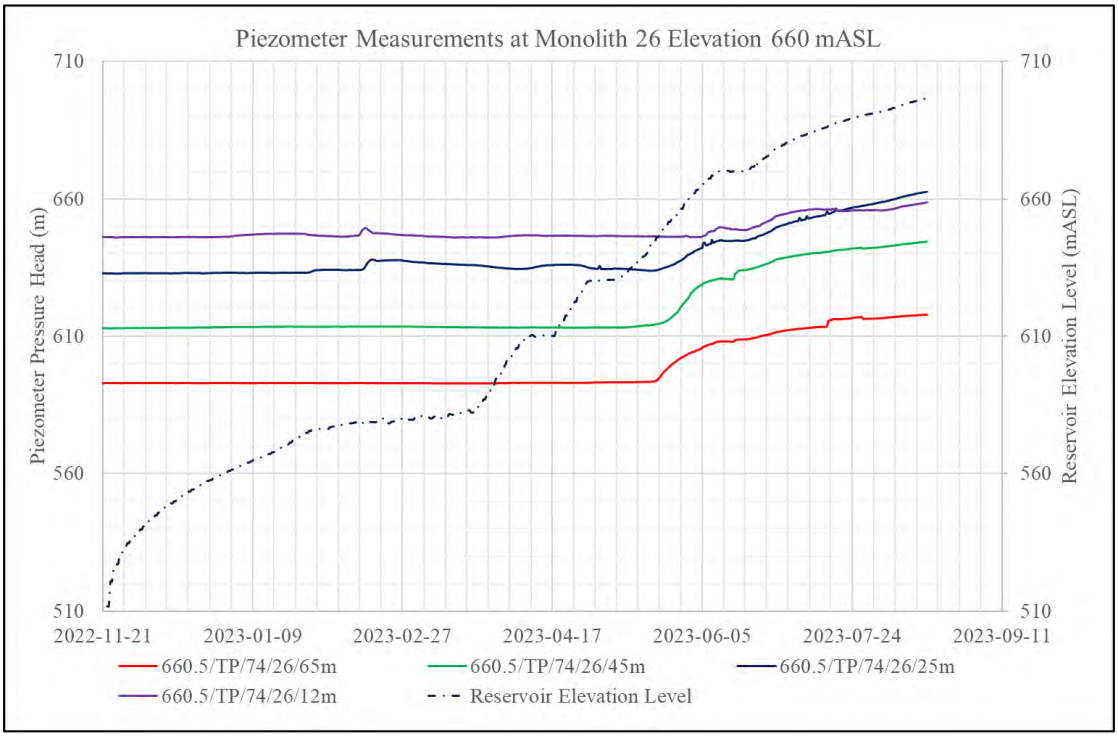

Figure 5-55: Piezometer Response at Elevation 660 mASL Monolith Block 26

5.10 SUMMARY

Various instrumentation devices were installed in the Yusufeli Dam whilst under construction to monitor its behaviour during first impoundment of the reservoir, and subsequently during operation of the dam. Monitoring of the dam behaviour during first impoundment allows for early detection of any signs of distress in the dam, as it is gradually loaded by the impounded reservoir.

In this chapter the instrumentation considered for the impoundment study of the dam and subsequent validation, or calibration of the FE model are presented and discussed. The physical locations of the instruments in relation to the dam body are depicted in various images, models and drawings of the dam. The various measurements and readings taken by the instruments during reservoir impoundment were presented as time-based curves over the impoundment period. The dam behaviour depicted by the curves were analysed and explained in terms of the response of the dam to the conditions imposed on it during impoundment. The following chapter reports the results output by the FE analysis undertaken of the dam under reservoir impoundment loading.

6 FE ANALYSIS RESULTS

This chapter provides a detailed presentation of the predicted dam behaviour during impoundment of the reservoir, as simulated by the results output by the FE analyses of the dam, under staged impoundment loading for stages 1 (580 mASL) to 5 (696 mASL). The results presented are the validated results after calibration of the FE model was achieved. A suite of sensitivity analysis results derived during calibration of the FE model are provided in Section 8.

The reservoir elevation levels for the 5 stages of impoundment are reproduced here for ease of reference against analysis results and are shown in Figure 6-1.

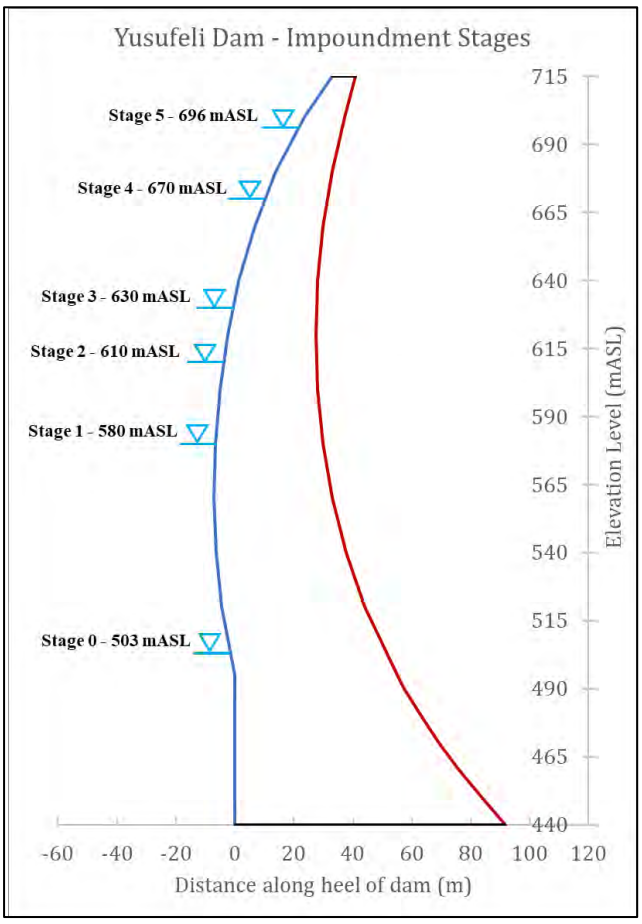

Figure 6-1: Yususfeli Dam reservoir level impoundment stages

The resultant hydrostatic force that is transferred by the dam into the foundation under the respective reservoir level impoundment stages, is shown in Figure 6-2. The plotted curve indicates that due to the non-linear/parabolic shape of the river valley and the curvature of the upstream face of the dam, the hydrostatic forces imposed on the dam by the water reservoir is a non-linear function of the rising reservoir level. This is especially evident within the upper portion of the dam body where the river valley slopes flatten out and the curvature of the dam is greatest.

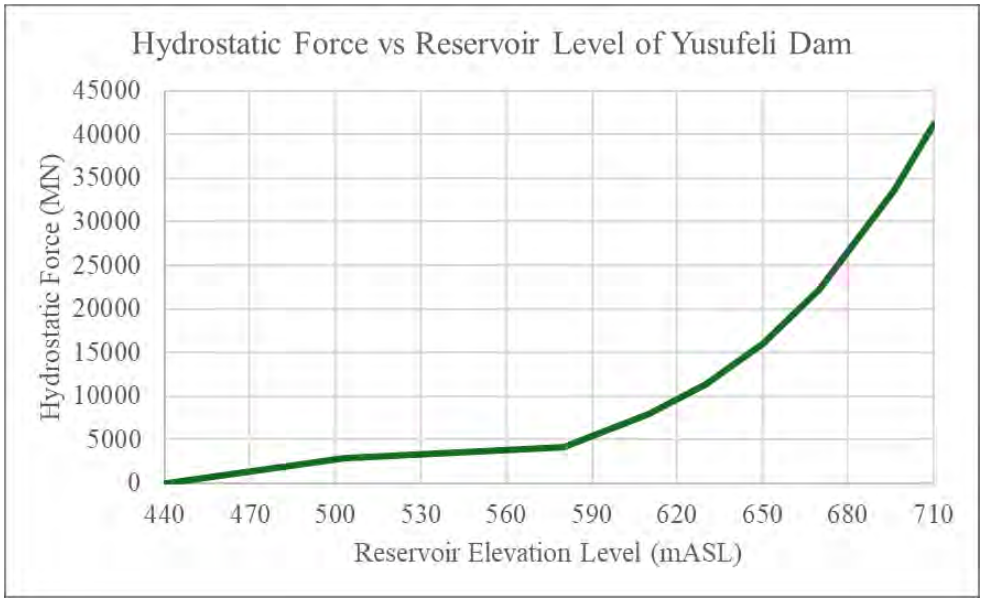

Figure 6-2: Resultant hydrostatic force vs reservoir level of Yusufeli Dam

The FE analysis results computed at each of the impoundment stages are shown in the form of graphical post-processed contour plots extracted from the FE analysis outputs.

The provided results plots were interrogated at nodal/elemental locations in the dam mesh body, coincident with the locations of the relevant installed instruments against which the measurements are compared, for validation and calibration of the model. The nodal/elemental results extracted for comparisons against instrument readings were summarized in table form for each instrument type at the end of the chapter.

Selected additional results plots not directly comparable with any instrument of the dam were also shown and evaluated in terms of the overall modelled dam behaviour and in terms of the acceptable design criteria.

For early stages of impoundment (stages 1 to 3) only the displacements of the dam body external faces in relation to survey beacons, and the relative movement (opening/closing) of the expansion joints in relation to jointmeters were considered. The measurement values of other instruments, at the early stages of impoundment, are too small to provide meaningful comparisons between the modelled and observed behaviour of the dam and were omitted.

At stage 4 of impoundment, the relative rotational displacement results in relation to pendulum movements were also considered.

At stage 5 of impoundment additional FEA dam behaviour results such as stress, strain and temperature values were also interrogated for comparison with measured dam behaviour.

6.1 1ST STAGE OF IMPOUNDING TO 580 MASL

6.1.1 Temperature Results

The simulated temperature state of the dam as computed at analysis stage 1 (T_{580}) is shown in Figure 6-3. The average temperature of the dam is 10.5 ° C, with a maximum of 17 ° C and minimum of 1.5 ° C. The impact of the ambient and water reservoir temperature conditions experienced during the cold Winter season of February, are evident from the computed low temperatures on the upstream and downstream face of the dam. The core temperature of the dam ranges from 8 ° C at the base to 17 ° C near the crest. The reference temperature state (T_0) at commencement of impoundment was shown in Figure 4-18.

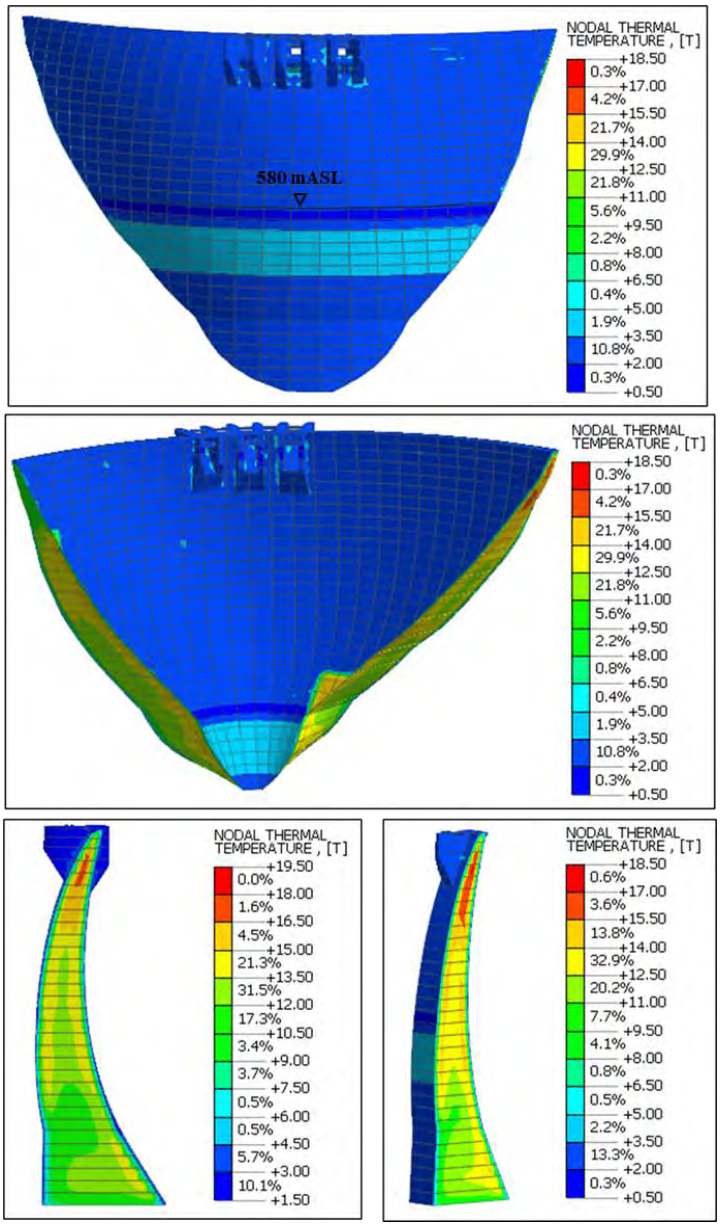

Figure 6-3: Temperature state of the dam at analysis stage 1 (Reservoir level 580 mASL, on 13/02/2023)

6.1.2 Displacement Results

The deformation analysis results were probed at nodal locations in the model corresponding to the respective location of each of the survey beacons B1 – B12. The simultaneous reservoir level was also sketched as a dark line on the downstream face of the dam FE model output plots for reference.

A local cylindrical coordinate system was implemented in the dam model to transpose horizontal displacement results into radial and tangential (axial) components. The radial (TX), tangential (TY) and vertical displacement (TZ) results computed through the structural FE analysis for an impounded water level of 580 mASL are illustrated in Figure 6-4 through Figure 6-6. Negative radial displacement values indicate downstream movement, and positive axial displacements indicate movement towards the right abutment of the dam. The resultant horizontal displacements (TXY) for the dam as predicted by the analyses on 13/02/2023 are illustrated in Figure 6-7.

The modelled deformation behaviour of the dam at this early stage of impoundment, shows the lower portion of the dam moving forward (downstream) under cantilever action due to the hydrostatic loading, whilst the crest also experiences downstream displacement due to the drop in ambient temperature, causing it to contract and move forward. The exaggerated deformed mode of the dam is shown in Figure 6-8. The maximum anticipated radial displacement of the dam is expected to be 13.5 mm occurring in the downstream direction, at the crest of the crown cantilever.

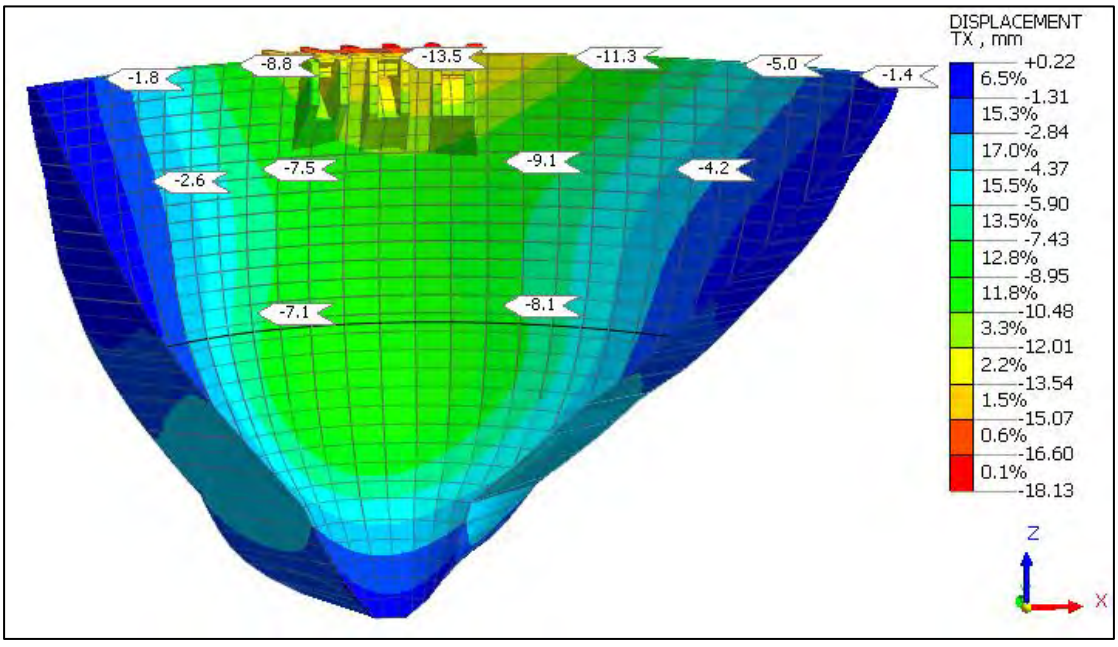

Figure 6-4: Radial (TX) displacements for impoundment to 580 mASL on 13/02/2023 (DS face)

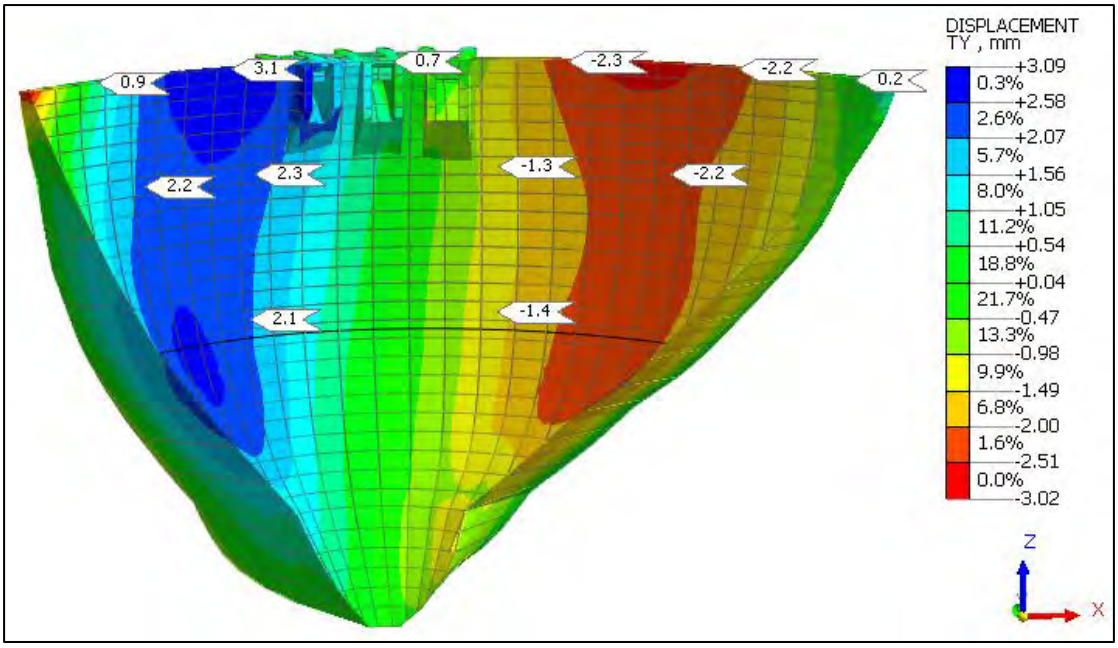

Figure 6-5: Tangential (TY) displacements for impoundment to 580 mASL on 13/02/2023 (DS face)

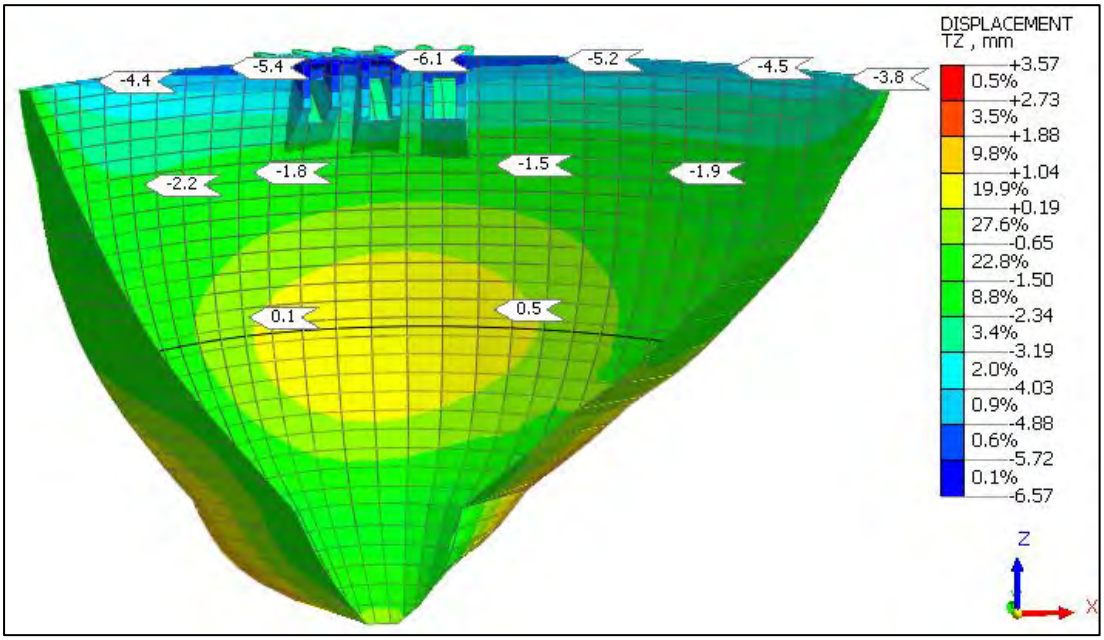

Figure 6-6: Vertical displacements for impoundment to 580 mASL on 13/02/2023 (DS face)

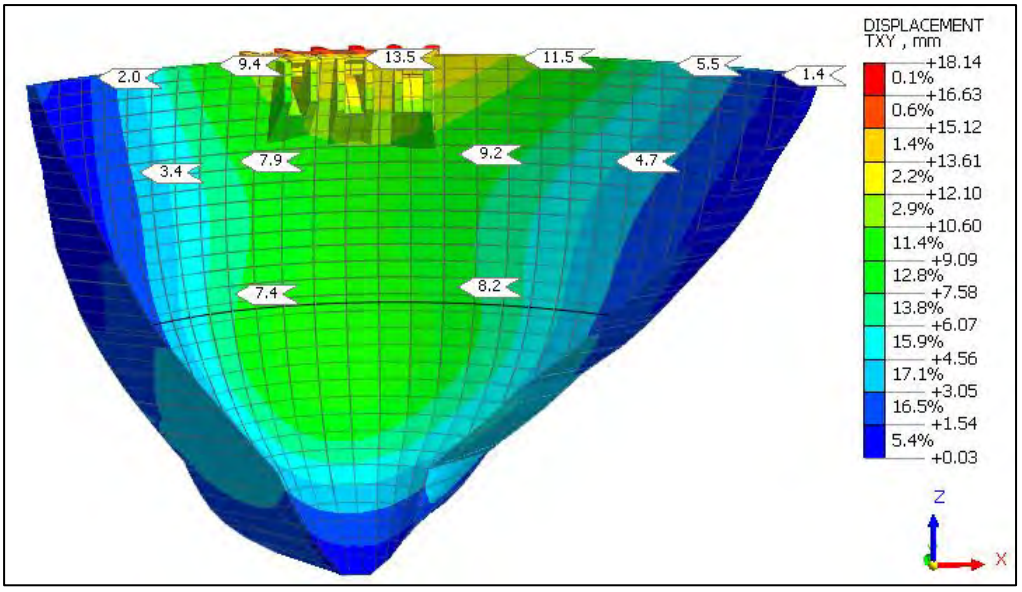

Figure 6-7: Horizontal displacements for impoundment to 580 mASL on 13/02/2023 (DS face)

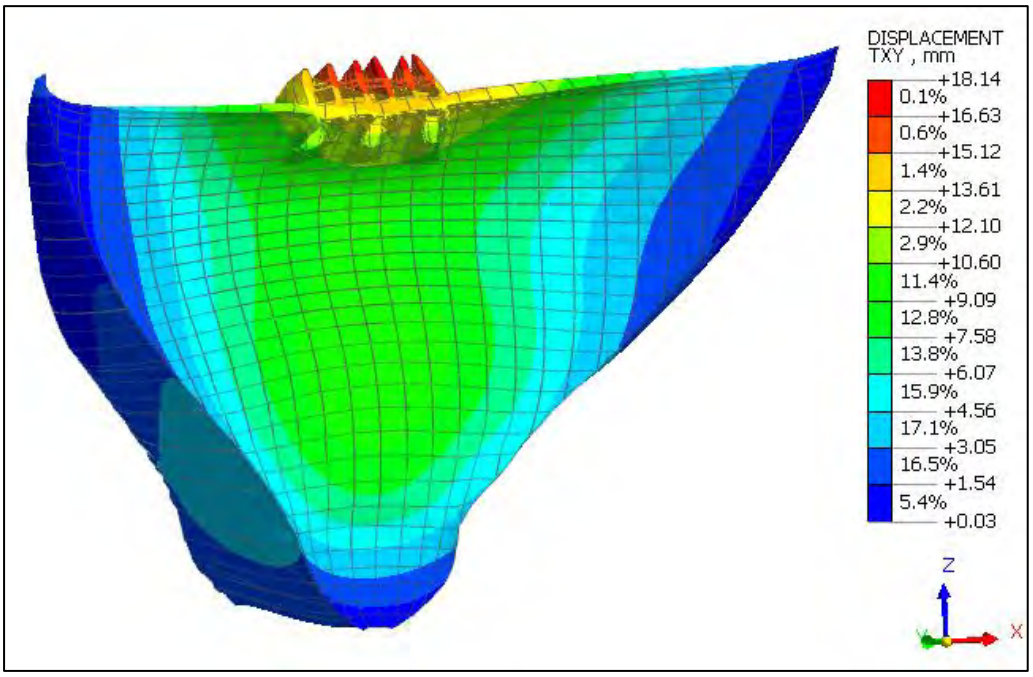

Figure 6-8: Exaggerated deformed shape of dam with horizontal displacement plot on 13/02/2023

6.1.3 Stress Results

Contours plots of the P3 principal compressive stress results output from the structural analysis are illustrated in Figure 6-9 and Figure 6-10. Vector plots presented in Figure 6-11 and Figure 6-12 demonstrate that the primary compressive load mechanism of the dam remains vertical. Hydrostatic loading from water reservoir level at 580 mASL is not sufficiently high to induce arching (axial) compression along the dam axis as the primary compressive load mechanism.

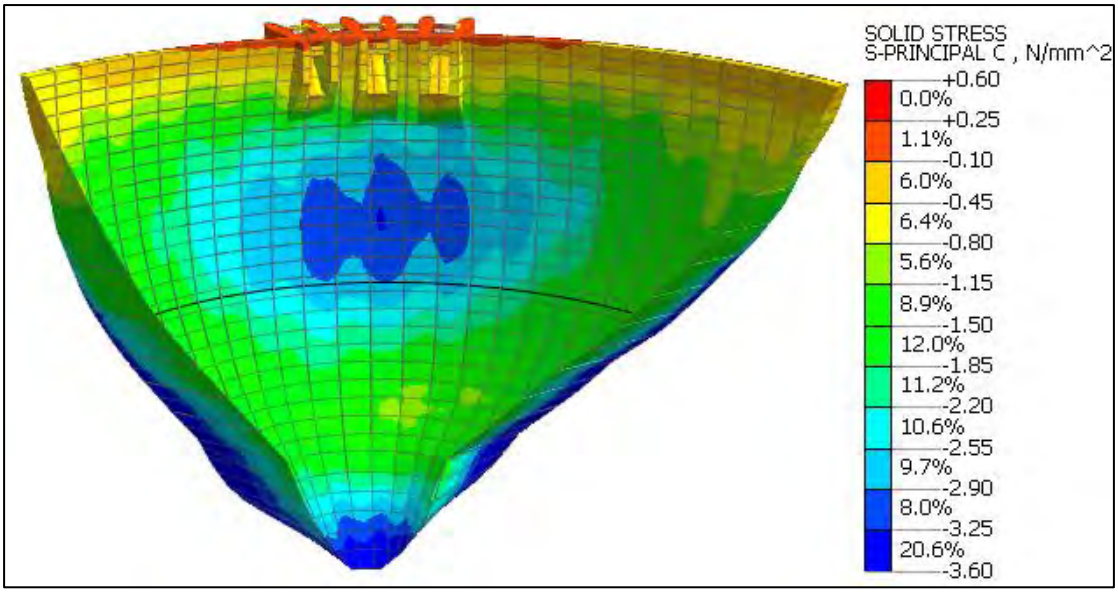

Figure 6-9: P3 principal stress results for reservoir impoundment to 580 mASL on 13/02/2023 (DS face)

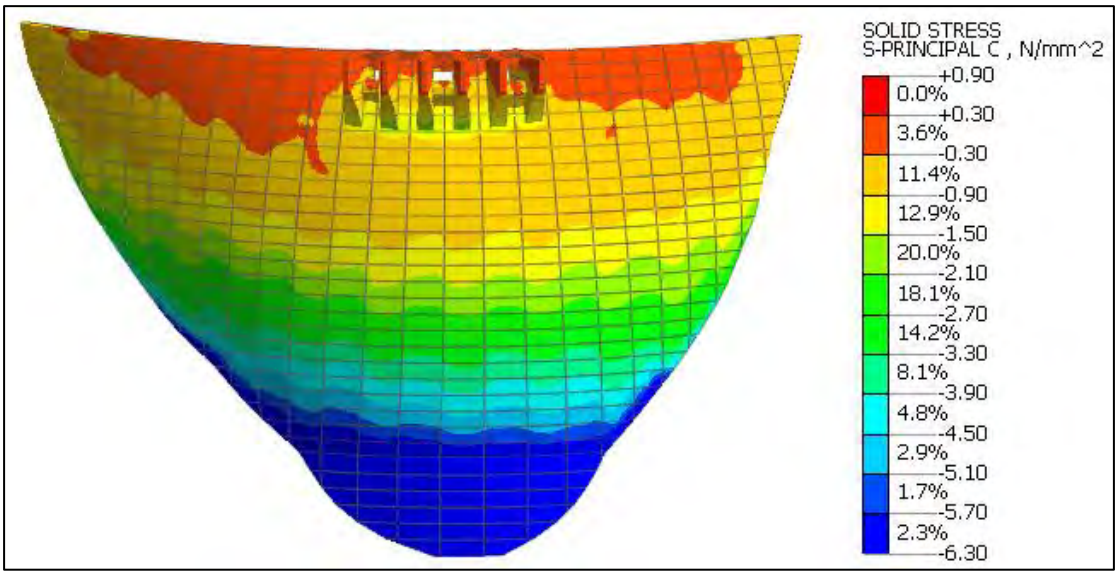

Figure 6-10: P3 principal stress results for reservoir impoundment to 580 mASL on 13/02/2023 (US face)

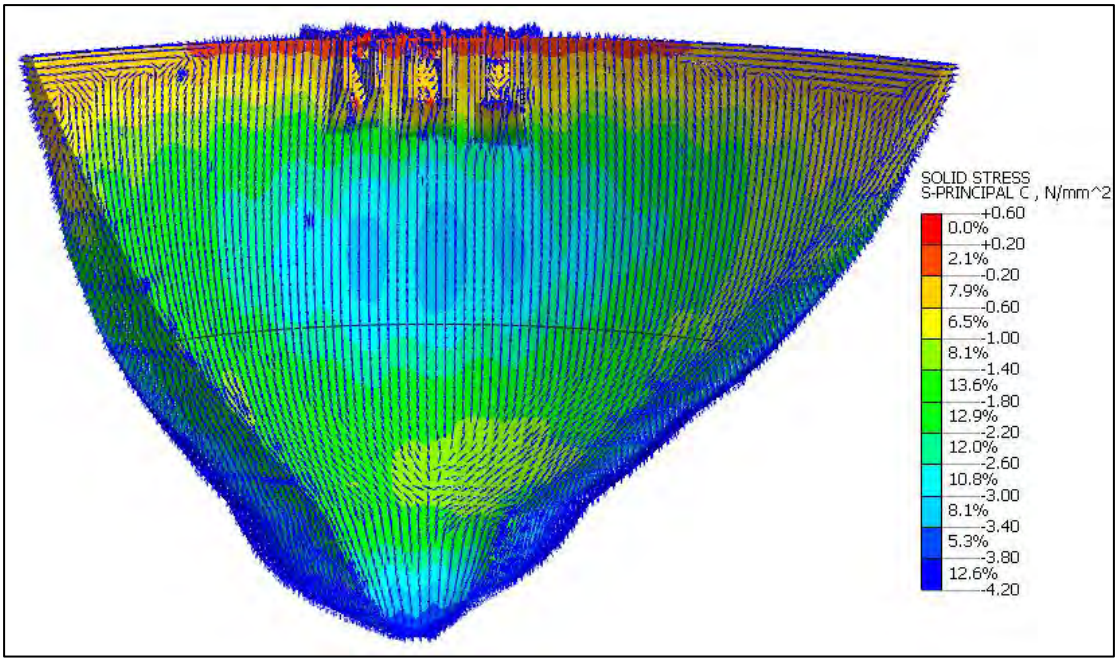

Figure 6-11: P3 principal stress vectors for impoundment to 580 mASL on 13/02/2023 (DS face)

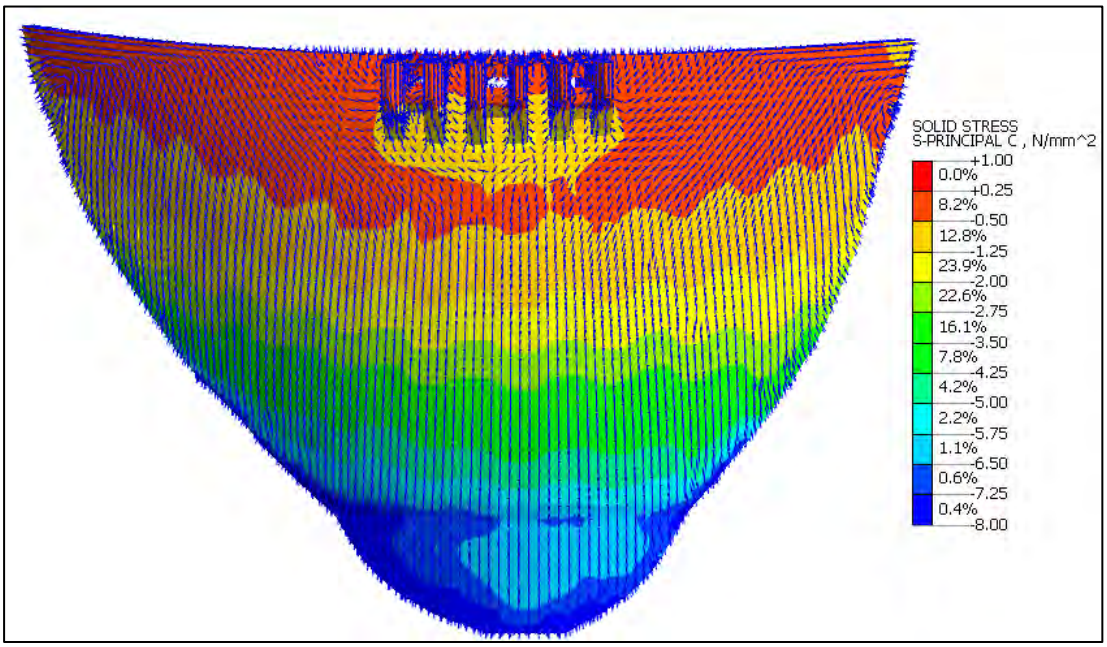

Figure 6-12: P3 principal stress vectors for impoundment to 580 mASL on 13/02/2023 (US face)

6.1.4 Interface Element Results

The normal displacements (X) predicted on the contraction joints between the individual construction monoliths of the dam are plotted in Figure 6-13. These plots indicate the relative displacements between monoliths, normal to the plane of the joint interface. Essentially these are the expected joint openings modelled under the applicable analysis loadings.

The results plots indicate that under the applied loading conditions of Stage 1 impoundment, the dam joints are only expected to open at the crest, with openings of between 0.5 and 1.7 mm.

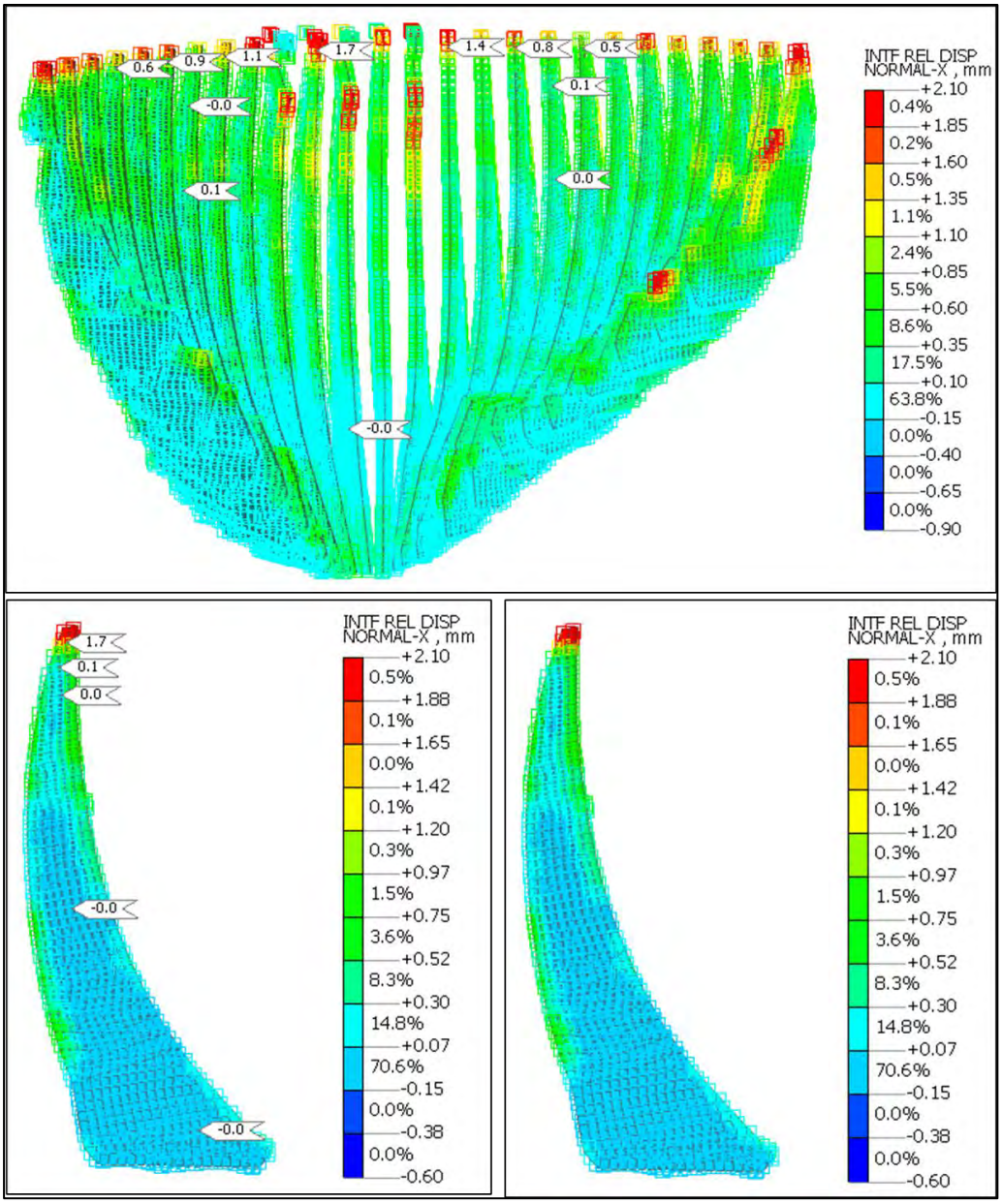

Figure 6-13: Axial displacement results on joints for impoundment to 580 mASL on 13/02/2023

6.2 2ND STAGE OF IMPOUNDING TO 610 MASL

6.2.1 Temperature Results

The simulated temperature state of the dam as computed at analysis stage 2 (T_{610}) is shown in Figure 6-14. The average temperature of the dam is 11.5 ° C, with a maximum of 16.5 ° C and minimum of 2 ° C. The contrast between the cold-water reservoir temperature conditions and

the mild Spring ambient temperatures are evident from the modelled temperature state on the upstream and downstream face of the dam. The core temperature of the dam ranges from 7.5 ° C at the base to 16.5 ° C near the crest.

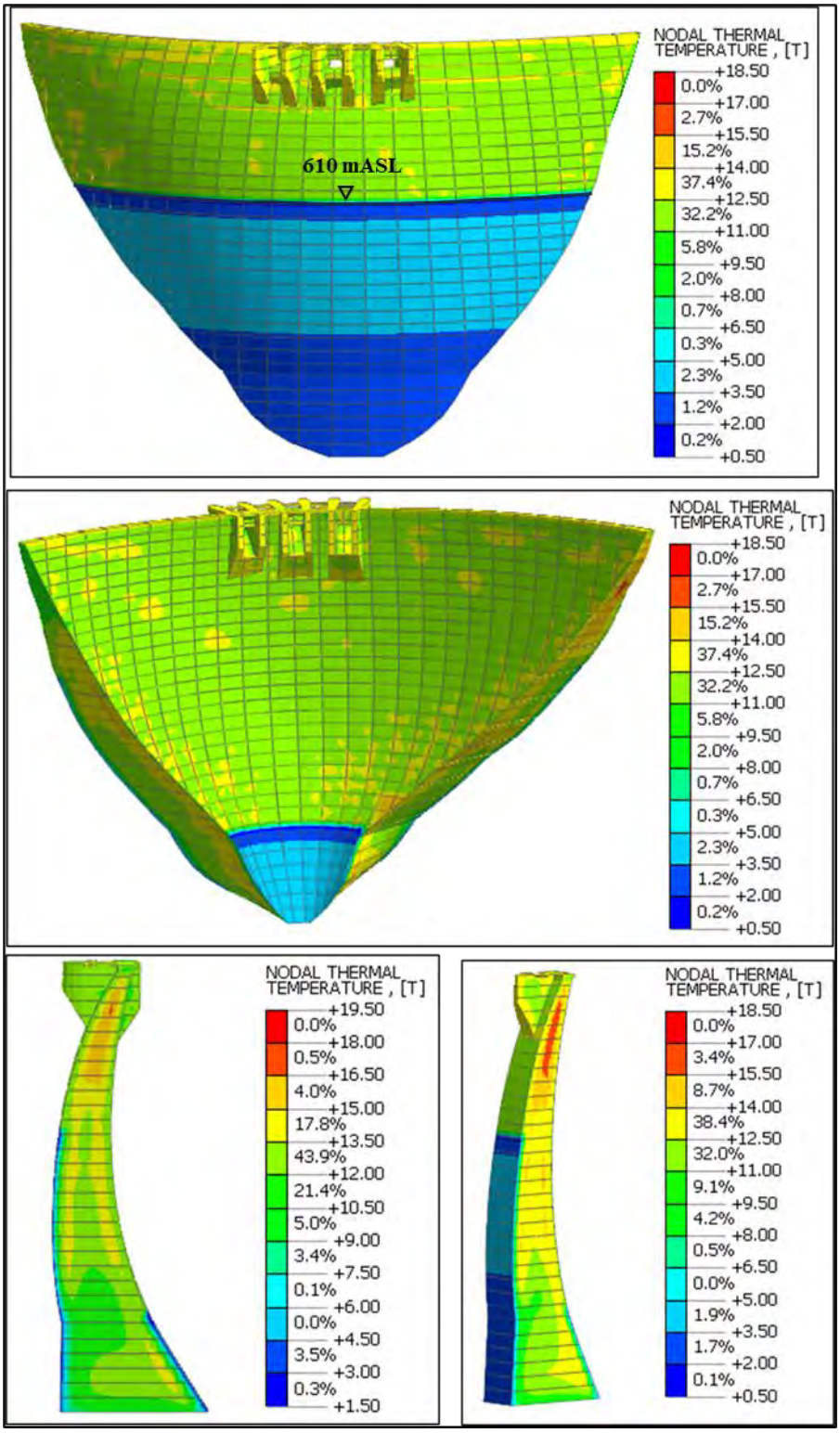

Figure 6-14: Temperature state of the dam at analysis stage 2 (Reservoir level 610 mASL, on 08/04/2023)

6.2.2 Displacement Results

The deformation analysis results were probed at nodal locations in the model corresponding to the respective location of each of the survey beacons B1 – B12. The simultaneous reservoir level was also sketched as a dark line on the downstream face of the dam FE model output plots for reference.

The radial (TX), tangential (TY) and vertical displacement (TZ) results computed through the structural FE analysis for an impounded water level of 610 mASL, are illustrated in Figure 6-15 through Figure 6-19. Negative radial displacement values indicate downstream movement, and positive axial displacements indicate movement towards the right abutment of the dam. The resultant horizontal displacements (TXY) for the dam as predicted by the analyses at 08/04/2023 are illustrated in Figure 6-18.

The modelled deformation behaviour of the dam at this early stage of impoundment shows the lower portion of the dam moving forward (downstream), under cantilever action due to the hydrostatic loading, whilst the crest also experiences downstream displacement due to the drop in ambient temperature causing it to contract and move forward. The exaggerated deformed mode of the dam is shown in Figure 6-19. The maximum anticipated radial displacement of the dam is expected to be 19.5 mm occurring in the downstream direction, just below mid height of the crown cantilever.

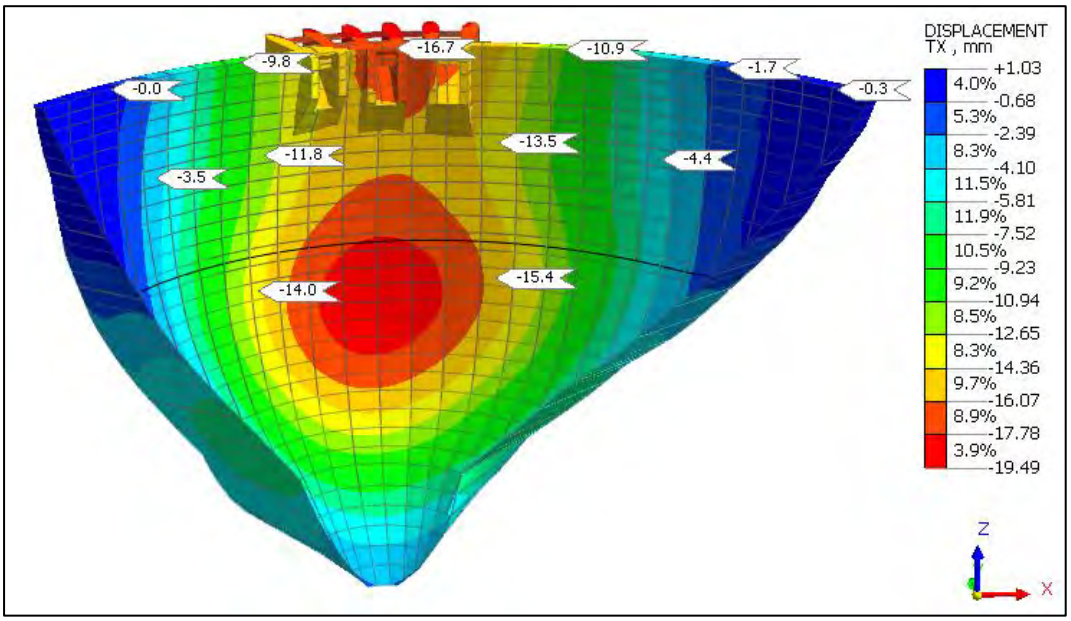

Figure 6-15: Radial (TX) displacements for impoundment to 610 mASL on 08/04/2023 (DS face)

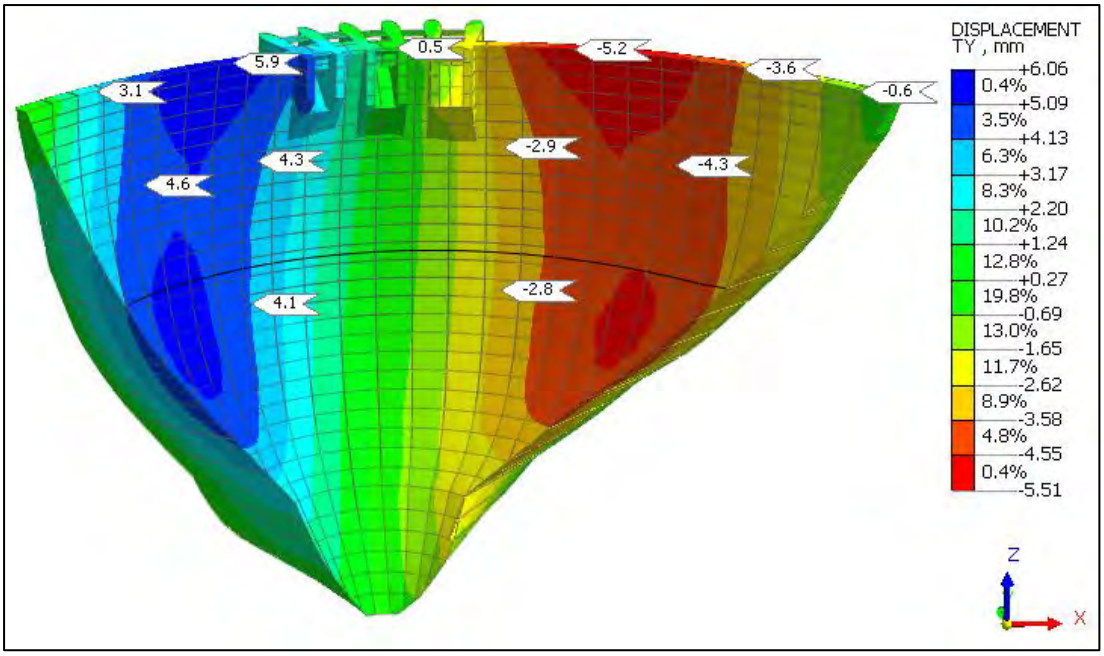

Figure 6-16: Tangential (TY) displacements for impoundment to 610 mASL on 08/04/2023 (DS face)

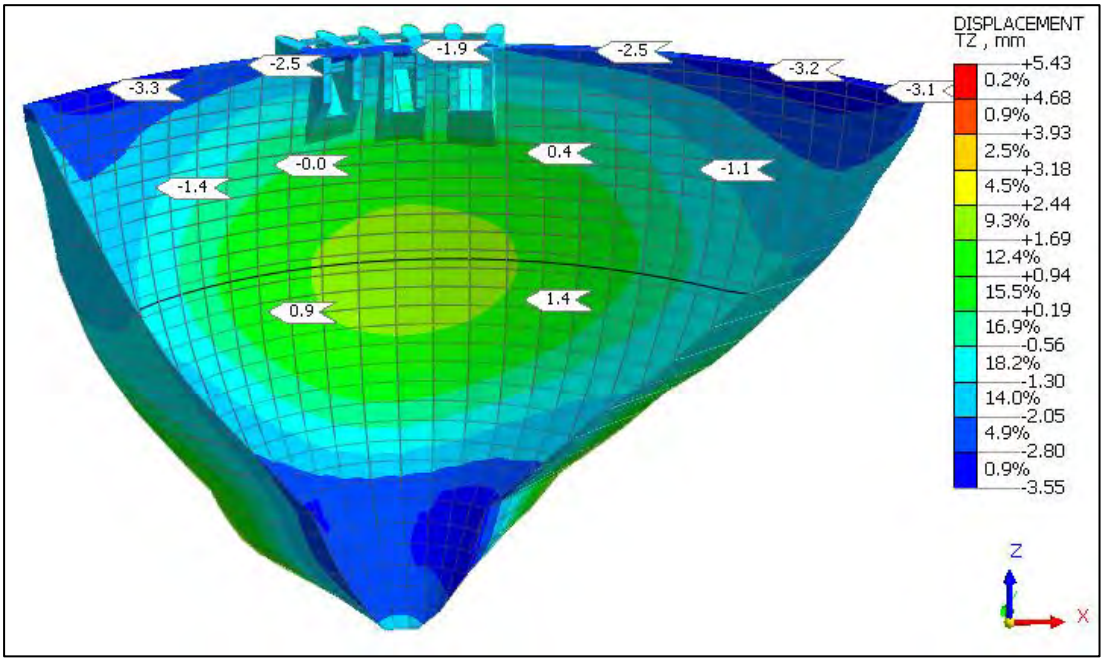

Figure 6-17: Vertical displacements for impoundment to 610 mASL on 08/04/2023 (DS face)

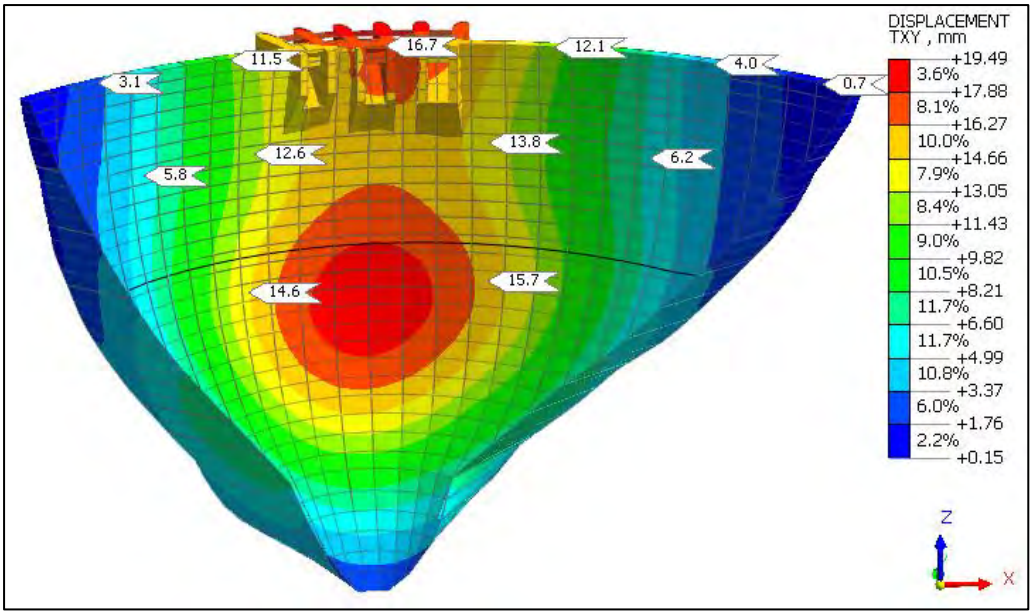

Figure 6-18: Horizontal displacements for impoundment to 610 mASL on 08/04/2023 (DS face)

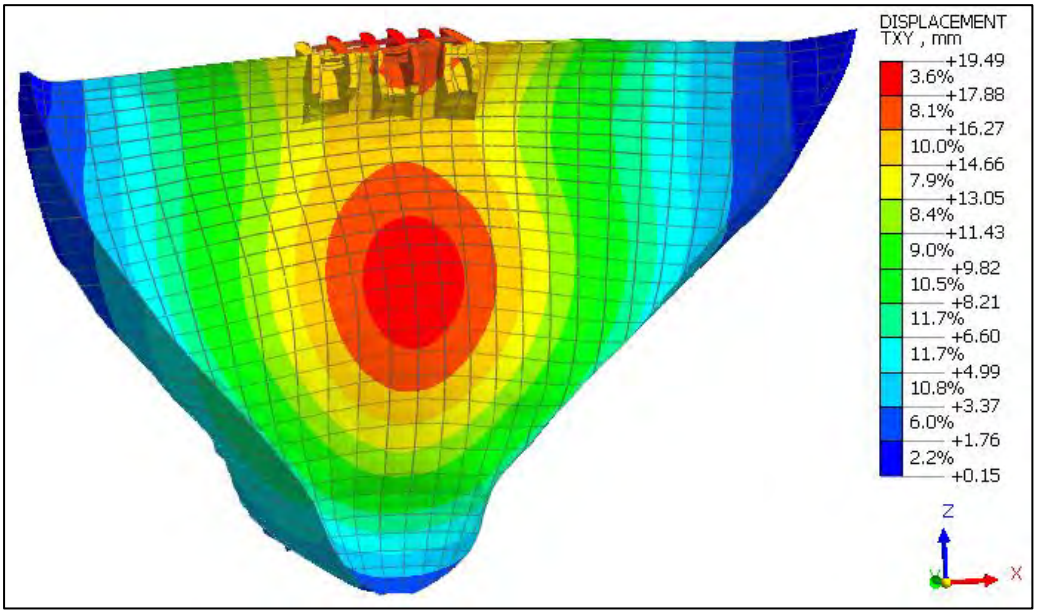

Figure 6-19: Exaggerated deformed shape of dam with horizontal displacement plot on 08/04/2023

6.2.3 Stress Results

Contours plots of the P3 principal (compressive) stress results output from the structural analysis are illustrated in Figure 6-20 and Figure 6-21 . Vector plots illustrated in Figure 6-22 and Figure 6-23 indicate that the primary compressive load mechanism of the dam is vertical at this stage, as expected.

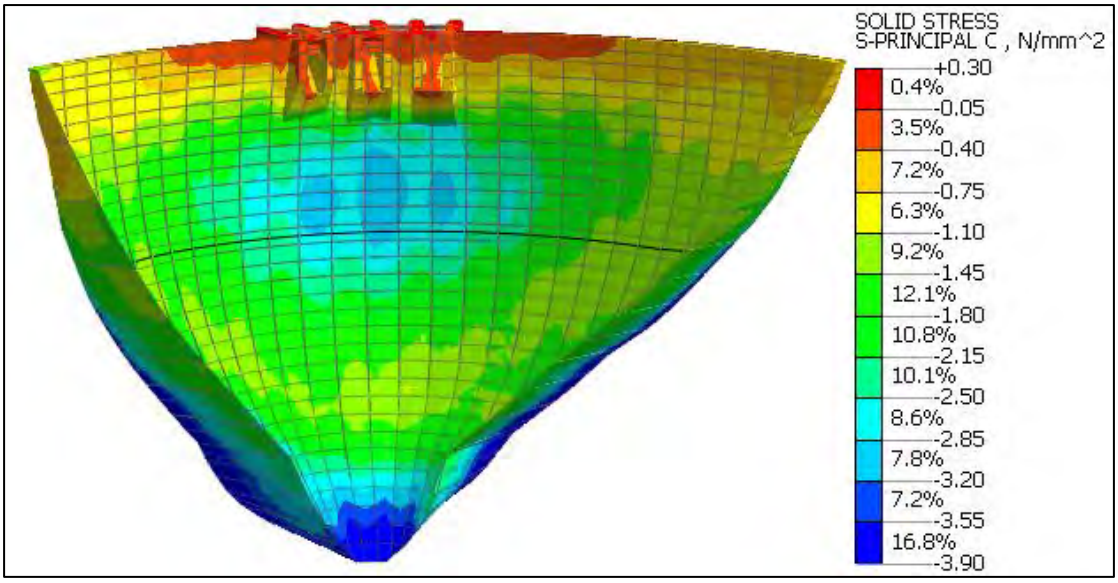

Figure 6-20: P3 principal stress results for reservoir impoundment to 610 mASL on 08/04/2023 (DS face)

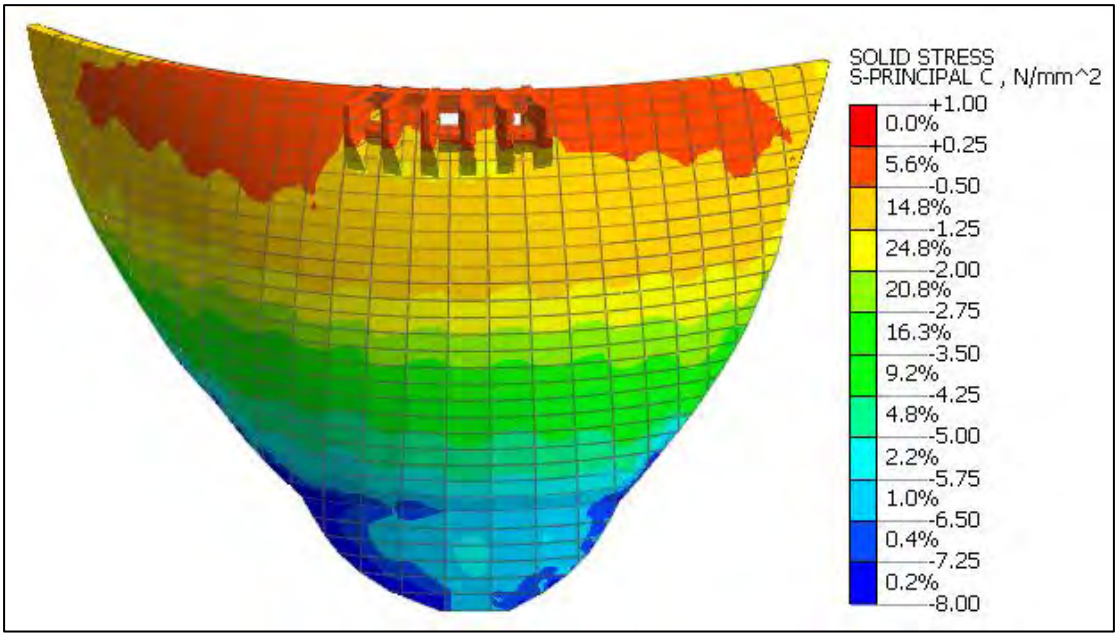

Figure 6-21: P3 principal stress results for reservoir impoundment to 610 mASL on 08/04/2023 (US face)

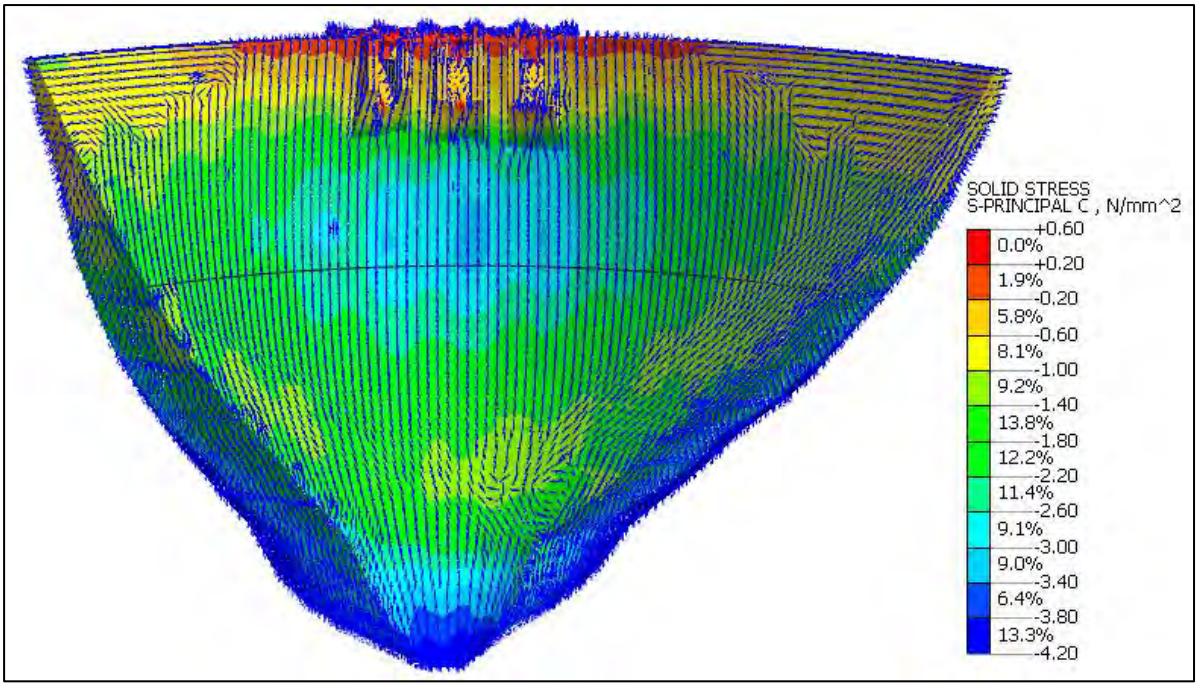

Figure 6-22: P3 principal stress vectors for impoundment to 610 mASL on 08/04/2023 (DS face)

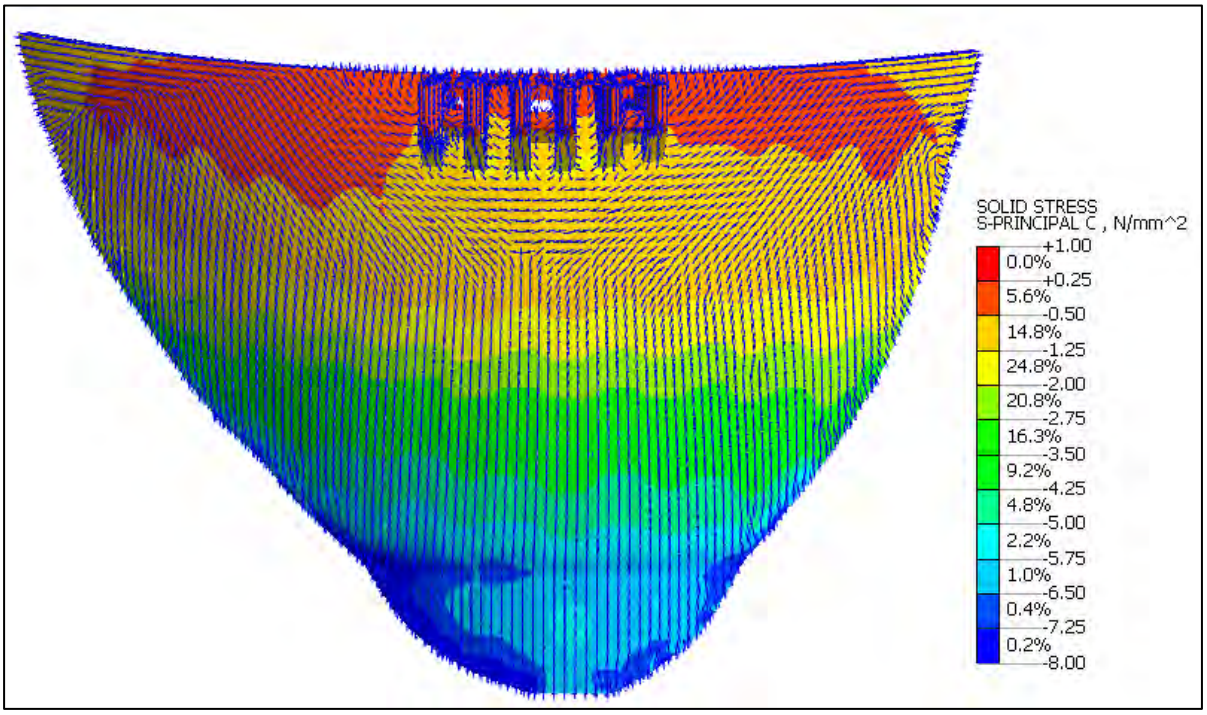

Figure 6-23: P3 principal stress vectors for impoundment to 610 mASL on 08/04/2023 (US face)

6.2.4 Interface Element Results

The normal displacements (X) predicted on the contraction joints between the individual construction monoliths of the dam, are plotted in Figure 6-24. These plots indicate the relative

displacements between monoliths, normal to the plane of the joint interface. Essentially these are the expected joint openings modelled under the applicable analysis loadings.

The results plots indicate that under the applied loading conditions of Stage 2 impoundment, the dam joints are only expected to open at the crest, with openings of between 0 and 0.6 mm.

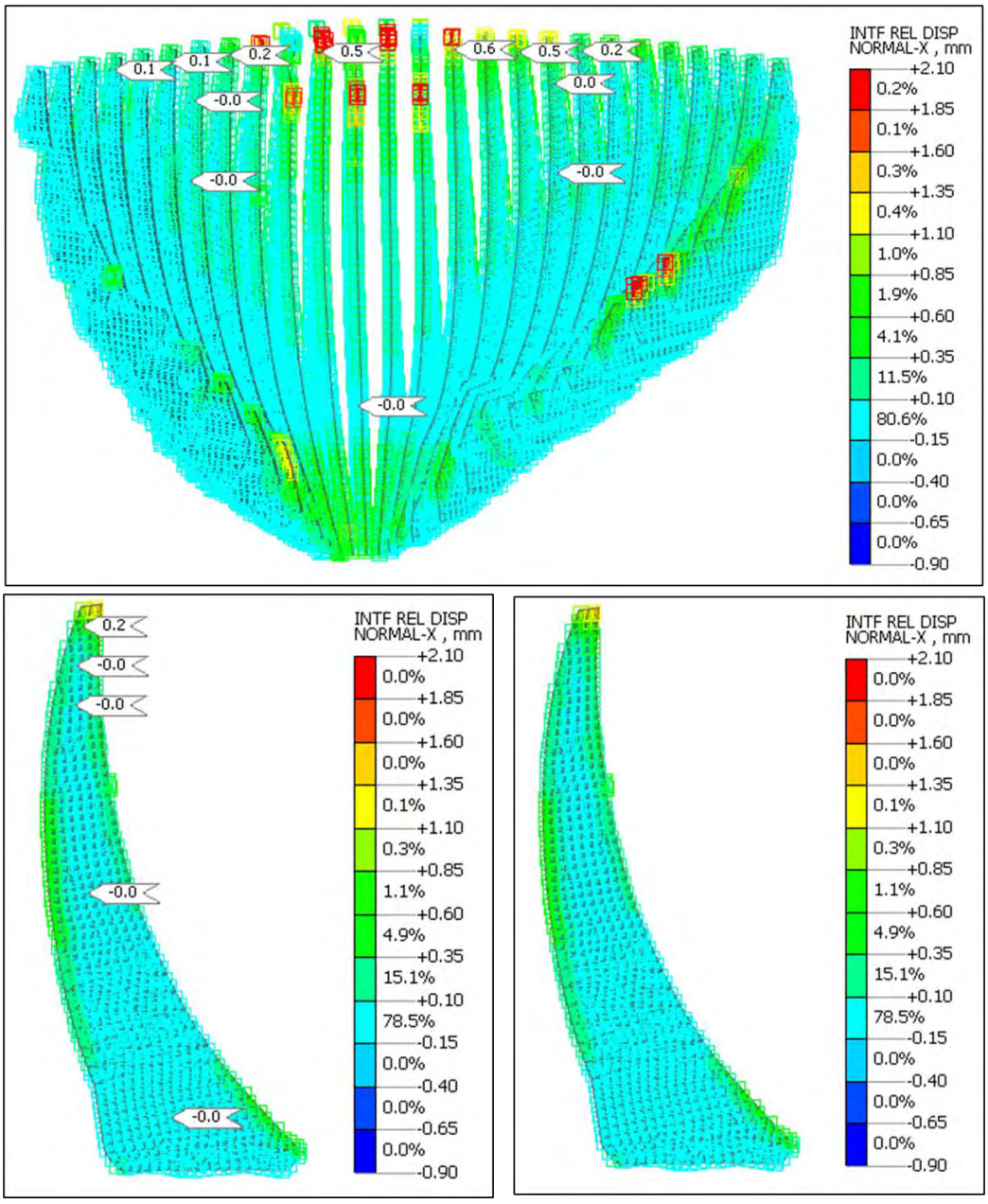

Figure 6-24: Axial displacement results on joints for impoundment to 610 mASL on 08/04/2023

6.3 3RD STAGE OF IMPOUNDING TO 630 MASL

6.3.1 Temperature Results

The simulated temperature state of the dam as computed at analysis stage 3 (T_{630}) is shown in Figure 6-25. The average temperature of the dam is 11.9 ° C, with a maximum of 17 ° C and minimum of 3.5 ° C. The contrast between the cold-water reservoir temperature conditions and the Spring ambient temperatures, are evident from the modelled temperature state on the upstream and downstream face of the dam. The core temperature of the dam ranges from 8 ° C at the base to 17 ° C near the crest.

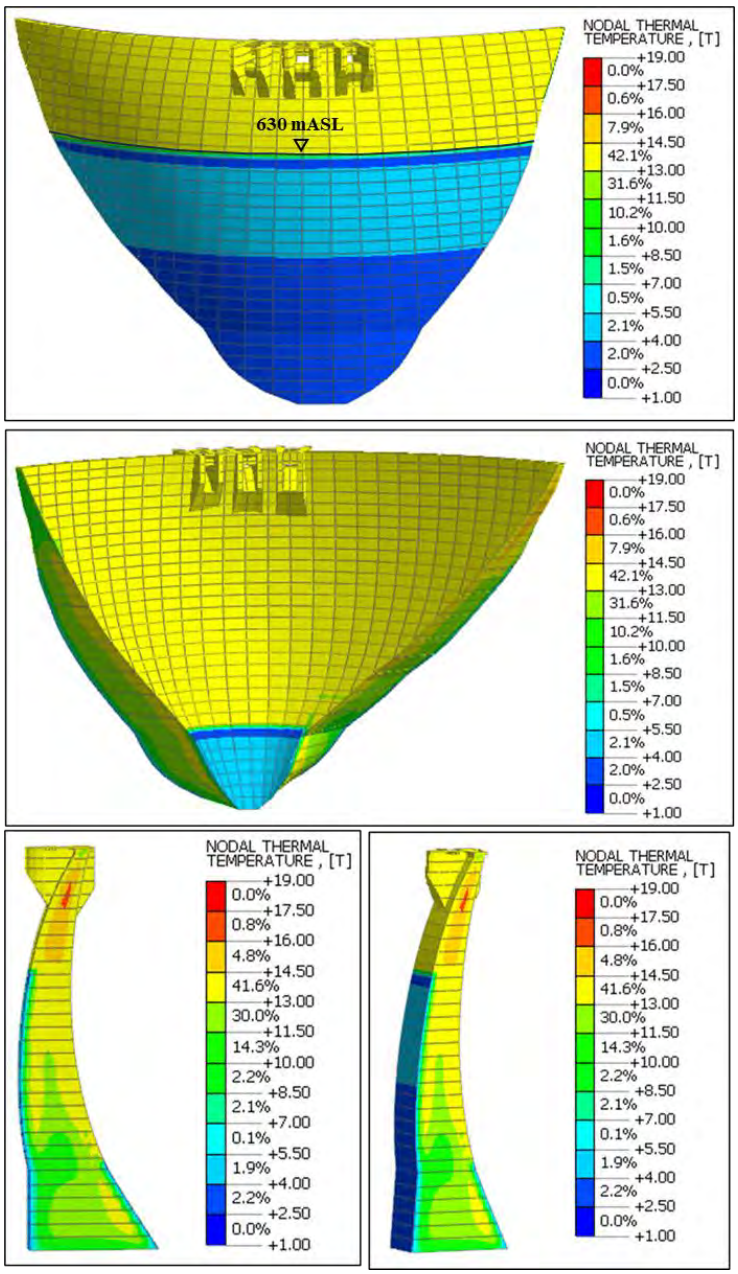

Figure 6-25: Temperature state of the dam at analysis stage 3 (Reservoir level 630 mASL, on 29/04/2023)

6.3.2 Displacement Results

The deformation analysis results were probed at nodal locations in the model corresponding to the respective location of each of the survey beacons B1 – B12. The simultaneous reservoir level was also sketched as a dark line on the downstream face of the dam FE model output plots for reference.

The radial (TX), tangential (TY) and vertical displacement (TZ) results computed through the structural FE analysis for an impounded water level of 630 mASL, are illustrated in Figure 6-26 through Figure 6-30. Negative radial displacement values indicate downstream movement, and positive axial displacements indicate movement towards the right abutment of the dam. The resultant horizontal displacements (TXY) for the dam as predicted by the analyses at 29/04/2023, are illustrated in Figure 6-29.

The modelled deformation behaviour of the dam at this stage of impoundment shows the lower portion of the dam moving forward (downstream) under cantilever action due to the hydrostatic loading, whilst the crest marginally undergoes local upstream displacement due to the rise in ambient temperature causing the crest to expand and move backward. The exaggerated deformed mode of the dam is shown in Figure 6-30. The maximum anticipated radial displacement of the dam is expected to be 28.5 mm occurring in the downstream direction, mid-height of the dam at the crown cantilever.

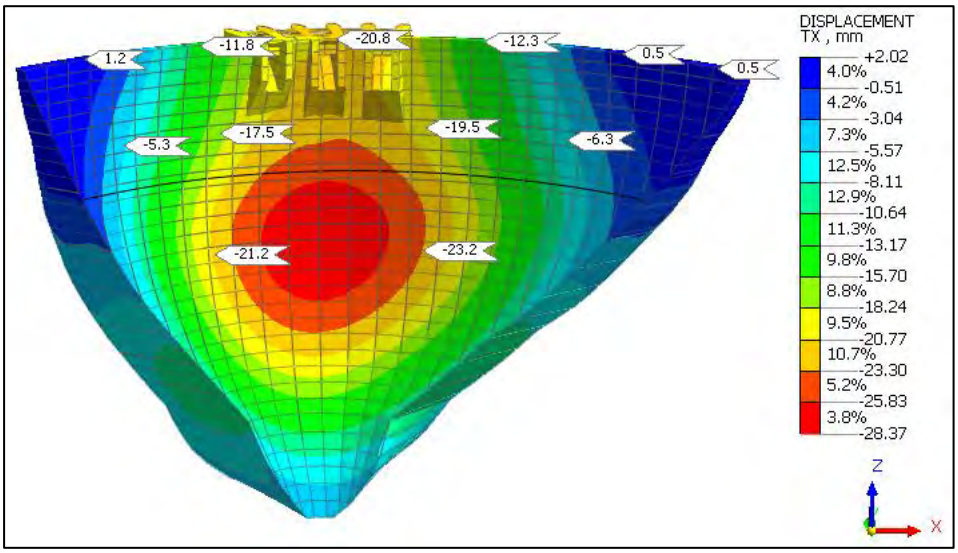

Figure 6-26: Radial (TX) displacements for impoundment to 630 mASL on 29/04/2023 (DS face)

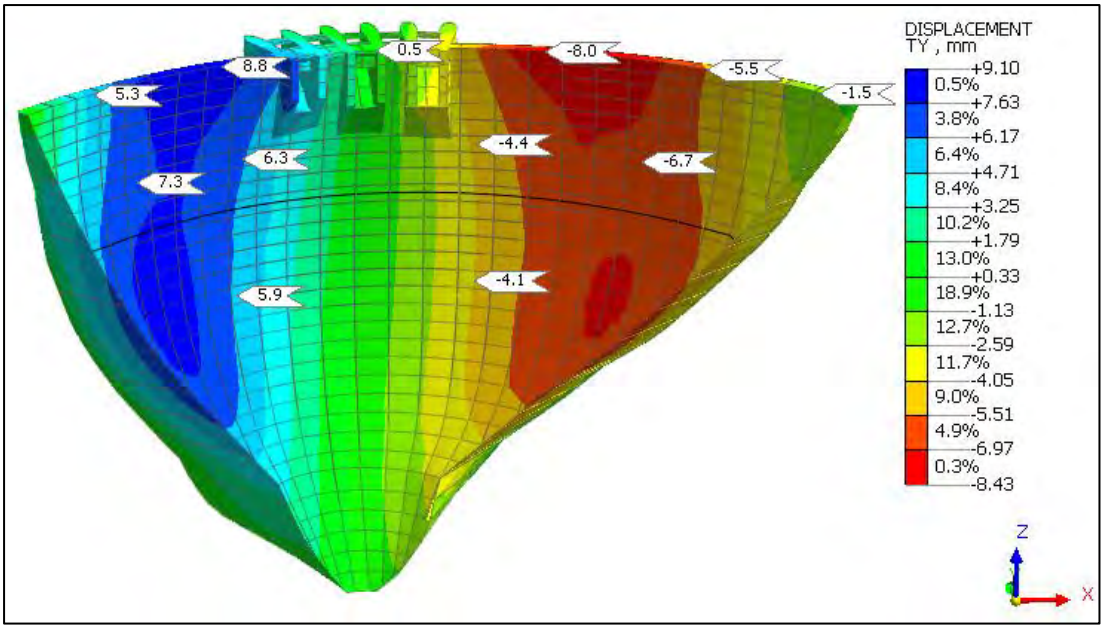

Figure 6-27: Tangential (TY) displacements for impoundment to 630 mASL on 29/04/2023 (DS face)

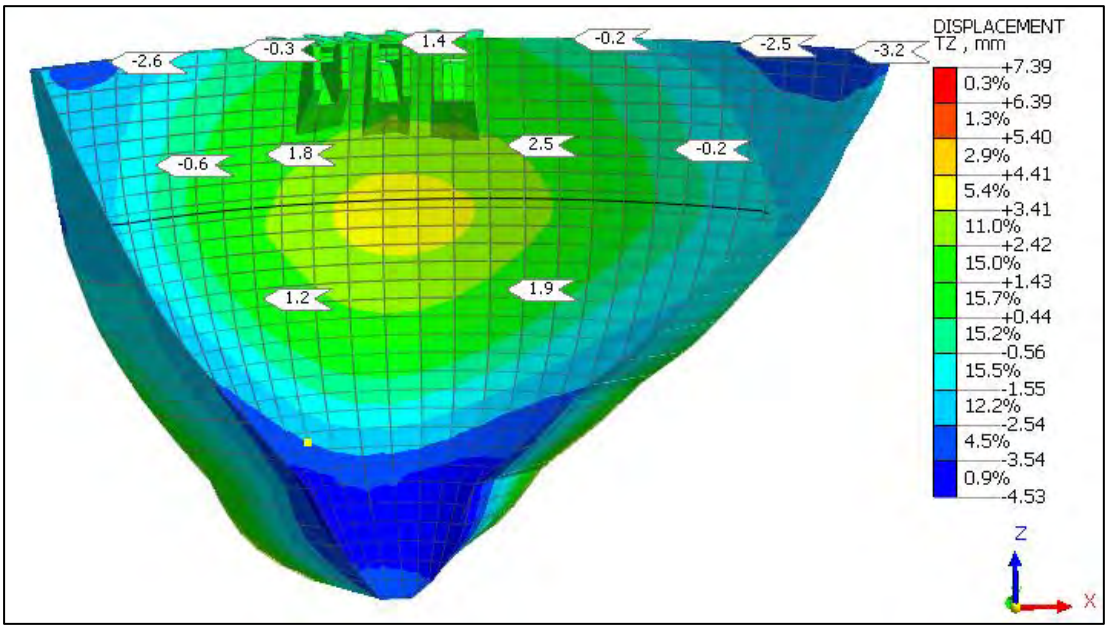

Figure 6-28: Vertical displacements for impoundment to 630 mASL on 29/04/2023 (DS face)

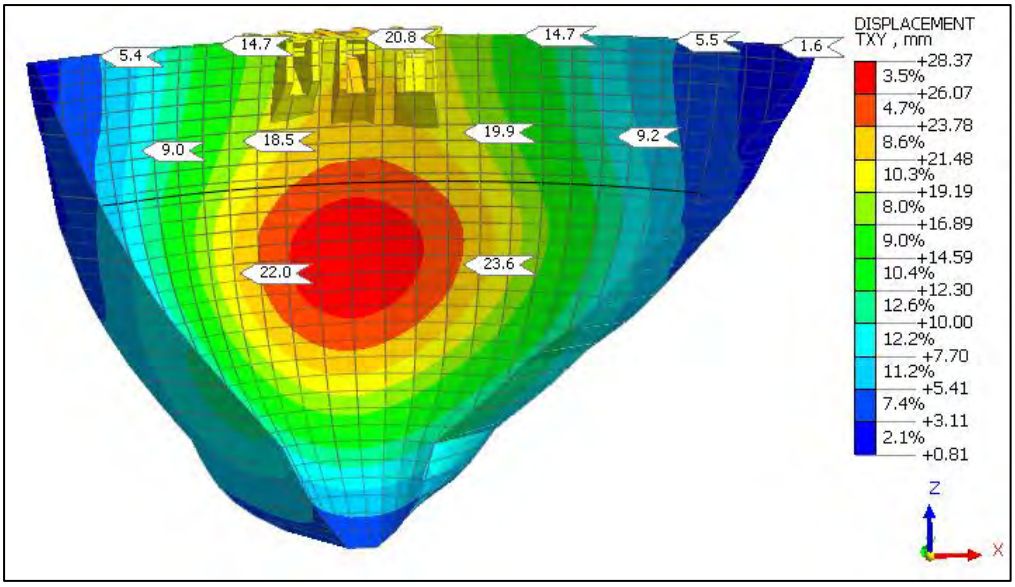

Figure 6-29: Horizontal displacements for impoundment to 630 mASL on 29/04/2023 (DS face)

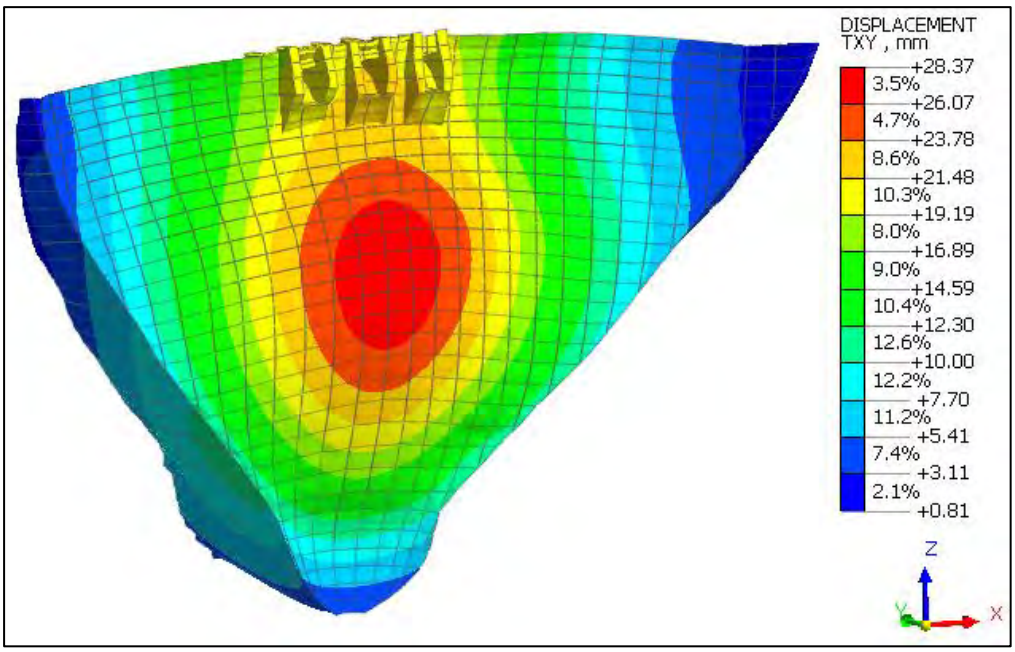

Figure 6-30: Exaggerated deformed shape of dam with horizontal displacement plot on 29/04/2023

A displacement vector plot is shown in Figure 6-31 to indicate the vector direction of the horizontal displacement of the dam. It can be seen that the horizontal displacement at the crown cantilever is almost completely radial, whilst near the abutments it is mostly axial (tangential), with a smooth transition from arch crown to abutments. This is synonymous with displacement behaviour reported by other large arch dams as shown in Figure 6-32 (Dungar, 1985).

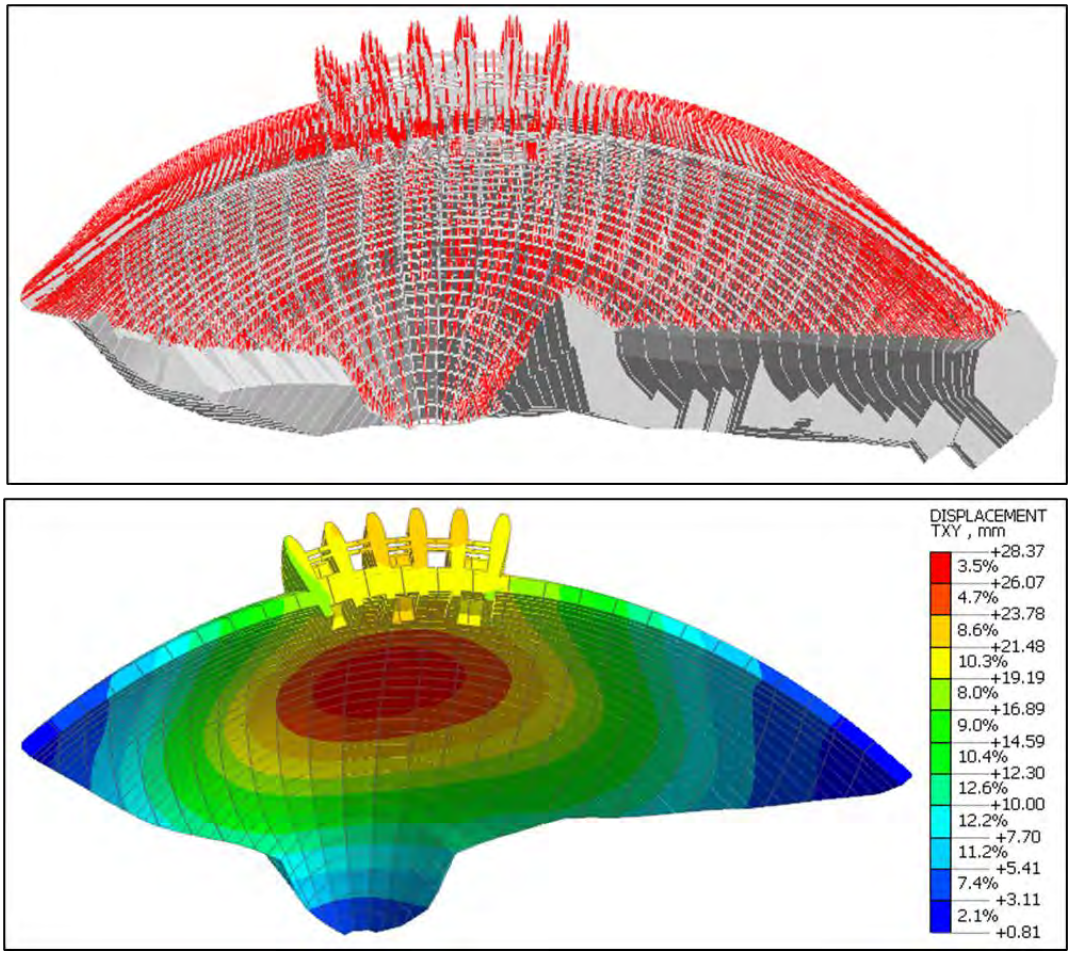

Figure 6-31: Displacement vector plot of dam for impoundment to 630 mASL on 29/04/2023

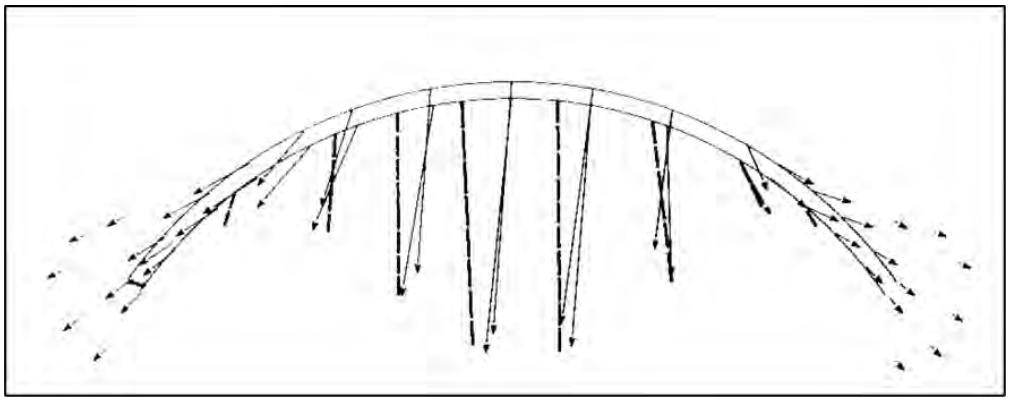

Figure 6-32: Typical 2-dimensional displacement vectors at crest arch dam from geodetic survey results (Dungar, 1985)

6.3.3 Stress Results

Contour plots of the P3 principal (compressive) stress results output from the structural analysis are illustrated in Figure 6-33 and Figure 6-34. Vector plots illustrated in Figure 6-35 and Figure 6-36 indicate that the primary compressive load mechanism of the dam is vertical at this stage, as expected. Early signs of axial horizontal compression (arching) of the upper third of the dam

is starting to show on the upstream face.

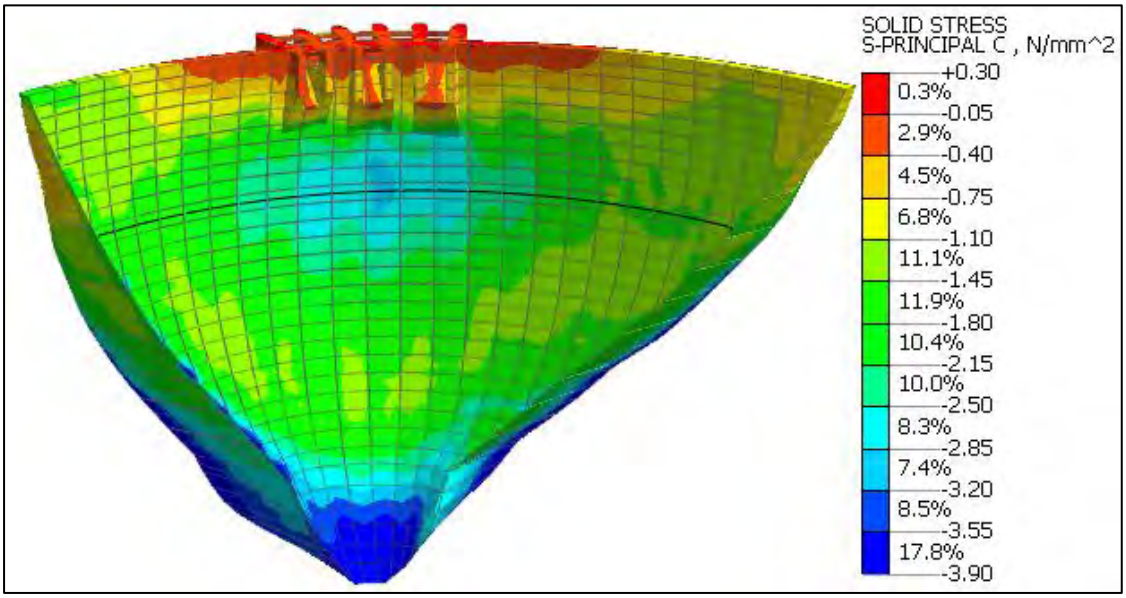

Figure 6-33: P3 principal stress results for reservoir impoundment to 630 mASL on 29/04/2023 (DS face)

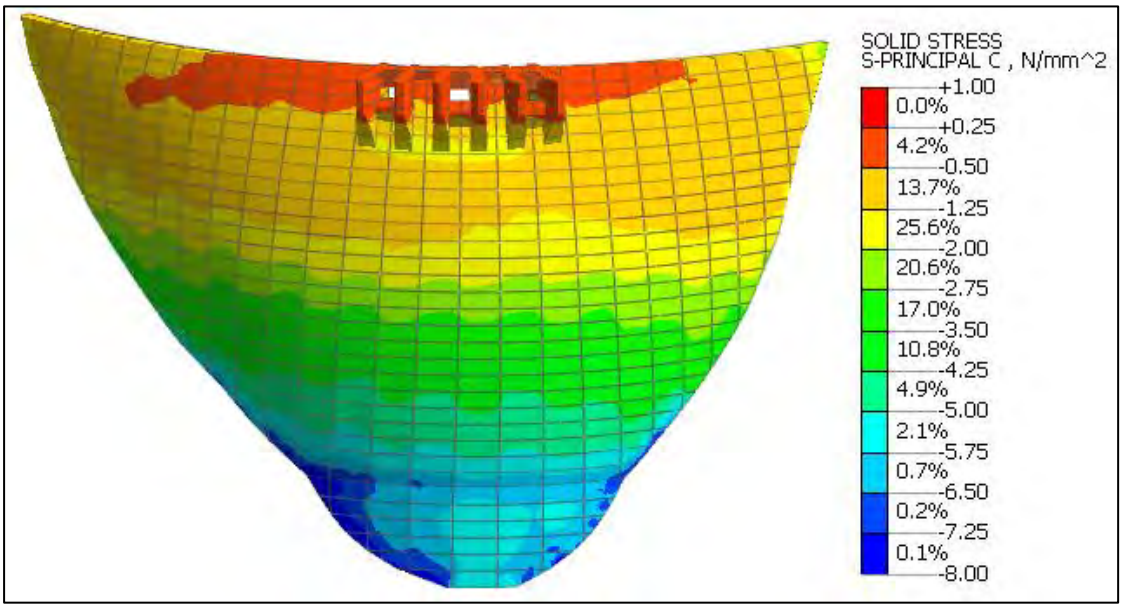

Figure 6-34: P3 principal stress results for reservoir impoundment to 630 mASL on 29/04/2023 (US face)

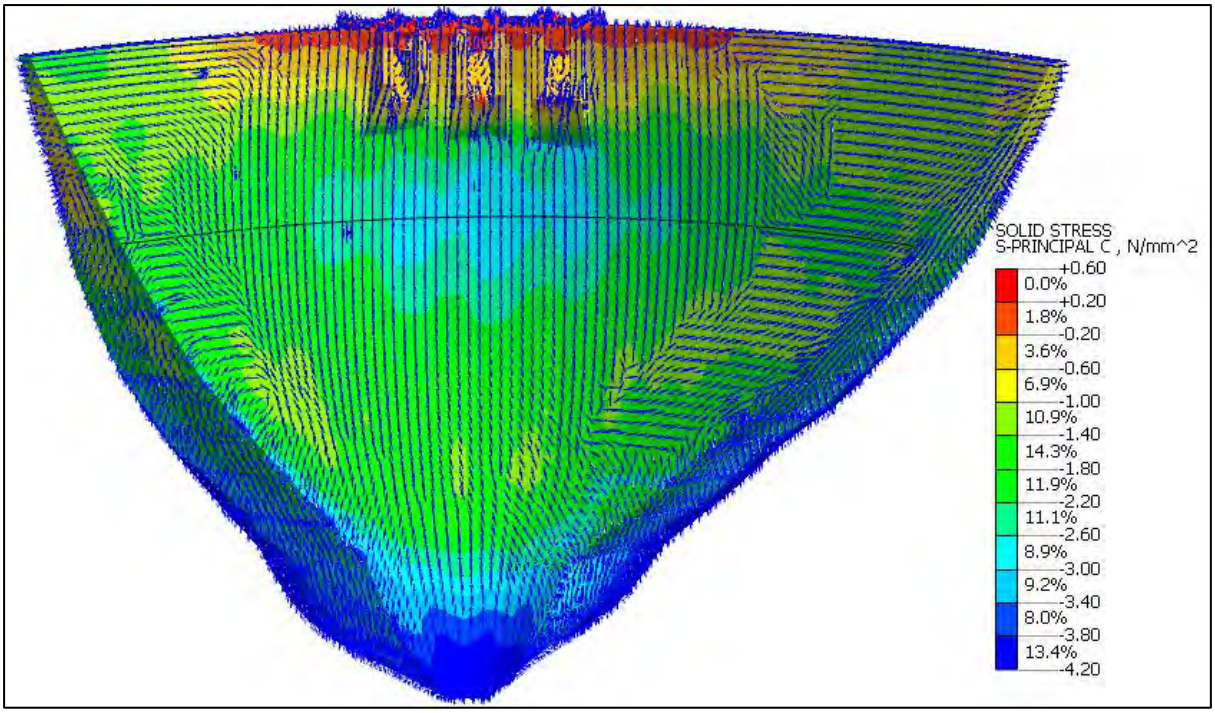

Figure 6-35: P3 principal stress vectors for impoundment to 630 mASL on 29/04/2023 (DS face)

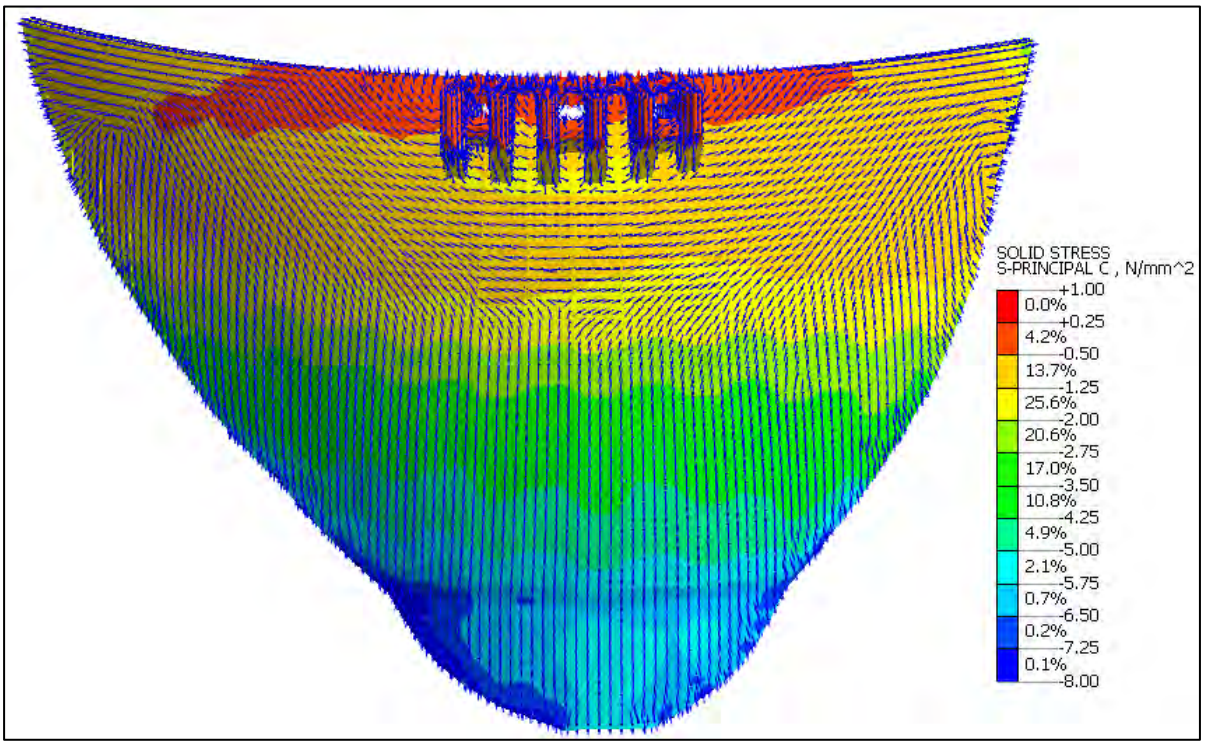

Figure 6-36: P3 principal stress vectors for impoundment to 630 mASL on 29/04/2023 (US face)

6.3.4 Interface Element Results

The normal displacements (X) predicted on the contraction joints between the individual monoliths of the dam are plotted in Figure 6-37. These plots indicate the relative displacements

between monoliths, normal to the plane of the joint interface. Essentially these are the expected joint openings modelled under the applicable analysis loadings.

The results plots indicate that under the applied loading conditions of Stage 3 impoundment, the dam joints are only expected to open at the crest, with openings of between 0 and 0.3 mm.

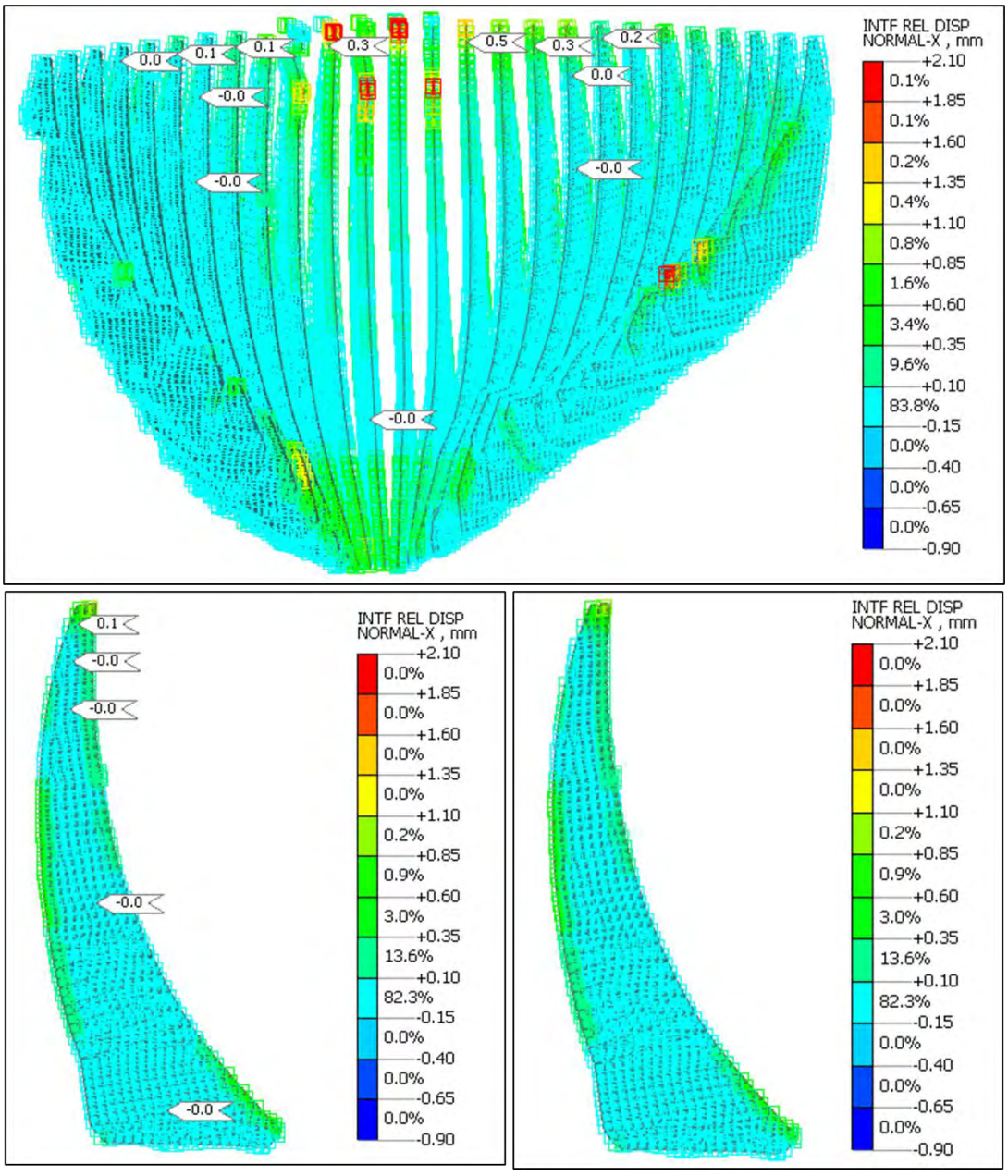

Figure 6-37: Axial displacement results on joints for impoundment to 630 mASL on 29/04/2023

6.4 4TH STAGE OF IMPOUNDING TO 670 MASL

6.4.1 Temperature Results

The simulated temperature state of the dam as computed for analysis stage 4 (T_{670}) is shown in Figure 6-38. The average temperature of the dam is 13.1 ° C, with a maximum of 26.5 ° C and minimum of 5.9 ° C. The contrast between the cold-water reservoir temperature conditions and the early Summer ambient temperatures, are evident from the modelled temperature state on the upstream and downstream face of the dam. The core temperature of the dam ranges from 9.5 ° C at the base to 19 ° C near the crest. The effect of solar radiation from sunshine experienced by the left flank of the dam is indicated by the modelled temperatures on the surface of the dam.

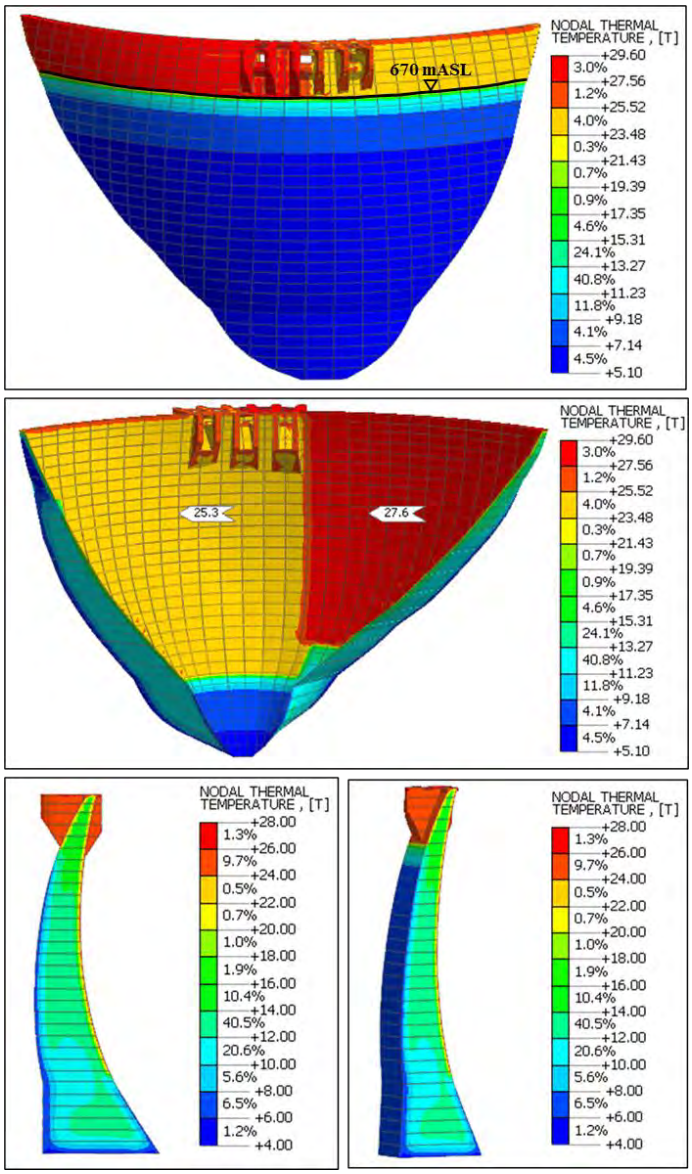

Figure 6-38: Temperature state of the dam at analysis stage 4 (Reservoir level 670 mASL, on 10/06/2023)

6.4.2 Displacement Results

The deformation analysis results were probed at nodal locations in the model corresponding to the respective location of each of the survey beacons B1 – B12. The simultaneous reservoir level was also sketched as a dark line on the downstream face of the dam FE model output plots for reference.

The radial (TX), tangential (TY) and vertical displacement (TZ) results computed through the structural FE analysis for an impounded water level of 670 mASL are illustrated in Figure 6-39 through Figure 6-43. Negative radial displacement values indicate downstream movement, and positive axial displacements indicate movement towards the right abutment of the dam. The resultant horizontal displacements (TXY) for the dam as predicted by the analyses at 10/06/2023 are illustrated in Figure 6-42.

The modelled deformation behaviour of the dam at this advanced stage of impoundment shows the lower portion of the dam moving forward (downstream) under cantilever action due to the hydrostatic loading, whilst the crest undergoes local upstream displacement due to the rise in ambient temperature causing it to expand and move backward. The exaggerated deformed mode of the dam is shown in Figure 6-43. The maximum anticipated radial displacement of the dam is expected to be 50 mm occurring in the downstream direction, just above mid-height of the dam at the crown cantilever.

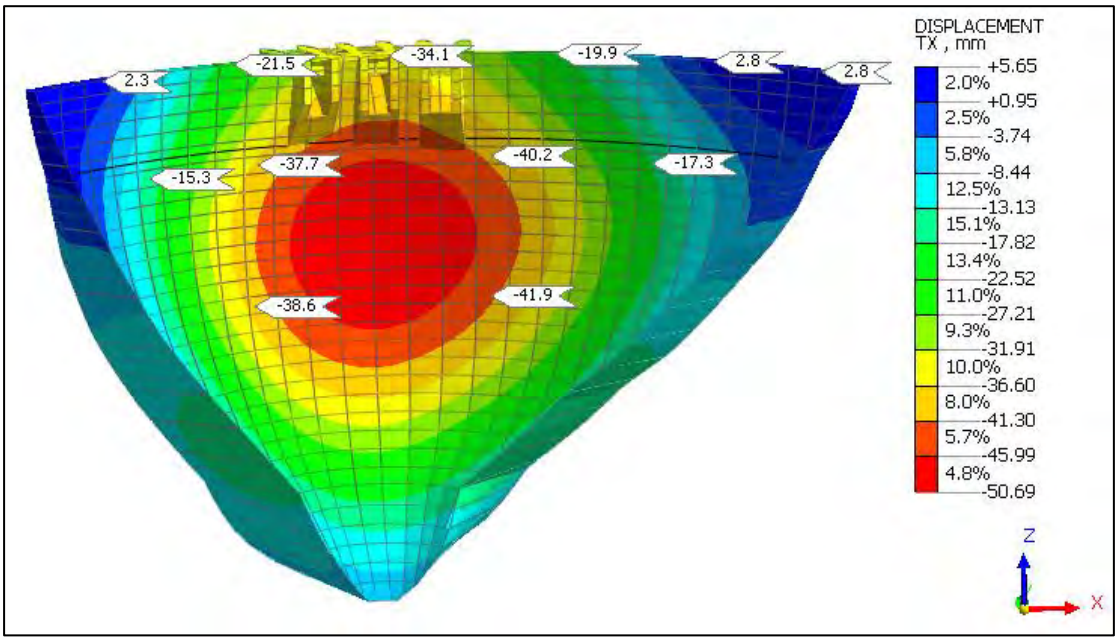

Figure 6-39: Radial (TX) displacements for impoundment to 670 mASL on 10/06/2023 (DS face)

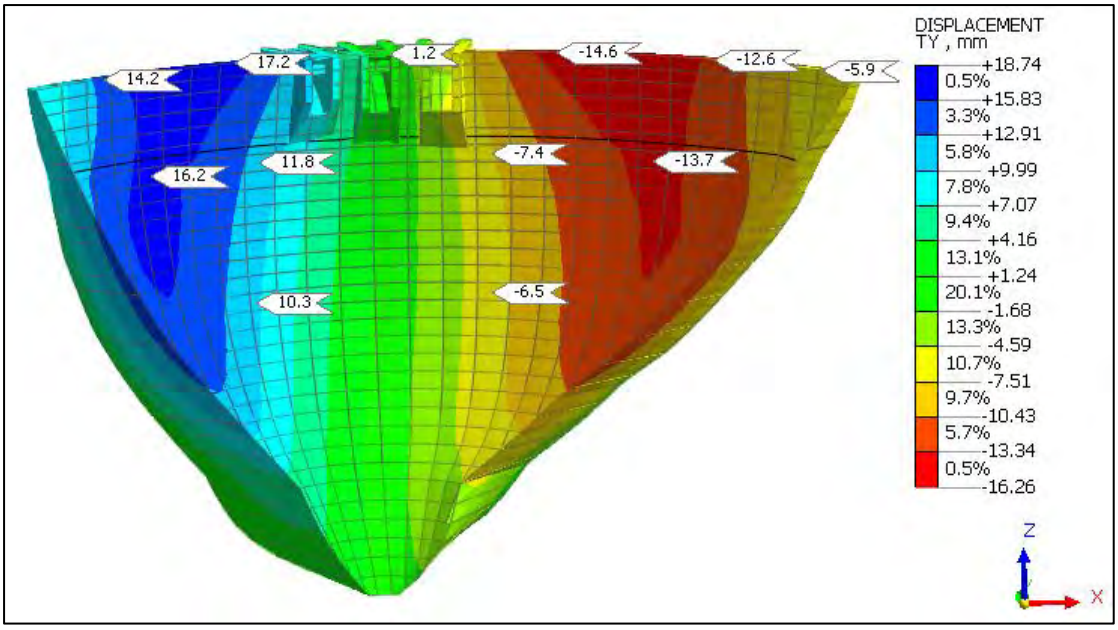

Figure 6-40: Tangential (TY) displacements for impoundment to 670 mASL on 10/06/2023 (DS face)

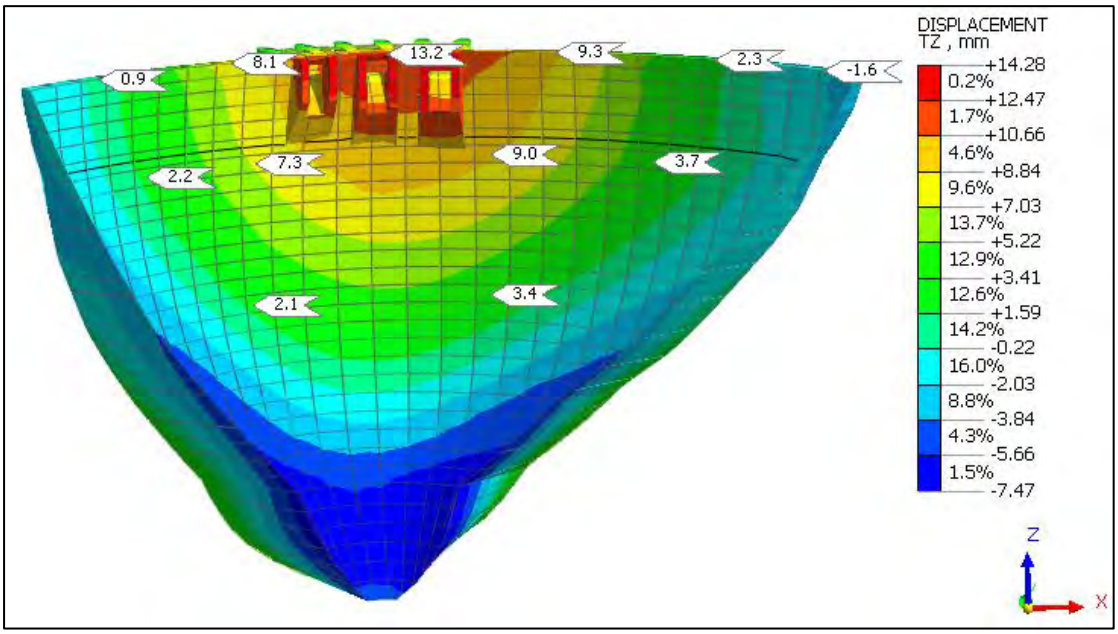

Figure 6-41: Vertical displacements for impoundment to 670 mASL on 10/06/2023 (DS face)

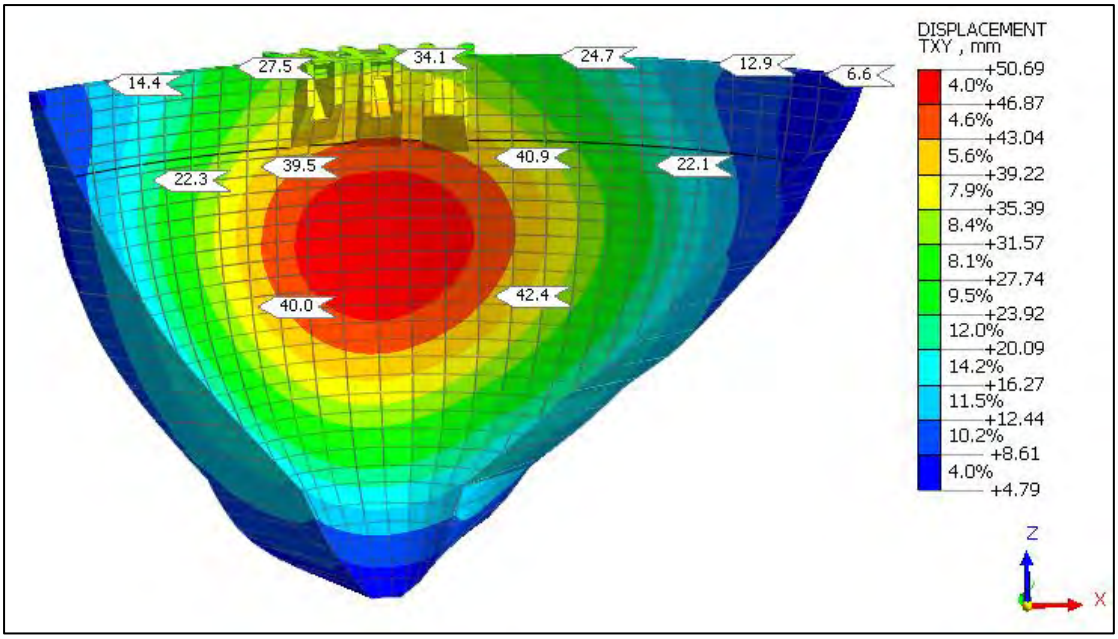

Figure 6-42: Horizontal displacements for impoundment to 670 mASL on 10/06/2023 (DS face)

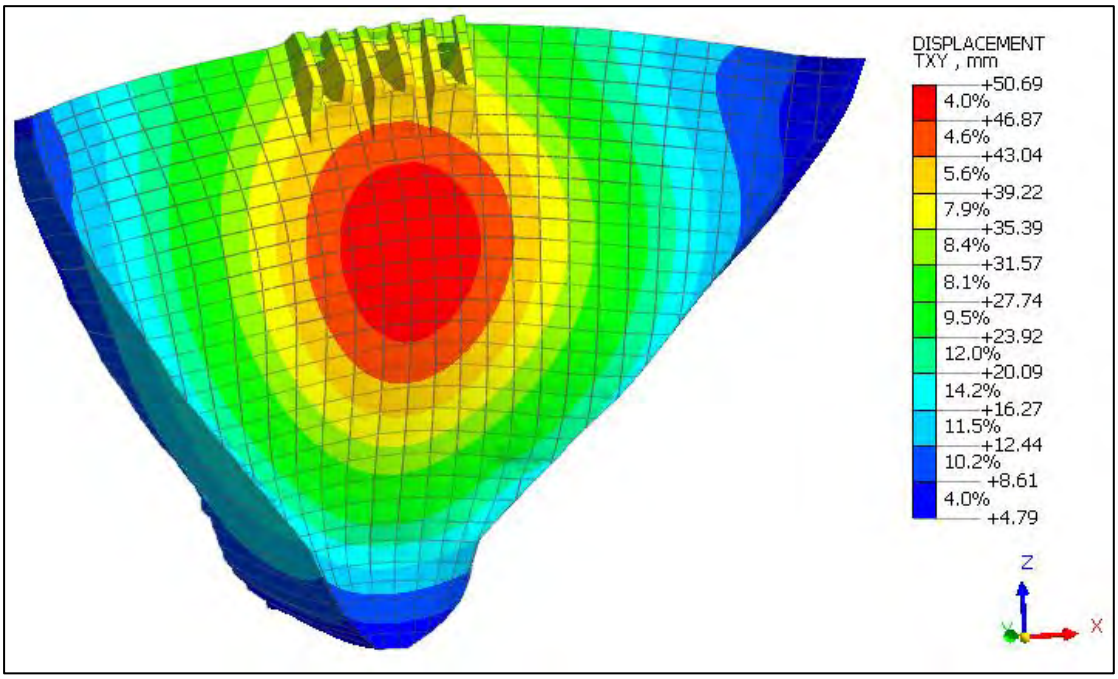

Figure 6-43: Exaggerated deformed shape of dam with horizontal displacement plot on 10/06/2023

A displacement vector plot is shown in Figure 6-44 to indicate the vector direction of the horizontal displacement of the dam. It can be seen that the horizontal displacement at the crown cantilever is almost completely radial, whilst that near the abutments it is mostly axial (tangential), with a smooth transition from arch crown to abutments. This is synonymous with displacement behaviour reported by other large arch dams as shown in Figure 6-45 (Dungar, 1985).

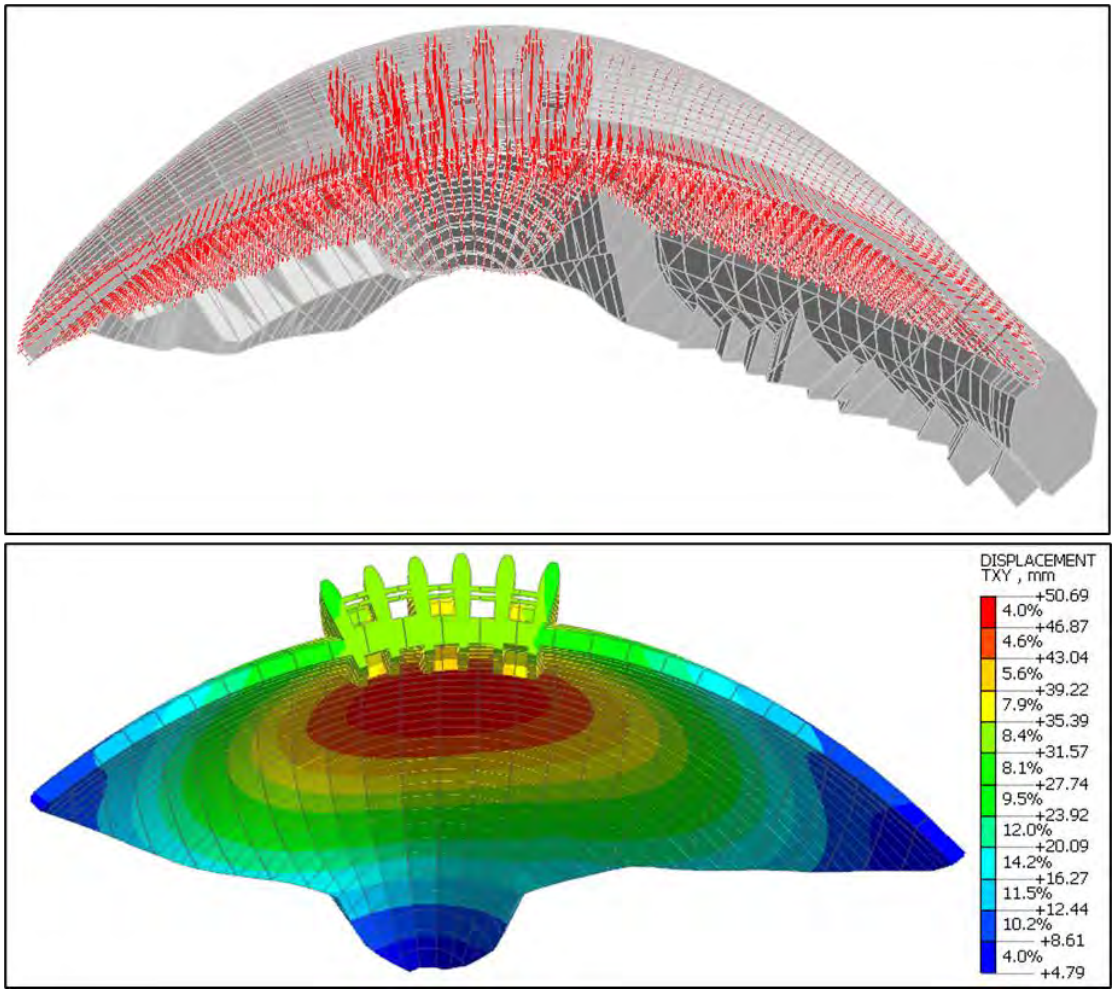

Figure 6-44: Displacement vector plot of dam for impoundment to 670 mASL on 10/06/2023

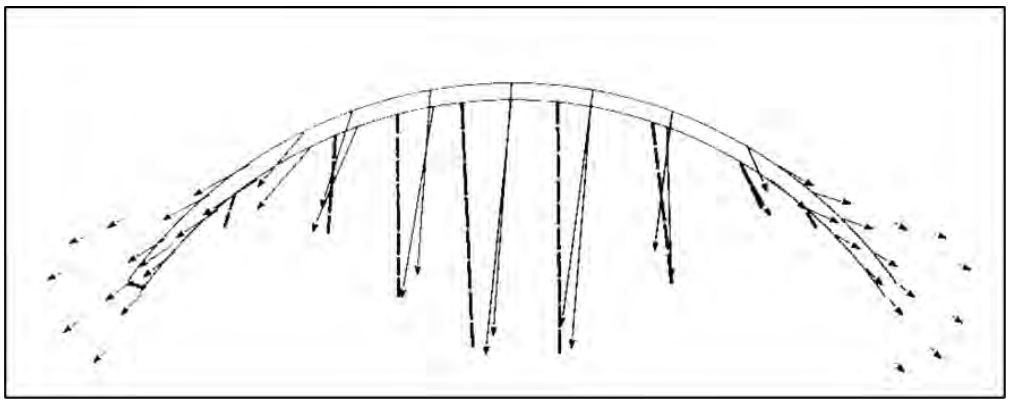

Figure 6-45: Typical 2-dimensional displacement vectors at crest arch dam from geodetic survey results (Dungar, 1985)

6.4.3 Stress Results

Contour plots of the P3 principal (compressive) stress results output from the structural analysis are illustrated in Figure 6-46 and Figure 6-47. Vector plots illustrated in Figure 6-48 and Figure 6-49 indicate that the primary compressive load mechanism of the dam has transitioned from

vertical to horizontal axial compression (arching). The vectors show horizontal arching along the top two-thirds of the dam body.

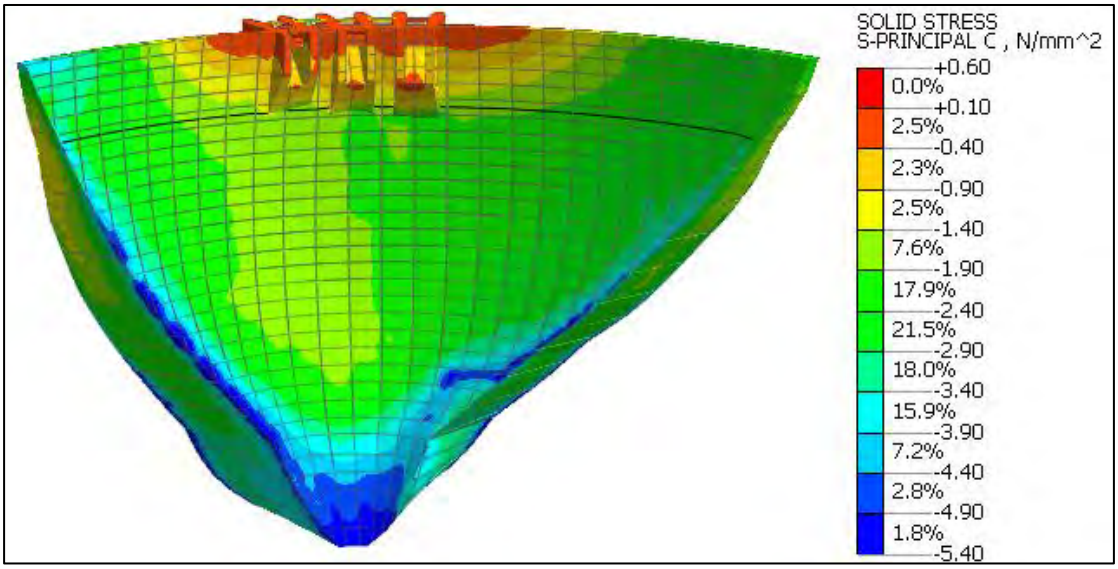

Figure 6-46: P3 principal stress results for reservoir impoundment to 670 mASL on 10/06/2023 (DS face)

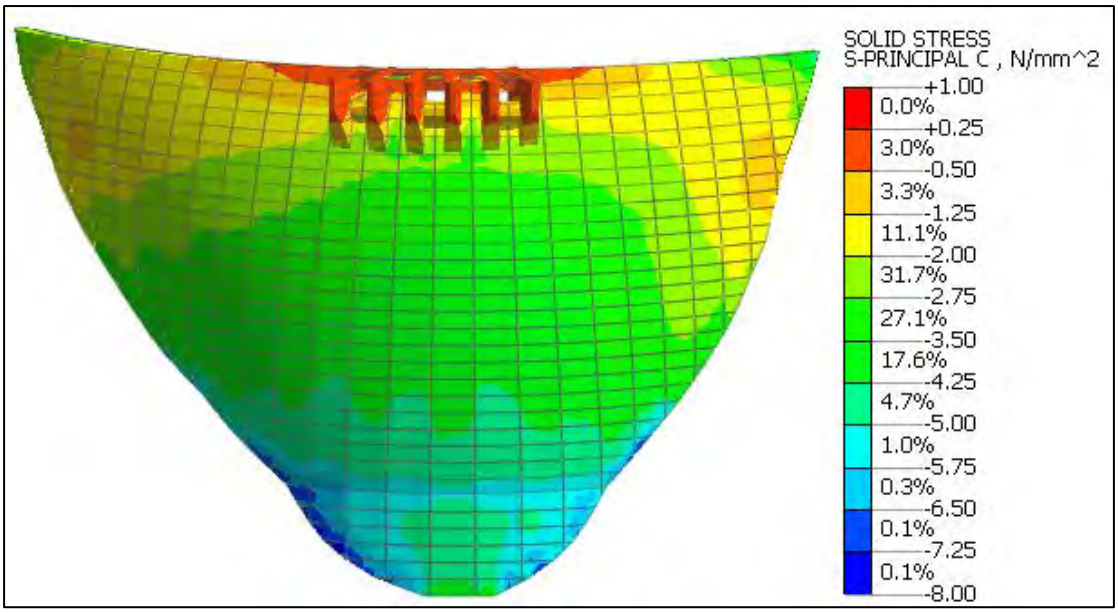

Figure 6-47: P3 principal stress results for reservoir impoundment to 670 mASL on 10/06/2023 (US face)

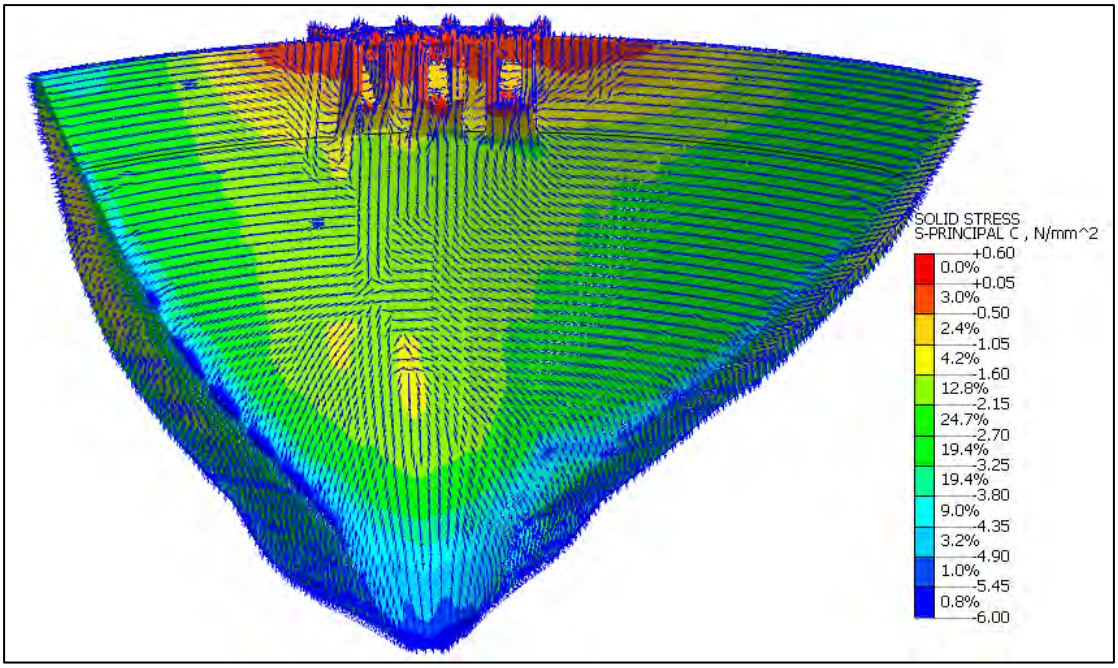

Figure 6-48: P3 principal stress vectors for impoundment to 670 mASL on 10/06/2023 (DS face)

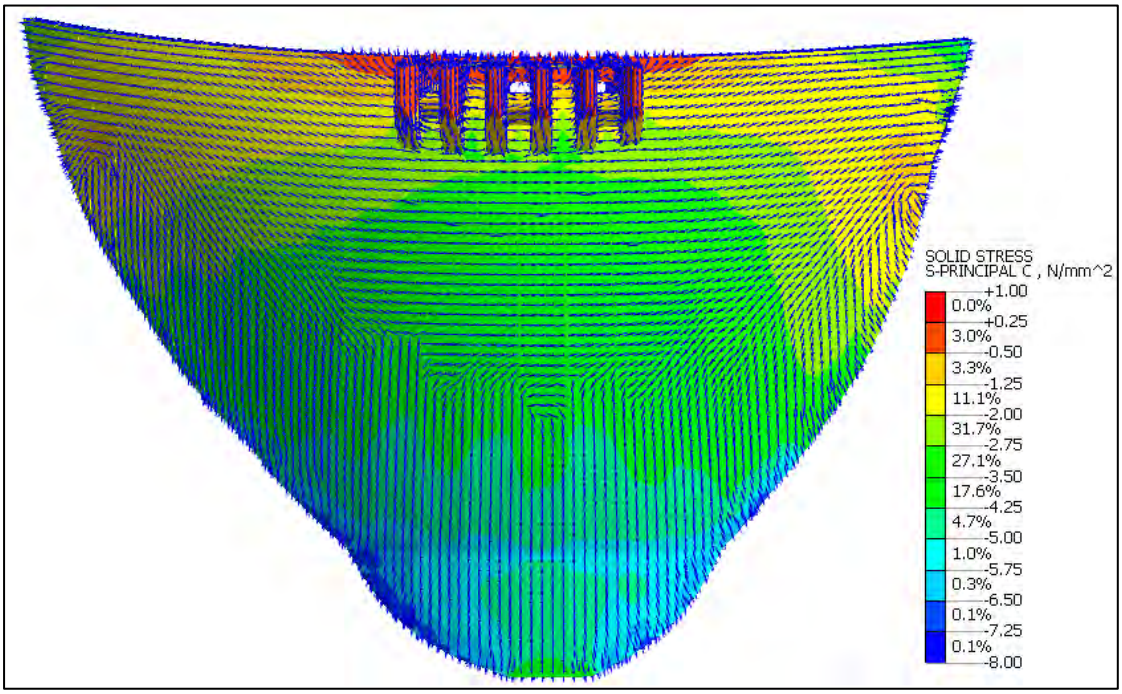

Figure 6-49: P3 principal stress vectors for impoundment to 670 mASL on 10/06/2023 (US face)

6.4.4 Interface Element Results

Measured and predicted behaviour of the joint meters during the progressive impoundment loading period from commencement of reservoir filling (21 November 2022) to reservoir level 630 mASL (29 April 2023), have shown that the joints have closed since impoundment. The closure is relative to the initial joint opening position at commencement of reservoir filling and

is due to the compressive stress response in the arch under hydrostatic loading. This can be seen in Figure 6-37 reproduced as Figure 6-50.

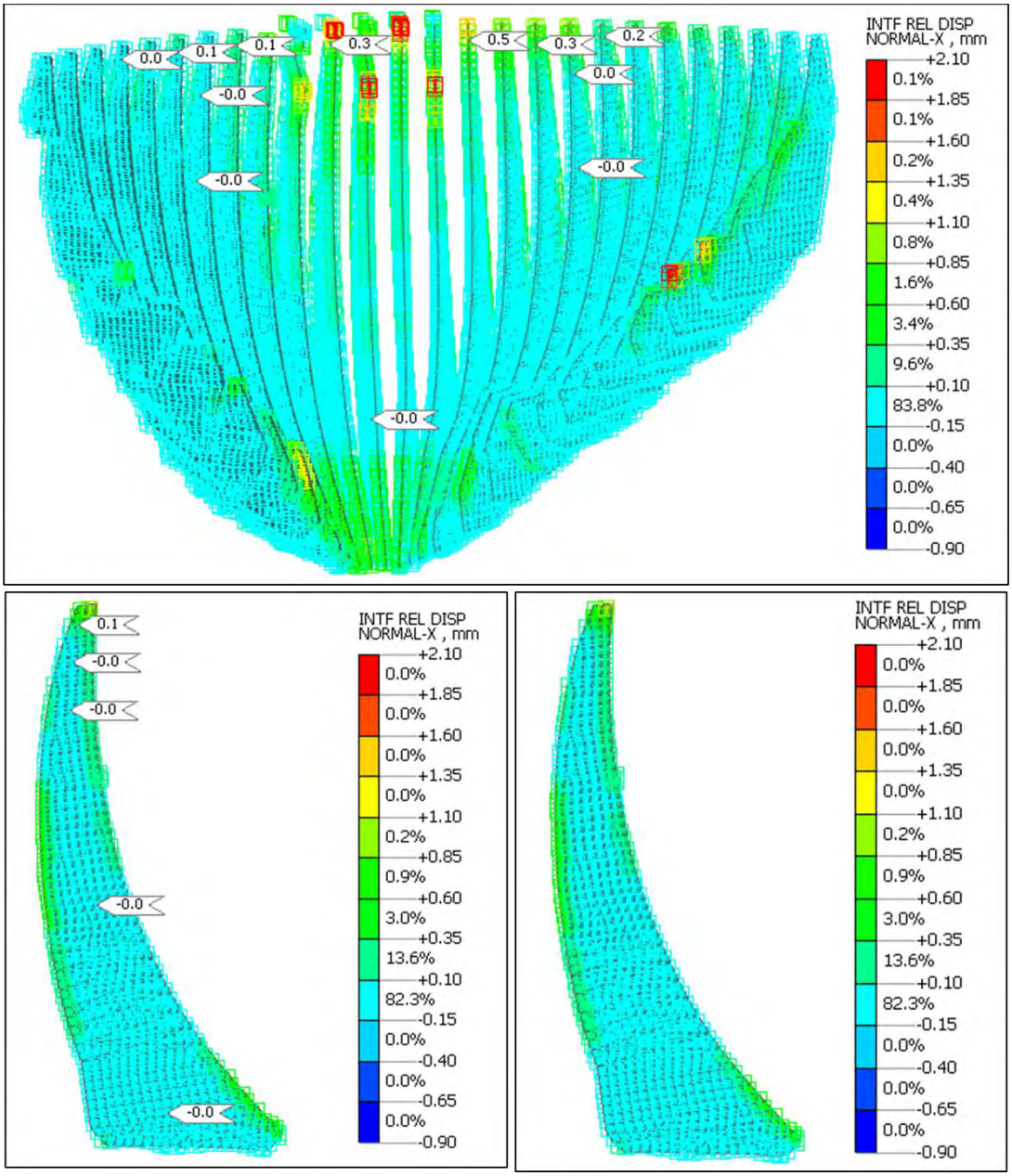

Figure 6-50: Axial displacement results on joints for impoundment to 630 mASL on 29/04/2023

6.4.5 Relative rotational displacement results (pendulums)

The movements predicted for the hanging and inverted pendulums of monolith 13, 16 and 19 as measured at elevation 525.5 mASL, are shown in Figure 6-51 and Figure 6-52 for impoundment stage 670 mASL on 10/06/2023. The pendulums measure differential movement between the hanging point and the measurement station point. Predicted measurements are obtained by subtracting the modelled displacement at the measurement point from that modelled at the hanging/anchor point.

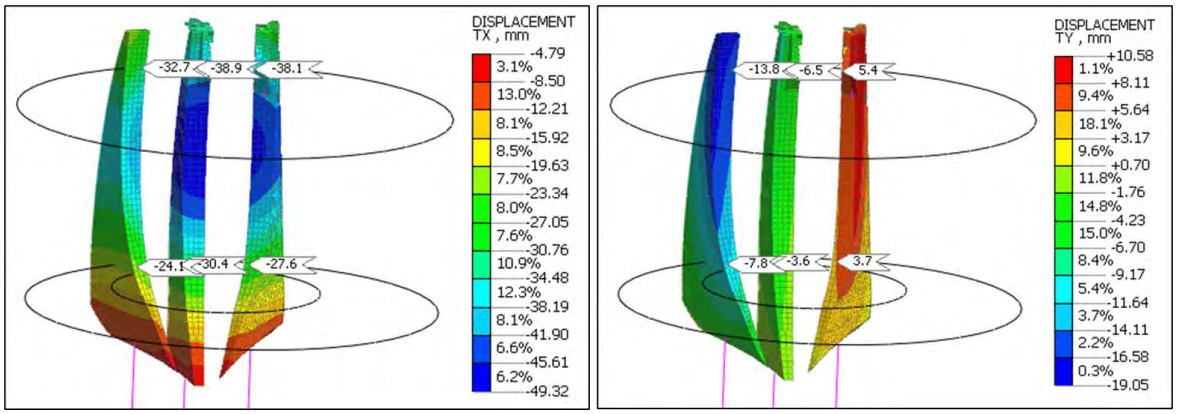

Figure 6-51: Radial (left) and tangential (right) predicted movements of hanging pendulums in monolith 13, 16 and 19 for impoundment to 670 mASL on 10/06/2023

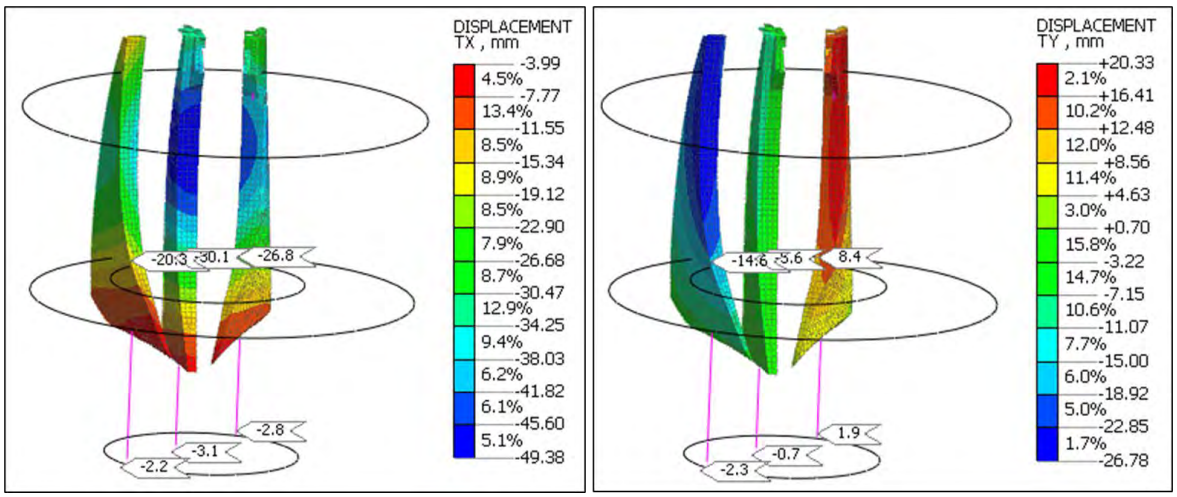

Figure 6-52: Radial (left) and tangential (right) predicted movements of inverted pendulums in monolith 13, 16 and 19 for impoundment to 670 mASL on 10/06/2023

6.5 5TH STAGE OF IMPOUNDING TO 696 MASL

6.5.1 Temperature Results

The simulated temperature state of the dam as computed at analysis stage 5 (T_{696}) is shown in Figure 6-53. The average temperature of the dam is 14.9 ° C, with a maximum of 33.8 ° C and minimum of 7.5 ° C. The contrast between the cool water reservoir temperature conditions and the hot Summer ambient temperatures, are evident from the modelled temperature state on the upstream and downstream face of the dam. The core temperature of the dam ranges from 10 ° C at the base to 21 ° C near the crest. The effect of solar radiation from sunshine experienced by the left flank of the dam is indicated by the modelled temperatures on the surface of the dam.

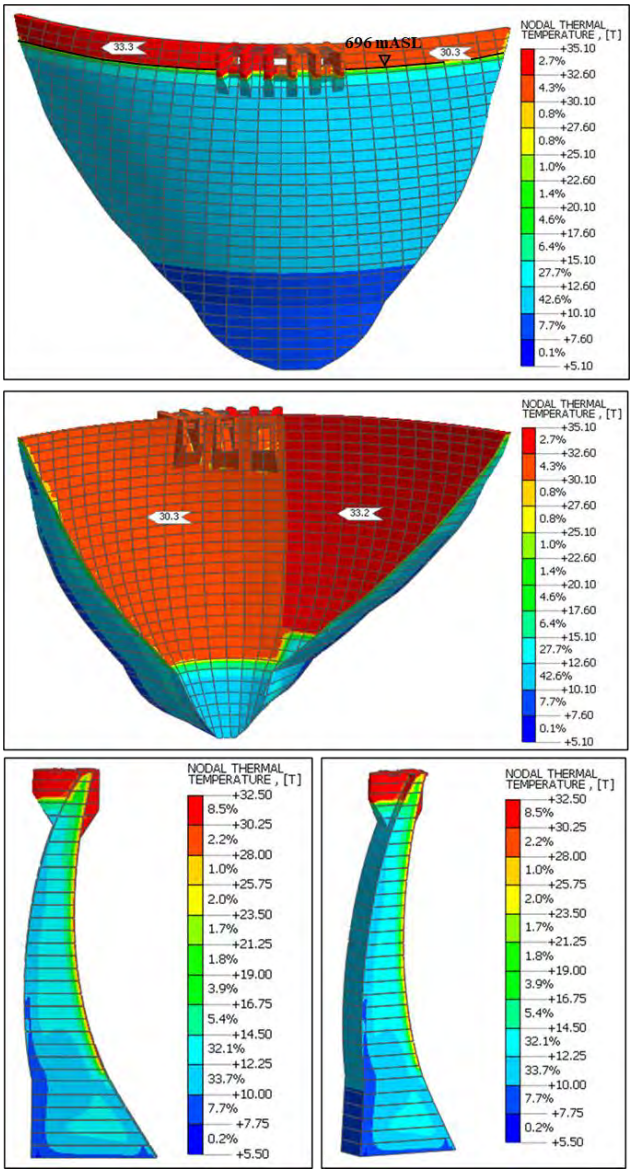

Figure 6-53: Temperature state of the dam at analysis stage 5 (Reservoir level 696 mASL, on 18/08/2023)

6.5.2 Displacement Results

The deformation analysis results were probed at nodal locations in the model corresponding to the respective location of each of the survey beacons B1 – B12. The simultaneous reservoir level was also sketched as a dark line on the downstream face of the dam FE model output plots for reference.

The radial (TX), tangential (TY) and vertical displacement (TZ) results computed through the structural FE analysis for an impounded water level of 696 mASL, are illustrated in Figure 6-54 through Figure 6-58. Negative radial displacement values indicate downstream movement, and positive axial displacements indicate movement towards the right abutment of the dam. The resultant horizontal displacements (TXY) for the dam as predicted by the analyses at 18/08/2023 are illustrated in Figure 6-57.

The modelled deformation behaviour of the dam at this late stage of impoundment, shows the mid-height portion of the dam moving forward (downstream) under cantilever-arch action due to the hydrostatic loading, whilst the crest undergoes local upstream displacement due to the rise in ambient temperature causing it to expand and move backward. The exaggerated deformed mode of the dam is shown in Figure 6-58. The maximum anticipated radial displacement of the dam is expected to be 69 mm occurring in the downstream direction, two thirds of dam height at the crown cantilever.

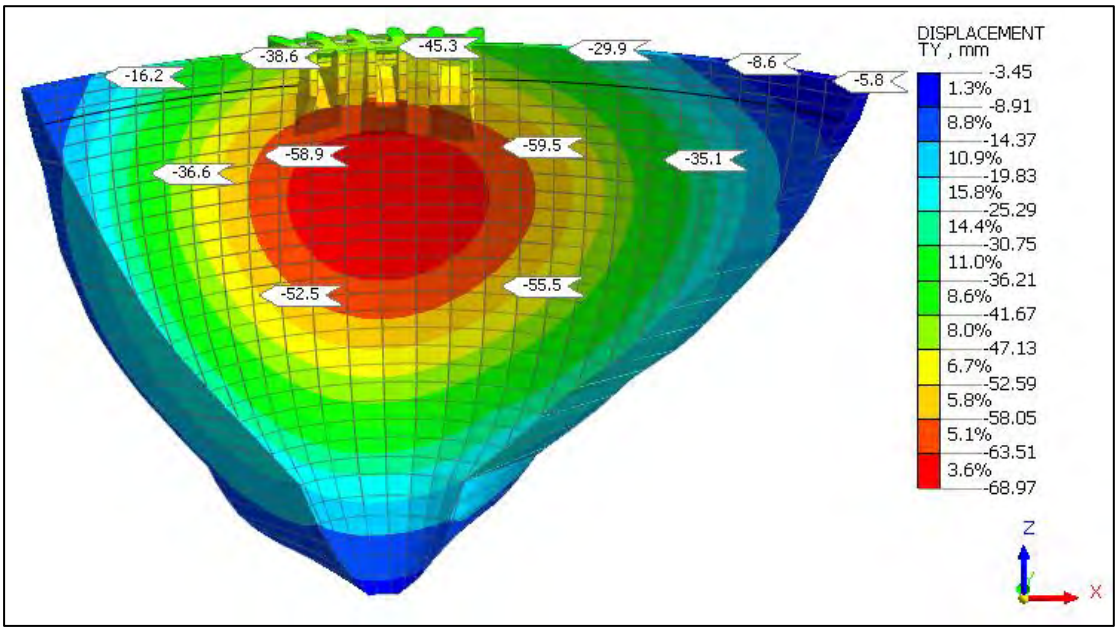

Figure 6-54: Radial (TX) displacements for impoundment to 696 mASL on 18/08/2023 (DS face)

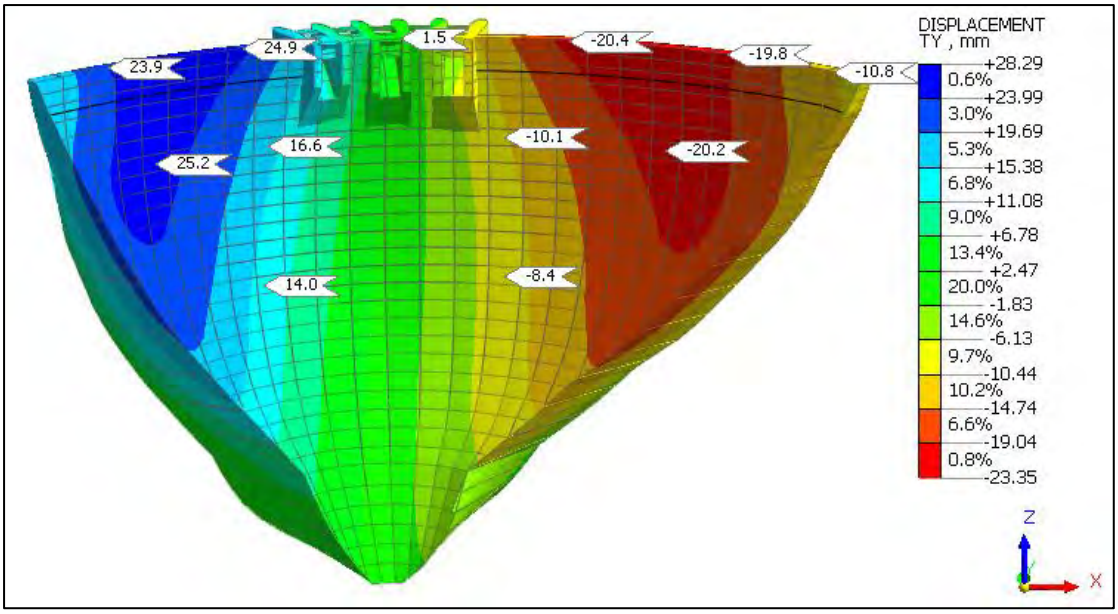

Figure 6-55: Tangential (TY) displacements for impoundment to 696 mASL on 18/08/2023 (DS face)

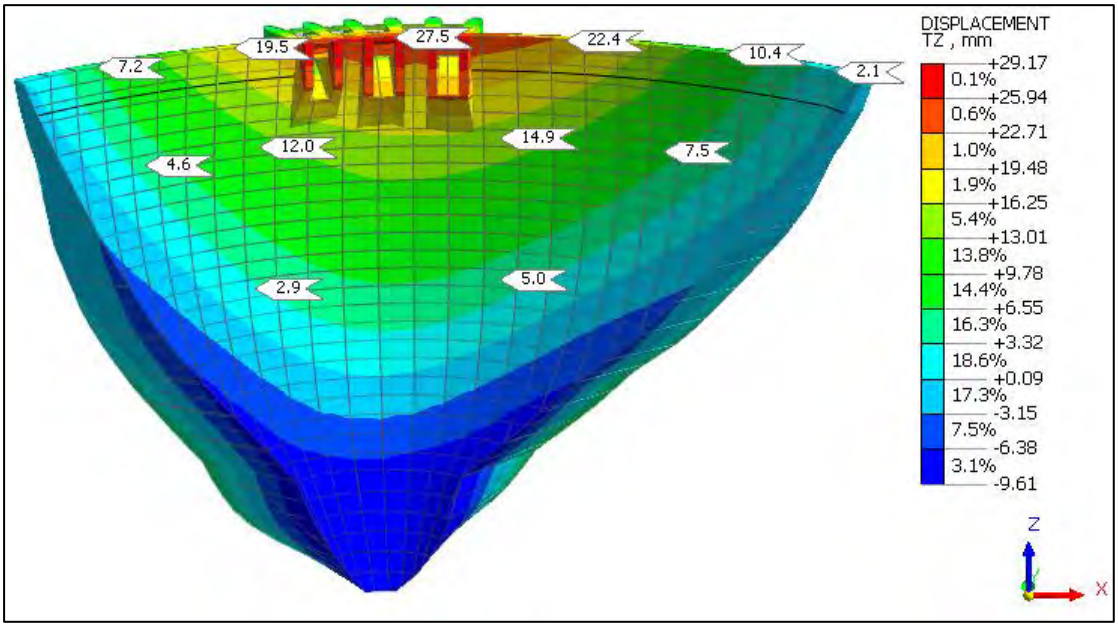

Figure 6-56: Vertical displacements for impoundment to 696 mASL on 18/08/2023 (DS face)

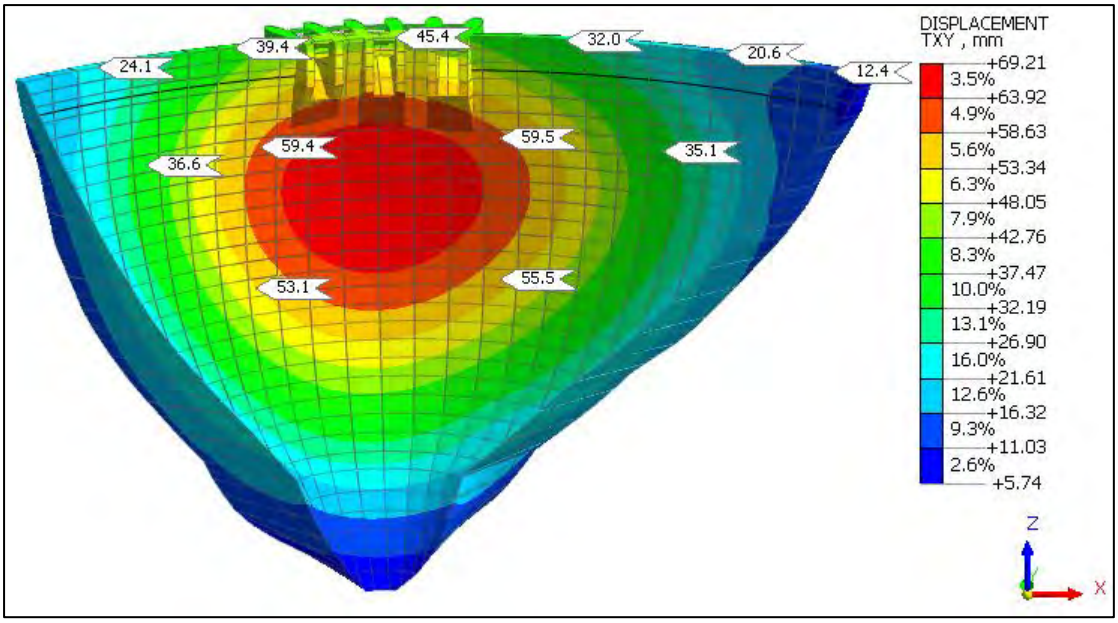

Figure 6-57: Horizontal displacements for impoundment to 696 mASL on 18/08/2023 (DS face)

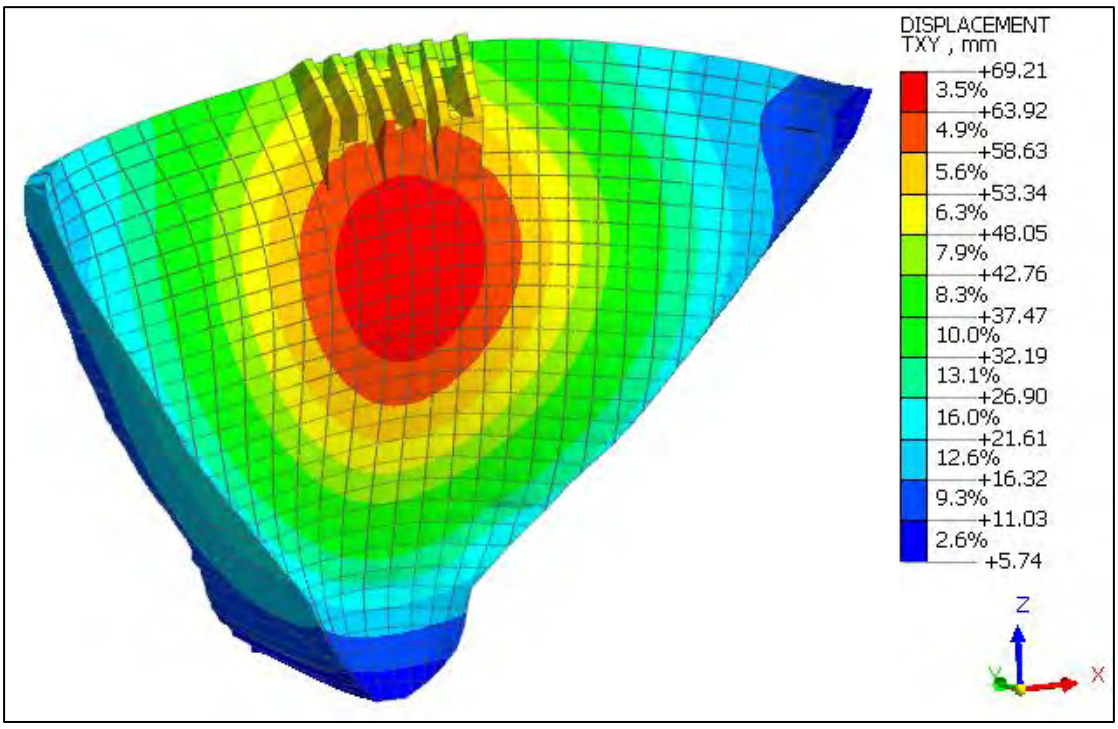

Figure 6-58: Exaggerated deformed shape of dam with horizontal displacement plot on 18/08/2023

A displacement vector plot is shown in Figure 6-59 to indicate the vector direction of the horizontal displacement of the dam. It can be seen that the horizontal displacement at the crown cantilever is almost completely radial whilst that near the abutments it is mostly axial (tangential), with a smooth transition from arch crown to abutments. This is synonymous with displacement behaviour reported by other large arch dams as shown in Figure 6-60 (Dungar, 1985).

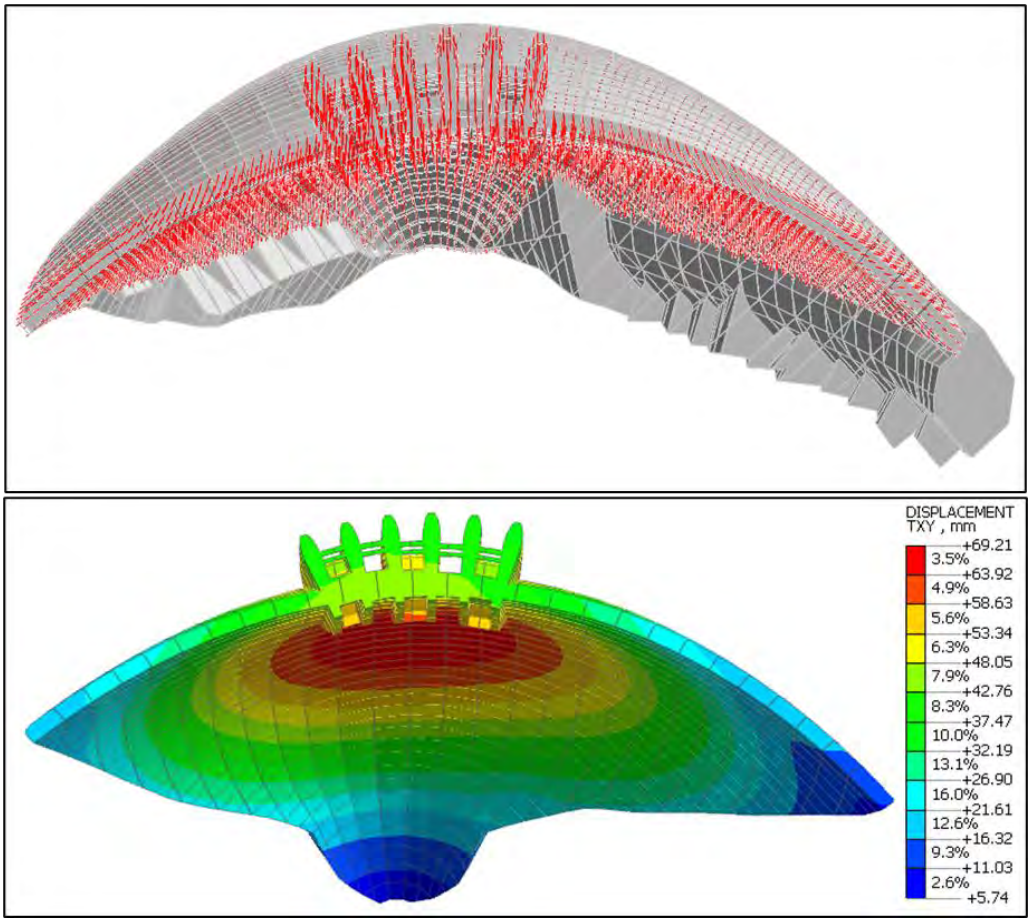

Figure 6-59: Displacement vector plot of dam for impoundment to 696 mASL on 18/08/2023

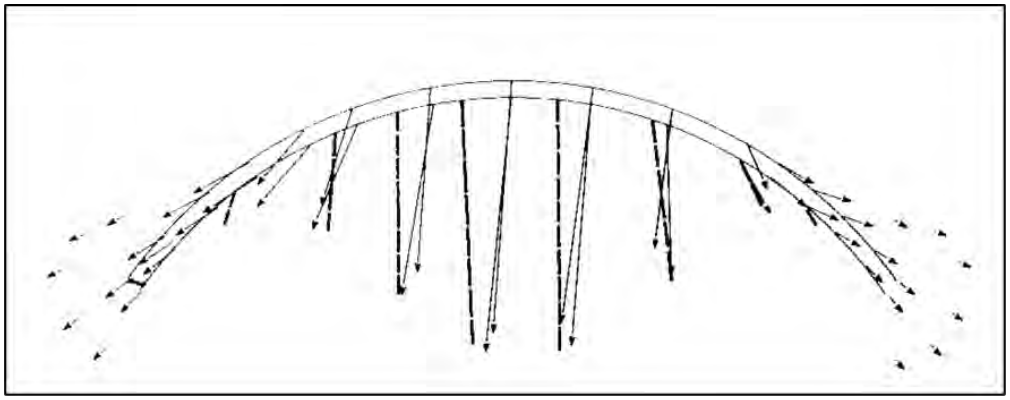

Figure 6-60: Typical 2-dimensional displacement vectors at crest arch dam from geodetic survey results (Dungar, 1985)

6.5.3 Stress Results

Contours plots of the P3 principal (compressive) stress results output from the structural analysis are illustrated in Figure 6-61 and Figure 6-62. Vector plots illustrated in Figure 6-63 and Figure 6-64, indicate that the primary compressive load mechanism of the dam has transitioned from vertical to horizontal axial compression (arching). The vectors show horizontal arching along the top 70% of the dam body.

The largest compressive stresses expected to develop in the dam of approximately 7 – 7.5 MPa, are within the allowable compressive design strength of 8 MPa. This is based on concrete compressive cube strength of the 32 MPa for the dam, assuming a material factor of 4 for normal loading conditions. Compressive stress values of 8 - 9 MPa at the toe of the arch along the abutment, are considered concentrations due to a combination of a re-entrant corner occurring in the modelling geometry and the discrete change in stiffness between the dam and foundation material. Modelling features that cause stress concentrations are discussed in section 2.5.9.

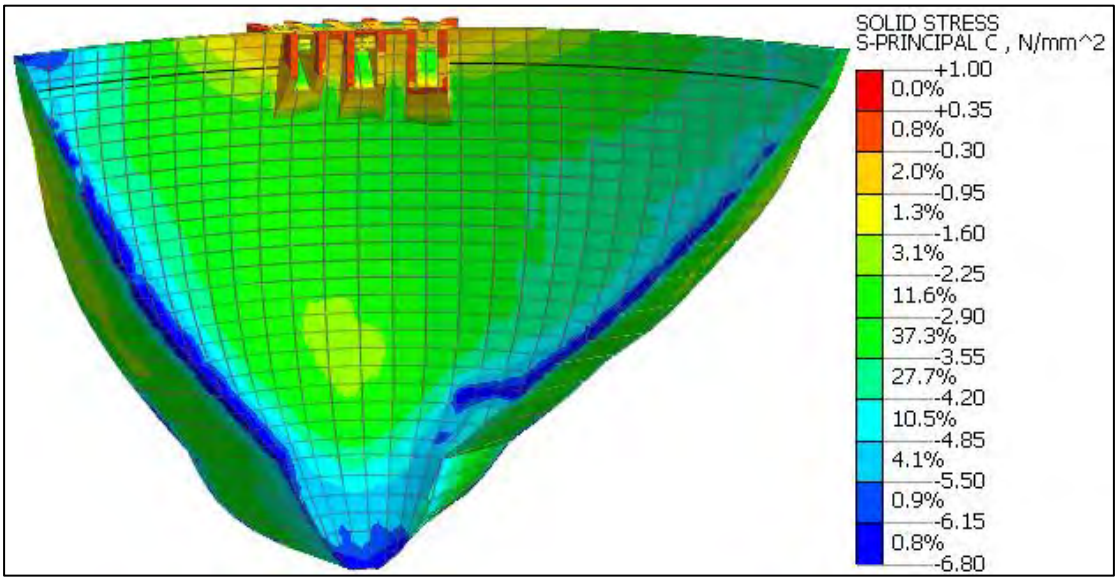

Figure 6-61: P3 principal stress results for reservoir impoundment to 696 mASL on 18/08/2023 (DS face)

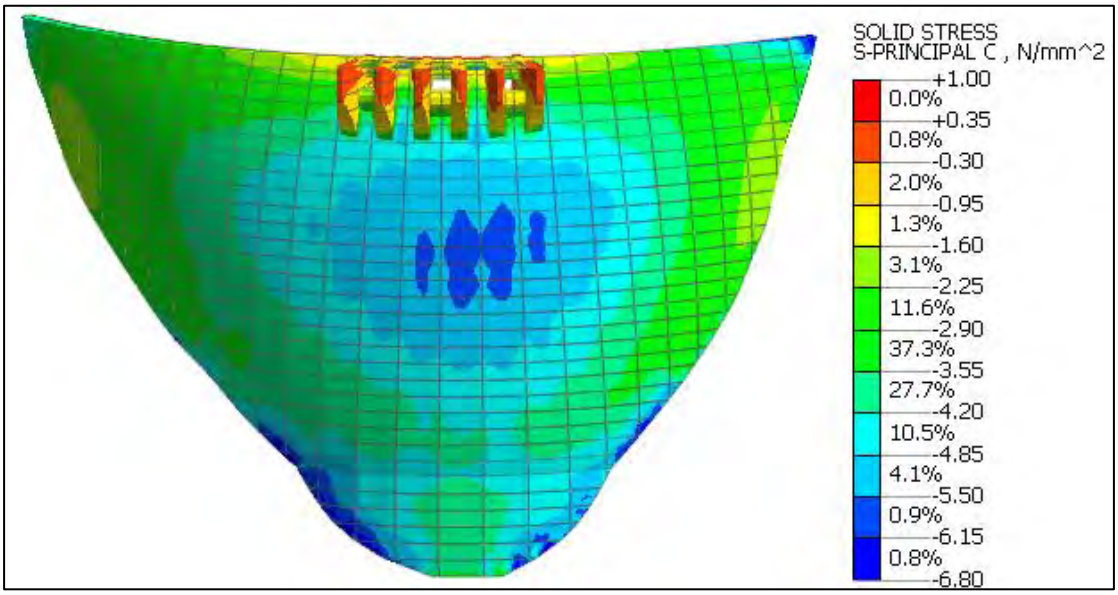

Figure 6-62: P3 principal stress results for reservoir impoundment to 696 mASL on 18/08/2023 (US face)

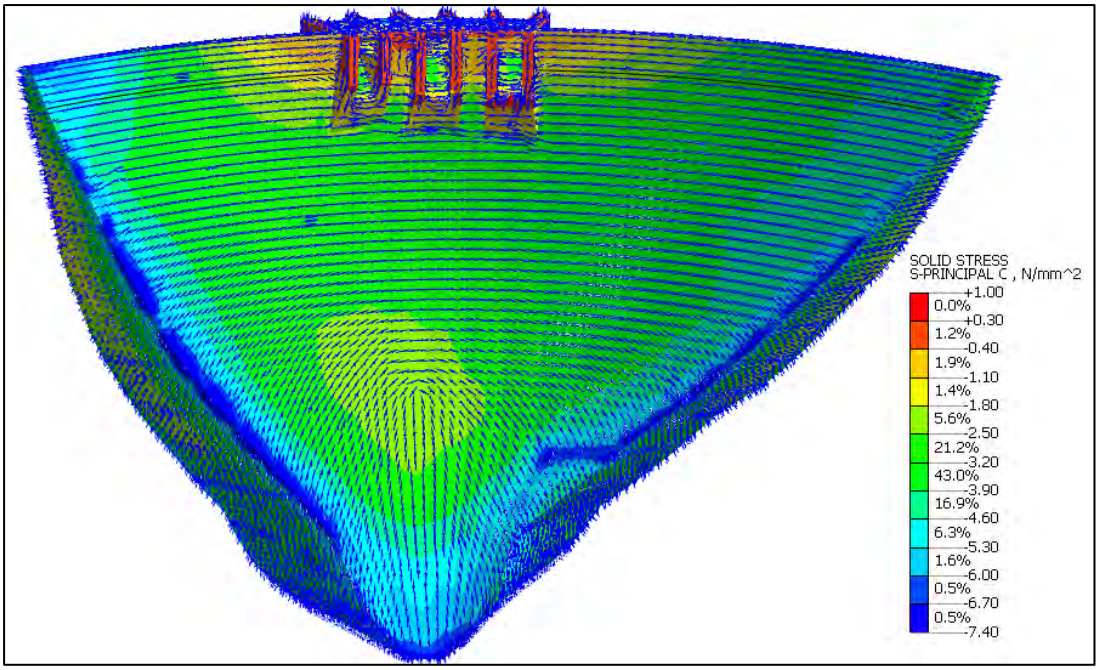

Figure 6-63: P3 principal stress vectors for impoundment to 696 mASL on 18/08/2023 (DS face)

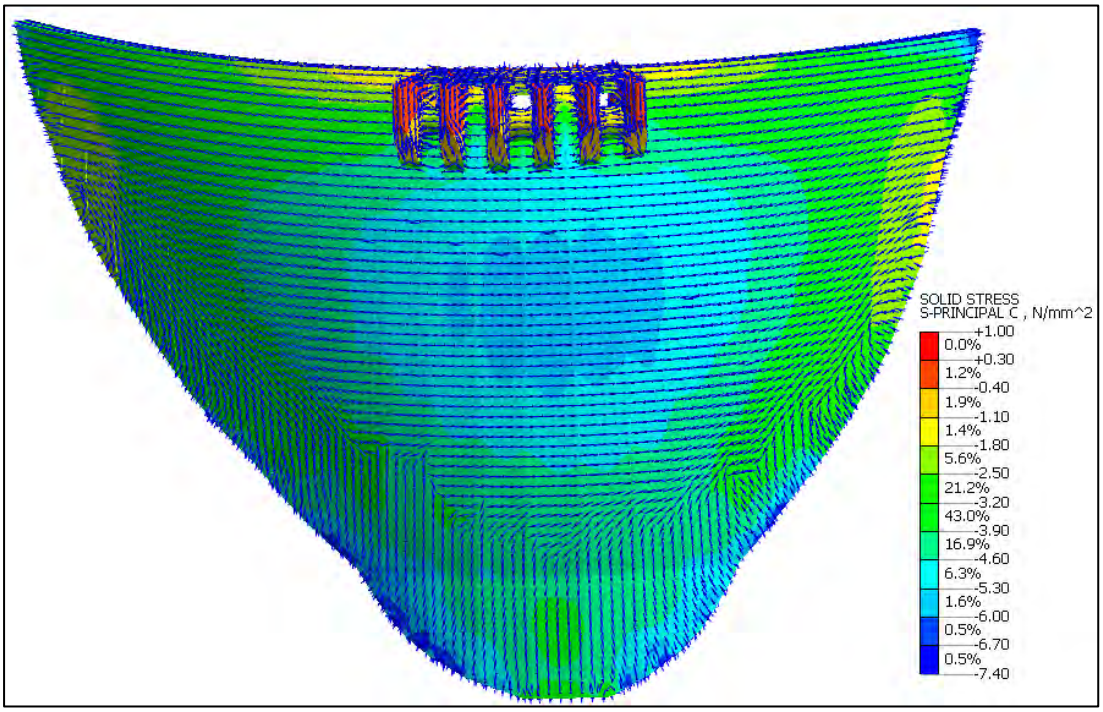

Figure 6-64: P3 principal stress vectors for impoundment to 696 mASL on 18/08/2023 (US face)

Vertical, axial and major principal stress results for analysis stage 5 is shown in Figure 6-65 through Figure 6-70. The peak compressive stress values of 6 – 8 MPa computed by the FE analysis are within the allowable compressive design strength based on a cube strength of 32 MPa, assuming a material safety factor for usual loading conditions of 4.

The maximum anticipated tensile stress of 0.6 MPa is within the dam concrete allowable direct tensile strength of 3 MPa.

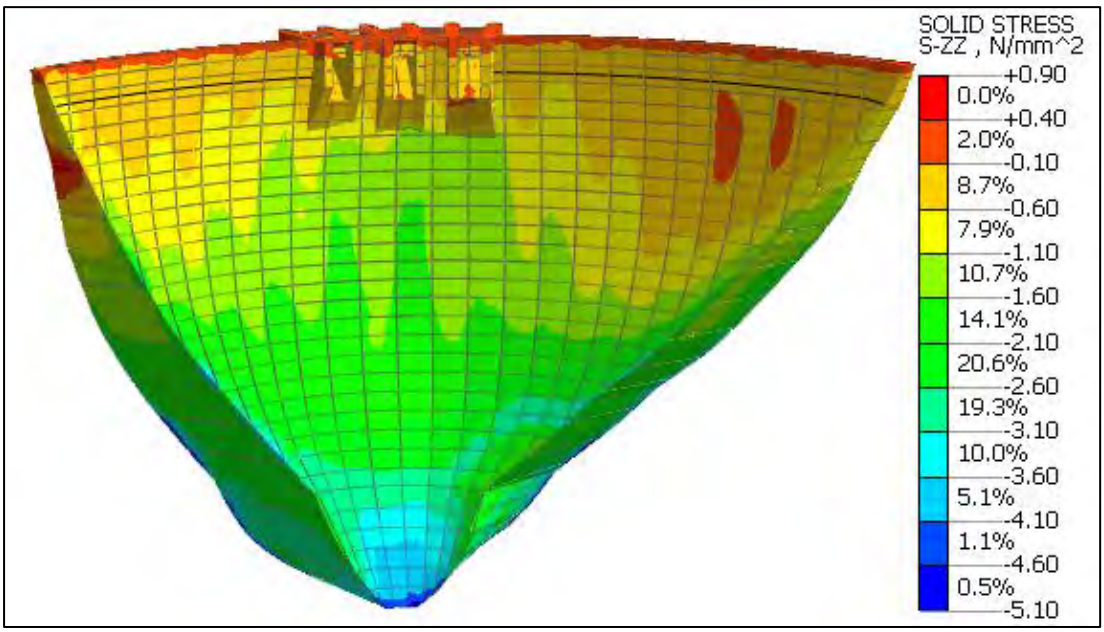

Figure 6-65: Vertical stress results for reservoir elevation 696 mASL on 18/08/2023 (DS face)

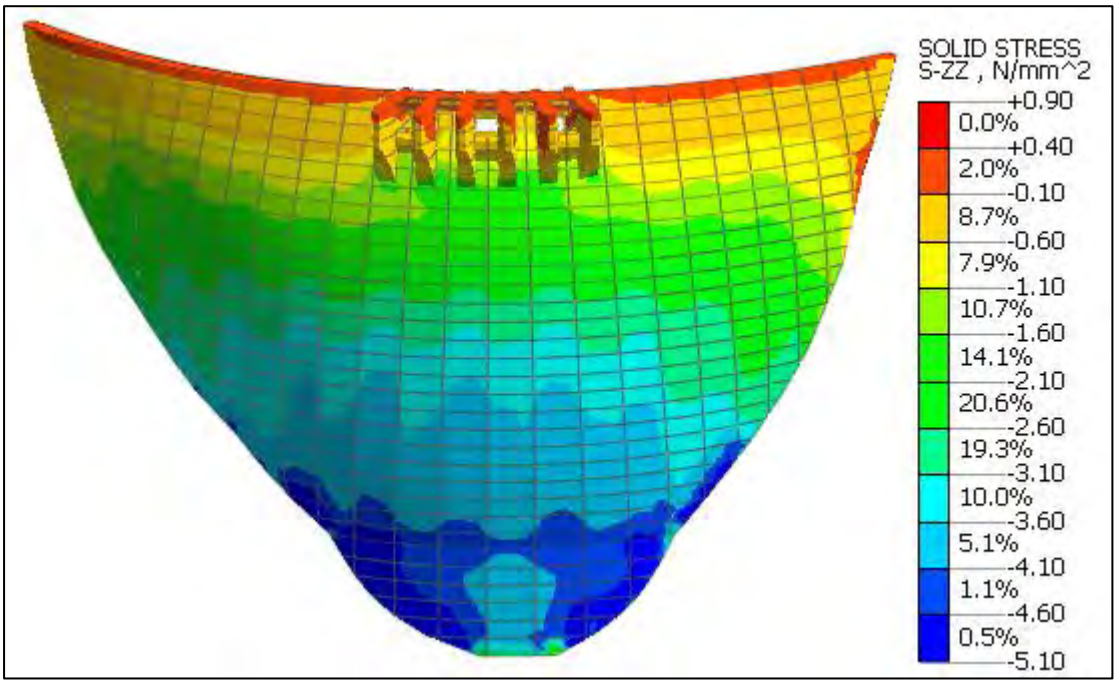

Figure 6-66: Vertical stress results for reservoir elevation 696 mASL on 18/08/2023 (US face)

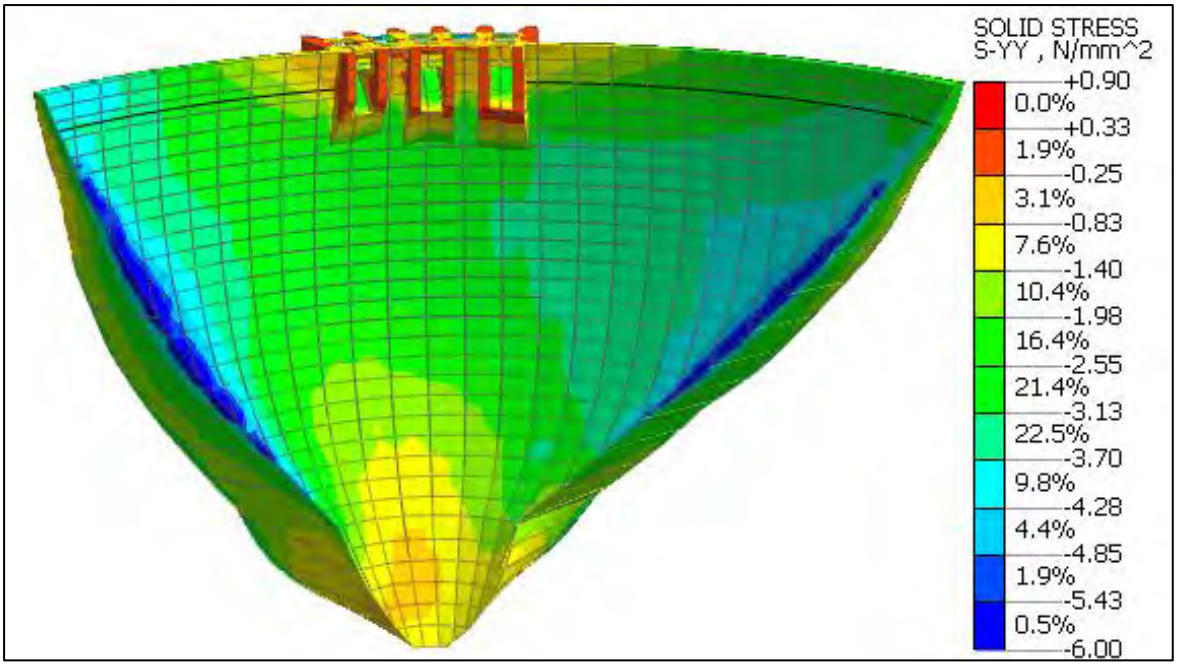

Figure 6-67: Axial (hoop) stress results for reservoir elevation 696 mASL on 18/08/2023 (DS face)

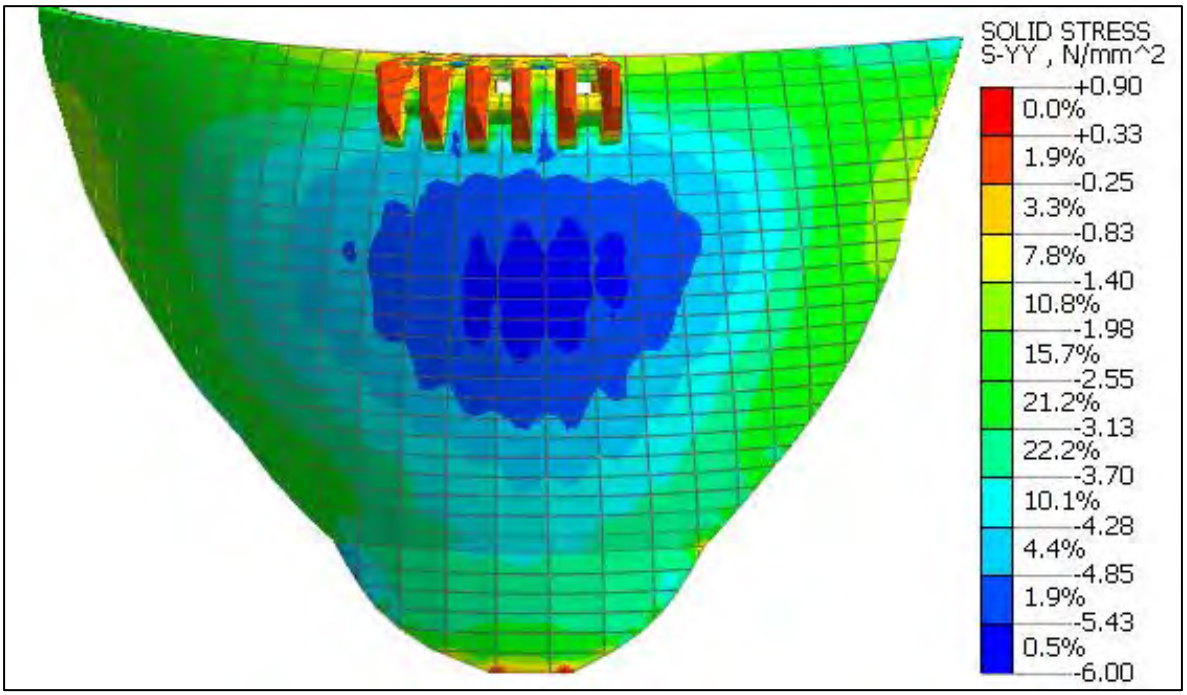

Figure 6-68: Axial (hoop) stress results for reservoir elevation 696 mASL on 18/08/2023 (US face)

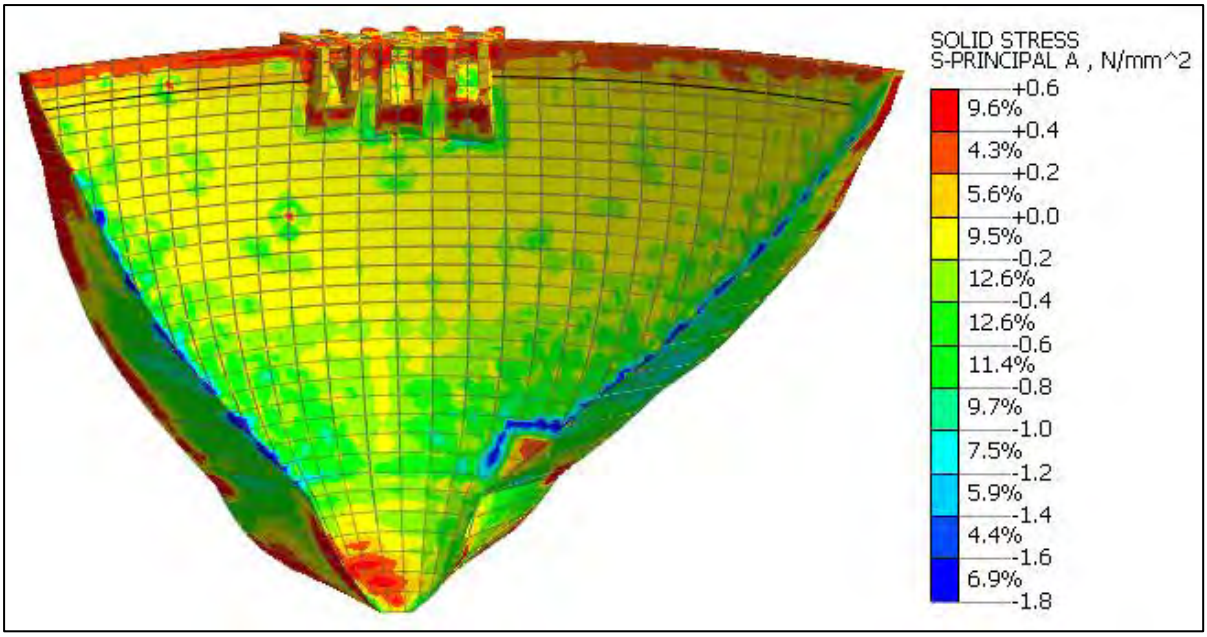

Figure 6-69: P1 principal stress results for reservoir elevation 696 mASL on 18/08/2023 (DS face)

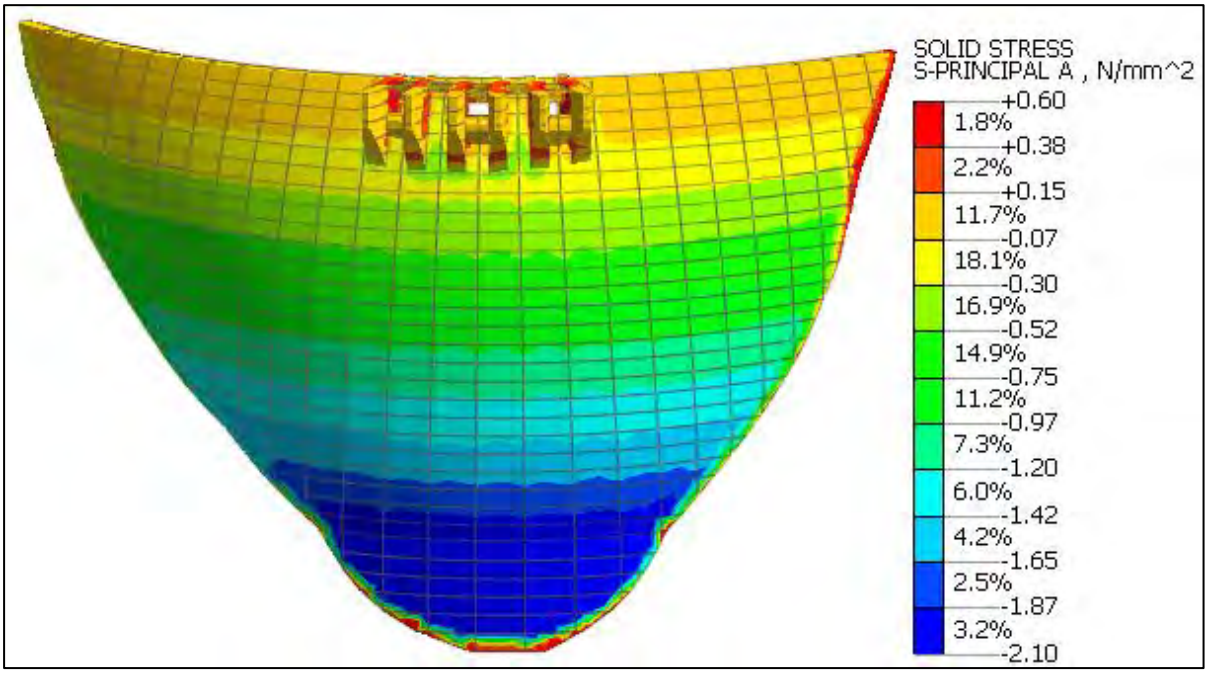

Figure 6-70: P1 principal stress results for reservoir elevation 696 mASL on 18/08/2023 (US face)

6.5.4 Interface Element Results

Measured and predicted behaviour of the joint meters during the progressive impoundment loading period from commencement of reservoir filling (21 November 2022) to reservoir level 630 mASL (29 April 2023), have shown that the joints have closed since impoundment. The closure is relative to the initial joint opening position at commencement of reservoir filling and

is due to the compressive stress response in the arch under hydrostatic loading. This can be seen in Figure 6-37 reproduced as Figure 6-71.

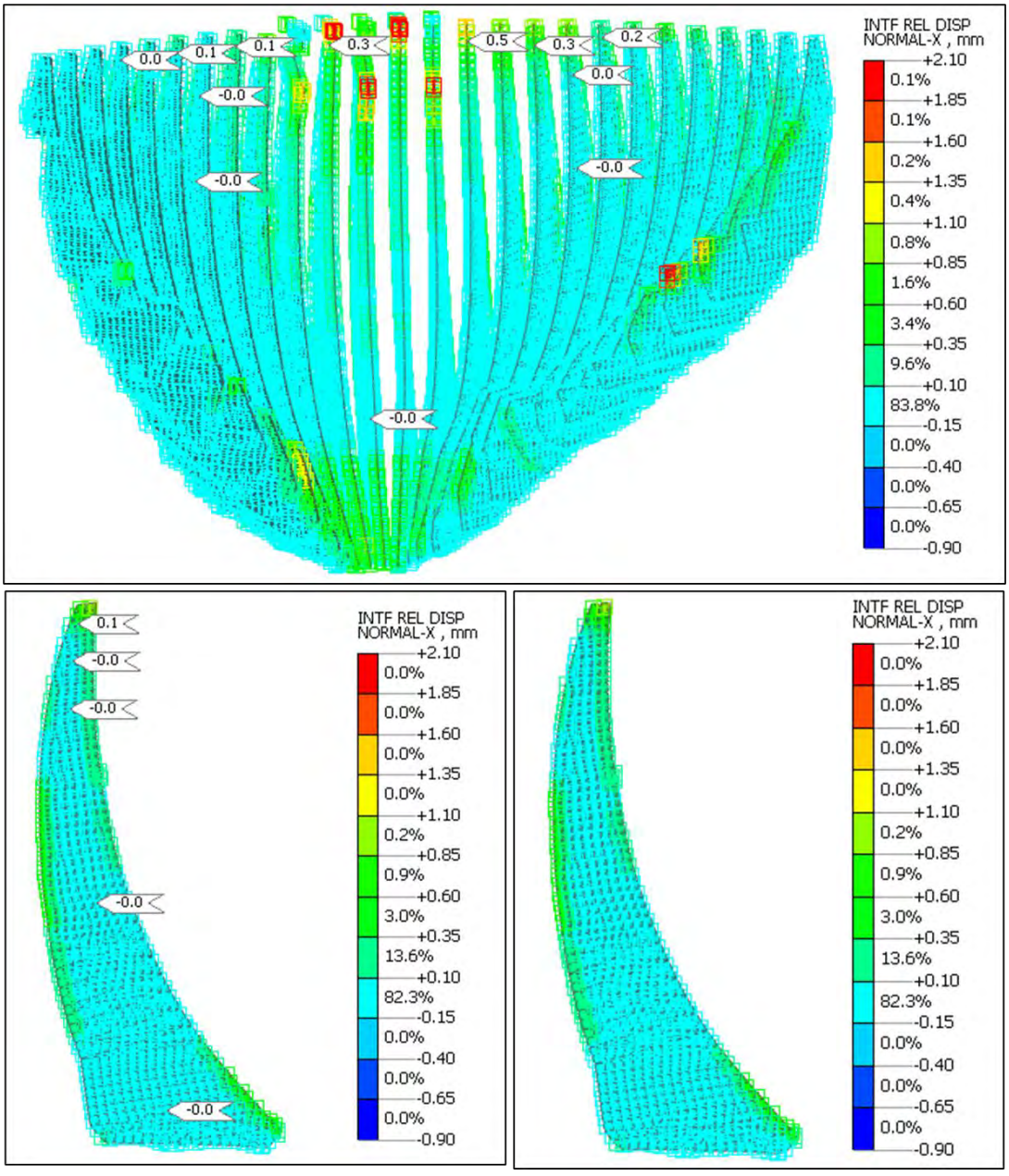

Figure 6-71: Axial displacement results on joints for impoundment to 630 mASL on 29/04/2023

6.5.5 Relative Rotational Displacement Results (pendulums)

The movements predicted for the hanging and inverted pendulums of monolith 13, 16 and 19 as measured at elevation 525.5 mASL, are shown in Figure 6-72 and Figure 6-73 for impoundment stage 696 mASL, on 18/08/2023. The pendulums measure differential movement between the hanging point and the measurement station point. Predicted measurements are

obtained by subtracting the modelled displacement at the measurement point from that modelled at the hanging/anchor point.

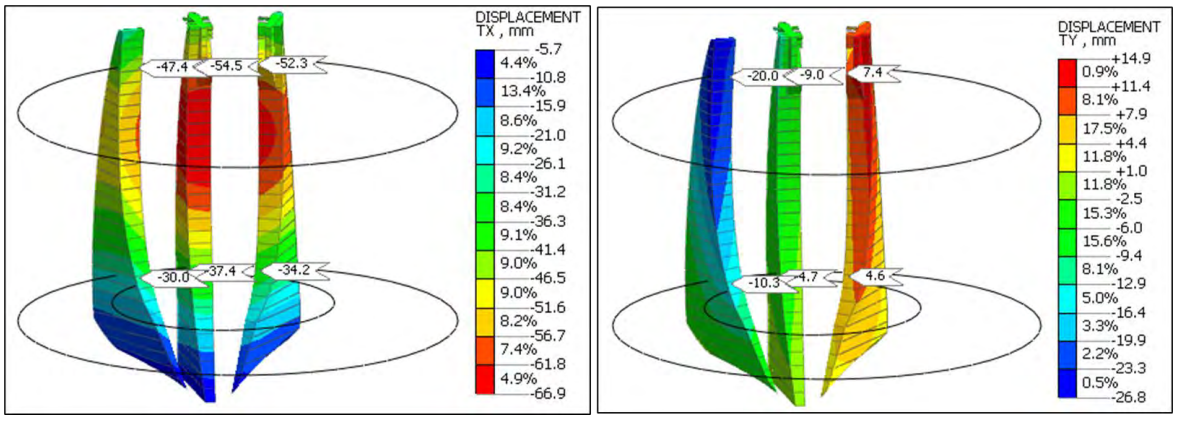

Figure 6-72: Radial (left) and tangential (right) predicted movements of hanging pendulums in monolith 13, 16 and 19 for impoundment to 696 mASL on 18/08/2023

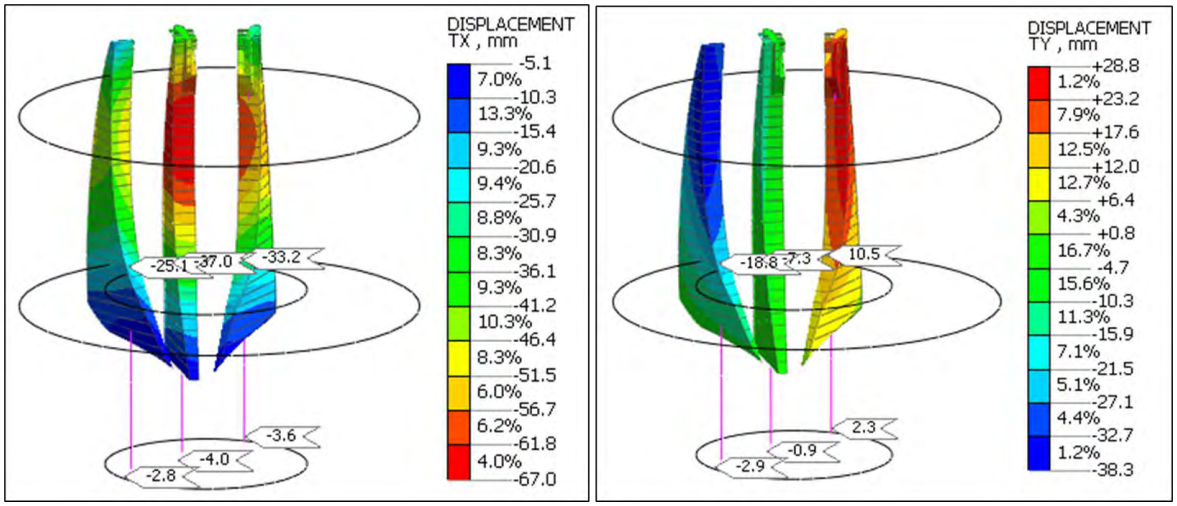

Figure 6-73: Radial (left) and tangential (right) predicted movements of inverted pendulums in monolith 13, 16 and 19 for impoundment to 696 mASL on 18/08/2023

6.5.6 Selected Stress Results

The analysis stress results for loading at impoundment reservoir level 696 mASL, were probed at element locations in the model corresponding to the respective locations of stress meters cast in the dam at elevations 471.5 mASL and 525.5 mASL. These instruments measure the normal stress between the dam concrete and foundation as a result of the dam thrusting into the foundation.

Analysis stress results were extracted just prior to impoundment and at the latest filling level of 696 mASL, to determine the increase in stress that occurred during the period of reservoir impoundment. Effectively the stress state at commencement of impoundment is taken as the reference stress.

The element stress results at dam elevation 471.5 mASL and 525.5 mASL, are shown in Figure 6-74 and Figure 6-75.

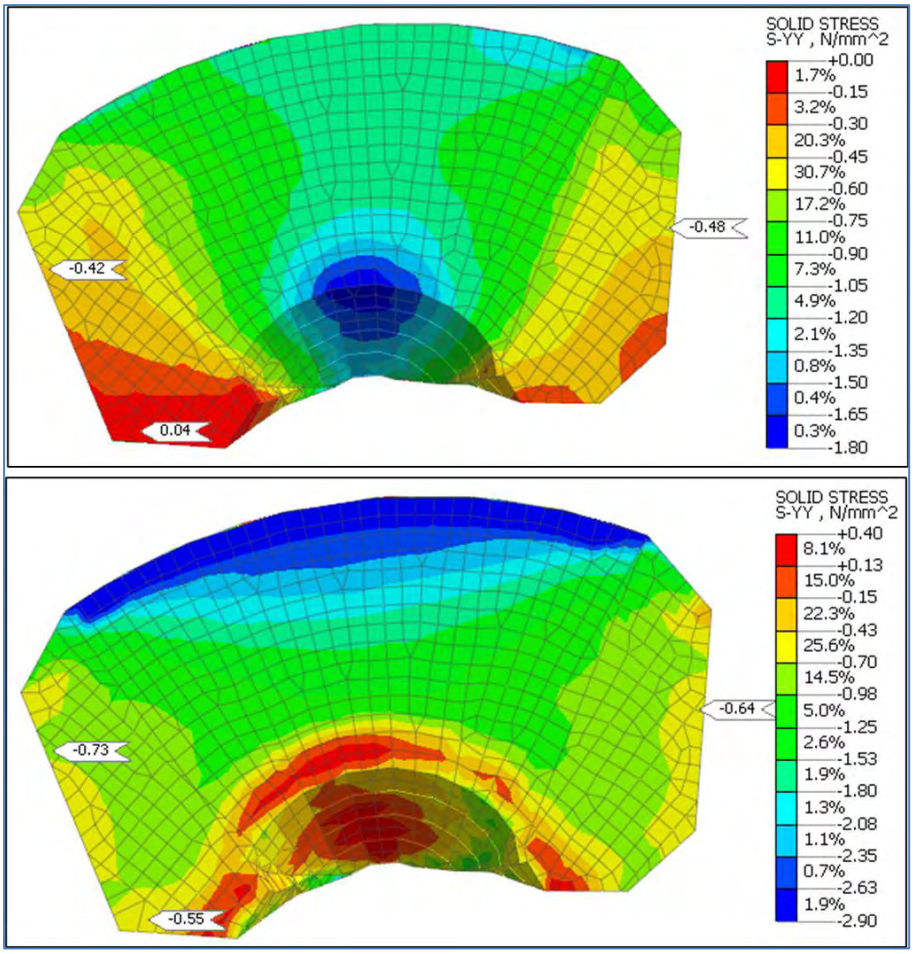

Figure 6-74: Analysis tangent (axial) stress results at dam elevation 471.5 mASL at impoundment commencement stage (top) and impoundment reservoir level 696 mASL stage (bottom)

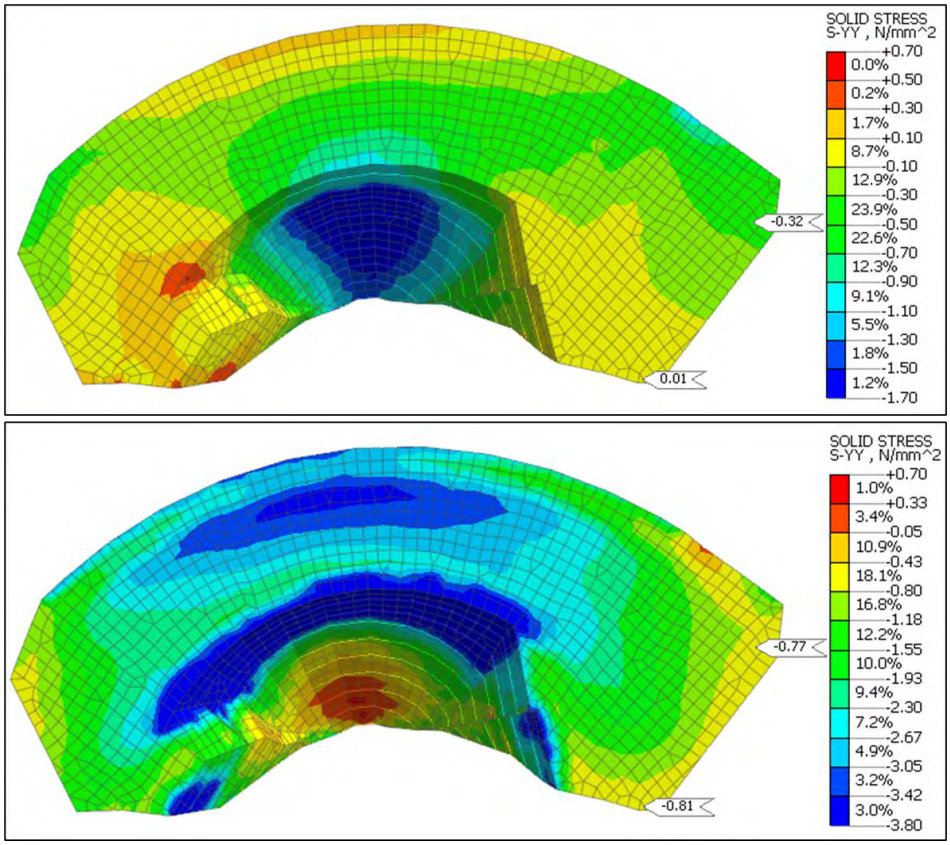

Figure 6-75: Analysis tangent (axial) stress results at dam elevation 525.5 mASL at impoundment commencement stage (top) and impoundment reservoir level 696 mASL stage (bottom)

6.5.7 Selected Strain Results

The computed strain results for analysis loading at impoundment reservoir level 696 mASL, were probed at element locations in the FE model corresponding to the respective locations of strain gauges cast in the dam at elevations 453.5 mASL and 471.5 mASL. The strain gauges placed at elevation 435.5 mASL are aligned to measure radial strains in the dam body and those placed at 471.5 mASL measure axial strains.

Strain results were extracted just prior to commencement of impoundment and at the latest reservoir filling level of 696 mASL, to determine the increase in strain that occurred during the period of reservoir impoundment. Effectively the strain state at commencement of impoundment is taken as the reference value.

The element strain results at dam elevation 453.5 mASL and 471.5 mASL are shown in Figure 6-76 and Figure 6-77.

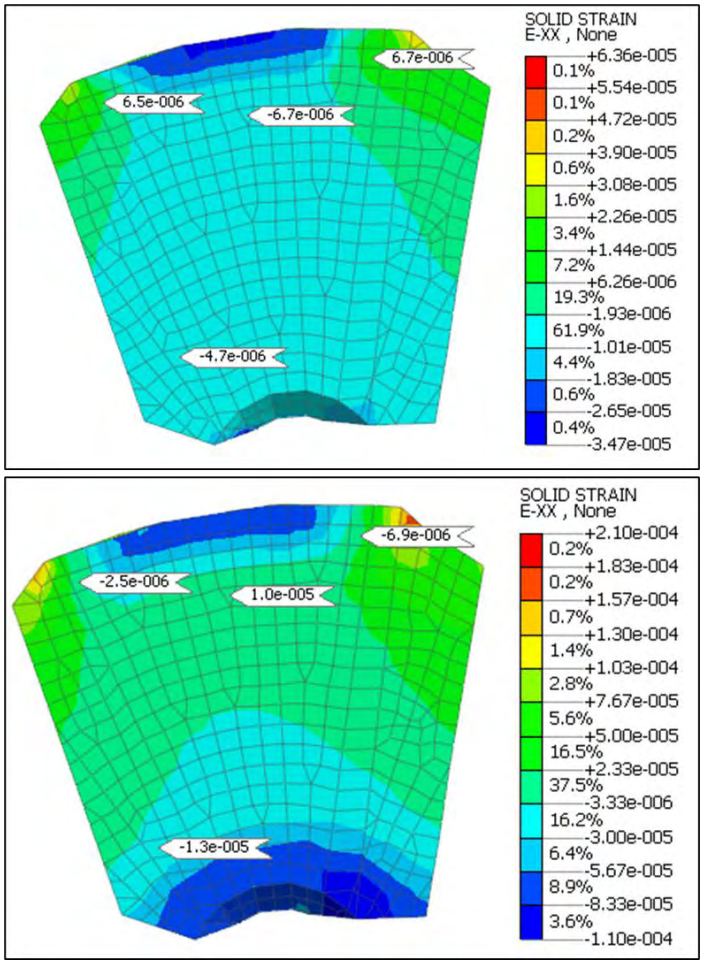

Figure 6-76: Computed radial strain results at dam elevation 453.5 mASL at impoundment commencement stage (left) and impoundment reservoir level 696 mASL stage (right)

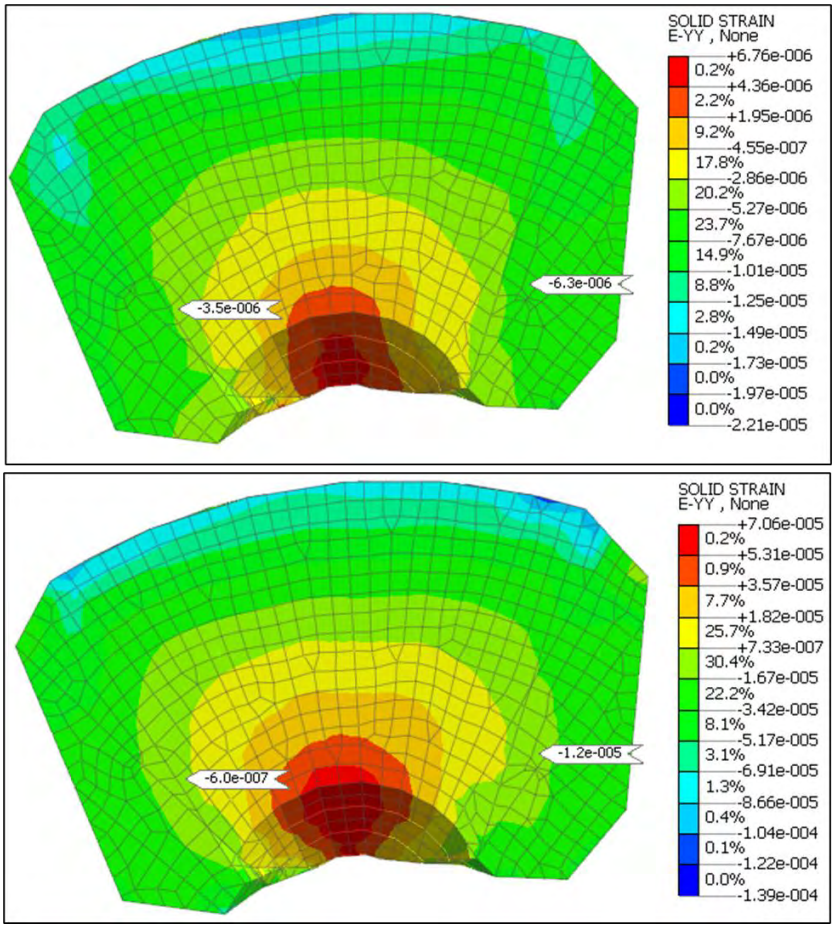

Figure 6-77: Computed tangential (axial) strain results at dam elevation 471.5 mASL at impoundment commencement stage (top) and impoundment reservoir level 696 mASL stage (bottom)

6.5.8 Selected Temperature Results

A thermal heat transfer analysis of the dam was carried out to determine the temperature state of the dam at commencement of impoundment and at each stage of impoundment, to derive the change in temperature state during the period of dam impoundment.

The temperature state analysis results of the dam indicating the modelled temperature state on 18/08/2023, were probed in locations of the FE model coincident with location of thermocouples installed during construction, to allow comparison of measured against modelled temperatures.

The modelled temperature state of the dam at elevations 462.5 mASL, 465.5 mASL, 516 mASL and 570 mASL are shown in Figure 6-78 through Figure 6-81.

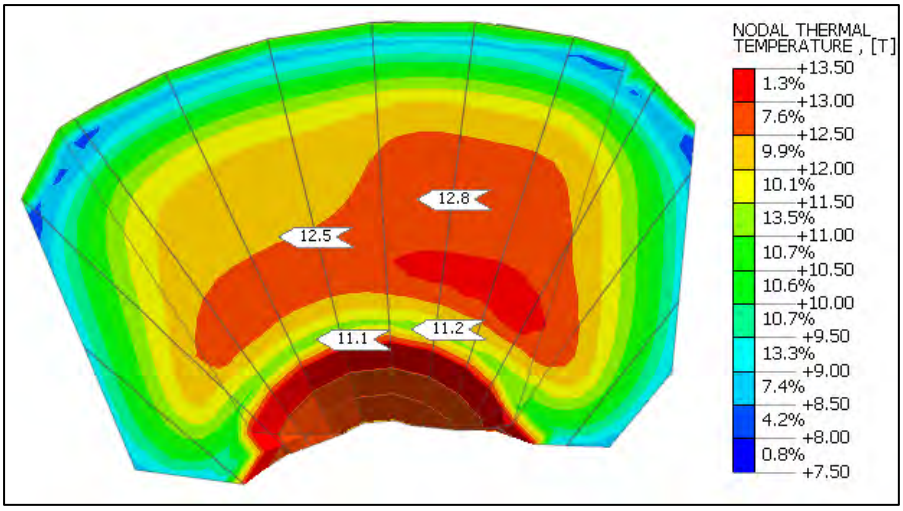

Figure 6-78: Thermal analysis results showing temperature state of dam at 462.5 mASL on 18/08/2023

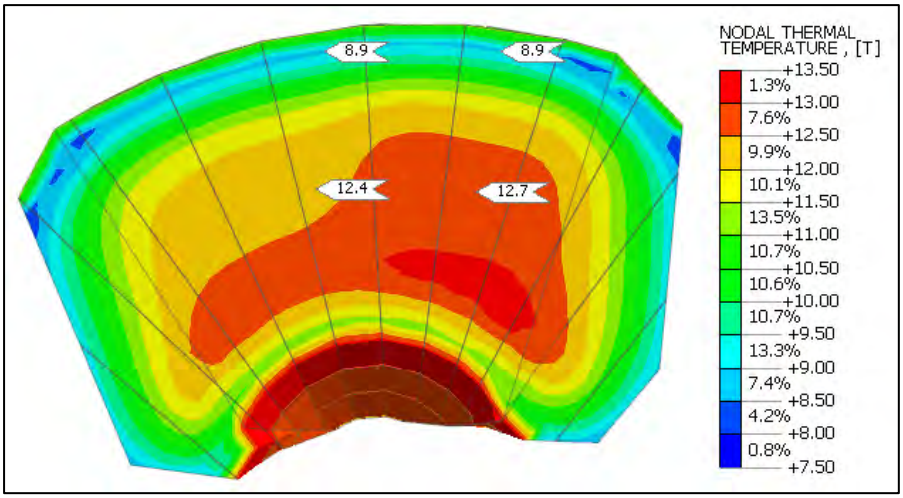

Figure 6-79: Thermal analysis results showing temperature state of dam at 465.5 mASL on 18/08/2023

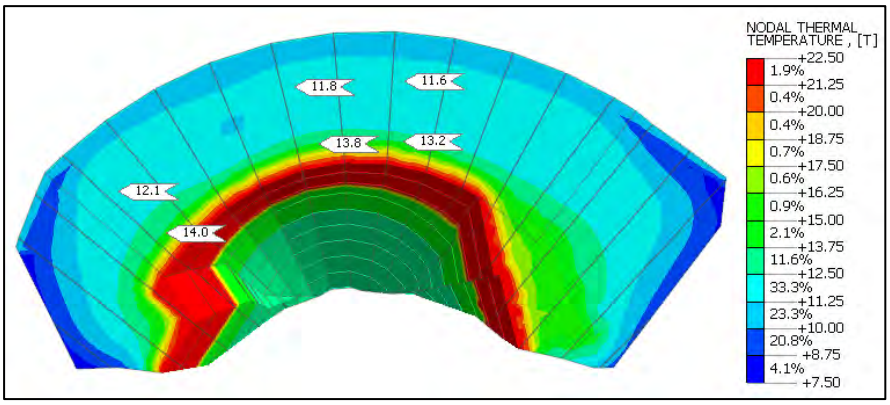

Figure 6-80: Thermal analysis results showing temperature state of dam at 516 mASL on 18/08/2023

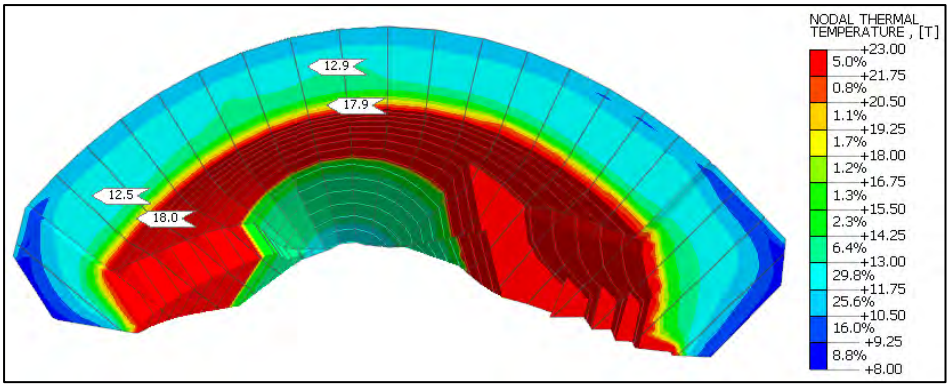

Figure 6-81: Thermal analysis results showing temperature state of dam at 570 mASL on 18/08/2023

6.6 EVALUATION OF PROGRESSIVE LOADING BEHAVIOUR

6.6.1 Displacement Behaviour

A summary of the resultant horizontal deformation results of the dam along the height of the crown cantilever, for the various impoundment stages is shown in Figure 6-82. The progressive deformation curves indicate how the maximum point of deformation along the height of the dam, moves upwards towards the crest as the reservoir elevation level rises. The maximum deformation at stage 5 of the impoundment programme shows the maximum deformation to occur at elevation level 640 mASL which is approximately 70 % of the dam height from the base. This is noted since at Stage 5 the reservoir elevation level of 696 mASL is still 19 m below the crest and 14 m below the normal operating elevation or FSL.

The impact of the ambient thermal loading conditions is evident, as the crest portion of the dam is seen to displace downstream during the Winter period and upstream during the Summer period. The cooling of the dam and associated contraction/shrinkage causes it to deflect downstream, while the warming of the dam and associated expansion causes it to move upstream. The Winter period coincides with impoundment stage 1 and the Summer period with stages 4 and 5. Stages 0, 2 and 3 are reached mid-season. The upper portion of the dam is more sensitive to ambient temperature changes due to the thinning of the dam width towards the crest. The thicker potion of the dam near the base has a larger thermal inertia, meaning the large core making up a significant portion of the width, is relatively insensitive to temperature changes, due to the relatively low thermal conductivity value of concrete.

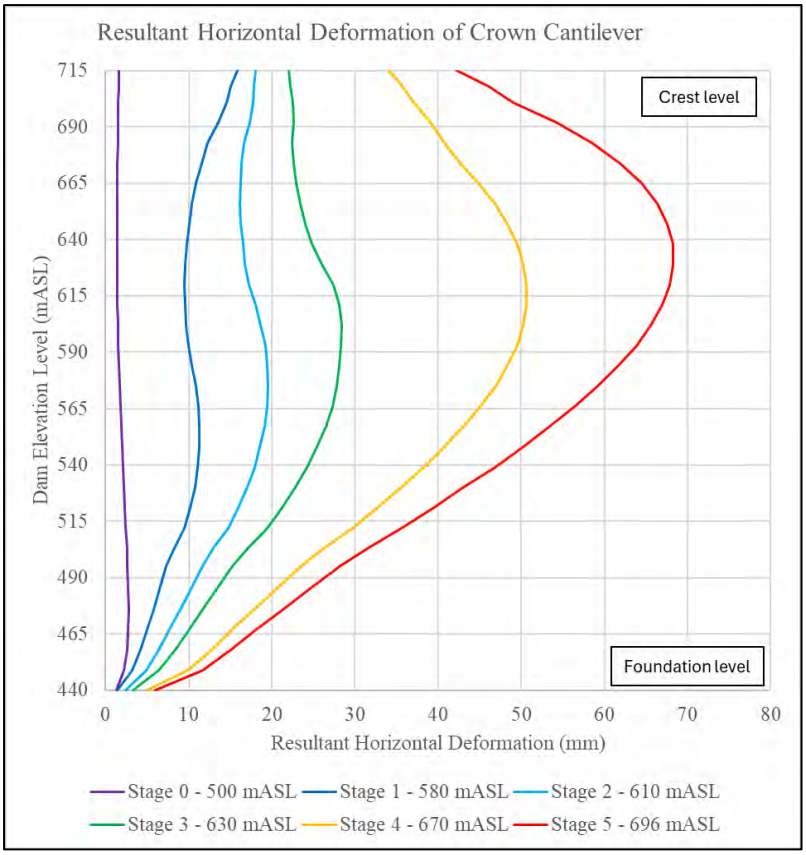

Figure 6-82: Staged representation of resultant horizontal deformation along height of crown cantilever

For a mass concrete structure, the depth below the surface that is influenced by external ambient temperature variations, is exponentially proportional to the time period of the temperature variations.

Generally only the outer 6 to 7 metre shell of concrete on the upstream and downstream face of a large dam experiences a significant variation in annual temperature state, with less than 10 % of the ambient temperature variation amplitude between Winter and Summer, penetrating further than 7 metres beneath the surface face (Bofang, 2014).

Curves representing the temperature variation ratio vs depth beneath concrete surface, for different temperature variation time-periods is shown in Figure 6-83. It is also noted from the curves of Figure 6-83, that less than 10 % of daily ambient temperature variation penetrates further than 0.3 m beneath the surface of a concrete dam. Consequently, a 20˚C surface temperature variation would only result in a variation of less than 2˚C, at a depth of 0.3 m beneath the surface.

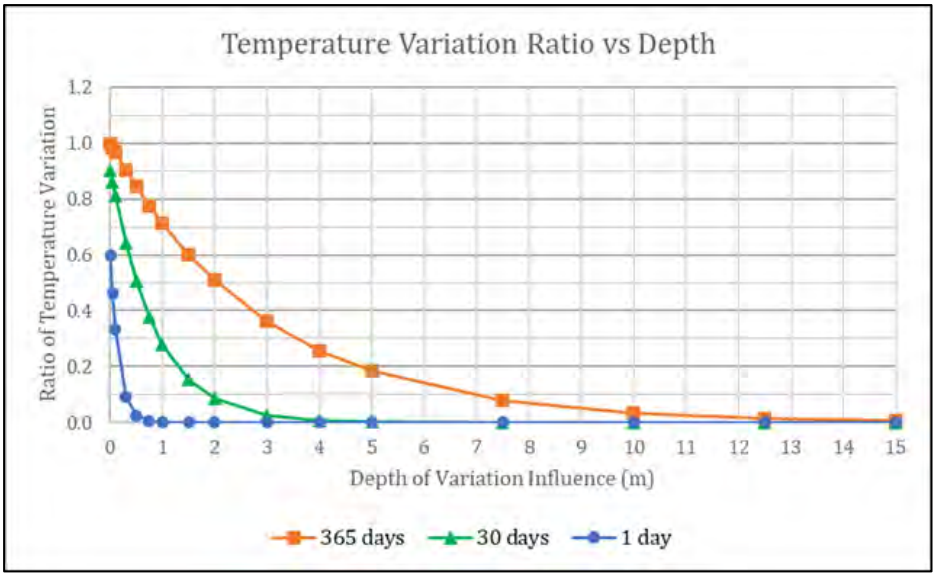

Figure 6-83: Temperature variation ratio vs depth of typical dam concrete (Bofang, 2014)

A set of horizontal displacement curves of the dam along its axis at elevation level 638 mASL, representing the modelled deformation of the dam, at the various impoundment stages is shown in Figure 6-84. The curves depict the significant increase in horizontal displacement towards the downstream side, especially at the central portion of the arch where the maximum displacement approaches 70 mm at stage 5 of impoundment. The curves also indicate the relative symmetry in the deformed shape of the arch.

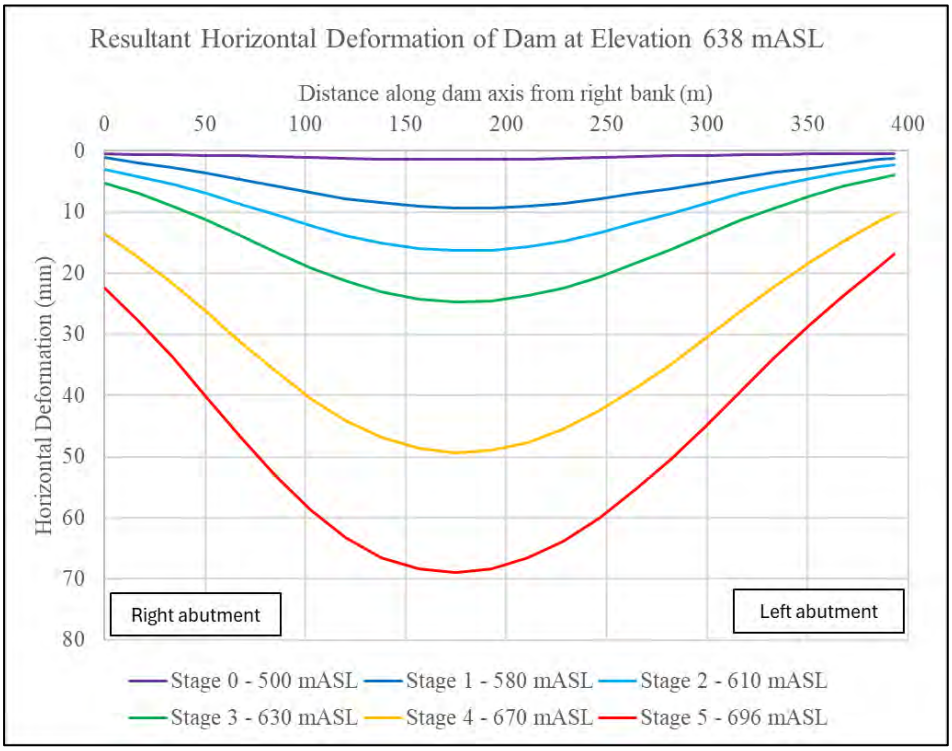

Figure 6-84: Horizontal displacement curves along dam axis at elevation level 638 mASL

6.6.2 Stress Behaviour

The progressive vertical stress development of the dam upstream face along the height of the crown cantilever, for the various impoundment reservoir levels is shown in Figure 6-85. The series of stress curves are relatively smooth with the exception of two significant kinks at elevation 495 mASL and 675 mASL, where the dam experiences distinct changes in geometrical stiffness of the cantilever in the vertical plane.

At elevation 495 mASL the upstream face of the dam experiences a discrete change in profile from a vertical to curved surface. This is the point where the curvature in the vertical plane of the dam commences and progress forming the undercut of the dam. Between elevation 665 mASL and 685 mASL the geometrical stiffness reduces due to the openings of the spillway.

The vertical stress curves show that the upstream face of the dam remains in vertical compression through all stages of reservoir impoundment. After construction of the dam and prior to hydrostatic loading from the reservoir, the dam structure leans backwards and the heel of the dam experiences significant vertical compressive stresses that decrease along the height of the dam, to approximately zero at the crest. As the reservoir level rises, the increasing hydrostatic load pushes the dam forward and into its abutments causing the cantilever to rotate and deflect towards the downstream.

During the advanced stages of impoundment (stage 4 – 6), the vertical compression stress at the lower portion of the dam has decreased significantly in comparison with the early stages (stage 0 – 3). The vertical compression stress at the heel of the dam is shown to decrease from approximately 9 MPa to 3 MPa.

It is noted that significant vertical compressive stress develops mid-height of the dam, at the advanced stages of impoundment from around 1 MPa to 3 MPa. This is caused by vertical hydrostatic loading of the arch curvature in the vertical-radial plane of the dam, and occurs when the reservoir level rises above the inflection point of the vertically curved upstream face. This observation depicts the effective behavioural functioning of the double-curvature of the arch, in keeping the concrete in compression during hydrostatic force transfer from reservoir to foundation. Single curvature arch dams do not exhibit this favourable form of structural behaviour.

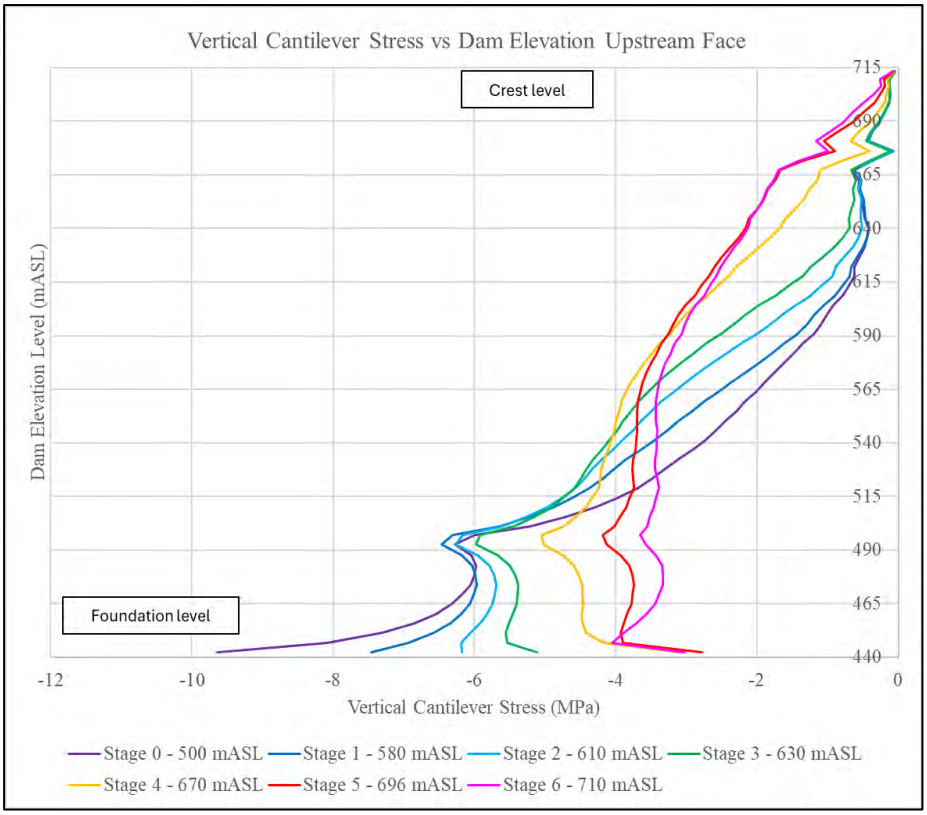

Figure 6-85: Staged representation of vertical stresses along height of crown cantilever on dam upstream face

The progressive vertical stress development of the dam downstream face along the height of the crown cantilever, for the various impoundment reservoir levels is shown in Figure 6-86. The series of stress curves are relatively smooth showing the downstream face to remain in vertical compression from commencement of dam filling to the point when the reservoir reaches FSL.

The vertical compression at the toe of the dam increases from a stress value of 2.5 MPa to 4.5 MPa during the term of impoundment, as the dam is seen to lean progressively forward as it takes up the rising hydrostatic load.

The vertical stresses expected to develop just above mid-height of the dam, have a significant compression value of 2 – 3 MPa during early stages of impoundment. These stresses are induced by the vertical gravity loading of the concrete as a result of the overhang of upper portion of the arch structure. The rising reservoir level and associated increase in hydrostatic load, causes the vertical cantilever action of the downstream deflecting central arch, to transition from a free vertical cantilever to a propped cantilever, whereby the stiffening effect of the crossing loaded horizontal arch units acts as series of supporting elastic springs. This analogy was demonstrated by Zimbabwean arch dam designer Wild (1980).

The propped cantilever structural mode of the downstream deflecting dam, causes a hogging moment to develop in the region of the propped elastic support, inducing tension which reduces the vertical precompression of the overhang from 2 – 3 MPa to less than 1.5 MPa.

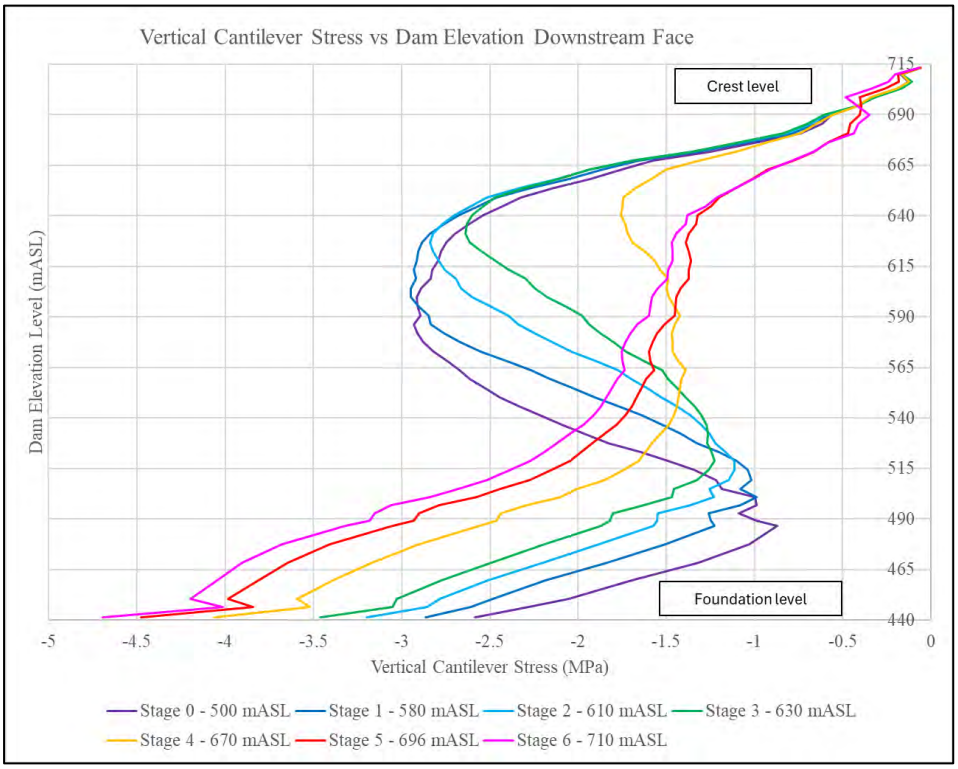

Figure 6-86: Staged representation of vertical stresses along height of crown cantilever on downstream face

The set of horizontal (axial) stress curves plotted in Figure 6-87, indicate the sequential horizontal arch stress development along the height of the crown cantilever, on the upstream face of the dam. Prior to hydrostatic loading of the dam, the dam leans back under its own weight and the horizontally spanning arch units undergo elongation and an increase in aperture. This externally caused behaviour induces the development of horizontal tensions as the arches effectively hang back from their supports. The purple curve of the plot shows the mid-height section of the dam undergoing horizontal tensile stress development ranging from 0 to nearly 1 MPa.

During filling of the reservoir, the horizontal arch units gradually develop horizontal compressive stresses along their axes. At stage 6 of the impoundment process significant compressive horizontal stresses of more than 6 MPa develop at an elevation level of 630 mASL, which is approximately 70 % of the dam height above foundation. At this height the horizontal stiffness of the arch units is greater than the vertical stiffness of the cantilever unit, resulting in the horizontal load transfer of the hydrostatic forces into the abutments. The horizontal compressive arch stress of the dam at FSL (stage 710 mASL), decreases significantly along the height of the dam from 70 % height to the crest as the hydrostatic load decreases. Despite the

zero hydrostatic load at the crest of the dam, the dam still develops a substantial horizontal compression stress of 2.5 MPa at the crest. This indicates that although the vertical stiffness of the cantilever is relatively low, it is still sufficient to transfer hydrostatic load vertically across arch units to the arch unit at the crest of the dam.

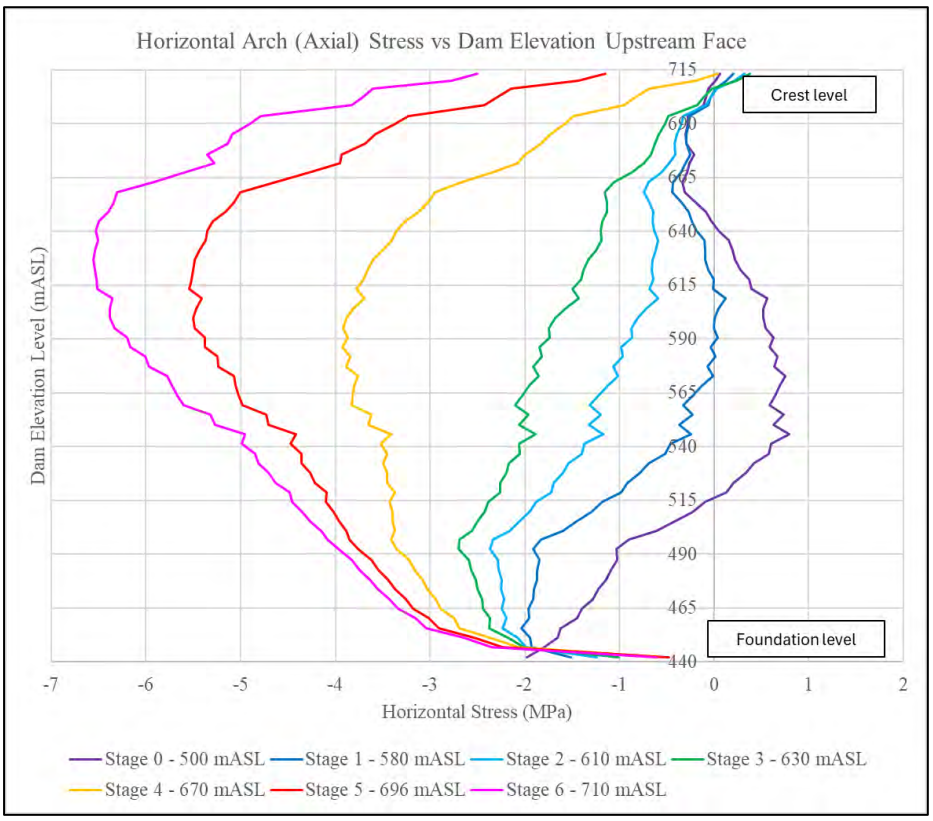

Figure 6-87: Staged representation of horizontal stresses along height of crown cantilever on upstream face

The set of horizontal (axial) stress curves plotted in Figure 6-88, indicate the sequential horizontal arch stress development along the height of the crown cantilever, on the downstream face of the dam. The progressive horizontal stress behaviour on the downstream face is similar to that of the upstream face, except for the lower portion of the dam where additional hydrostatic load decreases the horizontal compressive stress.

The horizontal arch units at the bottom of the dam have a small radius, high curvature and the horizontal displacement of these arches towards the downstream side causes the arch to open up on the concave side, reducing the curvature and increasing the radius. Effectively the lower arches have a larger bending stiffness than the upper arches meaning a significant portion of the load is transferred by rotation, as opposed to axial thrust which is seen to occur at the upper more flexible arches. Bending of the lower arch units under increased hydrostatic loading induces marginal horizontal tensile stresses (bursting stress), which effectively reduces the precompression horizontal stress that develops under lower hydrostatic loading experienced at

early stages of impoundment. The horizontal compressive stress in the lower portion of the arch decreases from approximately 2 MPa to 1 MPa during impoundment of the dam.

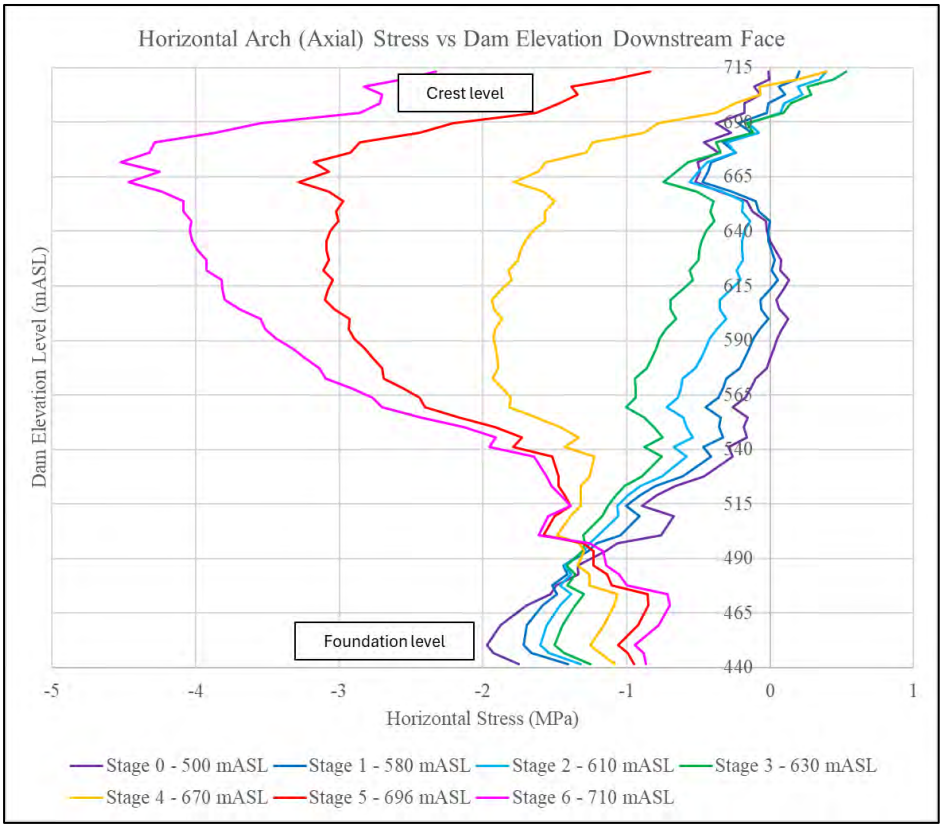

Figure 6-88: Staged representation of horizontal stresses along height of crown cantilever on downstream face

The maximum equivalent compressive stresses of an arch dam under FSL reservoir loading conditions, normally develops at the toe of the dam along the lower abutments. This is the part of the dam body where the vertical compressive cantilever force vectors and horizontal compressive arch force vectors converge and meet as shown in Figure 6-89, by the dark blue contour of the principal stress plot. The compressive minor principal stress that develops in the Yusufeli Dam, at the toe along the lower abutments, ranges from 7 – 9 MPa during the advanced stages of impoundment.

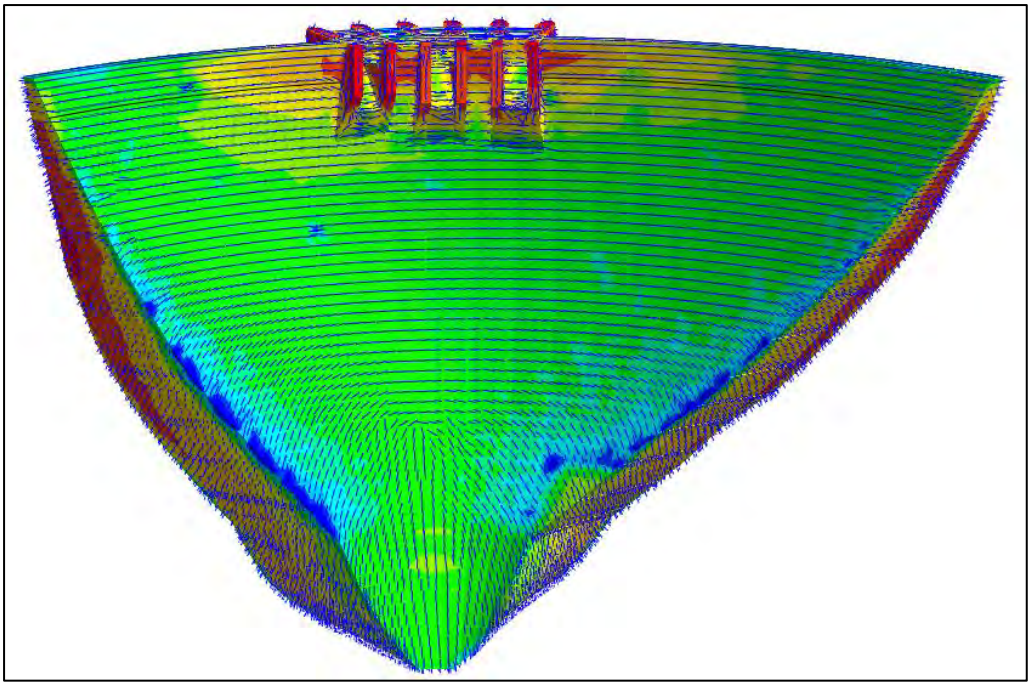

Figure 6-89: P3 principal stress vectors for impoundment to 696 mASL on 18/08/2023 (DS face)

The progressive minor principal stress development of the dam toe along the height of the left and right abutments, for the various impoundment reservoir levels are shown in Figure 6-90 and Figure 6-91. The series of stress curves are relatively jagged due to the re-entrant corner FE modelling phenomenon, between dam toe and foundation abutment, causing localised stress concentrations to be computed. Notwithstanding the localised high/low points along the stress curves, the overall average form of the curve is evident.

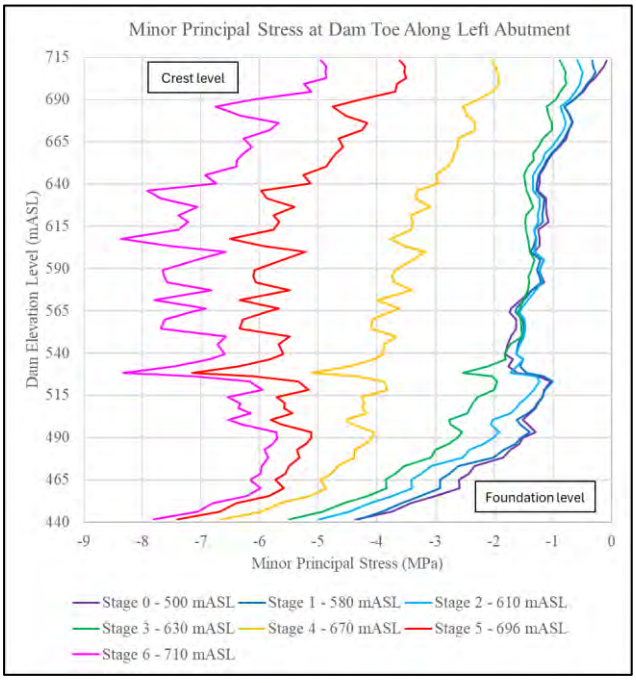

Figure 6-90: Staged representation of minor principal stresses at dam toe along height of left abutment

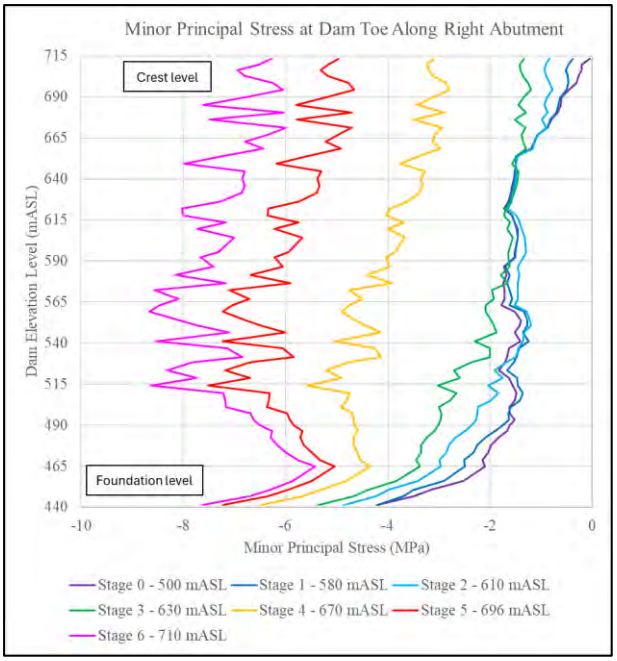

Figure 6-91: Staged representation of minor principal stresses at dam toe along height of right abutment

To understand the development of the equivalent stress state of the dam at the abutment toe in terms of the Mohr-Coulomb stress state, at the various stages of reservoir impoundment, a sequence of Mohr-Coulomb curves is presented in Figure 6-92. The set of semi-circle curves depict the sequential increase in multiaxial compressions (effective stress/confining stress) and deviatoric stress. As the maximum shear stress increases at each successive rise in reservoir level, the favourable effective stress increases at a greater rate. This behaviour is testament to the inherent structural strength of an arch structure which is a result of its geometrical shape and favourable mode of load transfer.

It is noted that just prior to filling of the reservoir (stage 0), the Mohr Coulomb stress state indicates the development of marginal major principal tensions at the abutment toe. These tensile stresses are subsequently reversed into compressive stresses after the early stages of filling when the dam undergoes hydrostatic loading. This observation confirms the well-known premise that a loaded concrete arch dam is safer than an unloaded one. A line plot showing the shear stress development along the dam abutment toe in terms of the critical stress state is shown in Figure 6-93.

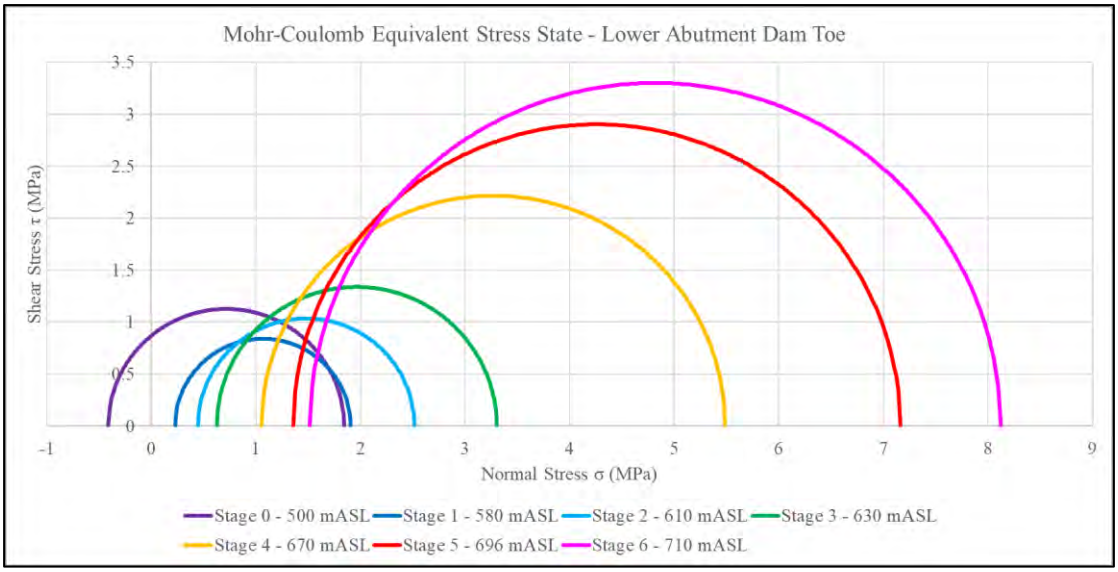

Figure 6-92: Progressive development of Mohr-Coulomb Equivalent stress state at dam abutment toe

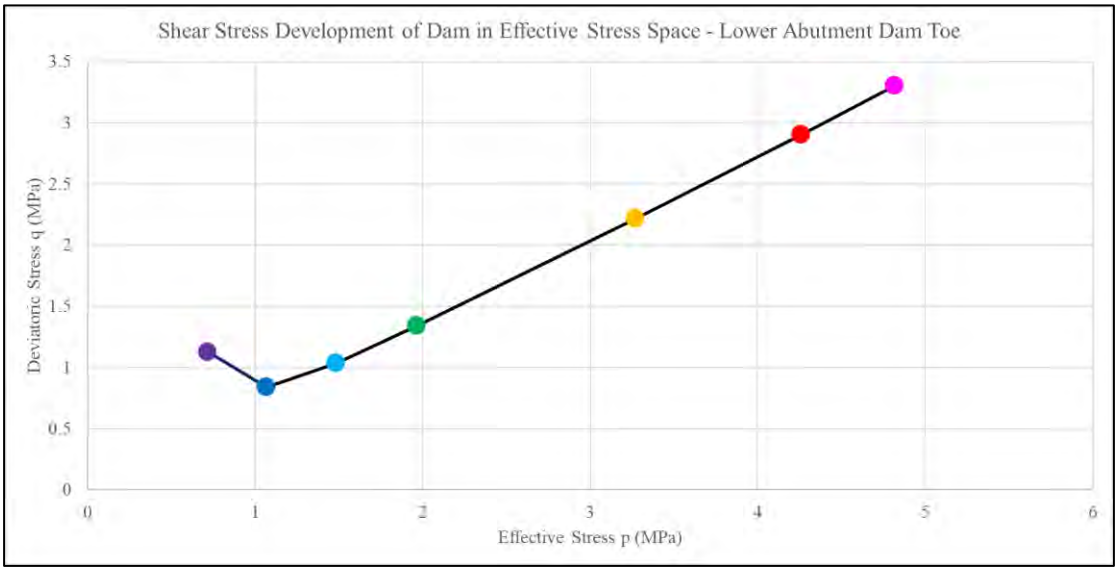

Figure 6-93: Progressive development of shear stress at the dam abutment toe in the effective stress space

6.6.3 Results Coinciding with Instrument Locations

A summary of the various FE analysis results as computed during the impoundment analysis study, and that were used to predict the different dam structural behaviour modes are provided in this section.

The dam deformation analyses results, extracted at nodal locations in the FE model coinciding with the positions of the dam geodetic surveys beacons for stage 1 to stage 5 of impoundment are shown in Table 6-1. Curves representing the predicted displacement of the various dam survey beacons as a function of reservoir elevation level is shown in Figure 6-94. The points on the curve represent actual predicted values whilst the lines plotted are merely interpolations between these values. The maximum displacement predicted after 5 stages of impoundment is approximately 59 mm occurring at survey beacons B4 and B5.

Table 6-1: Summary of predicted dam external displacement results from FE validation analysis

Survey Beacon	Resultant Horizontal Displacement (mm)				
	Stage 1: 580 mASL (2023-02-13)	Stage 2: 610 mASL (2023-04-08)	Stage 3: 630 mASL (2023-04-29)	Stage 4: 670 mASL (2023-06-10)	Stage 5: 696 mASL (2023-08-18)
B1	7.5	14.6	22.0	40.0	53.1
B2	8.2	15.7	23.6	42.4	55.5
B3	3.4	5.8	9.0	22.3	36.6
B4	7.8	12.6	18.5	39.5	59.3
B5	9.2	13.8	19.9	40.8	59.5
B6	4.7	6.2	9.2	22.0	35.2
B7	2.1	3.1	5.4	14.3	24.1
B8	9.4	11.5	14.8	27.5	39.4
B9	13.5	16.6	20.7	34.1	45.4
B10	11.5	12.1	14.6	24.7	32.0
B11	5.5	4.0	5.5	13.0	20.7
B12	1.3	0.7	1.6	6.6	12.4

*positive displacement indicates movement towards the downstream

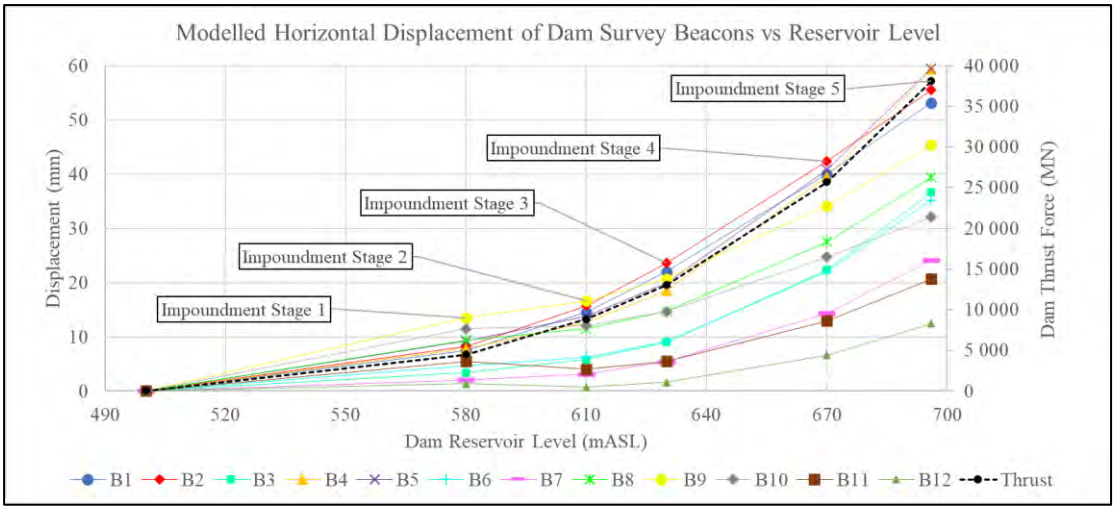

Figure 6-94: Predicted horizontal displacement of dam survey beacons

Relative displacement results across dam expansion joints as modelled by interface elements of the FE model are shown in Table 6-2. As discussed in results presentation, for all practical purposes the dam expansion joints had closed by the time the reservoir impoundment reached elevation level 610 mASL.

Table 6-2: Summary of predicted movements across dam joints

Joint meter	Elevation (mASL)	Relative Displacement Across Joint (mm)		
		Stage 1, 580 mASL (2023-02-13)	Stage 2, 610 mASL (2023-04-08)	Stage 3, 630 mASL (2023-04-29)
JM-9	715	0.5	0.2	0.2
JM-11	715	0.8	0.5	0.3
JM-13	715	1.4	0.6	0.5
JM-16	715	1.7	0.5	0.3
JM-17	715	1.1	0.2	0.1
JM-19	715	0.9	0.1	0.1
JM-21	715	0.6	0.1	0.1

*positive displacement denotes joint opening

A summary of the modelled dam deformation behaviour during reservoir impoundment as derived from the FE analysis, in terms of the relative internal (rotational) movement of the pendulums at impoundment stage 4 and stage 5 are shown in Table 6-3 and Table 6-4.

Table 6-3: Summary of predicted dam pendulum movements from outputs of FE analysis at impoundment stage 4 (El 670 mASL)

Pendulum	FEA Predicted Radial Movement (mm)			FEA Predicted Tangential Movement (mm)		
	Suspension Point	Measuring Point	Relative Movement	Suspension Point	Measuring Point	Relative Movement
P13-H-525.5	-38.1	-27.6	-10.5	5.4	3.7	1.7
P16-H-525.5	-38.9	-30.4	-8.5	-6.5	-3.6	-2.9
P19-H-525.5	-32.7	-24.1	-9.0	-13.8	-7.8	-6.0
P13-I-525.5	-2.8	-26.8	24.0	1.9	8.4	6.5
P16-I-525.5	-3.1	-30.1	27.0	-0.7	-5.6	-4.9
P19-I-525.5	-2.2	-20.3	18.1	-2.3	-14.6	-12.3

*positive displacement indicates upstream movement for hanging pendulums and downstream for inverted pendulums

**positive displacement indicates movement to the right bank for hanging and inverted pendulums

Table 6-4: Summary of predicted dam pendulum movements from outputs of FE analysis at impoundment stage 5 (El 696 mASL)

Pendulum	FEA Predicted Radial Movement (mm)			FEA Predicted Tangential Movement (mm)		
	Suspension Point	Measuring Point	Relative Movement	Suspension Point	Measuring Point	Relative Movement
P13-H-525.5	-52.3	-34.2	-18.1	7.4	4.6	2.8
P16-H-525.5	-54.5	-37.4	-17.1	-9.0	-4.7	-4.3
P19-H-525.5	-47.4	-30.0	-17.0	-20.0	-10.3	-9.7
P13-I-525.5	-3.6	-33.2	29.6	2.3	10.5	8.2
P16-I-525.5	-4.0	-37.0	33.0	-0.9	-7.3	-6.4
P19-I-525.5	-2.8	-25.1	22.3	-2.9	-18.8	-15.9

*positive displacement indicates upstream movement for hanging pendulums and downstream for inverted pendulums

**positive displacement indicates movement to the right bank for hanging and inverted pendulums

Stress and strain results computed from the FE analysis for impoundment stage 5 are shown in Table 6-6 and Table 6-5.

Table 6-5: Summary of stress results computed by FE validation analysis for impoundment stage 5

Stress meter No	FEA Axial Stress (MPa)		
	2023/11/22	2023/08/18	Change
471.5/ST/10/11/1	-0.48	-0.64	-0.17
471.5/ST/10/20/1	-0.42	-0.73	-0.30
471.5/ST/10/20/2	0.04	-0.55	-0.59
525.5/ST/28/7/1	-0.32	-0.77	-0.45
525.5/ST/28/7/2	0.01	-0.81	-0.82

*negative values denote compressive stress

Table 6-6: Summary of strain results computed by FE validation analysis for impoundment stage 5

Strain gauge No	FEA Strain (m/m)10^{-6}		
	2023/11/22	2023/08/18	Change
453.5/SR/1/15/1	6.7	-6.9	-13.6
453.5/SR/1/16/1	-6.7	10.0	16.7
453.5/SR/1/17/1	6.5	-2.5	-9.0
453.5/SR/1/17/2	-4.7	-13.0	-8.3
471.5/SR/10/11/1	-6.3	-12.0	-5.7
471.5/SR/10/20/1	-3.5	-0.6	2.9

*positive values denote expansive strain

A summary of the final modelled temperature state of the dam in terms of post-processed interrogated nodal temperature values selected coinciding with thermocouple locations in the dam is shown in Table 6-7.

Table 6-7: Summary of anticipated temperature state of dam as derived by results of thermal FE analysis at impoundment stage 5

Thermocouple No	Elevation Level (mASL)	FEA Nodal Temperature (°C)
471.5/TK/7/15/1	462.5	11.2
471.5/TK/7/15/2	462.5	12.8
471.5/TK/7/17/1	462.5	11.2
471.5/TK/7/17/2	462.5	12.5
471.5/TK/8/14/1	465.5	12.7
471.5/TK/8/14/2	465.5	8.9
471.5/TK/8/16/1	465.5	12.4
471.5/TK/8/16/2	465.5	8.9
525.5/TK/26/14/1	516	11.6
525.5/TK/26/14/2	516	13.2
525.5/TK/26/16/1	516	11.8
525.5/TK/26/16/2	516	13.8
525.5/TK/26/20/1	516	12.1
525.5/TK/26/20/2	516	14.0
588.5/TK/43/16/1	570	12.9
588.5/TK/43/16/2	570	17.9
588.5/TK/43/22/1	570	12.4
588.5/TK/43/22/2	570	18.0

6.7 SUMMARY

A detailed presentation and discussion of the expected dam behaviour during impoundment of the reservoir, as obtained from the results output by the FE analyses of the dam, were provided in this chapter. The expected behaviour of the dam in terms of deformation of the structure, development of internal stresses/strains and temperature state were provided. Interrogations of computed FE analysis results were made from plots of the output values in locations consistent with those of relevant instruments installed on the dam, against which the results are compared for validation of the FE model.

A direct comparison of the measured behaviour of the dam against the behaviour predicted by the FE model of the dam is addressed in the following chapter.

7 COMPARISON OF MEASURED VS PREDICTED BEHAVIOUR OF DAM

This chapter presents a direct comparison between the dam behaviour observed and measured during reservoir impoundment, with the predicted behaviour as simulated by the outputs of the impoundment FE analysis of the dam.

7.1 TIME-BASED SUMMARY OF EXTERNAL DISPLACEMENTS

The external deformation of the dam was measured by daily geodetic surveys taken of beacons placed on the downstream face of the dam, and provided as resultant horizontal displacements of each of the installed survey beacons. The anticipated deformation of the dam was derived from the nodal displacement values extracted from the results of the FE analysis impoundment study.

A time-based comparison of the measured vs modelled external deformation over the period of impoundment for each survey beacon B1 – B12 is provided in Figure 7-1 through Figure 7-12. The plotted line curve indicates the surveyed progressive deformation of the dam over the rise in reservoir level, whilst the points denoted in the legend as FEM indicate the predicted displacement of the dam at the various stages of impoundment, as per the FE modelled behaviour of the dam. It is noted that due to size and complexity of the FE model mesh and the associated lengthy analysis run times, deformation analyses were only run for the selected discrete reservoir impoundment stages and not for a continuous range of range of reservoir levels.

The results provided are after convergence of the modelled deformation results against measured values was attained through the calibration process. A presentation of the sensitivity analysis results obtained from the model calibration process is provided in Section 8. The comparison study shows that the FE model provides a very good prediction of the dam deformation behaviour at all survey beacon location points on the dam body. In most cases the model marginally overpredicts the deformation behaviour of the dam, meaning that the calibrated model errs marginally on the conservative side.

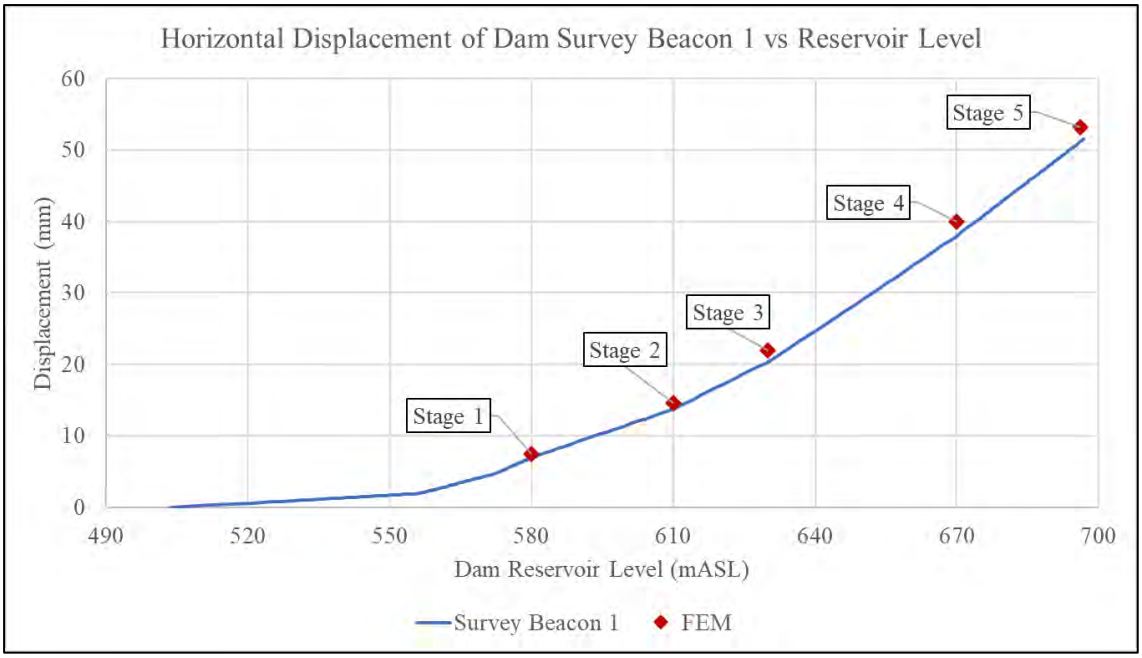

Figure 7-1: Comparison of surveyed vs modelled horizontal displacement of dam survey beacon 1

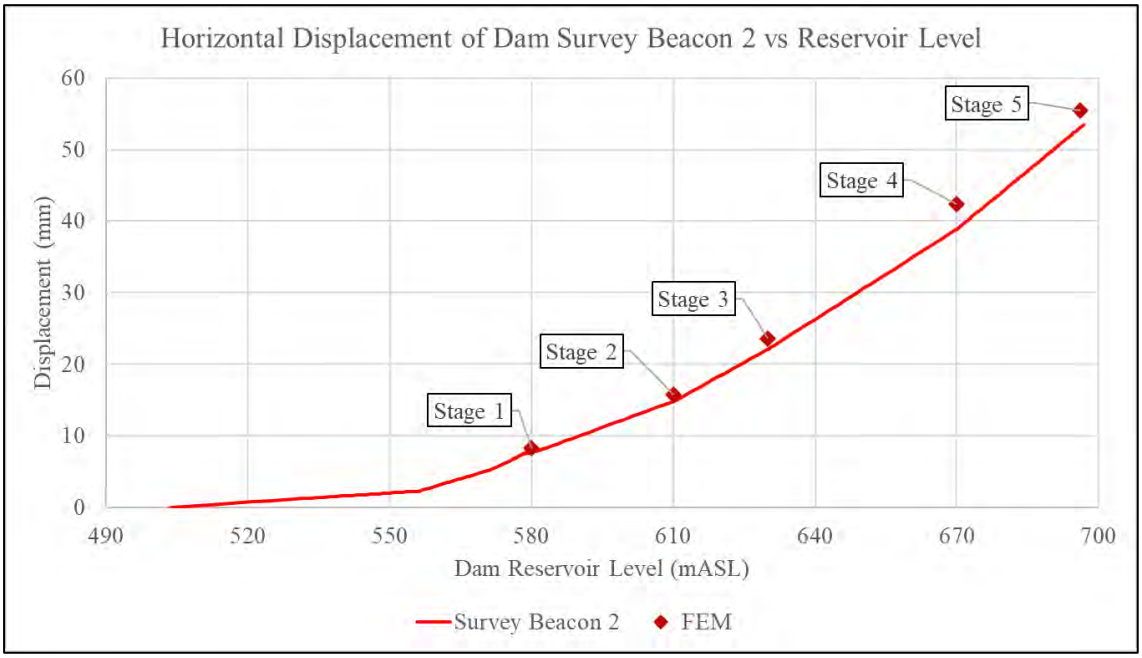

Figure 7-2: Comparison of surveyed vs modelled horizontal displacement of dam survey beacon 2

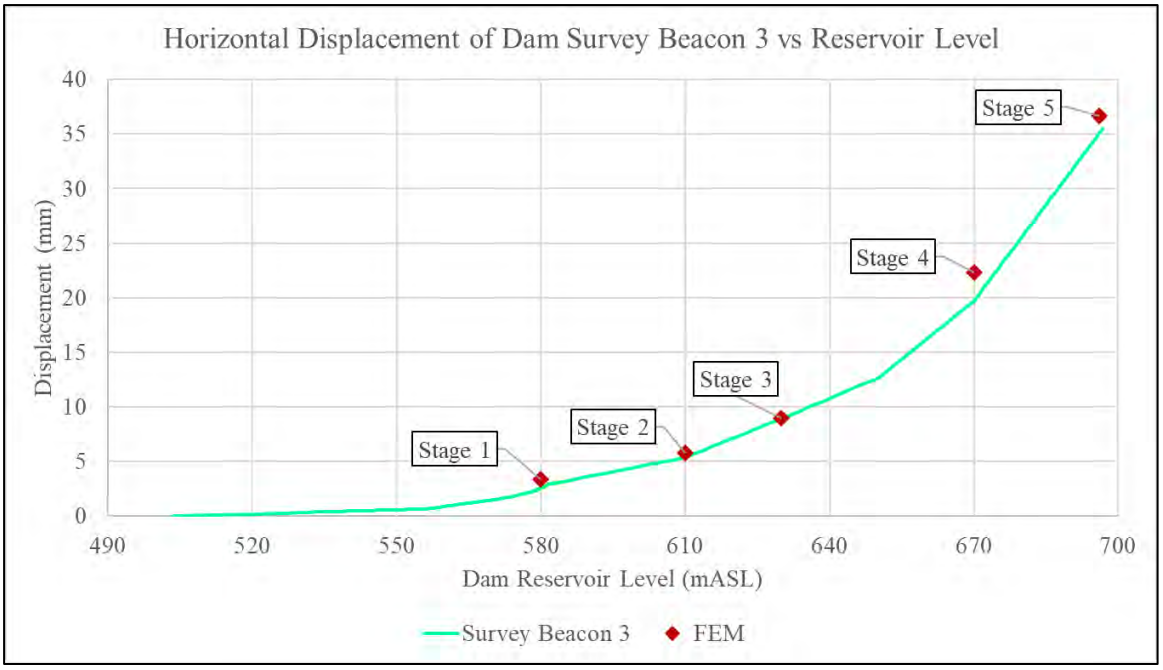

Figure 7-3: Comparison of surveyed vs modelled horizontal displacement of dam survey beacon 3

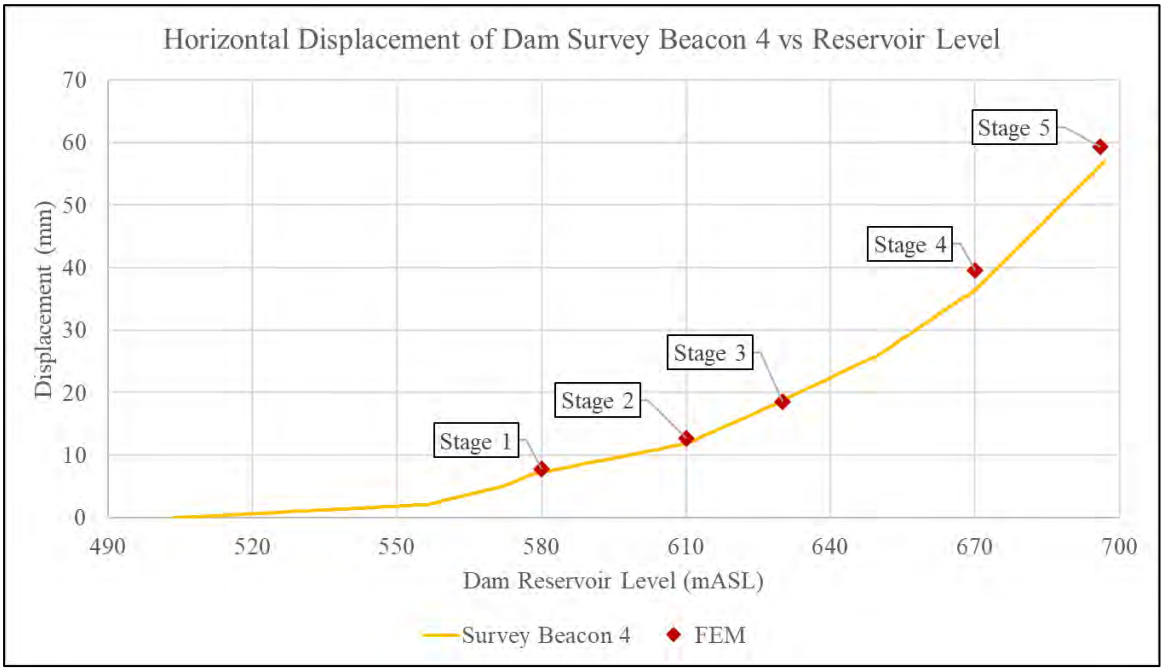

Figure 7-4: Comparison of surveyed vs modelled horizontal displacement of dam survey beacon 4

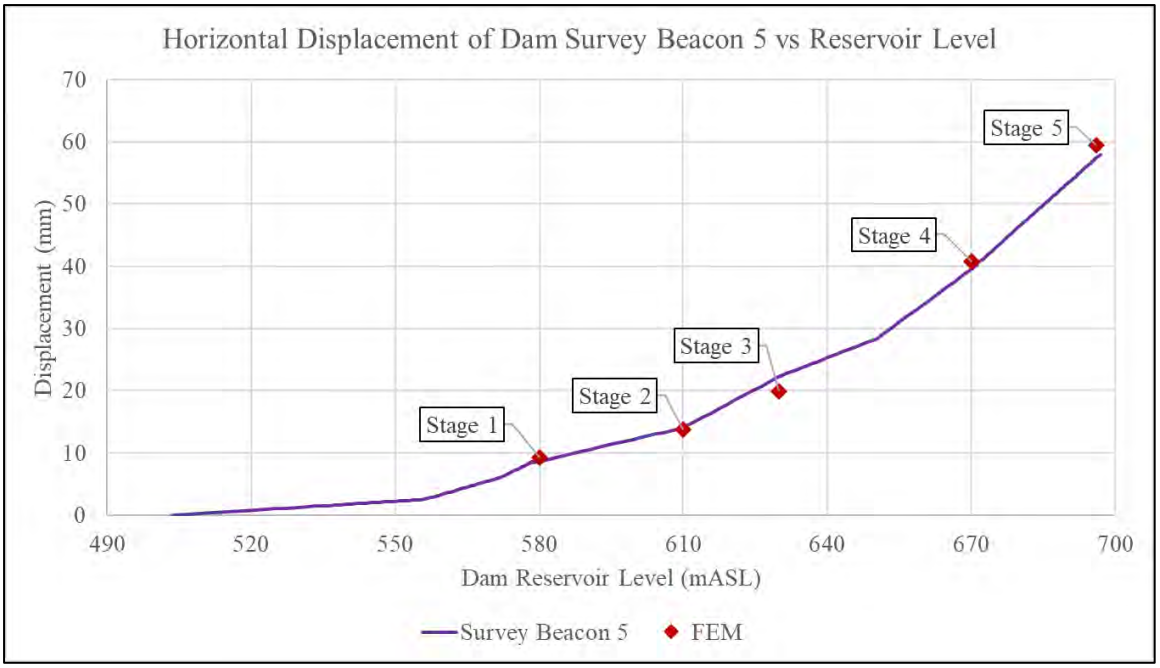

Figure 7-5: Comparison of surveyed vs modelled horizontal displacement of dam survey beacon 5

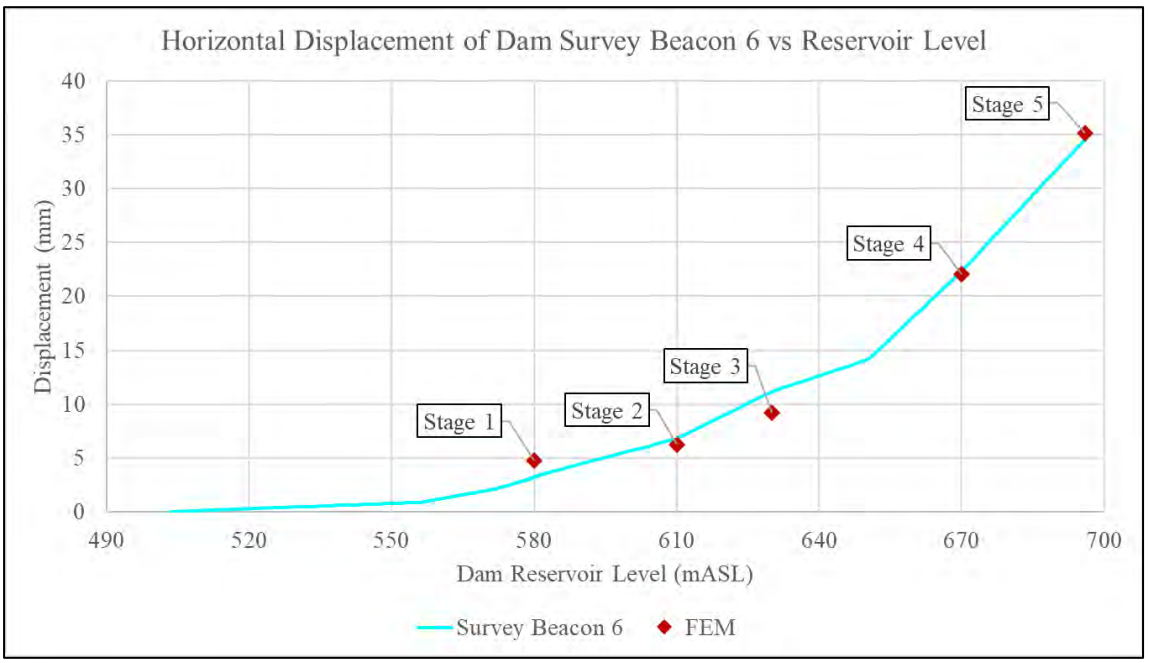

Figure 7-6: Comparison of surveyed vs modelled horizontal displacement of dam survey beacon 6

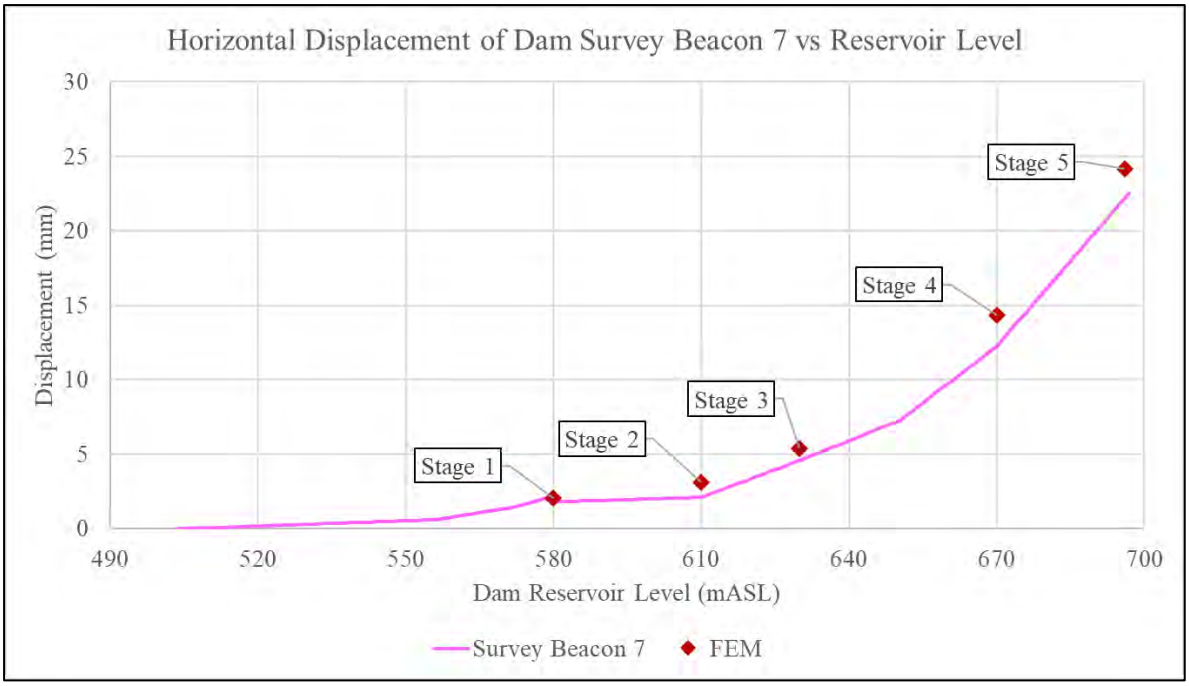

Figure 7-7: Comparison of surveyed vs modelled horizontal displacement of dam survey beacon 7

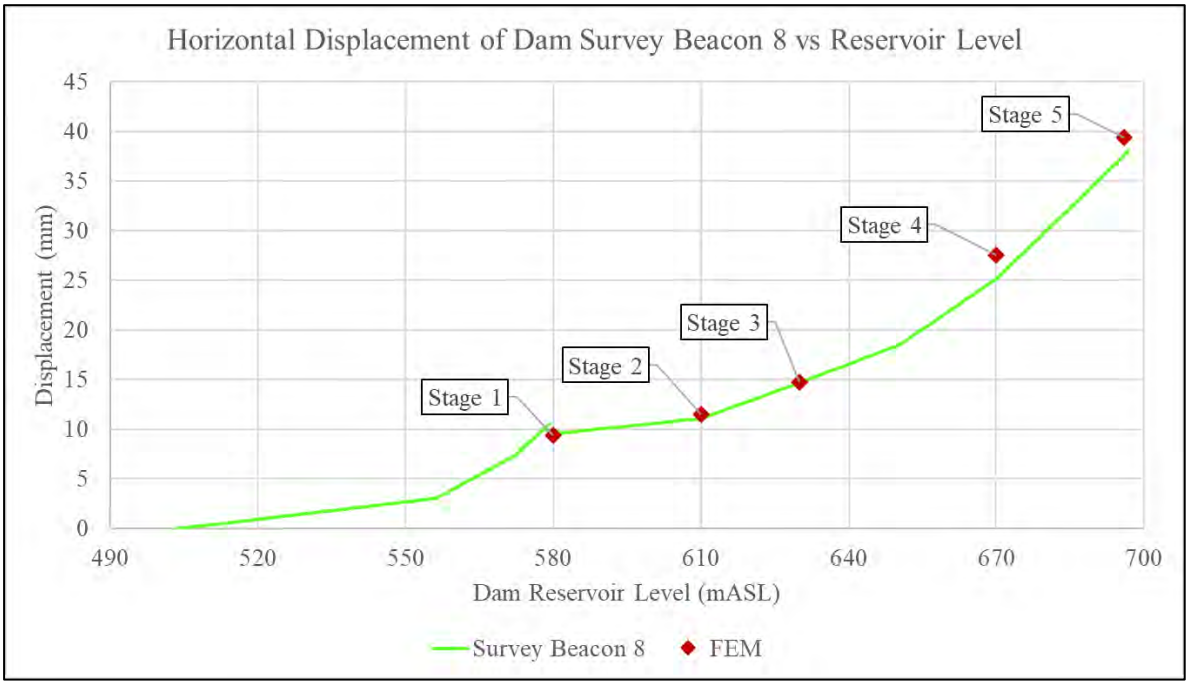

Figure 7-8: Comparison of surveyed vs modelled horizontal displacement of dam survey beacon 8

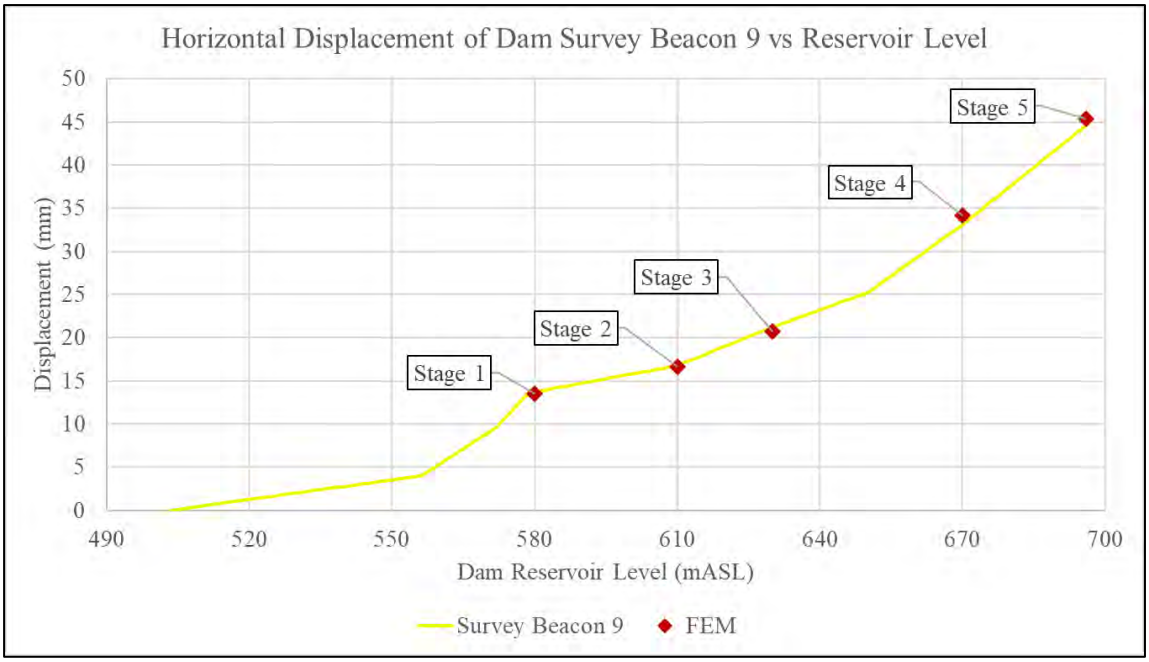

Figure 7-9: Comparison of surveyed vs modelled horizontal displacement of dam survey beacon 9

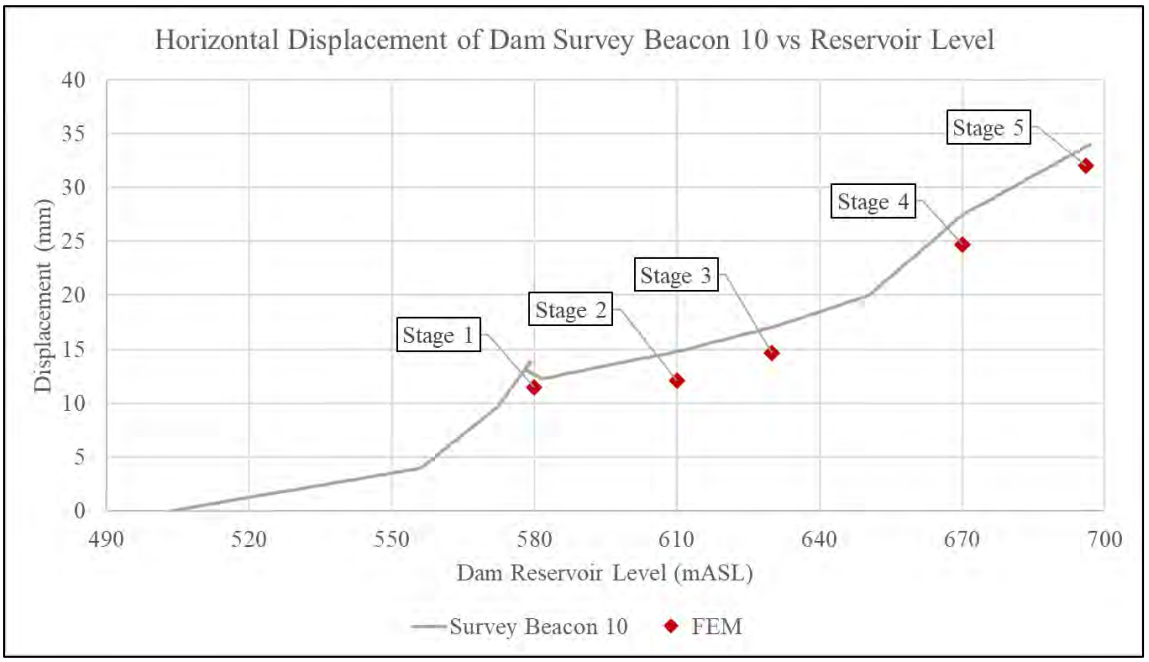

Figure 7-10: Comparison of surveyed vs modelled horizontal displacement of dam survey beacon 10

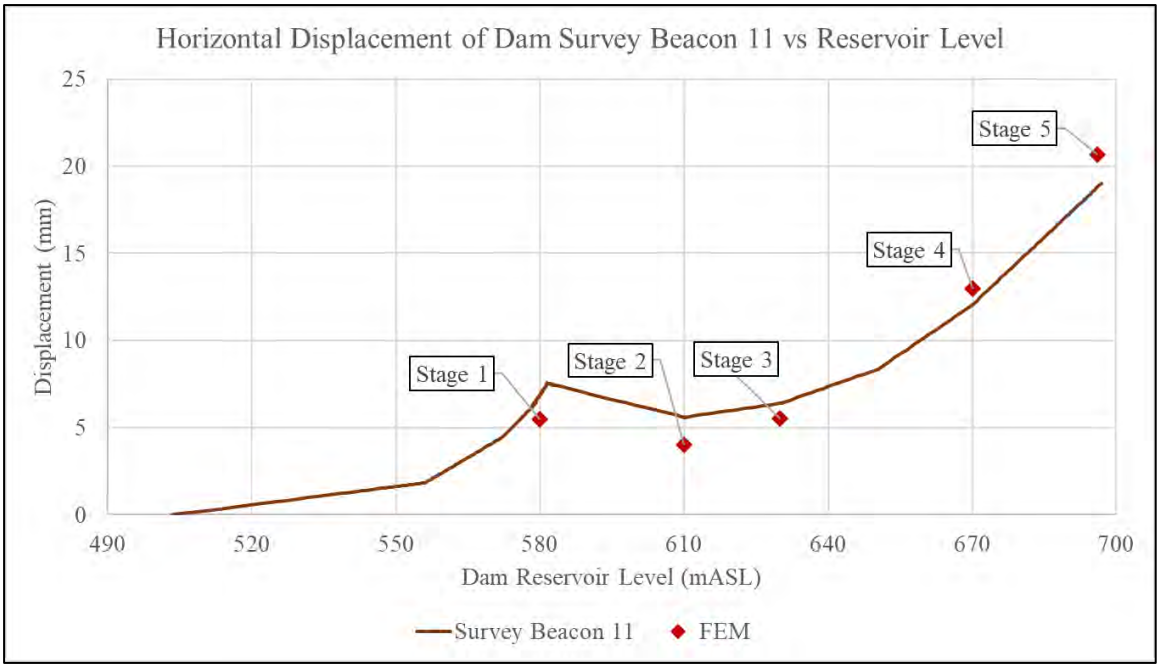

Figure 7-11: Comparison of surveyed vs modelled horizontal displacement of dam survey beacon 11

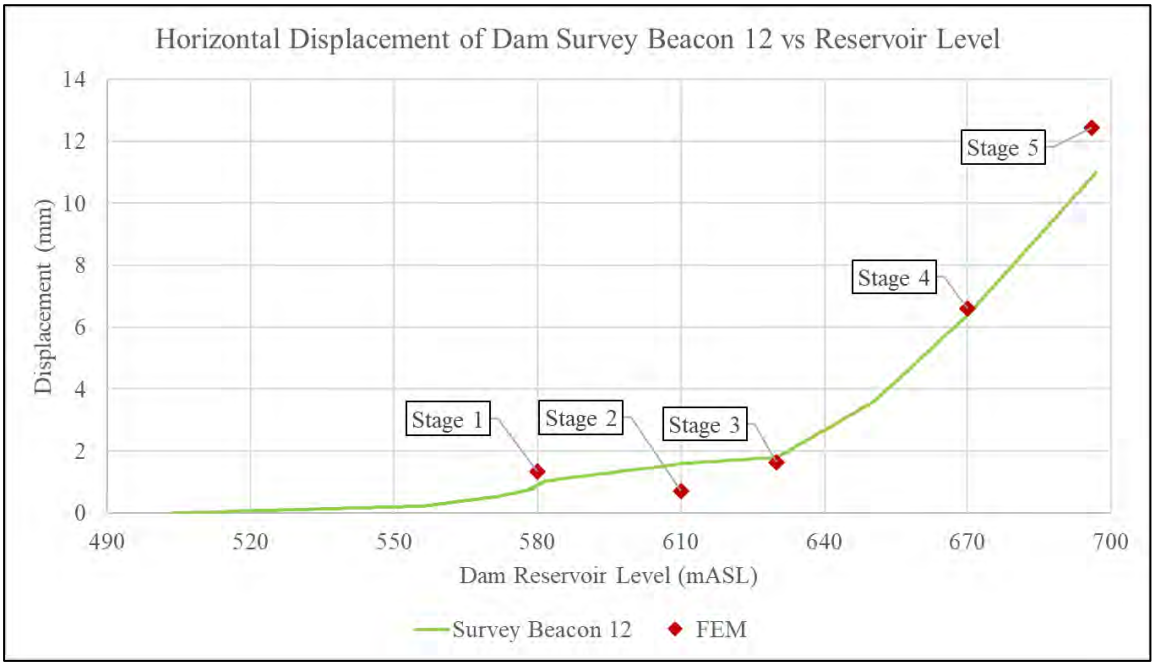

Figure 7-12: Comparison of surveyed vs modelled horizontal displacement of dam survey beacon 12

7.2 EXTERNAL DISPLACEMENTS SUMMARY AT EACH IMPOUNDMENT STAGE

A comparison of the measured vs predicted displacement values of the dam for stage 1 of impoundment is shown in Table 7-1 and plotted comparison curves across the survey measurement beacons are depicted in Figure 7-13. The comparison shows that apart from the displacement of the dam at survey beacon B6, all the modelled displacements are within 1 mm of the measured value.

The difference between modelled and measured displacements of the dam, in terms of percentage, is practically within 10 % for all instances except survey beacons B6 and B12 which are showing relatively high percentage differences. It is noted that although these percentages are high, they are misleading when considered in terms of the accuracy of the geodetic survey being of the order of +- 2 mm. The average difference for all beacons is 10 %, showing the model marginally overpredicts the dam deformation behaviour at impoundment stage 1 and is thus conservative.

Table 7-1: Comparison of measured and modelled external horizontal displacement of dam at impoundment stage 1 (580 mASL)

Survey Beacon	Measured Displacement (mm)	Modelled Displacement (mm)	Difference (mm)	Difference (%)
B1	6.8	7.5	0.7	10
B2	7.4	8.2	0.8	11
B3	3.4	3.4	0	0
B4	7.2	7.8	0.6	8
B5	9.1	9.2	0.1	1
B6	3.5	4.7	1.2	34
B7	2.0	2.1	0.1	5
B8	9.9	9.4	-0.5	-5
B9	13.4	13.5	0.1	1
B10	12.3	11.5	-0.8	-7
B11	5.6	5.5	-0.1	-2
B12	0.8	1.3	0.5	63

*positive difference indicates overprediction of values

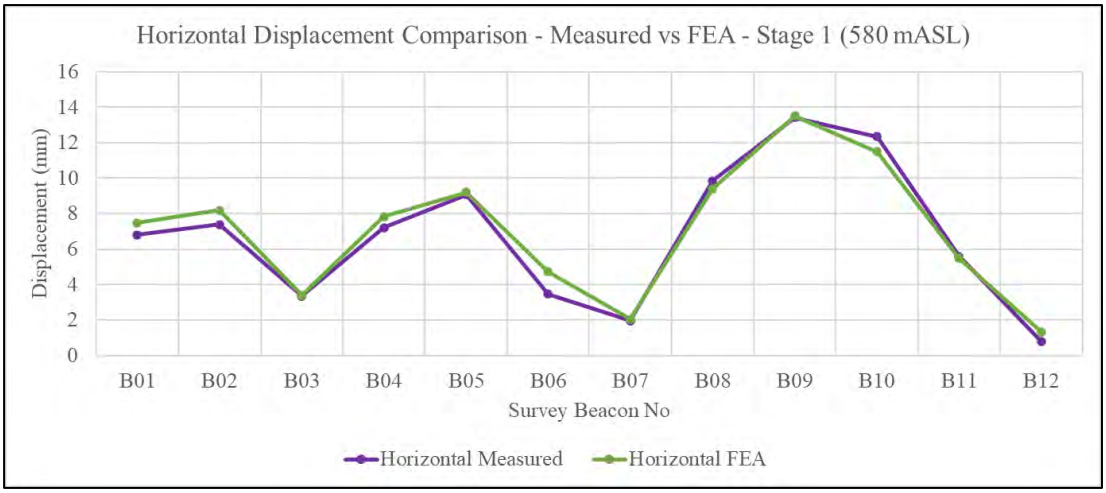

Figure 7-13: Comparison of measured displacement with FEA predicted value at impoundment stage 1

A comparison of the measured vs predicted displacement values of the dam for stage 2 of impoundment is shown in Table 7-2, and plotted comparison curves across the survey measurement beacons are depicted in Figure 7-14. The comparison shows that apart from the displacement of the dam at survey beacon B10, all the modelled displacements are within 1.5 mm of the measured value.

The difference between modelled and measured displacements of the dam in terms of percentage is within 20 % for all instances except survey beacons B7, B11 and B12 which are showing relatively high percentage differences. It is noted that although these percentages are high, they are misleading when considered in terms of the accuracy of the geodetic survey being of the order of +- 2 mm. The average difference for all beacons is -1 %, showing the model very marginally underpredicts the dam deformation behaviour at impoundment stage 2.

Table 7-2: Comparison of measured and modelled external horizontal displacement of dam at impoundment stage 2 (610 mASL)

Survey Beacon	Measured Displacement (mm)	Modelled Displacement (mm)	Difference (mm)	Difference (%)
B1	13.7	14.6	0.9	7
B2	15.2	15.7	0.5	3
B3	5.4	5.8	0.4	7
B4	11.9	12.6	0.7	6
B5	13.4	13.8	0.4	3
B6	6.3	6.2	-0.1	-2
B7	2.1	3.1	1	48
B8	10.6	11.5	0.9	8
B9	16.8	16.6	-0.2	-1
B10	14	12.1	-1.9	-14
B11	5.4	4	-1.4	-26
B12	1.5	0.7	-0.8	-53

*positive difference indicates overprediction of values

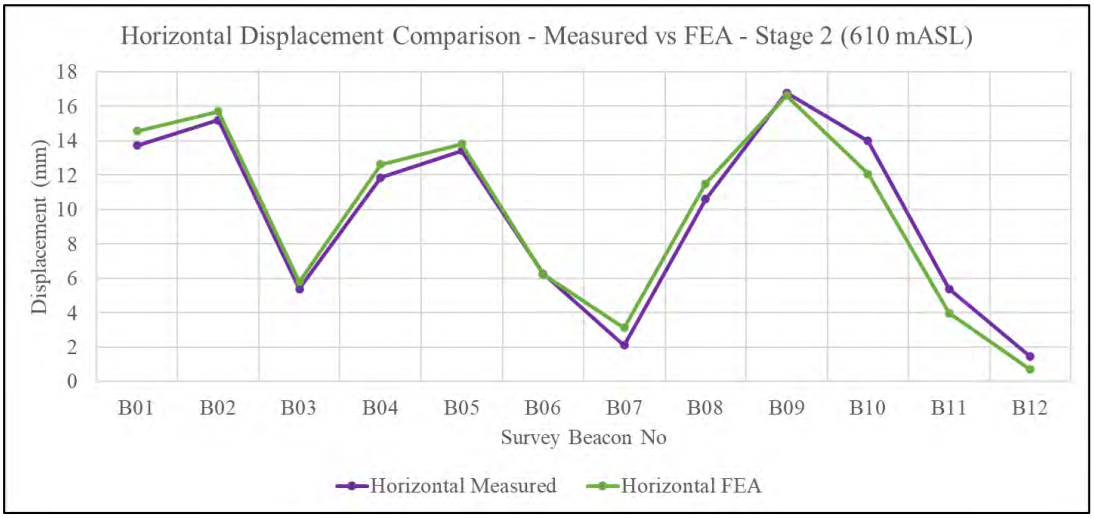

Figure 7-14: Comparison of measured displacement with FEA predicted value at impoundment stage 2

A comparison of the measured vs predicted displacement values of the dam for stage 3 of impoundment is shown in Table 7-3, and plotted comparison curves are depicted in Figure 7-15. The comparison shows that all the modelled displacements are within 2 mm of the measured value.

The difference between modelled and measured displacements of the dam, in terms of percentage, is within 10 % for all instances except survey beacon B7 which shows a relatively high percentage difference of 32%. It is noted that although this percentages is high, it is

misleading when considered in terms of the accuracy of the geodetic survey being of the order of +- 2 mm. The average difference for all beacons is 3 %, showing the model marginally overpredicts the dam deformation behaviour at impoundment stage 3 and is thus conservative.

Table 7-3: Comparison of measured and modelled external horizontal displacement of dam at impoundment stage 3 (630 mASL)

Survey Beacon	Measured Displacement (mm)	Modelled Displacement (mm)	Difference (mm)	Difference (%)
B1	20.4	22	1.6	8
B2	22.1	23.6	1.5	7
B3	8.9	9	0.1	1
B4	18.4	18.5	0.1	1
B5	20.4	19.9	-0.5	-2
B6	9.4	9.2	-0.2	-2
B7	4.1	5.4	1.3	32
B8	14.2	14.8	0.6	4
B9	19.9	20.7	0.8	4
B10	16.1	14.6	-1.5	-9
B11	5.7	5.5	-0.2	-4
B12	1.6	1.6	0	0

*positive difference indicates overprediction of values

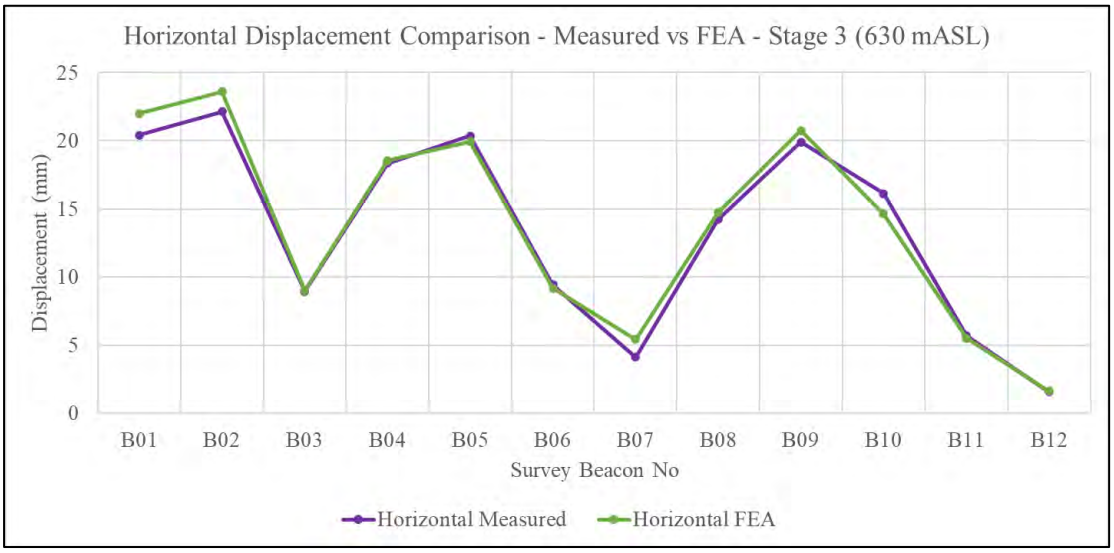

Figure 7-15: Comparison of measured displacement with FEA predicted value at impoundment stage 3

A comparison of the measured vs predicted displacement values of the dam for stage 4 of impoundment is shown in Table 7-4 and plotted comparison curves are depicted in Figure 7-16.

The comparison shows that all the modelled displacements are within 3.4 mm of the measured value.

The difference between modelled and measured displacements of the dam in terms of percentage is practically within 15 % for all instances. The average difference for all beacons is 6 %, showing the model marginally overpredicts the dam deformation behaviour at impoundment stage 4 and is thus conservative.

Table 7-4: Comparison of measured and modelled external horizontal displacement of dam at impoundment stage 4 (670 mASL)

Survey Beacon	Measured Displacement (mm)	Modelled Displacement (mm)	Difference (mm)	Difference (%)
B1	38.4	40	1.6	4
B2	39.4	42.4	3	8
B3	19.7	22.3	2.6	13
B4	36.1	39.5	3.4	9
B5	39.1	40.8	1.7	4
B6	22.4	22	-0.4	-2
B7	12.3	14.3	2	16
B8	25.1	27.5	2.4	10
B9	33.1	34.1	1	3
B10	27.5	24.7	-2.8	-10
B11	12	13	1	8
B12	6.4	6.6	0.2	3

*positive difference indicates overprediction of values

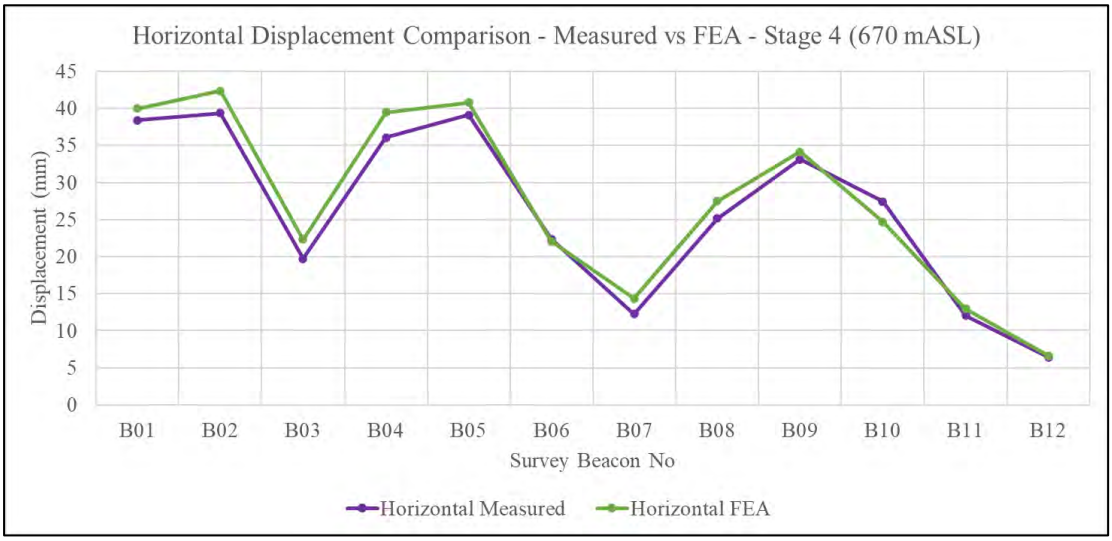

Figure 7-16: Comparison of measured displacement with FEA predicted value at impoundment stage 4

A comparison of the measured vs predicted displacement values of the dam for stage 5 of impoundment is shown in Table 7-5, and plotted comparison curves are depicted in Figure 7-17. The comparison shows on average the modelled displacements are within 1.1 mm greater than the measured value.

The average difference between modelled and measured displacements of the dam in terms of percentage is 4 %, showing the model marginally overpredicts the dam deformation behaviour at impoundment stage 5 and is thus conservative.

Table 7-5: Comparison of measured and modelled external horizontal displacement of dam at impoundment stage 5 (696 mASL)

Survey Beacon	Measured Displacement (mm)	Modelled Displacement (mm)	Difference (mm)	Difference (%)
B1	51.5	53.1	1.6	3
B2	53.5	55.5	2.0	4
B3	35.5	36.6	1.1	3
B4	57.0	59.3	2.3	4
B5	58.0	59.5	1.5	3
B6	35.0	35.2	0.2	0
B7	22.5	24.1	1.6	7
B8	38.0	39.4	1.4	4
B9	45.0	45.4	0.4	1
B10	34.0	32	-2.0	-6
B11	19.0	20.7	1.7	9
B12	11.0	12.4	1.4	13

*positive difference indicates overprediction of values

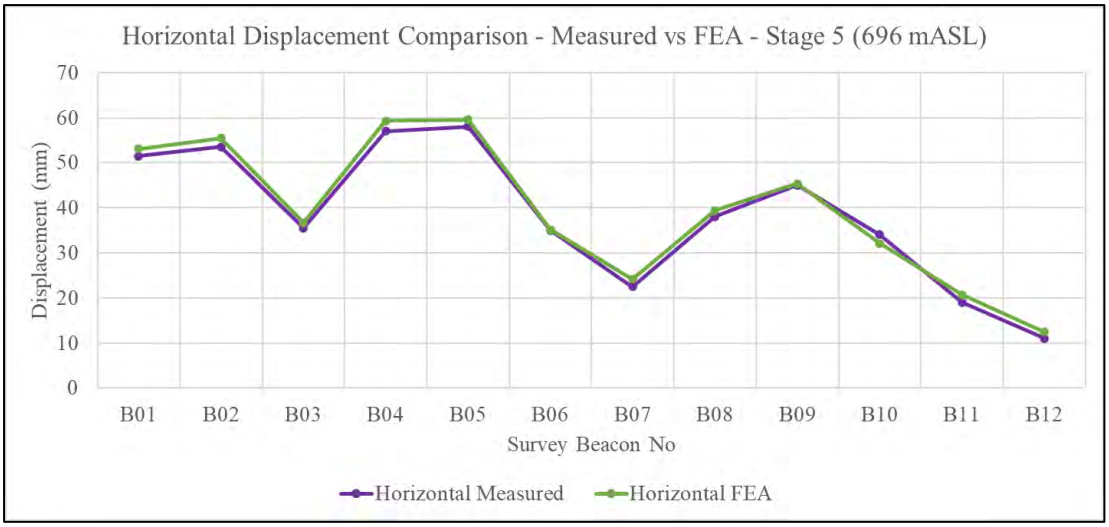

Figure 7-17: Comparison of measured displacement with FEA predicted value at impoundment stage 5

7.3 DAM EXPANSION JOINT OPENINGS

The opening and closing of the expansion/contraction joints between dam monoliths during reservoir impoundment, were measured by jointmeters placed across these joint interfaces. The anticipated movements between dam monoliths at the joints were obtained from the relative nodal displacements computed by low stiffness modulus interface elements, modelled at the interfaces between dam monoliths in the dam FEA mesh.

A comparison of the measured vs modelled dam joint openings for impoundment stages 1 and 2 is shown in Table 7-6. Subsequent to stage 2 of impoundment, all jointmeters showed closing of joints as the dam arch structure developed compressive hoop stresses along its axis, causing positive contact to be made between monoliths. The difference between measured and modelled dam joint openings indicate that at stage 1 of impoundment the FE model overpredicts joint opening by 0.1 mm and at stage 2 by 0.3 mm. In light of the accuracy of jointmeter measurements these values are considered negligible, indicating that the modelling of dam joints using low stiffness modulus interface elements is satisfactory.

Table 7-6: Comparisons between measured and modelled dam joint openings for impoundment stages 1 and 2

Joint meter	Elevation (mASL)	Stage 1 Joint Opening (mm)			Stage 2 Joint Opening (mm)		
		Measured	Modelled	Difference	Measured	Modelled	Difference
JM-9	715	0.8	0.5	-0.3	0	0.2	0.2
JM-11	715	0.9	0.8	-0.1	0	0.5	0.5
JM-13	715	1.3	1.4	0.1	0	0.6	0.6
JM-16	715	1.3	1.7	0.4	0	0.5	0.5
JM-17	715	0.9	1.1	0.2	0	0.2	0.2
JM-19	715	0.9	0.9	0	0	0.1	0.1
JM-21	715	0.5	0.6	0.1	0	0.1	0.1

*positive difference indicates overprediction of values

7.4 DAM RELATIVE INTERNAL DISPLACEMENTS

The evaluation of the dam internal relative displacement behaviour against that predicted by the FE model, in terms of pendulum measurements, was only included in this study for impoundment stage 4 and 5. Pendulum measurements at earlier stages were very small and not considered reliable enough for calibration due to the small measurement values.

A comparison of the measured and predicted radial and tangential movement of the pendulums installed in the dam for impoundment stage 4 and 5, are shown in Figure 7-18 and Figure 7-19. The plotted curves indicated the pendulum movements with time, whilst the diamond points indicate the predicted pendulum movements at impoundment stages 4 and 5. The readings taken for the hanging pendulum in dam monolith 19 (P-19-H-525.5) show some inconsistencies in behaviour, which compromises the reliability of this instrument. A comprehensive discussion on the measured pendulum movements was provided in Section 5.3.

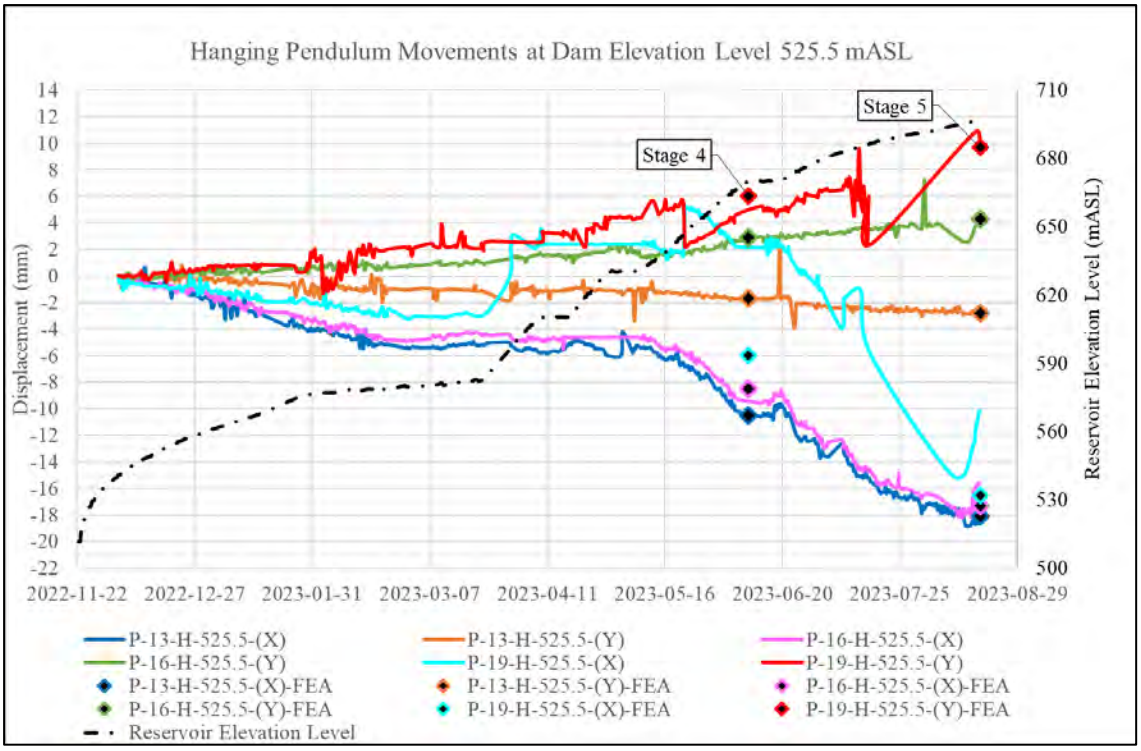

Figure 7-18: Comparison of hanging pendulum movements vs modelled deformation of dam for monolith 13, 16 and 19

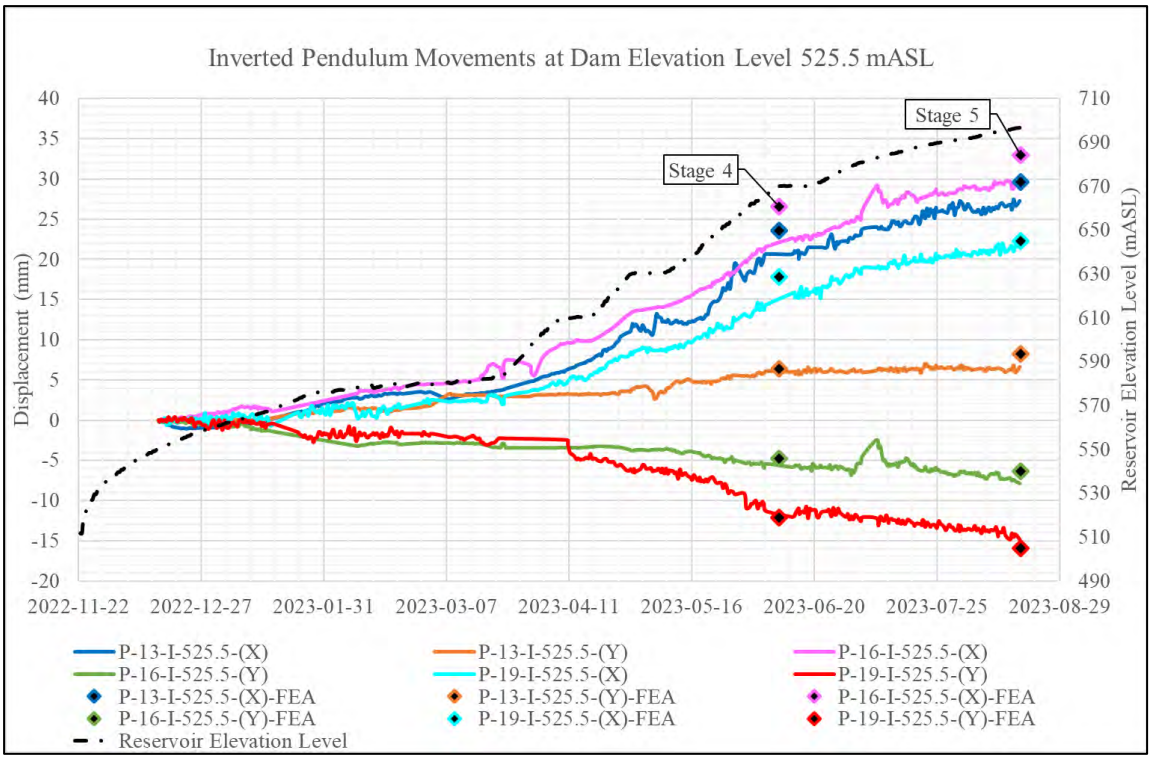

Figure 7-19: Comparison of hanging pendulum movements vs modelled deformation of dam for monolith 13, 16 and 19

A comparison summary of the predicted and measured radial and tangential movement of the pendulums, installed in the dam for impoundment stage 4, are shown in Table 7-7 and Table 7-8 and for stage 5, are shown in Table 7-9 and Table 7-10.

Considering that the mesh size of the dam is 4.5 m, the predicted relative pendulum movements show a good correlation to that measured on site. It is noted that pendulum measurements indicate tilting or leaning of the dam and are very sensitive to small rotational leaning, as a result differences between predicted and measured dam behaviour of 0 – 4 mm are deemed acceptable. On average the FE model overpredicts the pendulum movement by 5 - 8 % showing again that the model is marginally conservative in predicting deformation behaviour of the dam.

Table 7-7: Comparison of predicted and measured pendulum radial movements of dam at impoundment stage 4

Pendulum	FEA Predicted Radial Movement (mm)			Measured Radial Relative Movement (mm)	Difference (mm)	Difference (%)
	Suspension Point	Measuring Point	Relative Movement			
P13-H-525.5	-38.1	-27.6	-10.5	-10.0	-0.5	5
P16-H-525.5	-38.9	-30.4	-8.5	-9.0	0.5	-6
P19-H-525.5	-32.7	-24.1	-9.0	-8.0	-0.6	8
P13-I-525.5	-2.8	-26.8	24.0	21.0	3.0	14
P16-I-525.5	-3.1	-30.1	27.0	22.8	4.2	18
P19-I-525.5	-2.2	-20.3	18.1	16.0	2.1	13

Table 7-8: Comparison of predicted and measured pendulum tangential movements of dam at impoundment stage 4

Pendulum	FEA Predicted Tangential Movement (mm)			Measured Tangential Relative Movement (mm)	Difference (mm)	Difference (%)
	Suspension Point	Measuring Point	Relative Movement			
P13-H-525.5	5.4	3.7	1.7	1.75	-0.0	-3
P16-H-525.5	-6.5	-3.6	-2.9	-2.5	-0.4	16
P19-H-525.5	-13.8	-7.8	-6.0	-5.5	-0.5	9
P13-I-525.5	1.9	8.4	6.5	6.0	0.5	8
P16-I-525.5	-0.7	-5.6	-4.9	-5.0	0.1	-2
P19-I-525.5	-2.3	-14.6	-12.3	-11.0	-1.3	12

Table 7-9: Comparison of predicted and measured pendulum radial movements of dam at impoundment stage 5

Pendulum	FEA Predicted Radial Movement (mm)			Measured Radial Relative Movement (mm)	Difference (mm)	Difference (%)
	Suspension Point	Measuring Point	Relative Movement			
P13-H-525.5	-52.3	-34.2	-18.1	-19.0	0.9	-5
P16-H-525.5	-54.5	-37.4	-17.1	-18.0	0.9	-5
P19-H-525.5	-47.4	-30.0	-17.0	-16.0	-1.4	9
P13-I-525.5	-3.6	-33.2	29.6	27.5	2.1	8
P16-I-525.5	-4.0	-37.0	33.0	29.0	4.0	14
P19-I-525.5	-2.8	-25.1	22.3	22.0	0.3	1

Table 7-10: Comparison of predicted and measured pendulum tangential movements of dam at impoundment stage 5

Pendulum	FEA Predicted Tangential Movement (mm)			Measured Tangential Relative Movement (mm)	Difference (mm)	Difference (%)
	Suspension Point	Measuring Point	Relative Movement			
P13-H-525.5	7.4	4.6	2.8	2.75	0.1	2
P16-H-525.5	-9.0	-4.7	-4.3	-4.0	-0.3	8
P19-H-525.5	-20.0	-10.3	-9.7	-9.0	-0.7	8
P13-I-525.5	2.3	10.5	8.2	7.3	1.0	13
P16-I-525.5	-0.9	-7.3	-6.4	-6.5	0.1	-2
P19-I-525.5	-2.9	-18.8	-15.9	-15.0	-0.9	6

7.5 DAM INTERNAL STRESS DEVELOPMENTS

The observed internal stress development of the dam from loading during impoundment, was measured by stress meters placed in the lower portion of the dam. The expected internal stress development of the dam during impoundment was derived from element stress values extracted from outputs of the dam impoundment structural FE analysis.

A comparison of the axial stress development measured by stress meters in the lower portions of the dam, with stresses computed by the FE analysis is shown in Table 7-11. The comparison looks at the change in axial stress of the dam from commencement of impoundment (stage 0) to current stage 5 of impoundment.

The stress values show a good agreement between the measured values and predicted values except for instrument 525.5/ST/28/7/1. The high stress value reported by instrument

525.5/ST/28/7/1, is a clear outlier in comparison to the other stress meters at similar elevations. It seems the reading is unreliable and should be discarded. Except for instrument 525.5/ST/28/7/1, the average difference between measured and modelled stresses occurring in the dam is 0.12 MPa.

Table 7-11: Comparison of measured and anticipated stress development in dam at impoundment stage 5

Stress meter No	FEA Axial Stress (MPa)			Measured Change in Axial Stress (MPa)	Axial Stress Difference (MPa)
	Stage 0	Stage 5	Change		
471.5/ST/10/11/1	-0.48	-0.64	-0.17	-0.30	0.13
471.5/ST/10/20/1	-0.42	-0.73	-0.30	-0.35	0.05
471.5/ST/10/20/2	0.04	-0.55	-0.59	-0.70	0.11
525.5/ST/28/7/1	-0.32	-0.77	-0.45	-1.50	1.05
525.5/ST/28/7/2	0.01	-0.81	-0.82	-1	0.18

*positive difference indicates overprediction of compressive stress values

7.6 DAM INTERNAL STRAIN DEVELOPMENTS

The internal strain development of the dam from loading during impoundment was measured by strain gauges placed in the lower portion of the dam. The expected strain developments of the dam during impoundment, were derived from element strain values extracted from the dam impoundment structural FE analysis results.

A comparison of the strain development measured by the strain gauges in the lower portions of the dam, with strains computed by the FE analysis is shown in Table 7-12. The comparison looks at the strain of the dam from commencement of impoundment (stage 0) to stage 5. An average difference of -1 x 10^{-6} was observed between predicted and measured strain values. It is noted that the changes in strain values are very small and may not necessarily be very reliable in comparison to the sensitivity of the strain gauges.

Table 7-12: Comparison of measured and anticipated strain development in dam at impoundment stage 5

Strain gauge No	FEA Strain (m/m)10^{-6}			Measured Change in Strain (m/m)10^{-6}	Strain Difference (m/m)10^{-6}
	Stage 0	Stage 5	Change		
453.5/SR/1/15/1	6.7	-6.9	-13.6	-18.0	4.4
453.5/SR/1/16/1	-6.7	10.0	16.7	18.0	-1.3
453.5/SR/1/17/1	6.5	-2.5	-9.0	-7.0	-2.0
453.5/SR/1/17/2	-4.7	-13.0	-8.3	-6.0	-2.3
471.5/SR/10/11/1	-6.3	-12.0	-5.7	-5.0	-0.7
471.5/SR/10/20/1	-3.5	-0.6	2.9	2.0	0.9

*positive strain indicates expansive strain

7.7 DAM TEMPERATURE DEVELOPMENT

The measured temperature state of the dam body during reservoir impoundment was measured by thermocouples cast into the concrete dam. The simulated temperature state of the dam as modelled and analysed for determining the thermomechanical behaviour of the dam during impoundment, was obtained from the temperature plots produced by the thermal analysis of the dam.

A comparison of the observed temperature state of the dam, with that simulated by the FE analysis is shown in Table 7-13. The modelled temperature state of the dam is relatively accurate showing values not differing by more than 2.5 °C, from those measured by the thermocouples. The average of the absolute value of the difference between temperature measured and modelled is approximately 1 °C. It is noted that the temperature measurement of thermocouple 525.5/TK/26/20/2 was deemed unreliable as explained in Section 5.7.

Table 7-13: Comparison of measure and modelled temperature state in dam at impoundment stage 5

Thermocouple No	Elevation Level (mASL)	Measured Temperature (°C)	FEA Nodal Temperature (°C)	Temperature Difference (°C)
471.5/TK/7/15/1	462.5	12.7	11.2	-1.5
471.5/TK/7/15/2	462.5	13.3	12.8	-0.5
471.5/TK/7/17/1	462.5	12.7	11.2	-1.5
471.5/TK/7/17/2	462.5	13.3	12.5	-0.8
471.5/TK/8/14/1	465.5	11.6	12.7	1.1
471.5/TK/8/14/2	465.5	8.9	8.9	0
471.5/TK/8/16/1	465.5	10.9	12.4	1.5
471.5/TK/8/16/2	465.5	8.9	8.9	0
525.5/TK/26/14/1	516	11	11.6	0.6
525.5/TK/26/14/2	516	13.1	13.2	0.1
525.5/TK/26/16/1	516	11.5	11.8	0.3
525.5/TK/26/16/2	516	13.1	13.8	0.7
525.5/TK/26/20/1	516	11	12.1	1.1
525.5/TK/26/20/2	516	12.4	14.0	1.6
588.5/TK/43/16/1	570	14.8	12.9	-1.9
588.5/TK/43/16/2	570	16.8	17.9	1.1
588.5/TK/43/22/1	570	14.8	12.4	-2.4
588.5/TK/43/22/2	570	17.0	18.0	0.3

*positive difference indicates overprediction of temperature value

7.8 SUMMARY

Direct comparisons between the observed response of the Yusufeli concrete arch dam, as indicated by instrumentation measurements, and the anticipated response of the dam as reported by the outputs of the impoundment FEA study, were provided and discussed in this chapter.

The comparisons show that the FE model of the dam provides a very reliable and accurate simulation of the dam behaviour during reservoir impoundment, in terms of its displacement response, internal stress/strain development and temperature state.

Predicted deformation of the dam, as derived from the FE model was on average 5 – 10 % greater than the dam deformations measured by geodetic surveys, jointmeters and pendulums installed on the dam. The observed deformation of Yusufeli dam, especially that provided by the geodetic survey was the most reliable structural behaviour mode used for calibration/validation of a dam FE model. Deformation instrumentation installed on the dam covered the whole body of the dam and had numerous redundancies, ensuring comprehensive and global monitoring of the dam behaviour.

The stress and strain measurements obtained of the dam during impoundment were less reliable than the deformations measured. The stress/strain measurements obtained from stress meters and strain gauges installed in the dam, were only placed in limited isolated locations near the base of the dam and do not provide a global picture of the stress/strain response of the whole dam during impoundment. Various instruments also proved to be faulty or non-responsive and were not considered in the calibration study. The FEA modelled stress and strain behaviour of the dam, did provide a reasonable prediction of the behaviour measured by the limited stress meters and strain gauges installed in the dam.

The measured temperature state of the dam was very well modelled by the thermal heat transfer FE analysis. The average difference between measured and simulated temperatures within various locations of the dam section, was within 1 - 2 °C.

Installing delicate instruments during the construction of a large dam is never without challenges and it is inevitable that some instruments are damaged, fail, or become unreliable. In general, and considering the scale of the instrumentation installed in Yusufeli Dam, the instruments have performed well so far and have proved reliable. Most importantly, a very good correlation between predicted and measured behaviour has been confirmed, not only corroborating the good performance of the dam, but the instruments themselves as well.

8 SENSITIVITY AND BEHAVIOUR ANALYSES

This chapter discusses the results of investigations undertaken whereby the behaviour of the Yusufeli Dam is analysed under various theoretical conditions, to devise a deeper understanding of the global structural and thermal functioning of the concrete structure. Such investigations provide valuable insight into the load transfer mechanisms of the dam and modes of response associated with these.

Parametric analyses were undertaken of the dam under a range of material parameters, to establish the sensitivity of the dam behaviour to changes in such parameter value. Similarly, direct evaluations were derived of the physical relationship between different loadings and the response mode of the dam.

The computed behaviour of the FE model of the dam and foundation was validated against the measured behaviour of the dam during impoundment, under known loadings. As a result, the numerical model can be used as a "digital twin" to monitor the dam safety during its operational life and provide valuable information to the owner, should possible adverse conditions or behaviour of the dam arise in future.

8.1 PARAMETRIC STUDY OF ELASTIC MODULUS

According to Hooke's law, the extent and mode of deformation of the dam and its foundation under loading, is directly proportional to the stiffness of the dam-foundation structural system. The stiffness of the dam and foundation is a function of its geometrical configuration and the elastic modulus of the material.

Good quality survey control on site during construction, means that the geometrical configuration of a concrete arch dam can be defined with a good level of accuracy. The elastic modulus of the material may however vary from assumed or adopted design parameters, due to the inherent limitations of material testing and the time-based effects on the material, such as creep, porous plastic deformation or material deterioration (ICOLD, 2009).

Derivation of the dam behaviour sensitivity to changes in the elastic modulus of the concrete and foundation material, is a valuable insight to have on the dam that can be considered when designing or evaluating other existing large concrete arch dams of a similar size, and with similar foundation conditions.

8.1.1 Dam Elastic Modulus

Calibration of the FE model of the dam, under impoundment loading, indicated that the deformation response was most sensitive to changes of the elastic modulus of the dam. A comparison of the modelled dam resultant horizontal deformation values for a range of dam elastic moduli, in relation to the measured dam survey beacons displacement, is shown in Figure 8-1. The plot indicates the dam deformation at crest level (715 mASL) taken along its axis for impoundment stage 5 when the reservoir level is at 696 mASL and indicates measured deformations of survey beacons 7 to 12.

The curves indicate that the deformation of the dam is more sensitive to change in elastic modulus near the central portion of the arch and substantially less at the abutment supports. The plot also indicates that modelled deformation correlates very well to that measured for an assumed dam elastic modulus of 28 GPa. The other curves indicate elastic modulus values with increments of 25 % and 50 % higher and lower than the calibrated value of 28 GPa.

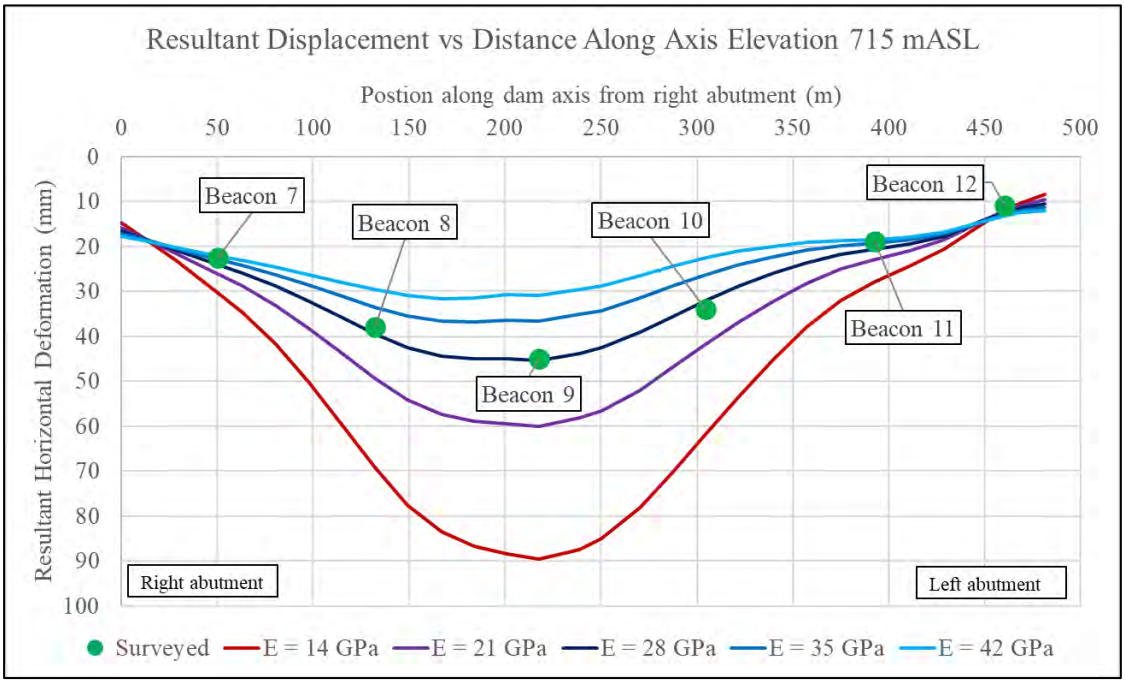

Figure 8-1: Sensitivity curves of modelled dam deformation response in relation to that measured - 715 mASL

Similarly, a comparison of the modelled dam resultant horizontal deformation values for a range of dam elastic moduli, in relation to the measured deformation at dam elevation 662 mASL and 590 mASL, are shown in Figure 8-2 and Figure 8-3. These plots indicate the dam deformation for impoundment stage 5 when the reservoir level is at 696 mASL in comparison to measured displacements of survey beacons 1 to 6.

The plots also indicate that modelled deformation correlates very well to that measured for a dam elastic modulus of 28 GPa.

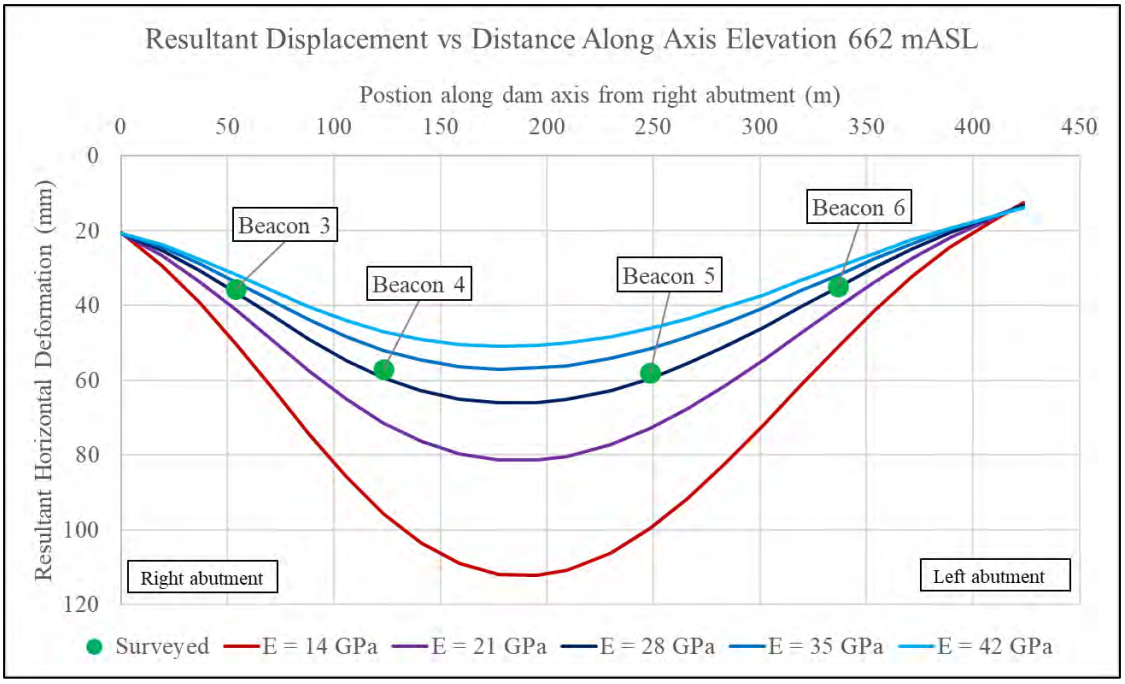

Figure 8-2: Sensitivity curves of modelled dam deformation response in relation to that measured - 662 mASL

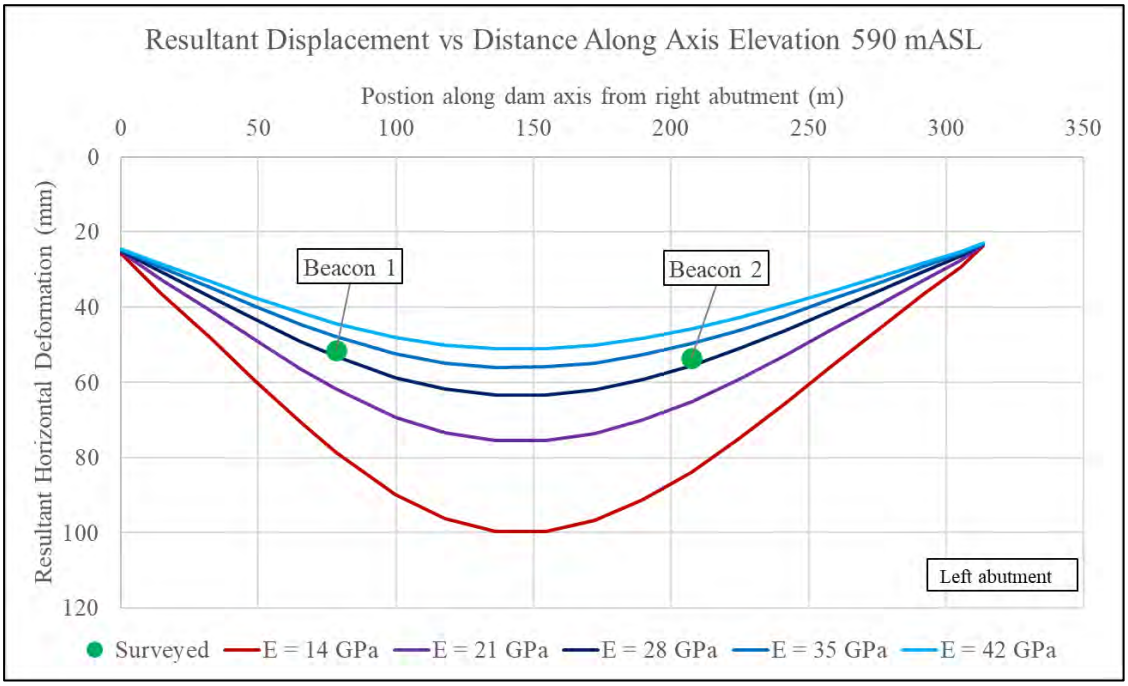

Figure 8-3: Sensitivity curves of modelled dam deformation response in relation to that measured - 590 mASL

A comparison of the modelled dam resultant horizontal deformation values for a range of dam elastic moduli, in relation to the measured deformation along the height of the dam near the centre cantilever, is shown in Figure 8-4. This plot indicates the dam deformation for impoundment stage 5 when the reservoir level is at 696 mASL in comparison to measured displacements of survey beacons 1, 4 and 8. The plot indicates that modelled deformation correlates very well to that measured for a dam elastic modulus of 28 GPa.

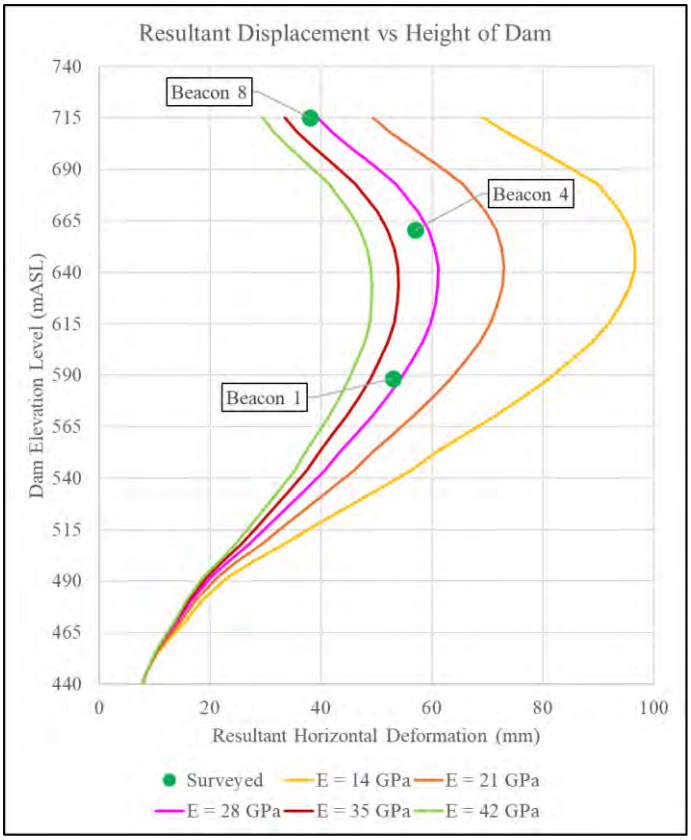

Figure 8-4: Sensitivity curves of modelled dam deformation response in relation to that measured along height

Numerous validations were undertaken to calibrate the dam FE model against its measured behaviour throughout impoundment, until reservoir level 696 mASL was reached. It can be assumed that the behaviour predicted by the model for the final stage of impoundment, when the reservoir level is raised to FSL at elevation 710 mASL, will provide a reliable and accurate simulation of actual behaviour under the ultimate operational conditions of the dam.

To predict the deformation of the dam at completion of impoundment, when the reservoir level reaches FSL (710 mASL), the date will need to be known to model the ambient temperature state. At the time of writing this dissertation such information was not available as this would be largely influenced by unpredictable precipitation and associated flood conditions, which dictate the time taken for the impoundment process can be completed.

Assuming temperature loadings are disregarded, the modelled deformation of the dam at the various impoundment stages is shown in Figure 8-5 and Figure 8-7 and can be compared to Figure 6-84 and Figure 6-85 where actual temperature conditions were considered. The curves depict the significant increase in horizontal displacement towards the downstream side, especially at the central portion of the arch where the maximum displacement approaches 103 mm at stage 6 of impoundment when the reservoir level reaches elevation 710 mASL. The curves also indicate the relative symmetry in the deformed shape of the arch.

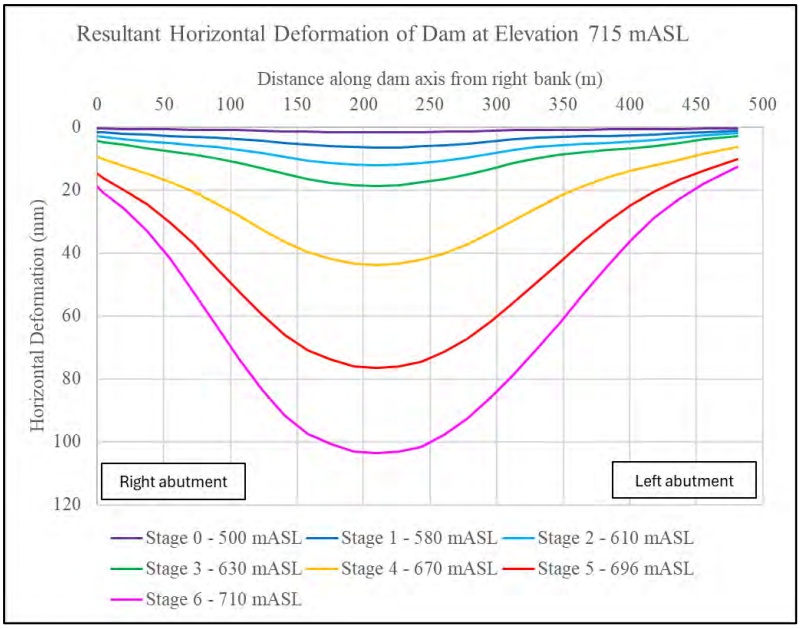

Figure 8-5: Anticipated horizontal deformation curves along dam axis at elevation level 715 mASL

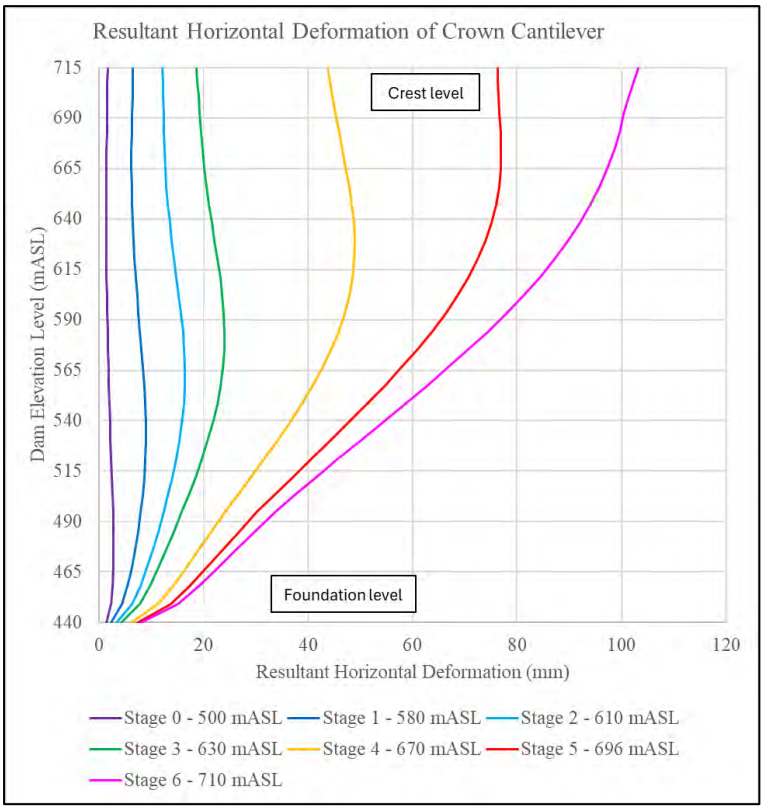

Figure 8-6: Anticipated horizontal deformation curves along dam axis at elevation level 715 mASL

Although it has been shown that the ambient temperature loading has a significant influence on the deformation response of the dam, the hydrostatic water loading still dominates the structural load transfer mechanism of a large arch dam. This warrants a detailed investigation of the sensitivity of the dam behaviour under a range of elastic moduli values for FSL hydrostatic loading.

A set of sensitivity curves indicating the modelled deformation of the dam at final stage of impoundment, disregarding temperature loading, when the reservoir level reaches elevation 710 mASL, being FSL, is shown in Figure 8-7 and Figure 8-8.

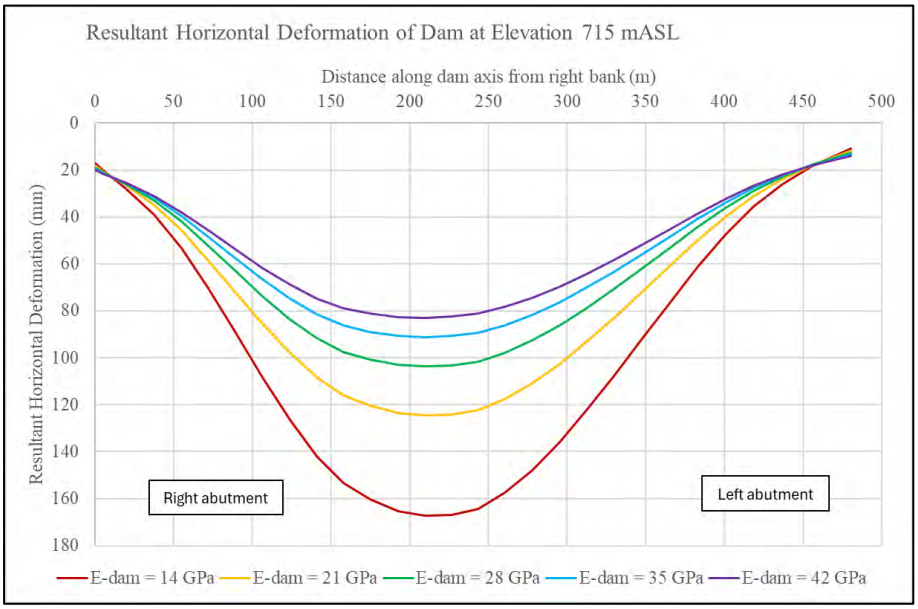

Figure 8-7: Sensitivity curves of modelled dam deformation response at crest level under FSL loading

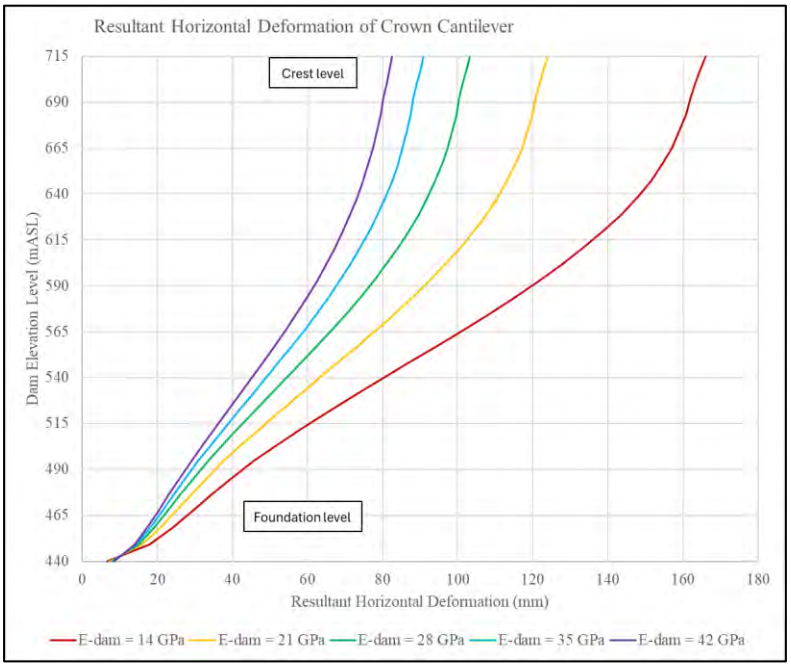

Figure 8-8: Sensitivity curves of modelled dam deformation response along height of dam under FSL loading

The range of vertical stresses expected to develop on the upstream face of the dam, along the height of the crown cantilever, for various dam elastic moduli are shown in Figure 8-9. The set of stress curves depict that a change in dam elastic modulus, results in a substantial change in vertical stresses along the lower half of the dam where vertical compressive stresses are

greatest, whilst a relatively insignificant change is evident along the top half of the dam. Along the full height of the dam a higher elastic modulus results in a stiffer cantilever function and development of higher vertical stresses.

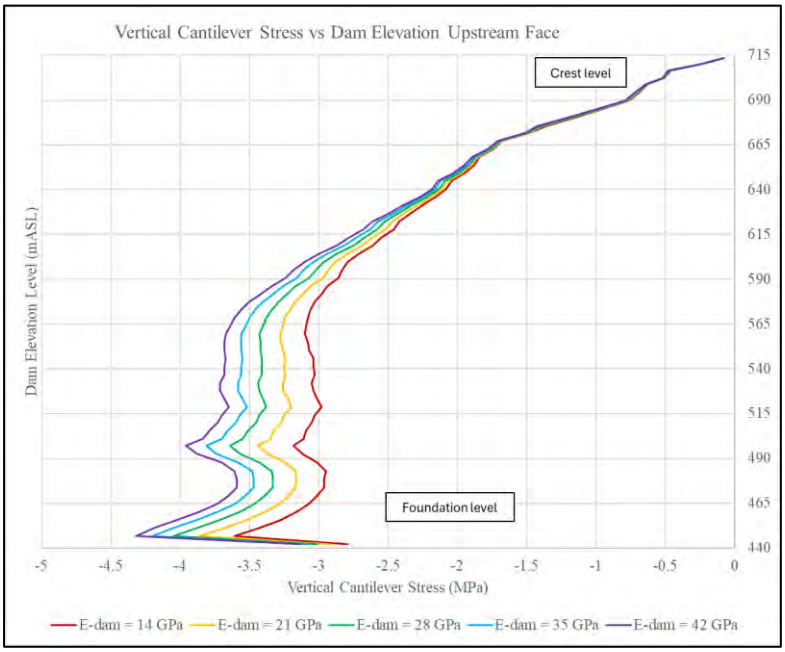

Figure 8-9: Sensitivity curves of dam vertical stresses on upstream face along dam height under FSL loading

The range of vertical stresses expected to develop on the downstream face of the dam, along the height of the crown cantilever, for various dam elastic moduli are shown in Figure 8-10. The set of stress curves depict that a change in dam elastic modulus, results in a substantial change in vertical stresses along the lower half of the dam where vertical compressive stresses are greatest, whilst a relatively insignificant change is evident along the top half of the dam.

It is interesting to note that mid-height of the dam, a lower elastic modulus results in higher vertical stresses on the downstream face. This is indicative of the development of vertical bursting stresses that may form on the downstream face of an arch if it is either overloaded, or not stiff enough. A more flexible arch will transfer a greater portion of the load to its foundation via bending moments as opposed to compressive thrusting causing these bursting stresses to develop. A significant portion of the vertical stresses expected to form on the downstream face of the arch mid-height are due to the curvature of the dam in the vertical plane.

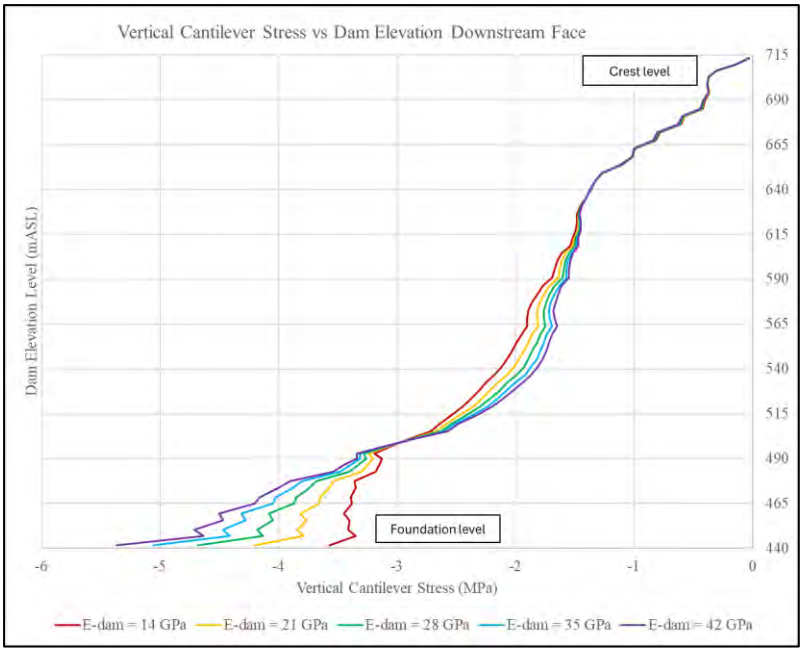

Figure 8-10: Sensitivity curves of dam vertical stress on downstream face along dam height under FSL loading

The range of horizontal axial (arch) stresses expected to develop on the upstream face of the dam, along the height of the crown cantilever, for various dam elastic moduli are shown in Figure 8-11. The set of stress curves depict that a change in dam elastic modulus, results in a substantial change in horizontal axial stresses along most of the dam. Along the full height of the dam a higher elastic modulus results in a stiffer arching function and higher development of arch stresses.

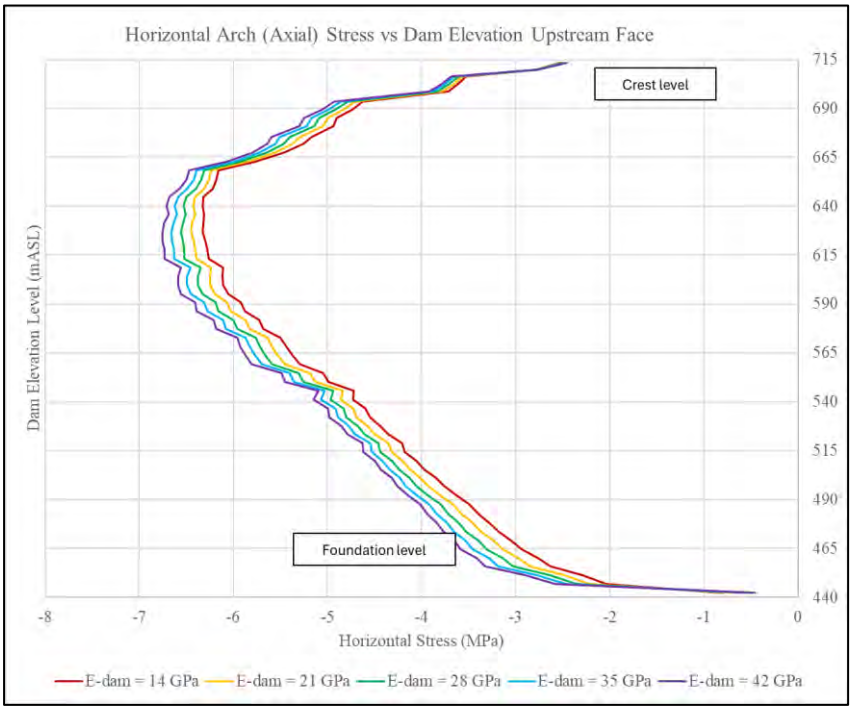

Figure 8-11: Sensitivity curves of dam axial stress on upstream face along dam height under FSL loading

The range of horizontal axial (arch) stresses expected to develop on the downstream face of the dam, along the height of the crown cantilever, for various dam elastic moduli are shown in Figure 8-12. The set of stress curves depict that a change in dam elastic modulus, results in a substantial change in arching stresses along the lower half of the dam, whilst a lower change is evident along the top half of the dam.

It is interesting to note that mid-height of the dam a lower elastic modulus results in higher vertical stresses on the downstream face. This is indicative of the development of horizontal bursting stresses that may form on the downstream face of an arch if it is either overloaded, or not stiff enough. A more flexible arch will transfer a greater portion of the load to its foundation via bending moments as opposed to compressive thrusting causing these bursting stresses to develop. A significant portion of the vertical stresses expected to form on the downstream face of the arch mid-height, are due to the curvature of the dam in the vertical plane.

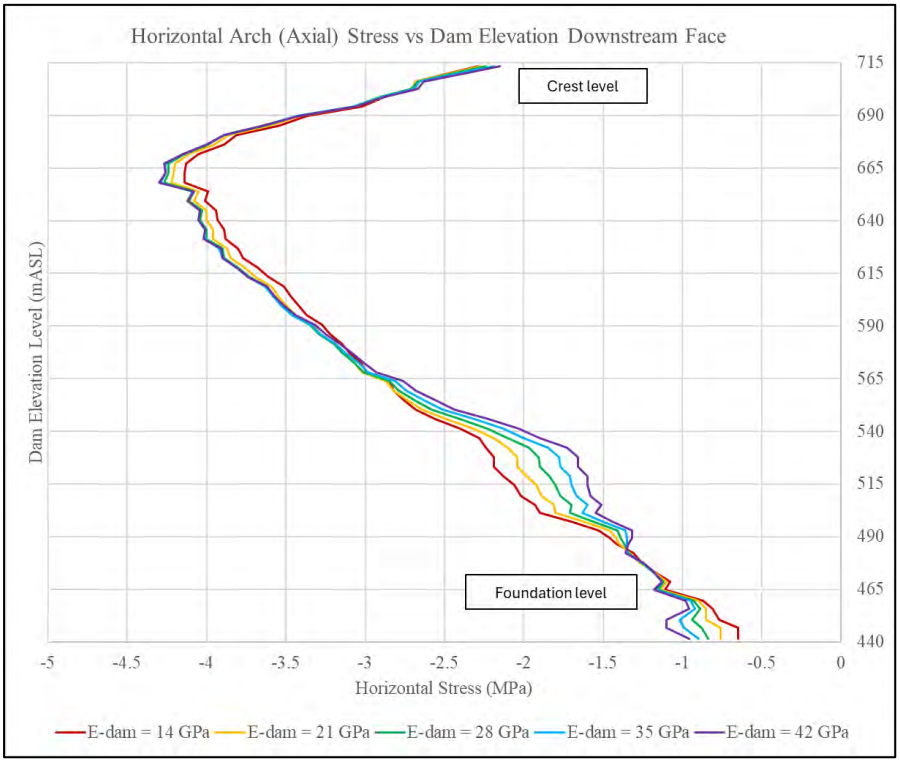

Figure 8-12: Sensitivity curves of dam axial stress on downstream face along dam height under FSL loading

A set of sensitivity curves indicating the minor principal stresses expected to develop at the toe of the arch along its left and right abutment, for various dam elastic moduli, are shown in Figure 8-13 and Figure 8-14. The stress curves indicate that a lower dam elastic modulus will cause higher minor principal stresses to form at the toe of the dam. A lower elastic modulus causes the dam to deflect further forward and transfer more load into the foundation at the toe portion of its ligament.

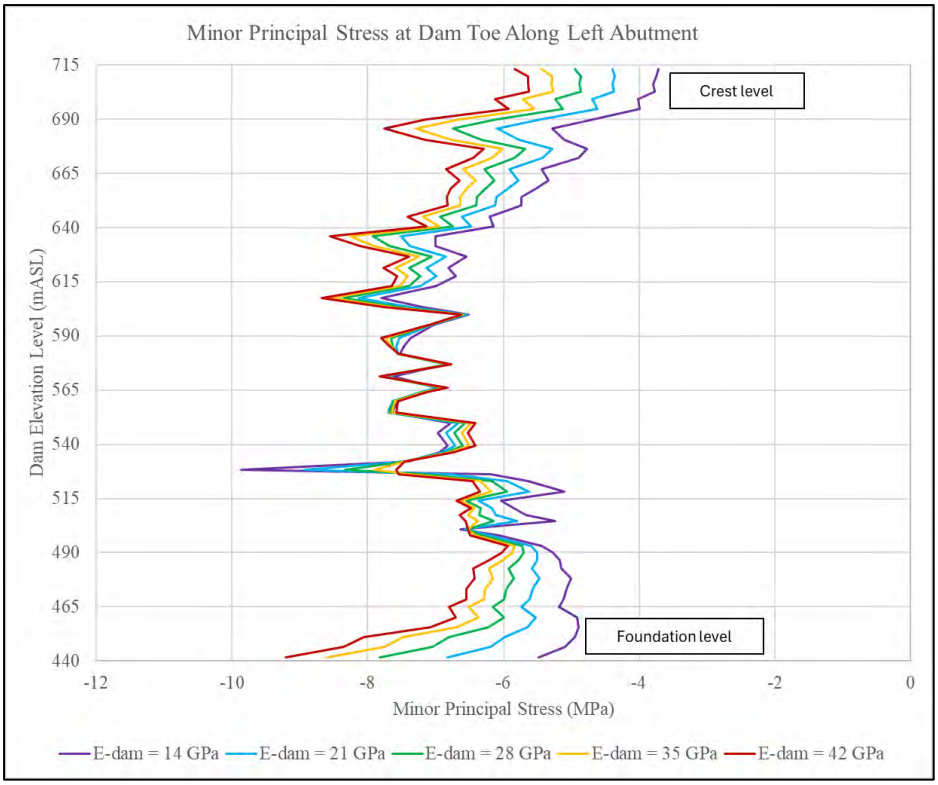

Figure 8-13: Sensitivity curves of dam minor principal stresses at toe of dam along left abutment height under FSL loading

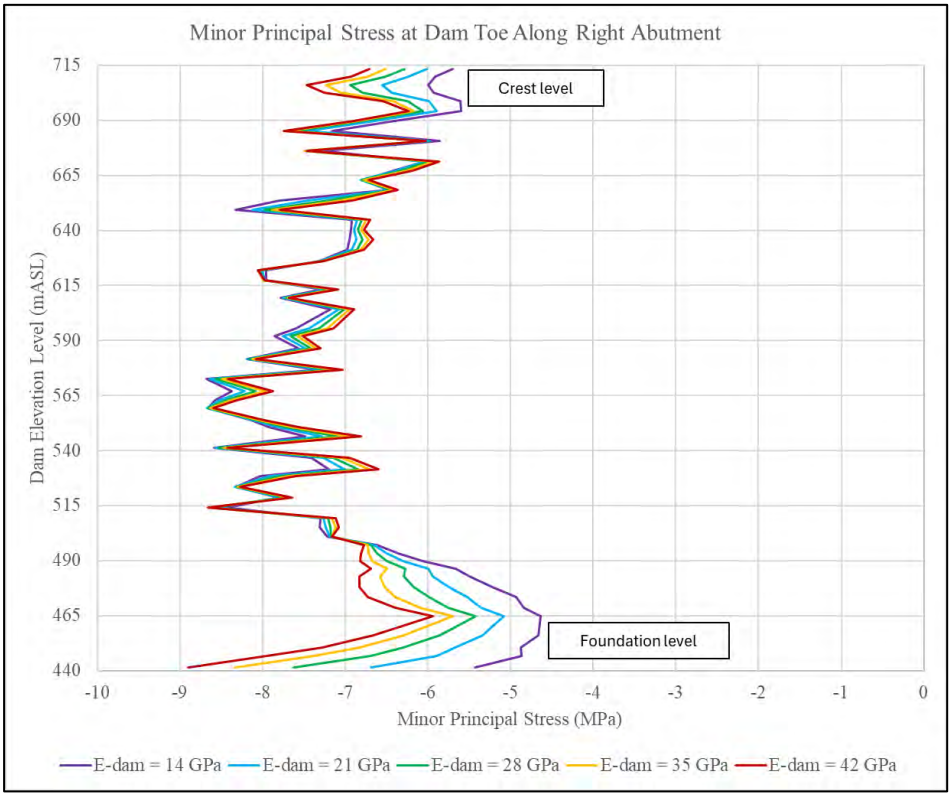

Figure 8-14: Sensitivity curves of dam minor principal stresses at toe of dam along right abutment height under FSL loading

8.1.2 Foundation Elastic Modulus

Calibration of the FE model of the dam indicated that the deformation response was approximately 50 % less sensitive to changes in foundation elastic modulus, than to that of the dam body.

Extensive geotechnical investigations done on site as described in section 3.2, provided relatively accurate insitu pre and post consolidation grouting rock mass foundation stiffness parameters, as shown in Table 3-1.

Due to the varying elastic modulus of the heterogenous foundation, the sensitivity analysis was done by changing the elastic modulus of the various rock mass zones by a common ratio denoted by Ef, for each of the analysis case runs. The range of Ef values evaluated are Ef = 0.5, Ef = 0.75, Ef = 1, Ef = 1.5 and Ef = 2. An Ef value of 2 represents a FE model analysis case where all foundation rock mass elastic modulus values are multiplied by 2, and inversely an Ef value of 0.5 is indicative of an FE model analysis case where all rock mass elastic modulus values are halved.

A comparison of the modelled dam resultant horizontal deformation values for the range of foundation elastic moduli, in relation to the measured dam survey beacons displacement, is shown in Figure 8-15 . The plot indicates the dam deformation at crest level (715 mASL) taken along its axis for impoundment stage 5 when the reservoir level is at 696 mASL and indicates measured deformations of survey beacons 7 to 12.

The curves indicate that the sensitivity of the deformation of the dam near the central portion of the arch, in comparison to the abutments, is substantially less for the variation in foundation elastic modulus than for that of dam elastic modulus. The plot also indicates that modelled deformation correlates very well to that measured for an assumed foundation elastic modulus of Ef = 1.

Similarly, a comparison of the modelled dam resultant horizontal deformation values for a range of foundation elastic moduli, in relation to the measured deformation at dam elevation 662 mASL and 590 mASL, are shown in Figure 8-16 and Figure 8-17. These plots indicate the dam deformation for impoundment stage 5 when the reservoir level is at 696 mASL, in comparison to measured displacements of survey beacons 1 to 6.

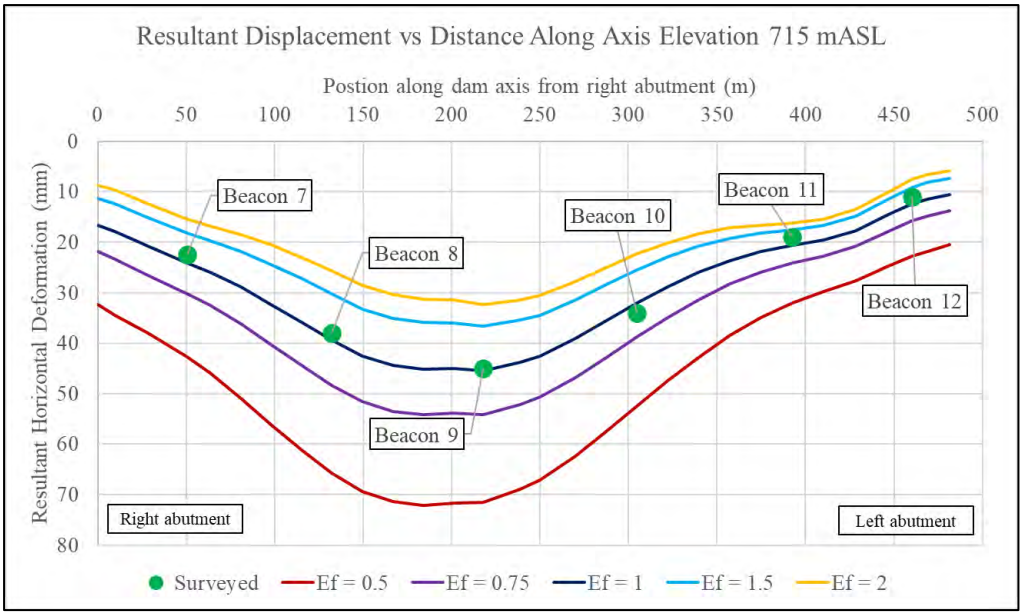

Figure 8-15: Sensitivity curves of modelled dam deformation response at crest as a function of Ef value

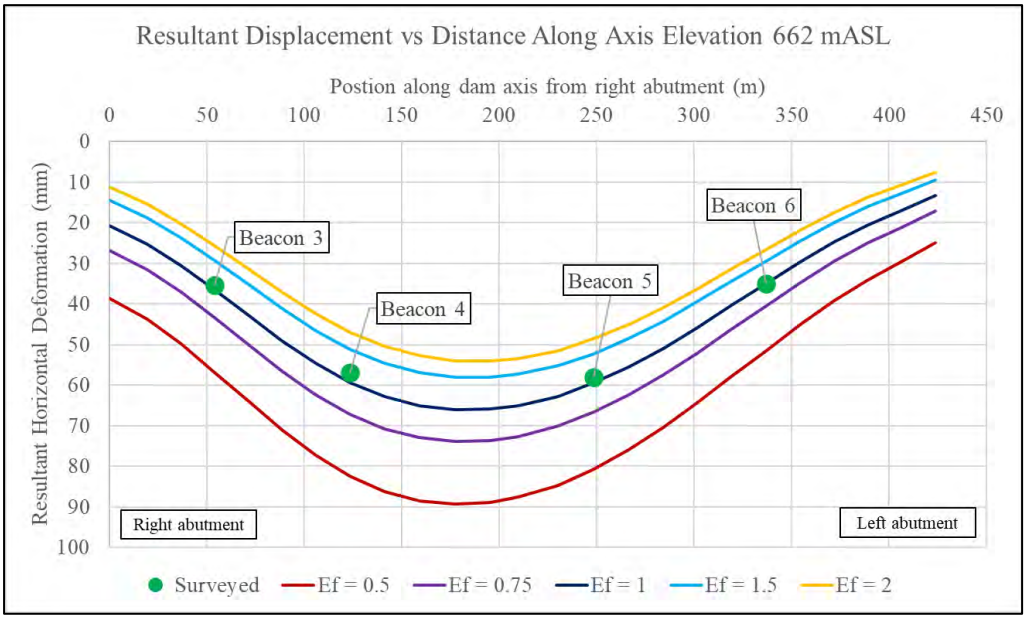

Figure 8-16: Sensitivity curves of modelled dam deformation response at 662 mASL as a function of Ef value

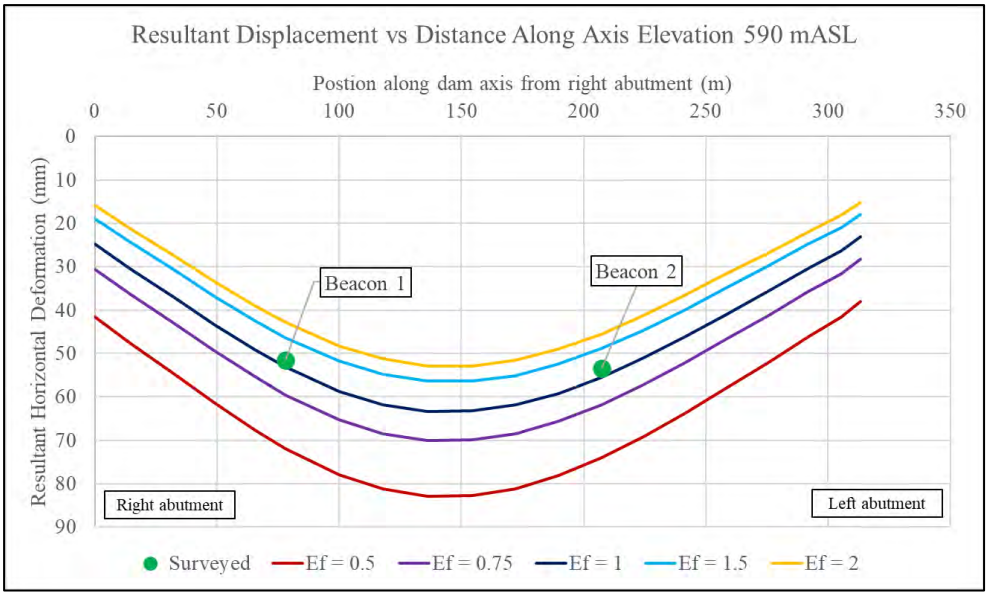

Figure 8-17: Sensitivity curves of modelled dam deformation response at 590 mASL as a function of Ef value

A comparison of the modelled dam resultant horizontal deformation values for a range of Ef values, in relation to the measured deformation along the height of the dam near the centre cantilever, is shown in Figure 8-18. This plot indicates the dam deformation for impoundment stage 5 when the reservoir level is at 696 mASL in comparison to measured displacements of survey beacons 1, 4 and 8. The plot also indicates that modelled deformation correlates very well to that measured for an assumed foundation elastic modulus of Ef = 1.

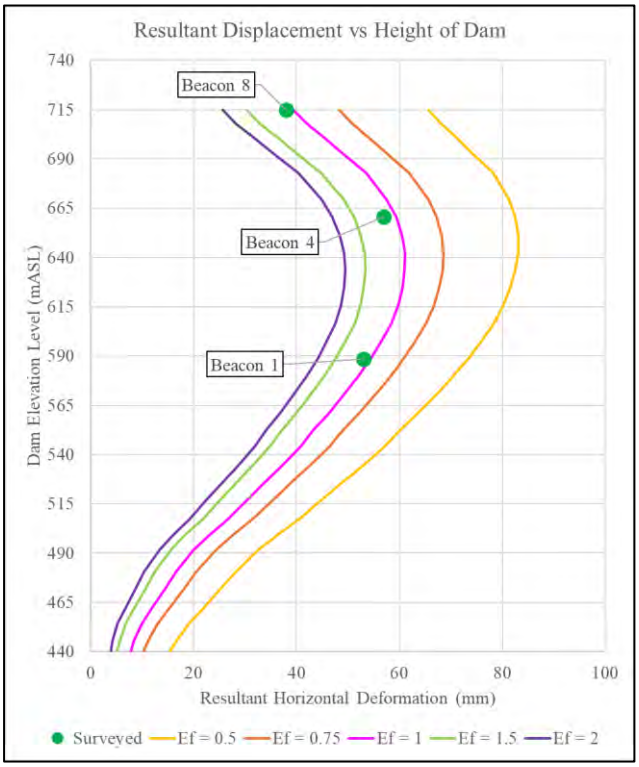

Figure 8-18: Sensitivity curves of modelled dam deformation in relation to that measured along height

A set of foundation elastic modulus sensitivity curves indicating the modelled deformation of the dam at final stage of impoundment, disregarding temperature loading, when the reservoir level reaches elevation 710 mASL, being FSL, is shown in Figure 8-19 and Figure 8-20.

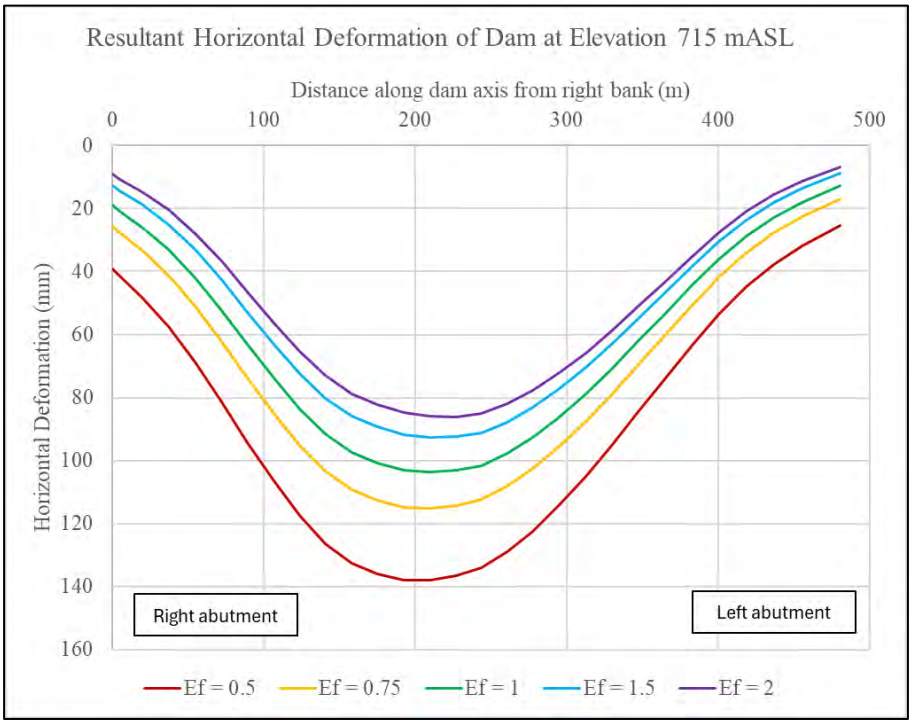

Figure 8-19: Sensitivity curves of modelled dam deformation response at crest level under FSL loading

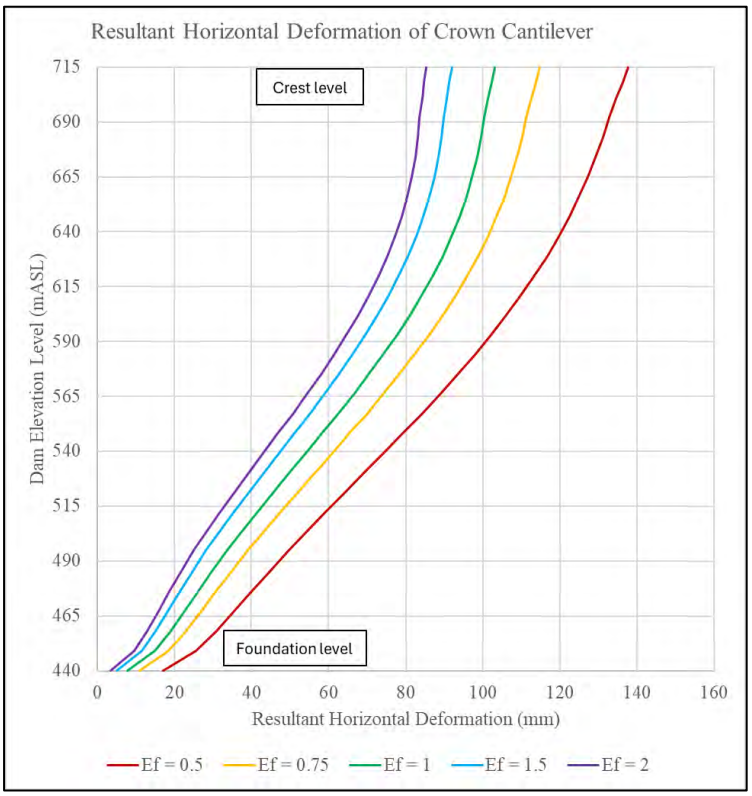

Figure 8-20: Sensitivity curves of modelled dam deformation response along height of dam under FSL loading

The range of vertical stresses expected to develop on the upstream face of the dam, along the height of the crown cantilever, for various Ef values are shown in Figure 8-21. The set of stress curves depict that a change in foundation elastic modulus, results in a substantial change in vertical stresses along the lower half of the dam where vertical compressive stresses are greatest, whilst a relatively insignificant change is evident along the top half of the dam. Along the full height of the dam a lower Ef value results in the development of higher vertical stresses.

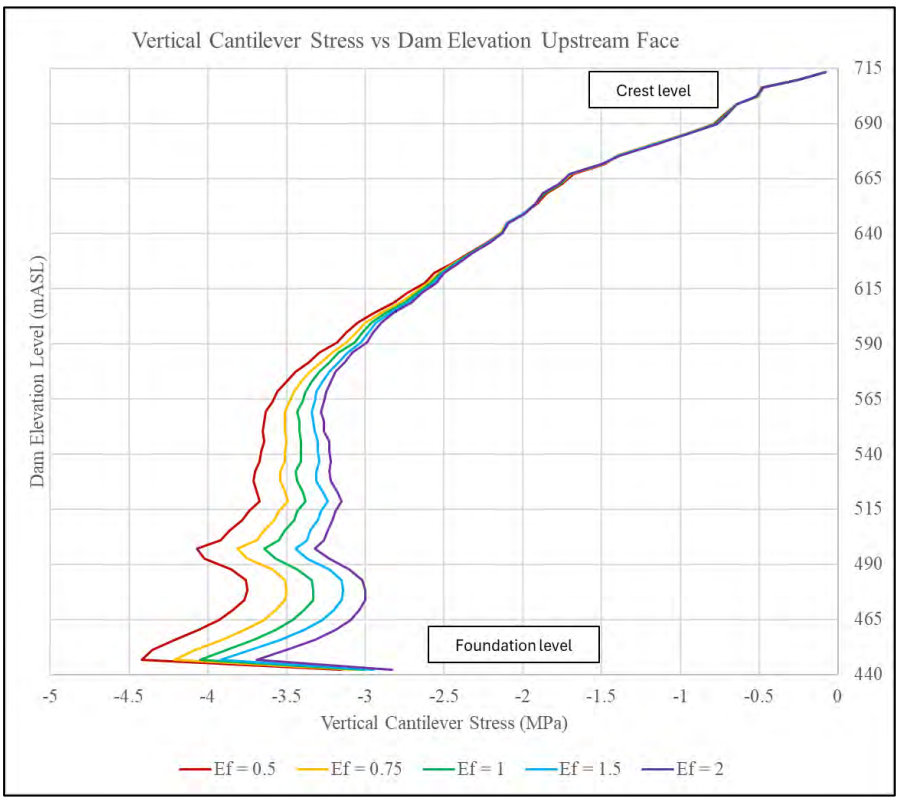

Figure 8-21: Sensitivity curves of dam vertical stresses on upstream face along dam height under FSL loading

The range of vertical stresses expected to develop on the downstream face of the dam, along the height of the crown cantilever, for various Ef values are shown in Figure 8-22. The set of stress curves depict that a change in foundation elastic modulus, results in a substantial change in vertical stresses along the lower half of the dam, whilst a relatively insignificant change is evident along the top half of the dam.

It is interesting to note that mid-height of the dam a higher Ef value results in higher vertical stresses on the downstream face. This is indicative of the development of vertical bursting stresses that may form on the downstream face of an arch if it is either overloaded, or not stiff enough in relation to the foundation. A more flexible arch will transfer a greater portion of the load to its foundation via bending moments, as opposed to compressive thrusting, causing these bursting stresses to develop.

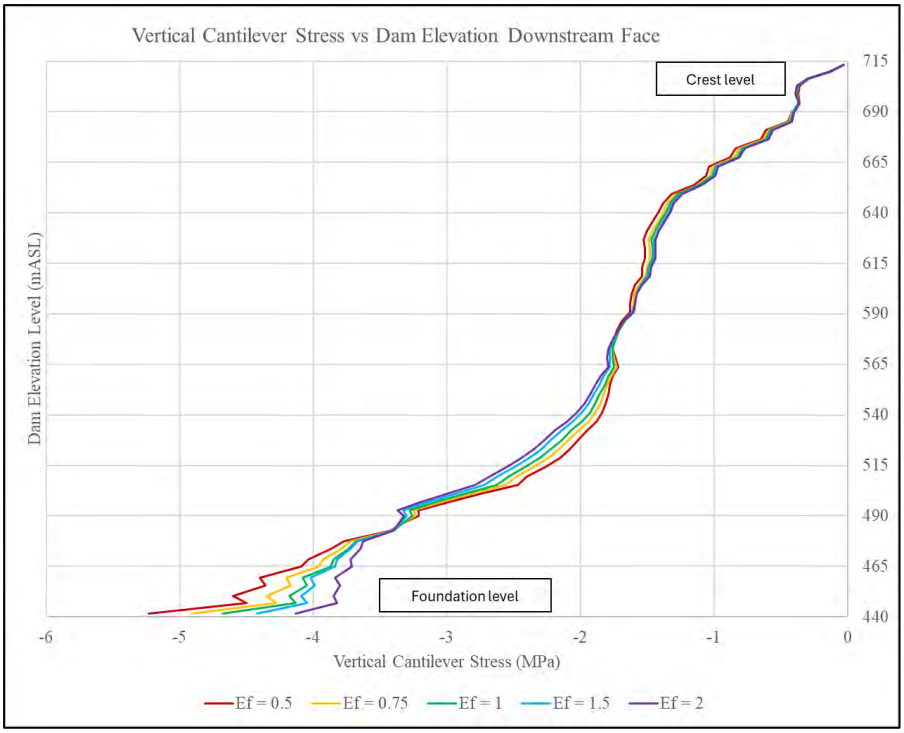

Figure 8-22: Sensitivity curves of dam vertical stress on downstream face along dam height under FSL loading

The range of horizontal axial (arch) stresses expected to develop on the upstream face of the dam, along the height of the crown cantilever, for various dam elastic moduli are shown in Figure 8-23. The set of stress curves depict that a change in foundation elastic modulus, results in a substantial change in horizontal axial stresses along most of the dam height. Along the full height of the dam a lower Ef value results in a higher development of arch stresses.

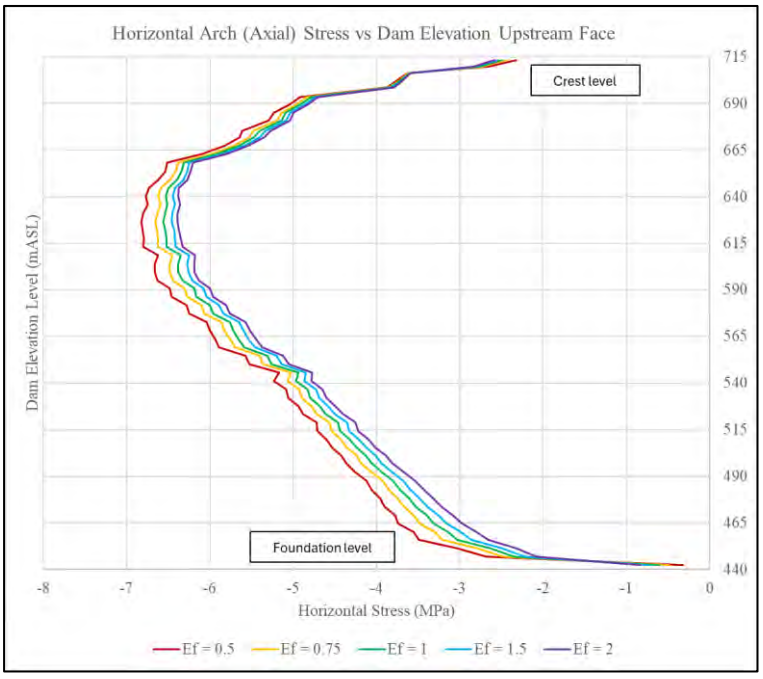

Figure 8-23: Sensitivity curves of dam axial stress on upstream face along dam height under FSL loading

The range of horizontal axial (arch) stresses expected to develop on the downstream face of the dam, along the height of the crown cantilever, for various Ef values are shown in Figure 8-24. The set of stress curves depict that a change in foundation elastic modulus, results in a substantial change in arching stresses along the lower half of the dam, whilst a lower change is evident along the top half of the dam.

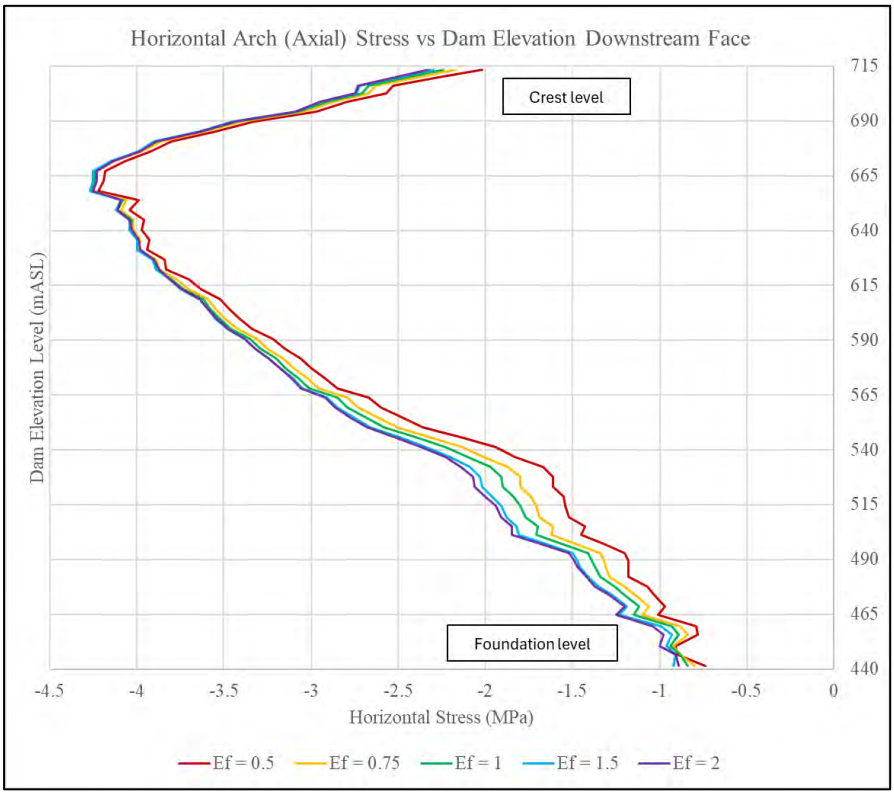

Figure 8-24: Sensitivity curves of dam axial stress on downstream face along dam height under FSL loading

A set of sensitivity curves indicating the minor principal stresses expected to develop at the toe of the arch along its left and right abutment, for various Ef values, are shown in Figure 8-25 and Figure 8-26. The stress curves indicate that a lower foundation elastic modulus will cause higher minor principal stresses to form at the toe of the dam. A lower elastic modulus causes the dam to deflect further downstream and transfer more load into the foundation at the toe portion of its ligament.

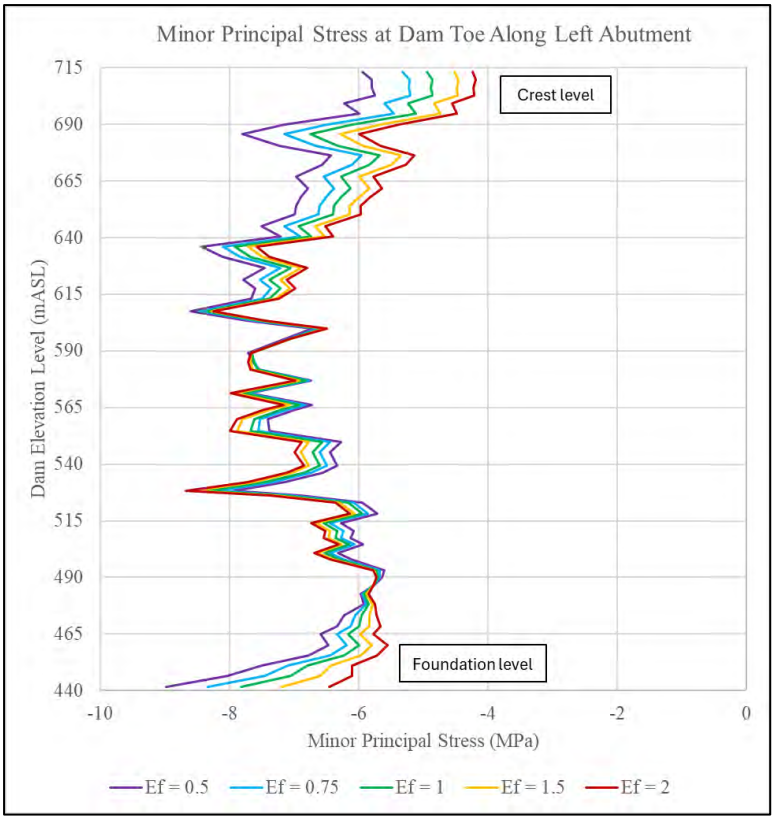

Figure 8-25: Sensitivity curves of dam minor principal stresses at toe of dam along left abutment height under FSL loading

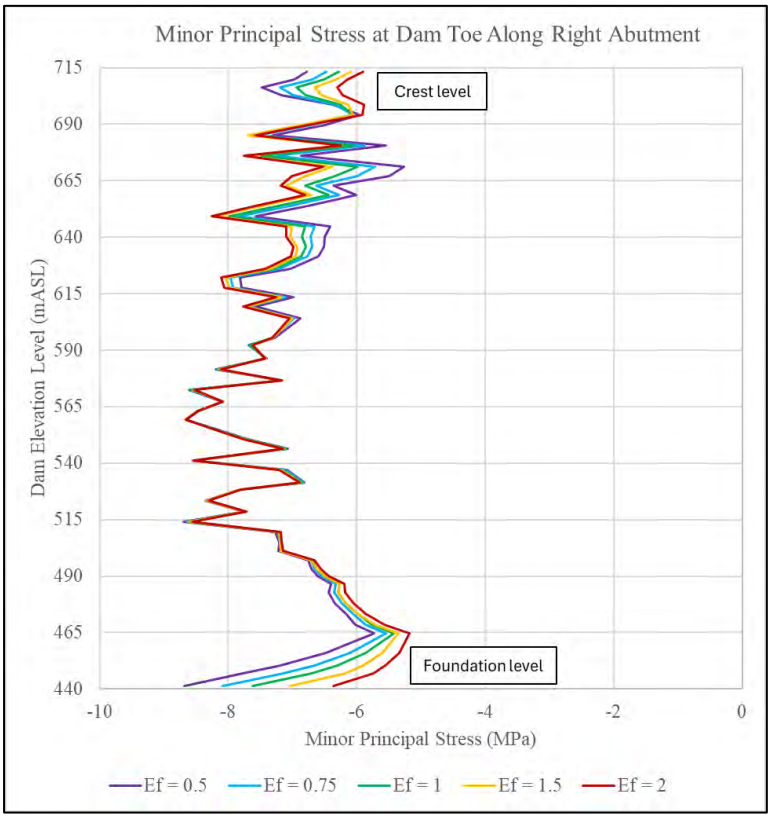

Figure 8-26: Sensitivity curves of dam minor principal stresses at toe of dam along right abutment height under FSL loading

A set of sensitivity curves indicating the major principal stresses expected to develop mid width of the dam base along the dam axis, from right to left abutment, for various Ef values, are shown in Figure 8-27. The stress curves indicate that a lower foundation elastic modulus will cause higher major principal stresses (tensions) to form along the base of the dam. A lower foundation elastic modulus causes the development of higher tensile stresses at the dam foundation contact, similar to the structural system of a loaded rigid beam on a flexible foundation as shown in Figure 3-4.

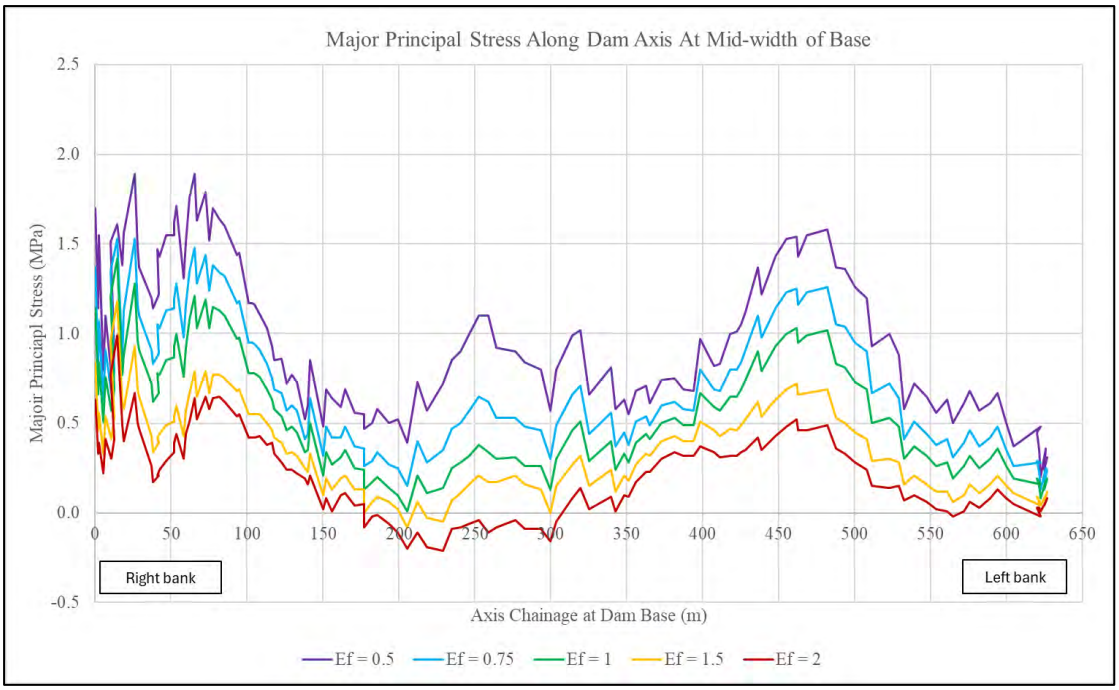

Figure 8-27: Sensitivity curves of dam major principal stresses at contact between base of dam and foundation under FSL loading

A set of sensitivity curves indicating the major principal stresses expected to develop along the ligament of the dam crown cantilever, at the contact between dam base and foundation, for various Ef values, are shown in Figure 8-28. The stress curves indicate that a lower foundation elastic modulus will cause higher major principal stresses (tensions) to form along the ligament the dam.

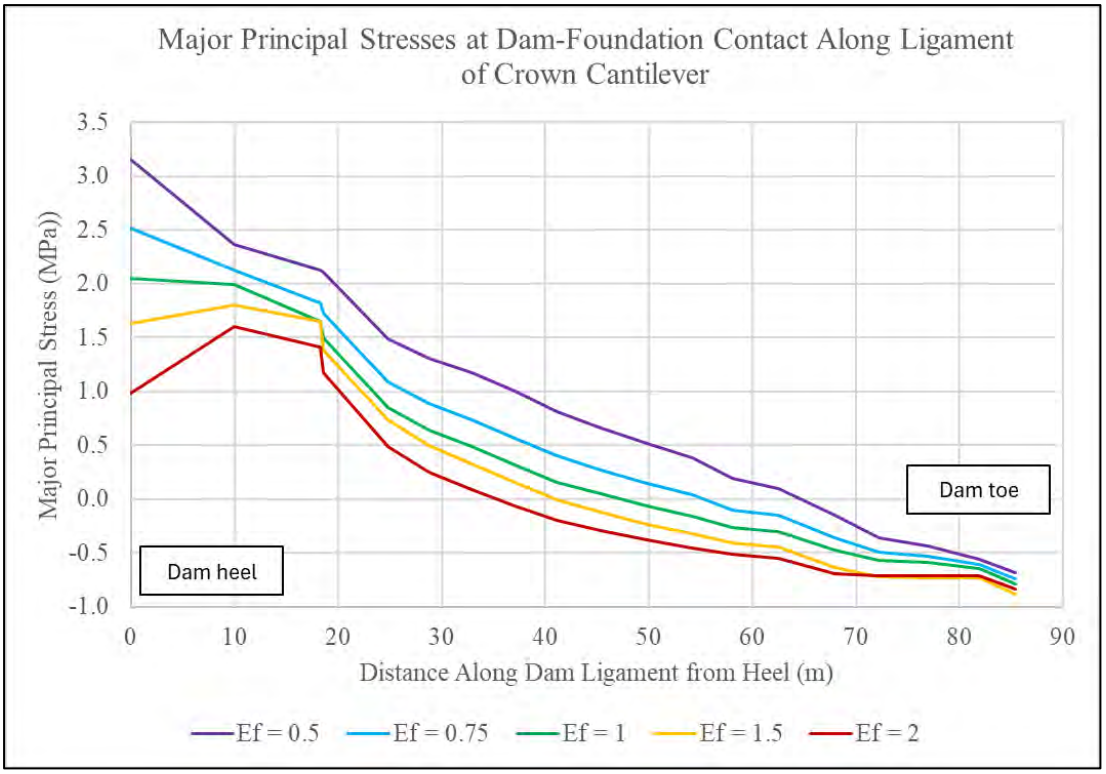

Figure 8-28: Sensitivity curves of dam major principal stresses at contact between base of dam and foundation under FSL loading

8.2 PARAMETRIC STUDY OF THERMAL EXPANSION COEFFICIENT

The extent of the deformation response of the dam caused by ambient temperature conditions on site, is directly related to the thermal expansion coefficient of the dam concrete. Changes in the temperature state of the dam between Summer and Winter conditions will induce a change in the volume of the dam, and an associated expansion or contraction response of the concrete body as dictated by its thermal expansion coefficient.

A comparison of the modelled dam resultant horizontal deformation values for a range of dam thermal expansion coefficients, in relation to the measured dam survey beacons displacement, is shown in Figure 8-29. The plot indicates the dam deformation at crest level (715 mASL) taken along its axis for impoundment stage 5 when the reservoir level is at 696 mASL and indicates measured deformations of survey beacons 7 to 12.

The curves indicate that the deformation of the dam is more sensitive to change in thermal expansion coefficient near the central portion of the arch, and substantially less at the abutment supports. The plot also indicates that modelled deformation correlates very well to that measured for an assumed dam thermal expansion coefficient (α) of 10×10^{-6} 1/°C. The other

curves indicate thermal expansion coefficient values with increments of 20 % and 40 % higher and lower than the calibrated value of 10×10^{-6} 1/°C.

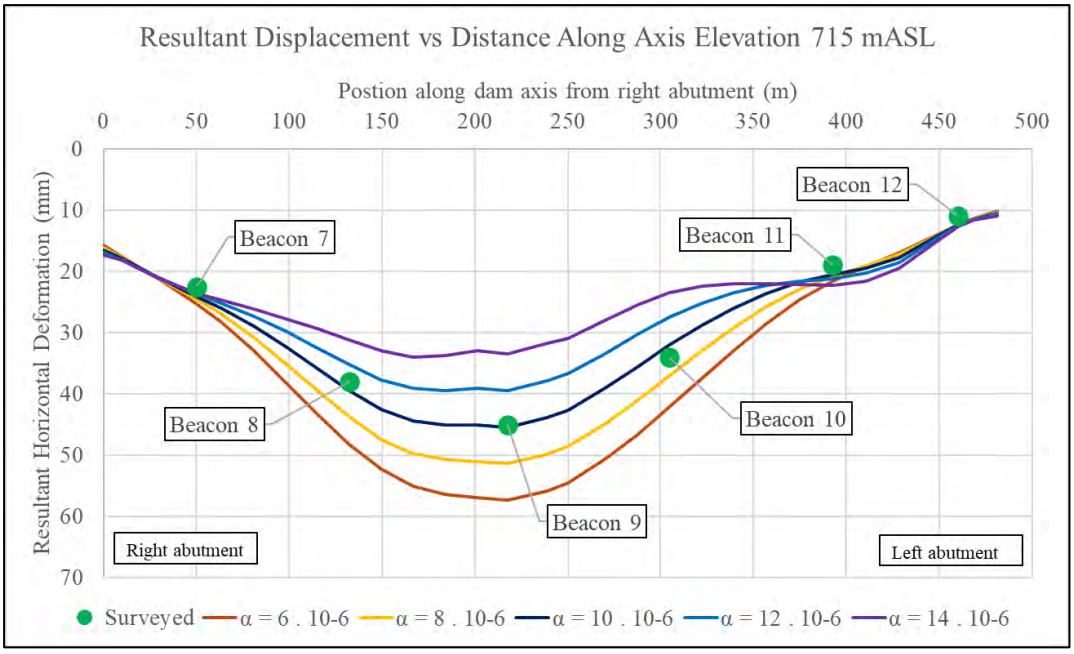

Figure 8-29: Sensitivity curves of modelled dam deformation response at 715 mASL as a function of α vlaue

Similarly, a comparison of the modelled dam resultant horizontal deformation values for a range of thermal expansion coefficients, in relation to the measured deformation at dam elevation 662 mASL and 590 mASL, are shown in Figure 8-30 and Figure 8-31. These plots indicate the dam deformation for impoundment stage 5 when the reservoir level is at 696 mASL, in comparison to measured displacements of survey beacons 1 to 6.

The plots also indicate that modelled deformation correlates very well to that measured for a dam thermal expansion coefficient of 10×10^{-6} 1/°C. It can be seen from the plots that the deformation response of the dam at elevation level 662 mASL, is not very sensitive to changes in the thermal expansion coefficient of the dam concrete, whilst at elevation level 590 mASL the change in thermal expansion coefficient has a negligible effect on the deformation response of the dam.

The noticeable decrease in sensitivity of the dam response to changes in the thermal expansion coefficient value, is due to the increasing thickness and associated rise in thermal inertia of the dam towards the base. It was shown in Figure 6-83 that the annual ambient temperature variation between Summer and Winter, typically only has a substantial impact on the temperature state of the outer 5 – 6 m shell of concrete of the dam, whilst the core remains relatively constant throughout the seasons.

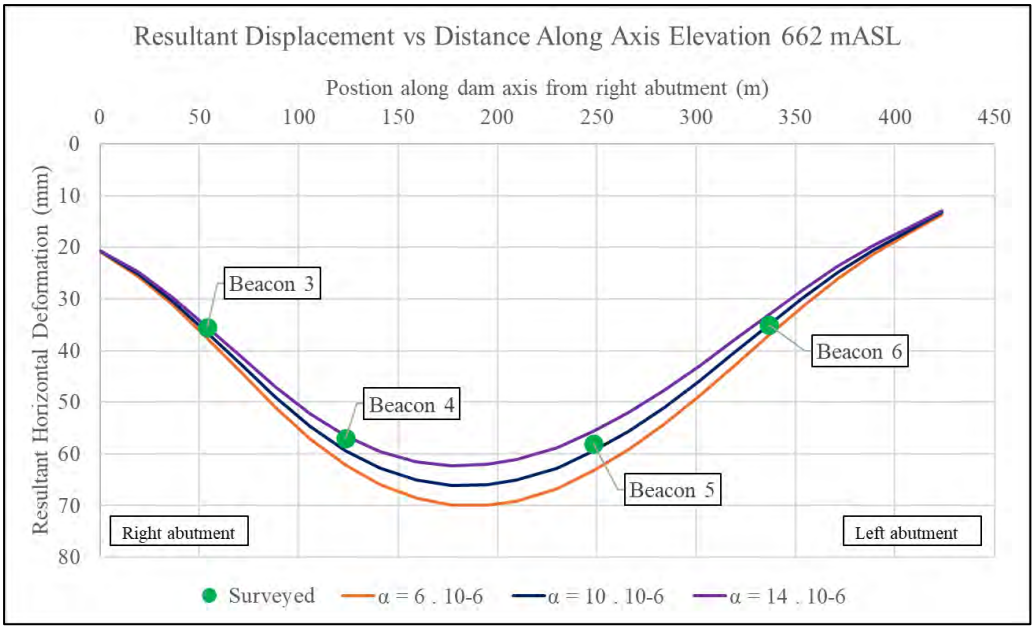

Figure 8-30: Sensitivity curves of modelled dam deformation response at 662 mASL as a function of α value

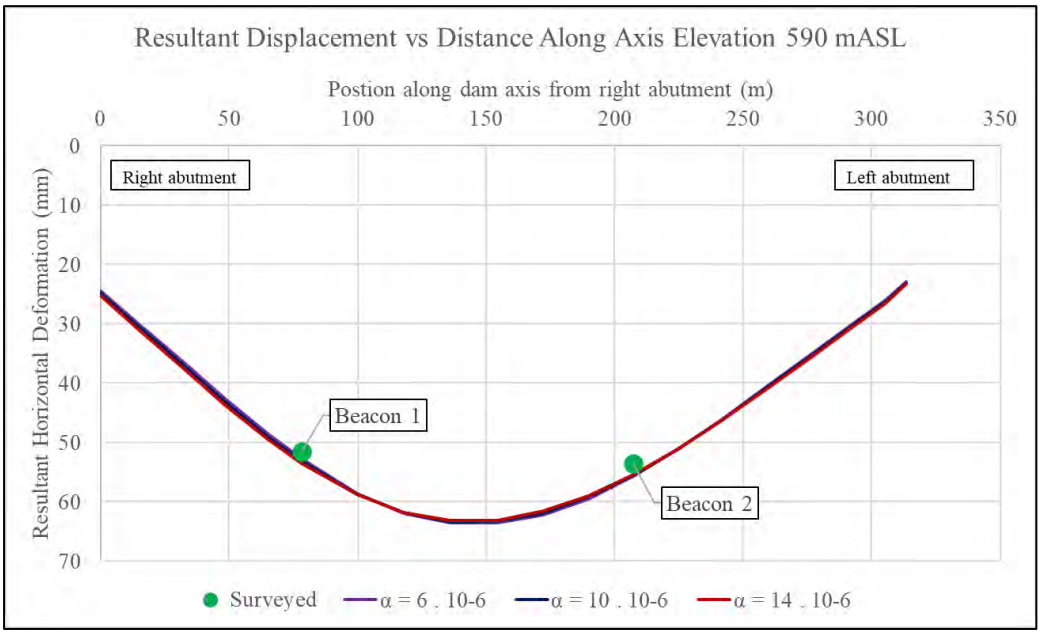

Figure 8-31: Sensitivity curves of modelled dam deformation response at 590 mASL as a function of α value

8.3 THERMAL BEHAVIOURAL ANALYSIS

The displacement and stress behaviour of the dam under progressive stages of hydrostatic loading were discussed in Section 6.6 and Section 8.1. The instantaneous elastic response of the dam to changes in hydrostatic loading is evident for the full range of possible flood levels up to FSL. The operating behaviour of the dam according to the seasonal changes in reservoir flood level can be predicted from the design model, and threshold values can be derived against which future dam deformations can be evaluated for dam safety purposes. It is seen from Figure

8-5 that the maximum expected deflection of the dam under neutral temperature conditions is expected to not exceed 103 mm.

The operating thermomechanical behaviour of the dam is caused by expansion and contraction of the dam body, due to a time-based variation in temperature state of the dam, between different points in time along a seasonal temperature cycle. The temperature state of the dam body is a complex three-dimensional time-based function which varies according to the spatial location within the dam body. The temperature state of the dam at any arbitrary location within the dam body, (at a point in time) is influenced by the proximity of the location to the upstream and downstream face, the thickness of the dam, the depth below reservoir level, the height of the dam and its exposure to solar radiation.

The modelled operational temperature state of the dam across the width of the crown cantilever, for a period of 5 years after completion of impoundment, at various elevation levels, provides an illustration of the spatial temperature cycle of the dam body. The largest time-based variation in the dam body occurs at the outer 3 – 5 m shell of the dam. Temperature time-history plots of the dam were extracted from the FE model at five locations along the width of the dam being the upstream face of the dam (dark blue), 4 m beneath upstream face (light blue), the dam core (green), 4 m beneath downstream face (yellow) and on the downstream face (red) as shown in Figure 8-32.

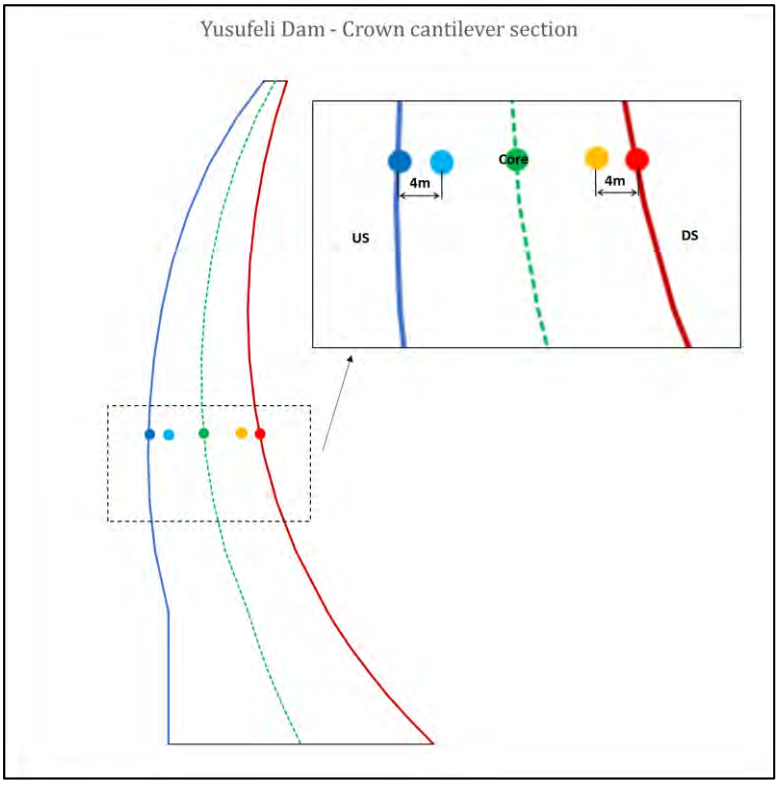

Figure 8-32: Locations across dam width where temperature histories were extracted from FE model

The dam elevation levels at which temperature time histories were extracted is shown in Figure 8-33. Each elevation level represents a physical location in the dam body with a different width, height and depth below the operating reservoir level of the dam.

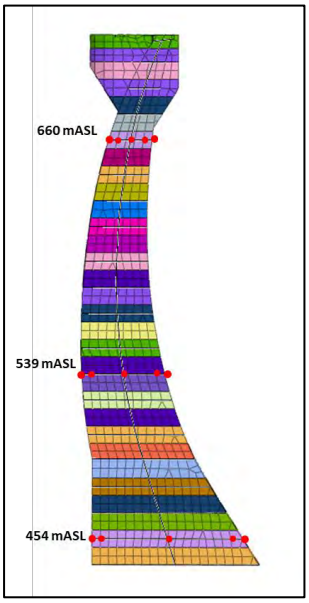

Figure 8-33: Dam elevation levels at which temperature histories were extracted

The simulated time-based temperature cycles of the dam at elevation 660 mASL are shown in Figure 8-34. The temeprature cycle on the US (dark blue curve) and DS (red curve) face of the dam, are comparable to that of the ambient temperature of the water reservoir and atmosphere. At elevation level 660 mASL the DS face experiences a maximum temperature of 30.5 °C at the end of warmest Summer month being July and a minimum temperature of 3.5 °C at the end of the coldest Winter month, which is January. The US face experiences a maximum temperature of 13 °C in mid September and a minimum temperature of 3.5 °C in January. The core temeprature of the dam (green dashed curve) is relatively constant throughout the year at 12 °C. The average temperature of the dam varies between 9.2 °C and 13.4 °C as depicted by the purple dotted curve.

The plots indicate there is a lower seasonal temperature variation experienced on the wet side of the dam, due to the thermal buffer of the water reservoir, which also causes the maximum and minimum temperature of the reservoir to lag behind that of the air temperature. Similarly the thermal buffer created by the outer 4 m shell of concrete induces a lower variation in cyclic temperatures beneath the shell of the dam, as indicated by the light blue and yellow curves.

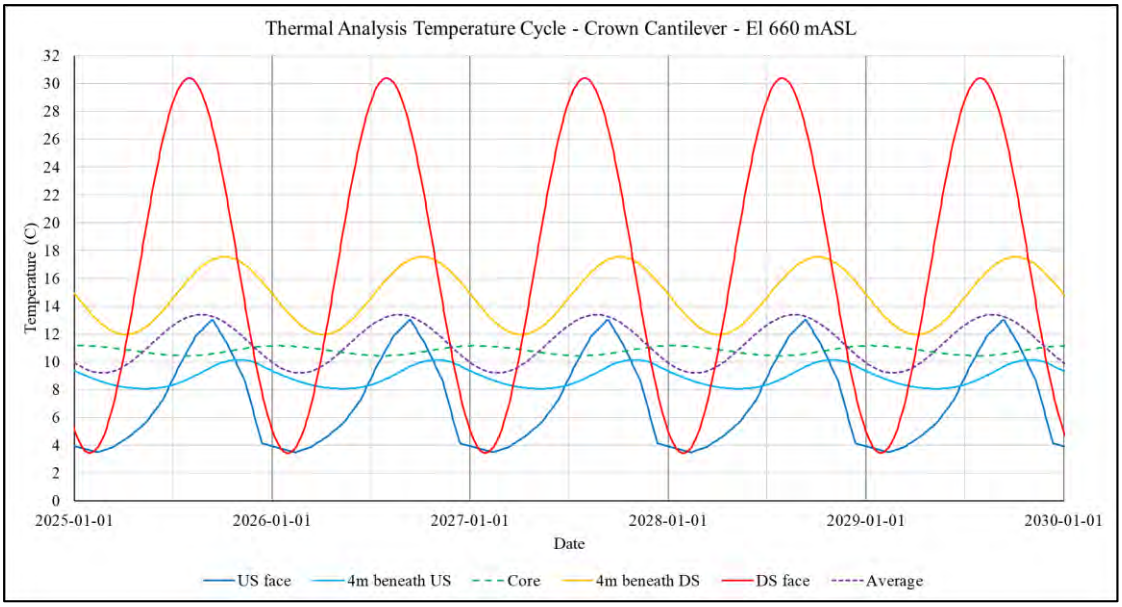

Figure 8-34: FEA simulated operating temperature cycles at elevation level 660 mASL

The temperature time-history curves of the dam at elevation 539 mASL is shown in Figure 8-35. The general form of these curves is similar to those representing temperatures at 660 mASL, with minor differences of 1 °C to 2 °C notable between maximum and minimum temperature values of the US portion of the dam body.

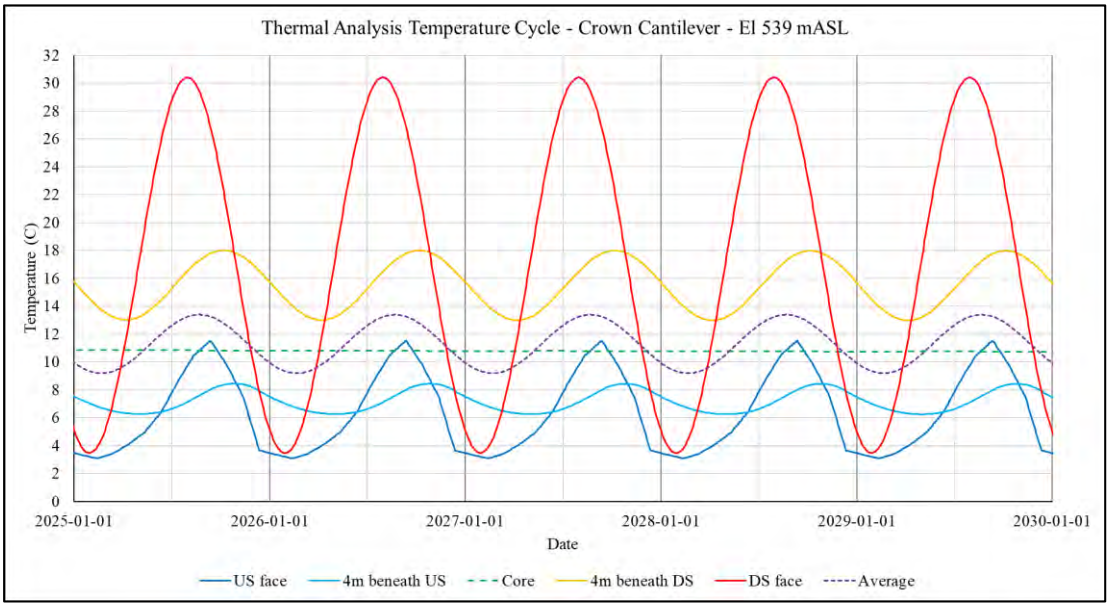

Figure 8-35: FEA simulated operating temperature cycles at elevation level 539 mASL

The temperature time-history curves of the dam at elevation 454 mASL is shown in Figure 8-36. Elevation level 454 mASL is below the dam tailwater level of 500 mASL, and as a result the temperature variation on both the US and DS face of the dam is low, with the US temperatures being marginally lower than the DS temperatures throughout the seasonal cycle.

The marginally lower temperature state on the US side of the dam is due to the larger depth below reservoir level on the US face of the dam.

Due to the cool water reservoir body on both the US and DS face of the dam at elevation 454 mASL, the core temperature of the dam of 8 °C, is significantly lower than the 12 °C at elevation 539 mASL and 660 mASL where the DS face is dry. Similarly, the core temperature at elevation 454 mASL is significantly larger than the average dam temperature.

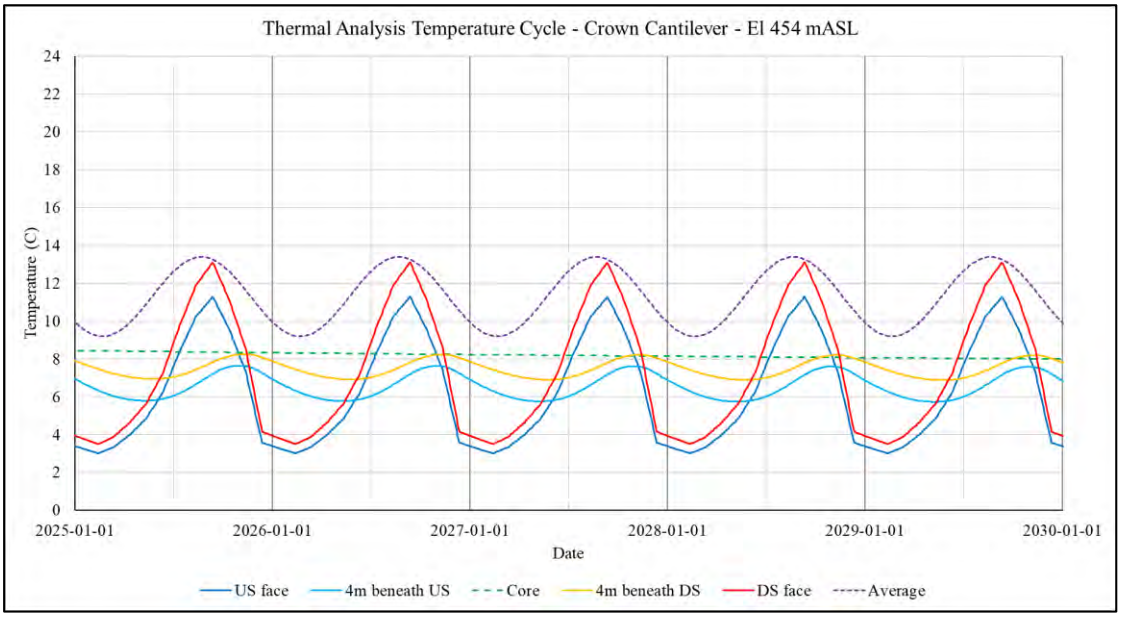

Figure 8-36: FEA simulated operating temperature cycles at elevation level 454 mASL

The core temperature of the dam varies with height above foundation level. The core temperature increases towards the crest of the dam as the section width gets thinner, the average reservoir temperature rises, and the crest of the dam is exposed to greater levels solar radiation. The time-varying dam core temperature at various elevation levels is shown in Figure 8-37.

Although the temperature state at the core has stabilised for most of the dam, it is evident that the bottom 50 m of the dam experiences marginal cooling as the wave of temperature decrease caused by the reservoir on both sides of it, is seen to be passing through the 90 m thick lower dam body from surface to core. The core temperature state of the dam experiences small seasonal variations of 1 – 2 ˚ C towards the thinner crest.

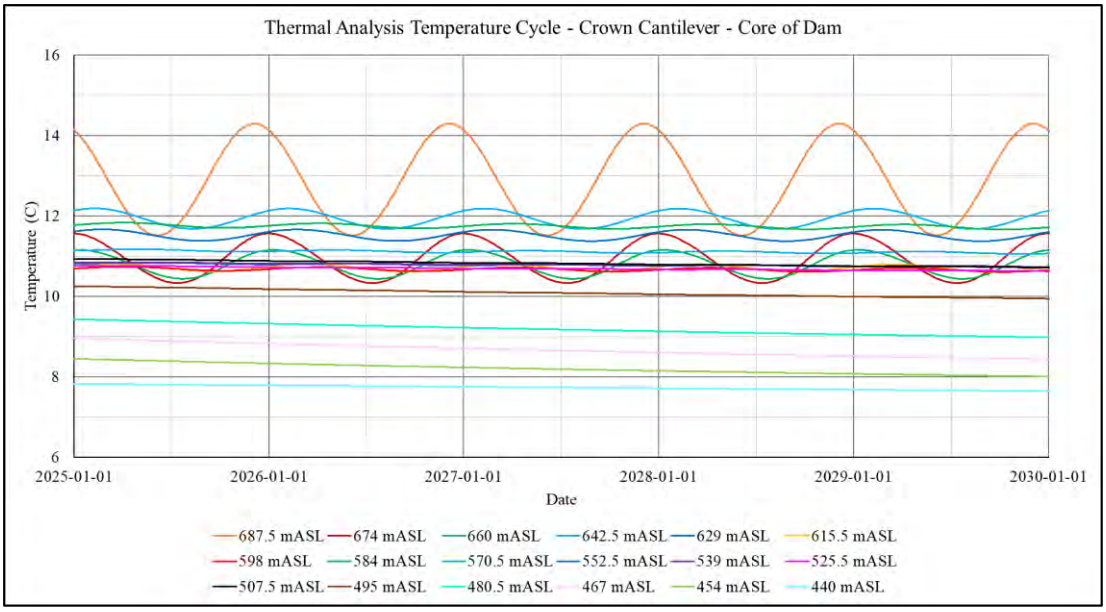

Figure 8-37: FEA simulated operating temperature cycles at dam core

The average core temperature of the dam as a function of elevation level is shown in Figure 8-38. The curve shows a substantial increase in the dam core temperature from 7.5° C at the base to 19.5° C at the crest. The curve shows a larger gradient of temperature increase with height near the base where the dam is exposed to water reservoir on both US and DS sides, and near the crest where the top portion of the dam is exposed to atmosphere on both sides due to the freeboard distance between reservoir level and dam crest.

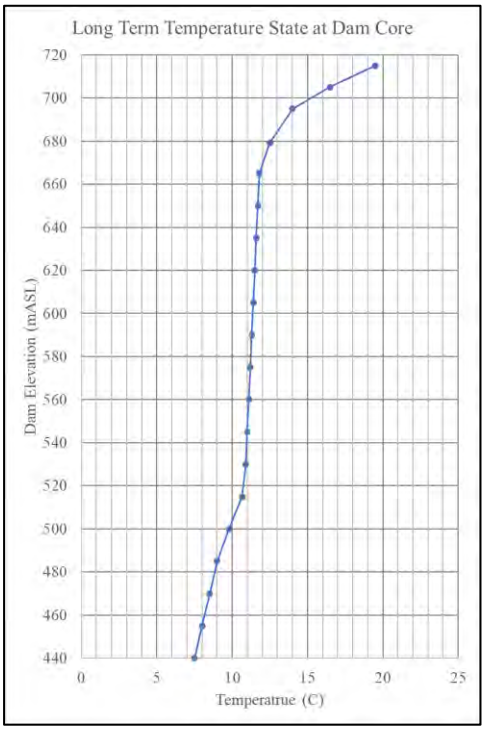

Figure 8-38: Average core temperature of dam at various elevation levels

The time-based temperature plots of the dam under operating conditions when the reservoir is at FSL, indicate that the dam is at its warmest state approximately at the end of July and at its coldest state at the end of January. The temperature of the dam body on 31 July is taken as the Summer temperature state and on 31 January as the Winter temperature state. The Spring and Autumn temperatures of the dam fall between these dates on 30 April and 31 October. Temperature contours of the dam crown cantilever section at the four seasonal temperature states is shown in Figure 8-39.

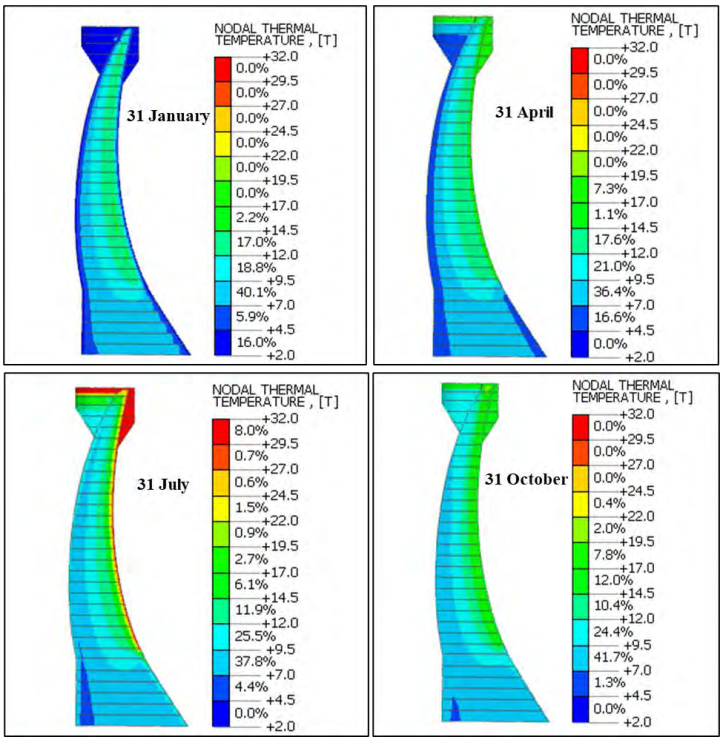

Figure 8-39: Seasonal operating temperature states of dam

8.4 THERMOMECHANICAL BEHAVIOURAL ANALYSIS

Large concrete arch dams exposed to relatively extreme temperature conditions, such as Yusufeli Dam, experience a significant degree of cyclic deformation under operating conditions as the seasons change. The Yusufeli Dam receives reliable annual water inflow due to the snow-melt runoff from the high altitude, mountainous catchment area of Yusufeli dam. The dam reservoir level is expected to remain relatively constant and the cyclic thermomechanical response of the dam will contribute to the majority of its seasonal deformation.

The range of operational temperature induced deformation of the dam crest, under FSL reservoir conditions, between Winter and Summer is shown in Figure 8-40. Positive deformations are taken as acting downstream and negative as upstream. The plot indicates that a maximum downstream deformation value of 21.5 mm is anticipated to occur when the dam

is in its Winter temperature state, around 31 January (purple curve), and a maximum upstream value of 21.5 mm is expected to occur in Summer around 31 July (red curve). In relation to the maximum deformation of the dam the zero-deformation curve associated with the neutral operating temperature state occurs in Spring and Autumn around 30 April and 31 October as shown by the turquoise and green curves. The light blue and dark blue curves indicate the downstream deformation of the dam during early Spring and early Winter, whilst the orange and yellow curves represent the upstream deformation of the dam during early Summer and early Autumn.

Similarly, the range of temperature induced deformation of the dam along the height of the crown cantilever, under FSL conditions, between Winter and Summer is shown in Figure 8-41.

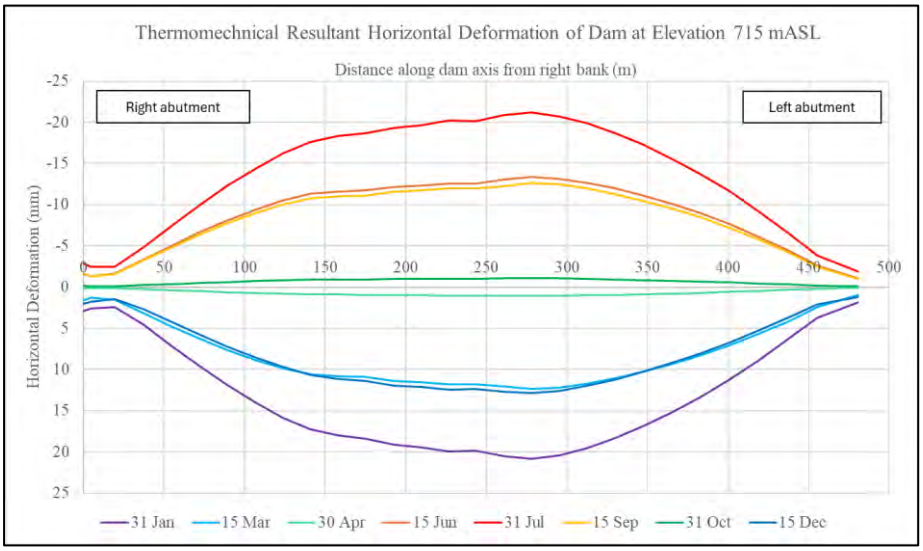

Figure 8-40: Seasonal temperature induced deformation of dam crest level under operating conditions

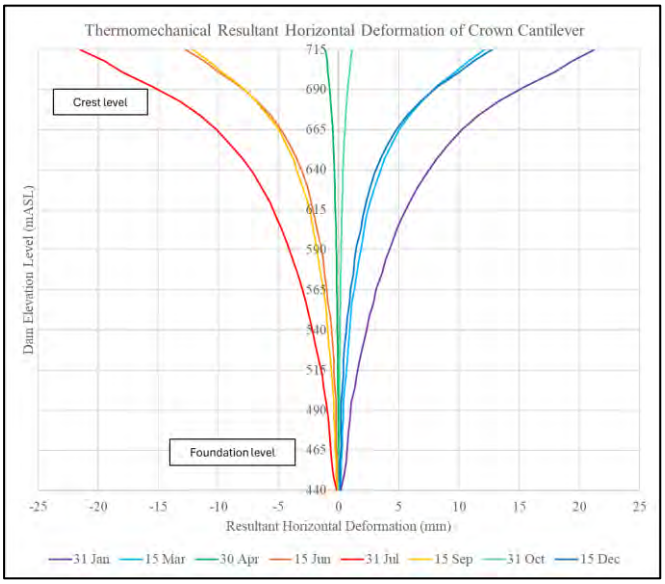

Figure 8-41: Seasonal temperature induced deformation of dam crown cantilever under operating conditions

9 CONCLUSION AND RECOMMENDATIONS

9.1 SUMMARY

The recently constructed Yusufeli arch dam in Turkey was used as the prototype structure for conducting this study. Yusufeli Dam is a 275 m high, double-curvature concrete arch dam for which the final arch configuration was designed according to the outcome of a suite of FE analyses. FE modelling and analysis was used extensively throughout the design development and verification studies of the dam.

The Yusufeli Dam is well instrumented and the deformation response of the dam during impoundment was comprehensively monitored by a geodetic survey, joint meters and pendulums. The stress/strain development of the dam and its temperature state were also monitored by stress meters, strain gauges and thermocouples. The FE model created for the design of the dam was calibrated against the observed dam behaviour during impoundment of the reservoir.

Calibration was achieved by performing validation studies at the various stages of impoundment, whereby the instrumentation measurements taken of the dam during filling, were directly compared to the outputs of related analysis cases for each of the stages of impoundment. These analysis cases were defined according to actual loading conditions observed and measured during impoundment, rather than design assumptions which are often more conservative than actual conditions. An example of this being dam uplift pressure loading.

Outputs from the dam FE analysis were used to predict how the dam should behave during impoundment, and this was validated by comparing it to the observed behaviour of the dam, as obtained from the dam instrumentation readings data.

This dissertation study focussed on investigating the accuracy with which the structural behaviour of a super high concrete arch dam can be modelled and analysed, under normal static loading, using the FE method, adopting practical material model assumptions.

The practical material model comprised assuming a linear elastic stress-strain material model for both the dam and foundation, and accurately modelling non-linearities of discrete joints between dam monoliths and at the dam foundation interface, through the inclusion of interface elements.

Although concrete and foundation materials are known to have a non-linear stress-strain response under loading, concrete arch dams are designed with substantial factors of safety under

normal loading conditions. As a result, concrete arch dams normally display linear elastic behaviour under operating conditions, as the stress-strain state remains within the linear portion of the non-linear stress-strain curve.

When conducting advanced FE analyses, for the design or safety evaluation of large concrete arch dams with complex foundation conditions, it may not be necessary to adopt elaborate and computationally expensive non-linear material models. This is especially relevant for large three-dimensional dam-foundation FE models with many degrees of freedom, making the analysis inherently computationally expensive to solve.

Performing FE analyses of large complex dam-foundation structures, assuming non-linear material models, should only be considered if a linear elastic analysis indicates significant exceedances of design stress/strain criteria, with likely formation of plastic deformation zones and stress re-distribution within the dam-foundation structure.

9.2 OUTCOMES

A comparison between the measured and modelled behaviour of the Yusufeli Dam, showed that generally all predicted deformations were no more than 5 – 10 % greater than the measured deformation of the dam. This behaviour comparison demonstrates very good correlation between the predicted and measured deformation behaviour, confirming the accuracy of the complex dam-and-foundation FE model developed for Yusufeli Dam, assuming linear elastic material properties.

The fact that the predicted displacements are close to those measured, but generally exceed the measured values, furthermore, confirms the excellent behaviour of the dam structure during the reservoir impoundment and that the model is marginally conservative.

The stress/strain response of the dam was well modelled by the FE model. Only limited instrumentation data was available from stress meters and strain gauges installed in the dam. Of the limited comparisons made between stress meter readings and predicted stress values, apart from one unreliable measurement, the average difference between predicted and measured stresses were low, considering that accurate stress measurement is especially challenging.

The temperature state of the dam due to heat transfer under ambient temperature conditions, was accurately simulated by the thermal heat transfer analysis of the dam with an average difference of only 1 - 2 °C between measured and modelled values.

A set of sensitivity analyses undertaken on the calibrated dam FE model allowed for

observations to be made in terms of how sensitive the dam response is to changes in selected material properties and loadings. The outcomes of the sensitivity analyses are summarised below:

- The deformation response of the dam to hydrostatic loading is significantly sensitive to the dam concrete elastic modulus value, and this is the primary parameter considered for calibration of the dam FE model against measured behaviour during impoundment.
- Changes in the assumed elastic modulus of the foundation rock mass material has an impact on the dam deformation response, but the deformation is approximately 50 % less sensitive to changes in the foundation elastic modulus above or below the calibrated value.
- The temperature loading induced deformation response of the dam is relatively sensitive to changes in the thermal expansion coefficient of the concrete, specifically towards the upper portion of the dam body. The mid portion of the dam is less sensitive to changes in thermal expansion coefficient and the lower portion shows negligible sensitivity to changes in this. This is a result of the increasing thickness of the dam towards the base and the associated increase in the size of the thermally insulated core of the dam.
- The temperature state at the core of a large concrete arch dam remains stable throughout the seasons under normal operating conditions, whilst the outer 5 m shell experiences a significant annual temperature variation through convective heat transfer at the surface.
- Seasonal temperature changes of the outer shell of the dam, induce a substantial cyclic deformation behaviour under normal FSL operating conditions, which can cause a maximum Winter and Summer deformation of +- 20 mm at the crest of the central cantilever of the dam.
- Generally, the vertical and horizontal stress response of the dam increases when the elastic modulus of the dam is increased with the exception of the “bursting” stresses that develop mid-height, mid-span of the dam on the downstream face. A decrease in dam elastic modulus and associated increase in arch flexibility, causes the arch downstream face to open increasing the radius and decreasing the curvature, effectively reducing its efficiency. This deflection mechanism is discussed in section 2.2.3.
- The minor principal (compressive) stress response of the dam at the toe increases as the dam and foundation elastic modulus is decreased. The more flexible dam/foundation system causes the arch to deflect and lean further forward (DS) transferring more compressive stress onto the toe of the dam.
- The major principal (tensile) stress response of the dam at the heel increases as the dam

and foundation elastic modulus is decreased. The more flexible dam/foundation system causes the arch to deflect and lean further forward (DS) inducing higher tensile stress at the heel.

- In a well-designed arch dam with sufficient structural redundancies, unwanted tensile stresses that may typically form at the heel of the dam, are normally re-distributed by the formation of a tensile plastic hinge. The hinge allows for some tensile cracking or delamination of the heel from the foundation, releasing the transfer of further tension as the dam leans forward and the abutments take up additional compressive loading.

Noteworthy observations made of the modelled and measured dam behaviour during the incremental loadings stages of impoundment are summarised below:

- The non-linear relationship between the rising reservoir level and the hydrostatic thrust force of the dam, indicates that the dam is subject to approximately 15 % of the FSL hydrostatic loading at 50 % of the FSL reservoir height. The remaining 85 % loading is taken up over the rise in reservoir level from 50 % to 100 % of FSL height. This is caused by the parabolic shape of the river valley and resulting parabolic increase in hydrostatic force with reservoir height.
- The non-linear relationship between the rising reservoir level and the hydrostatic load, paired with the increased flexibility of the arch towards the crest, results in a large portion of the dam deformation occurring towards the end of the reservoir impoundment process.
- The development of the Mohr-coulomb equivalent stress state at the toe of the dam, during the various incremental stages of hydrostatic loading during impoundment, indicates that the effective/confining stress of an arch dam increases at a larger rate than the deviatoric stress, and confirms the theory that a hydrostatically loaded arch dam is safer than an unloaded empty dam.

Other outcomes and findings were also obtained from the dissertation study. These are summarised below:

- The design uplift pressure assumed for a concrete dam is normally conservative in comparison to actual uplift pressure, if the drainage curtain and internal drain system is functioning properly.
- The geodetic survey of dam displacement behaviour is the most reliable form of dam displacement monitoring.
- Concrete dam structures are exposed to harsh environments during, and post construction and monitoring instruments often get damaged or misused.

- Pendulums and more specifically hanging pendulums, are the most sensitive deformation measurement devices to be installed in a dam and proper maintenance and operation of them is very critical. If properly used these devices can have an accuracy of 0.5 mm when measuring dam deformation, but practically this is often not the case due to external interference from wind in the shaft, water condensation and resulting dripping, spider webs and general bumping of the device by technicians.
- It is important to ensure there are redundancies in dam instrumentation installations to ensure instrument readings can be corroborated against each other and that failed or malfunctioning instruments can be covered by others.
- The deformation of large concrete arch dams is relatively sensitive to seasonal ambient temperature changes. At Yusufeli Dam a decrease in daily average ambient temperature of 25 °C, when moving from Summer to Winter, caused the dam to displace downstream 20 mm at the crest of the crown cantilever.

9.3 RECOMMENDATIONS

This dissertation study proves that the structural response of a concrete arch dam under normal static loading conditions, can be very well modelled and analysed using the FE method, assuming linear elastic constitutive material parameters, comprising simply of an elastic deformation modulus, Poisson value and unit weight.

It is suggested practical FEA techniques should be investigated and validated for modelling other advanced modes of structural behaviour observed in dams. Examples of such complex behaviour mechanisms may comprise:

- Dynamic response of the dam due to transient loading such as seismic loading or other dynamic loads (ambient vibrations).
- Structural response due to swelling/expansion from alkali aggregate reaction in concrete dams.
- Advanced thermomechanical effects of low stress relaxation creep behaviour of RCC dams.
- Poro-plastic behaviour of large concrete dams.
- Long-term permanent deformation or creep of large concrete dams.
- Non-linear response of dams due to cracking of concrete or delamination of heel of the dam from the foundation, due to development of tensions normal to the dam-foundation interface.

10 REFERENCES

ACI 207.1R-96 1996. Mass Concrete: Reported by ACI Committee 207.

Alfatlawi, T.J.M., Kadhim, M.J. & Hussein, M.N. 2021. Relation Between Cracks Behaviour and Curvature in Cracked Concrete Arch Dam Under Earthquake. In *Materials Today*. Babylon, Iraq, 2021 Elsevier Ltd: 1-13.

Allen, A., Achsendorf, J. & West, M. 2016. Structural Intelligence in Flexible Materials. In *The Fabric Formwork Book*. 1st ed. London: Taylor and Francis. 40-47.

Andersson, O. & Seppälä, M. 2015. *Verification of the Response of a Concrete Arch Dam Subjected to Seasonal Variations*. Master of Science Thesis. Stockholm: KTH Royal Institute of Technology, Sweden.

ASCE Task Committee 2018. *Monitoring Dam Performance: Instrumentation and Measurements*. 1st ed. Reston, Virginia: ASCE.

Bieniawski, Z.T. & Orr, C.M. 1976. Rapid Site Appraisal for Dam Foundations by the Geomechanics Classification. *ICOLD Congress Mexico* 483-497.

Bofang, Z. 1997. Prediction of Water Temperature in Deep Reservoirs. *Dam Engineering* 18(1): 13-26.

Bofang, Z. 2014. *Thermal Stresses and Temperature Control of Mass Concrete*. 1st ed. Oxford: Elsevier Inc.

Boggs, H.L., Tarbox, G.S. & Jansen, R.B. 1988. Arch Dam Design and Analysis. In R.B. Jansen (ed.) *Advanced Dam Engineering for Design, Construction and Rehabilitation*. New York: Van Nostrand Reinhold. 493-539.

Brown, E.T. 2016. Reducing Risks in the Investigation, Design and Construction of Large Concrete Dams. *Journal of Rock Mechanics and Geotechnical Engineering* 9(2): 197-209.

Casagrande, A. 1961. *Control of Seepage Through Foundation and Abutments of Dams*. First Rankine Lecture. London: ICE.

Cassells, R.O. & Roberts, G.D. 2017. The Study of Three-dimensional Stability For a Complex Arch Dam Abutment. In Roberts, P. (ed.) *SANCOLD Conference - Management of Dams and Reservoirs in South Africa*. Centurion, Tshwane, 2017 SANCOLD: 377-386.

Cassells, R.O. & Shaw, Q.H.W. 2022. Validated Numerical Modelling of the Stress-strain Response of a Super-High Concrete Arch Dam. In Blaeser, M. (ed.) *SANCOLD Conference - Evolving Dams in a Climate of Change*. Johannesburg, 2022 SANCOLD: 1-11.

Cassells, R.O. & Shaw, Q.H.W. 2023. Validated Numerical Modelling of the Deformation Response of a Super-High Concrete Arch Dam During Early Stages of First Filling. In Blaeser, M. (ed.) *SANCOLD Conference - Dams - A Critical Resource in Present Time*. Sandton, Johannesburg, 2023 SANCOLD: 237-248.

Cassells, R.O., Shaw, Q.H.W., Çevik, F.V. & Aydoğan, D. 2024. Calibrated Numerical Modelling of the Stress-strain Response of the 275 m High Yusufeli Concrete Arch Dam During First Filling. In *ICOLD Symposium - 92nd Annual ICOLD Meeting - Dams for People, Water, Environment and Development*. New Delhi, 2024 ICOLD

Cassells, R.O. & Wright, H.J. 2023. Effective Finite Element Analysis of a Multiple-Arch Buttress Dam by Modelling of Plastic Hinge Deformation. In *SANCOLD: Dams - A critical resource in present time*. Pretoria, 2023: 303-315.

Cassells, R.O. & Wright, H.J. 2023. Nonlinear Finite Element Analyses of a rubble masonry concrete arch buttress dam. In *ICOLD - 91st Annual ICOLD Meeting - Management for Safe Dams*. Gothenburg, 2023: 1056-1065.

Cement and Concrete Institute 2009. *Fulton's Concrete Technology*. 9th ed. Midrand, South Africa: Cement and Concrete Institute.

Chemaly, A.G. 1995. *Gravity Dams and Fracture Mechanics*. Masters Dissertation. University of Pretoria.

Chopra, A.K. 2020. *Earthquake Engineering for Concrete Dams*. 1st ed. Oxford: John Wiley and Sons.

Cook, R.D. 1995. *Finite Element Modelling for Stress Analysis*. 1st ed. New York: John Wiley and Sons.

Coyne, A. 1956. Arch Dams: Their Philosophy. *Journal of the Power Division, ASCE, Paper No 959* 82(2): 1-17.

Da Silva, V.D. & Julio, E.N.B.S. 1995. Design and Analysis of Arch Dams by the Membrane Method. *Education, Practice and Promotion of Computational Methods in Engineering Using Small Computers* 1(4): 533-538.

Dam Safety Rehabilitation Directorate 2018. *Guidelines for Instrumentation of Large Dams*. New Delhi: Central Dam Safety Organisation Central Water Commission of India.

Daoudu, M., Galanis, N. & Ballivy, G. 1997. Calculation of the Periodic Temperature Field in a Concrete Dam. *Canadian Journal of Civil Engineering* 24: 772-784.

Davis, G.N. 2010. Rock Mass Characterisation as Input in the Development of Founding Criteria for Dams, some South African Examples. In Williams, A.L.e.a. (ed.) *Geologically Active*. Auckland, 2010 Taylor and Francis Group: 293-302.

Djoudi, M.S. & Sabir, A.B. 1995. Finite Element Analysis of Singly and Doubly Curved Dams of Constant or Variable Thickness. *Thin-walled Structures* 21(3): 279-289.

Duffaut, P. 2013. Traps Behind the Failure of Malpasset Arch Dam, France, in 1959. *Journal of Rock Mechanics and Geotechnical Engineering* 5(5): 335-341.

Dungar, R. 1985. Analysis of Plastic Deformation Leading to Cracking of Grouted Contraction Joints in Zervreila Arch Dam. In *Proceedings of 15 ICOLD Congress*. Lausanne, 1985 ICOLD: 343-365.

Dungar, R., Soubrier, G. & Riemer, W. 2018. Arch Dam Design for an Adversely Jointed Abutment. In *Proceedings of the ICOLD 2018 Congress*. Vienna, 2018: 86-106.

Dunnicliff, J. 1988. *Geotechnical Instrumentation For Monitoring Field Performance*. 1st ed. John Wiley and Sons Inc, USA.

Durieux, J.H. 2008. *Development of a Practical Methodology for the Analysis of Gravity Dams Using the Non-linear Finite Element Method*. Masters Thesis. Pretoria: University of Pretoria University of Pretoria - Civil Engineering Department.

Durieux, J.H. & van Rensberg, B.W.J. 2016. Development of a Practical Methodology for the Analysis of Gravity Dams Using the Non-linear Finite Element Method. *Journal of South African Institution of Civil Engineering* 58(2): 2-13.

Emiroglu, E. 2008. Influences on Selection of Dam Type. *International Journal of Science and Technology* 3(2): 173-189.

Federal Energy Regulatory Commission 1999. *Engineering Guidelines for the Evlaution of Hydropower Projects - Chapter 11 Arch Dams*. Washington DC: Division of Dam Safety Inspections.

Fell, R. *et al.* 2015. *Geotechnical Engineering of Dams*. 2nd ed. London: CRC Press/Balkema.

Fu, C. & Haflioason, B. 2015. *Progressive Failure Analyses of Concrete Buttress Dams: Influence of Crack Propagation on the Structural Dam Safety. Trita-BKN-Examensarbete, 457*. Masters' Dissertation. Stockholm: KTH Royal Institue of Technology.

Ghanaat, Y. 1993. *Theoretical Manual for Analysis of Arch Dams - ITL-93-1*. Technical Report. Washington: United States Army Corps of Engineers.

Ghanaat, Y. 2004. Failure Modes Approach to Safety Evaluation of Dams. In *13th World Conference on Earthquake Engineering*., 2004: Paper 1115.

Gillian, C., Lund, G. & Weldon, J. 2011. Three Predominate Failure Modes of Thin Arch Dams. *Proceedings of the 31st Annual USSD Conference: 21st Century Dam Design - Advances and Adaptions* 173-187.

Goulas, E. 2016. *Design of Double-Curvature Arch Dams in Terms of Geometric and Stress Constraints by Using Script-based Finite Element Modelling*. Masters Thesis. The Hague: TNO Diana Delft University of Technology.

Greyling, R.P. & Zhang, C. 2017. State of the Art Thermal Analysis for Neckartal Dam. In *International Journal of Hydropower and Dams - Water Storage and Hydropower Development for Africa*. Marrakech, 2017 Aqua-Media International

Gunn, R. 2001. Non-linear Design and Safety Analysis of Arch Dams Using Damage Mechanics. *Hydropower and Dams* (2): 67-74.

Hattingh, L. *et al.* 2019. The Use of Ambient Vibration Monitoring in the Behavioural Assessment of an Arch Dam with Gravity Flanks and Limited Surveillance Records. In *ICOLD*. Ottawa, Canada, 2019: 2819-2831.

Hoek, E. 1993. *Practical Rock Engineering*. 1st ed. Toronto: University of Toronto.

Hollingworth, G. & Geringer, J.J. 1994. Concrete Dams. In J.M. Jordaan (ed.) *Large Dams and Water Systems in South Africa*. Pretoria: J.P. van der Walt and Son (Pty) Ltd. 128-149.

IC Consulenten 2018. *Yusufeli Dam Foundation Area: Geotechnical Model Rev 5*. Salzburg.

ICOLD 1987. *Dam Safety Guidelines - Bulletin 59*. Paris: ICOLD.

ICOLD 1988. *Dam Monitoring General Considerations - Bulletin 60*. Paris: ICOLD.

ICOLD 1988. *Development of Dam Engineering in the United States - Commemoration of the 16th Congress of the International Commission on Large Dams by the USCOLD*. 1st ed. New York: Pergamon Press USA.

ICOLD 1989. *Selecting Seismic Parameters for Large Dams - Bulletin 72*. Paris: ICOLD.

ICOLD 1992. *Selection of Design Flood - Bulletin 82*. Paris: ICOLD.

ICOLD 2001. *Computational Procedures for Dam Engineering - Bulletin 122*. Paris: ICOLD.

ICOLD 2009. *The Physical Properties of Hardened Conventional Concrete*. Paris: ICOLD Committe on Concrete Dams.

ICOLD 2010. *Selecting Sesimic Parameters for Large Dams - Bulletin 148*. Paris: ICOLD.

ICOLD 2013. *Guidelines For Use of Numerical Models in Dam Engineering - Bulletin 155*. Paris: ICOLD.

ICOLD 2018. *Proceedings of the 14th ICOLD Benchmark Workshop on Numerical Analysis of Dams*. Stockholm: ICOLD Royal Institute of Technology (KTH) - Department of Civil and Architectural Engineering.

ICOLD 2022. *Validation of Dynamic Analyses of Dams and Their Equipment - ICOLD Proceedings Volume 1*. 1st ed. Paris: CRC Press.

ICOLD 2024. *Arch Dam Design*. Paris: ICOLD.

IMIESA 2023. Turkey's Yusufeli Dam is one of history's most iconic structures. September. 16-19.

Jansen, R. 1988. *Advanced Dam Engineering for Design, Construction and Rehabilitation*. 1st ed. New York: Van Nostrand Reinhold.

Jonker, M. & Espandar, R. 2014. Evaluation of Existing Arch Dam Design Criteria in Lieu of ANCOLD Guidelines., 2014 ANCOLD

Kabell, T.C. 2014. *Arch Dams in Zimbabwe*.

Karnovsky, I.A. 2012. *Theory of Arched Structures*. 1st ed. New York: Springer.

Kijko, A., Cassells, R.O., Wieland, M. & Hattingh, L. 2023. Seismic Hazard Assessment Considerations for Large Dams in Southern Africa. In Blaeser, M. (ed.) *SANCOLD Conference - Dams - A Critical Resource in Present Time*. Sandton, Johannesburg, 2023 SANCOLD: 29-43.

Kirn, F.D. & Sarkaria, G.S. 1955. The Influence of Canyon Shape on the Design of Concrete Dams. *Civil Engineering and Public Works Review. London. UK* 20(585).

Kreuzer, H. 2000. Thoughts on the Aesthetics of Dams. *International Journal of Hydropower and Dams* (1).

Kreuzer, H. & Leger, P. 2013. The Adjustable Factor of Safety: A Reliability-based Approach to Assess the Factor of Safety for Concrete Dams. *International Journal of Hydropower and Dams* 20(1): 67-90.

Leitao, N.S., Castilho, E. & Farinha, M.L.B. 2023. Towards a Better Understanding of Concrete Arch Dam Behaviour During the First Filling of the Reservoir. *Civil Engineering* 4(1): 157-173.

Li, Z. 2011. *Advanced Concrete Technology*. 1st ed. Hoboken, New Jersey: John Wiley & Sons Inc.

Linsley, R.K. & Franzini, J.B. 1992. *Water-Resources Engineering*. 3rd ed. London: McGraw-Hill International Book Company.

Liu, G.R. & Quek, S.S. 2003. *The Finite Element Method*. 1st ed. Oxford: Butterworth-Heinemann.

Logan, D.L. 2019. *A First Course in the Finite Element Method*. 6th ed. Boston, USA: Cengage.

Lombardi, G. 1989. The FEA - Model and Foundations for Concrete Dams. In *De Mello Volume*. Sao Paulo, Brasil: Edgar Blucher Ltds. 270-283.

Lombardi, G., Amberg, G. & Darbre, G.R. 2008. Algorithm for the Prediction of Delays in Behaviour of Concrete Dams. *The International Journal of Hydropower and Dams* 15(3): 111-116.

Lombardi, G. & Fanelli, M. 1992. Practice and Theory of Arch Dams. In *Proceedings of the International Symposium on Arch Dam*. Nanjing, China, 1992: 1-4.

Londe, P. 1987. The Malpasset Dam Failure. *Engineering Geology* 24(3): 395-329.

Love, A.E.H. 1906. *A Treatise on the Mathematical Theory of Elasticity*. 2nd ed. Cambridge: Cambridge University Press.

Malm, R. 2016. *Guideline for FE Analysis of Concrete Dams*. Energiforsk AB.

Midas 2024. *FEA NX User Manual*. Korea: MidasSoft Inc.

Milavanovic, D. 1990. Case Studies of Foundations: Appropriate Foundations for Arch Dams. *Proceedings International Workshop on Arch Dams*.

Miranda, M.P. & Farinha, M.L.B. 2012. Arch Dam Foundations. In R. Sousa (ed.) *Innovatice Numerical Modelling in Geomechanics*. London: Taylor and Francis Group. 95-124.

Moyo, P. & Oosthuizen, C. 2013. Structural Health Monitoring of Arch Dams Using Dynamic and Static Measurements. *Report to the Water Research Commission, Report No 2025/1/13*.

Myburgh, R.I.D.M. 1960. *The Optimal Design of Double Curvature Arch Dams*. Masters Thesis. Pretoria: University of Pretoria.

National Water Act 1998. Government Gazette of South Africa. Cape Town.

Neville, A.M. 2011. *Properties of Concrete*. 5th ed. Essex: Pearson Education Limited.

Novak, P., Moffat, A.I.B., Nalluri, C. & Narayanan, R. 2006. *Hydraulic Structures*. 3rd ed. New York: Taylor and Francis.

Nzuza, M.H.S. 2013. *Thermo-mechanical Modelling of Arch Dams for Performance Assessment*. MSC Thesis. Cape Town: University of Cape Town.

O'Brien, K., O'Brien, T. & Robinson, B. 2021. Using the NorSand Constitutive Model as a Tool in Assessing the Static and Dynamic Stability of Tailings Slopes Containing Contractive Material. In Blaeser, M. (ed.) *SANCOLD - Resilient Dams in a Challenging Environment*. Pretoria, 2021: 1-10.

O'Brien, K., O'Brien, T. & Robinson, B. 2022. The "Critical State" of Our Tailings. *SAICE Civil Engineering* 30(3): 10-16.

Oliveira, R. 1990. Probabilistic Approach to the Assessment of Foundation Properties. In *International Workshop on Arch Dams*. Coimbra, 1990: 314-319.

Peng, L., Pengchen, W., Weihao, W. & Hongfei, H. 2018. Cracking Risk and Overall Stability Analysis of Zulong High Arch Dam: A Case Study. *Applied Sciences Journal* 8(2555): 1-18.

Perner, F. & Obernhuber, P. 2010. Analysis of Arch Dam Deformations. *Frontiers of Architecture and Civil Engineering in China* 4(1): 102-108.

Pourbehi, M.S. 2018. *Numerical Modelling of Alkali Silica Reaction in Concrete Dams*. Doctor of Philosophy Dissertation. Stellenbosch University.

Pretorius, C.J., Schmidt, W.F., van Staden, C.S. & Egger, K. 2001. The Extensive Geodetic System Used for the Monitoring of a 185 m High Arch Dam in Southern Africa. In *The 10th FIG International Symposium on Deformation Measurements*. California, USA, 2001: 203-213.

Prins, Z.J. 2017. *Investigating the Operational Behaviour of a Double Curvature Arch Dam*. Masters Thesis. University of Cape Town.

Qixiang, F., Shaowu, Z. & Ning, Y. 2015. Optimisation Design of Foundation Excavation for Xiluodu Super-high Arch Dam in China. *Journal of Rock Mechanics and Geotechnical Engineering* 7(2): 120-135.

Raphael, J.M. 1984. Tensile Strength of Concrete. *ACI Journal* 81(17): 158-165.

Ren, Q., Li, Q., Jiang, Y. & Jiang, X. 2011. Theory and Methods of Global Stability Analysis for High Arch Dams. *Science China* 54(1): 9-17.

Ren, H., Li, T.C., Niu, Z.W. & Zhao, L.H. 2009. General Displacement Arch-cantilever Element Method for Stress Analysis of Arch Dam. *Water Science and Engineering* 2(1): 32-42.

Roberts, G.D. 2017. Methods of Assessing Stability Under Seismic Loading for Gravity Dams. In Roberts, P. (ed.) *SANCOLD conference - Management of Dams and Reservoir in Southern Africa*. Centurion, Tshwane, 2017 SANCOLD: 365 - 376.

Roberts, G.D. 2017. Methods of Assessing Stability Under Seismic Loading for Gravity Dams. In *SANCOLD Conference Proceedings: Management of Dams and Reservoirs in Southern Africa*. Centurion, 2017 SANCOLD: 365-376.

Rocha, M. 1965. Statement of the Physical Problem of the Arch Dam. In *International Symposium on the Theory of Arch Dams*. Southampton, 1965 Pergamon Press: 3-22.

Rockey, K.C., Evans, H.R., Griffiths, D.W. & Nethercot, D.A. 1975. *The Finite Element Method*. 1st ed. Frogmore: Granada Publishing.

Romana, M. 2003. DMR, a New Geomechanics Classification for Use in Dams Foundations, Adpated from RMR. In *4th International Symposium on Roller Compacted Concrete Dams*. Madrid, Spain, 2003: 1-9.

Sarkaria, G.S. 1997. Lessons from Serious Incidents at Seven Arch Dams. *Proceedings of the 1997 Annual Conference of the Association of State Dam Safety Officials* 433-443.

Schleiss, A. & Pougatsch, H. 2022. *Design, Safety and Operation of Dams*. 1st ed. Lausanne: EPFL Press.

Serafim, J.L. & Clough, R.W. 1990. Arch Dams. *International Workshop on Arch Dams: AA Balkema*.

Serafim, J.L. & Pereira, J.P. 1983. Considerations on the Geomechanical Classification of Bieniawski. In *International Symposium of Engineering Geology and Underground Construction Theme 2 Vol 1*. Lisbon, 1983: 33-42.

Shaw, Q.H.W. 2010. *A New Understanding of the Early Behaviour of Roller Compacted Concrete in Large Dams*. PhD Thesis. University of Pretoria.

Shaw, Q.H.W. 2015. The Structural Function of Different Arch Dam Types. *Proceeding of SANCOLD Conference: Dam safety, maintenance and rehabilitation of dams in Southern Africa*.

Shaw, Q.H.W. 2017. Concrete Dam Types and the Circumstances and Conditions that Favour One Type Over Another. In Roberts, J. (ed.) *SANCOLD Conference 2017 - Management of Dams and Resevoirs in Southern Afirca*. Centurion, 2017 SANCOLD: 79-88.

Shaw, Q.H.W. 2023. *Personal communications*.

Shaw, Q.H.W. & Becerik, U. 2016. Structural Design to Accommodate Challenging Rock Mass Conditions at Yusufeli Dam. *10th ICOLD European Club Symposium*.

Shaw, Q.H.W. & Cassells, R.O. 2023. Calibrated Finite Element Modelling of the Low Stress Relaxation Creep Behaviour of an Arch-gravity Dam. In *International Conference and Exhibition on Water Storage and Hydropower Development for Africa*. Kampala, Uganda, 2023 International Journal on Hydropower and Dams

Shaw, Q.H.W., Cevik, F.Y. & Yavuz, O. 2020. Thermal Conctrol Systems to Enable Rapid Concrete Placement at Yusufeli Dam. In *ICOLD 88th Annual Meeting - Symposium on Sustainable Development of Dams and Rivers*. New Delhi, 2020: 6-22.

Sheibany, F. & Ghaemian, M. 2006. Effects of Environmental Action on Thermal Stress Analysis of Karaj Concrete Arch Dam. *Jounral of Engineering Mechanics* 132(5): 532-544.

Song, S., Feng, X., Rao, H. & Zheng, H. 2013. Treatment Design of Geological Defects in Dam Foundation of Jinping I Hydropower Station. *Journal of Rock Mechanics and Geotechnical Engineering* 5(5): 342-349.

Swaminathan, K.V. 1965. Development of Arch Action in Arch Dams. *Journal of the Power Division - Proceedings of the American Society of Civil Engineers* 91(P01): 39-57.

Takalloozadeh, M. & Ghaemian, M. 2014. Shape Optimisation of Concrete Arch Dams Considering Abutment Stability. *Scientia Iranica* 21(4): 1297-1308.

Tardieu, B. & Carrere, A. 1994. On Katse Dam. In *Proceedings of ICOLD Congress*. Durban, 1994 ICOLD: 724-769.

Terzaghi, K. 1929. Effects of Minor Geological Details on Safety of Dams. *AIMME Technical Publication* (215).

United States Department of the Interior Bureau of Reclamation 2006. *State-of-the-Practice for the Nonlinear Analysis of Concrete Dams at the Bureau of Reclamation*. Engineering Manual. Washington DC: USBR.

USACE 1987. *EM 1110-2-4300 Instrumentation for Concrete Structures*. Engineering Manual. Washington, DC: United States Army Corps of Engineers.

USACE 1994. *EM 1110-1-2908 Rock Foundations*. United States Army Corps of Engineers.

USACE 1994. *EM 1110-2-2201 Arch Dam Design*. United States Army Corps of Engineers.

USACE 1995. *EM 1110-2-2200 Gravity Dam Design*. United States Army Corps of Engineers.

USACE 1995. *EP 1110-2-12 Seismic Design provisions for Roller Compacted concrete Dams*. Engineering Pamphlet. United States Army Corps of Engineers.

USACE 1997. *ETL 1110-2-542 - Thermal Studies of Mass Concrete Structures*. Technical Letter. United States Army Corps of Engineers.

USACE 2005. *EM 1110-2-2100 Stability Analysis of Concrete Structures*. United States Army Corps of Engineers.

USACE 2018. *EM 1110-2-1009 Structural Deformation Surveying*. United States Army Corps of Engineers.

USBR 1977. *Design of Arch Dams, Design Manual for Concrete Arch Dams*. Denver, Colorado: A Water Resources Technical Publication.

USBR 1987. *Concrete Dam Instrumentation Manual*. Denver: United States Bureau of Reclamation.

USBR 2013. *Design of Double-Curvature Arch Dams Planning, Appraisal, Feasibility Level. Technical Memorandum EM36-86-68110*. Denver, Colorado: US Department of the Interior.

Van den Berg, M. & Parrock, A.L. 2009. Major Dam Foundation Design and Validation. In Basson, G.R. (ed.) *SANCOLD Conference - Sustainable Development of Dams in South Africa*. Drakensberg, 2009 SANCOLD: 153-162.

Wang, R. 2016. Key Technologies in the Design and Construction of 300 m Ultra-High Arch Dams. *Engineering* 2(3): 350-359.

Watermeyer, C. 2006. A Review of the Classical Method of Design of Medium Height Gravity Dams and Aspects of Base Shortening With Uplift. *Journal of SAICE* 48(3): 2-11.

Wieland, M. 2005. Tensile Stresses in Concrete Dams. *Water Power and Dam Construction*.

Wieland, M. 2018. Application of Pseudo-static Analysis in Seismic Design and Safety Evaluation of Embankment Dams. In *16th European Conference on Earthquake Engineering*. Thessaloniki, 2018: 2-9.

Wieland, M. 2023. A Need to Reassess Dam Safety. *International Water Power and Dam Construction*.

Wild, R.M. 1980. The Design of Small Arch Dams in Wide U-shaped Valleys. *Zimbabwe Engineer, Paper No 12* 293-297.

Williams, G.P. 1963. *Heat Transfer Coefficients for Natural Water Surfaces*. Ottawa: National Research Council Canada, Division of Building Research.

Wu, S., Cao, W. & Zheng, J. 2016. Analysis of Working Behaviour of Jinping I Arch Dam During Initial Impoundment. *Water Science and Engineering, Science Direct* 9(3): 240-248.

Yang, H., Haynes, M., Winzenread, S. & Okada, K. 1999. *The History of Dams*. Centre for Watershed Sciences. University of California, Davis.

Zhang, L., Peng, M., Chang, D. & Xu, Y. 2016. *Dam Failure Mechanisms and Risk Assessment*. 1st ed. Singapore: John Wiley and Sons.

Zhong, H., Li, H., Ooi, E.T. & Song, C. 2017. Hydraulic Fracture at the Dam-foundation Interface Using the Scaled Boundary Finite Element Method Coupled with the Cohesive Crack Model.

APPENDIX A: DAM CONSTRUCTION DRAWINGS

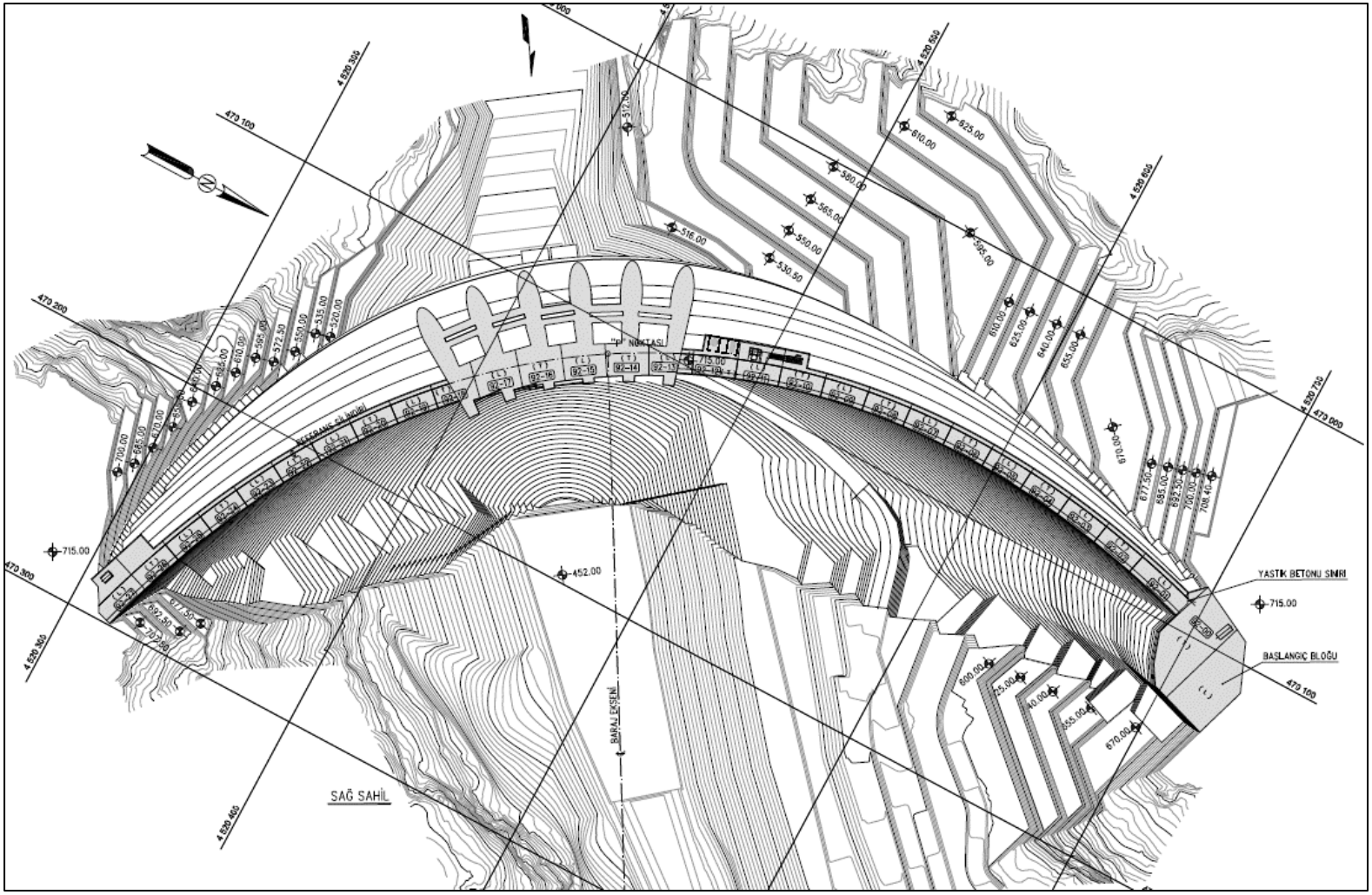

Figure 10-1: Yusufeli Dam body concrete drawing

Figure 10-2: Yusufeli Dam excavation drawing

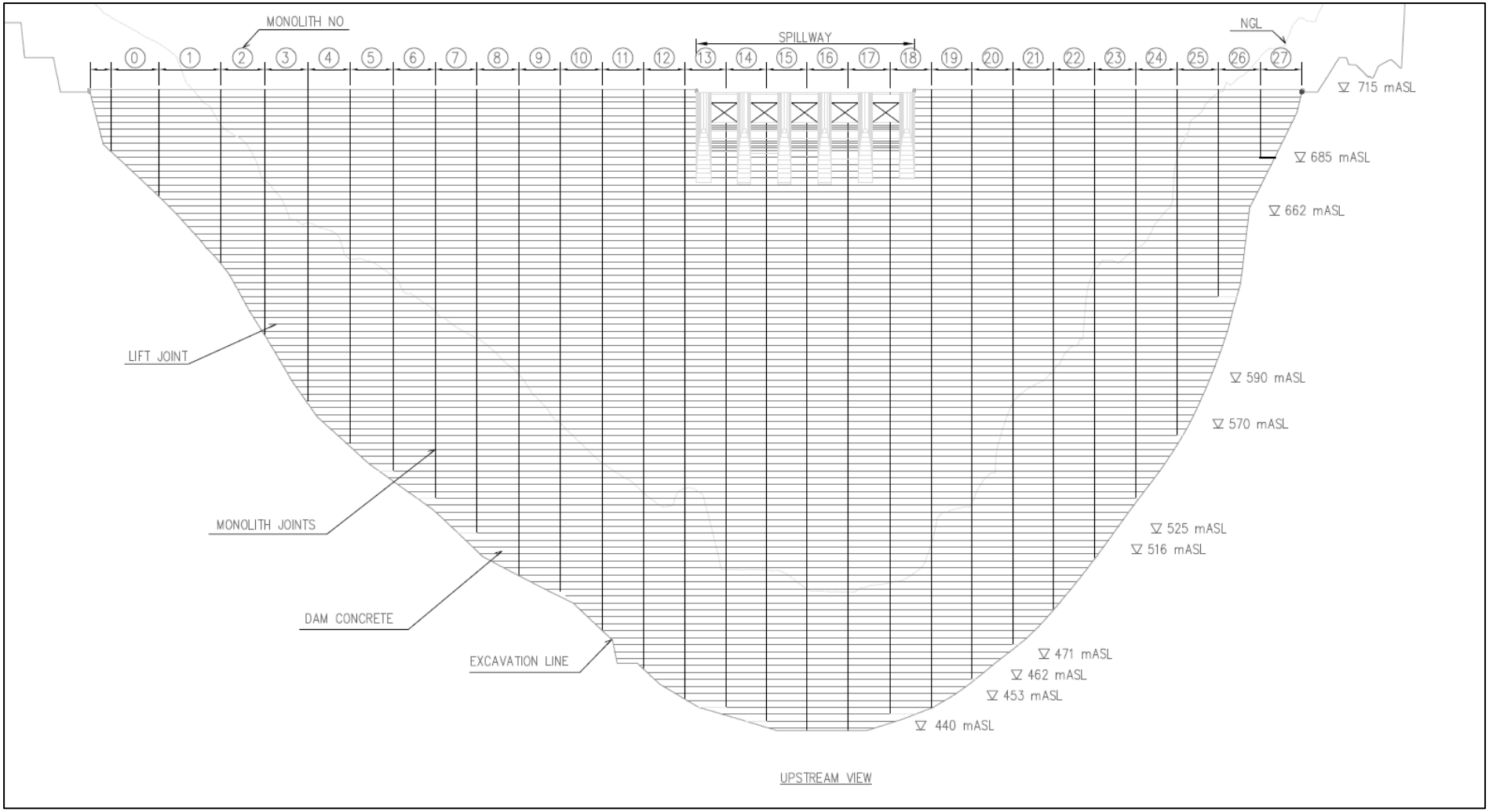

Figure 10-3: Developed downstream view of Yusufeli Dam body

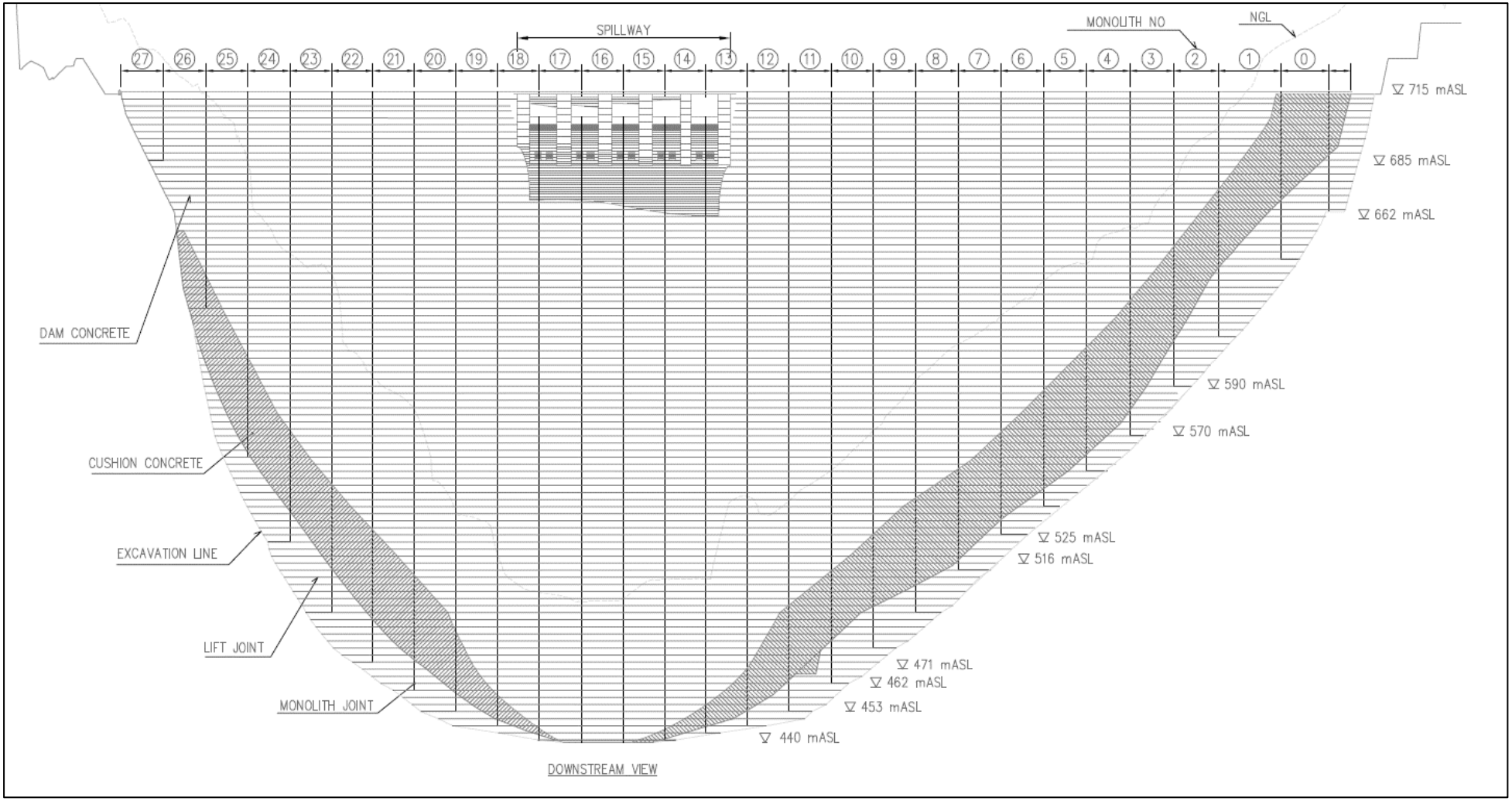

Figure 10-4: Developed upstream view of Yusufeli Dam body

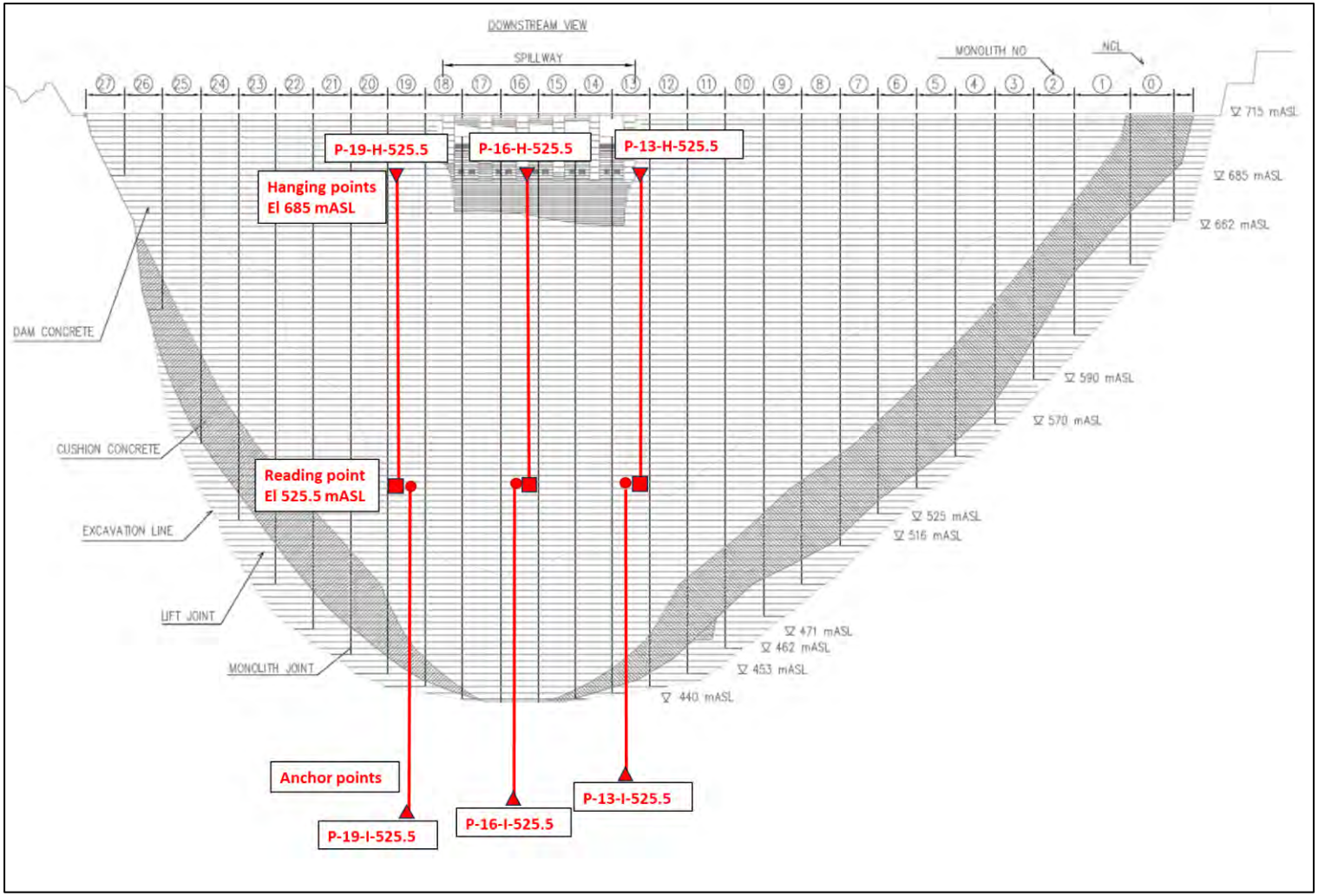

Figure 10-5: Developed upstream view of Yusufeli Dam body showing pendulum locations

APPENDIX B: DAM IMPOUNDMENT PLAN

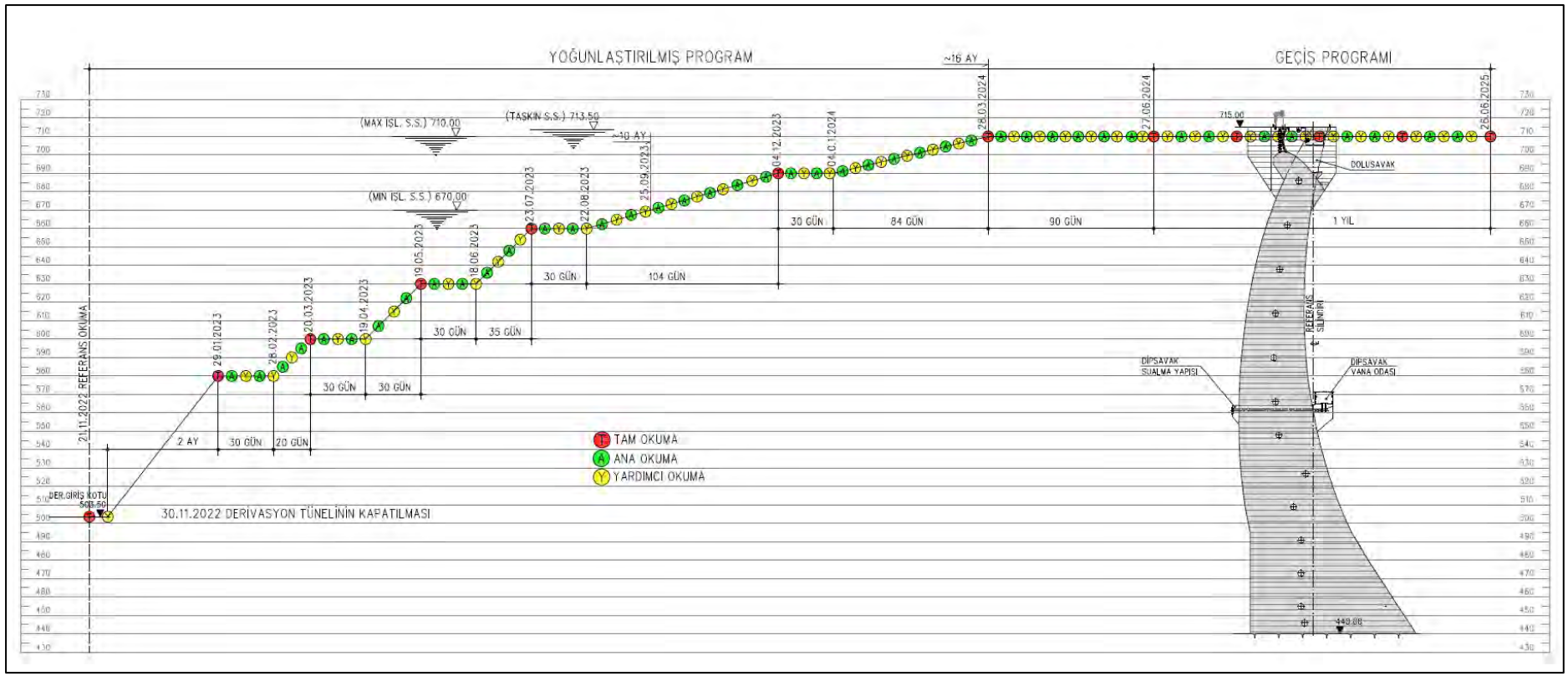

Figure 10-6: Yusufeli Dam - Original reservoir impoundment plan

APPENDIX C: DAM IMPOUNDMENT PHOTOS

Figure 10-7: Yusufeli Dam reservoir elevation 503 mASL, shortly before commencement of reservoir impoundment (15 November 2022)

Figure 10-8: Yusufeli Dam reservoir elevation 529 mASL, 4 days after commencement of impoundment (26 November 2022)

Figure 10-9: Yusufeli Dam reservoir elevation 536 mASL, 8 days after commencement of impoundment (30 November 2022)

Figure 10-10: Yusufeli Dam reservoir elevation 550 mASL, 22 days after commencement of impoundment (14 December 2022)

Figure 10-11: Yusufeli Dam reservoir elevation 561.5 mASL, 41 days after commencement of impoundment (2 January 2023)

Figure 10-12: Yusufeli Dam reservoir elevation 574 mASL, 63 days after commencement of impoundment (24 January 2023)

Figure 10-13: Yusufeli Dam reservoir elevation 577 mASL, 74 days after commencement of impoundment (4 February 2023)

Figure 10-14: Yusufeli Dam reservoir elevation 580 mASL, 96 days after commencement of impoundment (26 February 2023)

Figure 10-15: Yusufeli Dam reservoir elevation 582 mASL, 117 days after commencement of impoundment (19 March 2023)

Figure 10-16: Yusufeli Dam reservoir elevation 588 mASL, 124 days after commencement of impoundment (26 March 2023)

Figure 10-17: Yusufeli Dam reservoir elevation 610 mASL, 137 days after commencement of impoundment (8 April 2023)

Figure 10-18: Yusufeli Dam reservoir elevation 630 mASL, 159 days after commencement of impoundment (30 April 2023)

Figure 10-19: Yusufeli Dam reservoir elevation 630 mASL, 159 days after commencement of impoundment (30 April 2023)

Figure 10-20: Yusufeli Dam reservoir elevation 670 mASL, 200 days after commencement of impoundment (10 June 2023)

Figure 10-21: Yusufeli Dam reservoir elevation 670 mASL, 200 days after commencement of impoundment (10 June 2023)

Figure 10-22: Yusufeli Dam reservoir elevation 696 mASL, 269 days after commencement of impoundment (18 August 2023)

Figure 10-23:Yusufeli Dam reservoir elevation 696 mASL, 269 days after commencement of impoundment (18 August 2023)

APPENDIX D: FE MODEL MESH

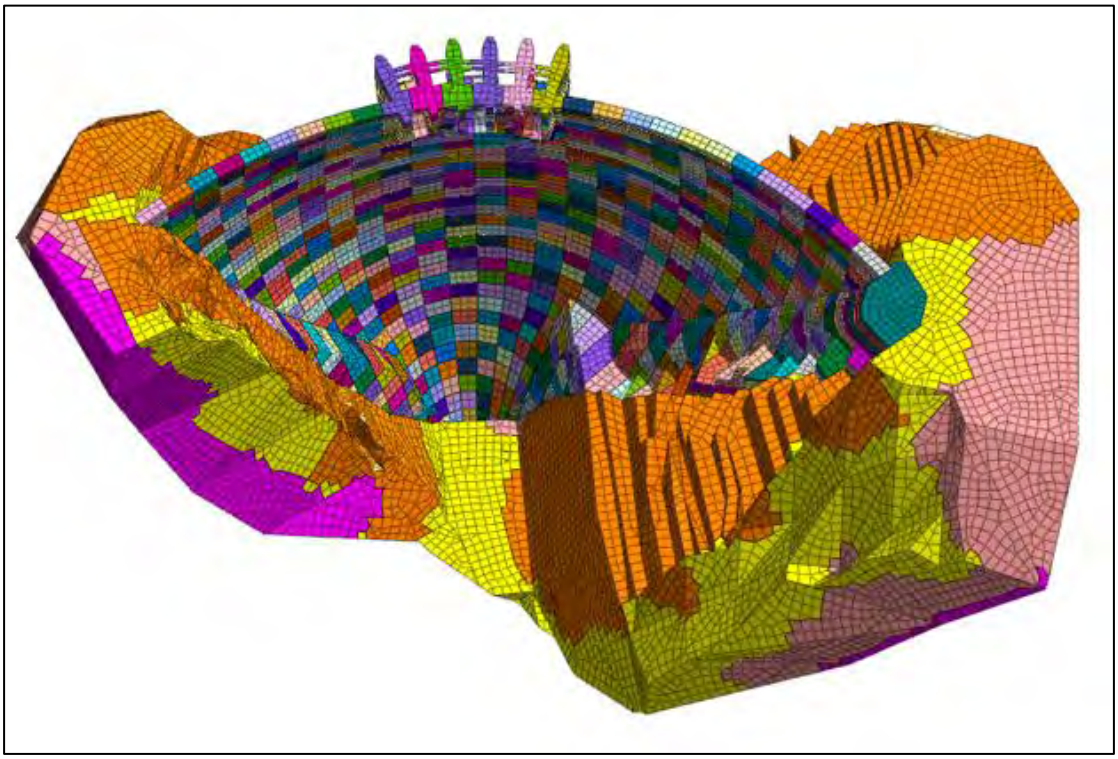

Figure 10-24: Three-dimensional perspective view of FE model mesh showing front of dam and portions of rock mass improved by consolidation grouting

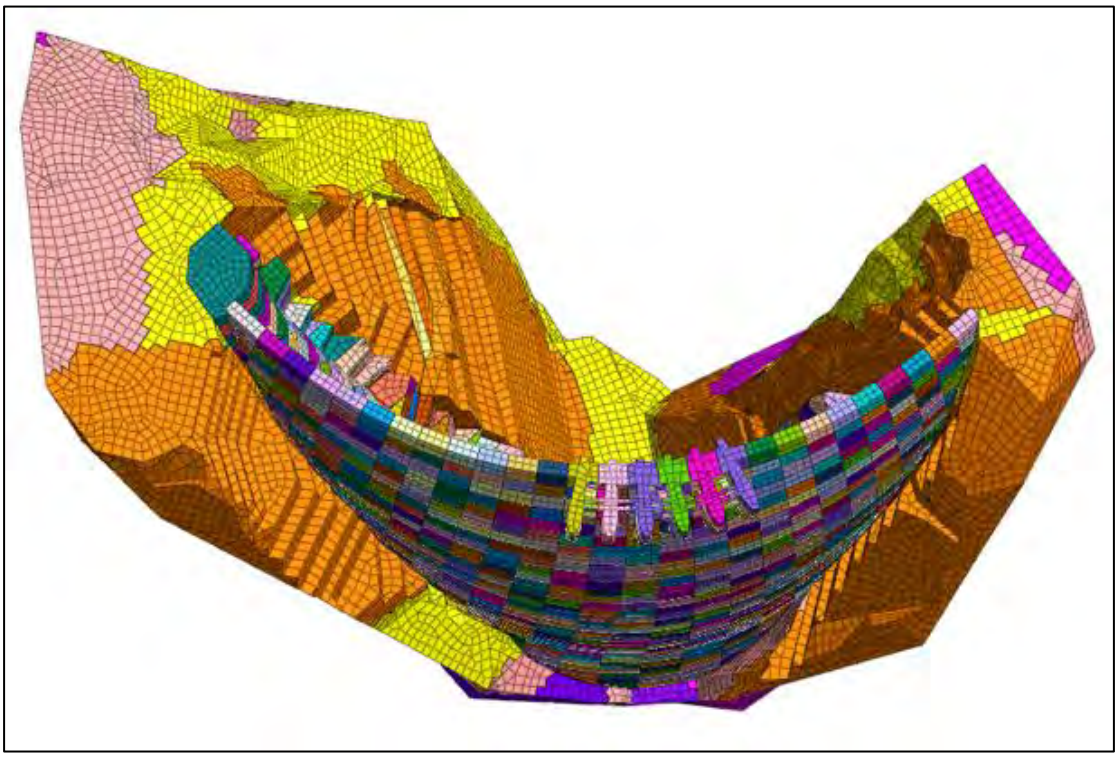

Figure 10-25: Three-dimensional perspective view of FE model mesh showing back of dam and portions of rock mass improved by consolidation grouting

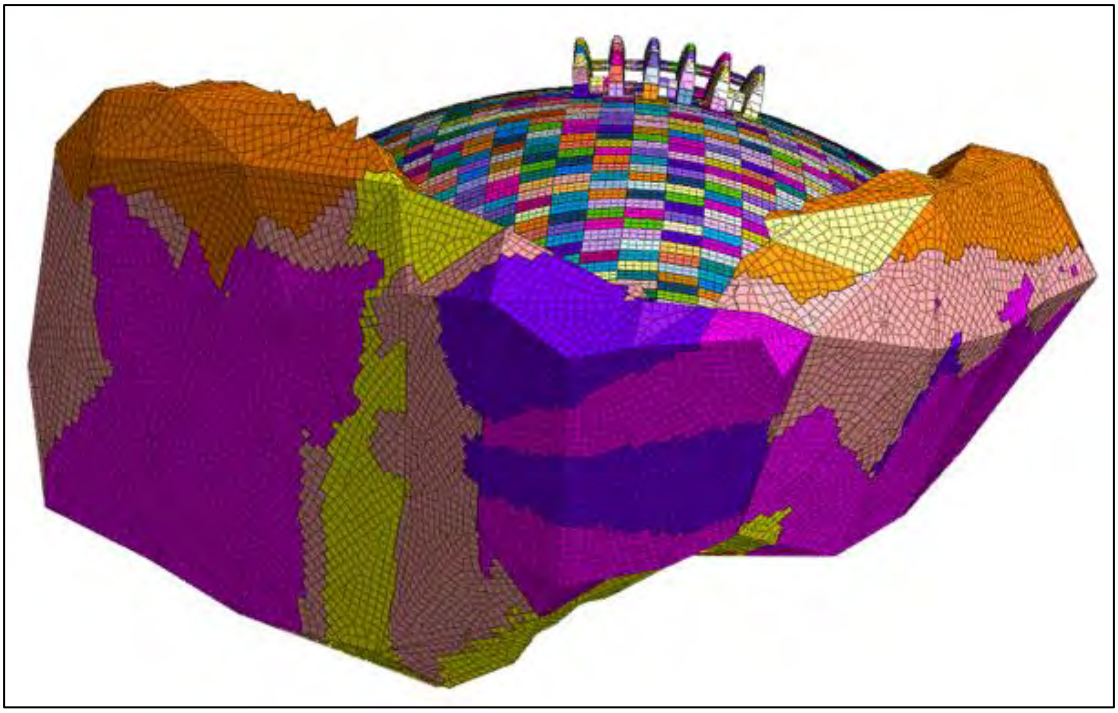

Figure 10-26: Three-dimensional perspective view of FE model mesh showing back of dam and portions of rock mass improved by consolidation grouting

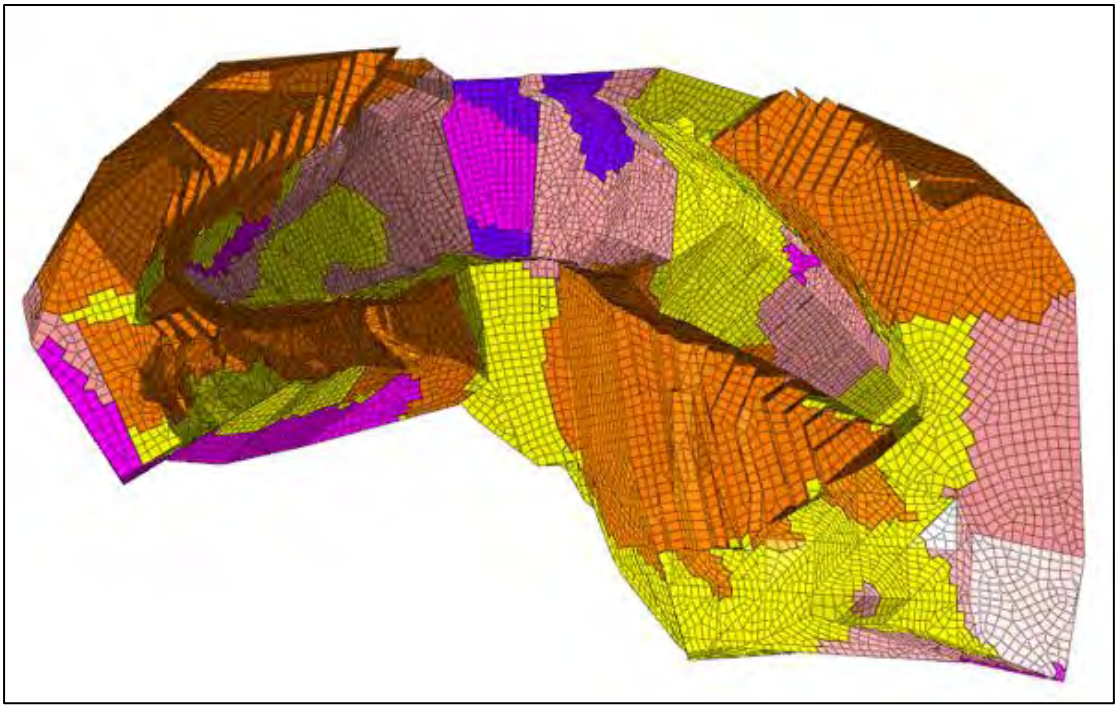

Figure 10-27: Three-dimensional perspective view of FE model mesh showing dam excavation footprint and portions of rock mass improved by consolidation grouting

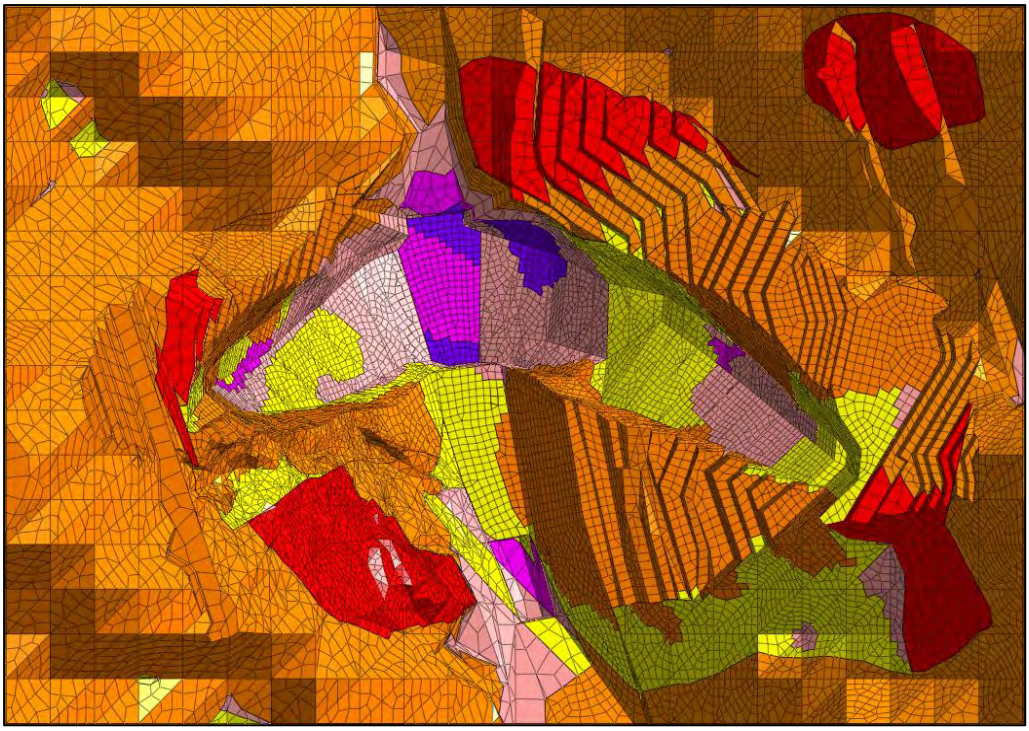

Figure 10-28: Three-dimensional perspective view of FE model mesh showing dam excavation footprint and rock mass foundation

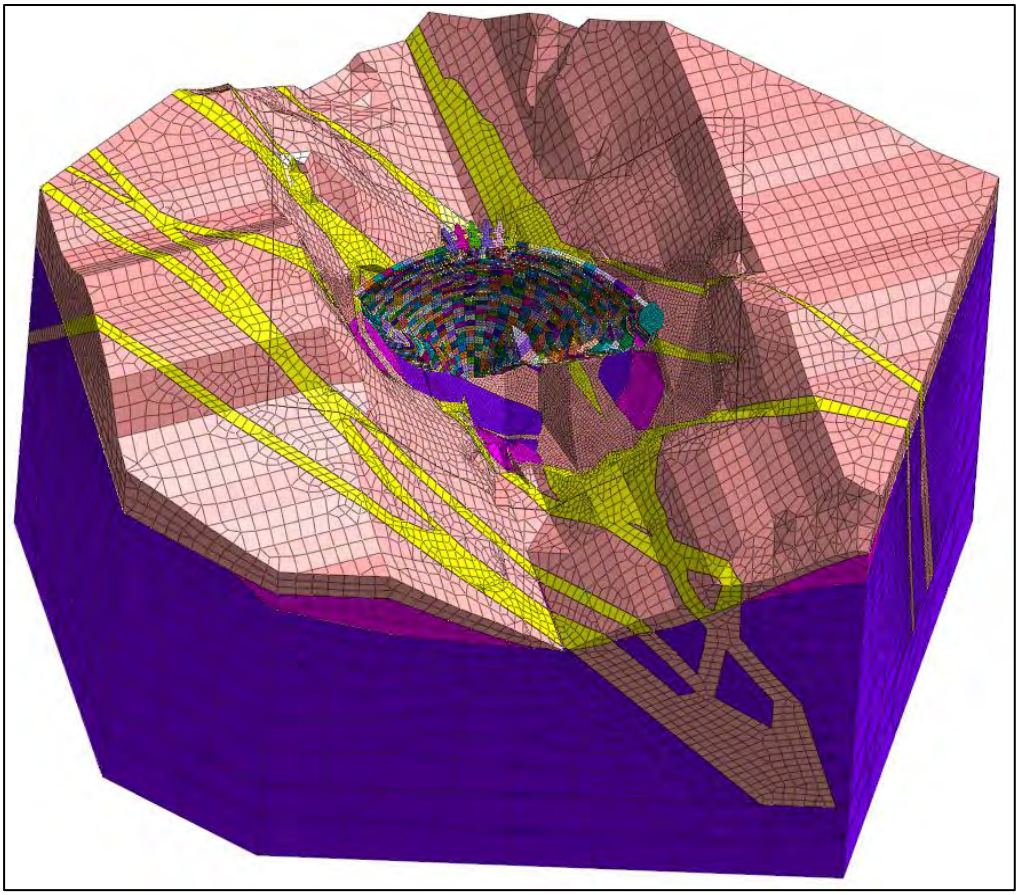

Figure 10-29: Three-dimensional perspective view of FE model mesh showing dam and layers of rock mass foundation

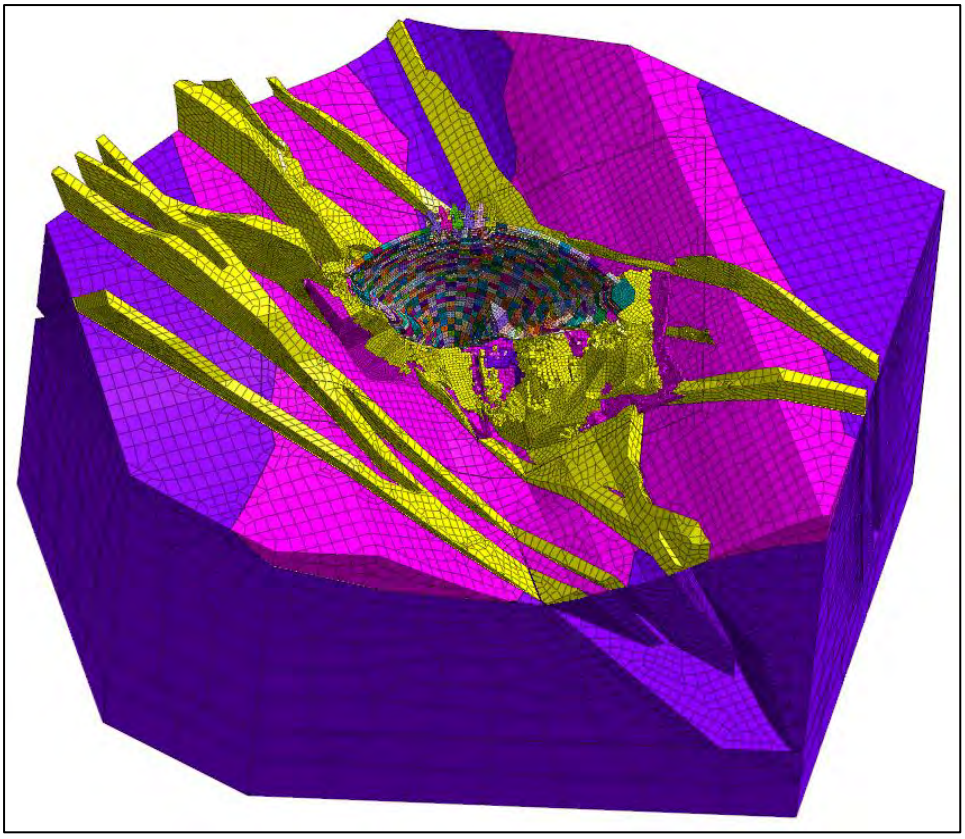

Figure 10-30: Three-dimensional perspective view of FE model mesh showing dam and lower layers of rock mass foundation

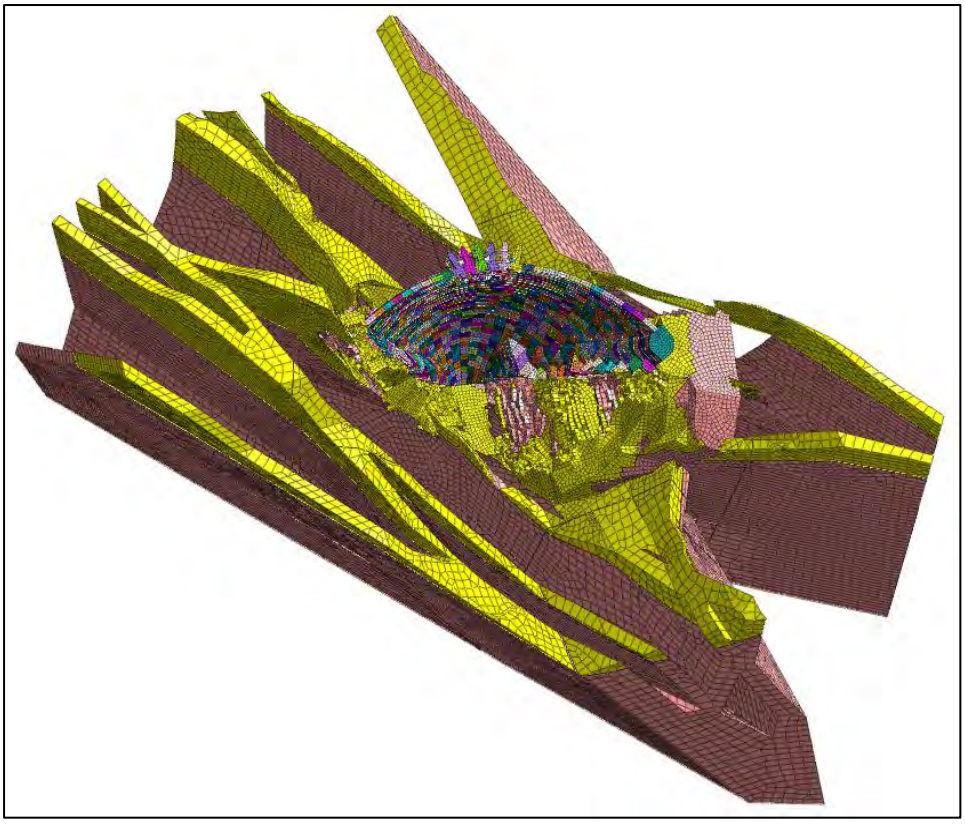

Figure 10-31: Three-dimensional perspective view of FE model mesh showing dam and vertical layers of rock mass foundation